An investigation of a polymetamorphic terrain using ^{40}Ar-^{39}Ar geochronology

Thesis

An Investigation of a Polymetamorphic Terrain Using ^{40}Ar-^{39}Ar Geochronology

A thesis presented for the degree of Doctor of Philosophy

by

Hazel Jane Roberts, BSc.(Hons.)

Department of Earth Sciences
The Open University

September 1999

Acknowledgements:

Professional:

I would like to start by thanking those people who helped me in a professional capacity by providing technical assistance, samples, or simply some good advice.

Firstly, of course, I must thank my supervisors: Simon Kelley and Peter Dahl. I am grateful to Simon for his relaxed, undemanding approach that perfectly suited the way I work. I'm sure on occasions he hadn't a clue what I was up to but trusted that I was doing something productive. I appreciate too, his open door policy that allowed me to drop by with a quick question (or a whole list!) and know that more often than not he would stop what he was doing to answer it. Thanks must go to Peter for so successfully bridging the few-thousand-mile-gap between the Open University and Kent State, Ohio. I imagine that on occasions it must be difficult to feel you are having a significant input into a project from such a distance. Nonetheless, he was an equal member in my supervisory partnership and we managed to maintain good contact and have some interesting discussions via the wonders of e-mail. This was supplemented by two face-to-face meetings where we talked non-stop for several days until my brain boiled over! I feel that Simon and Peter complimented each other well for this project, each focusing on different aspects of the work, relative to their expertise, yet seeing it as a whole. I'm grateful to them for both pulling in the same direction and not trying to lead me off on opposite paths.

Next I would like to thank Jo-Anne Wartho, for endlessly changing light bulbs and remedying other such technical problems in the argon lab – and for pointing out when it was just something stupid I had done! She deserves thanks for all the sample changes, for having the patience to mount awkward samples in foil and for figuring out which "H-number" was which. I think here is a good place to acknowledge her outstanding ability to nag without which the helium experiment would never have happened. Thanks also for allowing me to use her computer now and again.

I would also like to thank Sarah Sherlock for being my field assistant during the two weeks spent in Montana collecting samples, and for other general help throughout the first two years of study. Certainly without her driving skills learnt on and off roads in Turkey, I think we would have ended up in a ditch somewhere in Montana or we might still be stuck in the mud!

Other people I am grateful to for making my fieldtrip possible (and cheap!) are, particularly Susie and Elena Dahl, for their hospitality during a three day stay at their home in Ohio prior to the Montana fieldwork; Pat and Donna Christensen for allowing us to stay free of charge in their ideally situated ranch house in the Ruby Range; and Jim Brophy, Director of the Indiana University Geological Field Station (recently renamed the Judson Mead Geologic Field Station of Indiana University) in the Tobacco Root Mountains for allowing us to stay at the station and for loan of a field vehicle.

People within the Open University that deserve thanks are Kay Green, for making all thin-, probe- and thick-sections, and for advise on how to mount garnets in blocks; Mabs Gilmour, for providing valuable lab training prior to PbSL dating in Copenhagen; Andy Tindle, for training on the electron microprobe and digital photographs; John Watson and Arabelle Saxton for carbon coating of probe sections; Naomi Williams, for assistance with using the SEM; and Geoff Railley for providing me with some else's cast-off computer.

I am also extremely grateful to Robert Frei for supervision of the PbSL garnet dating experiment and valuable related advise. I'm grateful for the time he dedicated to me during my stay in Copenhagen, and for his hospitality. On that note, I'm also eternally grateful to the shop assistant who overcame the language difficulties and sold me the radio that saved my sanity during that trip!

For providing me with samples, I thank Eric Erslev, Colorado University for donating 9 thin-section off-cuts of rocks from the South Madison Range, for loan of thin sections and for other related information. Also, Tibor Dunai, Vrije Universiteit, Amsterdam, and Richard Brooker, University of Bristol, for donating gem-quality garnets for the helium diffusion experiment. And Steve Elphick, University of Edinburgh for conducting isothermally heated runs to dope garnet with helium

Personal:

Top of my list of people who helped me on a personal level is, of course, Steve who was always encouraging and supportive. I'm grateful to him for patiently listening to the endless instalments of the "how my day went" story, for some intelligent discussions and for providing necessary distractions. His pedantic nature (although sometimes irritating) was a valuable asset when proof-reading my first drafts.

Next on my list are my parents whose support, encouragement, tolerance and love has got me this far. I am grateful to them for this and I'm glad that they are proud of me.

Thank you to Mark, Cheryl and Yvonne for being great office mates. I think we made a good combination and we seemed to get the balance right being moments of silence for working and time for a good gossip. I would also like to thank the regulars at lunch for some interesting topics of conversation. Thanks too to Jessica for good chats about gardening.

Finally, I would like to thank Robyn for continuing to be a good friend.

Abstract

This research is an exploration both of the Precambrian metamorphic geology of south-western Montana and the UV laser ablation microprobe ^{40}Ar-^{39}Ar geochronological technique. Using the high spatial resolution of the UV laser microprobe it has been possible to produce systematic ^{40}Ar-^{39}Ar ages within individual mica grains. Further, the UV laser has been used to drill into biotite inclusions within garnet to look at the shielding effect of the garnet lattice, and to drill depth profiles into garnet to measure helium diffusion in laboratory experiments.

The south-western Montana region of the Precambrian Wyoming Province was believed to have undergone at least three separate periods of metamorphism: M1- granulite facies in the Archæan, M2 - amphibolite facies in the Early Proterozoic, and M3 - greenschist to epidote-amphibolite facies in the Mid-Proterozoic. Because of the relatively low blocking temperature of the ^{40}Ar-^{39}Ar geochronological system in mica (c.300-350 °C), it is readily reset by regional metamorphic events and previous K-Ar and ^{40}Ar-^{39}Ar geochronology had found that the Early Proterozoic event dominated the ages obtained.

UV laser ^{40}Ar-^{39}Ar dating of the matrix mica constrained the timing of cooling from the Early Proterozoic metamorphic event to between 1780 to 1740 Ma with a cooling rate between 1 and 8 °C/m.y. ^{40}Ar-^{39}Ar analyses of individual biotite inclusions in garnet also produced similar ages. However, Pb-Pb step leach dating of a small subset of garnet yielded ages between 1808 and 1765 Ma, demonstrating that the garnet did not grow during an Archæan event but, rather, during the Early Proterozoic metamorphic event. Thus, the shielding properties of garnet on biotite inclusions could not be easily assessed in these samples. However, where matrix biotite had been partially reset by the Cretaceous plutons, there was some evidence to suggest that a minority of the biotite inclusions in the same sample had been shielded from resetting. The influence of fractures, defects and other fast diffusion paths is believed to have prevented most of the inclusions from being shielded. No evidence was found to show that the rocks in south-western Montana were

metamorphosed during the Archæan and it seems likely that the M1 and M2 events were not greatly separated in time and were both Early Proterozoic in age.

The high spatial resolution of the UV laser microprobe was used in order to date highly altered biotite within rocks that had undergone later (M3) greenschist metamorphism. Biotite was interlayered with chlorite, clinozoisite and prehnite but using the UV laser it was possible to separately analyse areas of unaltered biotite and areas of alteration within a single mineral and produce ages from both. It was thus possible to measure two ages from one sample: an unaltered age consistent with the timing of the Early Proterozoic metamorphism, and a younger age that could be linked to the c.1500-1360 Ma timing of Belt basin formation to the north and west of the region. This technique therefore was able to overcome the difficulties associated with producing meaningful ages from altered samples whilst constraining the timing of the M3 metamorphic event.

Table of Contents

List of Figures

List of Plates

List of tables

Chapter 1 - Introduction

1.1. Aim

Geochronological techniques provide information about the timing of the last major geological event encountered by the study rocks; that is, an event that reached a temperature in excess of the blocking temperature of the geochronological system in question. In the ^{40}Ar-^{39}Ar geochronological technique that is the time that a potassium bearing mineral last went through its blocking temperature. As an example, for biotite that will be approximately 280 °C (Grove and Harrison, 1996). Above this temperature the mineral is an open system and any previously accumulated argon is lost and with it any information about the previous geological events. As the blocking temperature for argon in biotite is relatively low, the system is readily reset by geological events such as metamorphism, hydrothermal alteration and igneous intrusion. In theory this means that within a complex geological setting, such as the polymetamorphic terrain of south-western Montana, only the timing of the last major event will be recorded by the ^{40}Ar-^{39}Ar system. This research is focused on the further development of laser techniques associated with ^{40}Ar-^{39}Ar dating; the overall aim being to determine how much information can be obtained from a polymetamorphic terrain using this high spatial resolution, single geochronological technique.

1.2. Study Area

The study area comprises four mountain ranges in south-western Montana, USA, within the Precambrian Wyoming Province. These are the Ruby Range, Tobacco Root Mountains, Highland Mountains and South Madison Range. This area has well-documented geology, and geochronological investigation here has been ongoing since the mid 1960s. The Precambrian rocks of south-western Montana are examples of polymetamorphic rocks, believed to have undergone at least three major metamorphic events. These are: an Archæan granulite facies event, an Early Proterozoic amphibolite facies event, and a greenschist facies metamorphic event thought to be Mid-Proterozoic in age. These rocks have been chosen in order to determine whether the ^{40}Ar-^{39}Ar

geochronological technique can be used to obtain information on events both pre-dating and post-dating the main metamorphic event, and to determine the cooling history of the main event.

1.3. ^{40}Ar-^{39}Ar Geochronology

1.3.1. Dating the Last Major Geological Event

Previous geochronological work for the field area was accomplished using Rb-Sr age techniques (Giletti, 1966; Mueller and Cordua, 1976; James and Hedge, 1980), K-Ar (Giletti, 1966; Vitaliano *et al.*, 1979), and, more recently, stepped heating (Brady *et al.*, 1991; 1994; Harlan *et al.*, 1996) and single crystal laser fusion (Kovaric *et al.*, 1996) ^{40}Ar-^{39}Ar techniques. This current research provides the first high spatial resolution laser based ^{40}Ar-^{39}Ar dates for the area. Rb-Sr whole rock dating has yielded an age between 2760 ± 115 and 2600 ± 200 Ma and is believed to record the timing of the first metamorphic event (Giletti, 1966; Mueller and Cordua, 1976; Peterman, 1979; James and Hedge, 1980). Other dating techniques used (i.e. K-Ar, ^{40}Ar-^{39}Ar, U-Pb) have recorded younger events between 1800 and 1600 Ma, and are believed to date the second metamorphic event (Giletti, 1966; O'Neill *et al.*, 1988; Brady *et al.*, 1991; 1994; Kovaric *et al.*, 1996; Harlan *et al.*, 1996). The third metamorphic event has not previously been dated.

Straightforward ^{40}Ar-^{39}Ar dating of matrix mica and amphibole provides information on the last time the minerals were at their blocking temperature. Differences between apparent ages of different mineral species within the same rock or from the same area is due to the different blocking temperatures of the minerals and can be used as a gauge of peak metamorphism reached and cooling rate from the metamorphic peak. Dodson (1986) postulated that slow cooling would produce a characteristic age variation across a single mineral grain. As Precambrian polymetamophic rocks of this type often experience periods of protracted cooling in the middle crust these rocks provided an ideal opportunity to investigate this theory of slow cooling, using the high spatial resolution of the UV laser microprobe technique, and to establish whether these rocks underwent slow cooling, and, if so, at what rate.

Within a polymetamorphic terrain the age of matrix minerals represents the age of one metamorphic event and determining this age is essential for comparison to other ages that attempt to date other events in the geological history these rocks.

1.3.2. Dating Events Pre-dating the Last Major Geological Event

In order to gain information on events that occurred before the last major geological event it is necessary to date minerals that have not been reset. Normally this might involve using a geochronological technique that has a higher blocking temperature than the temperature reached during the event. However, this could also be achieved by dating a mineral that was protected from reheating.

DeWolf *et al.* (1993) found lead isotope ages for monazites within garnets were older than the ages of groundmass minerals, suggesting that the tightly packed garnet lattice was shielding the monazite from later events. An investigation by Kelley *et al.* (1997), using the UV laser microprobe technique to extract argon from biotite inclusions completely enclosed within garnet from a Proterozoic metamorphic assemblage of southern India, found that one in six of the inclusions yielded ages significantly older than groundmass ages. This further supports the notion that garnet has a shielding effect on inclusions within it.

An aim of this research was to build on the work carried out by Kelley *et al.* (1997) and to further investigate the value of the information contained within inclusions in garnet. To do this biotite inclusions within garnet were dated and the age compared to that of matrix biotite from the same rock. In addition, a subset of garnets were dated using the Pb-Pb step-leaching technique (Frei and Kamber, 1995) in order to constrain the age of the inclusions within them.

In order to establish the shielding properties of garnet for biotite inclusions, it is necessary to determine the blocking temperature of argon in garnet. Dunai and Roselieb (1996) have shown that helium diffusion in garnet has a closure temperature of 580-630 °C. Argon has a larger atomic radius than helium so will diffuse at a slower rate through garnet. This project measured the

diffusion rate of helium within garnet in order to add to the data obtained by Dunai and Roselieb (1996) and to interpret the diffusional characteristics of argon in garnet.

1.3.3. Dating Events Younger than the Last Major Geological Event

Events that occurred after the last major geological event can be detected by selection of the appropriate samples for dating. For example, hydrothermal alteration can be dated by identifying those samples that contain minerals indicative of alteration, such as chlorite, sericite and epidote. Since this study area has also experienced the emplacement of a major Cretaceous batholith, sampling of rocks close to this intrusion has been undertaken to investigate isotopic resetting caused by the batholith.

Chapter 2 - Regional Setting and Geology of the Study Area

2.1. The Wyoming Province

The Precambrian geology of the Wyoming Province was outlined by Condie, 1976. Below is a summary of Condie's findings augmented by other publications where cited.

Although a major part of the North American continent is unlain by Precambrian rocks, 90% of this Precambrian terrain is covered by Phanerozoic rocks (Peterman, 1981). The main exposures of Archæan rocks in the North American continent are in the Canadian Shield-Lake Superior Region, and the Wyoming Province. The Wyoming Province comprises Archæan rocks in Wyoming and adjacent states (Figure 2.1). Exposures differ from those of most other shield areas in that they consist of discrete blocks uplifted during the Laramide orogeny (Wooden *et al.* 1988), with the Archæan rocks forming the cores of the young mountain ranges. Unlike the Superior Province, where there is little relief and exposures are almost continuous, the Archæan rocks of the Wyoming Province are characterised by more than 1 km of topographic relief and as much as 10 km of structural relief (Wooden *et al.* 1988). The blocks are separated by basins containing thick sequences of Phanerozoic sedimentary rocks (Peterman, 1979) and this wide separation of exposures prevents widespread correlation of structural or lithological trends (Wooden *et al.* 1988). Due to inadequate exposure in places, the exact outer boundary of the province is unknown (see also 9.2.2).

Between the Canadian Shield and Wyoming Province is the Northern Great Plains. Relict Archæan ages from basement cores and geophysical samples in North Dakota and Manitoba suggest that Archæan basement continues underneath. However, a narrow zone of high electrical conductivity known as the North American Central Plains Conductivity Anomaly (NACP) exists in the basement

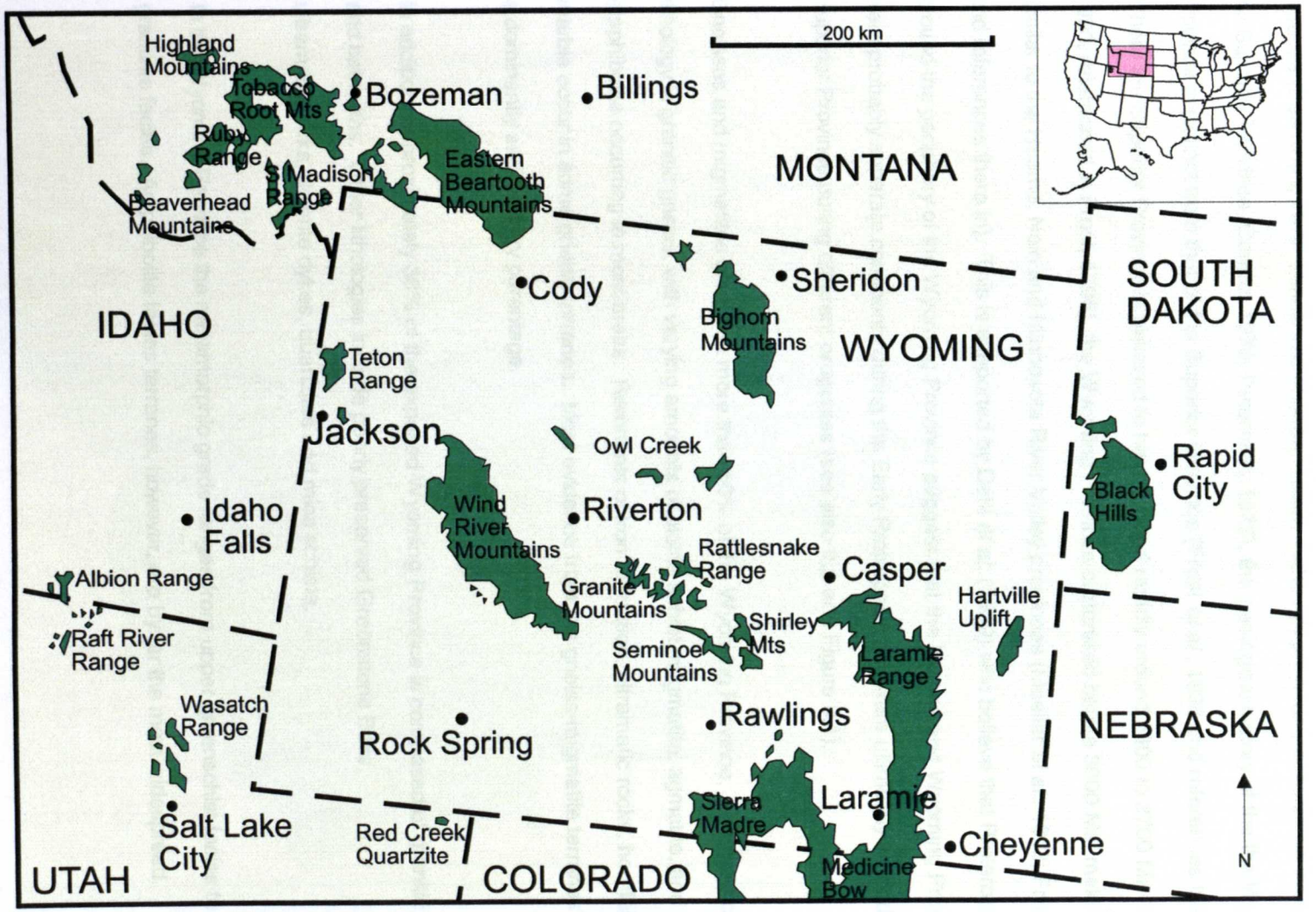

Figure 2.1: Map of the Precambrian Exposures of the Wyoming Province
(After Condie, 1975)

of the Great Plains. Because this anomaly appears to connect two major shear zones (the Cheyenne Belt in the northeast and Rottenstone-La Ronge Belt in Saskatchewan) it is interpreted as a possible Proterozoic plate boundary, implying an earlier separation of the two major Archæan terranes (Peterman, 1979; Dutch and Neilsen, 1990). Although previously considered be an arm of the Superior Province (Condie, 1976; Peterman, 1979), the geological history of the the Wyoming Province is distinct from that of the Superior Province (Frost *et al.*, 1998 and references therein). Where the Superior Province is believed to have formed rapidly around 2800 to 2700 Ma (Card, 1990, referenced in Frost, 1998), the Wyoming Province cratonised before 3000 Ma, making it similar to the Hearne, Nain and Minnosota River Valley provinces (Mueller *et al.*, 1993; Frost, 1998 and references there in). This is supported by Dahl *et al.* (1999) who believe that Proterozoic dates around the periphery of the Wyoming Province suggest that the Hearne and Wyoming Provinces were probably separate continents during the Early Proterozoic and were ultimately welded to the Superior Province during different orogenies (see also 9.2 and Figure 9.1).

Gneisses and migmatites compose more than 60% of the Wyoming Province. The most common lithology is granitic gneiss, with varying amounts of biotite schist, migmatite, agmatite, and amphibolite occurring in most areas. Remnants of iron formation, ultramafic rocks, hornfels, and marble occur in some gneiss terranes. Most evidence from the gneiss-migmatite terranes indicates a dominantly sedimentary parentage.

In addition, approximately 30% of the exposed Wyoming Province is composed of granitic plutons and batholiths. Other lithologies include poorly preserved Greenstone Belts, ultramafic rocks, dolerite dykes, quartzites and mica schists.

In the Wyoming Province the metamorphic grade ranges from upper greenschist facies to lower granulite facies. Amphibolite facies terranes, however, are by far the most widespread.

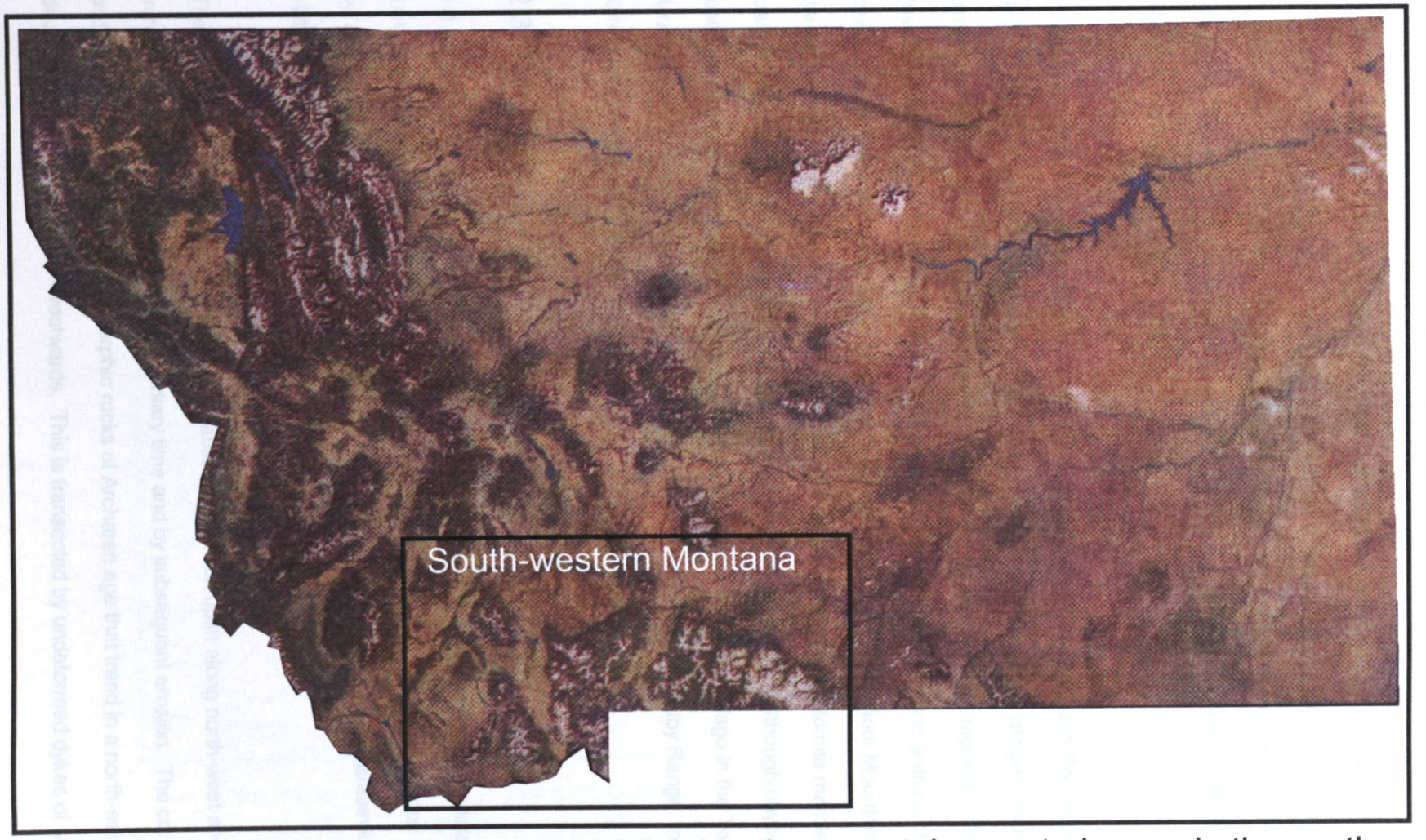

Plate 2.1: Satellite view of Montana highlighting the mountainous study area in the south-west

2.2. Geology of South-western Montana

The mountain ranges in south-western Montana represent the north-western corner of the Wyoming province (Figure 2.1). These Archæan rocks are exposed in a series of foreland block uplifts (Plate 2.1) from which younger strata have been stripped, wholly or in part, to expose a Precambrian core (Figure 2.2). These uplifts are separated by broad valleys and basins underlain largely by continental deposits of Tertiary age (James, 1990).

The areas of interest for this study are principally the Ruby Range, the Tobacco Root Mountains, the Highland Mountains and the South Madison Range. Within these ranges lithologies containing coarse grained micas and garnets were of most use for the experimentation required. For this present study these four mountain ranges will be considered as three separate entities. Previous attempts to correlate the rocks between the Ruby Range and the Tobacco Root Mountains have had little success. Correlation was based mainly on the relationship between dolomite marble and quartzofeldspathic gneiss (James, 1990). However, it was concluded that although physical continuity and general character indicate that the metasedimentary assemblage in the Tobacco Root Mountains are at least partially stratigraphically equivalent to those of the Ruby Range, more specific correlations are not justified (James, 1990).

2.3. The Ruby Range

It is not within the scope of this project to investigate the geology of the study area in detail and thus it will rely upon the work done by others. Detailed studies of the Ruby Range have been carried out by, amongst others, Heinrich, 1960; Garihan, 1979a, 1979b; Dahl, 1979; 1980; Karasevich *et al.*, 1981 and James, 1990. Below is a summary of James, 1990.

The general form of the Ruby Range was established by block uplift along north-west and north-east trending faults that culminated in Late Tertiary time and by subsequent erosion. The core is underlain by crystalline and metamorphic rocks of Archæan age that trend in a north-easterly direction and dip steeply north-westwards. This is transected by undeformed dykes of Middle

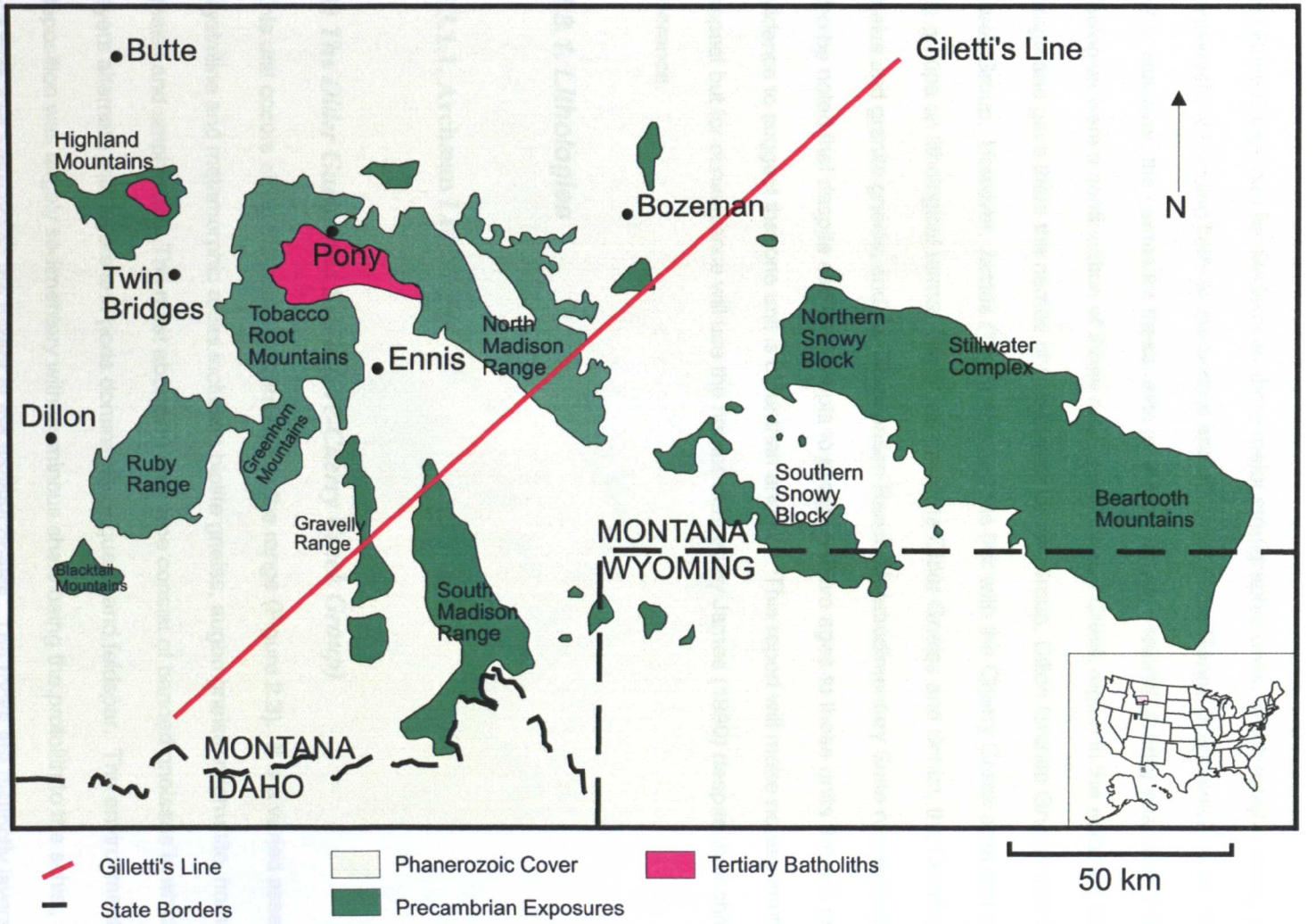

Figure 2.2: Map of the Precambrian Exposures in South-western Montana
(modified from Erslev and Sutter, 1990)

Proterozoic age that follow, and are structurally related to, north-west trending faults (see also sections 9.3.7.3, 9.3.7.4, and Figure 9.4). The Archæan core was exposed by Laramide uplift and subsequent erosion (Dahl, 1979).

The Ruby Range can be divided into three major stratigraphic units, which roughly occupy three north-easterly trending belts in the central and southern Ruby Range (Karasevich *et al.* 1981) (Figure 2.3.). However, the names for these units is under dispute. Heinrich (1960) assumed that these lithologies were a continuation of those seen in the Cherry Creek region in the adjacent Gravelly Range and gave them the names of Pre-Cherry Creek Group, Dillon Granite Gneiss and Cherry Creek Group. However, James (1990) disputed the link with the Cherry Creek area and renamed the groups on lithological terms. He called them the Older Gneiss and Schist, the Quartzofeldspathic gneiss and granite gneiss, and the Christensen Ranch Metasedimentary Suite respectively. It should also be noted that despite earlier attempts to assign relative ages to these units there is no strong evidence to suggest that one unit is older than another. This report will make no assumptions in this respect but for convenience will use the names derived by James (1990) despite their chronological inference.

2.3.1. Lithologies

2.3.1.1. Archæan Lithologies

A) The Older Gneiss and Schist (Pre-Cherry Creek Group)

This unit occurs along the south-eastern side of the range (Figure 2.3). It is a varied assemblage of crystalline and metamorphic rocks including biotite gneiss, augen gneiss, migmatite, hornblende gneiss and amphibolite. The most abundant rock type consist of banded gneisses in which dark layers alternate with layers and pods dominantly of quartz and feldspar. The environment of deposition was largely sedimentary with aluminous shale being the protolith to the schist, and impure quartzite and greywackes the parent of the banded gneiss. The rocks are distinctly layered

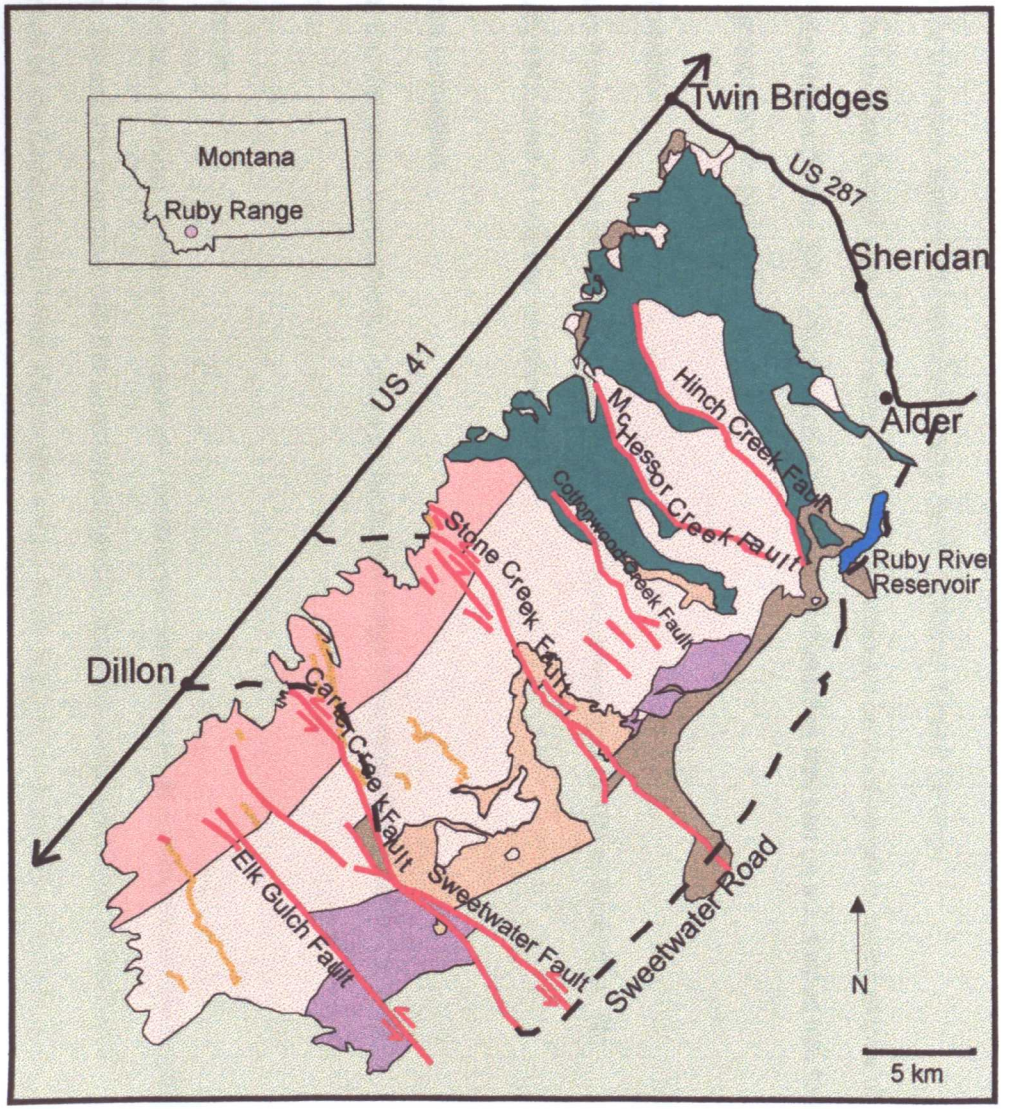

Phanerozoic Rocks

- Tertiary Volcanic Rocks
- Cretaceous and Tertiary Sedimentary Rocks
- Paleozoic Sedimentary Rocks

Precambrian Rocks

- Christensen Ranch Metasedimentary Suite
- Quartzofeldspathic Gneiss and Granitic Gneiss
- Older Gneiss and Schist

- Fault
- Dolerite Dyke
- Paved Road
- Unpaved Road
- Town

Figure 2.3: Map of the Basic Geological Subdivisions of the Ruby Range
(modified from Karaserich *et al.*, 1981)

and have conspicuous tight complex folding with a north-easterly trend. The main fault affecting these rocks is the Carter Creek fault (Figure 2.3) which has considerable left-lateral displacement.

B) Quartzofeldspathic gneiss and granitic gneiss (Dillon Granite Gneiss)

This is the central, north-east-trending belt, flanked on the east by Older Gneiss and Schist and on the west by strata of the Christensen Ranch Metasedimentary Suite (Figure 2.3). It is a tabular body that is structurally concordant with adjoining rock units and is dominated by massive to foliated medium grained grey to reddish brown gneiss of granitic composition. Foliation and compositional layering dip consistently north-westerly at moderate to steep angles and isoclinal folding is present. Peak metamorphism is amphibolite facies. Within this body are separately mapped bodies of amphibolite and narrow belts of infolded (or infaulted) dolomite marble of the Christensen Ranch Metasedimentary Suite. The unit is believed to have a diverse origin. It is partly is derived from sedimentary and volcanic precursors and partly from granitic intrusions.

C) Christensen Ranch Metasedimentary Suite (Cherry Creek Group)

The Christensen Ranch Metasedimentary Suite is well-exposed on north-westerly facing slopes of the Ruby Range (Figure 2.3). It has a complex variety of lithologies that can be subdivided into four main groups on the basis of lithology only.

1) Quartzite

Occurs throughout the suite in layers varying in size from centimetres to 100 m thickness. No primary structures or textures are preserved.

2) Iron formation

Minor but distinctive component. Occurs as beds that range from tens of centimetres to tens of metres.

3) Marble

Constitutes the most prominent component - several thousand metres in outcrop in steeply dipping belts. Where it is in contact with the Quartzofeldspathic Gneiss it is considered to be the basal member of the Christensen Ranch Metasedimentary Suite, infolded or infaulted. However, it is

believed that marble occupies more than one - possibly as many as three - stratigraphic positions in the initial sedimentary sequence.

4) Undifferentiated metasedimentary rocks

Form interbeds within more prominent or distinct lithological units. Three main types occur as follows:

a) Quartz-mica schist and quartzose gneiss, including sillimanitic, garnetiferous, and corundum-bearing varieties, derived from initial sediments of shale or sandy shale composition. They comprise a substantial percentage of bedrock in the area but in general are poorly exposed. All are well foliated rocks, typically made up mainly of quartz, biotite, plagioclase, and K-feldspar in varying proportions. Sillimanite and garnet are also common constituents.

b) Calc-silicate gneiss and schist, derived from shaly carbonate sediments.

c) Anthophyllite schist of uncertain origin.

All units have a north-easterly trend. There are complex interference patterns resulting from isoclinal folding and cross folding, and a general lack of cross or graded bedding. Because of this, and structural thinning and thickening due to flexural flow, no stratigraphic subdivisions can be allocated.

D) Minor Lithologies

1) Ultramafic rocks

Intrusive bodies of ultramafics are found throughout the area as pods or lenses tens of metres to kilometres in size. Initial rocks range in composition from harzburgite to pyroxenite but these are extensively modified by serpentinization and post-emplacement metamorphism. It is likely that most of the ultramafic bodies in the strata of the Christensen Ranch Metasedimentary Suite were emplaced tectonically by plastic flow rather than by intrusion of magma.

2) Amphibolite

Bodies of amphibolite ranging in size from a few metres to kilometres can be found throughout the area. The majority are derived from mafic igneous rocks and were emplaced as dolerite or gabbro sills. At least two, and probably several, episodes of mafic intrusion are represented.

3) Granite gneiss

Granite gneiss exists as sills or concordant lenses in strata of the Christensen Ranch Metasedimentary Suite, or as larger masses in or engulfing quartzite bearing strata of the range-front-terrain in the south-western part of the area.

2.3.1.2. Proterozoic Lithologies

A) Pegmatites

Pegmatites are abundant in the Ruby Range, and two varieties can be distinguished. 1) Older pegmatite - these are the most abundant and occur as thick concordant sheets and straight-walled dykes exhibiting yellowish weathering and simple composition; and 2) younger pegmatite - occurs as smaller pod-like bodies that commonly are crudely zoned to quartz-rich cores. General cataclasis and local development of foliation suggests that the older pegmatites were intruded at the end of the Late Archæan orogeny that has been dated as c.2750 Ma by James and Hedge (1980) (see Appendix 2.1 and 2.7.4.3 below). The younger pegmatites post-date this event and are cut by dolerite dykes that have a Rb-Sr whole rock age of about 1424 Ma (Wooden *et al.*, 1978) (see Appendix 2.1 and 2.7.4.2 below). Muscovite from a zoned pegmatite was dated by Giletti (1966) using K-Ar and Rb-Sr techniques to give ages of 1643 and 1640 Ma respectively (corrected for decay constant after Steiger and Jäger, 1977).

B) Middle Proterozoic Dolerite Dykes

Dolerite dykes transect the generally north-easterly trends of crystalline rocks in the area and clearly are related structurally to the north-easterly trending fault system (Figure 2.3; see also Figure 9.4). Outcrop thickness varies from as much as 150 m to the more usual 30 m, and are traceable for no more than a kilometre or so. The rock has little resistance to erosion and outcrops are rare. Instead they are recognisable by marked topographic sags and by the presence of spheroidally weathered

boulders. These are part of a swarm of generally north-westerly trending dykes that cut older Precambrian rocks of the Ruby Range and of the adjacent Tobacco Root Mountains. Wooden *et al.* (1978) class the dolerite in the Ruby Range as "low potassium tholeiite".

2.3.1.3. Phanerozoic Lithologies

A) Cambrian to Carboniferous

On the northern tip of the Ruby Range about 450 m of Palaeozoic marine sedimentary rocks nonconformably overlie the Precambrian (Figure 2.3). They range in age from Middle Cambrian to Young Carboniferous (Pennsylvanian) (Garihan, 1979b).

B) Cretaceous

The Beaverhead formation is the only preserved Mesozoic strata in the Ruby Range. The occurrences are generally small and scattered throughout the range. However, a large area of exposure of "Red Conglomerate" (Dorr and Wheeler, 1964 referenced in Garihan, 1979b) is located in the central-east region. It consists principally of carbonate- and quartzite-clast conglomerate. The formation overlies the Quartzofeldspathic Gneiss and in turn is overlain by Tertiary sedimentary rocks.

C) Tertiary

North-westerly trending wedges of faulted and tilted Tertiary rocks unconformably rest on the basement units (Garihan, 1979). The rocks underlie the higher elevations of the northern one-third of the range. They consist of weakly lithified siltstone, sandstone, and conglomerate. The main Tertiary-Precambrian contact is generally obscured by a covering of Quaternary gravel.

In addition, basalt is found as remnants of valley flows in isolated patches in the western and north-western parts of the map area and in more extensive outcrop along the eastern margin. Equivalent flows in the south-east yield Pliocene whole-rock K-Ar ages of 4.2 ± 0.2 Ma (Marvin *et al.*, 1974; referenced in James, 1990).

D) Quaternary

1) Basin fill

Confined to the eastern part of the range where they underlie a wide area of low relief in the upper reaches of the Sweetwater Creek drainage system.

2) Stream alluvium

Sand and gravel, found in narrow strips along a number of streams in the area.

3) Colluvial debris

Mantles pediment surfaces on lower slopes.

2.3.2. Structures

Within the range the fabric is defined mainly by a general north-east trend of layering, foliation, and fold axes, modified by northern trending cross folds and by Middle Proterozoic movement on faults of the north-east trending system.

2.3.2.1. Faults

The north-westerly trending fault system is of regional importance throughout Idaho and south-western Montana. The main Precambrian faults (e.g. Stone Creek, Carter Creek, and Elk Gulch Creek faults) have considerable left lateral displacement of thousands of metres (Figure 2.3). Movement was later renewed, possibly in late Mesozoic (Laramide) time but certainly in late Tertiary.

2.3.2.2. Folds

There is some evidence of possible early low-angle structural displacement in the south-west Ruby Range that included at least local recumbent folding. Within the Ruby Range itself the physical evidence to support this fold generation is scarce but it is recorded by orientations present in Pre-Cherry Creek rocks in the South Madison Range. The oldest easily recognisable structures within the Ruby Range are isoclinal or similar folds that trend and plunge north-east and have axial planes that dip north-westerly, and could be the product of more than one deformation. The next generation of folds are contemporaneous with, or slightly younger than, the isoclinal folds and are on a

mesoscopic scale. These folds are only recogniseable in a few locations where they overprint or refold the isoclinal folds. They are upright, tight to open cross folds that trend and plunge to the north. Also overprinting the isoclinal folds are tight to gentle concentric folds that can be recognised by deformation of both compositional layering and axial plane schistosity of the isoclinal folds. The final fold generation is seen as open to gentle concentric folds in the northern Ruby Range and geometric in the southern Ruby Range.

2.3.3. Metamorphism

All of the Precambrian strata of the area, except pegmatites and dolerite dykes have been metamorphosed to upper amphibolite facies.

2.3.3.1. Prograde Metamorphism

Prograde metamorphism is amphibolite facies. It was characterised by James (1990) to be within the sillimanite-K-feldspar zone based on the association of sillimanite-perthitic microcline in quartz-feldspar gneiss and schist, and by the general absence of prograde muscovite. Kyanite is also generally absent but has been preserved as a relict phase in some metapelite. Using ultramafic assemblages Desmarais (1981) gave an estimate of 710 °C; 5-7 Kb for the metamorphic peak. Dahl (1979, 1980) used garnet-pyroxene, garnet-biotite, garnet-hornblende and alkali feldspar to plagioclase to give an estimate of 645 ± 45 °C; 6.2 ± 1.2 Kb for the Carter Creek area in the south-western Ruby Range. These temperature estimates are lower than for the northern part of the range where rocks reached granulite facies (Karasevich *et al.*, 1981). For the Kelly area in the north-eastern Ruby Range Dahl (1979, 1980) produced an estimate of 745 ± 50 °C; 6-8 Kb for peak metamorphism.

2.3.3.2. Retrograde Metamorphism

All prograde assemblages have been modified by retrograde metamorphism. James (1990) characterised the retrograde metamorphism by the following mineralogical conventions:

Forsterite → serpentine

Pyroxenes → amphibole and epidote

Amphibole → epidote and chlorite

Biotite → chlorite and muscovite

Feldspar → clinozoisite and sericite

Dahl (1979) produced estimates for the temperature of metamorphism of 545 °C using iron-magnesium fraction between garnet and cordierite, and 475 °C using oxygen isotope fractionation between magnetite and quartz in the iron formation. Some of the apparent retrograde phenomena, such as exsolution of amphibole and cordierite coronas on garnet, can be attributed to continued chemical and mineralogical reaction during the slow decline of temperature from peak conditions. Other effects, such as widespread epidotisation and hornblendisation of diopside gneiss, however, represent a separate, later cycle of metamorphism superimposed on the earlier prograde assemblage.

2.3.3.3. Other Metamorphic Effects

All Middle Proterozoic dolerite dykes have been incompletely but extensively altered to a greenschist assemblage. These post-date the Proterozoic thermal rise and retrograde metamorphism so therefore represent a later metamorphic cycle of at least moderate intensity. This is assumed to be of Late to Late Middle Proterozoic age.

2.4. The Tobacco Root Mountains

What follows is a summary of the work carried out by Vitaliano *et al.* (1979). As with the Ruby Range there have been difficulties producing a relative stratigraphy within the Archæan lithologies. Instead, the rocks are dealt with in order of abundance.

In this range the Archæan lithologies occur as a series of metasedimentary and meta-igneous rocks mainly of upper amphibolite grade with scattered patches of granulite grade (Figure 2.4). A twofold lithological association has been established as follows:

1) Quartzofeldspathic gneiss and amphibolite.

2) A sequence of marbles, sillimanite schists, iron formations and quartzites that for convenience will be referred to as supracrustal rocks.

2.4.1. Lithologies

2.4.1.1. Archæan Lithologies

A) Quartzofeldspathic Gneiss and amphibolite

1) Quartzofeldspathic Gneiss

Within the quartzofeldspathic gneiss unit there are four subdivisions. These are 1) granoblastic to blastomylonitic granitic paragneiss rich in K-feldspar; 2) tonalitic paragneiss rich in plagioclase; 3) quartz-feldspar biotite gneiss; and 4) plagioclase-quartz-hornblende-biotite gneiss. These are interlayered with thin layers of amphibolite, quartzite, and sillimanite schist. Universally conformable contacts with the enclosing units suggest a predominantly sedimentary nature for its protoliths.

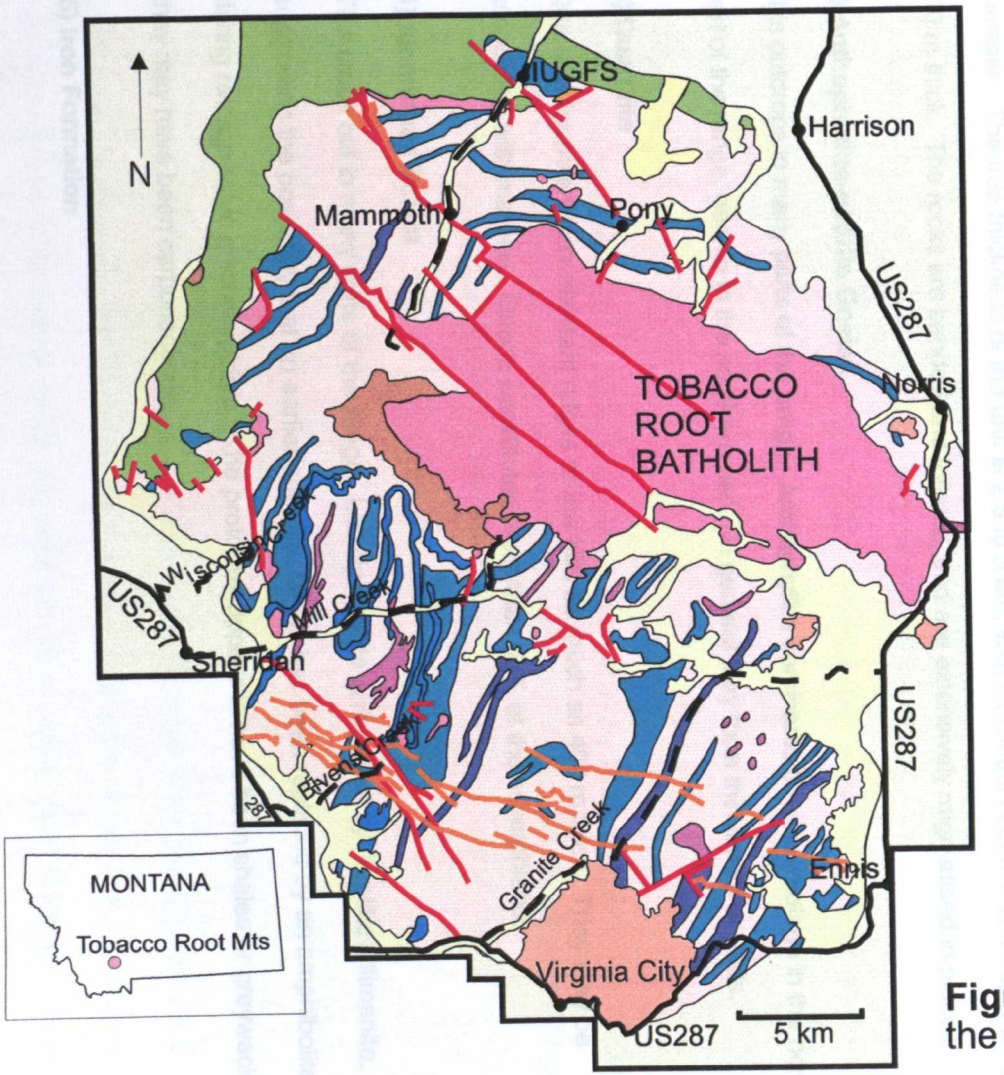

Fault
Lithological Boundary
Town
287 Paved Road
Unpaved Road
IUGFS Indiana University Geological Field Station

Tertiary and Quaternary
Alluvium
Volcanic Rocks

Paleozoic To Mesozoic
Silicic Plutonic Rocks
Phanerozoic Sedimentary Rocks

Precambrian
Dolerite Dykes
Metabasic Intrusive Rocks
Garnet Gneiss
Marble and Associated Calc-silicate Rocks
Iron Formation
Anthrophyllite-gedrite Gneiss Assemblage
Hornblende Gneiss, Granulite, and Pelitic and Quartoze Metasediments
Quartzofeldspathic Gneiss

Figure 2.4: Map of the Geology of the Tobacco Root Mountains

2) Amphibolite

The amphibolite crop out as sills, dykes and phacoliths throughout the range. In the sills, pinch- and-swell and boundinage structures are common. The dykes frequently form connecting links between sills, but occasional tabular bodies as much as 50 m thick transect the foliation for considerable distances. The phacoliths occur in the crests of sub-isoclinal folds. Many of the dykes and sills have been deformed, and some are cut by pegmatites. The presence of sharp contacts and chilled margins suggest that both sills and dykes were emplaced during or shortly after an earlier metamorphic event.

B) Supracrustal Rocks

1) Hornblende Gneiss

These hornblende-rich assemblages range from para-amphibolites to hornblende plagioclase gneisses. The true thickness of the unit is 2.5 to 3 km, with individual occurrences being as much as 900 m thick. The rocks are banded and foliated, and are extensively migmatised in places.

2) Anthophyllite-gedrite Gneiss

This outcrops in many parts of the range. Anthophyllite dominates the assemblage in the northern part of the range, gedrite in the southern part. In general they form thin layers or pods.

3) Quartzite

Quartzite forms erosion-resistant ridges or low hills as much as 400 m thick. They may be associated with marbles. Quartz constitutes more than 60% of the assemblage.

4) Aluminous Schist

This crops out in many parts of the range. Locally kyanite is replaced by fibrolitic sillimanite, suggesting the possibility that an earlier granulite facies has been replaced by an amphibolite facies during retrogressive metamorphism. The protoliths appear to have been shales or greywackes, and they may have been carbonaceous.

5) Iron Formation

Iron formation outcrops in relatively thin layers in the Copper Mountain and Carmichael Creek areas. Lesser deposits are scattered throughout the range. They consist of magnetite-bearing schists and gneisses, grunerite-magnetite schist, and garnet-quartz rocks.

6) Marble

Marble is found in prominent buff-coloured to dark brown ridges. Calcite and dolomite are the dominant minerals. In the vicinity of the Tobacco Root Batholith, the marble has been thermally metamorphosed.

2.4.1.2. Proterozoic Lithologies

A) Pegmatites

Lenses and streaks of pegmatite are found in outcrops in many parts of the range. Those considered to be the oldest are concordant with the foliation and have a similar mineralogy to the host rock. If these are equivalent to the older pegmatites in the Ruby Range than they are assumed to be Archæan in age. The other pegmatites are discordant to the foliation and occupy joints or faults. These are coarser grained. Again, if they are equivalent to younger pegmatites in the Ruby Range then they have a Proterozoic age.

B) Dolerite Dykes

These dykes are considered to be related to the dykes within the Ruby Range. In the Tobacco Root Mountains they are emplaced along a set of north-west trending faults in the southern and north-western parts of the range (Figure 2.4; see also Figure 9.4).

2.4.1.3. Phanerozoic Rocks

A) Cretaceous

The late Mesozoic Tobacco Root Batholith is the most important of the Mesozoic intrusives (Figure 2.4). It covers an area of 310 km^2 in the north-eastern part of the range. It is a zoned composite pluton ranging from hornblende diorite to granite with intermediate facies of tonalite, granodiorite, and

monzonite. It is believed to have been emplaced as a single injection and differentiated *in situ* during cooling.

B) Tertiary

Tertiary volcanic rocks flank the crystalline core on the east-central and south-eastern parts of the map area. Lavas and pyroclastic rocks form a prominent plateau in the Virginia City region, and a small area (both extrusive and intrusive) crop out west of McAllister (Figure 2.4).

2.4.2. Structures

2.4.2.1. Faults

Two major fault sets are present. One has a north-west trend and the other has a north-east trend to it. Both were emplaced within the Precambrian but movement continued into the early Tertiary.

2.4.2.2. Folds

The area is dominated by a major north-south trending, broad, open fold known as the Mill Gulch antiform. The antiform is flanked on the west and east by a series of sub-isoclinal folds of nearly parallel trend. Refolding is also common in the area.

2.4.3. Metamorphism

The metamorphic events within the Tobacco Root Mountains parallels those experienced by the Ruby Range. The oldest was a prograde metamorphism which may have reached granulite grade, but certainly reached amphibolite facies. Following this came a period of retrograde metamorphism which equilibrated mainly to almandine-amphibolite facies with some local granulite facies. The third event is less well constrained. It is possible that it began in very late Precambrian time but it is clearly represented in the thermal events accompanying the emplacement of the Tobacco Root Batholith in late Mesozoic time. Hornfels facies metamorphism was locally attained in the contact

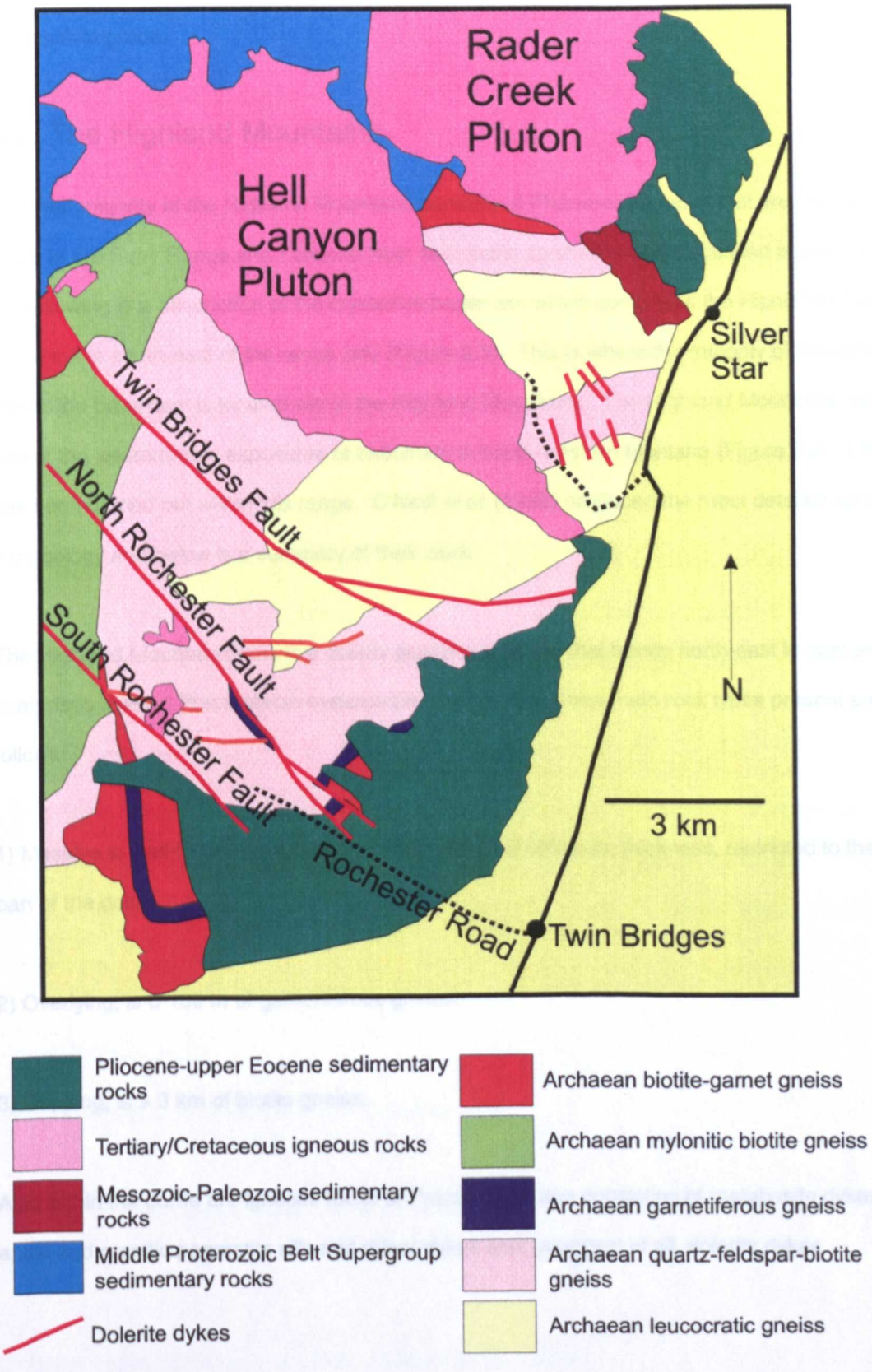

Figure 2.5: Map of the Geology of the Highland Mountain Dome (modified from O'Neill *et al.* 1988)

zone. Elsewhere, especially in zones of shearing, metamorphic conditions equilibrated to greenschist grade.

2.5. The Highland Mountains

The vast majority of the Highland Mountains consists of Phanerozoic rocks that are the same as those in the Ruby Range and Tobacco Root Mountains so shall not be discussed again. Therefore, the following is a description of the crystalline basement which comprises the Highland Mountain dome in the south-east of the range only (Figure 2.5). This is where the majority of the exposure of crystalline basement is located within the Highland Mountains. The Highland Mountains represents one of the westernmost exposures of basement in south-western Montana (Figure 2.2). Little work has been carried out within this range. O'Neill *et al.* (1988) produced the most detailed account of the geology and below is a summary of their work.

The Highland Mountain dome is a doubly plunging antiform that trends north-east to east and comprises layered Precambrian metamorphic rocks. The three main rock types present are as follows:

1) Massive to well-foliated quartzofeldspathic gneiss of unknown thickness, restricted to the central part of the dome.

2) Overlying, is 0-100 m of garnetiferous gneiss.

3) Capping, is > 3 km of biotite gneiss.

Also within the dome are igneous rocks of Precambrian age consisting of metabasite dykes and sills, aplite and granitic pegmatite sills and minor dykes and, youngest of all, dolerite dykes.

2.5.1. Lithologies

2.5.1.1. Archæan lithologies

A) Quartzofeldspathic Gneiss

In this region the quartzofeldspathic gneiss can be divided up into two major types as follows:

1) Massive leucocratic gneiss exposed in the core of the dome. The dominant rock type consists of massive, strongly deformed and lineated quartz-feldspar gneiss that contains only sparse biotite or muscovite.

2) Overlying is well-foliated quartz-feldspar-biotite gneiss. This is in gradational contact with the underlying leucocratic gneiss. The gneiss is fine to medium grained and displays a distinct, platy foliation defined by a regular alteration of leucocratic and biotite-bearing layers.

B) Garnetiferous Gneiss

This is an extremely diverse, garnet-rich unit that separates the quartzofeldspathic gneiss from the biotite-gneiss. It includes quartzofeldspathic and biotite gneiss similar to the contact rocks, but also includes amphibolite, quartz-plagioclase-garnet gneiss, anthophyllite-garnet gneiss, magnetite gneiss and marble.

C) Biotite Gneiss

The biotite gneiss is divided into two mappable units.

1) Lower mylonitic biotite gneiss - exhibits strong shearing leading to an extremely planar, nonfolded fabric.

2) Upper biotite garnet gneiss - more massive and contorted.

The biotite gneiss is medium to coarse grained and composed essentially of biotite, quartz and plagioclase, and contains conspicuous porphyroblasts of plagioclase and garnet. The contact between the two subdivisions is gradational for several hundred metres.

D) Amphibolite

Amphibolite is present in all major rock units. It is well-layered and occurs as concordant lenses 0.5-3 m in thickness and generally < 100 m in length.

2.5.1.2. Proterozoic Lithologies

A) Aplite and pegmatite

As in the Ruby Range and the Tobacco Root Mountains there are two series of pegmatites present in the Highland Mountains. They occur as sills and minor dykes in well-foliated gneisses that cap the core of the Highland Mountain dome. They are absent from the more massive leucocratic core rocks. One set of pegmatites has a massive character and occurs in non-layered sills, interconnected by dykes. These are the structurally highest group. The second set are non-layered quartz monzonite to well-foliated, leucocratic augen gneisses and finely laminated leucocratic sills.

B) Metabasite

This unit occurs solely as dykes in the leucocratic core rocks. It is weakly foliated, dark brown to black and ranges in thickness from < 1m to 10-15 m.

C) Dolerite Dykes

As in the Ruby Range and Tobacco Root Mountains, dolerite dykes are present in the Highland Mountains. These are subvertical, 3-100 m thick and have a north-westerly trend. Their emplacement is controlled by major north-west trending faults.

2.5.2. Structure

The major structures of the crystalline rocks of the Highland Mountains are, from south-east to north-west:

1) a dome cored with quartzofeldspathic gneiss.

2) an overlying, strongly sheared and mylonitic interval of biotite gneiss, more than 3 km thick that contains conspicuous sills of aplite to pegmatite and leucocratic mylonitic orthogneisses in its lower part.

3) a structurally higher synform composed of coarsely crystalline, strongly folded biotite-garnet gneiss.

Minor structures in these rocks, from small-scale folds to fabric elements, indicate that all rocks were affected by the doming event.

The Highland Mountain dome apparently formed by:

1) differential vertical rise of a mobile leucocratic core.

2) penetrative metamorphism of the mantling rocks and injection into these rocks of quartz monzonite sills and orthogneisses.

3) Extension and down-dip shearing of the overlying mylonitic gneiss off the hinge zone.

The dome is truncated on the east by Tertiary-Quaternary basin-bounding faults and covered on the east and south by Tertiary and Quaternary sedimentary deposits. On the north-east the nose of the dome is cut by the north-west trending, Laramide age, Silverstar fault that marks the partly exposed edge of the Cretaceous Highland uplift. To the north, metasedimentary rocks of the Middle

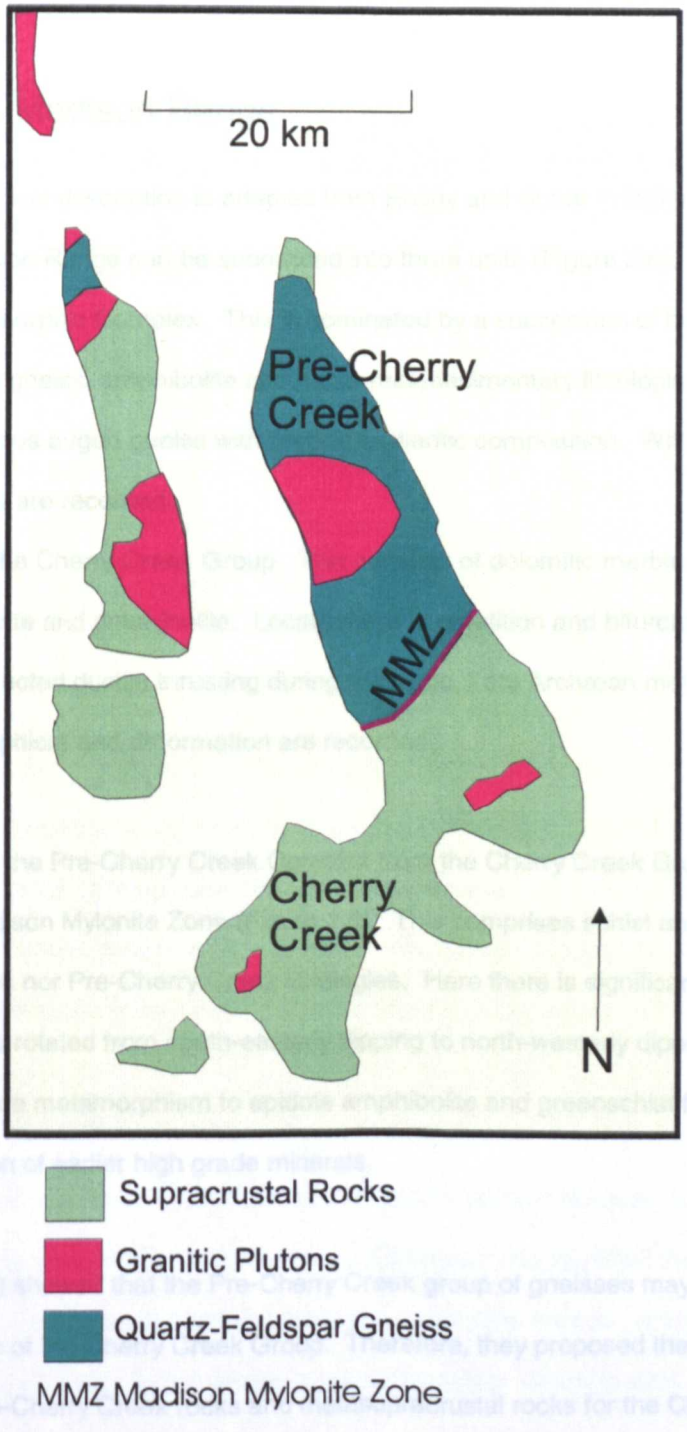

Figure 2.6: Map of the Basic Geological Subdivisions of the South Madison Range
(modified from Sumner and Erslev, 1988)

Proterozoic Belt Supergroup overlie basement rocks along the north-dipping Camp Creek fault of small displacement that cuts obliquely across the dome.

2.6. Southern Madison Range

The following geological description is adapted from Erslev and Sutter (1990) (see also chapter 8). The Southern Madison Range can be subdivided into three units (Figure 2.6). The first is the Pre-Cherry Creek Metamorphic Complex. This is dominated by a succession of heterogeneous migmatites, tonalitic gneiss, amphibolite and minor metasedimentary lithologies wrapped around a dome of homogeneous augen gneiss with granitic to diaritic composition. Within these rocks three metamorphic events are recorded.

The second unit is the Cherry Creek Group. This consists of dolomitic marble, biotite-staurolite-garnet schist, quartzite and amphibolite. Locally there is repetition and bifurcation of units as a result of north-westerly directed ductile thrusting during prograde, Late Archæan metamorphism. Two periods of metamorphism and deformation are recorded.

Spatially separating the Pre-Cherry Creek Complex from the Cherry Creek Group is a ductile shear zone called the Madison Mylonite Zone (Figure 2.6). This comprises schist and quartzite resembling neither Cherry Creek nor Pre-Cherry Creek lithologies. Here there is significant crustal discontinuity and the foliation has rotated from south-easterly dipping to north-westerly dipping. Mafic rocks have undergone retrograde metamorphism to epidote amphibolite and greenschist facies. However, there is some preservation of earlier high grade minerals.

Mueller *et al.* (1993) showed that the Pre-Cherry Creek group of gneisses may not have totally predated deposition of the Cherry Creek Group. Therefore, they proposed the terms central gneiss complex for the Pre-Cherry Creek rocks and metasupracrustal rocks for the Cherry Creek rocks. However, for simplicity the terms Pre-Cherry Creek and Cherry Creek will be used in this research.

2.7. Previous Geochronology of South-western Montana

2.7.1. Introduction

Appendix 2.1 provides a brief summary of previous geochronological work carried out within the Wyoming Province in general, with a more detailed listing of the geochronology undertaken within the south-western Montana portion of the province. Most of the isotopic studies that have been carried out in the Wyoming Province have used Rb-Sr whole-rock and U-Pb zircon techniques (Rosholt *et al.*, 1973; Wooden *et al.*, 1978; Peterman, 1979; James and Hedge, 1980; Peterman, 1981; Stuckless *et al.*, 1985; Wooden and Mueller, 1988; Wooden *et al.* 1988; Aleinikoff *et al.*, 1989; Mueller *et al.*, 1992, 1993). K-Ar and ^{40}Ar-^{39}Ar dates are less common. Most Rb-Sr whole rock isochron and zircon concordia dates fall in the range of 2700 - 2500 Ma for the timing of metamorphism (Condie, 1976).

The most widespread orogenic event in the Wyoming Province is the deformation, granitic plutonism, and regional metamorphism recorded by both whole rock Rb-Sr ages and U-Pb zircon ages at 2700 - 2600 Ma (Condie, 1976). This is coincidental with the Kenoran Orogeny in the Superior Province. It is recorded in all mountain ranges including the peripheral ones. Major granites were emplaced and there was a period of mafic dyke intrusion in the Beartooth Mountains (Condie, 1976).

2.7.2. The Giletti Line

Giletti (1966) first established ages for the rocks in south-western Montana using Rb-Sr and K-Ar techniques on whole rock, biotite, muscovite and K-feldspar. He identified that one or more episodes of regional metamorphism and/or igneous intrusion occurred in most of central and western Wyoming at 2600 ± 200 Ma. In the west of the south-western Montana area, in contrast, he could find no mineral age greater than 1800 Ma. Using these data he divided the region along the Giletti Line (Figure 2.7). This is a north-east/south-west trending line that crosses the Gravelly Range and the Gallatin River and Gallatin River Canyon. The rocks to the south-east of the line he

PAGE
NUMBERS
CUT OFF
IN THE
ORIGINAL

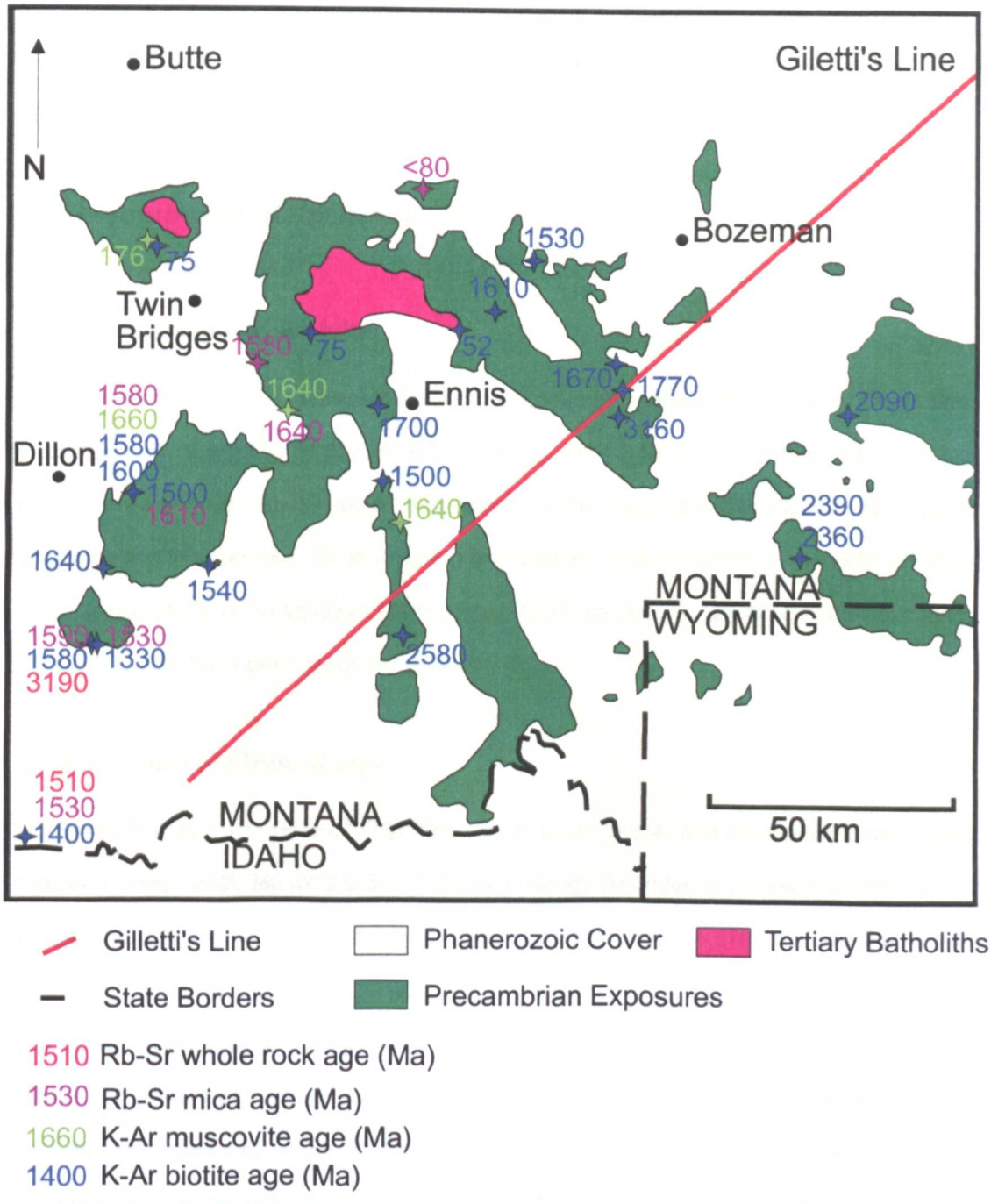

Figure 2.7: Map of south-western Montana showing the Rb-Sr and K-Ar ages obtained by Giletti (1966) relative to the sample locations (nb: all ages are corrected for decay constants after Steiger and Jager, 1977)

found to be 2600 Ma or older, whereas those to the north-west were no older than 1800 Ma. He tentatively suggested that some rocks on the north-west may be older and were re-metamorphosed at 1600 Ma.

2.7.3. South-east of the Giletti Line

2.7.3.1. Beartooth Mountains

The ages reported for the Beartooth Mountains (Eastern Beartooth, North Snowy Block, Stillwater Complex) vary depending on the technique used (U-Pb, Rb-Sr and Sm-Nd), as well as the location and rock unit (Figure 2.8). However, the majority of the dates are within a 2800 - 2700 Ma range (DePaolo and Wasserburg, 1979; Wooden and Mueller, 1988; Wooden *et al.*, 1988; Mueller *et al.*, 1992) (Appendix 2.1). In addition, U-Pb zircon, Rb-Sr whole rock, Sm-Nd chrondritic, and Pb ages of 3500 - 3000 Ma have been recorded (Figure 2.8).

2.7.3.2. South Madison Range

Rb-Sr whole rock, U-Pb zircon, $^{207}Pb/^{206}Pb$ zircon, Lu-Hf zircon, and Sm-Nd techniques give ages of between 3540 - 2500 Ma for the South Madison Range (Wooden *et al.*, 1988; Mueller *et al.*, 1993) (Appendix 2.1). However, the majority of these ages are within the 2700 - 2600 Ma field.

Erslev and Sutter (1990), undertook an ^{40}Ar-^{39}Ar study of the South Madison range. An age of 2500 - 2400 Ma for the Pre-Cherry Group was believed to represent cooling after a metamorphic maximum at 2750 Ma (Figure 2.8). Ages of 2520 (muscovite) and 2530 (biotite) Ma for the Cherry Creek Group were recorded but there was possible resetting by a granodiorite intrusion (Figure 2.8). The Madison Mylonite Zone proved problematic with very discordant hornblende ages, and biotite entrapping extraneous argon during mylonitization. A combined hornblende and muscovite age of 1900 - 1800 Ma is believed to date the last major ductile strain event within the Madison Mylonite Zone (Figure 2.8). See also Chapter 8.

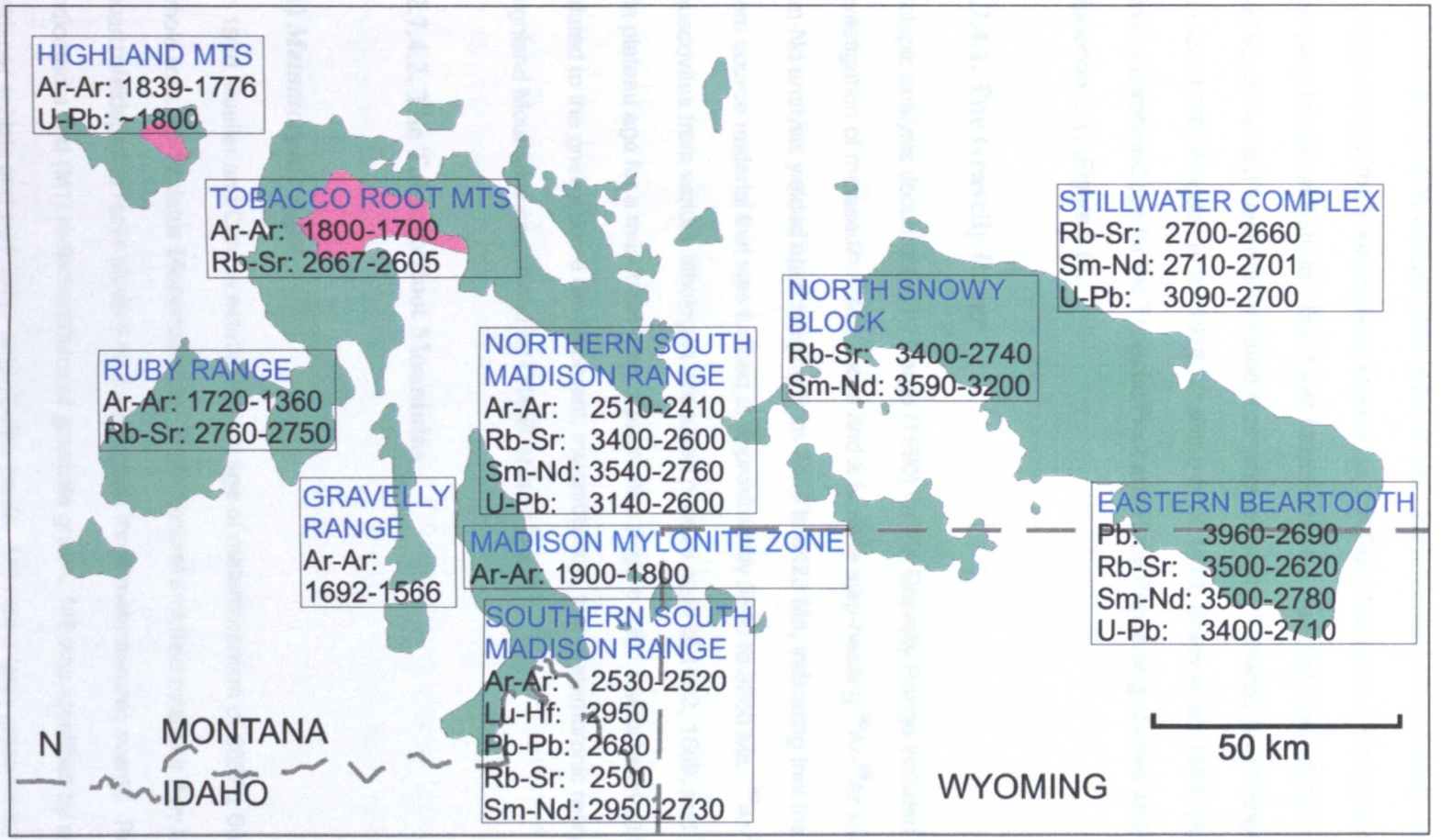

Figure 2.8: Map of south-western Montana showing previous geochronology by other authors
(See Appendix 2.1 for references)

2.7.4. North-west of the Giletti Line

Situated on the north-western side of the Giletti Line are most of the Gravelly Range, the North Madison Range, the Tobacco Root Mountains, the Ruby Range and the Highland Mountains. Compared to the well-studied Beartooth Mountains little work has been done in this area. Those studies carried out have mainly dated rock units within the Tobacco Root Range (e.g. Mueller and Cordua, 1976; Wooden *et al.*, 1978; Vitaliano *et al.* 1979; Brady *et al.*, 1994) (Appendix 2.1) or have given a combined age for the Tobacco Root and Ruby Range (e.g. James and Hedge, 1980) (Appendix 2.1) (Figure 2.8).

2.7.4.1. The Gravelly Range

Isotopic analysis documented by Vargo (1990) for the Gravelly Range included a Sm-Nd investigation of metasedimentary rocks and a furnace step-heating ^{40}Ar-^{39}Ar study (Appendix 2.1). Sm-Nd analysis yielded ages ranging from 3450 to 3423 Ma, indicating that the rocks were derived from source material that was formed at approximately 3500 to 3200 Ma. ^{40}Ar-^{39}Ar dating of several muscovites from various lithologies produced plateau ages of 1692, 1669, and 1676 Ma, and a 1566 Ma plateau age for a muscovite from a pegmatite (Figure 2.8). It was believed that these dates were related to the gneiss dome development, mylonitization, and metamorphic recrystallisation in the Highland Mountains as outlined by O'Neill *et al.* (1988).

2.7.4.2. The Tobacco Root Mountains

A) Metamorphic Ages

In 1976 Mueller and Cordua established an age of metamorphism of 2667 ± 66 Ma based on five whole rock Rb-Sr dates (Appendix 2.1). From textural and field relations they believed the quartzofeldspathic rocks studied had undergone three metamorphic events. Relict pyroxene indicated a first (M1) metamorphism of granulite grade. M2 was identified by sillimanite and K-feldspar schists and was upper amphibolite grade. M3 was a later greenschist grade event producing chlorite, epidote, sericite, and paragonite. The Rb-Sr age was believed to date the M2 amphibolite grade event. Younger K-Ar and Rb-Sr ages of Giletti (1966) were interpreted by these

authors as dating the M3 event. It was further inferred that M1 and M2 were not greatly separated in time.

Work by Vitaliano *et al.* (1979) quoted the ~ 2700 Ma age found by Mueller and Cordua (1976) but took this to be the date of a metamorphic event that "may have reached granulite facies intensity". They also stated that the metamorphic event at ~1600 Ma recorded by Giletti (1966) appeared to have equilibrated mainly at almandine-amphibolite grade. They went on to say that granulite facies assemblages may also have been produced during this event or that these two events could have been part of a single multiphase thermal event as suggested by Immega and Klein (1976). Vitaliano *et al.* (1979) also found evidence of a third thermal event but did not date this. They believed it could possibly have begun in very late Precambrian time but it was clearly represented in the thermal events accompanying emplacement of the Tobacco Root Batholith in late Mesozoic time. Hornfels grade conditions were attained locally within the contact zone and greenschist grade metamorphism occurred in zones of shearing.

More recently, Brady *et al.* (1994), carried out 9 ^{40}Ar-^{39}Ar age determinations on amphiboles from two suites in the Tobacco Root Mountains (Appendix 2.1). A mean age of 1800 Ma was found. They believed that these ages were consistent with evidence from the nearby Madison Range for a major Early Proterozoic orogeny in this region. Kovaric *et al.* (1996), produced further ^{40}Ar-^{39}Ar dates for the range (Appendix 2.1). A combined age for hornblende from each suite within the Tobacco Root Mountains was ~1700 Ma. They reported also that later reheating during Cretaceous granitoid emplacement appears to have affected the rocks of this range, with biotite samples yielding ^{40}Ar-^{39}Ar age spectra that have total gas ages of 112 and 125 Ma.

B) Igneous Ages

Wooden *et al.* (1978) dated the timing of intrusion for three dykes using Rb-Sr whole rock and established ages of 1455 and 1130 Ma (Appendix 2.1). The most important Phanerozoic crystalline rock in the range is the late Mesozoic Tobacco Root Batholith. The gradational character of the contacts and concentric nature of the zoning led Vitaliano *et al.* (1979) to conclude that the batholith

was emplaced as a single injection and differentiated *in situ* during cooling. K-Ar studies reported by Vitaliano *et al.* (1979) gave ages of 74 to 71 Ma for some of the units in the pluton (Appendix 2.1).

2.7.4.3. The Ruby Range

Limited work has been carried out specifically on the Ruby Range. The most well known study was the Rb-Sr whole rock investigation by James and Hedge (1980) which was extensively quoted by later texts (Desmarais, 1981; Wilson, 1981; Mogk and Henry, 1988; Wooden *et al.*, 1988; Erslev and Sutter, 1990; James, 1990; Mueller *et al.*, 1993.). A best-fit line for their data from both the Tobacco Root and the Ruby Range gave an age of 2760 ± 115 Ma (Appendix 2.1) and was considered to date the approximate time of metamorphism. The great uncertainty associated with this number results from the rocks analysed being from two distinct rock suites, one Middle Archæan and one Late Archæan (Erslev and Sutter, 1990). However, the age is consistent with the findings of Mueller and Cordua (1976) in the Tobacco Root Mountains and corresponds to the Beartooth orogeny.

Brady *et al.* (1991) published the first known ^{40}Ar-^{39}Ar dates for the Ruby Range (Appendix 2.1). This study established an ^{40}Ar-^{39}Ar age spectra for phlogopite, biotite and hornblende from an extensive metasomatic talc deposit that yielded a plateau and total gas age of ~ 1700 Ma. This age is consistent with the regional ages obtained by Giletti (1966). However, the mica age spectra were "disturbed" and this date can only be considered as a minimum age.

Support for these dates comes from a study by Kovaric *et al.* (1996) who obtained 1720 Ma ages from hornblende and two phlogopites from basement in the Ruby Range (Appendix 2.1). Also investigated was sericite that grew during the formation of the talc deposit. This exhibited a good ^{40}Ar-^{39}Ar plateau age of 1360 Ma, confirming the suggestions that the talc formed during the Proterozoic rifting that created the Belt basin (see also section 9.3.7). Phlogopite in marble from an adjacent talc deposit had a 1720 Ma plateau age.

2.7.4.4. The Highland Mountains

U-Pb zircon analysis of zircons from leucocratic gneiss from the core of the Highland Mountain dome, mylonitic biotite gneiss from the northwest flank of the dome, and similar zircons from

gneisses exposed in the Armstead anticline and the Tendoy Mountains (southeast of the Highland Mountains) reveal a complex isotopic pattern on a concordia diagram (O'Neill *et al.*, 1988). These data suggest metamorphic growth of zircon at about 1800 Ma, in part nucleating upon cores of an older generation of crystals (Appendix 2.1). O'Neill *et al.* (1988) believed that this implied that the quartzofeldspathic gneisses are at least as old as the 2750 Ma crystalline basement rocks of the Tobacco Root Mountains and Ruby Range. More recent geochronology by Harlan *et al.* (1996) supports the Proterozoic age found. Using ^{40}Ar-^{39}Ar dating, total gas ages of 1839 and 1776 Ma were achieved for biotite from layer gneiss and hornblende from metabasite sill, respectively (Appendix 2.1). Kovaric *et al.* (1996) also used ^{40}Ar-^{39}Ar on sericite in the talc deposit in the Highland Mountains. This yielded a disturbed total gas age of 122 Ma that is probably due to resetting by a nearby 75 Ma pluton (Appendix 2.1).

2.7.4.5. The Pioneer Mountains

The Pioneer Mountains are situated to the west of the Ruby Range. Dating of the Precambrian gneisses in the Pioneer Mountains was undertaken by Arth *et al.* (1986). Data from four samples of microcline-plagioclase gneiss and interbanded amphibolite yielded a linear Rb-Sr whole-rock isochron suggesting an age of 1640 Ma. Zircon separates from a leucocratic gneiss gave discordant U-Pb ages and a $^{207}Pb/^{206}Pb$ age of about 1800 Ma (Appendix 2.1).

The Pioneer Mountains Cretaceous batholith was dated by Marvin *et al.* (1983; referenced in Arth *et al.* 1986). K-Ar and ^{40}Ar-^{39}Ar on biotite and hornblende from the batholith yielded ages of 76 Ma for hornblende-biotite quartz diorite, 74 Ma for hornblende-biotite tonalite, 72 Ma for hornblende-biotite granodiorite and biotite granite, and 67 and 65 Ma for biotite granodiorite and 2-mica granite. It is believed that the source for the Pioneer batholith magmas was distinct from that of the Boulder batholith in the northeast, instead being sourced from Proterozoic gneiss or isotopically similar rocks of the lower continental lithosphere (Arth *et al.*, 1986).

Chapter 3 - The ^{40}Ar-^{39}Ar Geochronological Technique

3.1. Introduction

The main aim of this research is to further develop laser techniques associated with ^{40}Ar-^{39}Ar dating and to increase its potential use in geological applications. The evolution of the ^{40}Ar-^{39}Ar technique and the radioactive decay process will be summarised only since they have been described in detail by numerous authors already (see particularly Kelley, 1995; McDougall and Harrison, 1988; Faure, 1986). However, those aspects particularly relevant to this study and details of the actual technique used will be included. The technique is outlined in the order that is dealt within the laboratory situation, i.e. from sample selection and preparation, through the gas extraction stage, to calculation of the age and interpretation.

3.2. Sample Preparation

3.2.1. Thin Section Examination

Thin section examination is a vital step for sample selection. Thin sections for all rock specimens were produced and examined under a standard petrological microscope. A number of factors determined whether a sample was suitable for further experimentation. Ideally the samples should be relatively unaltered and unweathered in order to maximise reliability of the dating technique and the age produced. Also the samples need to contain a potassium-bearing mineral such as mica or amphibole that can be dated. Those samples selected for amphibole separate dating require numerous, good quality amphiboles. Samples selected for matrix and inclusion biotite dating need both pristine matrix biotites and well-formed garnets containing a high abundance of biotite inclusions. The presence of a high number of opaque inclusions within garnets in some samples meant that these were dismissed as opaque and biotite inclusions are difficult to distinguish at the laser ablation stage. For full details of the thin-section examination of the samples analysed see Chapter 4.

3.2.2. Probe and Laser Sections

Probe and laser sections were produced for each of the samples selected after thin section examination. Probe sections were used for detailed chemical analysis on a *Cameca SX100* electron microprobe (Appendix 3.2). The data produced from these sections were used to augment thin-section examination, to identify possible alteration, and to provide insight into possible chemical reasons for age variations.

A "laser" or "thick" section is designed for the *in situ* analysis of minerals using the UV laser ablation microprobe (see section 3.4.1). The sample preparation technique is similar to that of a thin section except the resultant section is 100-150 μm thick and is attached to its glass slide by *Canada Balsam* rather than epoxy resin. The advantage of a thick section over a mineral separate is that the mineral can be examined *in situ* and the analysis related to its position within the rock and its textual relationship to other mineral species. Furthermore, where the mineral separation technique can cause damage to the edges of mineral grains or reduce the size of the grain, minerals *in situ* are clearly unaffected by preparation, except by the polishing technique.

Photographs were taken of each section (e.g. Plate 3.1) and selected areas of interest within each section, such as garnets (e.g. Plate 3.2), using a camera attached to a *Leica Wild MZ8* binocular microscope. These were designed to be used as a reference "map" of the sample for use during analysis. This is particularly useful for the location of inclusions within the garnet as these are easier to see under the brighter conditions of a low powered binocular microscope than in the laser port.

The sections were heated to soften the *Canada Balsam* and carefully removed from their glass slide. Each section was then cleaned to remove the resin (see below) and broken into smaller pieces suitable for packing for irradiation (see section 3.3.3). When the sample was intended for biotite

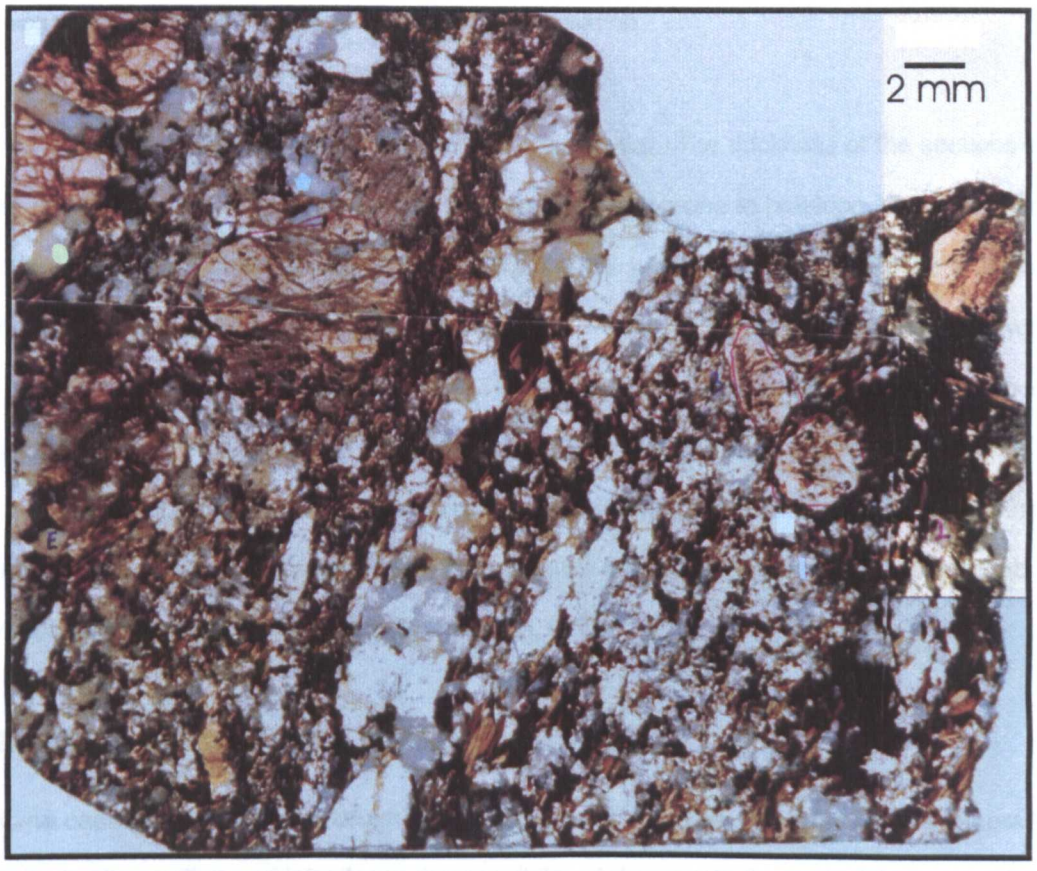

Plate 3.1: Photograph of Thick Section (Rm39)

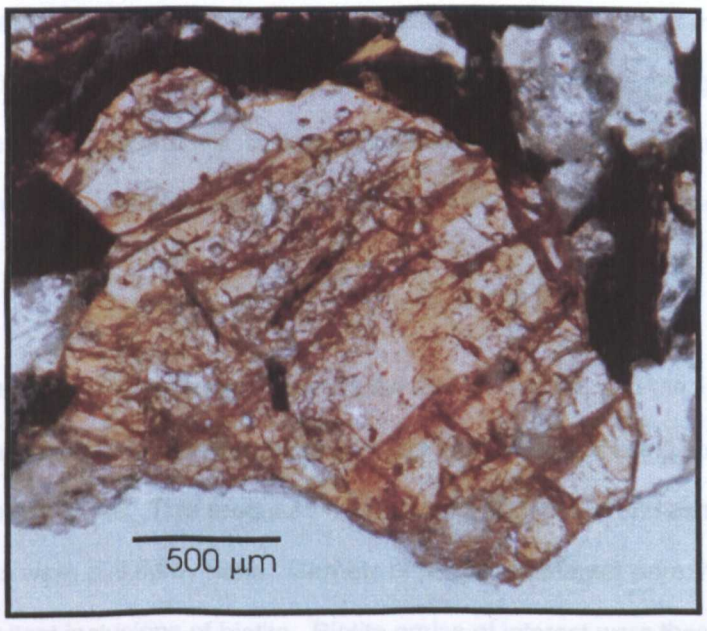

Plate 3.2: Photograph of Garnet Within a Thick Section (Rm40)

inclusion analysis, only those parts of the section containing the largest garnets were retained. Two to three pieces from each section were sent for irradiation.

Careful handling of the samples at this stage was essential. The thickness of the sections and the brittle nature of the rock type means that the samples were prone to breaking. Fragmentation of the sample makes the sample difficult to handle and the pieces tend to "jump" when the laser is applied to them. This is caused by the explosive degassing of hydrous minerals, such as biotite, when they are rapidly heated in the absence of water. This particularly affects small sample pieces because the degassing force is strong enough to move the fragment. Furthermore, the fragmentation of the sample renders the photographic maps useless and introduces difficulties in locating the inclusions in garnet. Most importantly, the advantage of being able to relate individual grain dates to fabric elements, usually associated with a thick section, is lost.

3.2.3. Rock Crushing and Mineral Separation

In some cases the sample was crushed and separated. Although this removes the mineral grain from its *in situ* position and introduces the possibility of damage to the grain, it has a number of advantages over the thick section method. The thick section is only a small fragment of the rock sample that may or may not contain the minerals of particular interest. When a rock is crushed and separated, suitable minerals can be specifically selected and more of that mineral type included in the analysis. The orientation of the mineral may also be controlled, allowing, for example, more frequent analysis of biotite grains in basal section than would naturally occur within a thick section. Furthermore, mineral separates are not as prone as a thick section to damage during cleaning and handling.

The rocks were crushed and sieved, retaining the 250 μm - 1 mm and the 1-2 mm fractions. The fractions were washed to remove fine dust particles and separated using sodium polytungstate heavy liquid with a density of 2.8. This produced concentrations of garnet and biotite grains from which individual grains were picked by hand. Garnets of particular interest were those that clearly contained abundant inclusions of biotite. Biotite grains of interest were those that appeared to have unbroken and unaltered edges when observed under a low powered microscope (e.g. Plate 3.3),

thus reducing the possibility of analysing grains with edges damaged by the preparation process or natural alteration.

3.2.4. Garnet Separate Polishing

In order to analyse biotite inclusions within a garnet separate, it is necessary to remove part of the garnet to expose a large surface area, and to polish the surface so that inclusions just beneath the surface are visible. To do this, picked garnets were mounted in resin blocks and ground down to the largest diameter. The blocks were then lapped using corundum powder and polished using water-based 0.5 μm aluminium oxide until a high polish was achieved. The blocks were examined under a low powered microscope to insure that the polish was adequate and to examine the abundance of inclusions within a reasonable distance from the polished surface of the garnet. Photographs of the most suitable garnets within the blocks were taken to serve as a map (e.g. Plate 3.4). The block was then soaked in acetone in an ultrasonic bath to soften the resin, and the garnets removed using a razor blade.

3.3. Irradiation to Sample Loading

3.3.1. Irradiation

The ^{40}Ar-^{39}Ar dating technique, like the K-Ar technique, is based upon the radioactive decay of unstable ^{40}K to its radiogenic daughter ^{40}Ar. ^{40}K has a half life of 1250 Ma, 89.5% decaying to ^{40}Ca by electron (β^-) emission, and 10.5% decaying to ^{40}Ar predominantly by orbital electron capture. Both daughter products are stable and although it is theoretically possible to use the ratio of ^{40}Ca to ^{40}K to obtain dates, ^{40}Ca is an abundant element in nature and isolating the ^{40}Ca that is produced by the decay of ^{40}K would be impossible in most situations. In contrast, ^{40}Ar is only ever present in trace amounts. A date can thus be calculated by measuring the ratio of the daughter ^{40}Ar to the parent ^{40}K.

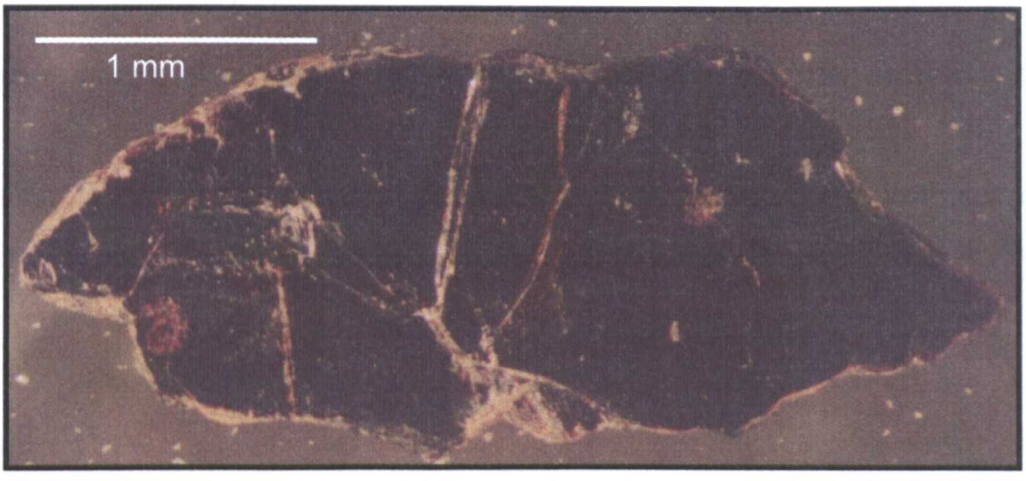

Plate 3.3: Photograph of biotite separate (RRCR2)

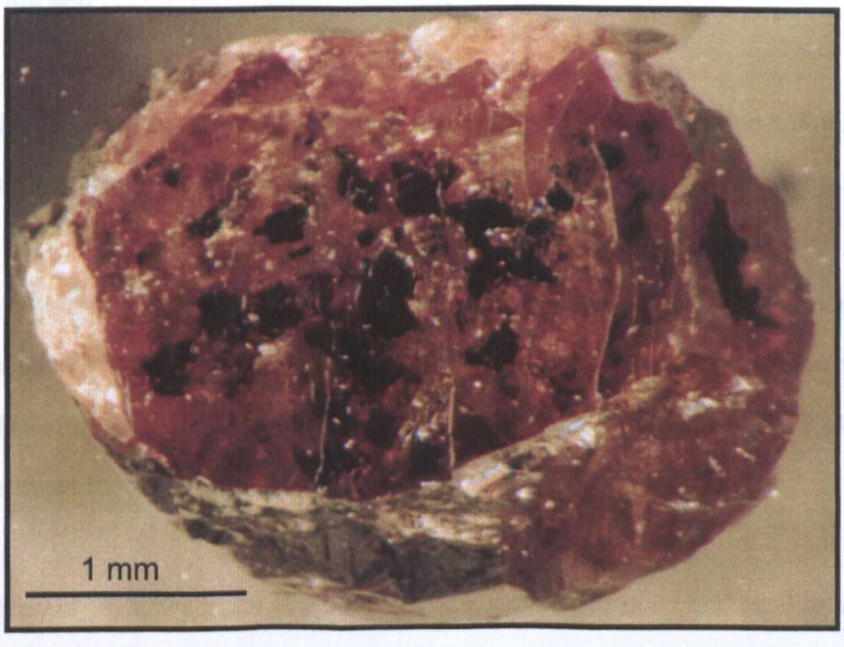

Plate 3.4: Photograph of garnet separate mounted in resin block (RRCR3)

For the K-Ar technique potassium and argon are measured separately on portions of the same sample but its reliability can be hampered by sample inhomogeneity. The ^{40}Ar-^{39}Ar method has the advantage of determining the argon/potassium ratio in one analysis by measuring the ratio of two isotopes of argon. The measurement of ^{39}Ar is an indirect method of determining the amount of ^{40}K.

The isotope ^{39}Ar is produced by the transformation of ^{39}K by bombardment by fast neutrons within a nuclear reactor. A neutron replaces a proton in the nucleus of the ^{39}K, transmuting it to ^{39}Ar, as shown below:

$$^{39}_{19}K(n,p)^{39}_{18}Ar$$

The K isotopes undergo very little fractionation in nature and, therefore, the $^{39}K/^{40}K$ ratio is essentially constant in nature. It has been measured as 0.0001167 (Steiger and Jäger, 1977), therefore, the $^{40}Ar/^{39}Ar$ ratio is proportional to the $^{40}Ar/^{40}K$ daughter/parent ratio in the sample, and can be used to calculate the age.

The resultant ^{39}Ar is radioactive and decays to ^{39}K by beta emission with a half-life of 269 years. This decay is corrected for but its effect is negligible between the irradiation time and the analysis.

Both the K-Ar and the ^{40}Ar-^{39}Ar dating techniques are dependant on several fundamental assumptions that are summarised below. Full discussion of the validity of these assumptions can be found in Dalrymple and Lanphere (1969). Although these refer specifically to K-Ar dating, they are equally relevant to the ^{40}Ar-^{39}Ar method.

1) The decay of ^{40}K takes place at a constant rate, regardless of its chemical or physical environment.

2) The present-day proportion of ^{40}K to $^{Total}K$ is the same in all materials to which the K-Ar method is applied.

3) All argon in the rock or mineral is either radiogenic or atmospheric; that is, there is no extraneous argon.

4) The rock or mineral has been a closed system since t_0; that is, there has been no loss or gain of ^{40}K or ^{40}Ar except for that which results from the radioactive decay of ^{40}K.

5) The time of formation of the rock or mineral is short compared to its age.

3.3.2. Interfering Reactions

The fast and slow neutron bombardment that transforms ^{39}K to ^{39}Ar also causes a number of other transformations within the sample (see Table 3.1). These interfering reactions are outlined in detail in McDougall and Harrison (1988). Many of the reactions occur at such low levels that they can be ignored. However, in addition to the conversion of ^{39}K to ^{39}Ar, the other important reactions convert chlorine nuclei to ^{38}Ar, calcium nuclei to ^{37}Ar and ^{36}Ar, and ^{40}K to ^{40}Ar.

Data from an irradiated sample that contains calcium must be corrected for the decay of ^{37}Ar to ^{37}Cl. The half life of ^{37}Ar is 35 days, therefore both the time since irradiation and the K/Ca ratio of the sample will influence the age. All samples containing calcium have to be analysed within 6 months of irradiation to prevent significant distortion to the ages produced. However, analysis too soon after irradiation can implant significant ^{37}Ar into the multiplier, causing high apparent background levels as the implanted ^{37}Ar decays. This problem affects amphiboles to a greater extent than micas due to the lower K/Ca ratio in amphiboles.

Table 3.1. Significant irradiation transformations

Original Isotope	Isotope Produced	Reaction for Transformation
^{40}K	^{40}Ar	$^{40}K(n,p)^{40}Ar$
^{42}Ca	^{39}Ar	$^{42}Ca(n,\alpha)^{39}Ar$
^{39}K	^{39}Ar	$^{39}K(n,p)^{39}Ar$
^{37}Cl	^{38}Ar	$^{37}Cl(n,\gamma)^{38}Cl \rightarrow \beta \rightarrow ^{38}Ar$
^{40}Ca	^{37}Ar	$^{40}Ca(n,\alpha)^{37}Ar$
^{40}Ca	^{36}Ar	$^{40}Ca(n,n\alpha)^{36}Ar$

where n = neutron, p = proton, α = alpha particle, γ = gamma ray, β = positron
Box in grey is the conversion of ^{39}K to ^{39}Ar, other boxes are interference reactions.

Each reactor has a different spectrum and level of neutron flux, and the flux varies depending on the location of the samples within the reactor. This neutron flux gradient is significant along the length and breadth of the sample containing tube, and is measured using standards of known age. The standards are later analysed and a J-value for each is calculated (see section 3.5). These can then be interpolated to obtain a J-value for each sample. The error on the J-value is ± 0.5%.

3.3.3. Irradiation Packing Procedure

It is important that the sample is clean as grease from fingerprints and resins used in the sample preparation stage can add hydrocarbons to the analysis. Hydrocarbons cause a scattering effect in the mass spectrometer that may interfere with the argon measurements, and ultimately they oxidise the filament. Furthermore, finger grease contains potassium that might affect the $^{40}Ar/^{39}Ar$ ratio. For this reason samples were cleaned in methanol in an ultrasonic bath for 15 minutes, and then for a further 15 minutes in deionsed water. Particularly dirty samples, such as those coated in *Canada Balsam* from thick section preparation were cleaned in methanol twice.

It is also important that the samples are dry, as water becomes hydrolysed in the reactor and can attack some minerals and the aluminium foil packaging, producing aluminium hydroxide. This reduces the foil to a fine grey powder that is extremely difficult to remove from the sample. Therefore, samples were left to dry overnight before packing commenced.

Each sample, whether it was a set of mineral separates or a piece of thick section, were wrapped in a small piece of aluminium foil. In addition, an appropriate number of packages (3-4) containing a standard were prepared. The size of the package is dependant on the size capacity of the reactor sample chamber and this varies for each reactor. In the case of the McMaster reactor, used most often in this study, the ideal package size was 10 mm^2. Each package was labelled with a simple one letter, one number system. Finally, each package was weighed. This is a backup safety precaution to the labelling system so that if the label should become illegible the sample can be identified by its unique weight.

The set of packages was carefully stacked, with standards spaced at regular intervals throughout the stack, and wrapped in a further layer of aluminium foil to keep the stack in place. An aluminium tube

with the dimensions of 84 mm in length by 20 mm in diameter was used to contain the aluminium foil package (Figure 3.1). At the reactor site the tube was fitted with a cadmium foil liner to reduce the slow neutron flux to the samples, and sealed. Slow neutrons are not required for the conversion of ^{39}K to ^{39}Ar but do increase the radioactivity of the sample so a reduction of these reaching the sample keeps the radioactivity of the sample at a minimum.

3.3.4. Irradiation Duration

The irradiation duration is designed to give the optimum neutron flux (see Turner, 1971). There must be sufficient flux to produce measurable ^{39}Ar and a measurable $^{40}Ar/^{39}Ar$ ratio but not too much that the interfering reactions degrade the precision of the $^{40}Ar/^{39}Ar$ ratio determined. The key factors when determining how long the irradiation should last is the approximate age of the sample and its K/Ca ratio. Older samples require more irradiation time than younger samples because they have only low levels of ^{39}K, and higher Ca minerals are more prone to interference reactions. Full discussion of optimising irradiation parameters can be found in Turner (1971) but Figure 3.2 gives a indication of how these parameters can be determined.

Following irradiation, samples will be kept at the reactor site until the radioactivity has decreased to a level which allows transport back to the laboratory.

3.3.5. Sample loading

After irradiation the samples are loaded into an ultra high vacuum laser port and baked overnight at 120 °C using a 250 W lamp to remove any absorbed atmospheric argon from the sample surface. The laser port is fitted with a UV grade fused silica window which has a high transmission coefficient for light at 266 nm. A sapphire window 1 mm thick is positioned between the laser port window and the sample to prevent ablation material coating the outer window. Ablated material on

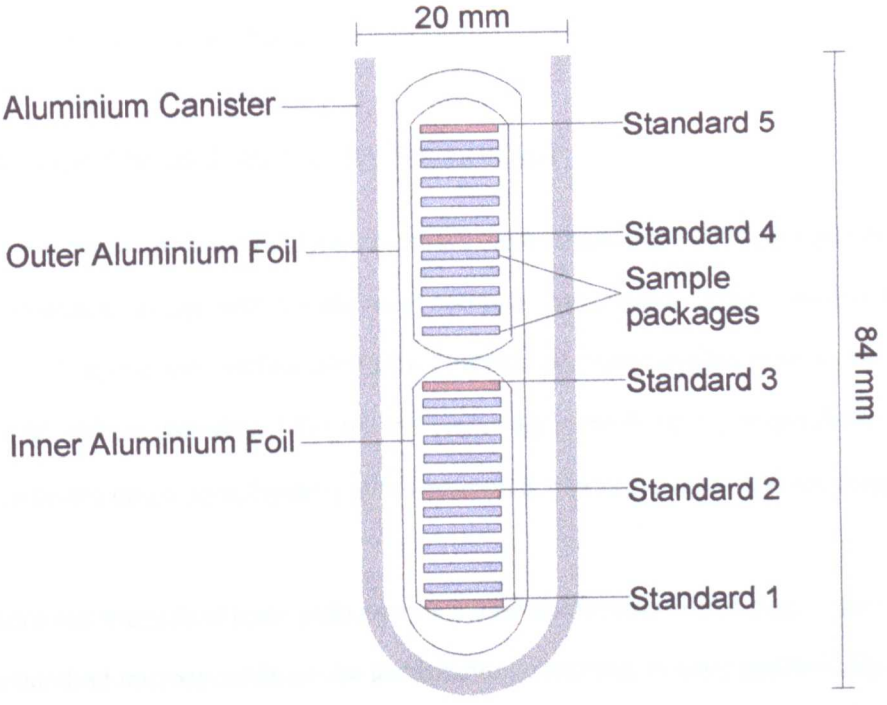

Figure 3.1: A cartoon to illustrate packing of the samples to be sent for irradiation

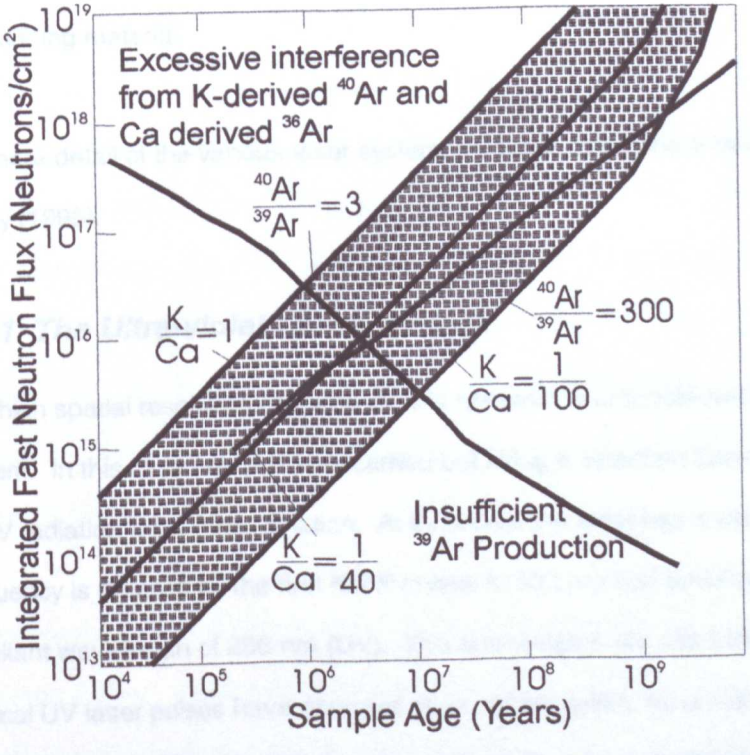

Figure 3.2: Integrated fast neutron flux requirements to maximize ^{39}Ar production and minimize ^{40}Ar and ^{36}Ar interference effects (after Turner, 1971)

the window eventually absorbs the laser beam and causes damage to the window but the sapphire window can be replaced cheaply.

3.4. The Laser Extraction Technique

Currently there are two main types of lasers: continuous wave (CW) and pulsed systems. Continuous wave systems are the most common and operate by the continuous pumping of high power. They can be used for both slow heating and instantaneous melting and have pit sizes varying from 50-250 μm diameter. This makes them very versatile and, consequently, popular. However, these lasers cause local heating of the surrounding material up to 500 μm away from the laser spot.

In contrast, the pulsed laser outputs as a series of microsecond spikes. High power densities for a few hundred microseconds cause instantaneous melting, making gentle heating impossible. However, this problem can be overcome with the Q-switching ultra-violet system which creates short pulses of light for a few nanoseconds, resulting in a small spot size that avoids large scale instantaneous melting. The result is a high spatial resolution system with no heating of the surrounding material.

For more detail of the various laser systems currently used and a history of their development see Kelley (1995).

3.4.1. The Ultra-violet Laser System

The high spatial resolution required for this research is only achievable using the UV-laser extraction system. In this case analysis was carried out using a *Spectron Laser Systems SL401* as the source of UV radiation for sample ablation. At its source the laser has a wavelength of 1064 nm (IR). This frequency is doubled by the first KD*P crystal to 532 nm and doubled again by the second crystal to a resultant wavelength of 266 nm (UV). The wavelengths are separated using a *Pellin Brocca* prism. Typical UV laser pulses have energies of ~1 mJ per pulse, for a pulse length of 10 ns and repetition rate of 10 Hz. The beam is directed into a customised *Leica DM* microscope by high-reflectance oxide-coated mirrors. Inside the microscope the beam is redirected through a UV-refracting

objective lens and focused to a spot size of ~10 μm at the sample surface. The sample is observed using a CCD camera, coaxial with the laser beam.

A computer controlled XY stage was used to move the sample beneath the laser beam. Stage movement can be programmed to cover the area of interest and can be activated when the laser is switched on. These capabilities give the analyst precise control over the area to be ablated. For general sample analysis, where the position within the grain is not critical, a 50 μm square was ablated. The laser beam was rastered over the same area 7 to 9 times within the ten minute analysis time. When a 50 μm square failed to release sufficient amounts of gas to produce acceptable errors, the analysis was repeated using a 100 μm square. In this instance the square was repeatedly ablated 3 times within the ten minute analysis time to yield a larger quantity of gas.

For detailed work on age variations within a single grain, linear pits were ablated with a width equivalent to the beam diameter. A traverse was made along the edge of a grain for 400-500 μm. This length is necessary in order to obtain sufficient gas to produce reasonable errors. The following analysis was a traverse immediately adjacent to the previous at a measurable distance, and so on. In this way a profile can be constructed from the edge of the grain inwards. Traverses were carried out in two different orientations. In the case of mineral separates, the biotite grains were oriented in basal section (Figure 3.3A) and ablation was in a series of linear pits within the *001* plane. When thick-sections were used, the polished surface of the biotite grains were often not the basal section. In this instance, ablation was carried out in a series of traverses perpendicular to the cleavage traces (Figure 3.3B). Both these orientations are capable of detecting any theoretical age variation due to cooling and will homogenise any apparent age effects caused by fast path diffusion along the cleavage planes.

Occasionally it was necessary to undertake detailed work of age variations that might occur along the cleavage planes. When analysing mineral separates in basal section this required a depth profile. Each analysis consists of a 150 μm square ablated once only within the 10 minute analysis

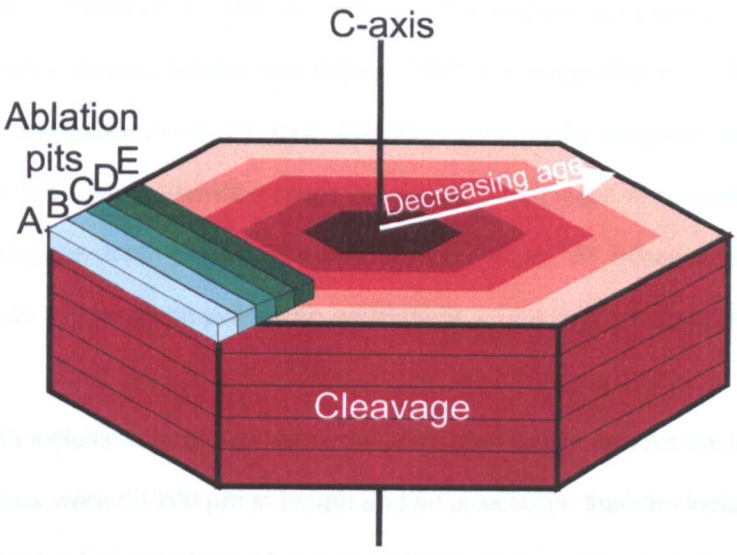

A) Basal section

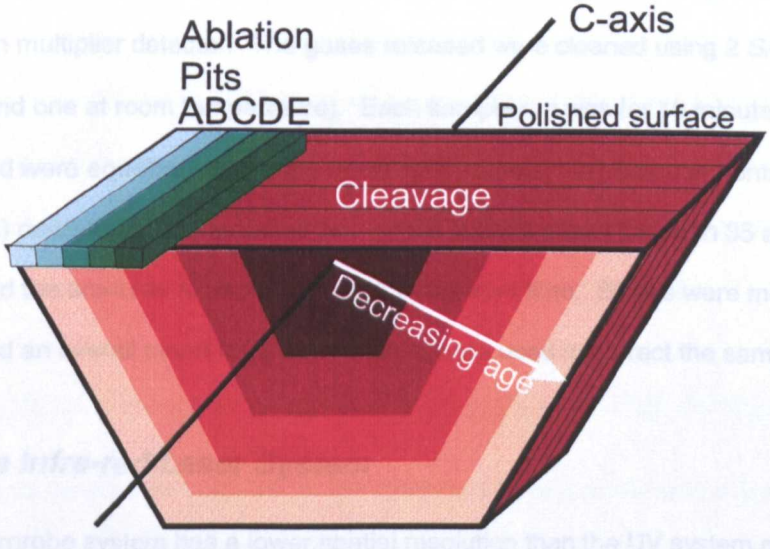

B) Thick section

Figure 3.3: A cartoon to illustrate the orientation of laser ablation pits in biotite depending on sample format

time. Successive analyses were performed over the previously ablated square. Each ablation step removed only a thin layer of material. Although ^{39}Ar release has been used to calculate pit depth in K-feldspar experiments (Arnaud and Kelley, 1997), it is impossible to back-calculate the exact amount of material removed with each ablation step in biotite using the amount of ^{39}Ar released alone. This is because alteration along the cleavage can result in potassium-depleted material being ablated during the depth profile. However, the maximum ^{39}Ar released from depth profile layers from biotite in this research yielded an estimate of ~1 μm depth of ablation with each analysis.

When biotite inclusions in garnet were analysed, attempts to remove the whole grain were made. The inclusions were 50-200 μm in length and an area larger than the inclusion was ablated. For inclusions buried beneath the surface several runs were necessary before the inclusion was ablated. As the garnet contained no detectable argon the ablation of garnet had no influence on the ages produced.

The released gases were measured in a *MAP 215-50* noble gas mass spectrometer using a *Balzers 219* electron multiplier detector. The gases released were cleaned using 2 *SAES AP 10* getters (one at 400 °C and one at room temperature). Each sample run was for 10 minutes and the gases accumulated were equilibrated into the mass spectrometer via computer controlled VAT valves (35 mm flanges) operated by compressed air. Argon isotope peaks between 35 and 41 were scanned 10 times and the amounts extrapolated back to the inlet time. Blanks were measured after every two samples and an overall mean for a day's blanks were used to correct the sample analyses.

3.4.2. The Infra-red Laser System

The IR laserprobe system has a lower spatial resolution than the UV system due to the longer wavelength of infra-red radiation and thus produces a spot size of >25 μm. This system is therefore inappropriate for the high spatial resolution work carried out for this research. However, all the standards were analysed on this system. This is because total-fusion of a whole grain is required to produce the bulk age expected. Furthermore, amphiboles were analysed on this machine because they contain lower concentrations of argon and cannot easily be analysed using the UV system.

The laser source was a *Spectron Laser Systems SL902* CW Nd YAG, producing a continuous infrared beam with a wavelength of 1064 nm. The beam, which has an output of approximately 15 W TEM_{00} and 45 W multimode (maximum) is directed into a customised *Leica Metallux 3* microscope using high reflectance, oxide coated mirrors. Focusing of the beam at the sample surface via the objective lens enabled a spot size of between 25 and 100 μm. The sample was observed using a CCD camera, coaxial with the laser beam.

Two different laser techniques were used on samples analysed with this system. For standards and total fusion amphibole ages the spot-fusion technique was used. This involves the rapid heating of the whole or part of a grain using a focused laser beam. Using this technique the grain melts almost instantly and all gas is released. The second technique is step-heating. In this instance the grain is gently and evenly heated using a defocused laser beam over a number of steps, gradually increasing the beam intensity with each step. Early steps release argon from clay minerals within the grain or from lattice sites close to the grain boundary. Later steps release more tightly held argon from mineral breakdown at high temperatures (see Wartho *et al.* 1991 for more detail).

The gases released by laser ablation were cleaned using 2 *SAES AP 10* getters, with one operated at 400 °C and one at room temperature. After 5 minutes the gas was equilibrated via automated valves into a *MAP 215-50* noble gas spectrometer. Once again blanks were carried out after every two analyses and a mean of the day's blanks used for blank correction.

3.5. Standard Analysis and Determination of the J-Value

The standards most commonly used in this study were Tinto biotite with a known age of 410.3 Ma (Rex and Guise, 1995) and Hb3gr with an age of 1072 Ma (Turner *et al.*, 1971). Ideally standards should be as close as possible to the age and composition of the samples being irradiated. In this study Tinto was chosen because it is a highly reliable biotite standard, and Hb3gr hornblende was chosen because of its closeness to the ages of the samples. On average 5 to 10 grains of the standard from each position within the reactor were analysed by total fusion using the IR laser system. The resultant data were then corrected for blank levels, mass spectrometer discrimination, calcium and potassium.

An age is calculated using the following equation:

$$\text{Age} = \frac{1}{\lambda} Ln\left[\frac{^{40}Ar}{^{39}Ar} \times J + 1\right] \qquad \text{Equation [3.1]}$$

Therefore:

$$\frac{^{40}Ar}{^{39}Ar} \times J = e^{(Age \times \lambda)-1} \qquad \text{Equation [3.2]}$$

where λ is the combined decay constant for ^{40}K .. This comprises the decay of ^{40}Ar to ^{40}Ca by beta emissions, the decay of ^{40}K to ^{40}Ar by electron capture and gamma emission, and the decay of ^{40}K to ^{40}Ar by electron capture. This has a combined decay constant of $5.543 \times 10^{-10} a^{-1}$.

If the standard Hb3gr is used then the age is known to be 1072 Ma. So $e^{(Age \times \lambda) - 1}$ can be calculated. The J-value is obtained by dividing this value by the $^{40}Ar/^{39}Ar$ ratio produced for the standard.

For each standard in a different reactor position a mean J-value can be calculated, giving an indication of the amount of flux throughout the sample column. The variation between standards can be calculated in terms of percentage and a separate J-value for each sample between the standards can be interpolated. This reduces the amount of error in the final age caused by the J-value.

3.6. Data Handling

The raw data from the mass spectrometers record the measurements of ^{36}Ar, ^{37}Ar, ^{38}Ar, ^{39}Ar and ^{40}Ar. These must first be corrected for the blank levels of these isotopes. Blank levels are determined by running the system in the same way as for a sample analysis but by not operating the laser. A correction for mass spectrometer discrimination is required. Discrimination can cause the atmospheric $^{40}Ar/^{36}Ar$ ratio to be measured as a different value to the 295.5 determined by Steiger

and Jäger (1977). Discrimination has been determined by the analysis of glass known to contain air only. For the UV system mass spectrometer it is 282, and 283 for the IR system mass spectrometer.

If calcium is present within the sample then the calcium correction should also be made to correct for any ^{36}Ar produced from the transformation of calcium in the reactor. To do this the ^{37}Ar measured is used, as the majority of this comes from the transformation of calcium and gives a good indication of the amount of calcium contained within the sample. Measured interference factors for many of the world's reactors are listed in McDougall and Harrison (1988). These were determined by measuring the relative production rates of the isotopes in a pure calcium salt (CaF_2) after neutron irradiation. In addition, details about the duration and date of the irradiation are required for this correction because of the rapid decay of ^{37}Ar.

A potassium correction may also be required to correct for the small amounts of ^{40}Ar produced from potassium during irradiation. Again correction is made using factors determined from the irradiation of pure potassium salt (K_2SO_4).

The age is calculated from the ratio of radiogenic ^{40}Ar and ^{39}Ar. The ^{40}Ar measured in the mass spectrometer is a measure of the total ^{40}Ar so includes radiogenic ^{40}Ar, ^{40}Ar from the atmosphere and excess argon. It is therefore necessary to calculate the amount of atmospheric ^{40}Ar and to subtract this from the total to give the radiogenic ^{40}Ar (expressed as $^{40}Ar^*$) only. This is achieved using the ^{36}Ar content measured. Apart from a very minor amount of ^{36}Ar produced in the reactor from calcium (corrected for in the calcium correction), ^{36}Ar comes from the atmosphere, or from atmospheric argon dissolved within meteoric water or hydrothermal fluids, so it gives a good indication of the amount of atmospheric ^{40}Ar contained within the sample. Furthermore, the ratio of $^{40}Ar/^{36}Ar$ in the present-day atmosphere has been determined to be 295.5 (Steiger and Jäger, 1977). Using this it is possible to calculate the amount of atmospheric ^{40}Ar within the sample, and consequently, the amount of $^{40}Ar^*$.

The age is finally calculated using equation [3.1] above, inserting the appropriate J-value.

3.7. Interpretation of the Age Produced

3.7.1. The Isotopic Clock

When a rock or mineral is at a high temperature, argon can diffuse freely into and out of the mineral. However, when the mineral cools, argon diffuses more slowly. Below a certain temperature the distance argon diffuses over geological time is smaller than the size of the mineral grain and the argon becomes trapped. It is at this point that the isotopic clock is activated. This is known as the closure or blocking temperature and was proposed originally by Dodson (1973). It can be defined quantitatively as:

$$\frac{E}{RT_c} = Ln\left[\frac{-ART_c^2 D_o}{a^2 EdT/dt}\right] \qquad \text{Equation [3.3]}$$

where E is the activation energy per mole, D_0 is the pre-exponential factor, a is the effective diffusion dimension, R is the universal gas constant, dT/dt is the cooling rate, and A is the constant depending on the assumed diffusion geometry (slab, cylinder, sphere).

This concept is dependent upon the theory of volume diffusion, which involves the migration of solute atoms or ions (such as Ar) via point defects through a "homogeneous" crystal. In any individual mineral the closure temperature is controlled by its composition, grain size and cooling rate.

In rapidly cooled igneous rocks the point that the blocking temperature is reached is often coincident (within error) with the eruption or intrusion of the rock, so the age represents the time of emplacement. In metamorphic rocks it is more complicated. A given metamorphic event may be capable of heating a mineral to a temperature above the blocking temperature, thus resetting the isotopic clock. Any information about the previous history of the mineral is then lost. The isotopic clock will not restart again until the mineral cools back below the blocking temperature. If this happens slowly, different parts of the mineral may reach the closure temperature at different times (see section 3.7.2). In general, the age obtained for a metamorphic mineral will be the last time that

the mineral passed through its blocking temperature. A mild reheating event may, however, result in a partial resetting of the isotopic clock, and the resultant age is a mixture of two events.

3.7.2. Closure Profiles

3.7.2.1. Introduction

Although the exact closure temperature of a mineral grain is dependent on such factors as grain size, different minerals of comparable size have different blocking temperatures. For example, amphibole has a higher blocking temperature than muscovite, and muscovite higher than biotite. Ar analyses of each of these from the same rock can be used to give an estimate of cooling rate. For example, the amphibole age will indicate when the rock was at about 500 °C (Harrison, 1981), the muscovite age will indicate when the rock was about 350 °C (Hames and Bowring, 1994), and biotite at about 280 °C (Grove and Harrison, 1996). A mineral isochron can be constructed, with age versus temperature, using these estimates. The resultant line between these points gives a crude estimate of a linear cooling history (Figure 3.4).

However, it has been theorised that a rock that has undergone a protracted period of cooling will exhibit systematic apparent age variations within a single mineral grain (Dodson, 1986). If this theory is correct then a mineral grain that undergoes slow cooling will block firstly at its core, and later at the rim. This results in the grain exhibiting a slowly declining apparent age from core to

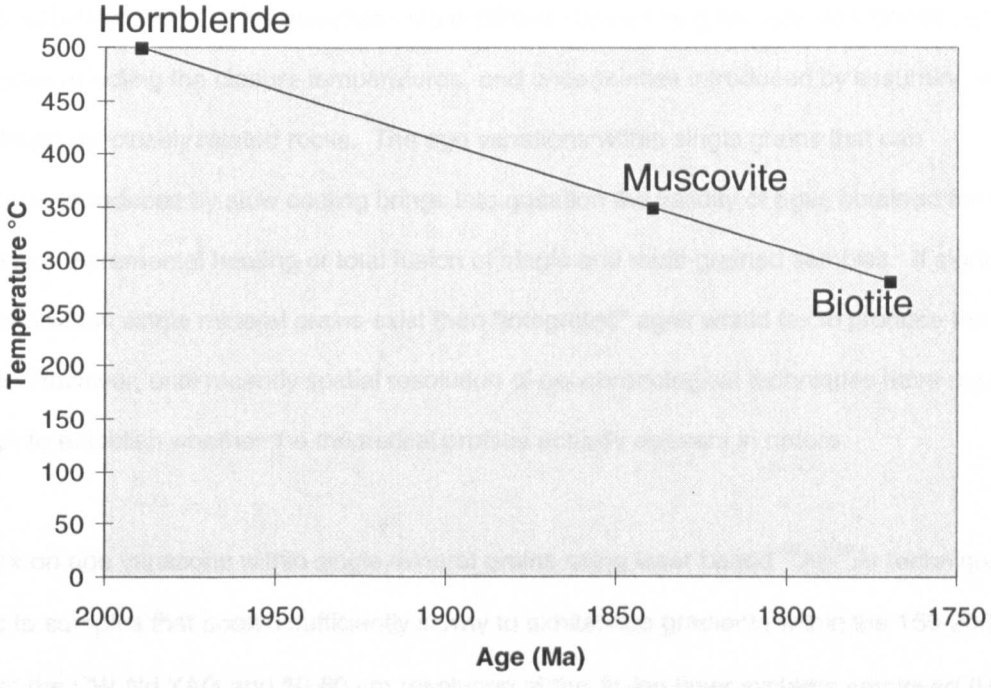

Figure 3.4: An example of a 3 point isochron indicating a cooling rate of 1 °C/m.y.

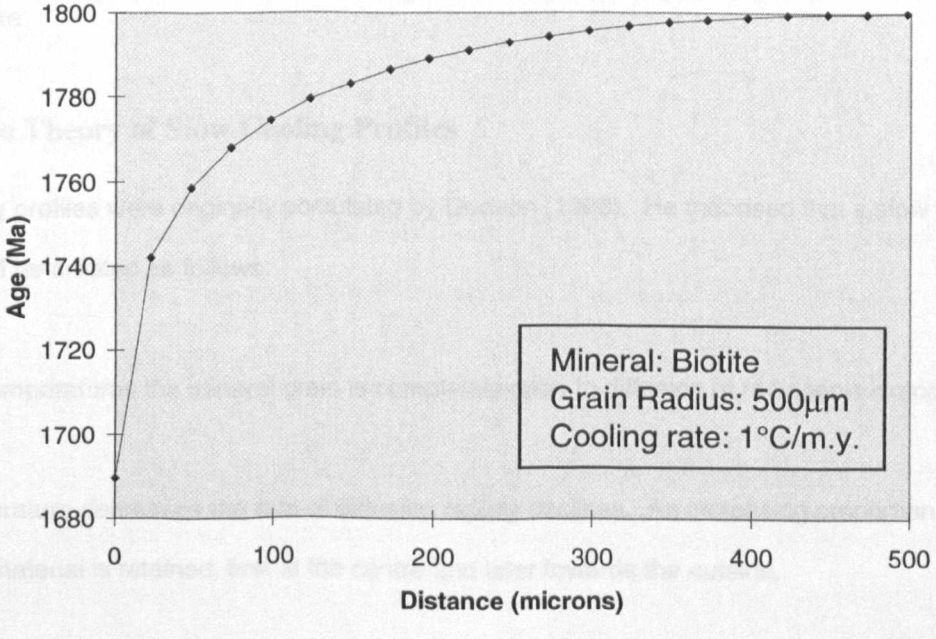

Figure 3.5: An example of a theoretical closure profile

near rim with a steep decline in ages occurring within the rim area (Dodson, 1986) (Figure 3.5) (section 3.7.2.2). By measuring these age variations within single mineral grains, and fitting the appropriate closure profile to it, the need for multiple mineral phase ages for determining cooling histories could be bypassed. This eliminates uncertainties caused by grain size differences between mineral phases affecting the closure temperatures, and uncertainties introduced by assuming similar cooling histories for closely related rocks. The age variations within single grains that can theoretically be introduced by slow cooling brings into question the validity of ages obtained for slowly cooled rocks by incremental heating or total fusion of single and multi-grained samples. If significant age variations within single mineral grains exist then "integrated" ages would fail to produce the correct age. However, until recently spatial resolution of geochronological techniques have not been high enough to establish whether the theoretical profiles actually appears in nature.

Recent work on age variations within single mineral grains using laser based ^{40}Ar-^{39}Ar techniques was limited to samples that cooled sufficiently slowly to exhibit age gradients within the 150-200 μm resolution of the CW Nd YAG and 50-80 μm resolution of the Ar-ion laser systems employed (Hames and Hodges, 1993; Hodges *et al.*, 1994; Hodges and Bowring, 1995; Hames and Andresen, 1996; Reddy *et al.*, 1996). However, using the UV laser microprobe it is now possible to carry out detailed age mapping to a 10 μm resolution and to more thoroughly determine whether slow cooling profiles exist in nature.

3.7.2.2. The Theory of Slow Cooling Profiles

Slow cooling profiles were originally postulated by Dodson (1986). He theorised that a slow cooling profile would be created as follows:

1) At high temperatures the mineral grain is completely open to diffusion of radiogenic isotopes.

2) As temperature decreases the rate of diffusion rapidly declines. An increasing proportion of the radiogenic material is retained, first at the centre and later towards the outside.

3) Eventually the blocking temperature is reached and the system begins to close. This occurs at the centre first and then nearer the outside until no more diffusion occurs.

4) A closure profile results from the variations across the grain. The system records a higher age in the centre than in its outer layers.

A theoretical profile can be constructed for any cooling system using the following equation:

$$E/RT_c(x) = Ln(\tau D_o / a^2) + G(x) \qquad \text{Equation [3.4]}$$

where :

E = activation energy

R = the gas constant

T_c = closure temperature

τ = time constant

D_0 = diffusion coefficient at an infinitely high temperature

a = linear grain size

G(x) = closure function (In micas this assumes an infinite cylinder geometry)

See Appendix 3.1 for more details.

The calculated ages are plotted against the position within the grain. In every case the model profile has an almost constant age from core to near rim, with a rapid decrease in age at the rim (Figure 3.5).

Once a series of analyses from the rim of a mineral grain has been made using the UV laser microprobe, the above equation can be used to construct a closure profile for the appropriate mineral species and grain size, adjusting the time constant until a reasonable fit to the data points is produced, thus giving an indication of the cooling history of the grain.

3.7.2.3. Previous Work on Slowly Cooled Rocks

1. Hames and Hodges, 1993

Muscovite and white mica pseudomorphs after kyanite were analysed from a complex terrain in the Vermont Appalachians. Initially analysis was carried out as incremental step-heating experiments from which muscovite yielded ^{40}Ar-^{39}Ar plateau and isochron ages of 420 ± 9 and 422 ± 3 Ma respectively. However, the data reflected a homogenous distribution of $^{40}Ar^*$ which resulted from only *in situ* decay of ^{40}K after Ordovician metamorphism and no appreciable loss of accumulated $^{40}Ar^*$ during the superimposed Devonian event. The white mica pseudomorphs from the same sample yielded plateau and isochron ages of 343 Ma. This was interpreted as a minimum estimate for the timing of the superimposed event. Some characteristics of the data from the step-heating experiments suggested that $^{40}Ar^*$ was distributed inhomogeneously and indicated that the sample had been disturbed and that a naturally varying isotopic distribution was partly homogenised by the analytical technique.

Micas from the same sample were subsequently analysed using an Ar-ion laser to produce melt pits 50 to 100 μm in diameter on a grain 3000 μm in diameter. These new data defined a broadly concentric age distribution with regions of lower ages inside the crystal. Core ages were a maximum of 462 Ma and ages along the edge varied from about 420 to 440 Ma. Younger ages were also found in association with *010* and *110* cleavage planes. No variations in major element distribution, atmospheric argon or excess argon were found. The age variations within the single mineral grain were believed to have formed during protracted cooling from 460 to 420 Ma, during an episodic loss event after 460 Ma, or as part of a complex combination of both. Defects were found to be at least locally important.

2. Hodges, Hames and Bowring, 1994

In this study muscovite and biotite from a monzogranite from the low-pressure-high-temperature metamorphic terrain in Crazy Basin, central Arizona were age dated. Both laser incremental heating of a single grain and detailed age mapping of a single grain using a focused laser beam was carried out and the results compared.

The incremental heating suggested an essentially uniform distribution of radiogenic ^{40}Ar in each crystal and yielded ages of 1412 ± 5 Ma for muscovite and 1410 ± 10 Ma for biotite. These findings suggest that rapid cooling in the order of 25 K/m.y. occurred after a reheating episode slightly before 1412 Ma.

The spot dating was achieved using an Ar-ion laser microprobe producing 50-100 μm pits. Numerous points on the grain were dated and a series of chrontours were fitted by eye. The spot dating highlighted age variations within a single crystal that were not apparent with incremental heating. The age variations were interpreted by the authors as indicating either a brief thermal pulse at ≤1270 Ma, which would cause episodic loss of radiogenic Ar, or extremely slow cooling over the interval between 1650 Ma and 1270 Ma. The episodic loss hypothesis was dismissed because no appropriate heat source is identifiable in the local geological setting.

3. Hodges and Bowring, 1995

Biotites from the Horse Mountain monzogranite were used in this study. Horse Mountain is about 5 km west of the Crazy Basin Pluton in central Arizona. As in the previous study, single crystals were incrementally heated as well as analysed using spot dating and the results compared. In addition, total fusion was undertaken on 25 biotite fragments and further comparisons were made.

The incremental heating using a defocused laser beam gave a flat age spectra with near-plateau ages of ~1190 Ma. There was no indication of intracrystalline ^{40}Ar inhomogeneity. Total fusion resulted in apparent ages ranging from 1212 to 1006.7 Ma. The detailed age mapping using a focused laser beam (~30 μm spot size) confirmed the dispersion of ages found using the total fusion technique. A 200 m.y age gradient within single crystals was evident.

Within the 2 crystals spot dated two mechanisms of diffusion are apparent. These are volume diffusion on the scale of the grain radius, and rapid diffusion along discrete zones of high crystal defect density. However, overall the age dispersion in the 2 crystals was interpreted by Hodges and

Bowring (1995) as being consistent with the development of the observed age gradients by slow cooling at an average rate of 0.5 K/m.y.

3.7.3. *Using* DIFFARG

Advancements in computer technology has allowed more sophisticated modelling of age variations within single mineral grains to be attempted. The closure profile equation devised by Dodson (1986) is limited to a linear cooling history but in nature rocks may undergo a complicated history involving reheating, rapid cooling followed by slow cooling, a period where very little cooling occurs, or even exposure to excess argon. In such situations, it would be unlikely that the Dodson equation closely fitted the data points produced.

DIFFARG is a Matlab 4.1 computer program that uses finite-difference algorithm to simulate argon diffusion profiles for any thermal history. As with the Dodson equation, volume diffusion through the mineral lattice is assumed to be the dominant process. However, the program has the ability to incorporate elements such excess argon, reheating, periods of quiescence and other events into the model. As before, known factors such as mineral species and grain size can be entered to the program and the thermal history altered until a profile that fits the data points is found. It is possible that several different models may closely fit the data points so any known geological history for the study area is useful to construct the most likely thermal history for the rocks in question.

For full details of *DIFFARG* see Wheeler (1996).

3.7.4. *Fast Diffusion Pathways*

Unfortunately, the concept of blocking temperatures and closure profiles are both dependent on the mineral grain in question being structurally perfect and volume diffusion being the dominant process. In reality, of course, mineral grains are never perfect and contain a number of different defects, cleavage traces, etc. that can all facilitate rapid diffusion of argon out of, or even into, the grain. Lee (1995) devised the term "multi-path" diffusion for this type of rapid diffusion.

Although the heterogeneous distribution of elements within a mineral caused by chemical reactions and contamination from impurities can be detected by techniques such as microprobe analysis, defect-enhanced diffusion is more difficult to identify. However, defect-enhanced diffusion may still have a significant impact on the overall distribution of elements within a mineral and this, clearly, will affect the apparent age obtained. In ^{40}Ar-^{39}Ar dating, for example, the distribution of potassium and argon within a mineral will be influenced by the different atomic radii and valencies of these elements. Argon has a larger atomic radius than its parent potassium so will potentially occupy different crystal sites. Argon may prefer to locate within structural defects which are larger and where the argon will have lower potential energy and/or higher binding energy (Lee, 1995). Such defects may include lattice dislocations, microfractures, and cleavage traces. When a high spatial resolution technique such as the UV laser microprobe is employed, heterogeneous concentrations of potassium and argon could potentially produce different apparent ages that may or may not be geologically meaningful. Therefore, multipath diffusion may result in significant age variations within a single grain.

According to Lee (1995), the impact of multi-path diffusion may change depending on grain size. When the grain size is small, volume diffusion will be the dominant diffusion mechanism because the length scale for lattice diffusion to the grain boundary will be short. However, in larger grains, multi-path diffusion will have a greater influence on solute transport because the diffusing solute species will be more likely to interact with the fast paths. Although volume diffusion theory predicts that cooling ages and closure temperatures will be affected by grain size, multipath diffusion may override that effect, resulting in cooling ages and closure temperatures that are independent of grain size. Instead, the effective diffusion dimension will be the influential factor but determining this can be difficult. When interpreting apparent ages and closure profiles, it is important to take the effect of multi-path diffusion into account as it can significantly affect the ages obtained and can change the shape, and therefore the apparent meaning, of any closure profiles produced. This study will, therefore, also attempt to use the high-spatial resolution of the UV laser microprobe to determine the effective diffusion dimensions influencing the age variations within single mineral grains.

Geochronological studies that have suggested that multipath diffusion may play an important role in the interpretation of the geochronological data include Onstott and Peacock (1987), Parson *et al.*

(1988), Kelley *et al.* (1989), Burgess *et al.* (1992), Kelley and Turner (1991), and Lee (1993, 1995). These studies found argon concentration profiles in single mineral grains that could not be explained by volume diffusion alone. Multipath diffusion may also be responsible for apparent ages in minerals with a high blocking temperature appearing younger than a mineral in the same rock with a lower blocking temperature (Harrison and Fitz Gerald, 1986; Davidson, 1991; Miller *et al.*, 1991). In these cases the pathways allowed either rapid diffusion of argon out of a mineral, yielding unusually low ages, or facilitated the introduction of excess water into the crystal as H_3O^+ that displaced radiogenic ^{40}Ar, causing a lowering of the K/Ar ratio.

Chapter 4 - Sample Locations and Descriptions

4.1. The Samples

4.1.1. Sample Selection

In order to undertake ^{40}Ar-^{39}Ar dating it was necessary to collect samples that contained K-bearing minerals. Of primary interest were rocks that contained abundant matrix mica and inclusion-rich garnets. These samples would allow the analysis of both matrix biotite and biotite inclusions in garnet from the same rock, facilitating direct comparison between the mean matrix biotite age and the age of included biotite. Rocks containing muscovite and hornblende were also of interest as the different blocking temperatures of these mineral species can be used to give an indication of the cooling rate of the rocks from the metamorphic peak.

The main focus of this project was the Ruby Range, Tobacco Root Mountains and Highland Mountains of the south-western Montana portion of the Wyoming Province (Figure 2.2). During a two week sampling excursion to Montana samples were collected from these three mountain ranges. Although a good geographical coverage was attempted, heavy rainfall and flood conditions made access to some regions impossible. In the Tobacco Root Mountains rocks in close proximity to the Tobacco Root Batholith were also collected to investigate the resetting properties of the batholith on the surrounding rocks (Figure 2.4).

The rocks collected in the field were supplemented by samples supplied by Dr Peter Dahl from his Ruby Range collection. Samples RM37, RM39, RM40, RM42, RMC93, RMC200, and 70-30-2 were selected by Dr Dahl because they contained large garnets with abundant biotite inclusions suitable for this research. These were used for initial experimentation before the field excursion. Sample RMC42 was selected because it contained both biotite and muscovite, allowing direct comparison between the apparent ages of the two mica species. A further 9 samples were supplied by Dr Eric

Erslev, collected from the South Madison Range in order to extend the area of investigation beyond the 'Giletti Line' (Figures 2.2 and 2.7).

4.1.2. Sample Description Format

The following descriptions are derived mainly from thin section observations, augmented with photomicrographs and backscatter images (Plates 4.1 to 4.16), together with microprobe analysis of the main minerals where available (Tables 4.1 to 4.4 and Appendix 4.1 to 4.4). Photomicrographs were taken using a *Polaroid* digital microscope camera attached to a *Leica DMRP* petrological microscope, using a magnification of x25, with image capture operated through *Adobe Photoshop 5.0.2*. All images in this chapter are presented at the same size to allow comparisons between grain sizes etc. Microprobe analysis was carried out on a *Cameca SX100* as described in Appendix 3.2. Results are given in Tables 4.1 to 4.4 as mean values of replicate analyses of one or more mineral grain in the same rock, and full probe data can be found in Appendix 4.1 to 4.4. Because of the selective nature of this research, these descriptions are not exhaustive and do not cover all the lithologies within the study area. Instead they provide a general picture of the petrology and the petrochemistry of the garnet, biotite and hornblende of the analytical samples. Lithological subdivisions used are those described in chapter 2.

4.2. The Ruby Range

Two of the three principle Precambrian rock units within the Ruby Range were sampled, with the majority of the samples collected from the Christensen Ranch Metamorphic Suite (Figure 4.1 and Figure 4.2) because this was the easiest to access and contained the minerals of interest. Some samples were also collected from the Older Gneiss and Schist in the central eastern Ruby Range.

4.2.1. Older Gneiss and Schist

4.2.1.1. The Cottonwood Creek Area

Sample 70-30-2 was located on the boundary between quartzofeldspathic gneiss and older gneiss and schist (Figure 4.1). The mineralogy is essentially biotite, quartz, andesine, almandine,

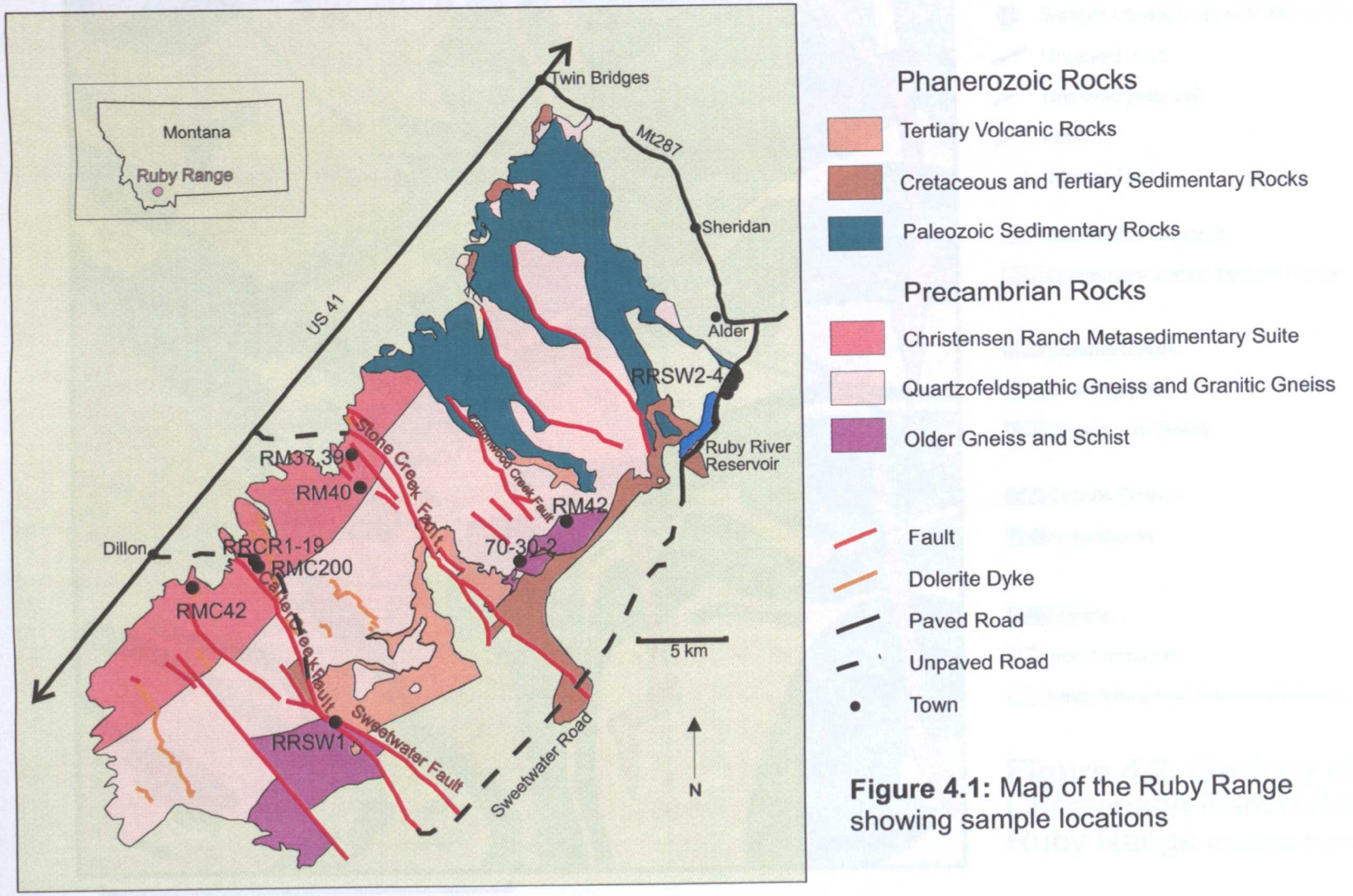

Figure 4.1: Map of the Ruby Range showing sample locations

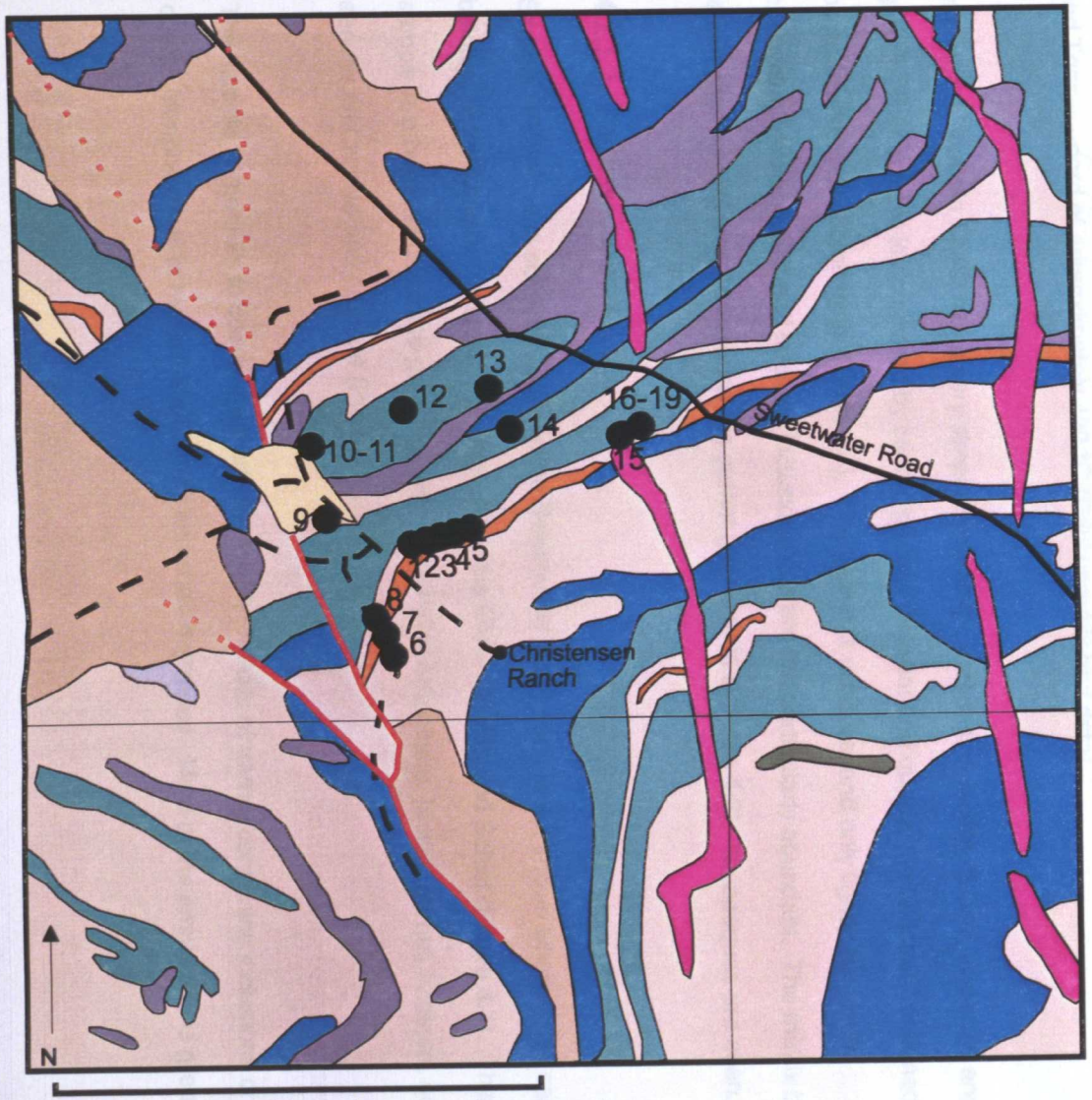

Sample Location (all samples prefixed with RRCR)

Unpaved road

Unpaved jeep trail

Fault

Inferred fault

Quaternary Deposits

Quaternary and/or Tertiary Rocks

Dolerite Dykes

Small Bodies

Sheets and Dykes

Granite Gneiss

Amphibolite

Marble

Iron Formation

Undifferentiated Metasedimentary Rocks

Figure 4.2: Geology of the Christensen Ranch Area of the Ruby Range (modified from James, 1990)

cordierite, sillimanite, apatite, opaques (rutile, ilmenite and perovskite) and unknown alteration product (Plate 4.1). This is the only cordierite-bearing rock examined from the Ruby Range with the cordierite occurring within the matrix (Plate 4.1) and as a coronal phase on the garnet. Probe data for the cordierite are shown in Table 4.4 and Appendix 4.4 along with data for sillimanite and andesine. 70-30-2 is a medium grained rock with porphyroblastic garnet. Garnets (probe data in Table 4.1) are only a maximum of few millimetres in diameter and some are elongate. They have a subhedral form and have a few inclusions of all matrix minerals seen. The biotite (probe data in Table 4.2) reveals a preferred orientation and is seen to wrap around garnet (Plate 4.1). It is fairly fine grained but pristine. Cordierite and sillimanite follow the preferred orientation, along with an unidentified alteration product (Plate 4.1). Although this alteration was also probed, the uneven surface of the mineral made probe results unreliable and it was not clear from the chemical analysis what the mineral was. Garnet/cordierite thermometry gave $Tgar_{(CORE)}$-cord of approximately 675 °C and $Tgar_{(RIM)}$-cord of approximately 490 °C (Dahl unpublished data).

In contrast, sample RM42 has a very simple mineralogy, comprising biotite, quartz, andesine and garnet. This sample is dominated by coarse grained feldspar and quartz, the feldspar confirmed to be andesine by probe analysis (Table 4.4). The garnet is euhedral and only lightly fractured, containing biotite, quartz and feldspar inclusions that are not particularly abundant. The matrix biotite is fine grained and wrapped around the garnet (probe data in Table 4.2). No opaques are seen.

4.2.1.2. The Sweetwater Area

Sample RRSW1 was collected close to the Sweetwater Fault but it is not known whether the sample belongs to the Quartzofeldspathic Gneiss unit or the Older Gneiss and Schist (Figure 4.1). This sample is a hornblende-biotite-garnet gneiss, comprising amphibole, biotite, garnet, feldspar, quartz, sericite and zoisite and prehnite (Plate 4.2).

The sample is medium to coarse grained with porphyroblasts of garnet containing inclusions of quartz. Amphibole is in highest abundance and coarse grained. Most of the amphibole is green

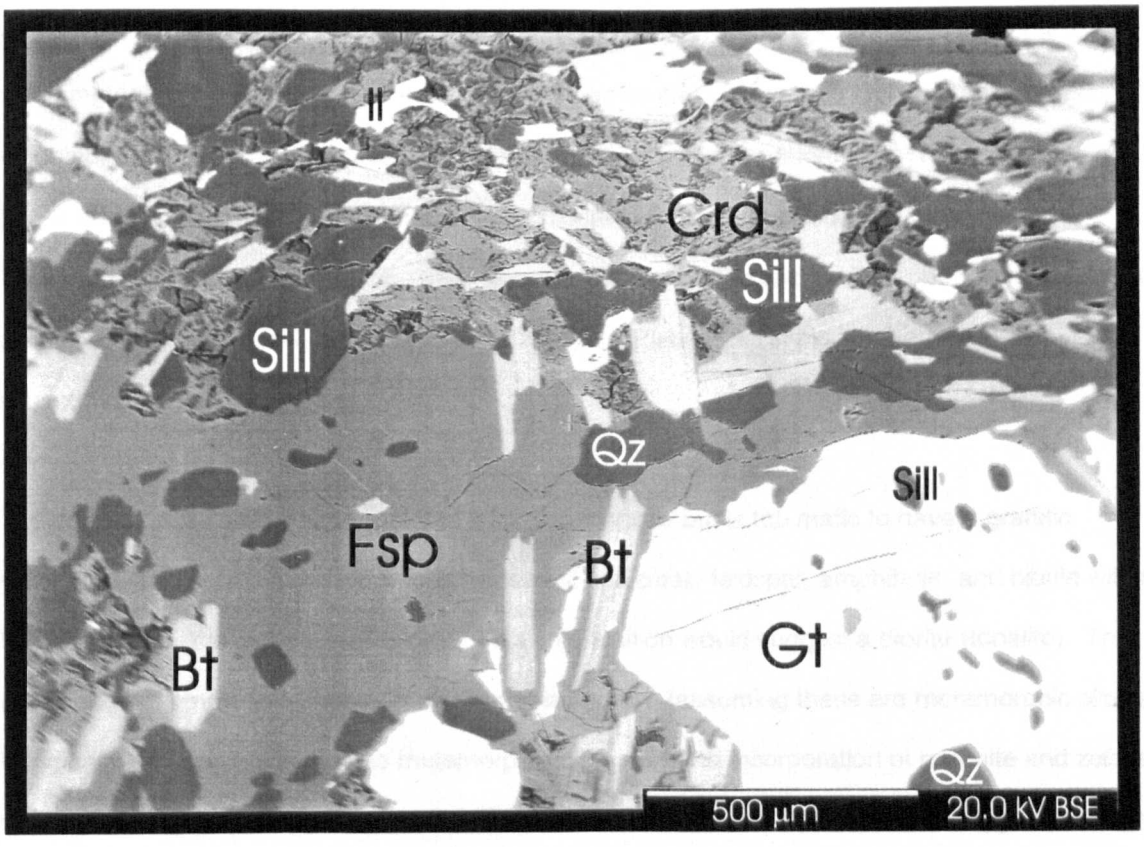

Plate 4.1: Backscatter image of 70-30-2 microprobe section showing occurrence of cordierite and sillimanite

and pleochroic, likely to be hornblende, but a colourless, non-pleochroic amphibole, probably cummingtonite also occurs (Plate 4.2). Studs of apatite can be found as included phases within the amphibole. Biotite is also relatively abundant and has a preferred orientation. However, most of the biotite is highly altered along the cleavage to chlorite together with zoisite and characteristic 'hourglass' formations of prehnite. (see Plate 4.2, Table 4.4, and section 7.2). Sericitised plagioclase occurs, still showing some occasional albite twinning (Plate 4.2). In places there is also saussuritisation of the feldspar.

The general texture would suggest that it is meta-igneous but is too mafic to have a granitic precursor. The protolith most probably contained sodic/calc feldspar, amphibole, and biotite with no K-feldspar and little evidence of quartz. This composition would suggest a diorite (tonalite). The occurrence of amphibole, biotite, garnet and plagioclase (assuming these are metamorphic phases) is indicative of amphibolite facies metamorphism. Finally, the incorporation of prehnite and zoisite within the biotite and plagioclase, and the presence of chlorite and sericite would suggest a low grade retrogressive metamorphic event.

The higher CaO in the garnet compared to other garnet analyses from the Ruby Range (Table 4.1) is consistent with a difference in bulk composition and the presence of amphibole. A high Al_2O_3 component in the biotite relative to other samples (Table 4.2) also suggests an influence from the bulk composition of the protolith.

4.2.2. Christensen Ranch Metamorphic Suite

4.2.2.1. The Christensen Ranch Area

Samples collected from this area were from the undifferentiated metasedimentary rocks of the Christensen Ranch Metamorphic Suite (Figures 4.1 and 4.2). Peak metamorphism for this area was amphibolite facies, estimated to be 710 °C; 5-7 Kb by Desmarais (1981) and 645 ± 45 °C; 6.2 ± 1.2 Kb by Dahl (1979, 1980) (see section 2.3.3.1),

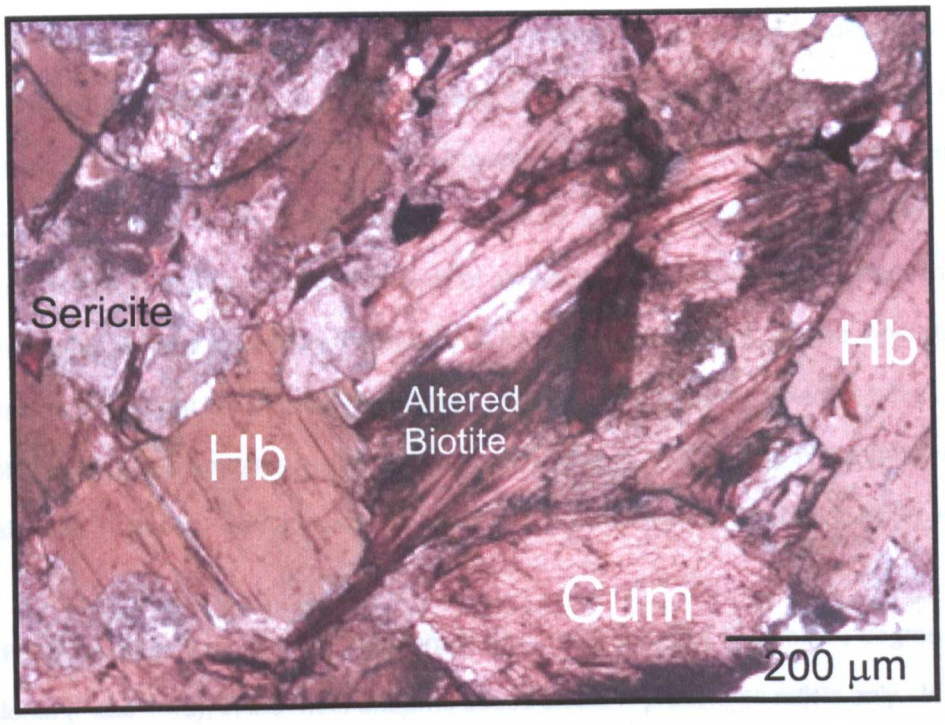

A) Photomicrograph of RRSW1 in PPL

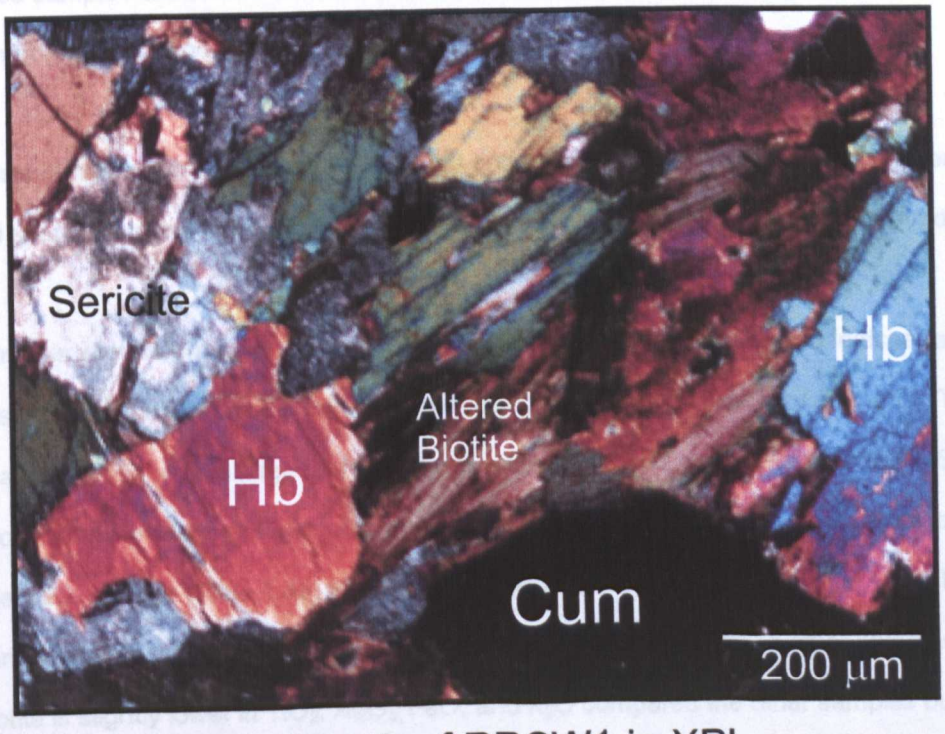

B) Photomicrograph of RRSW1 in XPL

Plate 4.2: Photomicrograph of RRSW1 showing association of amphibole and biotite, and degree of alteration

A) Biotite-garnet Gneiss

The biotite-garnet gneisses collected from this unit are medium grained rocks with a simple mineralogy, comprising biotite, garnet, quartz, plagioclase (albite and pericline twinning) and opaques (Plate 4.3). Banding is generally on a millimetre scale but can be poorly defined. Garnet is present as porphyroblasts, visible at millimetre scale in rock specimens. From probe data (Table 4.1) it is apparent that the garnet is predominantly of almandine composition. In thin-section the garnets are euhedral to skeletal and highly fractured and fragmented (Plate 4.3). In the most strongly banded samples the garnet is elongate, having been deformed by a strong flattening fabric. Inclusions of biotite, quartz and opaques are present within the garnet, the majority in communication with the matrix via fractures. Some samples show a rotated syn-tectonic fabric in the garnets (Plate 4.3).

In some samples the biotite appears pristine but most samples show some degree of alteration to chlorite (Plate 4.4a), in the most extreme cases biotite is present as relicts only. In samples RRCR2, 3 and 5 the biotite is pristine (Plate 4.3) and the mean matrix biotite chemistry from probe data from these samples are shown in Table 4.2. The biotite laths follow a preferred orientation and wrap the garnet (Plate 4.3 and 4.4b).

Felsic minerals include quartz, plagioclase and microcline. Opaques occur as accessories both as a rod shaped mineral following the orientation of the biotite grains, and as more rounded grain.

Samples with deformed and altered biotite often also contain fibrolite and feldspar extensively altered to sericite. Studs of epidote minerals may also be present in accessory amounts. This is indicative of a retrograde assemblage that may be the result of fluid flow or metamorphism. Sample RMC200 shows some evidence of this retrogression, containing warped and ragged biotite laths, slightly altered to chlorite (Plate 4.4a) with extensive sericitisation of feldspar (Table 4.4). The garnet in this sample shows higher MgO and lower FeO concentrations than in the other samples (Table 4.1). The biotite is slightly lower in TiO_2, Al_2O_3, FeO, and K_2O compared the other samples but has a higher concentration of Na_2O (Table 4.2).

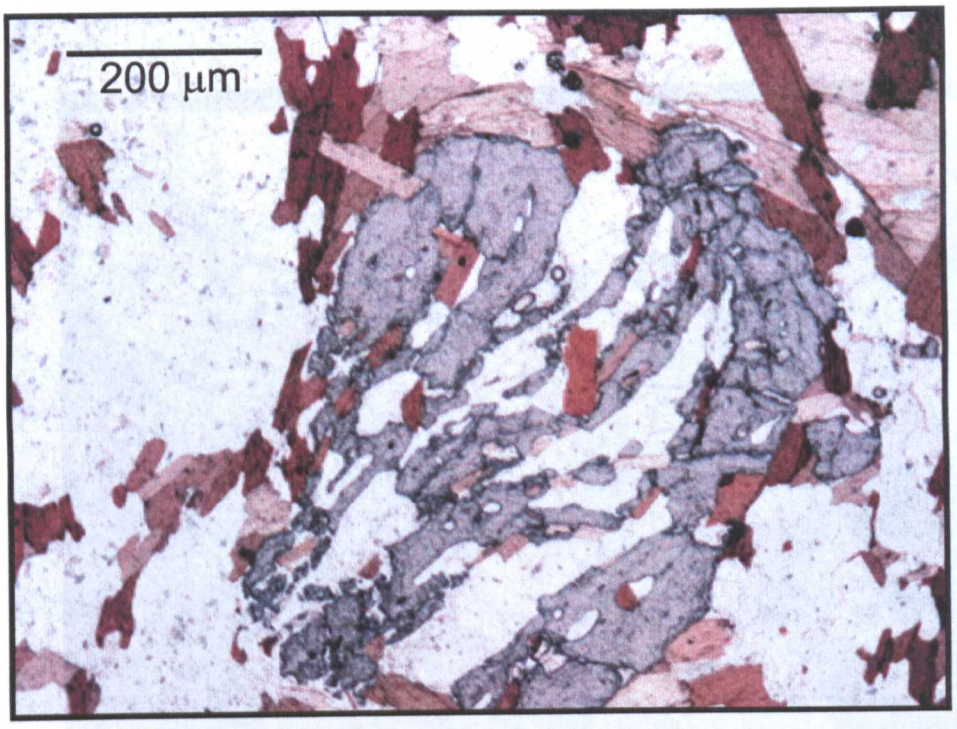

Plate 4.3: Photomicrograph of RRCR5 in PPL showing syntectonic fabric in garnet and pristine biotite

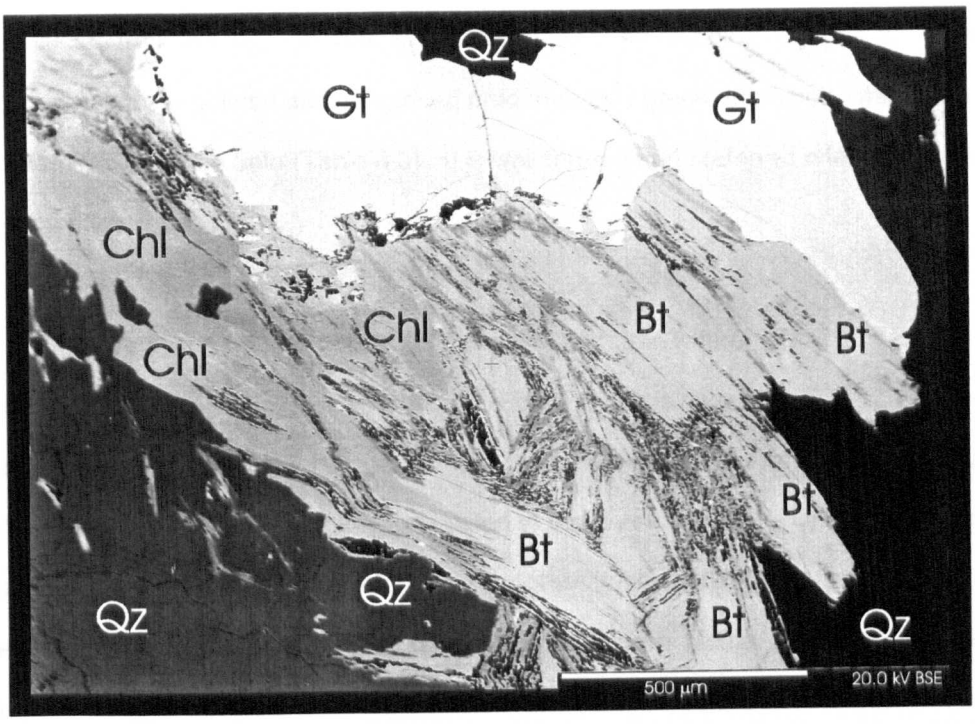

A) Backscatter image of RMC200 microprobe section showing alteration of biotite to chlorite

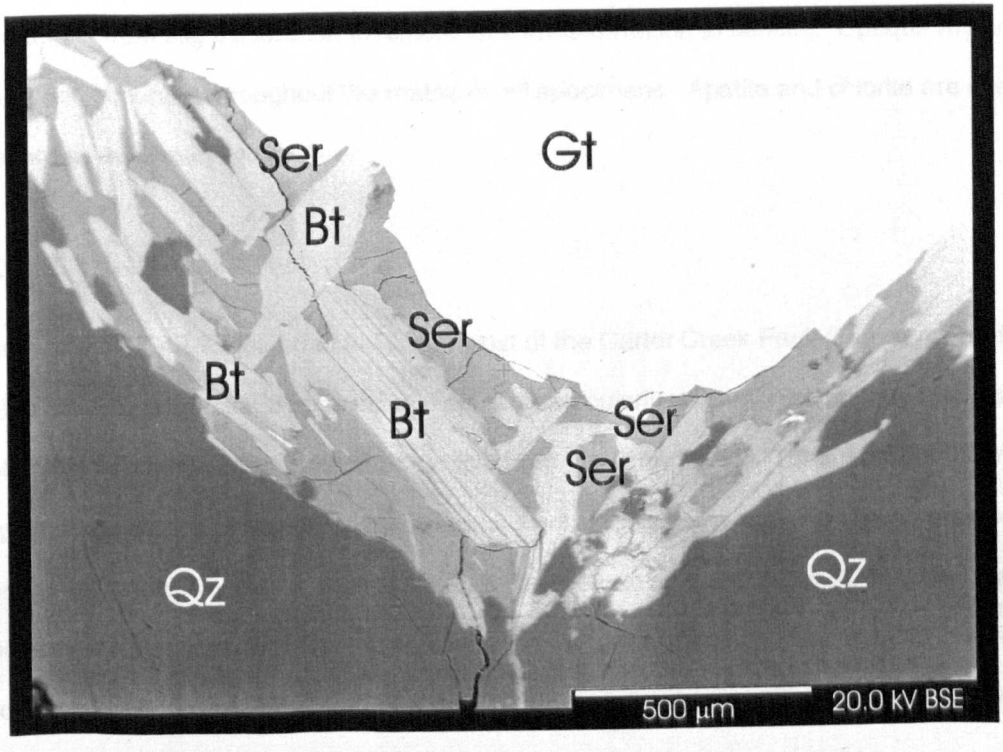

B) Backscatter image of RMC200 microprobe section showing a garnet corona texture

Plate 4.4: Backscatter image of RMC200 microprobe section

B) Amphibolite

Also collected from this location were several samples of amphibolite (Figure 4.2). These ranged from fine to medium grained and comprised predominantly green amphibole which was confirmed to be hornblende by probe data (Table 4.3). It is well formed and preferred orientation is apparent under the microscope.

Both garnetiferous and non-garnetiferous samples occur and where garnet is present it is as porphyroblasts ranging up to millimetre scale. Probe analysis showed that the garnet contained higher concentrations of CaO than garnet from the biotite-garnet gneisses (Table 4.1), probably resulting from different bulk composition related to the parentage of the lithologies. Garnets are generally sub- to euhedral and undeformed but poikiloblastic with numerous inclusions, concentrated in the core of the garnet, of quartz and opaques with very rare biotite. Biotite is not present in the matrix.

Other matrix minerals include quartz, plagioclase and opaques. In all samples feldspar is altered but this ranges from slight alteration to almost total transformation to sericite. Opaque minerals are abundant, occurring throughout the matrix on all specimens. Apatite and chlorite are occasionally present as accessory minerals.

4.2.2.2. The Carter Creek Area

Metapelite RMC42 is located to the south-west of the Carter Creek Fault (Figure 4.1 and 4.2), adjacent to a post-tectonic pegmatite. This is a particularly unusual rock sample because it contains both biotite and muscovite. No other sample from the Ruby Range, Tobacco Root Mountains, and Highland Mountains obtained for this research contains muscovite. It is a coarse grained rock, comprising principally biotite, muscovite, and very coarse quartz (Plate 4.5). Accessory amounts of opaques are also present. The muscovite, and to a lesser extent the biotite, in this sample are in the process of yielding to sillimanite (Plate 4.5). This is a prograde alteration process involving the reaction of muscovite and quartz to form sillimanite, K-feldspar and water. In

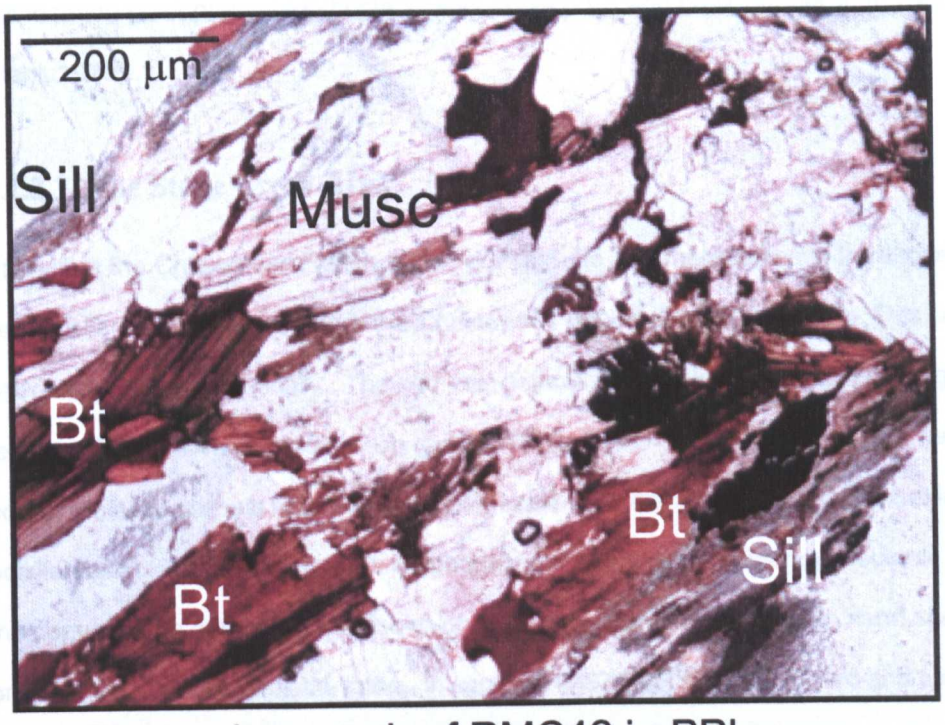

A) Photomicrograph of RMC42 in PPL

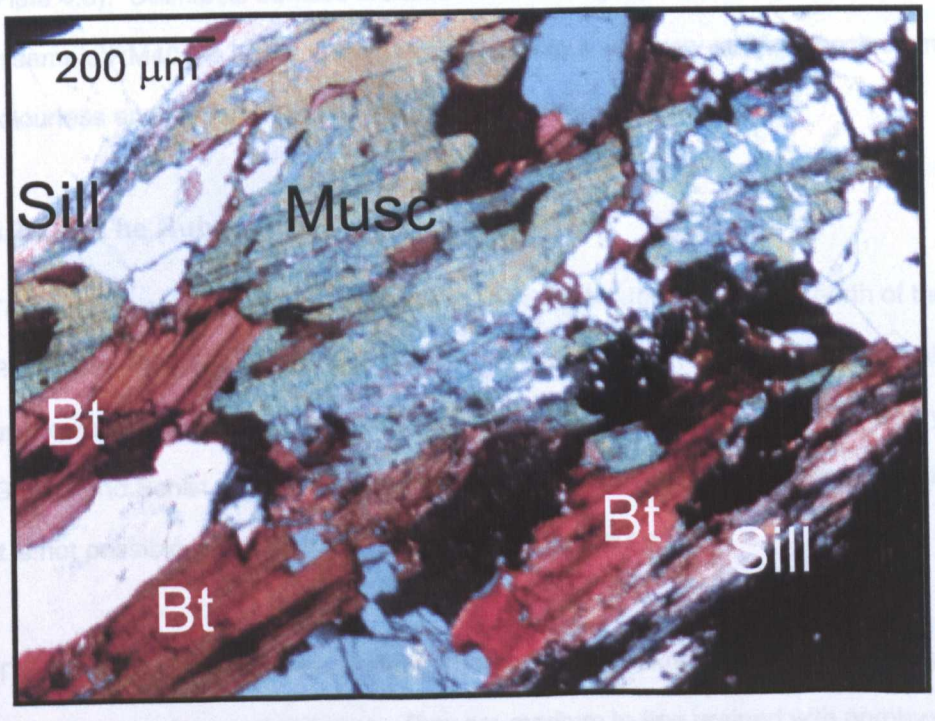

B) Photomicrograph of RMC42 in XPL

Plate 4.5: Photomicrographs of RMC42 showing association of biotite and muscovite and breakdown of muscovite to sillimanite

this location peak pressure (lithostatic) was about 6 Kb and peak temperature was about 660 ± 30 °C (Dahl, 1979).

4.2.2.3. The Stone Creek Area

Still within the Christensen Ranch Metamorphic Suite, the metapelites in the Stone Creek area are very similar to the gneisses from the Christensen Ranch area (Figure 4.1). This can be seen both petrologically and chemically. The samples generally comprise biotite, quartz, oligoclase/andesine feldspar (Table 4.4), almandine-rich garnet (Table 4.1) and ilmenite. They are medium grained with porphyroblastic garnets reaching millimetre scale. Garnet tends to be subhedral in form and poikiloblastic. Inclusions are mostly opaques and quartz with a clear syn-tectonic rotational fabric in the centre of the garnet but with inclusion free rims. Banding is visible in hand specimen with a preferred orientation of biotite laths. In sample RM37 the biotite is warped and turning to sillimanite (fibrolite) (Table 4.4). Fibrolite runs through the rock in thin threads, following the biotite orientation (Plate 4.6). Sillimanite bundles are also found infilling a pseudomorph, possibly of relict andalusite. In sample RM40 the biotite is a striking green colour with very strong pleochroism from dark green to colourless and chemically has a low TiO_2 concentration (Table 4.2).

4.2.2.4. The Ruby River Reservoir Area

These samples were situated adjacent to the Sweetwater Road to the north of the Ruby River Reservoir. They fall outside the geologically mapped area (Figure 4.1) of the Ruby Range so it is unknown to which unit they belong. As the mineralogy and microprobe chemistry of the Older Gneiss and Schist does not vary significantly from that of the Christensen Ranch Metamorphic Suite it is not possible to assign them to a unit on these grounds.

The rocks here appear to be biotite-garnet-quartz gneisses generally comprising garnet, biotite, quartz, plagioclase and opaques. They are medium to fine grained with porphyroblastic garnets ranging to centimetre scale. Garnet is present in all rocks but its abundance varies. The garnets are euhedral to subhedral and contain numerous inclusions of biotite, quartz and opaques. The matrix biotite is mostly only incipiently altered but some chlorite is present in some samples. There

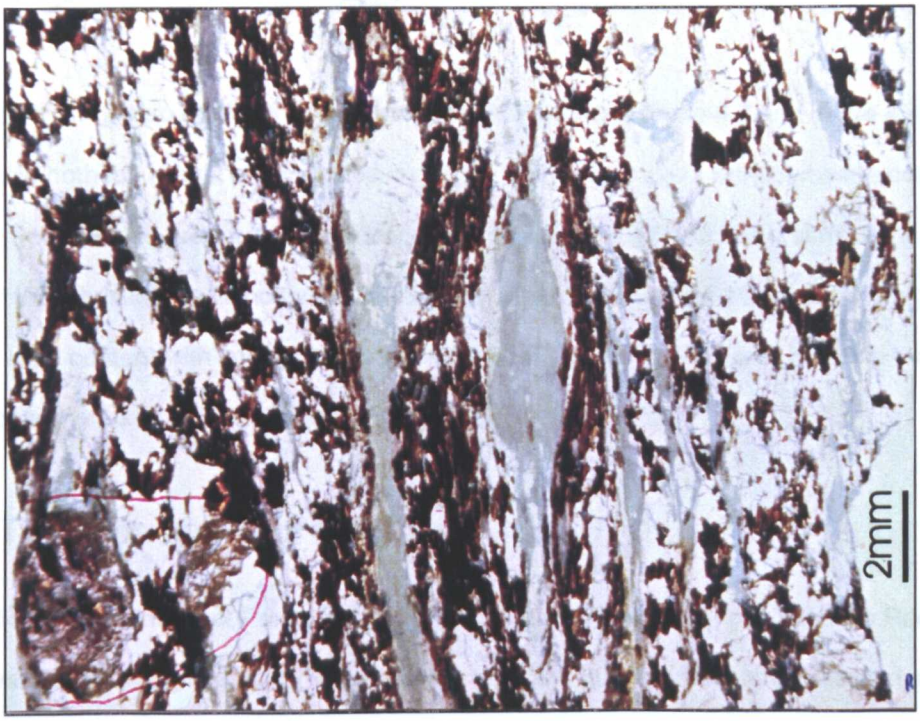

Plate 4.6: Photograph of thick section of sample Rm37 showing foliation and fibrolite

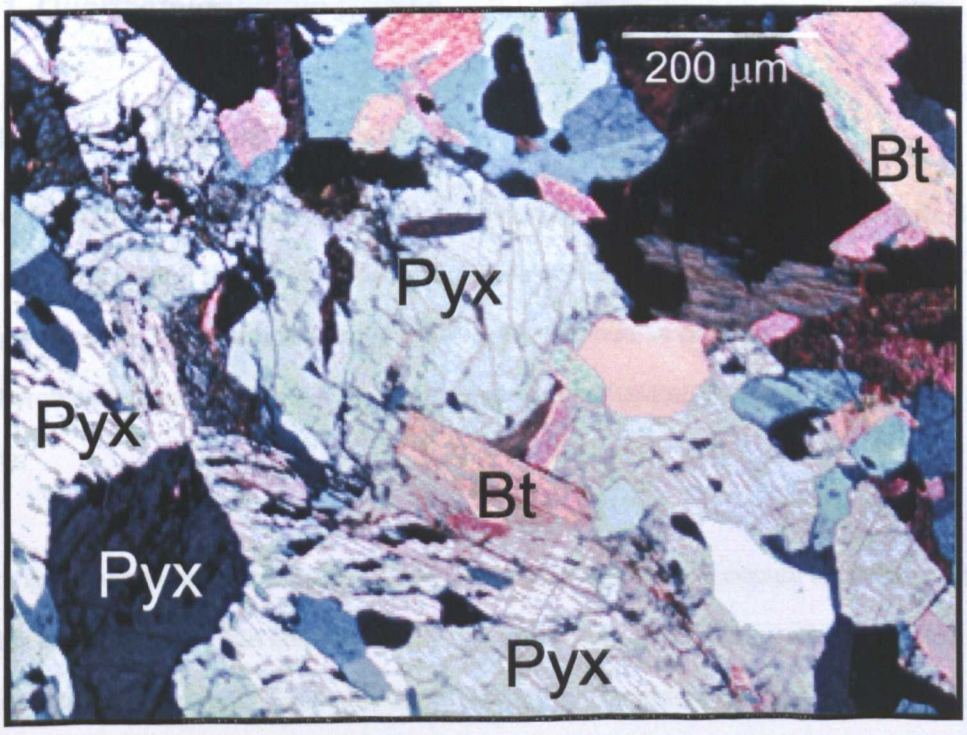

Plate 4.7: Photomicrograph of RRSW2 in XPL showing association of pyroxene and biotite

is a preferred orientation evident. Quartz and plagioclase in the matrix are also mainly unaltered with only a few patches of sericite seen in places.

Sample RRSW2 also contains large grains of orthopyroxene (Plate 4.7 and Table 4.4) and sphene is present in both the matrix and included in garnet. The presence of orthopyroxene could indicate a higher metamorphic grade. Although the garnet in sample RRSW3 has a similar chemistry to that seen in the Christensen Ranch area, garnet in sample RRSW2 and 4 both show a significantly higher MgO content with corresponding lower FeO (Table 4.1). Similarly, biotite in these samples have lower FeO and K_2O and higher MgO and Na_2O (Table 4.2).

4.3. The Tobacco Root Mountains

In section 2.4 a number of Precambrian lithologies are described for the Tobacco Root Mountains. However, of principle interest for this research were the quartzofeldspathic gneiss and amphibolite. Within the quartzofeldspathic gneiss unit, the sub-divisions of quartz-feldspar biotite gneiss and plagioclase-quartz-hornblende-biotite gneiss were sampled.

4.3.1. Quartzofeldspathic Gneiss

4.3.1.1. Quartz-feldspar Biotite Gneiss

As the name of this unit implies these rocks comprise essentially quartz, feldspar (plagioclase and K-feldspar), and biotite, but they also contain varying amounts of garnet and accessory amounts of opaque minerals. The samples range from medium to coarse grained, with a granular matrix and porphyroblasts of garnet (Plate 4.8). All samples are dominated by the felsic minerals, particularly quartz.

Banding is seen in hand specimen as thin layers of biotite. Biotite occurs as small, well formed laths in fairly low abundance but showing strong preferred orientation and, occasionally, flow banding around garnet (Plate 4.8). Examples of probe data for the matrix biotite are displayed in Table 4.2. The garnets range from euhedral with few fractures, to anhedral and fragmental.

Plate 4.8: Photograph of thick section of sample TRMR2 showing porphyroblastic texture and foliation

Fractures occasionally contain alteration products. Inclusions are mostly biotite and quartz with occasional feldspar and opaque minerals. Chemical analyses of garnet for samples TRER7, TRBC2 (Figure 4.3) and TRMR2 are shown in Table 4.1. Most samples appear unaltered but there is a range of alteration states to those with abundant sericite, chlorite and epidote (Table 4.4). In the most altered samples only relict biotite and feldspar survive. Occasionally sillimanite or studs of epidote occur in accessory amounts within the mafic bands.

4.3.1.2. Plagioclase-quartz-hornblende-biotite Gneiss

Again this rock unit is characterised by abundant felsic minerals including quartz, plagioclase, K-feldspar with some sericite in altered rocks. The rocks are medium to coarse grained with porphyroblasts of garnet. Banding is seen both on a large scale and as orientated minerals under the microscope.

Hornblende and biotite are present in all samples (Plate 4.9) but the abundance of these varies. The hornblende tends to occur as large grains (Plate 4.9), most showing preferred orientation but occasionally present as discrete bundles. Even in samples showing altered feldspar and biotite the hornblende remains apparently unaltered. Inclusions of biotite are occasionally found within the hornblende and in one sample the hornblende has a poikiloblastic texture, containing feldspar, biotite and opaque minerals. Biotite tends to be in lesser abundance and usually occurs in association with garnet or with the hornblende (Plate 4.9). However, in some samples the biotite occurs throughout the slide and occasionally it is as abundant as the hornblende. Probe data for hornblende and biotite for sample TRER6B (Figure 4.3) can be found in Tables 4.2 and 4.3. In Table 4.2 it can be seen that the biotite has a higher CaO concentration than for the biotite in the quartz-feldspar biotite gneisses. This is a common occurrence in biotite from hornblendic rocks and is related to bulk composition.

Garnet varies in size and abundance. It ranges from euhedral to anhedral and from containing few inclusions to being poikiloblastic. Included phases are generally quartz, biotite, and opaques, with

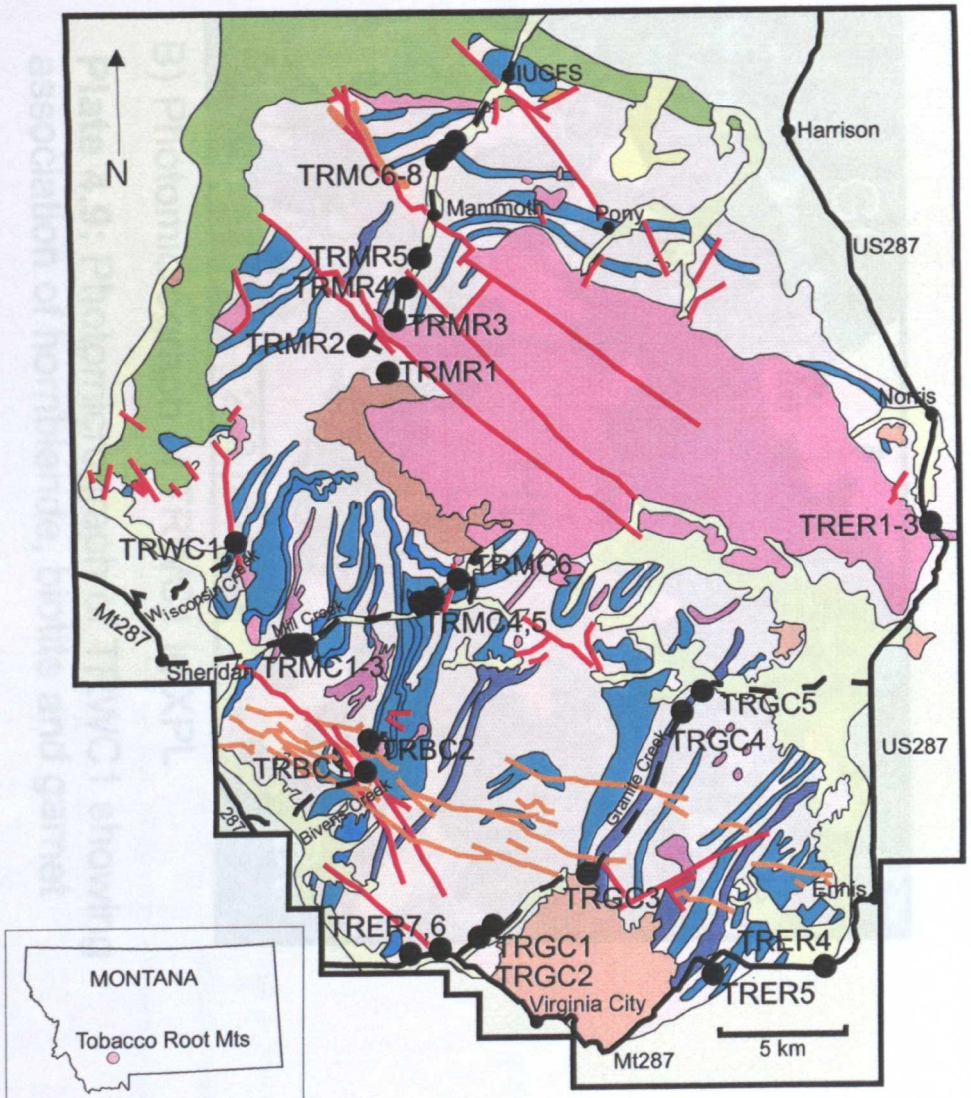

Fault
Lithological Boundary
Town
287 Paved Road
Unpaved Road
IUGFS Indiana University Geological Field Station

Tertiary and Quaternary
Alluvium
Volcanic Rocks

Paleozoic To Mesozoic
Silicic Plutonic Rocks
Phanerozoic Sedimentary Rocks

Precambrian
Dolerite Dykes
Metabasic Intrusive Rocks
Garnet Gneiss
Marble and Associated Calc-silicate Rocks
Iron Formation
Anthrophyllite-gedrite Gneiss Assemblage
Hornblende Gneiss, Granulite, and Pelitic and Quartzose Metasediments
Quartzofeldspathic Gneiss

Figure 4.3: Map of the Tobacco Root Mountains showing sample locations

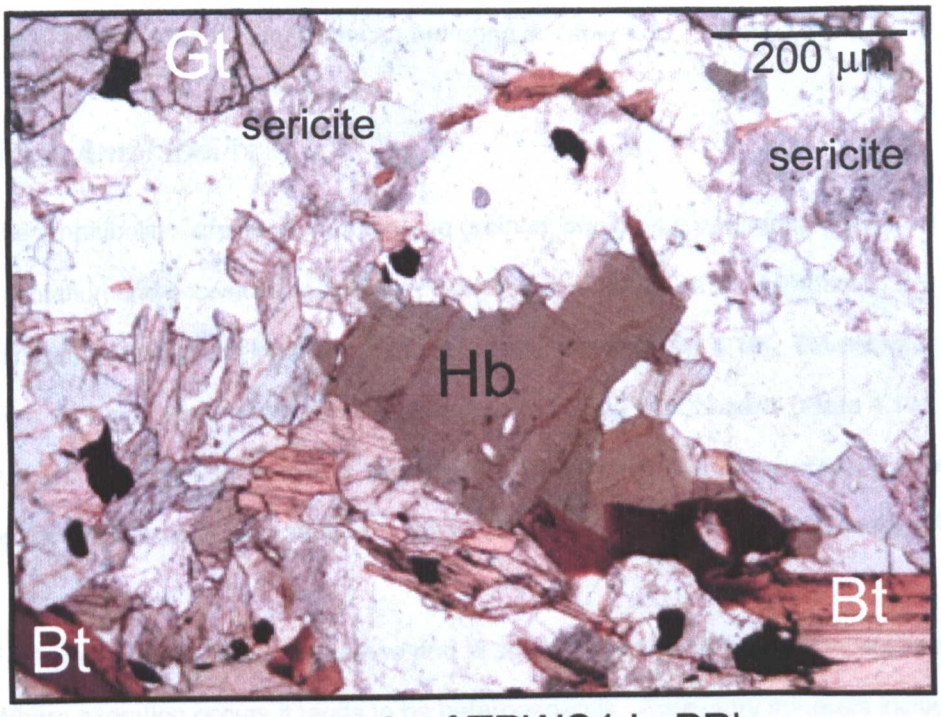

A) Photomicrograph of TRWC1 in PPL

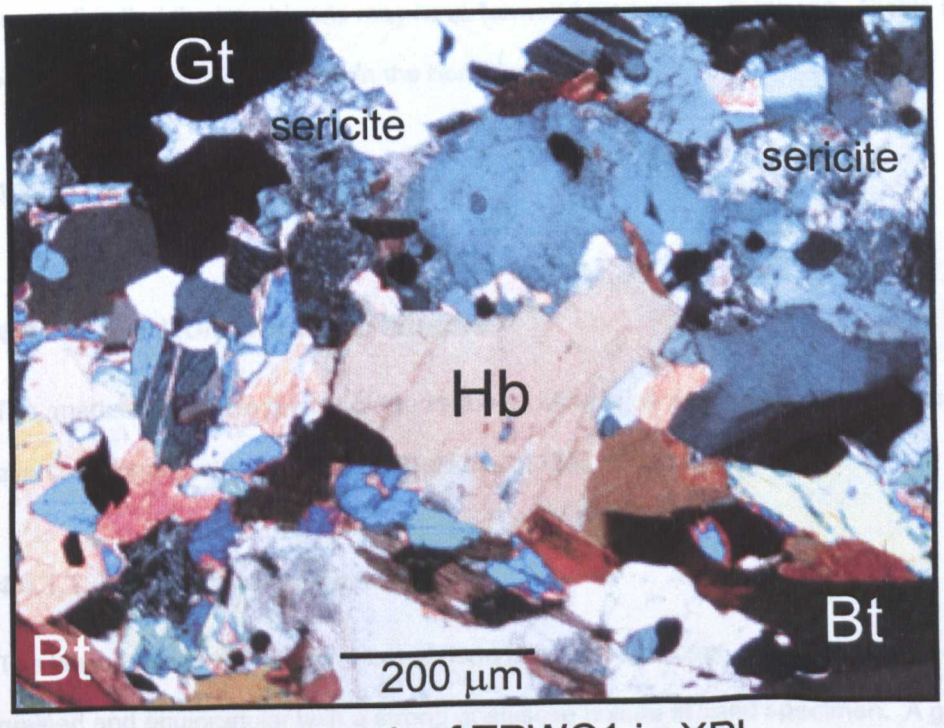

B) Photomicrograph of TRWC1 in XPL

Plate 4.9: Photomicrograph of TRWC1 showing association of hornblende, biotite and garnet

occasional chlorite. In one sample the garnet is apparently being replaced by cordierite. An example of a chemical analysis of garnet can be found in Table 4.1.

4.3.2. Amphibolite

The amphibolites are medium to coarse grained, equigranular, generally showing preferred orientation and occasionally exhibiting banding on a large scale. Hornblende is the dominant mineral, usually green in colour but occasionally brown (Plate 4.10). Garnet varies in abundance from very abundant to absent. It ranges from euhedral to subhedral (Plate 4.10), is usually well fractured with inclusions mainly of quartz and hornblende and lesser amounts of epidote and opaques. Cordierite and sericite coronas occur around the garnet in some samples.

Feldspar is in fairly high abundance and in some specimens is degrading to sericite (Plate 4.10). Where alteration occurs it tends to be heterogeneous. Accessory minerals include epidote, opaques and apatite. Relict pyroxene is also present in some samples associated with the hornblende, suggesting that the hornblende may have formed from primary pyroxene. Biotite is only rarely seen, occurring as very thin laths within the hornblende.

4.4. The Highland Mountains

4.4.1. Quartzofeldspathic Gneiss

The quartzofeldspathic gneiss of the Highland Mountains was subdivided into leucocratic gneiss and quartz-feldspar-biotite gneiss by O'Neill *et al.* (1988) (Figure 4.4).

4.4.1.1. Leucocratic Gneiss

The leucocratic gneiss (Figure 4.4) is dominated by K-feldspar, plagioclase, and quartz. It is medium grained and equigranular with a strong gneissose texture in hand specimen. A general preferred orientation is defined by matrix biotite and sillimanite in thin section. Alteration is heterogeneous. In places the biotite is pristine and elsewhere it is being altered to chlorite. In

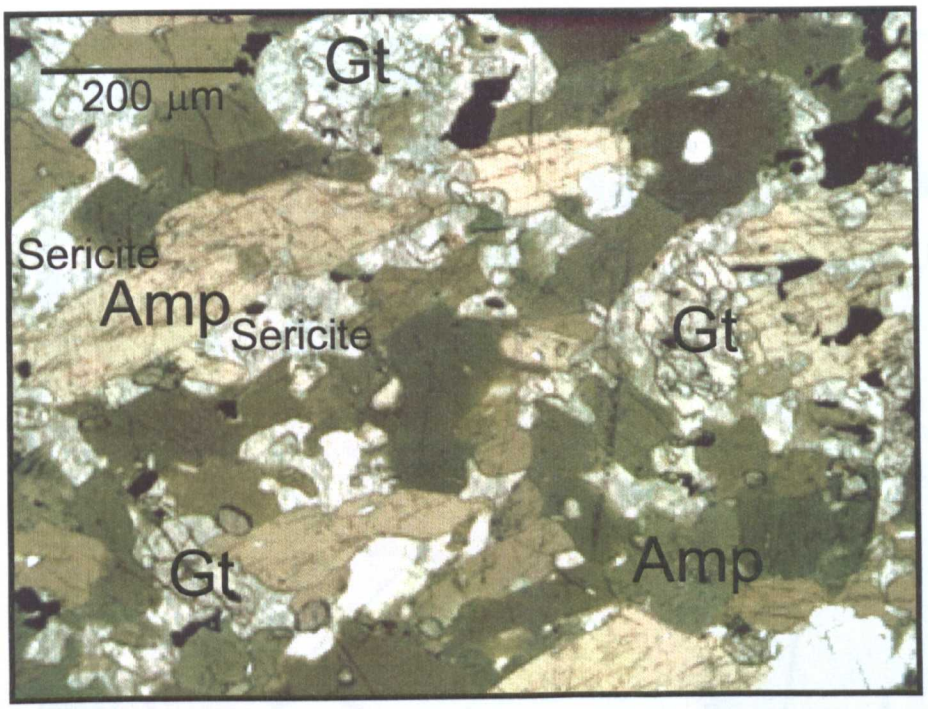

A) Photomicrograph of TRMR8B in PPL

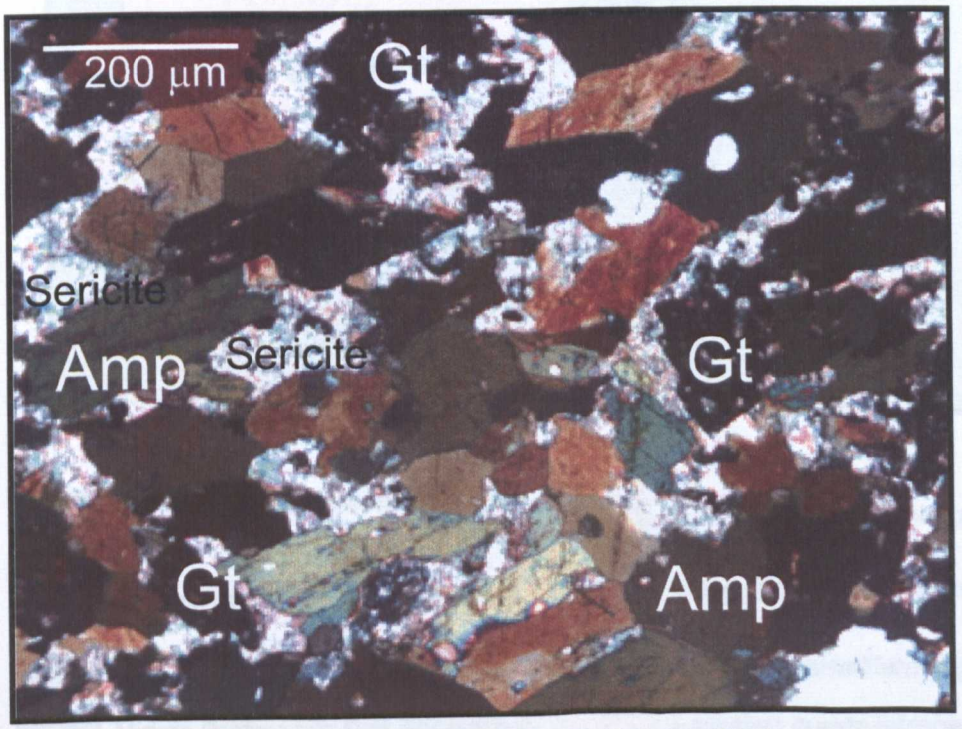

B) Photomicrograph of TRMR8B in XPL

Plate 4.10: Photomicrograph of TRMR8B showing typical amphibolite textures

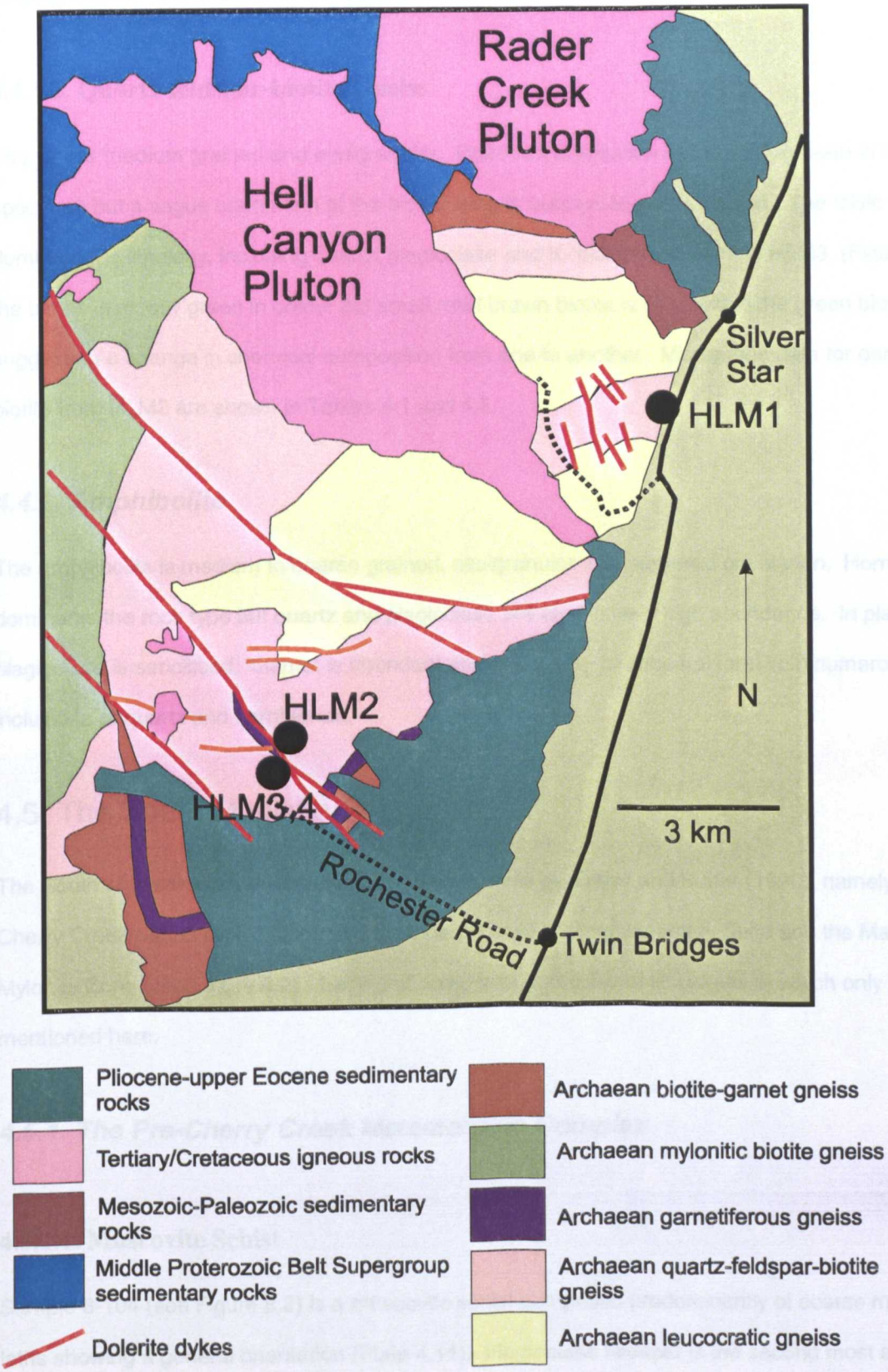

Figure 4.4: The Highland Mountains with sample locations (modified from O'Neill *et al.*, 1988)

some areas distinct knots of chlorite are observed. Garnet is fairly abundant and occurs as porphyroblasts. It is subhedral with abundant inclusions of biotite and quartz.

4.4.1.2. Quartz-feldspar-biotite Gneiss

This unit is medium grained and equigranular. Preferred orientation is more easily seen in hand specimen but a vague orientation of the biotite laths is noticeable in thin section. The felsic minerals dominate the lithology, including quartz, plagioclase and K-feldspar. In sample HLM3 (Figure 4.4) the biotite is mostly green in colour but small relict brown biotite is seen within the green biotite suggesting a change in chemical composition from one to another. Microprobe data for garnet and biotite from HLM2 are shown in Tables 4.1 and 4.2.

4.4.2. Amphibolite

The amphibolite is medium to coarse grained, equigranular with preferred orientation. Hornblende dominants the rock type but quartz and plagioclase are also in fairly high abundance. In places the plagioclase is sericitised. Garnet is abundant and has a sub- to anhedral form with numerous inclusions of quartz and hornblende.

4.5. The South Madison Range

The South Madison Range was divided into three units by Erslev and Sutter (1990), namely the Pre-Cherry Creek Metamorphic Complex, the Cherry Creek Metasedimentary Suite and the Madison Mylonite Zone (see Figure 8.2). Each unit comprises a number of lithologies of which only some are mentioned here.

4.5.1. The Pre-Cherry Creek Metamorphic Complex

4.5.1.1. Muscovite Schist

Sample 8-104 (see Figure 8.2) is a muscovite schist composed predominantly of coarse muscovite laths showing a general orientation (Plate 4.11). Plagioclase feldspar is the second most abundant mineral and is also coarse grained. Some large patches of sericite are evidence of degradation of

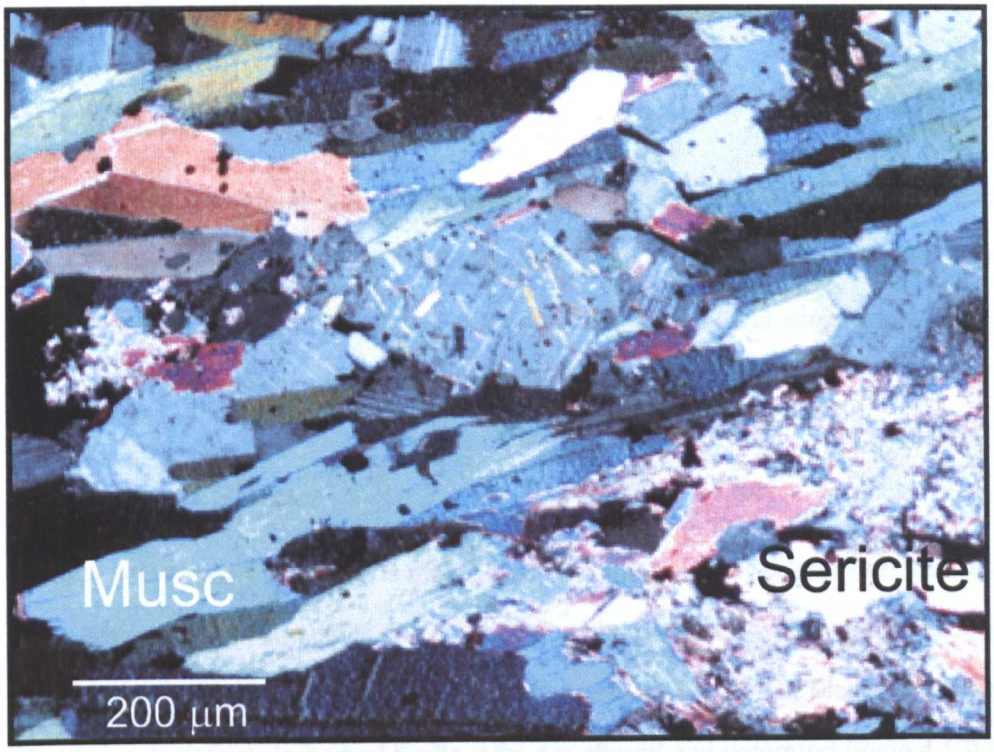

Plate 4.11: Photomicrograph of 8-104 in XPL showing general mineralogy

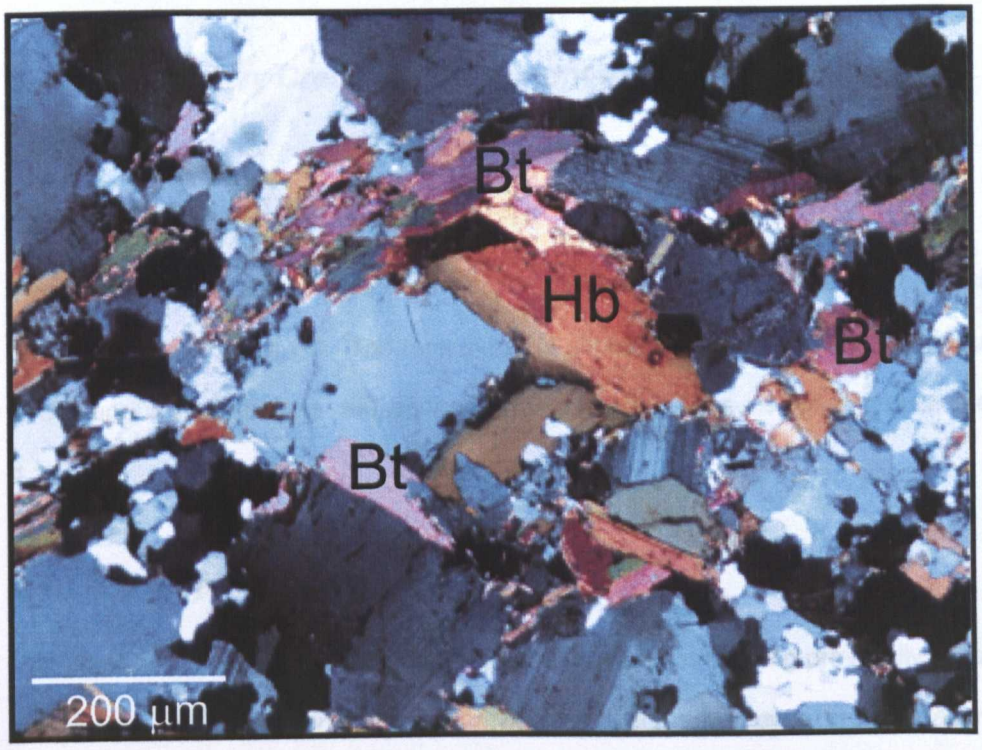

Plate 4.12: Photomicrograph of 8-152 in XPL showing general mineralogy

plagioclase (Plate 4.11). A few large grains of elongate quartz are also present. Scattered throughout the rock are tiny grains of sphene.

4.5.1.2. Biotite-hornblende Schist

Sample 8-152 (see Figure 8.2) is a biotite-hornblende schist. It is dominated by coarse plagioclase and K-feldspar with subordinate medium grained quartz (Plate 4.12). Hornblende is poorly formed with ragged edges. Also present are small laths of olive green biotite, slightly altered at the edges (Plate 4.12). There is no obvious preferred orientation. No opaques are present.

4.5.1.3. Biotite Schist

Sample 8-114 (see Figure 8.2) is a biotite schist. It is generally coarse grained but a whole range of sizes are seen. The sample is dominated by coarse grains of plagioclase, K-feldspar and quartz (Plate 4.13). Fine grained rounded quartz grains are also present. Biotite is medium grained and olive green in colour. Individual biotite laths are altered and deformed (Plate 4.13) and together they define an apparently folded fabric. Occasional porphyroblasts of garnet occur and are highly fractured, with no inclusions. Accessory opaques occur.

4.5.2. The Cherry Creek Metasedimentary Suite

4.5.2.1. Muscovite Quartzite

Sample SMR1 is a quartz-muscovite schist with a very simple mineralogy, comprising only quartz and muscovite (Plate 4.14). The rock consists almost entirely of coarse grained quartz showing strong undulose extinction. Muscovite is present as thin laths exhibiting preferred orientation (Plate 4.14).

4.5.2.2. Semi-pelitic Schist

The semi-pelitic schists are medium to coarse grained, comprising principally mica and quartz with lesser amounts of feldspar and garnet. The rocks generally show a strong foliation with orientation of the mica laths. However, the mica in sample 9-51 is apparently randomly orientated. Both biotite

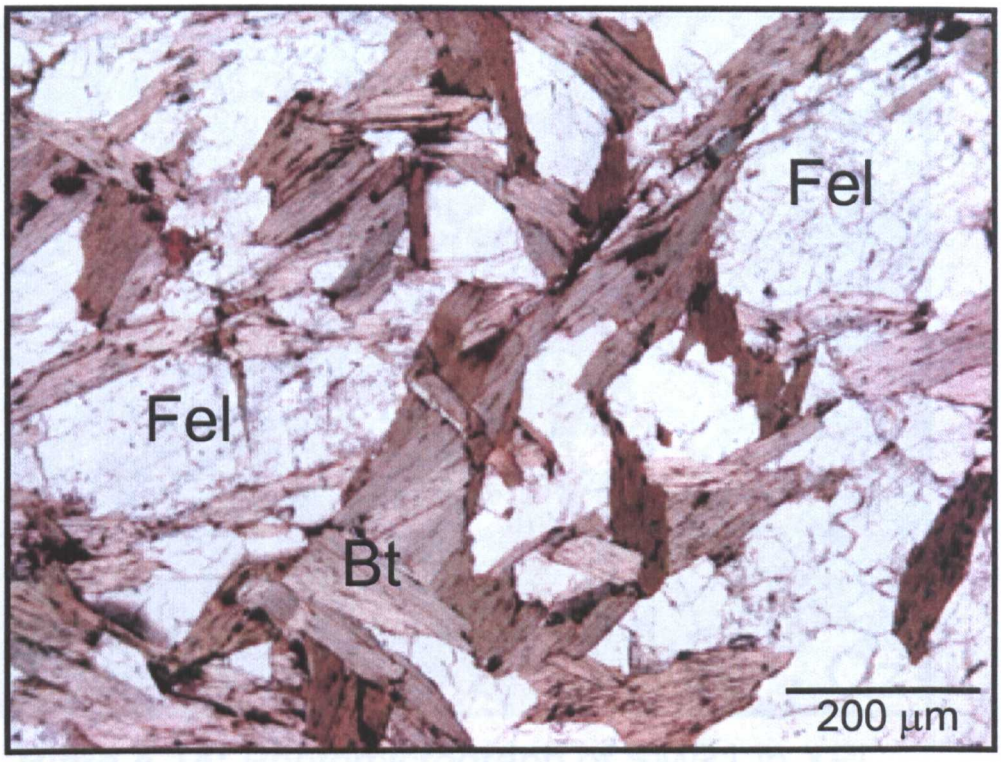

A) Photomicrograph of 8-114 in PPL

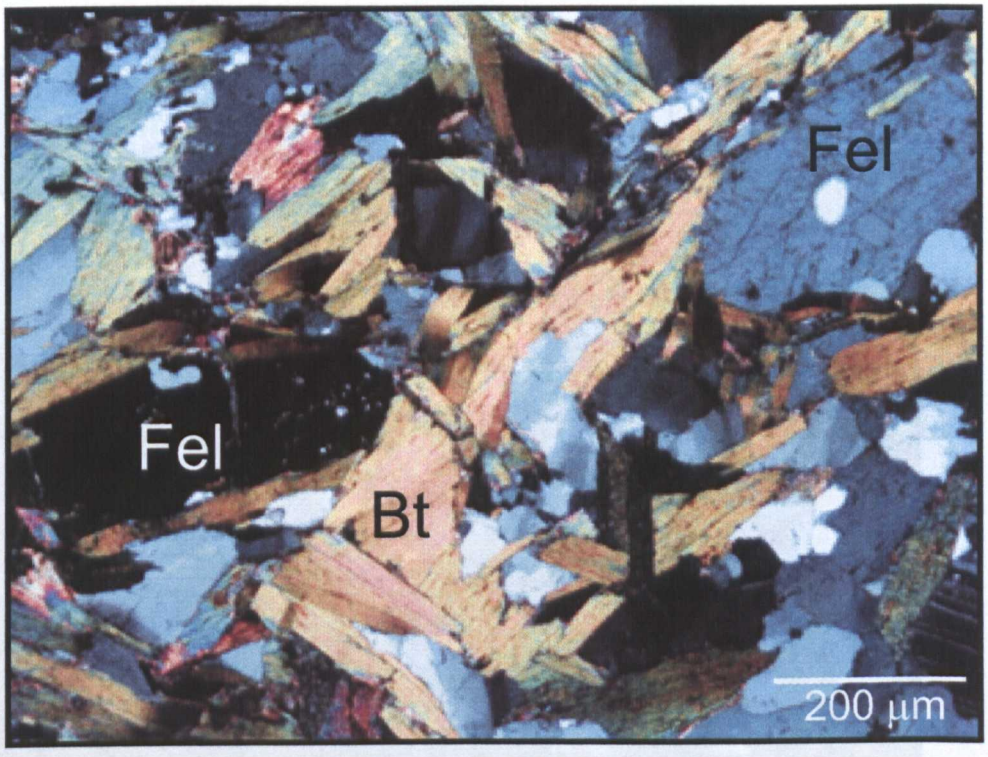

B) Photomicrograph of 8-114 in XPL

Plate 4.13: Photomicrograph of 8-114 showing general mineralogy and textures

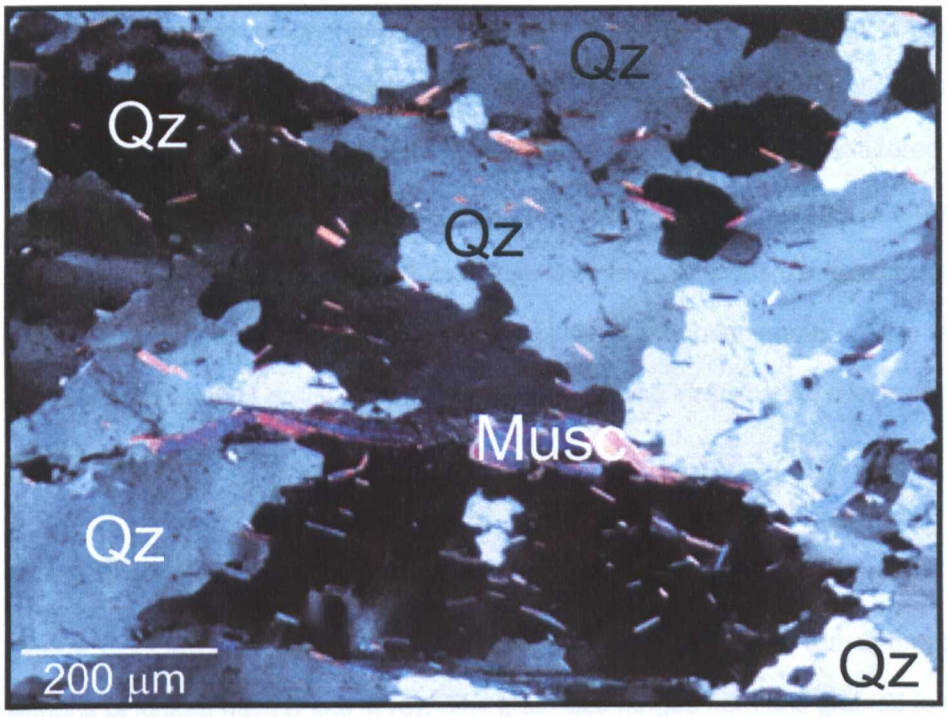

Plate 4.14: Photomicrograph of SMR1 in XPL showing simple quartz-muscovite mineralogy

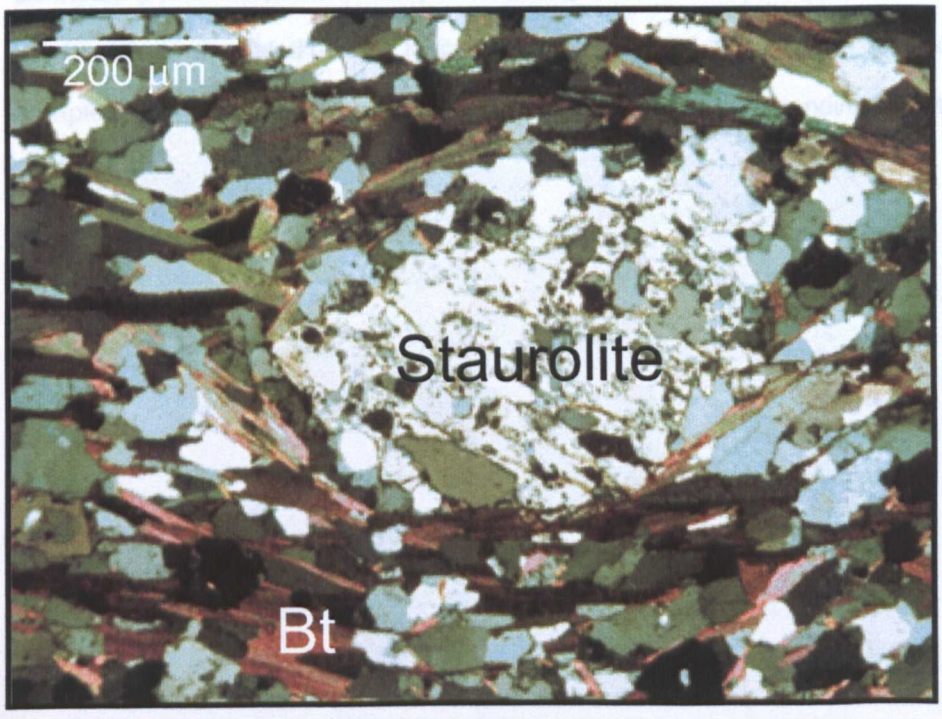

Plate 4.15: Photomicrograph of 9-49 in XPL showing staurolite porphyroblast and associated textures

and muscovite mica are present but muscovite is in lower abundance than biotite. There are degrees of alteration of the mica between different rock samples, however where biotite is altered to chlorite along the cleavage, coexisting muscovite shows only slight alteration. Quartz occurs as a granular groundmass with only occasional feldspar present. In the most altered samples the feldspar is extensively broken down to sericite. Garnet is present as small euhedral studs of comparable size to the other minerals in the rock. It contains only a few inclusions but is fractured and some show alteration along the fractures. Accessory amounts of opaque minerals occur. In sample 9-49 there are porphyroblasts of poikiloblastic staurolite, containing inclusions of quartz and biotite, wrapped by mica (Plate 4.15).

4.5.3. The Madison Mylonite Zone

These rocks are characterised by a fine to very fine grained texture with strong banding of quartz and ribbons of kinked mica (Plate 4.16). The grain size ranges from fine grained to ultra fine grains when observed under the microscope with occasional coarser grains of elongated quartz. No feldspar was observed. Samples 7-68 and 8-15a contain both biotite and muscovite, although muscovite is more abundant (Plate 4.16), and in sample 8-14b only muscovite is present. Accessory opaque minerals are frequently elongated parallel to the fabric. In sample 8-14b they are elongated and bent, and in sample 8-15a the opaques are small and rounded but follow the banding (Plate 4.16).

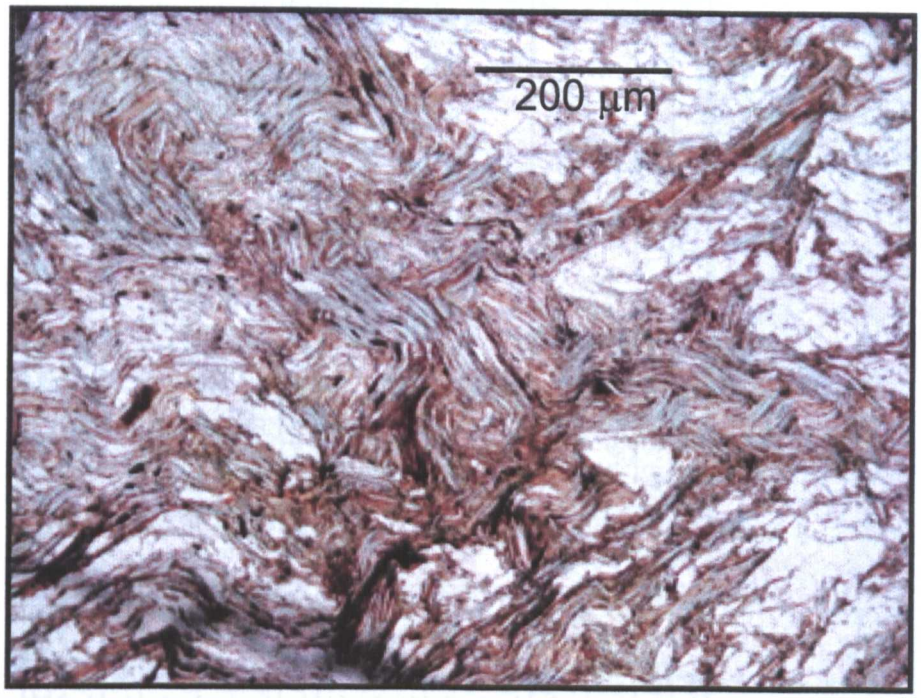

A) Photomicrograph of 8-15a in PPL

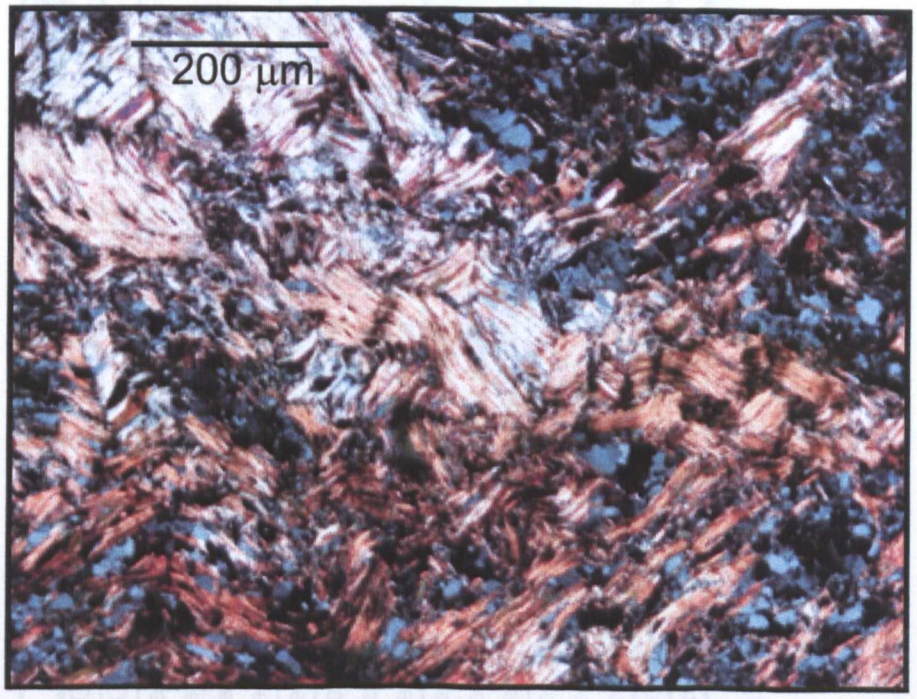

B) Photomicrograph of 8-15a in XPL

Plate 4.16: Photomicrographs of 8-15a showing fine grained and kinked micas

Table 4.1. Mean garnet electron microprobe analyses, expressed as oxide weight percent

Range	Unit	Sample	SiO_2	TiO_2	Al_2O_3	MgO	CaO	MnO	FeO	MgO/FeO	Total	No. Analyses
Ruby Range	Older Gneiss & Schist	70-30-2	37.66	0.01	21.84	6.66	1.43	0.70	31.68	0.21	99.98	5
Ruby Range	Older Gneiss & Schist	RRSW1	37.53	0.04	21.73	4.95	5.28	1.31	30.34	0.16	101.19	12
Ruby Range	Christensen Ranch Metamorphic Suite	RRCR2	36.64	0.01	21.27	3.16	2.05	1.05	36.24	0.09	100.42	7
Ruby Range	Christensen Ranch Metamorphic Suite	RRCR3	36.54	0.01	21.28	3.50	1.29	0.66	37.40	0.09	100.68	20
Ruby Range	Christensen Ranch Metamorphic Suite	RRCR5	36.54	0.01	21.26	3.03	1.10	0.93	38.12	0.08	101.00	19
Ruby Range	Christensen Ranch Metamorphic Suite	RMC200	38.21	0.02	21.53	6.69	2.13	0.33	32.02	0.21	100.9	29
Ruby Range	Christensen Ranch Metamorphic Suite	RRCR12	37.40	0.02	21.58	4.45	5.10	0.93	31.49	0.14	100.97	16
Ruby Range	Christensen Ranch Metamorphic Suite	RM37	37.04	0.05	20.87	2.52	1.38	0.69	38.38	0.07	100.93	5
Ruby Range	Christensen Ranch Metamorphic Suite	RM39	37.16	0.10	20.85	3.11	1.33	0.49	37.93	0.08	100.97	43
Ruby Range	Christensen Ranch Metamorphic Suite	RM40	37.13	0.04	21.06	4.10	1.36	2.77	34.16	0.12	100.65	10
Ruby Range	Christensen Ranch Metamorphic Suite	RRSW2	38.54	0.01	22.48	10.70	1.09	0.28	27.82	0.38	100.93	15
Ruby Range	Christensen Ranch Metamorphic Suite	RRSW3	36.34	0.01	21.35	3.71	2.13	1.87	35.08	0.11	100.48	13
Ruby Range	Christensen Ranch Metamorphic Suite	RRSW4	38.60	0.02	22.49	10.90	2.57	0.55	25.42	0.43	100.56	29
Tobacco Root Mountains	Quartz-feldspar-biotite Gneiss	TRBC2	38.72	0.01	22.52	10.06	1.45	0.50	28.08	0.36	101.34	67
Tobacco Root Mountains	Quartz-feldspar-biotite Gneiss	TRER7	37.26	0.01	21.86	6.39	1.52	1.79	31.80	0.20	100.63	19
Tobacco Root Mountains	Quartz-feldspar-biotite Gneiss	TRMR2	36.45	0.01	21.75	8.41	1.12	0.47	30.66	0.27	98.87	50
Tobacco Root Mountains	Plagioclase-quartz-hornblende Gneiss	TRER6B	37.17	0.05	21.28	3.53	7.82	1.08	29.69	0.12	100.63	26
Highland Mountains	Quartz-feldspar-biotite Gneiss	HLM2	36.61	0.01	21.39	3.47	2.08	2.14	34.96	0.10	100.65	25

(For full data tables see Appendix 4.1)

Table 4.2. Mean biotite electron microprobe analyses, expressed as oxide weight percent

A) Mean matrix biotite analyses

Range	Unit	Sample	SiO_2	TiO_2	Al_2O_3	MgO	CaO	MnO	FeO	Na_2O	K_2O	MgO/FeO	Total	No. Analyses
Ruby Range	Older Gneiss & Schist	70-30-2	35.36	4.18	17.57	11.06	0.05	0.00	16.51	0.13	9.27	0.67	94.16	4
Ruby Range	Older Gneiss & Schist	RM42	33.86	5.10	18.29	9.17	0.03	0.06	19.11	0.09	8.28	0.48	94.02	4
Ruby Range	Older Gneiss & Schist	RRSW1	35.33	3.36	17.97	11.86	0.11	0.04	16.37	0.29	8.59	0.89	93.95	9
Ruby Range	CRMS	RRCR2	33.65	3.26	18.18	7.11	0.03	0.05	22.15	0.17	9.25	0.32	93.85	12
Ruby Range	CRMS	RRCR3	33.88	3.69	18.39	7.26	0.02	0.02	21.98	0.24	9.21	0.33	94.69	15
Ruby Range	CRMS	RRCR5	33.86	3.52	18.75	6.91	0.00	0.03	21.98	0.20	9.34	0.31	94.58	15
Ruby Range	CRMS	RMC200	36.72	2.74	17.39	13.56	0.02	0.02	15.80	0.41	8.59	0.86	95.34	25
Ruby Range	CRMS	RM37	34.55	3.49	19.51	6.83	0.04	0.03	21.78	0.17	8.60	0.32	95.22	7
Ruby Range	CRMS	RM39	34.71	3.86	18.73	6.98	0.02	0.01	22.21	0.13	9.46	0.31	96.20	22
Ruby Range	CRMS	RM40	35.41	1.07	19.69	11.42	0.01	0.05	17.35	0.20	9.39	0.67	94.70	3
Ruby Range	CRMS	RRSW2	37.51	3.09	17.20	15.74	0.04	0.00	11.78	0.61	7.84	1.34	93.80	13
Ruby Range	CRMS	RRSW3	33.94	4.13	17.30	7.44	0.01	0.07	22.13	0.13	9.32	0.34	94.48	15
Ruby Range	CRMS	RRSW4	38.07	2.30	17.00	16.35	0.06	0.01	11.61	0.49	7.96	1.41	93.86	15
Tobacco Root Mountains	Quartz-feldspar-biotite Gneiss	TRBC2	35.44	5.03	16.76	13.63	0.73	0.03	12.72	0.22	7.79	1.07	92.35	14
Tobacco Root Mountains	Quartz-feldspar-biotite Gneiss	TRER7	35.20	3.63	17.72	11.64	0.00	0.04	16.06	0.21	9.38	0.73	93.90	15
Tobacco Root Mountains	Quartz-feldspar-biotite Gneiss	TRMR2	35.06	2.51	18.27	13.52	0.02	0.01	13.49	0.10	9.29	1.00	92.29	5
Tobacco Root Mountains	Plag-quartz-hornblende Gneiss	TRER6B	36.00	3.12	18.83	11.19	0.11	0.03	15.68	0.25	8.51	0.80	93.75	9
Highland Mountains	Quartz-feldspar-biotite Gneiss	HLM2	34.21	2.86	18.95	8.24	0.01	0.07	20.24	0.17	9.56	0.41	94.32	14

B) Mean analyses for biotite inclusions in garnet

Range	Unit	Sample	SiO_2	TiO_2	Al_2O_3	MgO	CaO	MnO	FeO	Na_2O	K_2O	MgO/FeO	Total	No. Analyses
Ruby Range	Older Gneiss & Schist	RRSW1	34.65	4.42	14.91	11.67	0.54	0.05	19.46	0.24	6.73	0.61	92.67	6
Ruby Range	CRMS	RRCR2	33.82	2.12	18.44	7.30	0.07	0.06	22.70	0.19	8.71	0.32	93.41	1
Ruby Range	CRMS	RRCR3	35.01	3.96	18.55	9.28	0.01	0.01	18.97	0.30	9.23	0.49	95.31	11
Ruby Range	CRMS	RRCR5	34.44	3.34	19.21	8.03	0.02	0.02	20.35	0.28	9.17	0.40	94.86	21
Ruby Range	CRMS	RMC200	37.07	2.51	17.91	14.88	0.03	0.02	13.51	0.50	8.67	1.11	95.22	10
Ruby Range	CRMS	RM37	35.10	3.64	19.70	8.59	0.00	0.00	19.52	0.29	9.44	0.44	96.77	1
Ruby Range	CRMS	RM39	34.90	3.43	18.88	8.22	0.03	0.02	21.12	0.18	9.11	0.39	95.96	28
Ruby Range	CRMS	RM40	35.56	1.02	19.77	12.04	0.01	0.03	16.42	0.21	9.38	0.74	94.57	5
Ruby Range	CRMS	RRSW2	37.66	2.55	17.78	17.90	0.06	0.00	8.00	1.03	7.70	2.24	92.69	2
Ruby Range	CRMS	RRSW3	34.98	3.37	18.43	9.97	0.03	0.04	18.01	0.31	9.10	0.57	94.23	11
Ruby Range	CRMS	RRSW4	35.35	3.21	18.34	10.73	0.04	0.04	17.21	0.33	9.01	0.71	94.26	1
Tobacco Root Mountains	Quartz-feldspar-biotite Gneiss	TRMR2	36.57	2.30	18.93	14.64	0.05	0.03	11.85	0.14	9.11	1.28	93.70	5
Tobacco Root Mountains	Plag-quartz-hornblende Gneiss	TRER6B	33.35	5.18	14.65	9.41	0.59	0.09	23.80	0.09	6.84	0.40	93.99	1

C) Mean analyses from biotite rimming garnet

Range	Unit	Sample	SiO_2	TiO_2	Al_2O_3	MgO	CaO	MnO	FeO	Na_2O	K_2O	MgO/FeO	Total	No. Analyses
Ruby Range	CRMS	RRCR2	33.70	2.51	19.14	7.06	0.03	0.05	22.03	0.20	8.96	0.32	93.67	5
Ruby Range	CRMS	RRCR3	34.57	3.56	18.70	7.40	0.01	0.02	21.87	0.26	9.19	0.34	95.58	9
Ruby Range	CRMS	RRCR5	34.38	3.13	19.27	7.20	0.02	0.03	21.76	0.27	9.22	0.33	95.28	16
Ruby Range	CRMS	RMC200	36.80	2.45	17.99	13.40	0.06	0.02	15.23	0.34	8.08	0.88	94.47	9
Ruby Range	CRMS	RM37	34.88	2.77	19.81	7.35	0.05	0.03	21.77	0.23	9.24	0.34	96.23	5
Ruby Range	CRMS	RM39	34.51	3.42	19.13	7.31	0.02	0.03	21.79	0.21	9.28	0.34	95.81	8
Ruby Range	CRMS	RM40	34.87	1.01	19.63	10.34	0.04	0.08	19.17	0.21	9.51	0.54	94.86	1
Ruby Range	CRMS	RRSW2	37.83	2.37	17.93	16.94	0.03	0.01	10.68	0.65	7.67	1.61	94.11	13
Ruby Range	CRMS	RRSW3	34.31	3.63	17.72	7.65	0.02	0.07	21.73	0.17	9.17	0.35	94.48	15
Ruby Range	CRMS	RRSW4	38.20	1.55	17.10	17.34	0.15	0.02	11.22	0.49	7.28	1.55	93.36	15
Tobacco Root Mountains	Quartz-feldspar-biotite Gneiss	TRBC2	36.20	4.04	16.44	14.88	0.05	0.03	12.62	0.25	8.84	1.19	93.35	12
Tobacco Root Mountains	Quartz-feldspar-biotite Gneiss	TRER7	35.40	3.16	17.88	12.32	0.03	0.03	15.71	0.22	9.29	0.79	94.03	15
Highland Mountains	Quartz-feldspar-biotite Gneiss	HLM2	34.20	2.41	19.31	8.52	0.01	0.05	19.88	0.15	9.64	0.43	94.18	15

(For full data tables see Appendix 4.2)

Table 4.3. Mean amphibole electron microprobe analyses, expressed as oxide weight percent

A) Mean matrix amphibole analysis

Range	Unit	Sample	SiO_2	TiO_2	Al_2O_3	MgO	CaO	MnO	FeO	Na_2O	K_2O	Total	No. Analysis
Ruby Range	Older Gneiss & Schist	RRSW1	43.87	1.41	10.66	10.46	10.67	0.18	17.94	1.31	0.51	96.82	16
Ruby Range	Christensen Ranch Metamorphic Suite	RRCR12	42.87	1.01	13.56	9.90	10.93	0.09	16.64	1.65	0.42	97.07	14
Tobacco Root Mountains	Plagioclase-quartz-hornblende Gneiss	TRER6B	41.18	2.14	11.07	8.64	10.98	0.15	19.19	1.70	0.91	95.96	11

B) Mean analyses for amphibole inclusions in garnet

Range	Unit	Sample	SiO_2	TiO_2	Al_2O_3	MgO	CaO	MnO	FeO	Na_2O	K_2O	Total	No. Analysis
Ruby Range	*Christensen Ranch Metamorphic Suite*	RRCR12	42.91	0.95	14.00	10.31	10.83	0.09	16.23	1.68	0.37	97.38	10
Tobacco Root Mountains	Plagioclase-quartz-hornblende Gneiss	TRER6B	43.02	1.97	11.42	9.77	11.10	0.09	17.58	1.63	1.02	97.59	25

C) Mean analyses for amphibole rimming garnet

Range	Unit	Sample	SiO_2	TiO_2	Al_2O_3	MgO	CaO	MnO	FeO	Na_2O	K_2O	Total	No. Analysis
Ruby Range	Older Gneiss & Schist	RRSW1	44.78	1.24	10.65	10.40	10.47	0.16	18.18	1.23	0.46	97.57	5
Ruby Range	Christensen Ranch Metamorphic Suite	RRCR12	42.57	0.98	14.01	10.01	10.90	0.08	16.43	1.70	0.40	97.09	10
Tobacco Root Mountains	Plagioclase-quartz-hornblende Gneiss	TRER6B	42.44	2.02	11.29	9.42	11.04	0.11	18.10	1.66	0.96	97.05	9

(For full data tables see Appendix 4.3.)

Table 4.4. Mean electron microprobe analyses for miscellaneous minerals, expressed as oxide weight percent

Range	Unit	Sample	Analysis	SiO_2	TiO_2	Al_2O_3	MgO	CaO	MnO	FeO	Na_2O	K_2O	Total
Ruby Range	Older Gneiss & Schist	70-30-2	Cordierite	49.05	0.01	32.90	9.73	0.01	0.03	6.17	0.12	0.02	98.04
Ruby Range	Older Gneiss & Schist	70-30-2	Feldspar	58.17	0.00	25.64	0.00	6.02	0.00	1.15	4.87	0.71	97.16
Ruby Range	Older Gneiss & Schist	70-30-2	Sillimanite	36.67	0.03	61.49	0.01	0.01	0.02	0.40	0.01	0.00	98.66
Ruby Range	Older Gneiss & Schist	RM42	Feldspar	59.20	0.00	24.96	0.00	7.07	0.00	0.03	7.30	0.34	98.91
Ruby Range	Older Gneiss & Schist	RRSW1	Chlorite	28.21	0.65	17.52	13.76	0.25	0.19	27.14	0.01	0.51	88.24
Ruby Range	Older Gneiss & Schist	RRSW1	Prehnite	42.56	0.07	23.01	0.02	27.10	0.00	1.39	0.07	0.01	94.23
Ruby Range	Christensen Ranch Metamorphic Suite	RMC200	Chlorite	26.56	0.05	22.50	18.62	0.01	0.04	20.14	0.03	0.07	88.01
Ruby Range	Christensen Ranch Metamorphic Suite	RMC200	Sericite	47.93	0.05	28.99	4.06	1.39	0.02	4.06	0.84	7.27	94.60
Ruby Range	Christensen Ranch Metamorphic Suite	RM37	Sillimanite	47.33	0.02	37.12	0.23	0.26	0.00	0.37	0.11	0.65	86.08
Ruby Range	Christensen Ranch Metamorphic Suite	RM39	Feldspar	61.43	0.00	24.02	0.00	5.66	0.00	0.04	8.19	0.22	99.56
Ruby Range	Christensen Ranch Metamorphic Suite	RRSW2	Rutile	0.09	99.38	0.03	0.00	0.00	0.01	0.24	0.02	0.00	99.76
Ruby Range	Christensen Ranch Metamorphic Suite	RRSW2	Pyroxene	46.52	0.56	12.56	17.40	0.21	0.07	18.52	1.24	0.00	97.08
Tobacco Root Mountains	Quartz-feldspar-biotite Gneiss	TRER7	Epidote	58.93	0.01	23.96	0.00	6.30	0.00	0.06	8.38	0.07	97.71

(For full data tables see Appendix 4.4)

Chapter 5 - ^{40}Ar-^{39}Ar Geochronology

5.1. Introduction

Determining the ^{40}Ar-^{39}Ar age of the matrix minerals of rocks from the polymetamorphic terrain of south-western Montana is essential for the comparison to ages that attempt to date other events in the geological history of the region. The different blocking temperatures of mineral species within the same rock or from the same area result in different apparent ages that can be used as a gauge of peak metamorphism reached and cooling rate from peak metamorphism. For this reason biotite, muscovite and amphibole have all been dated in this study. In addition, according to Dodson (1986), cooling rates can also be established by monitoring apparent age variations within a single mineral grain (section 3.7.2.2). He postulated that slow cooling would produce characteristic apparent age variations across a single mineral grain. Because Precambrian polymetamophic rocks often experience periods of protracted cooling in the middle crust, the rocks of south-western Montana provide an ideal opportunity to investigate the theory of slow cooling postulated by Dodson (1986) and to establish whether these rocks underwent slow cooling.

5.2. Matrix Mica Geochronology for South-western Montana

5.2.1. Aim

The aim of this experimentation was two-fold: to determine the ages of the matrix mica from the Ruby Range, Tobacco Root Mountains and Highland Mountains; and to construct closure profiles from mica that might lead to a better understanding of the cooling history of these rocks. This involved carrying out analyses using the UV laser microprobe either as 50 or 100 μm squares for general ages or as 100 to 500 μm linear traverses for the construction of closure profiles. Closure profiles are detailed further in this chapter (section 5.3) but dates achieved whilst constructing profiles are also used here to obtain mean ages for matrix mica.

5.2.2. Sample Preparation and Irradiation

Samples that contained both large, inclusion-rich garnets and abundant well-formed matrix mica were selected in order to allow direct comparison between matrix ages and ages for biotite inclusions in garnet within the same rock (section 6.3). In the metamorphic rocks of south-western Montana muscovite is extremely rare. Indeed, only sample RMC42 contained both biotite and muscovite, facilitating direct comparison between the apparent ages of the two micas.

Some samples were analysed from thick section, whilst others were crushed and separated and large single biotite grains picked by hand (section 3.2). Whether the sample was analysed as a thick section or as mineral separates is indicated in Appendix 5.1 under McMaster 1, 4 and 5. Mineral separates were of millimetre scale and provided good sample density. In contrast, grains from thick sections were generally smaller than 500 μm but were able to provide unequivocal analyses of the true grain edges. In addition, because a thick section consists of multiple mineral species, analysis of quartz and garnet was used in some samples to determine whether excess argon was present in the sample. As neither quartz nor garnet naturally contain potassium, argon will only be detected in these minerals if excess argon is present in the sample. The differences in grain size of the mica, from the millimetre scale separates to the micron scale thick section mica, enabled further investigation of the controls of argon diffusion in mica with grain size.

Details of the duration sample irradiation can be found in Appendix 5.1. Analysis of interlaboratory standards and calculation of the neutron flux within the reactor was used and the J-values obtained for each sample are also recorded in Appendix 5.1.

5.2.3. Results

The weighted mean of each sample is showed in Table 5.1. Apparent ages were excluded from the mean calculation if: a) they were anomalously young or old, b) had a 1 σ error greater than 50 m.y., and c) were at the edge of a profile and apparently affected by slow cooling. All data for mica analyses can be found in Appendix 5.2 and those apparent ages excluded from the mean are indicated. In some samples two distinct populations of apparent ages were recorded: an age

Figure 5.1: $^{39}Ar/^{40}Ar$ versus $^{36}Ar/^{40}Ar$ for quartz and garnet analyses to assess the presence of excess argon

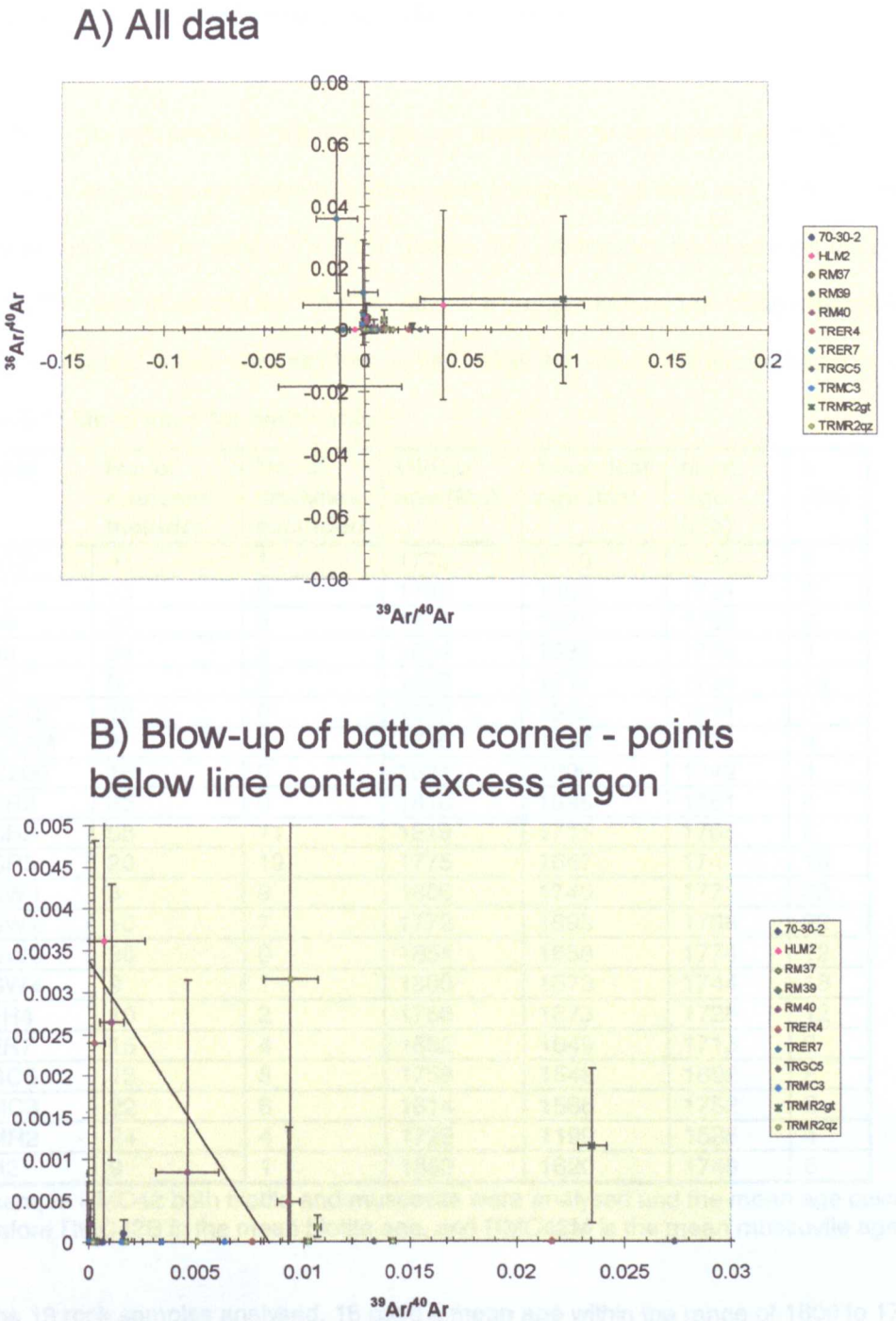

comparable to the ages achieved for the majority of the samples and a younger age population. In other samples just the younger age population was detected. Where two age populations were recorded, only the older population was used to determine the mean age shown below. The causes of younger ages are discussed in more detail in chapter 7.

In addition, the full results of quartz and garnet analyses can be found in Appendix 5.3. To assess whether excess argon was present in the quartz and garnet the data was plotted on an inverse isochron, with $^{39}Ar/^{40}Ar$ versus $^{36}Ar/^{40}Ar$ (Figure 5.1). A line was drawn across the graph based on the $^{36}Ar/^{40}Ar$ ratio in air and the $^{39}Ar/^{40}Ar$ ratio of a sample with an age of approximately 1750 Ma. Those quartz and garnet analyses that plotted below this line contained excess argon.

Table 5.1: Mean ages for matrix mica

Sample	No. of analyses included	No. of analyses excluded	Oldest age (Ma)	Youngest age (Ma)	Mean Age (Ma)	± (2σ)
70-30-2	9	1	1773	1710	1744	6
RM37	23	0	1798	1405	1731	4
RM39	10	5	1813	1675	1784	6
RM40	24	3	1854	1632	1772	4
RM42	6	4	1852	1717	1734	14
RMC42B*	10	0	1668	1522	1611	8
RMC42M*	9	0	1716	1639	1671	6
RMC200	16	0	1821	1690	1742	4
RRCR2	35	0	1818	1695	1761	4
RRCR3	58	11	1819	1715	1765	6
RRCR5	20	19	1775	1687	1741	10
RRSW1	6	9	1806	1740	1771	32
RRSW2	10	7	1772	1693	1738	22
RRSW3	30	0	1854	1658	1774	12
RRSW4	9	1	1800	1673	1744	18
TRER4	10	2	1758	1673	1728	12
TRER7	15	4	1852	1649	1713	8
TRGC5	13	8	1758	1548	1692	8
TRMC3	22	6	1814	1586	1752	8
TRMR2	24	4	1729	1199	1585	4
HLM2	9	1	1853	1620	1749	6

*In sample RMC42 both biotite and muscovite were analysed and the mean age calculated for both, therefore RMC42B is the mean biotite age, and RMC42M is the mean muscovite age.

Of the 19 rock samples analysed, 16 gave a mean age within the range of 1800 to 1700 Ma, and of those, 11 were within the range of 1780 to 1740 Ma. Figure 5.2. is a map showing the location of the rock sample within south-western Montana and the mean age obtained.

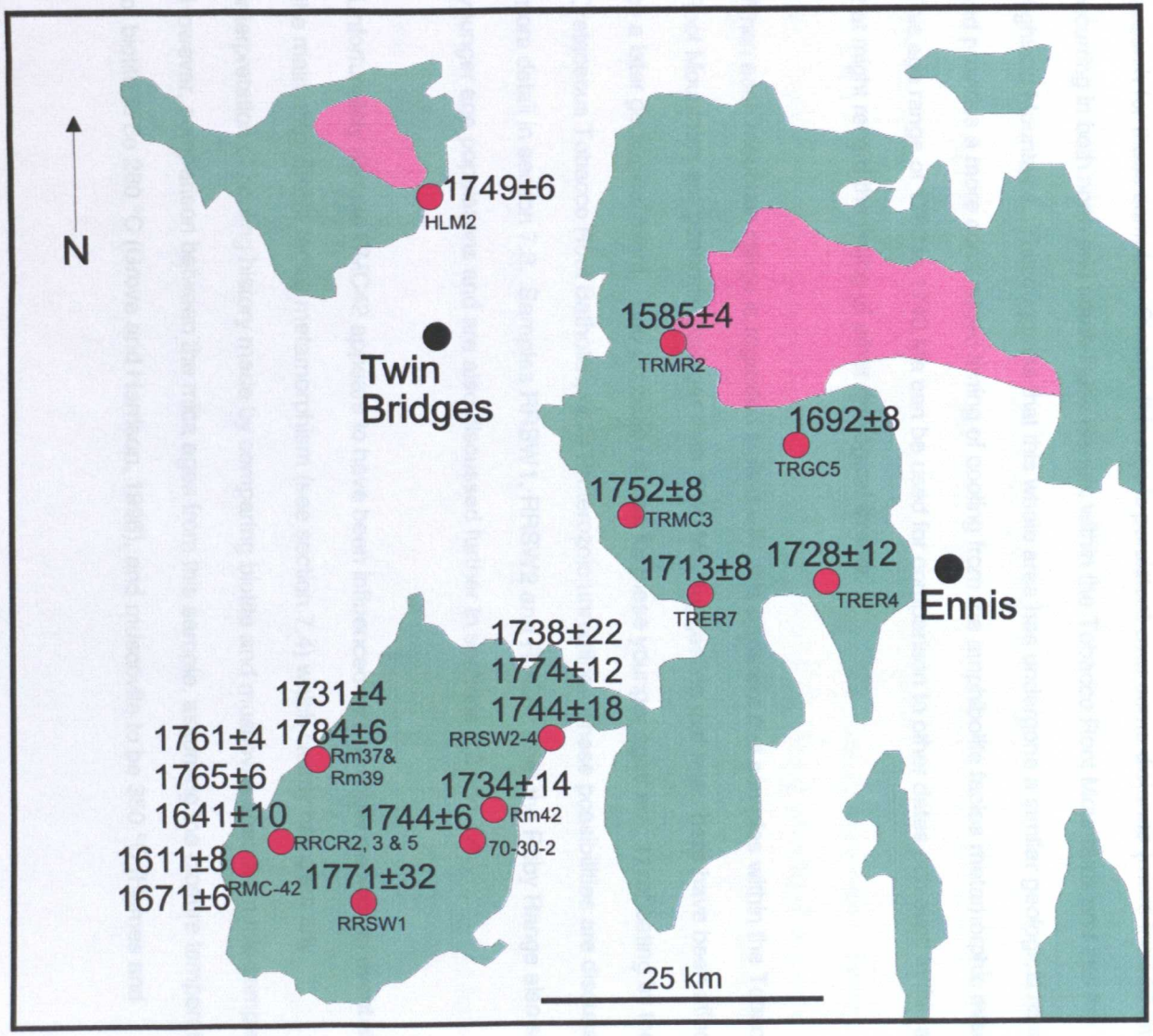

Figure 5.2: Map of South-western Montana with apparent mean matrix mica ^{40}Ar-^{39}Ar ages of samples related to sample location

5.2.4. Discussion

Most of the mean ages recorded in Table 5.1 fall within the 1800 to 1600 Ma age range found by Giletti (1966). Furthermore, these findings support the ages found by the previous authors who used ^{40}Ar-^{39}Ar geochronological techniques, particularly: Brady *et al.*, 1991 (~1700 Ma phlogopite, biotite and hornblende ages for Ruby Range); Brady *et al.*, 1994 (1800 Ma hornblende ages for Tobacco Root Mountains); Kovaric *et al.*, 1996 (~1700 Ma hornblende ages for Tobacco Root Mountains and 1720 Ma hornblende and phlogopite ages for Ruby Range); and Harlan *et al.*, 1996 (1776 and 1839 Ma total gas ages for Highland Mountains) (see Appendix 2.1).

A narrower age range from 1780 to 1740 Ma encompasses the majority of the ages achieved in this research for these samples. Clearly, this age is persistent over some distance (more than 50 km), occurring in both north and south Ruby Range, within the Tobacco Root Mountains and into the Highland Mountains. This suggests that this whole area has undergone a similar geological history and provides a more constrained timing of cooling from the amphibolite facies metamorphic event. This age range of 1780 to 1740 Ma can be used for comparison to other dates achieved in this area that might record the timing of other geological events.

When each mountain range is regarded individually, it is apparent that samples within the Tobacco Root Mountains are generally younger than 1740 Ma, suggesting that ages here have been affected by a later geological event. Two possible causes for these younger ages are: 1) reheating by the Cretaceous Tobacco Root Batholith; or 2) Proterozoic unroofing. These possibilities are discussed in more detail in section 7.3. Samples RRSW1, RRSW2 and RMC42 from the Ruby Range also show younger age populations and are also discussed further in sections 7.2 and 7.4.

Unfortunately sample RMC42 appears to have been influenced by a younger geological event after the main amphibolite facies metamorphism (see section 7.4) which clearly hampers any interpretation of cooling history made by comparing biotite and muscovite ages from this sample. However, comparison between the mica ages from this sample, assuming the closure temperatures of biotite to be 280 °C (Grove and Harrison, 1996), and muscovite to be 350 °C (Hames and

Bowring, 1994), gives a cooling rate of about 1.2 °C/m.y. between the two closure temperatures. This can be compared to the cooling rate estimated from closure profiles in 5.4.3.2 below.

5.2.5. Conclusion

This research supports the findings of previous ^{40}Ar-^{39}Ar dating attempts in south-western Montana and suggests a 1780 to 1740 Ma timing for the amphibolite facies metamorphic event. This age is consistent and persistent over three mountain ranges, but is locally absent in samples that have been reset by younger geological events.

5.3. Matrix Amphibole Geochronology for South-western Montana

5.3.1. Sample Preparation and Irradiation

Samples were chosen in order to provide a good geographical spread across the three mountain ranges. Samples RRCR4, RRCR11, RRCR12, TRMC5, TRWC1 and HLM4 were selected because it was believed they would provide straightforward results that would give a good indication of the age recorded by amphibole in this area that could be compared to the mica ages produced. Sample RRSW1 was chosen because the biotite in this sample was highly altered, affecting the apparent ages obtained (section 7.2). Dating the amphibole would determine whether the amphibole had similarly been affected and could constrain the temperature of the resetting event. Samples TRER1, TRER2, and TRMR3 were selected because of their close proximity to the Tobacco Root Batholith in order to investigate the effects of resetting in amphiboles by this pluton. Samples RRSW1, TRWC1, TRER2 and TRMR3 were of particular interest as these contained both amphibole and biotites, allowing direct comparisons to be made between the ages of two different mineral species from the same rock.

All samples were crushed and separated and single amphibole grains (and biotite where appropriate) were picked by hand. Analysis of the amphibole was carried out on the IR laser system using both step-heating and total fusion techniques (section 3.4.2). Biotite was analysed using the UV laser microprobe system (section 3.4.1). The method of analysis is indicated in Appendix 5.1.

All the samples were irradiated in the McMaster reactor in Canada and details of the duration and end date of the irradiation can be found in Appendix 5.1 under McMaster 1 and 5. Analysis of interlaboratory standards and calculation of the neutron flux within the reactor were used to obtain J-values for each sample as recorded in Appendix 5.1.

5.3.2. Results

Table 5.2 below contains the mean apparent ages obtained for the amphibole analysed in this experiment, together with biotite ages where coexisting with amphibole. Full data tables can be found in Appendix 5.4 and all apparent ages are shown relative to geographical location of the sample in Figure 5.3. The anomalously high apparent ages recorded in the amphibole in HLM4 suggests that excess argon was present in this sample. For this reason no meaningful information can be obtained from this sample. Similarly, amphibole from sample TRMC5 also appears to be exhibiting higher apparent ages than expected. An age of 2471 ± 60 Ma was recorded for this sample but was not included in the calculation of the mean (Appendix 5.4). However, other ages that were included in the mean calculation may also have been influenced by excess argon, leading to an anomalously high mean. For this reason the mean age of this sample should be regarded as a maximum age.

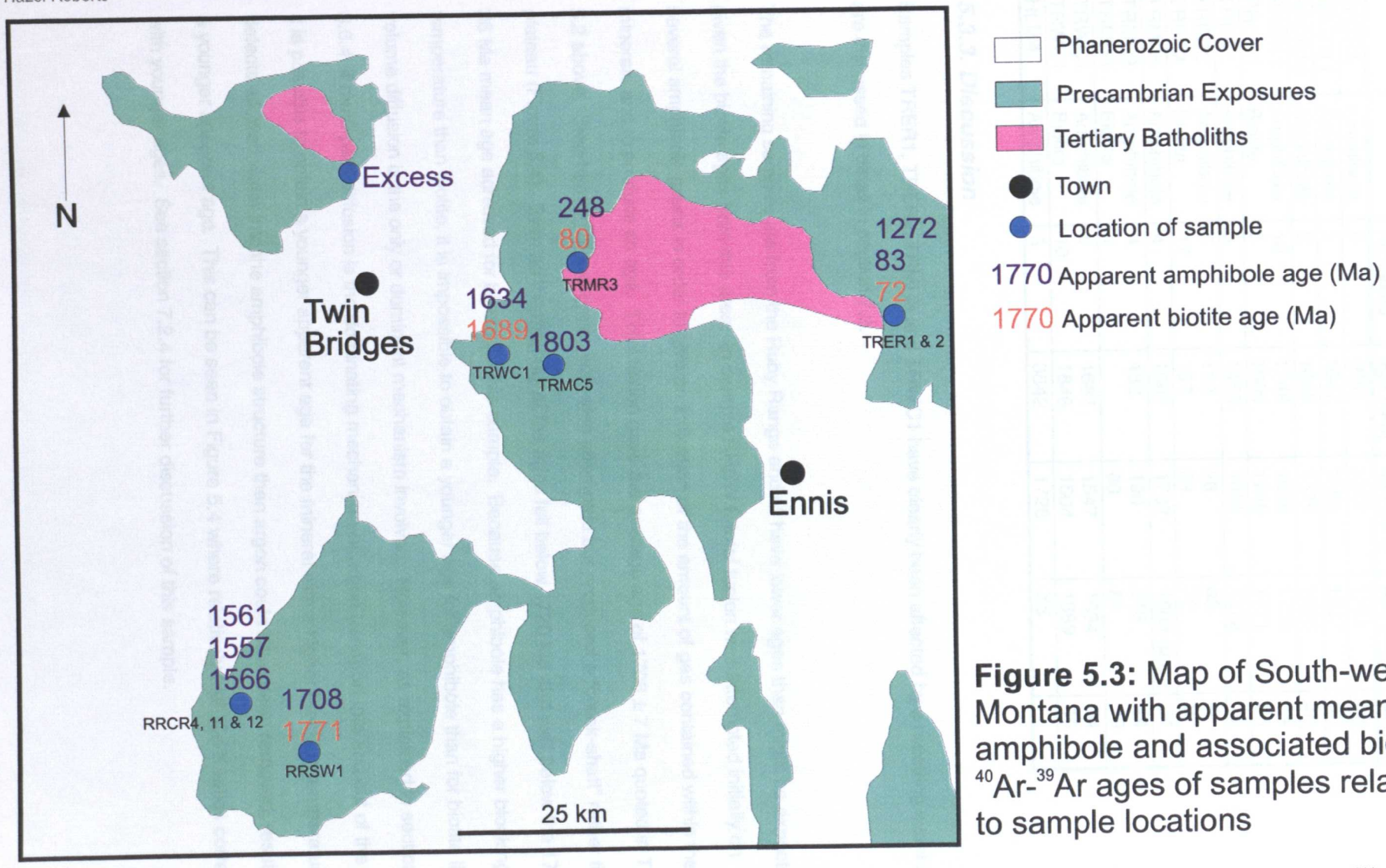

Figure 5.3: Map of South-western Montana with apparent mean amphibole and associated biotite ^{40}Ar-^{39}Ar ages of samples related to sample locations

Table 5.2: Ages obtained for amphibole and coexisting biotite where available

Sample	Mineral	No. of Analyses	Oldest age (Ma)	Youngest age (Ma)	Mean Age (Ma)	± (2σ)
RRCR4	Amphibole	5	1651	1377	1561	60
RRCR11	Amphibole	5	1667	1266	1557	60
RRCR12	Amphibole	5	1668	1375	1566	38
RRSW1	Amphibole	10	1748	1639	1708	14
RRSW1	Biotite	6	1806	1740	1771	36
TRER1	Amphibole	5	1456	1056	1272	16
TRER2	Amphibole	5	119	26	83	4
TRER2	Biotite	17	107	29	72	8
TRMC5	Amphibole	4	1997	1737	1803 (Max)	34
TRMR3	Amphibole	4	482	199	248	44
TRMR3	Biotite	1		80	80	39
TRWC1	Amphibole	5	1687	1547	1634	34
TRWC1	Biotite	10	1846	1604	1689	10
HLM4	Amphibole	5	3842	1728	XS	

5.3.3. Discussion

Samples TRER1, TRER2, TRMR3 and TRWC1 have clearly been affected by a resetting event and are discussed in detail in section 7.3.

The remaining samples are from the Ruby Range and all have lower ages than might be expected given the biotite ages from this area. In sample RRSW1, total fusion was attempted initially on several amphibole grains in order to give an indication of the amount of gas contained within the minerals and to produce an age. Total fusion gave the average age of 1708 ± 7 Ma quoted in Table 5.2 above. Step-heating of two grains was also attempted but produced a "crank-shaft" rather than a plateau (Figure 5.4). Even so the majority of the ages fell below 1720 Ma and well below the 1771 ± 36 Ma mean age achieved for biotite for this sample. Because amphibole has a higher blocking temperature than biotite, it is impossible to obtain a younger age for amphibole than for biotite if volume diffusion is the only or dominant mechanism involved. However, as explained in section 3.6.4, if multi-path diffusion is the dominating mechanism of argon transport into and out of the grain it is possible to obtain a younger apparent age for the mineral with a higher blocking temperature. If defects allowed water into the amphibole structure then argon could have been removed, resulting in a younger apparent age. This can be seen in Figure 5.4 where relatively high Ca/K ratios correlate with younger ages. See section 7.2.4 for further discussion of this sample.

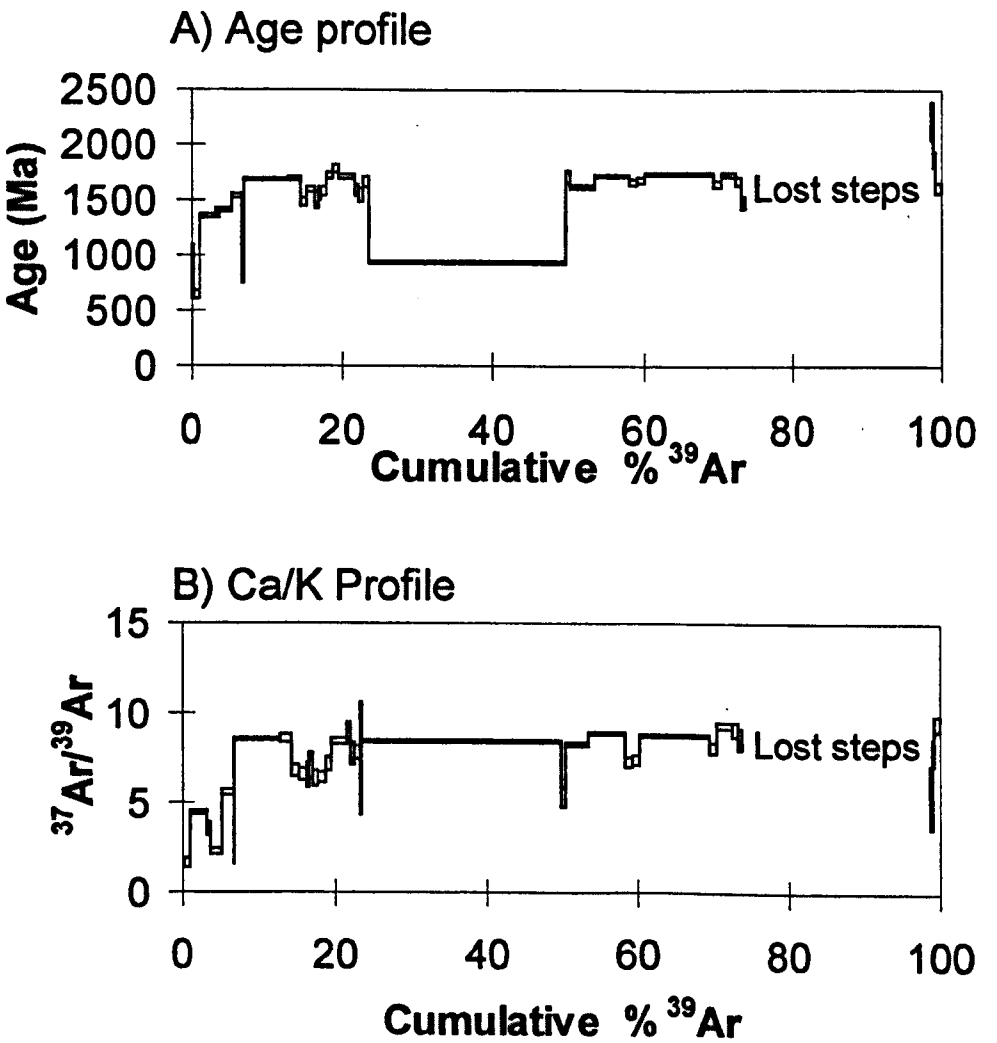

Figure 5.4: Step-heating profile for RRSW1 amphibole

Samples RRCR4, 11 and 12, from the Christensen Ranch area of the Ruby Range, gave very similar mean ages to each other, being in the range from 1566 ± 38 to 1557 ± 60 Ma, which suggests that these could be reliable ages, dating a younger event. However, the ages that make up these mean ages range from 1668 ± 70 to 1266 ± 122 Ma which is a relatively large variation considering that only 5 grains of amphibole were analysed in each case. Therefore, it seems more likely that the biotite ages achieved for the Christensen Range area of the Ruby Range are more reliable. This suggests that these amphiboles have also been influenced by such factors as loss of potassium via alteration, or contamination by younger potassium-rich, less retentive mineral phases (Wartho, 1995) resulting in anomalously young ages being recorded.

Because of the questionable nature of the amphibole dates obtained it is not possible to use the amphibole ages in a crude isochron with biotite to gauge the cooling rate of these samples.

5.3.4. Conclusion

This experiments highlights some of the difficulties associated with dating amphibole using the ^{40}Ar-^{39}Ar techniques. Sample RRSW1 in particular demonstrated that alteration in the sample reduced the apparent age of the amphibole within it when total fusion was undertaken. However, even when step-heating was attempted a poor profile was produced that was difficult to interpret and still appeared to produce ages younger than biotite from the same rock. Because of these difficulties the results produced here are not particularly reliable and instead the biotite ages for the region should be considered.

5.4. Closure Profiles

5.4.1. Introduction

Attempts to construct closure profiles were made in micas from samples RRCR2, 3 and 5, RRSW1, 2, 3, and 4, RMC42, TRMC3, TRER4 and 7, TRGC5 and TRMR2. These samples were chosen to provide a good geographical spread across the Ruby Range and Tobacco Root Mountains. Profiles were made principally in biotite with only one muscovite in RMC42 being analysed. A total of 24 profiles, ranging from 3 to 49 traverses, were made in samples from the Ruby Range, and a total of

12 profiles, ranging from 3 to 8 traverses, were made in samples from the Tobacco Root Mountains. As the slow cooling theory predicts that the largest age variations occur in the rim to near-rim area, only a few traverses were needed to determine whether age variations were apparent, therefore, the average length of profiles was 6 traverses. Some profiles were stopped after only 3 traverses either because it was clear that the profile was not producing systematic age variations, or the sample jumped due to explosive degassing (section 3.2.2).

For irradiation details, sample format, and analytical details see Appendix 5.1 and sections 5.2.2 and 5.2.3 above.

5.4.2. Results

Data tables in Appendix 5.2 and figures in Appendix 5.7 contain details of the apparent ages and profiles produced.

Of the 24 profiles produced for Ruby Range samples only 12 showed younger ages at the edge of the grain with a systematic increase in ages with distance, and of the 12 profiles produced for the Tobacco Root Mountains samples only 6 were successful. Another 8 profiles had the oldest age at the edge of which 5 systematically decreased in age from the edge inwards. The remaining profiles showed random age variations with no apparent relationship between the age and the position of the analysis within the grain.

5.4.3. Discussion

5.4.3.1. Older Ages at Edge of Grain

Similar work on ^{40}Ar-^{39}Ar age variations in micas by Reddy *et al.* (1996) and Pickles *et al.* (1997) found older apparent ages at the edge of mica grains. They attributed this to the occurrence of excess argon within the grain.

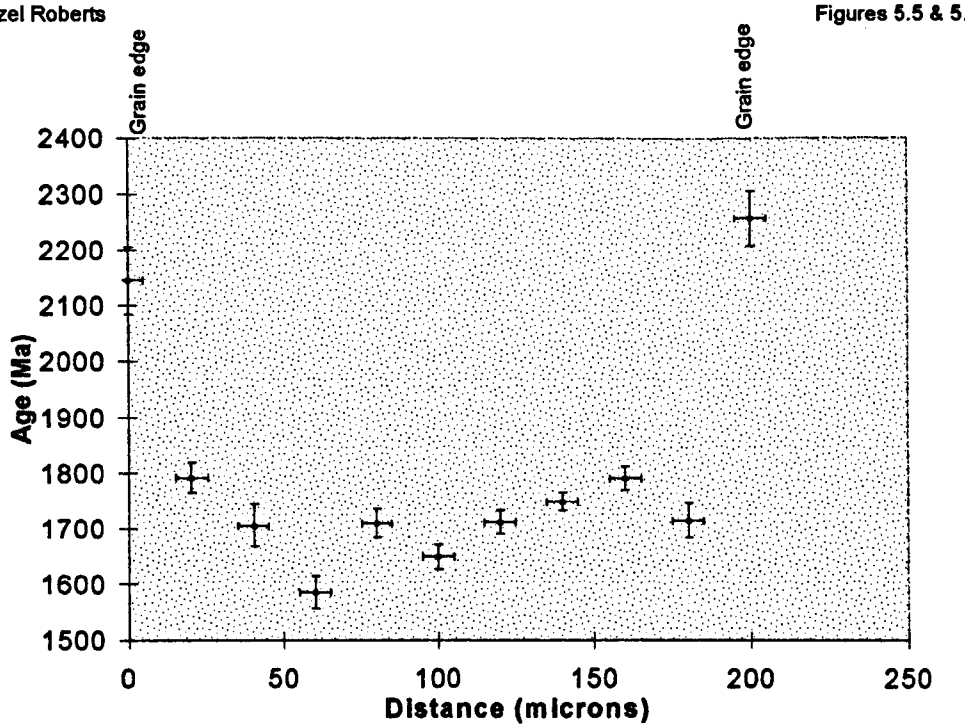

Figure 5.5: TRMC3 Profile B showing excess argon at either edge

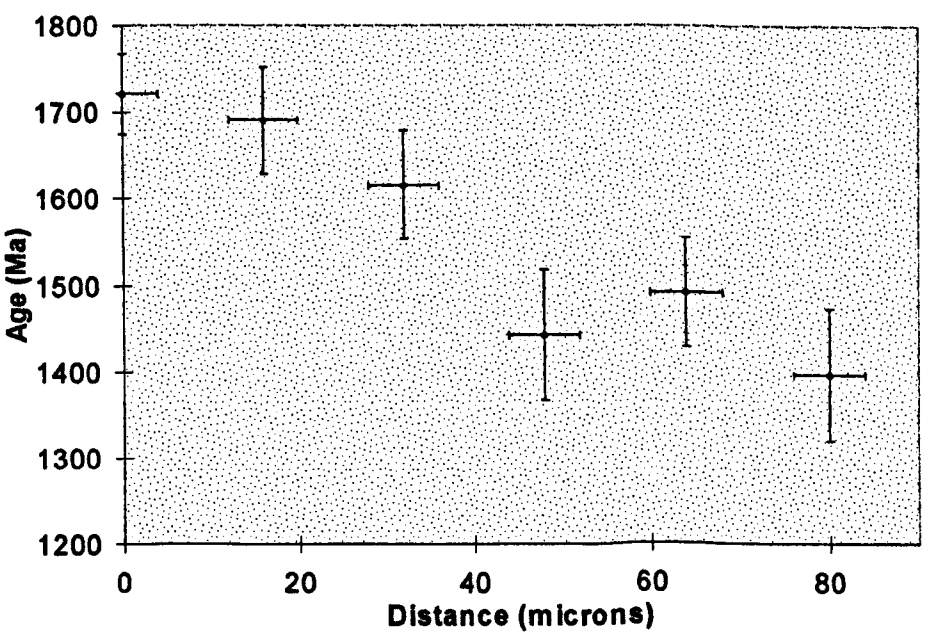

Figure 5.6: RRSW2 Profile A showing decreasing ages from edge

Profile B in TRMC3 extended from one edge of a grain to another and in Figure 5.5 it can be seen that both edges exhibit apparent ages in excess of 2100 Ma, significantly older than other ages from that profile, the sample as a whole and other samples from the area. Excess argon was found to be present within the quartz grains of this sample, as demonstrated in Figure 5.1, and the traverses at the edges of this profile were made on the edge of a biotite grain adjacent to quartz. It seems likely that the traverses at the edges of this grain included some quartz content, introducing excess argon into the analysis. This is notion is supported by the decrease in the amount of ^{39}Ar in the edge points of this profile (see Appendix 5.2), indicating that quartz was sampled as well as biotite. As the traverses away from the edge of the grain have ages close to those expected, it appeared that the excess argon had not diffused into the biotite. However, the length of the traverse extended across the width of this biotite grain and quartz may have been sampled by the traverse extending outside the biotite grain at any point in this profile. For this reason the ages achieved during traverses should be regarded as maximum ages.

It is not possible to assign the influence of excess argon to all samples where the oldest age occurs at the edge of the grain. Where mineral separates were used, presence or absence of excess argon could not be independently determined by analysing the quartz. However, in sample RRSW2 profile A (Figure 5.6), for example, there is a systematic decline in apparent ages from the edge of the grain that is unlikely to be caused by excess argon. Here the apparent age decreases from 1721 ± 92 Ma, close to the mean age achieved for this sample (1738 ± 22 Ma), to a low of 1396 ± 156 Ma, considerably younger than expected. The younger ages recorded can be attributed to the affects of alteration and is discussed further in section 7.2.

5.4.3.2. Interpretation of Closure Profiles Produced

Of the profiles that had the youngest age at the edge of the grain and a general increase of ages inwards, few produced a smooth curve. In most cases one or more of the points within the grain fell significantly outside the curve shape, suggesting that a mechanism other than volume diffusion influenced these dates (section 3.7.4). In other cases, e.g. profiles in RRCR2 (Figure 5.7A-D), although there was a systematic increase in ages within the first 100-200 μm this was followed by a decrease in ages and apparent random ages variations beyond the rim area. This also suggests

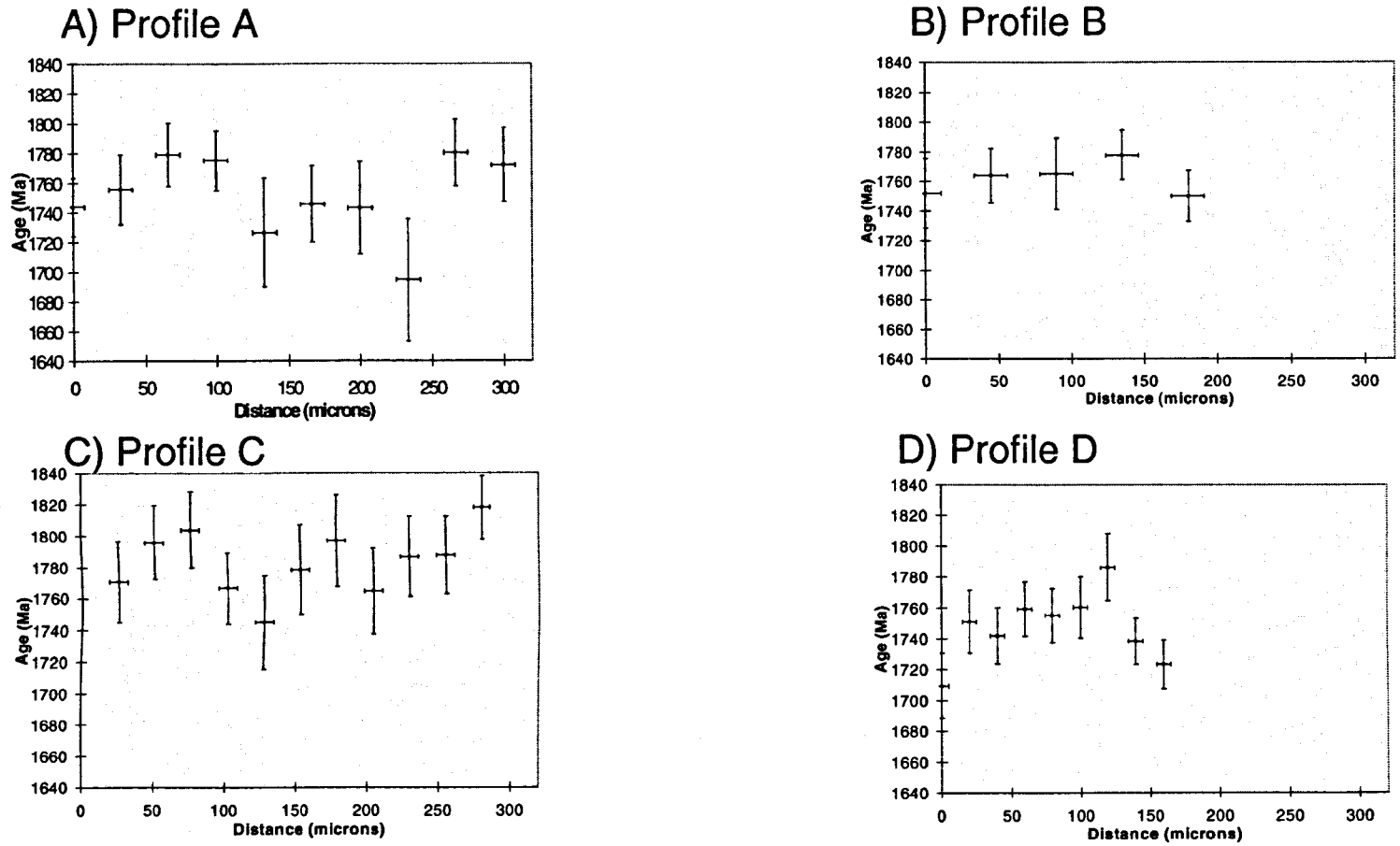

Figure 5.7: Closure profiles for RRCR2

that volume diffusion was not the only mechanism at work. These points will be discussed further in section 5.4.3.3 below. Because of these problems is it difficult to fit model curves to these data. Of the profiles that showed a crude curve shape, those in sample RRCR3 were the most convincing (Figure 5.8).

A good fit is found when the first 100 μm of profiles A to D of sample RRCR3 are plotted together (Figure 5.9). Using *DIFFARG* in *Matlab* (section 3.7.3) it is possible to construct possible cooling histories that fit the data produced (Figure 5.10). Although several scenarios can be crudely fitted to the data points, it is clear from Figure 5.10A that the linear cooling curves do not decrease in age sufficiently at the edge to fit the data. Excluding the edge point, the data would suggest a linear cooling history at a rate of between 1 and 3 °C/m.y. (Figure 5.10A). However, the large apparent age difference at the edge of the grain suggests a reheating event at some time during the cooling history and Figure 5.10B presents several possible histories involving reheating that fit the measured profiles within error. Alternatively, the edge point may have lost argon via another mechanism, such as alteration or defect enhanced diffusion, and should not be included within the closure profile. As a large number of possible T-t histories could fit the data points within their errors, it is impossible to further constrain the cooling history of this sample without other independently obtained information about the history of this rock sample.

In sample RRCR5 profiles A and E have very similar shaped curves, both showing younger ages at the edge, increasing with distance into the grain (Figure 5.11). However, there is about 120 m.y. age difference between these two curves. Profile A has an edge age of 1553 ± 36 Ma, reaching a peak of about 1650 ± 10 Ma after 150 μm, with a steady increase in ages in between; whereas profile E has an edge age of 1679 ± 32 Ma, reaching a peak of about 1730 ± 25 Ma after 100 μm. Both these profiles describe similar slopes to that seen in RRCR3 but do not have the large drop in age at the very edge seen in RRCR3. It is impossible to tell from the data (Appendix 5.2) which, if either, of these two apparent age profiles represents the "true" age and which is caused by other factors such as those discussed in section 7.2. However, it seems that whatever caused the discrepancy in ages between the profiles did not affect the shape of the profile produced. Because the ages in profile E are similar to those in sample RRCR3, this profile was used for modelling

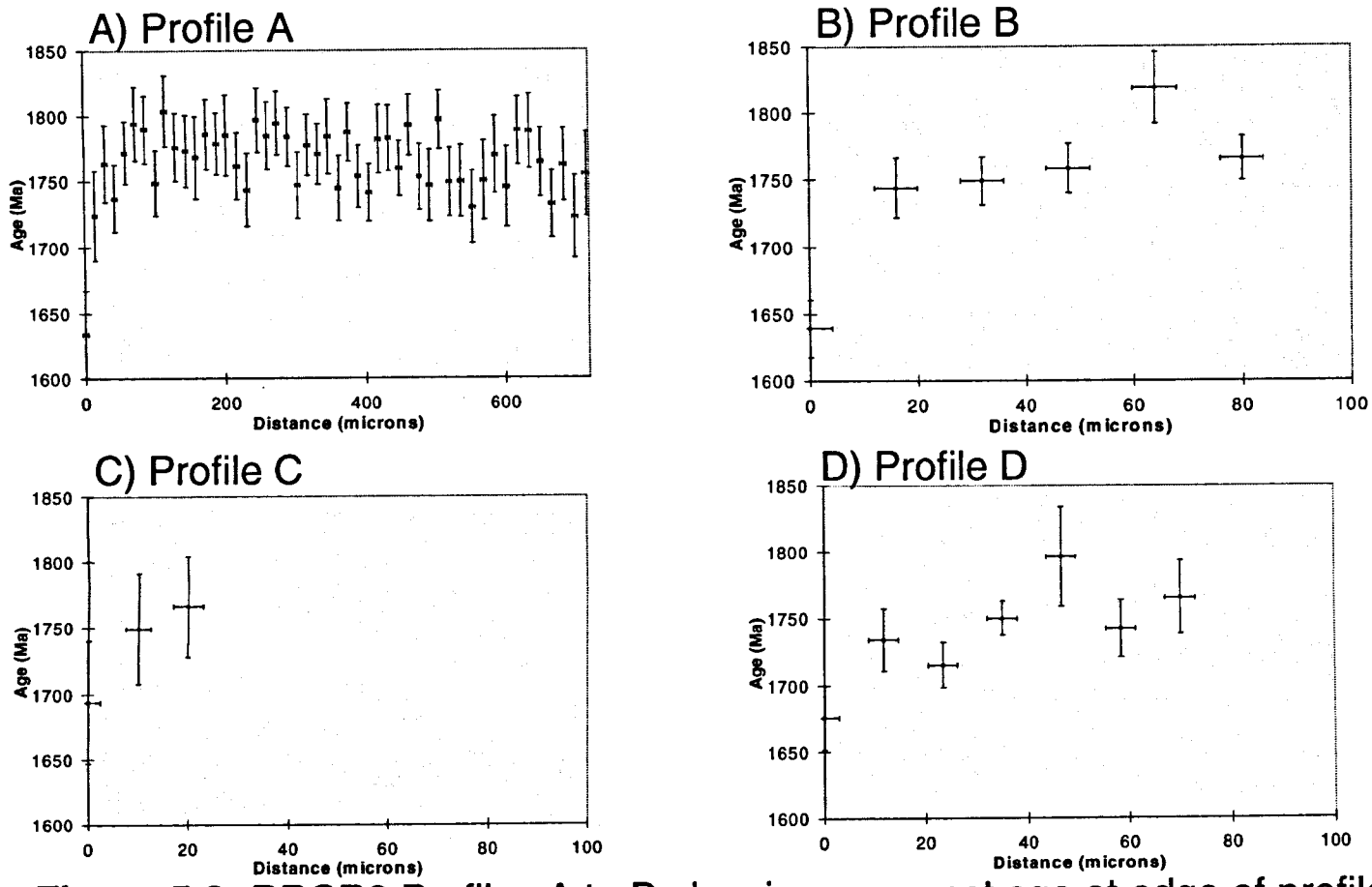

Figure 5.8: RRCR3 Profiles A to D showing youngest age at edge of profile

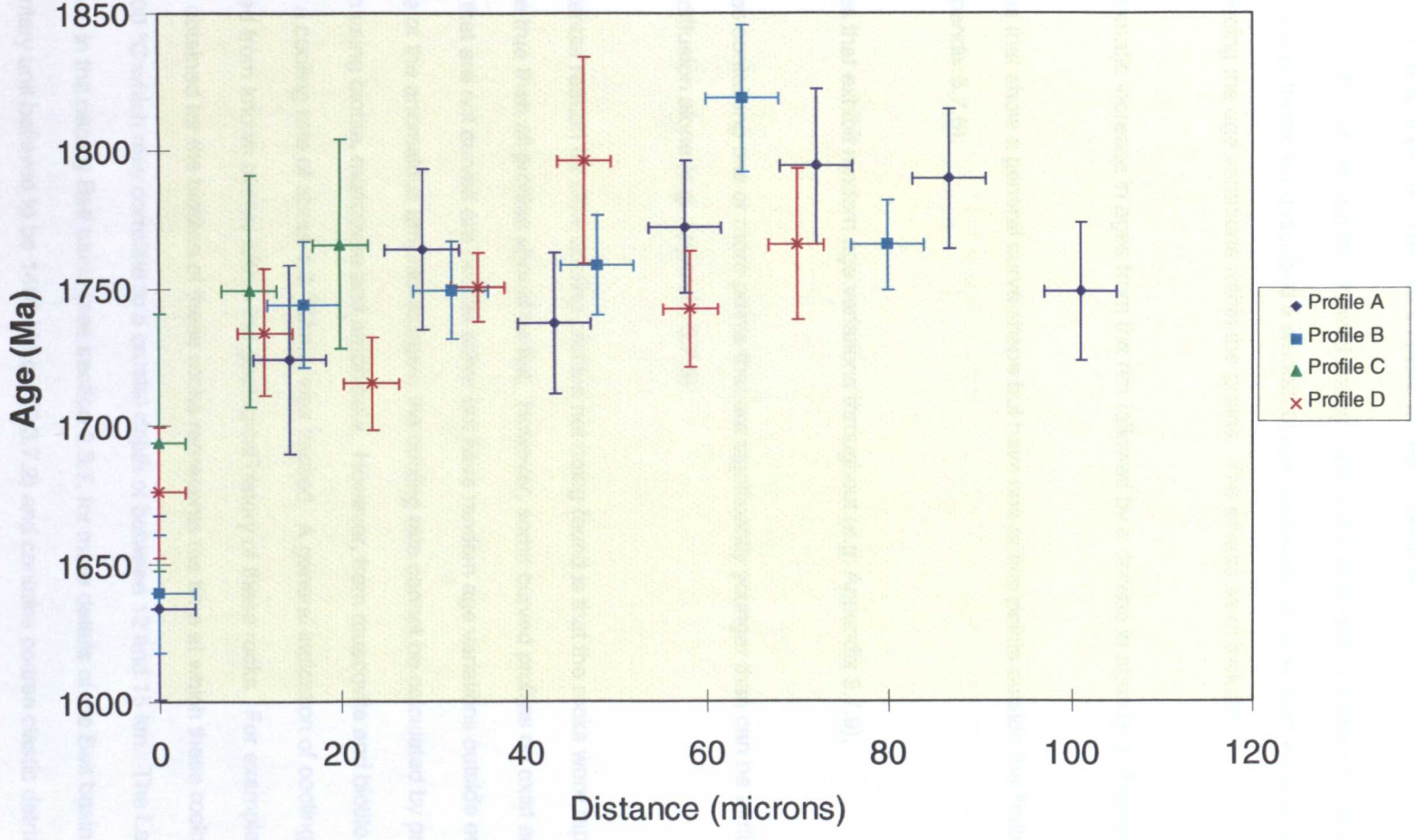

Figure 5.9: The first 100 microns of RRCR3 Profiles A-D plotted together

purposes. Using *DIFFARG* a linear cooling history of 2 °C/m.y. can be fitted to the data for this profile (Figure 5.12) which is consistent with the rate obtained for RRCR3.

5.4.3.3. Possible Reasons for No Profile being Produced

Because only 50% of the profiles showed young ages at the edge with a systematic increase in ages inwards, and of those few described a smooth curve, mechanisms other than volume diffusion must be influencing the age variations within the grains. The effects seen include:

a) a systematic increase in ages from the rim followed by a decline in ages (e.g. Appendix 5.7.4);

b) profiles that show a general curve shape but have one or two points outside the limits of the curve (e.g. Appendix 5.7.6);

c) profiles that exhibit random age variations throughout (e.g. Appendix 5.7.9);

d) profiles containing one or more points that are significantly younger than can be attributed to volume diffusion alone (e.g. Appendix 5.7.6).

One potential reason for slow cooling profiles not being found is that the rocks were rapidly cooled. If this were true then all profiles should be flat. However, some curved profiles do exist and those profiles that are not curved are not flat either but have random age variations outside errors. Because of the anomalous amphibole ages, the cooling rate cannot be calculated by producing an isochron using biotite, muscovite and amphibole. However, from muscovite and biotite from sample RMC42 a cooling rate of about 1.2 °C/m.y. was implied. A general indication of cooling rate can also be gained from known events within the geological history of these rocks. For example, the c.1780 Ma age obtained for the biotites of these rocks represents the time at which these rocks were at about 300 °C which may correlate to a crustal depth of between 12 and 15 km. The LaHood Formation in the nearby Belt basin (see section 9.3.7. for more details of the Belt basin) is a sedimentary unit believed to be 1400 Ma old (9.3.7.2) and contains coarse clastic detritus from

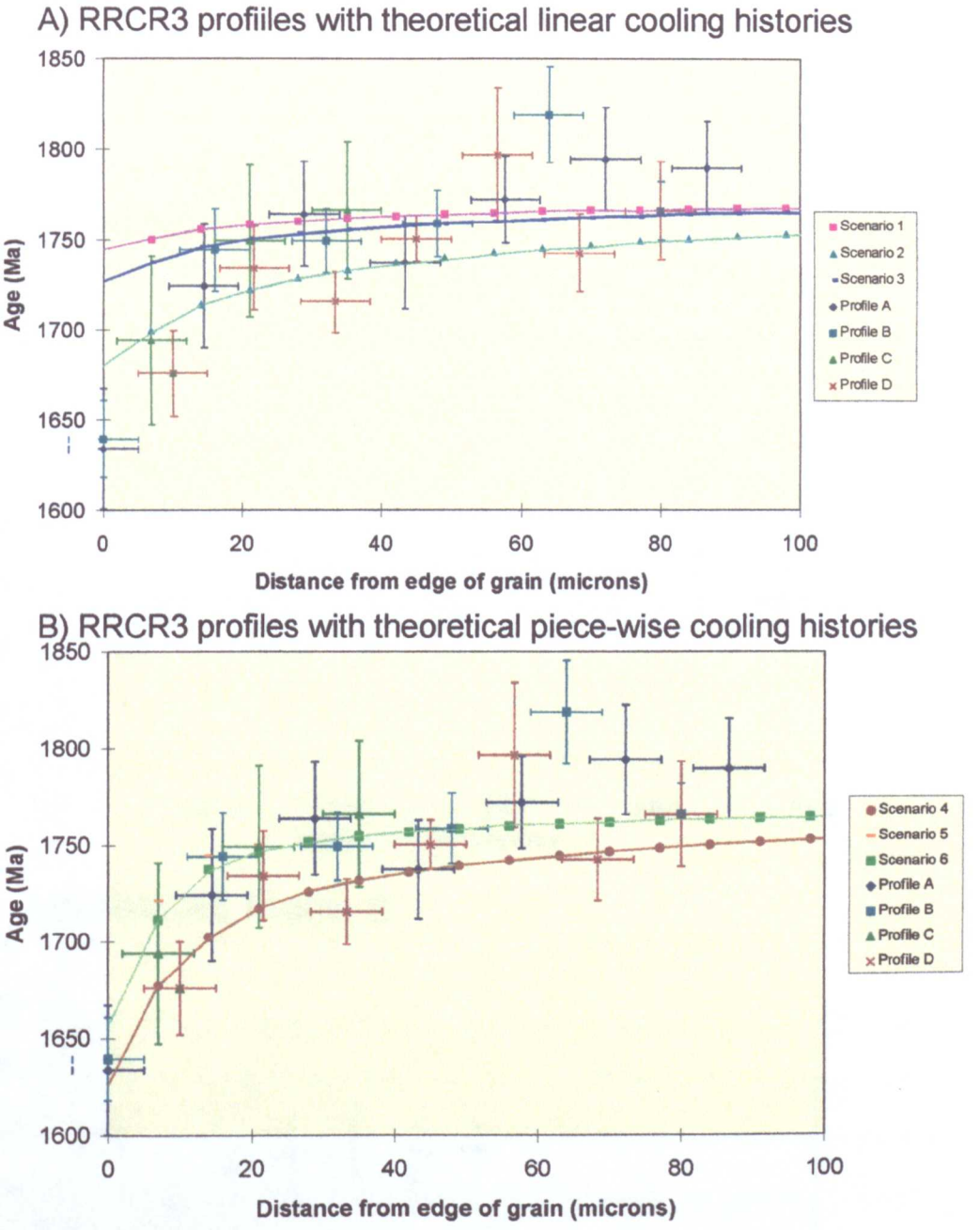

Scenario 1: Linear cooling from 350 °C from 1770 Ma at 3 °C/m.y.
Scenario 2: Linear cooling from 350 °C from 1770 Ma at 1 °C/m.y
Scenario 3: Linear cooling from 350 °C from 1770 Ma at 2 °C/m.y
Scenario 4: Linear cooling at 1 °C/m.y from 350 °C from 1770 Ma for 120 m.y., followed by a temperature increase to 250 °C, sustained for 10 m.y. before cooling to 25 °C at 1 °C/m.y.
Scenario 5: Linear cooling at 2 °C/m.y from 350 °C from 1770 Ma for 150 m.y., followed by a temperature increase to 200 °C, sustained for 10 m.y. before cooling to 25 °C at 2 °C/m.y.
Scenario 6: Linear cooling at 2 °C/m.y from 350 °C from 1770 Ma for 60 m.y., followed by a temperature increase to 250 °C sustained for 10 m.y., followed by a drop in temperature to 205 °C before cooling to 25 °C at 2 °C/m.y.

Scenarios 4 to 6 are designed to represent possible resetting events such as a greenschist facies metamorphism or igneous intrusion that might have disturbed the cooling history.

Figure 5.10: RRCR3 Profiles A-D plotted with theoretical closure profiles

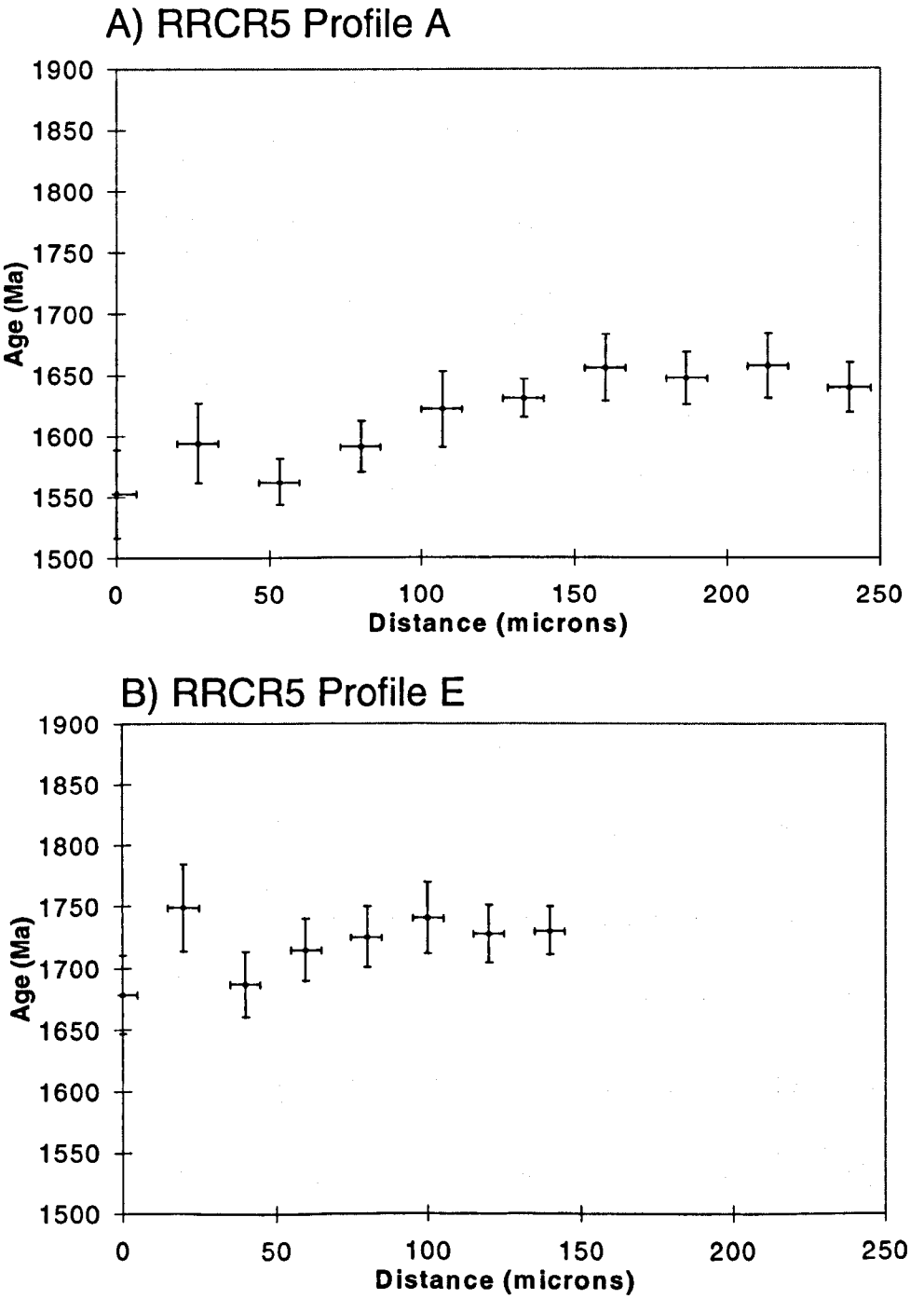

Figure 5.11: RRCR5 Profiles A and E showing similar curve shapes but different apparent ages

similar Precambrian rocks to those now exposed. This means that at 1400 Ma crystalline Precambrian rocks were near the surface. From this a time-integrated 1770-1400 Ma exhumation rate can be calculated, assuming a retrograde geotherm and an argon closure temperature. If the geotherm is 20-25 °C/km and the closure temperature for biotite is assumed for simplicity to be 300 °C, then the exhumation rate is 32 to 40 m/m.y. This is equivalent to an exhumation controlled cooling rate of c.0.8 °C/m.y., which is comparable to estimates from muscovite-biotite ages (RMC42) and biotite age profiles (RRCR3 and RRCR5). Therefore, theoretically slow cooling profiles should exist within these rocks and an explanation other than rapid cooling is required to explain the absence of profiles in some samples.

When no age variations were found at the edge of mineral separates when analysed, it could be assumed that the rim area was removed during the crushing process. In the profiles that do show age variations, significant variations occur within the first 50 μm or so and it is conceivable that this amount of material was lost during sample preparation. However, of the mineral separates analysed, 70% did show age variations, and of the thick sections analysed, 67% did not show age variations. This would suggest that although loss of the true edge of the grain is a possibility, it is of only minor significance and other causes for lack of age variations need to be sought.

The four profiles in RRCR2 are examples of profiles that initially increase systematically from the edge of the grain but then decrease in age (Figure 5.7A-D). In each case the drop in ages occurs between 130 and 170 μm in from the edge of the grain. This effect can be seen when all 4 profiles are plotted together (Figure 5.13). In profiles A and C the ages appear to then steadily increase again for a further 50 μm before once again decreasing (Figure 5.7.A-D and 5.13). To determine whether these oscillations in apparent ages occurred throughout the grain and whether they occurred at regular intervals, a profile was constructed from one edge of a grain to another in sample RRCR3. Such an effect would suggest a controlling factor within the structure of the biotite was responsible for the age variations, such as subgrains, rather than random multi-path diffusion (Section 3.7.4).

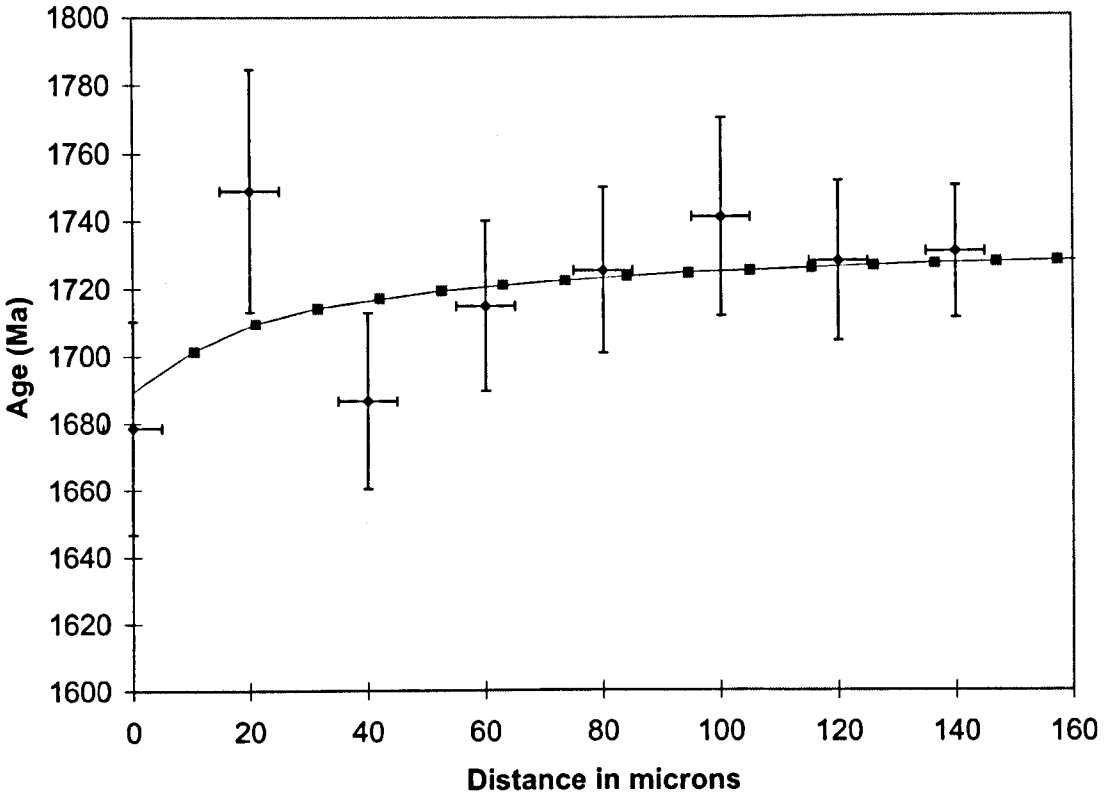

Figure 5.12: RRCR5 Profile E plotted with theoretical 2 °C/m.y. linear cooling curve

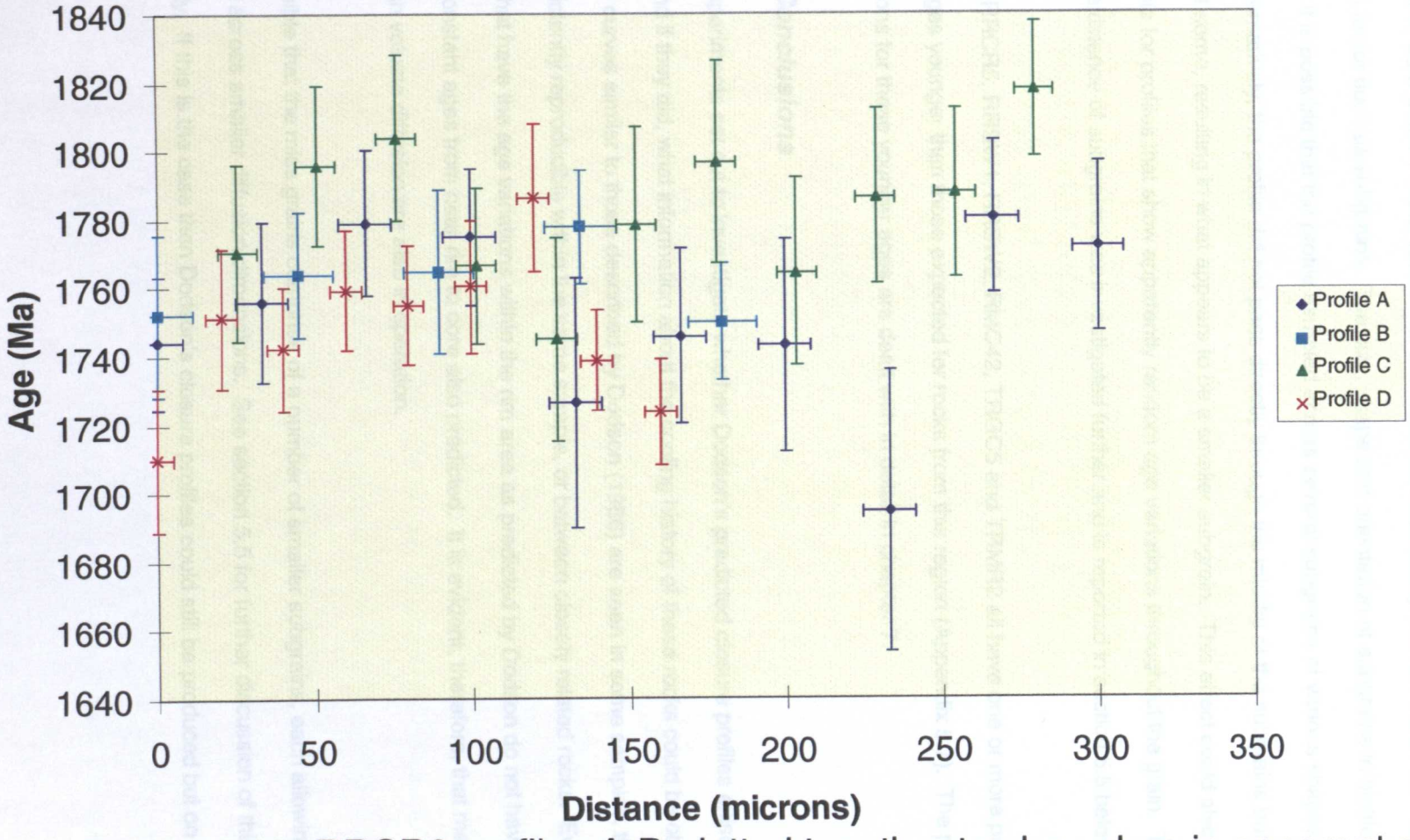

Figure 5.13: RRCR2 profiles A-D plotted together to show drop in apparent ages within profiles

To test this a grain 720 μm in diameter in sample RRCR3 (Profile A) was systematically analysed in a series of traverses from one edge to the other, requiring 49 traverses in total (Plate 5.1). The resultant profile showed that age variations occur across the length of a grain, therefore, in sample RRCR3 although the systematic age variations in the rim area predicted by Dodson (1986) were found, the almost constant ages from near-rim to core were not (Figure 5.8A). Although there does not appear to be a pattern to the variations, this does not necessarily rule out the possibility of a controlling factor such as subgrains. The size, shape and orientation of subgrains in biotite are not known so it is possible that the profile sampled across several subgrains of various shapes and sizes. Alternatively, the profile did not pass directly through the middle of the subgrains but crossed corners of some, resulting in what appears to be a smaller subgrain. This effect could also be responsible for profiles that show apparently random age variations throughout the grain. The possible existence of subgrains was investigated further and is reported in section 5.5 below.

Samples RRCR5, RRSW1, RRSW2, RMC42, TRGC5 and TRMR2 all have one or more profiles that contain ages younger than those expected for rocks from this region (Appendix 5.7). The possible explanations for these younger ages are dealt with in detail in chapter 7.

5.4.4. Conclusions

These experiments set out to investigate whether Dodson's predicted closure profiles existed in nature and if they did, what information about the cooling history of these rocks could be obtained. Although curves similar to those described by Dodson (1986) are seen in some samples, they are not consistently reproducible within the same sample, or between closely related rocks. Even profiles that have the age variations within the rim area as predicted by Dodson do not have the almost constant ages from near-rim to core also predicted. It is evident, therefore, that mechanisms other than volume diffusion are also in operation.

It is possible that the mica grains comprise of a number of smaller subgrains, each allowing volume diffusion across smaller diffusion dimensions. See section 5.5 for further discussion of this possibility. If this is the case then Dodson's closure profiles could still be produced but on a

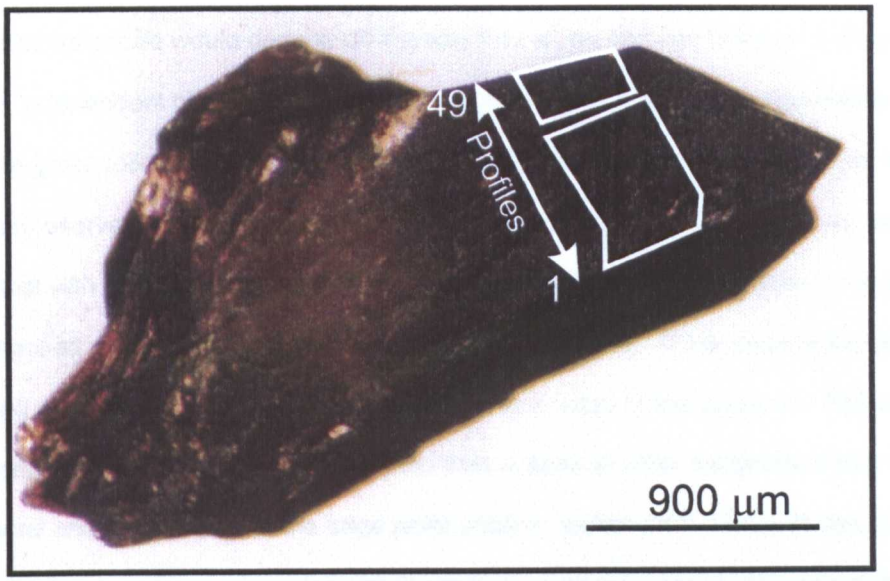

Plate 5.1: Photograph of biotite grain from RRCR3 showing location of ablation pits for analyses used to construct Profile A

subgrain scale, with multiple profiles existing within a single mineral grain. However, the shape of the closure profile would depend on the way that argon diffused between subgrains. If each subgrain were independent of the next then each subgrain would cool in the same way as predicted for a whole grain, following Dodson's assumption that the mineral grain is in contact with an infinite well-mixed reservoir, and a series of closure profiles would be found. If, however, subgrains in close contact with each other influenced the diffusion of argon from the adjacent subgrains, this infinite well-mixed reservoir assumption would no longer be valid. At the edge of the grain the infinite well-mixed reservoir assumption could be used for one edge of the subgrain. This could allow for a greater age variation within this subgrain than is seen in other subgrains within the body of the mineral and would result in the edge point analysis yielding the youngest age. Overall, a biotite grain comprising numerous subgrains would produce youngest ages at the edge of the grain, followed by continuous but smaller age variations throughout the grain, which is what is observed in some samples (e.g. RRCR3).

In addition to subgrains, it seems likely that multi-paths exist within these samples that affect some of the ages produced and result in either no apparent profiles being produced or ages that fall outside the profile. The existence of multi-paths can obscure the true shape of a profile or make the interpretation of profiles more difficult. It seems unlikely that in natural samples volume diffusion would be the only process in operation, therefore multi-paths will always affect the shape and validity of any profiles produced, or prevent a profile being produced altogether.

Despite the influences of multipath diffusion and/or subgrains, in some cases profiles can be seen and from these information about the cooling history of the rocks obtained. It is encouraging that both the profiles from samples RRCR3 and RRCR5 suggest a cooling rate of between 1 and 3 °C, and that this rate corresponds with the 1.2 °C/m.y. cooling rate inferred from biotite and muscovite ages from sample RMC42, and that both these estimates fit within the known geological history of the area. However, the very edge point in the profiles in RRCR3 suggest that simple linear cooling history was not followed and that a reheating event has influenced the ages produced. If, however, this edge was affected by multi-path diffusion or alteration then it should not be included within the closure profiles, returning the interpretation of the cooling history back to a linear cooling rate between 1 and 3 °C. For this reason, caution must be exercised when interpreting closure profiles

and, ideally, other information about the history of the rocks should be used to corroborate the interpretation of a closure profile. However, profiles have been useful in this experiment because they were able to provide some idea of the cooling rate of these rocks that was not possible to achieve through multiple mineral isochrons because all amphibole ages were affected by other factors.

5.5. High Spatial Resolution Investigation of Age Variations Within Biotite

5.5.1. Introduction

The possibility that large biotite grains comprise a number of smaller subgrains was investigated by Wright *et al.* (1991) who measured the relationship between apparent ages and measured grain size in an Archæan slowly cooled terrain. They found that grain size influenced apparent age below about 225 μm, with smaller grains yielding younger apparent ages. Above this grain size the apparent ages did not alter significantly with grain size. This, they believed, suggested that the grains contained subgrains and that the effective diffusion dimension never exceeded 225 μm. However, Lee (1995) suggested that these results could be due to multipath diffusion having a greater influence than volume diffusion on larger grains (section 3.7.4).

Spot dating of single mineral grains in this current study has also suggested that subgrains and multi-path diffusion were influencing the age variations produced. In order to test this idea further an experiment was designed using a very high spatial resolution dating technique to determine whether age variations on a small scale could be detected.

5.5.2. High Spatial Resolution Experiment Design

The spatial resolution of UV laser based ^{40}Ar-^{39}Ar geochronological technique is limited by two factors: the diameter of the laser beam, and the amount of gas released. The UV laser microprobe used for this research has a minimum laser diameter of about 5 μm which allows analysis at a resolution of around 10 μm, far in excess of any other experiment performed so far. Because these

samples are Precambrian in age, they contain a high concentration of ^{40}Ar. However, the precision of the age and, therefore, the amount of sample required for analysis, is limited by the concentration of ^{39}Ar released. Under irradiation conditions from other irradiation used in this study, a 50 μm pit in a Proterozoic biotite will release approximately 3×10^{-11} cc of ^{39}Ar. In order to obtain a similar concentration for a smaller ablation pit it is necessary to subject the sample to a high level irradiation, increasing the amount of ^{39}K transformed to ^{39}Ar, and thus increasing the ^{39}Ar concentration within the sample. Although a high level irradiation increases the influence of the interfering reactions, these biotite samples contain very little Ca so this does not greatly affect the $^{40}Ar/^{39}Ar$ ratio.

For this experiment sample TRMR2 was selected and prepared as a thick section. This sample was chosen because it had shown a considerable variation in ages when analysed previously (Table 5.1 and Appendix 5.2) that would be readily detectable when analysing smaller amounts of material. The sample was prepared for irradiation in the usual manner and sent to the McMaster reactor (McMaster 7 in Appendix 5.1). Normally irradiation is carried out for 15 to 50 hours, but this irradiation was sustained for 200 hours, and the sample was allowed to cool for four months before starting analysis. Analysis of standards determined the J-value as $0.04693 \pm 2.3 \times 10^{-4}$

Two experiments were undertaken on this sample. The first experiment (A) analysed a grain within the thick section in non-basal orientation. The grain was 150 by 70 μm and 20 analyses were carried out within a 50 μm square in part of the grain (Figure 5.14A). Each analysis was made by firing a low intensity laser beam for 3 minutes into the sample without moving the stage within a 5 minute analysis time, resulting in individual pits about 15 μm in diameter (Figure 5.14A). Approximately 2.5×10^{-12} cc of ^{39}Ar were released. Subsequent ablations were made adjacent to previous pits, analysing the sample in a grid fashion. Blanks were run after every two samples. However, in this orientation, analyses were carried out across cleavage planes so age variations were influenced by the cleavages. Although this could detect age variations caused by factors such

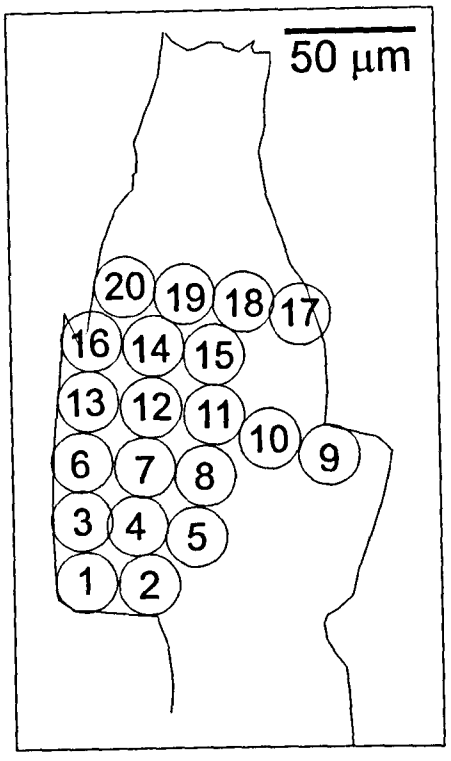

A) Sketch of biotite grain showing location of ablations pits

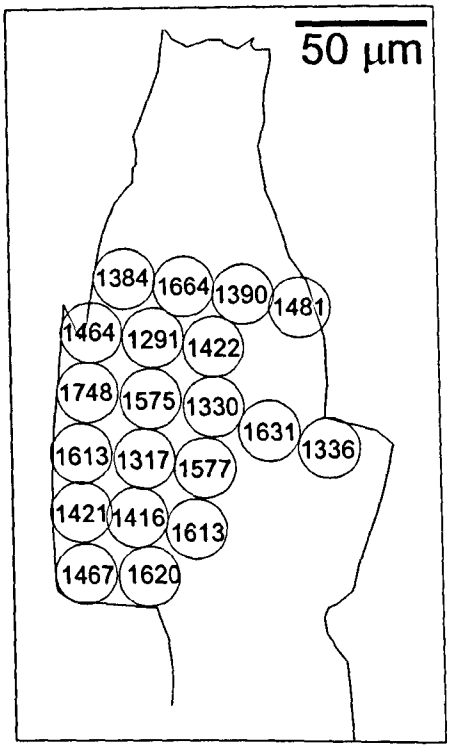

B) Sketch of biotite grain showing ablations pits with apparent ages (Ma)

Figure 5.14: Biotite grain from high spatial resolution experiment A on TRMR2

as alteration along the cleavage planes, it could not detect those caused by volume diffusion or subgrains which would dominate analyses in basal section. For this reason, the irradiated thick section was crushed and individual biotite grains picked for analysis.

For the second experiment (B) a grain 370 by 320 μm was analysed in basal section. The intensity of the laser beam was increased and laser was fired for 30 seconds within a 3 minute analysis time, resulting in ablation pits about 30 μm in diameter. This short ablation time resulted in shallow pits, potentially reducing the influence of cleavage alteration at depth. In this experiment approximately 6.75×10^{-13} cc of ^{39}Ar was released with each analysis, although towards the edge of the grain, the lath thinned, yielding too small a concentration of ^{39}Ar to produce an age. The location of the pits within the grain is illustrated in Figure 5.15A and B.

5.5.3. Results

Data in Appendix 5.6 provide the detailed results of this experiment. Figures 5.14B and 5.15C show the age obtained for each ablation pit relative to its position within the grain. Tables 5.3 and 5.4 below give the apparent age obtained from each ablation pit.

Table 5.3: Spot numbers and apparent ages for Experiment A

Spot	Age (Ma)	± 2 σ	Spot	Age (Ma)	± 2 σ
1	1467	282	11	1330	346
2	1620	196	12	1575	280
3	1421	192	13	1748	316
4	1416	248	14	1291	336
5	1613	166	15	1422	92
6	1613	169	16	1464	256
7	1317	338	17	1481	62
8	1577	182	18	1390	136
9	1336	224	19	1664	302
10	1631	246	20	1384	302

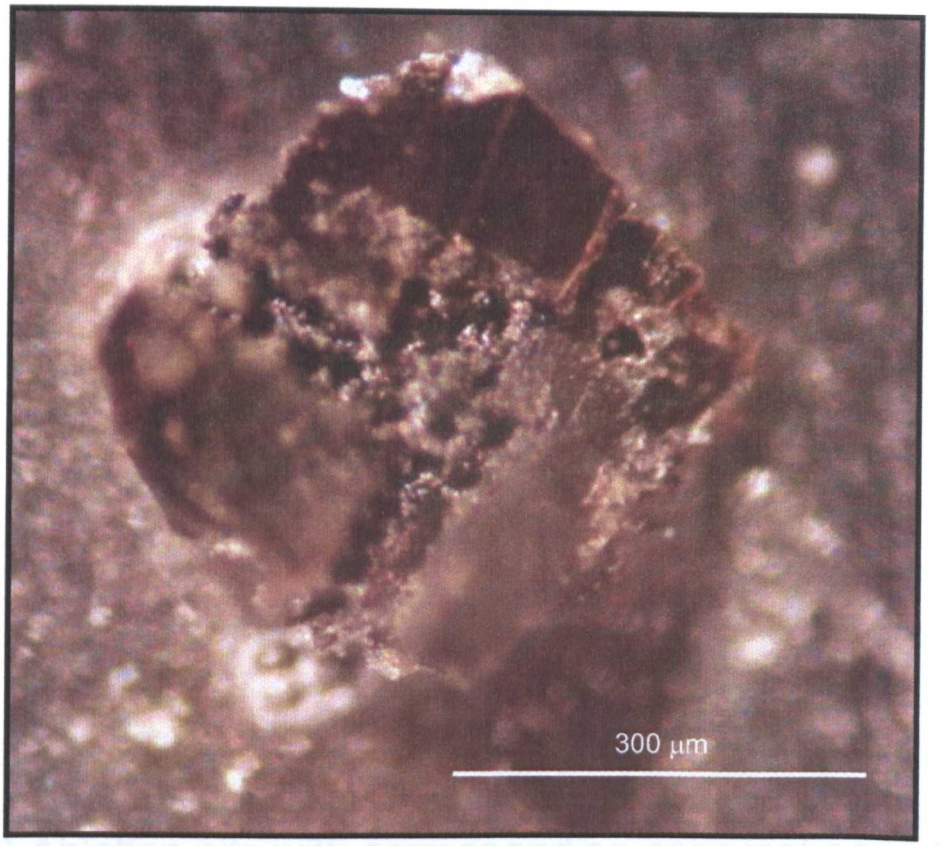

A) Biotite grain showing ablation pits

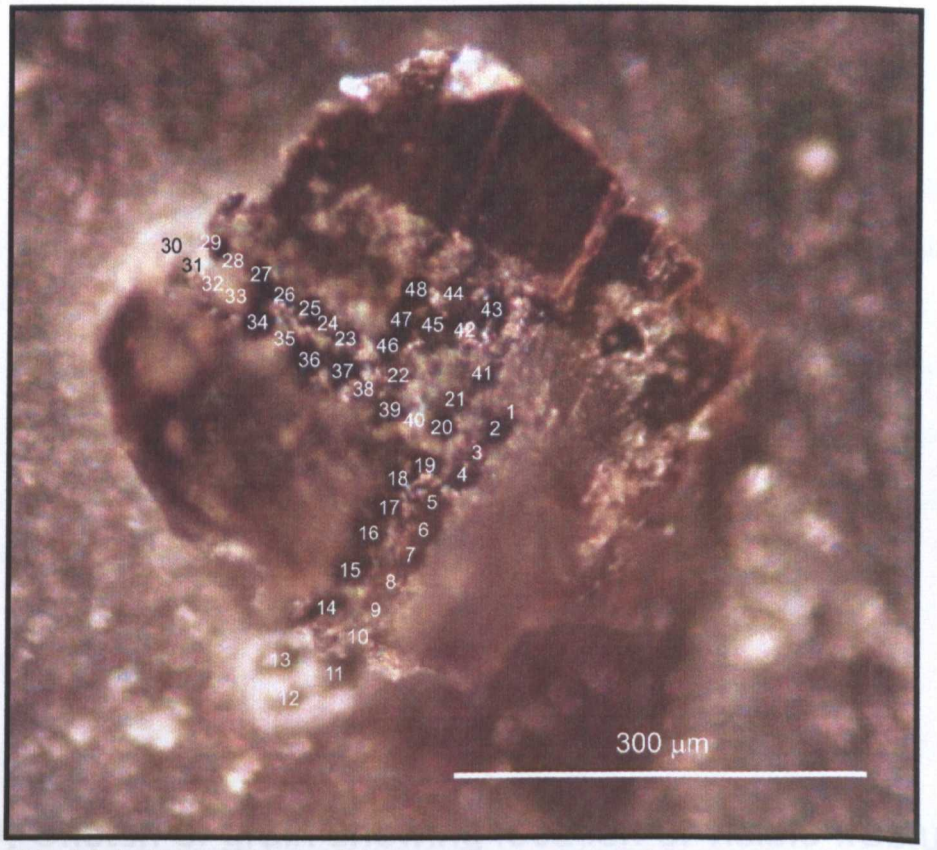

B) Ablation pits with analysis number

Figure 5.15: Biotite grain from high spatial resolution experiment 2 on TRMR2

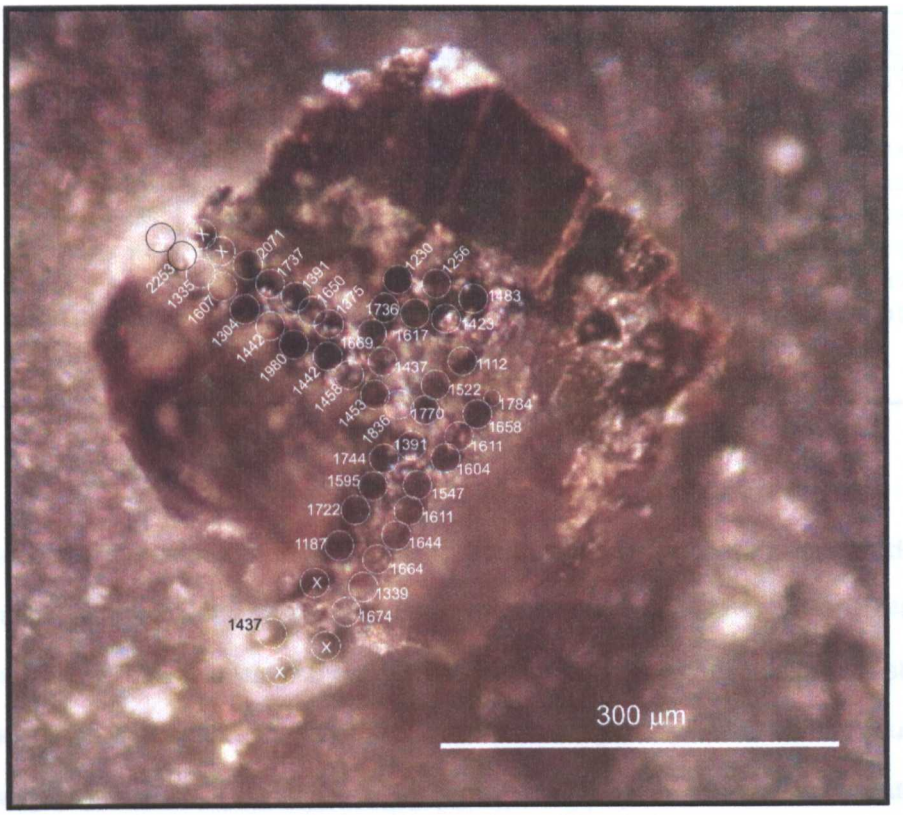

C) Ablation pits with corresponding apparent ages (Ma)

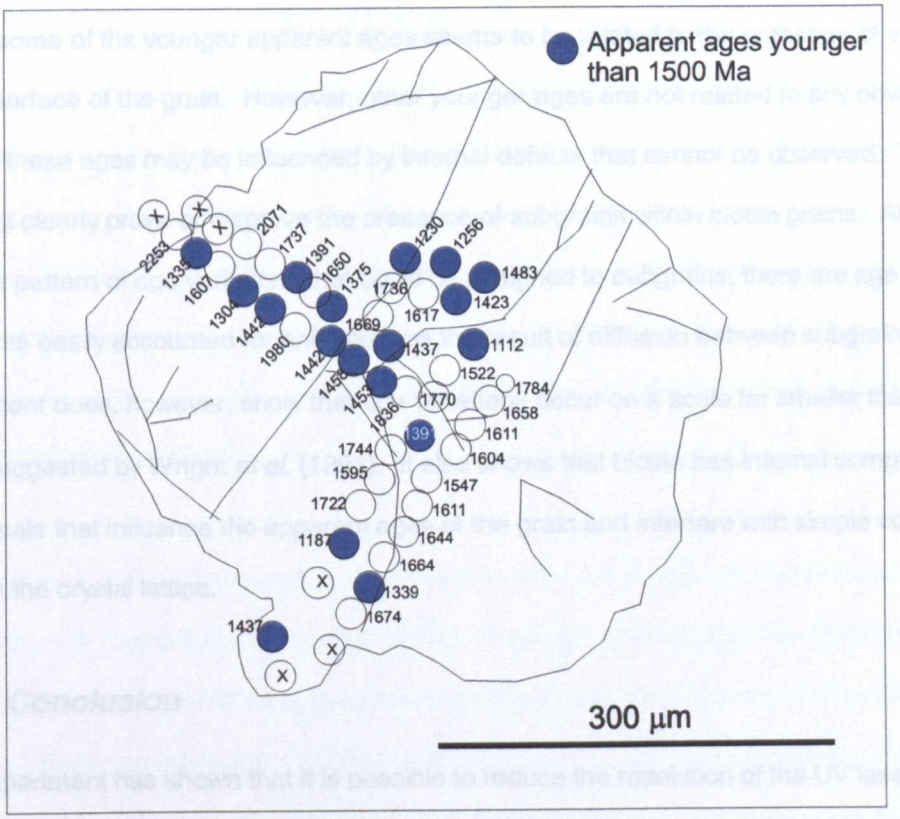

D) Sketch of grain showing location of visible fractures

Figure 5.15 continued

Table 5.4: Spot numbers and apparent ages for Experiment B

Spot	Age (Ma)	± 2 σ	Spot	Age (Ma)	± 2 σ	Spot	Age (Ma)	± 2 σ	Spot	Age (Ma)	± 2 σ	Spot	Age (Ma)	± 2 σ
1	1784	1008	11	3458	2300	21	1522	284	31	2253	1158	41	1112	402
2	1658	272	12	2441	8338	22	1437	510	32	1335	924	42	1423	338
3	1611	170	13	1437	1350	23	1375	554	33	1607	1090	43	1483	290
4	1604	304	14	601	2092	24	1650	366	34	1304	769	44	1256	552
5	1547	458	15	1187	794	25	1391	366	35	1442	650	45	1617	598
6	1611	458	16	1722	302	26	1737	428	36	1980	1524	46	1669	1008
7	1644	380	17	1595	280	27	2071	672	37	1442	620	47	1736	796
8	1664	742	18	1744	372	28	Blank		38	1458	374	48	1230	438
9	1339	1436	19	1391	532	29	Blank		39	1453	316			
10	1674	2124	20	1770	346	30	Blank		40	1836	438			

5.5.4. Discussion

Because of the small amount of gas released, the errors on the apparent ages produced are high, thus making interpretation problematic. However, there does appear to be 300 to 400 m.y. apparent age variations within the scale of the experiment, and some adjacent ablation pits show 1 to 2 hundred million year apparent age differences. Answering the question of what causes these apparent age variations is also difficult. In Figure 5.14B a line of younger age variations through the centre of the ablated area could be related to alteration along a cleavage plane. Similarly, in Figure 5.15D, some of the younger apparent ages seems to be related to the presence of visible fractures on the surface of the grain. However, other younger ages are not related to any obvious defects. Instead these ages may be influenced by internal defects that cannot be observed. This experiment does not clearly prove or disprove the presence of subgrains within biotite grains. Although there is no clear pattern of age variations that could be assigned to subgrains, there are age variations that cannot be easily accounted for and could be the result of diffusion between subgrains. This experiment does, however, show that age variations occur on a scale far smaller than the 225 μm scale suggested by Wright *et al.* (1991). It also shows that biotite has internal complexities on a very small scale that influence the apparent ages of the grain and interfere with simple volume diffusion through the crystal lattice.

5.5.5. Conclusion

This experiment has shown that it is possible to reduce the resolution of the UV laser microprobe to 15 μm spot sizes on biotites of Precambrian age by increasing the level of the irradiation to which the sample is subjected. This allows the study of age variations within single mineral grains in very fine

detail and the investigation of effects that are not detectable at higher resolution. Although this experiment was hampered by very high errors, further refinement of this method, involving lower blank levels, particularly on the ^{40}Ar and ^{36}Ar peaks; adjustment of the power of the laser beam; the length of analysis time; and degree of irradiation could reduce these errors to a reasonable level, facilitating meaningful interpretation of the apparent ages produced.

5.6. Overall Conclusions

The mean matrix biotite ages obtained in this study have constrained the timing of cooling to biotite blocking temperature from the metamorphic peak of amphibolite facies metamorphism within this part of south-western Montana to be between 1780 and 1740 Ma. It is clear that this event has extensively and consistently influenced the Ruby Range, Tobacco Root Mountains and Highland Mountains, implying that at this time these three mountain ranges were very closely related and that their exhumation was synchronous. There is no suggestion of a gradation of ages towards the margin of the Wyoming Province to the west or towards the Giletti Line in the east.

However, some of the ages have clearly been influenced by later geological events that have caused partial or total resetting (discussed in Chapter 7). This is particularly true for the Tobacco Root Mountains where the influence of the Tobacco Root Batholith is evident. Furthermore, the mean amphibole ages also show the effects of alteration and resetting. Although this does not provide a useful contribution to obtaining an age for the area, it does highlight some of the difficulties associated with dating even slightly altered amphibole. It demonstrates that both total fusion and step-heating dates obtained for amphibole should not be used in isolation from other geochronological information.

This chapter has demonstrated that slowly cooled rocks do exhibit age variations across single mineral grains as predicted by Dodson (1986). However, it has also shown that other factors can influence the way argon diffuses to and from a mineral and that the theoretical profiles predicted by Dodson (1986) are rarely seen in nature and are never perfect. The profiles detected the presence of excess argon in some samples but this was fortunately a rare occurrence that did not greatly hamper the interpretation. The influence of multi-path diffusion, such as caused by the presence of

fractures and cleavages, was a greater problem and appeared to have an influence on most profiles. Other factors that also disturbed the shape of the profiles produced were alteration (discussed in Chapter 7), a complex geological history involving resetting (also discussed in Chapter 7), and the possible presence of subgrains. However, where cooling profiles were found, together with a biotite and muscovite "isochron", they suggested a cooling rate of between 1 and 3 °C/m.y. for at least the part of the geological history for these rocks where muscovite and biotite were becoming closed to Ar diffusion. This is consistent with the known Proterozoic geological history of this region.

It is clear that the high spatial resolution capability of the UV laser microprobe technique for the application of ^{40}Ar-^{39}Ar geochronology provides a versatile tool that can reveal considerable geochronological information about an area that would not have been possible using bulk sample techniques. Mean ages help to provide general reference ages to which ages obtained from more detailed probing of individual grains can be compared. Linear traverses detect age variations caused by geological history (cooling and resetting), alteration, multi-path diffusion, and subgrains. The further refinement of the spot-dating technique reported in section 5.5 has made it possible to reduce the spatial resolution of the UV laser microprobe technique further for samples of this age, allowing even finer details to be characterised.

Chapter 6 - ^{40}Ar-^{39}Ar Dating of Biotite Inclusions in Garnet

6.1. Introduction

In order to date events that occurred before the last major geological event it is necessary to use minerals that were not reset by it. This has been achieved using direct dating of garnet (Vance and O'Nions, 1992). However, garnet contains only very small concentrations of potassium and cannot be dated directly by the ^{40}Ar-^{39}Ar technique. Potassic inclusions, such as biotite, however, might yield ^{40}Ar-^{39}Ar ages. The premise that garnet could have a shielding effect on inclusions within it that would protect the inclusions from resetting by later geological events was discussed first by DeWolf *et al.* (1993), reviewed below. Kelley *et al.* (1997) (also reviewed below) expanded this idea and investigated the possibility of similar shielding properties for biotite inclusions in garnet. This research is a further expansion of that work, repeating the use of a high spatial resolution ^{40}Ar-^{39}Ar dating technique to analyse biotite inclusions completely enclosed in garnet. The aim is to test the technique on polymetamorphic rocks from a different area to that studied by Kelley *et al.* (1997), whilst increasing the understanding of shielding properties of garnet.

From the geochronology of matrix minerals reported in chapter 5 it is clear that a significant metamorphic event occurred at 1780-1740 Ma, resetting or forming the mica in the matrix. In order for the biotite inclusions in garnets to preserve an age older than this the following criteria must be met:

1) the inclusion-rich garnets were formed during an older metamorphic event

2) the blocking temperature for argon in garnet is high enough to prevent resetting of biotite inclusions within it and the solubility of argon in garnet is lower than for argon in biotite

3) the inclusions are completely enclosed within garnet, preventing the loss of argon by fast path diffusion.

To test the first criterion, a small subset of the garnets were dated (section 6.4). The second criterion can be investigated by measuring the diffusion for argon in garnet (section 6.5), and third criterion can be assessed by examining garnet for the presence of fast diffusion paths (section 6.6).

6.2. Previous Dating of Inclusions in Polymetamorphic Garnets

6.2.1. U-Pb Dating of Monazite Inclusions in Garnet

A study by DeWolf *et al.* (1993) dated monazite inclusions within garnets in polymetamorphic rocks from the Archæan core complex of the Wind River Range, Wyoming. The Wind River Range lies within the central Wyoming Province (see Figure 2.1). Previous dating had focused upon the late Archæan granitoids for which whole rock ages between 2670 and 2550 Ma had been obtained (Stuckless *et al.*, 1985; Compston *et al.*, 1986; referenced in DeWolf *et al.*, 1993). DeWolf *et al.*'s study was designed to investigate the possible link between garnet and monazite growth by undertaking U-Pb dating of monazite inclusions within garnet using the high spatial resolution technique of secondary ion mass spectrometry (SIMS).

Below about 600 °C, diffusion rates in garnet are slow enough that the Rb-Sr, U-Pb and Sm-Nd isotopic systems appear to preserve the time of garnet growth. However, at upper amphibolite facies, U-Pb ages for garnet are generally older than Sm-Nd ages for the same rock. DeWolf *et al.* (1993) suggested that this is because Pb diffuses more slowly than Sm and Nd in garnet and at amphibolite facies temperatures the blocking temperature for the Sm-Nd dating system is exceeded. The concentrations for uranium in garnet are low (typically <1 μg/g) and the U-Pb age of garnet is strongly influenced by inclusions of zircon and monazite within the garnet. Zircon is commonly an inherited mineral so cannot be used to produce a reliable age for a garnet. Monazite may also be inherited but this is less common. Therefore, DeWolf *et al.* (1993) believed that dating monazite inclusions within garnet could prove to be a useful method for dating garnet growth if a link between garnet and monazite growth could be established, or if monazite U-Pb systematics remained "open" until incorporation in a growing garnet.

Reported in this study were the U-Pb ages of seven monazite inclusions. Of those, 4 were located in fractures in the garnet and gave ages of c.2600 Ma. One inclusion was next to a fracture and gave an age of 2764 ± 12 Ma, and two were away from visible fractures, giving ages of 2781 ± 6 Ma and 2809 ± 10 Ma. In comparison, a single large monazite inclusion from the matrix was dated, giving ages between 2788 and 2523 Ma. The oldest age was obtained from the rim of the monazite and was believed to be closest to the thermal maximum. The youngest age was from the core which was believed to be reset.

From this it was concluded that the monazite inclusions fully armoured by garnet were preserving dates related to a phase of metamorphism that pre-dated the emplacement of the Bridger Batholith (responsible for the apparent matrix ages) by >100 m.y. Therefore, it was believed that this dating method could provide estimates for the time of garnet growth, even in high grade terranes where most chronometers are reset.

6.2.2. ^{40}Ar-^{39}Ar Ages from Biotite Inclusions in Garnet

Kelley *et al.* (1997) investigated whether the shielding effect of garnet, demonstrated for monazite inclusions by DeWolf *et al.* (1993), could also work with biotite inclusions within garnets from polymetamorphic rocks. This investigation was undertaken using the high spatial resolution ^{40}Ar-^{39}Ar laserprobe technique to date individual biotite inclusions completely occluded within garnet from a Proterozoic metamorphic assemblage of southern India.

In this study five biotites from the matrix were dated and gave an age of 454 ± 4 Ma, which is consistent with both laser fusion ^{40}Ar-^{39}Ar ages for biotite and Rb-Sr biotite ages from the region. A total of 34 biotite inclusion ages were reported, of which the majority yielded ages identical to the matrix age. However, five inclusions gave ages between 2100 and 1800 Ma, corresponding to zircon ages from the same rock.

From this it was concluded that, in a small population of biotite inclusions, the ^{40}Ar-^{39}Ar system remained closed during the high-grade metamorphism of the Pan-African event that produced the

454 Ma ages in the unprotected matrix biotites and in the incompletely shielded biotites included in garnet.

6.3. New Experimental Attempts to Date Biotite Inclusions in Garnet

6.3.1. Sample Selection and Analytical Method

Initially experimentation using the UV laser microprobe was carried out on thick sections from Ruby Range samples supplied by Dr Dahl. Ages were obtained from matrix biotite, biotite adjacent to garnet, and biotite inclusions in garnet.

In order to increase the sample density and provide more inclusions to analyse, further experimentation was carried out using polished garnet separates (section 3.2.4). For this experiment samples RRCR3 and RRSW2 from the Ruby Range were chosen, samples TRBC2, TRER7 from the Tobacco Root Mountains, and HLM2 from the Highland Mountains. These specimens were selected because they contained a high abundance of both matrix biotite and garnet and some biotite inclusions in garnet. Furthermore, the samples provide a good geographical distribution across the field area. In addition, ages for biotite inclusions in samples TRGC5 and TRMR2 were obtained from thick sections whilst the samples were being analysed for matrix biotite ages (section 5.2). Irradiation details for these samples can be found in Appendix 5.1 under McMaster 2, McMaster 3 and McMaster 5.

Sample RRCR3 contained numerous large (3 - 6 mm diameter) garnets with abundant biotite inclusions of various sizes, thus providing a high sample density. The disadvantage of this sample was that the large size of the garnets meant that some biotite inclusions were deep within the garnet and beyond the depth that the laser can penetrate. Unfortunately, viewing the sample through the camera attached to the laser probe produces a two-dimensional image and it is impossible to judge the depth of the inclusions. To reduce this problem photographs were taken of the garnets prior to analysis and the sample was viewed under a low powered binocular microscope. On the photograph each inclusion was marked with a red dot if judged to be too far below the surface for analysis or a green dot if close enough to the surface for analysis (Plate 3.4). The highly fractured nature of the

sample was a further problem because inclusions situated away from fractures were limited in number (Plate 3.2).

Sample RRSW2 was chosen mainly on the basis of thin-section and microprobe analysis. Thin-section analysis revealed the presence of orthopyroxene, suggesting that this rock could have reached granulite facies conditions of metamorphism. This was supported by probe data that revealed a higher MgO/FeO ratio in the garnet (Table 4.1), suggesting a slightly higher pyrope component consistent with this rock being of higher grade. Because the Archæan age obtained by James and Hedge (1980) was believed to have dated a granulite facies metamorphic event (section 2.7.4), it seemed conceivable that the garnets of this rock (RRSW2) were Archæan in age and would be most likely to preserve older inclusions. However, there were very few biotite inclusions within the garnets of this rock and some inclusions of sphene and opaques. Nevertheless, the low density of fractures in the garnets meant that the inclusions were more likely to be completely enclosed within garnet.

Rocks TRER7, TRBC2 and HLM2 were selected principally because they contained abundant garnets and were from suitable geographical locations to provide good distribution across the field area.

Samples TRGC5 and TRMR2 were of interest because of their close proximity to the Tobacco Root Batholith. In these rocks the biotite inclusions may have been protected from resetting by the batholith. This allowed the investigation of the shielding properties of garnet without the need to know if the garnets were formed in the Proterozoic or Archæan metamorphic event.

6.3.2. Results

Table 6.1 below shows the number of inclusions analysed for each sample and the number of those that released enough argon to obtain ages from them (full analytical results are in Appendix 6.1). A weighted mean of inclusion ages for each sample was obtained to 2σ error and for comparison mean matrix biotite ages for each sample are provided where obtained.

Some attempts to analyse included biotite failed to release any argon above blank levels so no ages were obtained. In some cases the inclusions were so deeply buried that even after repeated ablations the inclusion was not reached. In other instances it is likely that opaque minerals or sphene inclusions were analysed by mistake instead of biotite and hence did not contain argon.

Table 6.1. Apparent ages of matrix biotite versus included biotite

Sample	Mean Matrix Biotite Age (Ma) (± 2σ)	Mean Included Biotite Age (Ma) (± 2σ)	No. of Inclusions Analysed	No. of inclusions giving age
70-30-2	1744 ± 6	NA	7	0
RM37	1731 ± 4	1731 ± 22	8	8
RM39	1784 ± 6	2054 ± 860	16	1
RM40	1772 ± 4	1769 ± 50	3	3
RM42	1734 ± 14	NA	16	0
RRCR3	1765 ± 6	1766 ± 10	66	24
RRSW2	1738 ± 22	1719 ± 11	27	3
TRER4	1728 ± 12	1720 ± 28	4	3
TRER7	1713 ± 8	NA	8	0
TRBC2	NA	NA	13	0
HLM2	1749 ± 5	NA	2	0
TRGC5	1692 ± 8	1693 ± 12	6	6
TRMR2	1585 ± 4	1649 ± 3	29	25

NA = None achieved, meaning that no ages for biotite inclusions in garnet were obtained.

6.3.3. Discussion

In both RRCR3 and RRSW2 no significant variation in ages was found between those inclusions clearly on the surface of the garnet and those buried beneath the surface. Within error, the mean inclusion ages of 1766 ± 10 Ma and 1719 ± 11 Ma, respectively, are concordant with matrix biotite ages of 1765 ± 6 Ma and 1738 ± 22 Ma obtained in these same samples. This concordance suggests either that the garnet host and biotite inclusions are the same age or that the garnet had no shielding effect. Similarly, samples RM37 and RM40 show almost perfect agreement between the inclusion ages of 1731 ± 22 and 1769 ± 50 Ma and matrix ages of 1731 ± 4 and 1772 ± 4 Ma, respectively.

All inclusions analysed for samples TRER7, TRBC2 and HLM2 failed to release argon above blank so no ages were obtained.

The majority of matrix biotite ages for TRMR2 were between 1700 and 1500 Ma and are believed to have been partially reset by the Tobacco Root Batholith (section 7.3). Clearly, this is also the case for the majority of the inclusions. However, whereas only c.10% of the matrix biotites record an age in excess of 1700 Ma, c.33% of inclusions are older than 1700 Ma (Figure 6.1). This would suggest that in some cases garnet shielded the biotite inclusions from the thermal resetting influence of the Tobacco Root Batholith.

Similarly, sample TRGC5 also appears to have undergone some degree of resetting (section 7.3). The ages of the matrix biotite range from 1758 ± 26 to 1205 ± 52 Ma and the inclusion ages ranged from 1766 ± 24 to 1397 ± 40 Ma. Although 3 of the 6 inclusions analysed yielded ages over 1740 Ma, suggestive of shielding by the garnet host, the difference between the ages achieved for the matrix biotite and the included biotite is not significant enough for this to be confirmed.

6.3.4. Conclusion

It is clear from these results that the age of the biotite inclusions in the garnets from the Ruby Range samples are consistent with the ages of the matrix biotite and that they have been equally influenced by the Proterozoic metamorphic event. Similarly, the majority of the inclusions in TRMR2 are also comparable to matrix ages, with only a few inclusions suggesting that shielding might have occurred.

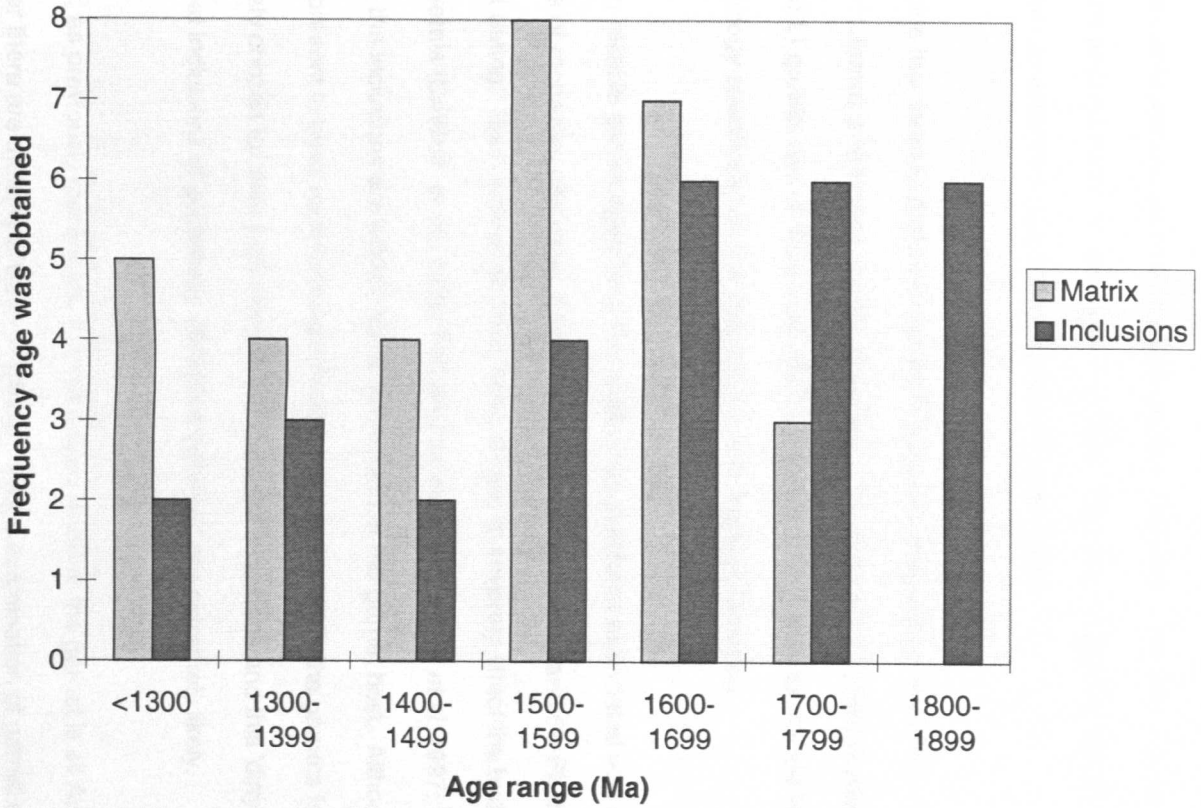

Figure 6.1: Frequency histogram of ^{40}Ar-^{39}Ar apparent ages of included and matrix biotite in sample TRMR2

6.4. Garnet Dating in South-western Montana

6.4.1. Reason for Dating Garnets from South-western Montana

Both the Archæan granulite facies event and the Proterozoic amphibolite metamorphic event reached grades clearly reached temperatures high enough to form garnet (sections 2.3.3 and 2.4.3) and it is possible that the garnets in south-western Montana were formed solely in the first event, solely in the second event, or during both events. Knowing the growth age of a small subset of the garnets can constrain the age of any inclusions within them.

The premise that there is Archæan garnet in this area is based on the 2760 ± 115 Ma Rb-Sr whole rock age of James and Hedge (1980). However, until Dahl *et al.* (1998) produced a lead-lead step-leach (PbSL) growth age of 1822 ± 32 Ma for a garnet from the Ruby Range there had been no geochronology specifically on the garnets in south-western Montana.

Producing reliable garnet ages from this region has problems associated with it. Firstly, any inclusions of monazite, allanite or zircon could disturb the Sm-Nd and Pb-Pb dating systematics used for garnet dating. Such inclusions have been shown to severely affect the budgets of U, Pb, Sm and Nd in minerals (DeWolf *et al.*, 1996; Frei and Kamber, 1995; Frei *et al.* 1997; Vance *et al.*, 1998) such that the inclusions are effectively dated instead of the garnet host. Although these inclusions are omnipresent in most rock-forming silicates (Frei *et al.*, 1997) the garnets for this study were deliberately chosen for their high abundance of biotite inclusions and this 'dirty' nature of the garnets means that inclusions of potentially disruptive minerals are extremely likely.

Secondly, as previously mentioned, it is not known whether the garnet is all Archæan, all Proterozoic, or whether there are multiple phases of garnet. Visual examination of garnet separates under a low powered microscope suggests that there are two phases of garnets in some rocks. Sample RRCR2, for example, contained a well-formed, relatively clear and unfractured, dark red phase, and a poorly formed, inclusion-rich pink phase with abundant fractures (Plate 6.1). If

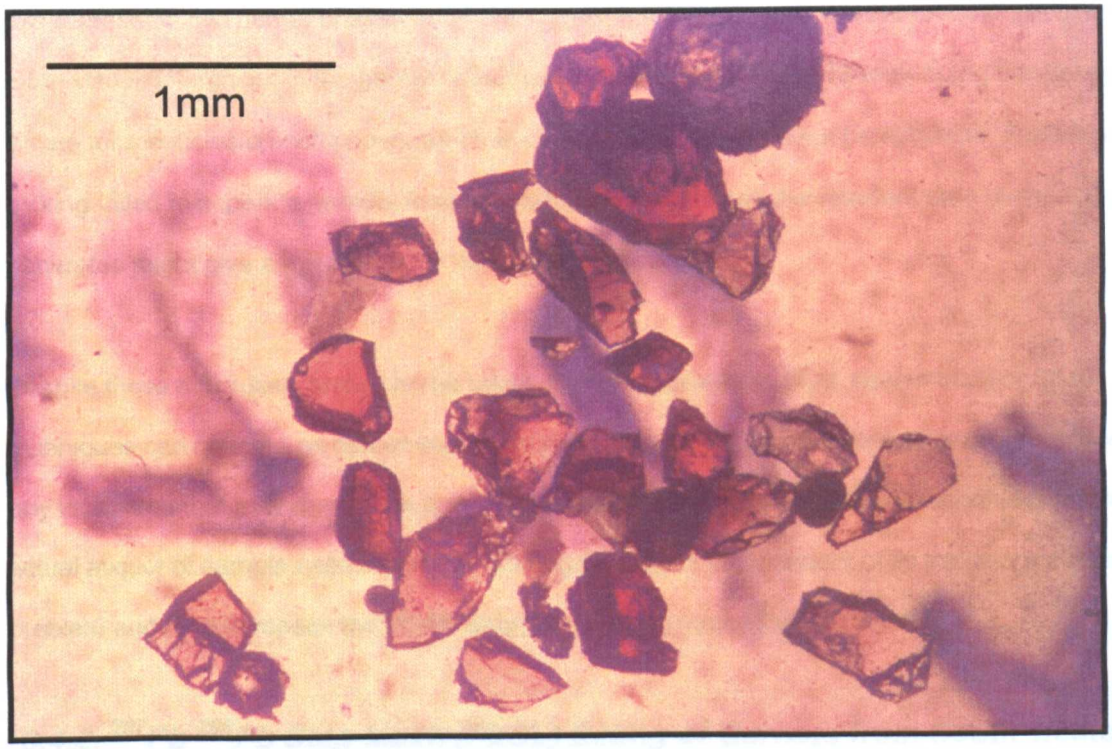

A) RRCR2A garnet separates showing good form and low abundance of fractures (mounted in epoxy resin)

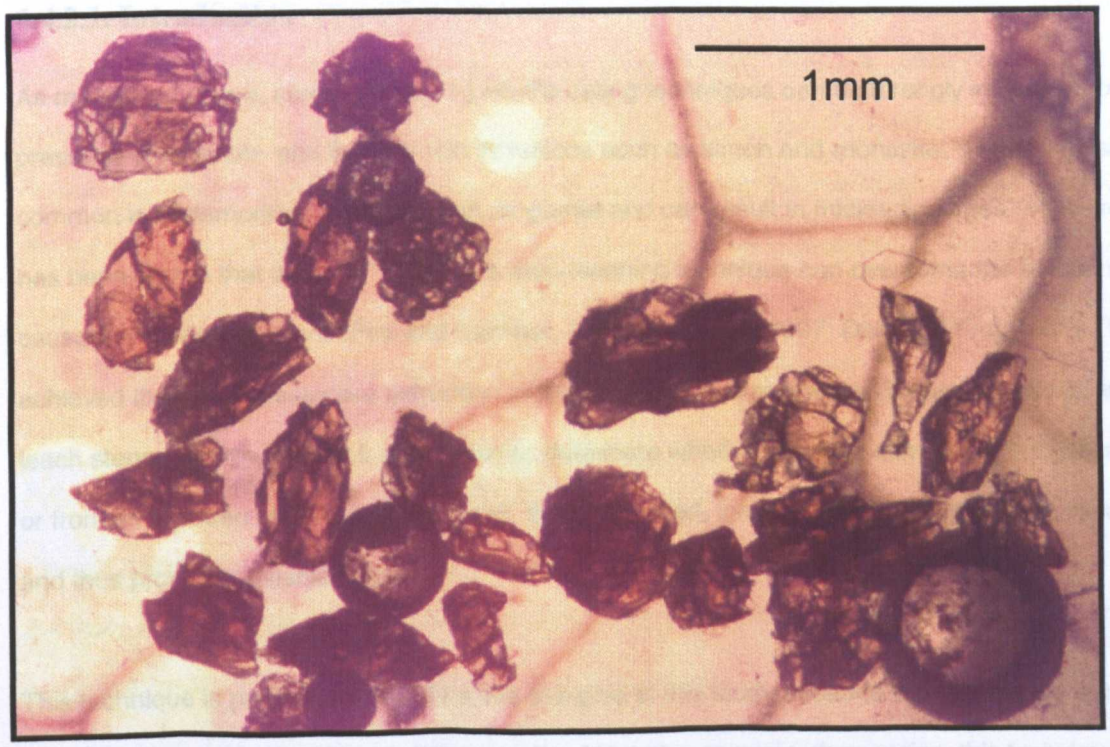

B) RRCR2B garnet separates showing poor form and high abundance of fractures (mounted in epoxy resin)

Plate 6.1: Photographs of two apparent phases of garnet from sample RRCR2

this represents two garnet phases of different ages, it will cause problems when dating is attempted. If the visual differences in the garnet reflect two different phases then by only dating the clear phase, a date for the inclusion-rich phase, which is of most interest, would not be obtained. Furthermore, if picking failed to separate garnets from two different phases then the resultant date of several garnet separates might give a mixed age for the two phases.

Despite these difficulties, steps can be taken to limit unreliability. SEM, fission track or SIMS techniques can be used on garnet separates from the sample before dating to reveal the presence of any inclusions that may disrupt the age. However, it is difficult to apply these techniques on the actual aliquot of sample used for dating. Dating the garnet independent of its inclusions avoids this problem and for this reason the Pb-Pb step-leach dating method was chosen.

6.4.2. ^{207}Pb-^{206}Pb Step-leach (PbSL) Dating of Garnets from South-western Montana

6.4.2.1. Introduction

As mentioned above, conventional (U-) Pb-Pb dating techniques can be strongly influenced by the presence of uranium- and thorium-rich inclusions such as zircon and monazite. These inclusions are common in metamorphic minerals such as garnet and can result in misleading ages. However, it has been shown that the new ^{207}Pb-^{206}Pb step-leaching technique can overcome the problems caused by these inclusions (Frei and Kamber, 1995; Frei *et al.*, 1997; Dahl and Frei, 1998). This is achieved through the selective extraction of lead from various reservoirs during successive acid-leach steps. By this method it is possible to determine whether the lead came from the garnet lattice or from an included phase. Isochrons can then be plotted, ignoring points obtained from inclusions and thus providing reliable ages.

This technique is particularly useful for the samples in this study because the garnets are extremely likely to contain such inclusions. Whereas Sm-Nd dating requires clear grains, this technique can use garnets with obvious biotite and opaque inclusions that may also contain U- and Th-rich inclusions. In addition to providing an age unaffected by these inclusions, it also means that the

inclusion-rich garnet phase can be dated. This gives a far more useful age for constraining the ages of biotite inclusions within the garnets. Furthermore, as this method only deals with a single element (Pb) it is not hampered by element fractionation during chemical procedures applied in the laboratory (Frei *et al.*, 1997).

6.4.2.2. How the Technique Works

What follows is a brief summary of the mechanisms behind the PbSL technique. For a more detailed explanation see Frei and Kamber (1995) and Frei *et al.* (1997).

The PbSL technique involves subjecting 50-300 mg of single mineral species sample to a series of steps (4-7) of acid leaching. The acids used have different properties, resulting in a series of dissolution-reprecipitation reactions in the mineral. If the crystal contains inhomogeneities, such as inclusions, then it can be regarded as a multi-component system. Each component responds differently to successive leaching steps, producing a spread in the $^{208}Pb/^{204}Pb$, $^{207}Pb/^{204}Pb$ and $^{206}Pb/^{204}Pb$ arrays. The release of Pb during leaching is controlled by two mechanisms occurring at different rates. These are a fast surface hydrolysis of cations at the reaction front and a slow remobilisation of initially trapped cations from the leached zone. Because these processes operate at different rates, an effective separation of common and radiogenic Pb results. This may yield a $^{207}Pb/^{204}Pb$ versus $^{206}Pb/^{204}Pb$ isochron giving the mineral age, along with a non-linear array in the $^{208}Pb/^{204}Pb$ versus $^{206}Pb/^{204}Pb$ plot that betrays the presence of inclusions. This non-linear array does not invalidate the $^{207}Pb/^{204}Pb$ versus $^{206}Pb/^{204}Pb$ age but can be used to assess whether or not the inclusions are in isotopic equilibrium with their host as it crystallised.

6.4.2.3. Sample Selection and Preparation

Five samples were selected for analysis, intending to give a good geographical distribution across the three mountain ranges. All five samples had also undergone ^{40}Ar-^{39}Ar dating of biotite or amphibole so that comparisons could be made between the garnet ages and the ^{40}Ar-^{39}Ar ages for the same samples.

Sample RRCR2, from the Ruby Range, was chosen because it produced a reliable mean ^{40}Ar-^{39}Ar biotite age of 1761 Ma. However, as previously mentioned, two apparently different phases of garnet were identified petrographically (Plate 6.1). An attempt was made to hand pick both phases separately for dating. Sample RRSW1 contained altered biotite that produced a broad range of ^{40}Ar-^{39}Ar ages, including anomalously young ages as detailed in section 7.2. It was selected for garnet dating to determine whether the garnet had also been influenced by the alteration event. TRMR2 was chosen because it was close to the Tobacco Root Batholith. ^{40}Ar-^{39}Ar dating of both the matrix biotite and biotite inclusions within the garnet of this sample showed that although the matrix biotite was apparently partially reset by the batholith, some of the inclusions within the garnet had apparently been shielded (sections 5.2, 7.3 and 6.3). Samples TRWC1 and HLM2 were chosen to represent standard samples from the Tobacco Root Mountains and Highland Mountains, respectively, and to compare the garnet ages with the ^{40}Ar-^{39}Ar dates from these samples (sections 5.2, 5.3).

All samples were crushed and sieved, and the 250 μm or 125 μm fractions separated using the heavy liquid sodium polytungstate to produce a concentrated garnet fraction. The fractions were rinsed thoroughly in water to remove the heavy liquid and dried. From the garnet concentrate approximately 300 mg of garnet were hand picked for each sample. The garnet was then washed in deionsed water in an ultrasonic bath for 15 minutes and dried overnight. The garnet separates were ground down using a pestle and mortar to reduce the grain size to about 50-75 μm before the leaching procedure was undertaken.

6.4.2.4. Analytical Procedure

Analytical procedure was carried out at the Geologisk Institut, Kobenhavns Universitet under the supervision of Dr Robert Frei. The garnet separates were transferred into 7 ml Savillex® screw-top beakers for step-leaching. Seven 120 °C acid-leach steps were performed on each mineral separate following the step-wise leaching technique of Frei and Kamber (1995) with modifications of leaching intervals as detailed in Table 6.2.

Table 6.2. Acid leach steps performed on each sample

Step	Acid	Time
1	12:1 mix 1.5N HBr: 2N HCl	30 minutes
2	1N HBr	1.5 hours
3	4N HBr	5 hours
4	8N HBr	16 hours
5	8N HBr	48 hours
6	HF	24 hours
7	HF	72 hours

For each step, Pb was separated conventionally in 0.5 ml glass columns charged with AG 1×8 100-200 mesh anion exchange resin, followed by a clean-up in 200 µl Teflon columns using a standard HBr-HCl elution recipe (Appendix 6.2). Total procedural blanks for Pb were less than 53 pg. Pb was loaded together with silica gel and phosphoric acid onto 20 µm Re filaments (Appendix 6.2). Isotopic analyses were carried out on a VG Sector 54-IT mass spectrometer. Fractionation for Pb was controlled by repetitive analysis of the NBS 981 standard (values of Todt *et al.*, 1993) and amounted to 0.063 ± 0.007 %/amu (2σ; n=11).

6.4.2.5. Results

The analytical results are given in Table 6.3, and Figures 6.2 to 6.7 present the leaching spectra in the form of uranogenic ($^{206}Pb/^{204}Pb$ versus $^{207}Pb/^{204}Pb$) and thorogenic ($^{206}Pb/^{204}Pb$ versus $^{208}Pb/^{204}Pb$) diagrams. Diagrams were constructed using *Isoplot/Ex 1.00* (Ludwig, 1998) run through *Microsoft Excel 5.* Isochrons were plotted using Model 2 regression (Appendix 6.2.3).

A) RRCR2

The two phases of garnet visually identified in sample RRCR2 were labelled A (dark red, well formed) and B (light pink and inclusion rich) (Plate 6.1) and analysed separately. Sample A produced a standard leaching pattern (Figure 6.2A). All data define an isochron of 1808 ± 3 (MSWD = 4.3) which falls within the ^{40}Ar-^{39}Ar biotite age range for this sample (1818-1695 Ma; 1765 ± 6 Ma mean) and is in good agreement with the 1822 ± 32 Ma PbSL age obtained by Dahl *et al.* (1998) for a garnet from the same location. There is only a small offset from the line of the residue (step 6) on the $^{206}Pb/^{204}Pb$ versus $^{208}Pb/^{204}Pb$ diagram (Figure 6.2B) and this is interpreted

Table 6.3. PbSL analytical results

Sample	Step	$^{206}Pb/^{204}Pb$	± 2σ	$^{207}Pb/^{204}Pb$	± 2σ	$^{208}Pb/^{204}Pb$	± 2σ	$^{207}Pb/^{206}Pb$	± 2σ	$^{208}Pb/^{206}Pb$	± 2σ	r^{1*}	$r^{2\dagger}$
RRCR2A	1	28.696	0.107	16.791	0.064	55.918	0.213	0.585	0.000	1.9486	0.0014	0.978	0.981
RRCR2A	2	30.212	0.181	17.060	0.103	67.327	0.409	0.565	0.000	2.2285	0.0019	0.990	0.991
RRCR2A	3	225.960	0.632	38.271	0.111	799.888	2.346	0.169	0.000	3.5400	0.0027	0.973	0.966
RRCR2A	4	2311.330	160.579	268.952	18.755	8320.081	578.125	0.116	0.001	3.5997	0.0041	0.996	1.000
RRCR2A	5	167.834	3.359	32.180	0.812	480.408	9.722	0.192	0.003	2.8624	0.0085	0.793	0.989
RRCR2A	6	140.827	1.931	28.915	0.398	47.328	0.651	0.205	0.000	0.3361	0.0003	0.997	0.998
RRCR2A	7	36.810	0.015	17.632	0.074	44.972	0.188	0.479	0.000	1.2217	0.0009	0.982	0.986
RRCR2B	1	31.920	0.241	17.124	0.130	77.078	0.586	0.536	0.001	2.4148	0.0018	0.992	0.995
RRCR2B	2	28.847	0.188	16.895	0.113	73.299	0.490	0.586	0.001	2.5409	0.0035	0.979	0.979
RRCR2B	3	325.677	2.607	49.030	0.394	1312.714	10.555	0.151	0.000	4.0307	0.0025	0.996	0.997
RRCR2B	4	3406.901	145.696	381.360	16.315	14075.892	602.113	0.112	0.000	4.1316	0.0036	1.000	1.000
RRCR2B	5	110.976	1.828	25.642	0.445	331.328	5.722	0.231	0.001	2.9856	0.0154	0.950	0.954
RRCR2B	6	88.234	1.210	23.172	0.319	42.188	0.580	0.263	0.000	0.4781	0.0004	0.997	0.998
RRCR2B	7	24.349	0.169	16.262	0.114	41.226	0.288	0.668	0.001	1.6931	0.0012	0.989	0.995
RRSW1	1	21.129	0.274	15.993	0.209	40.034	0.522	0.757	0.001	1.8948	0.0022	0.992	0.996
RRSW1	2	18.869	0.023	16.003	0.023	42.676	0.068	0.848	0.001	2.2617	0.0020	0.887	0.832
RRSW1	3	18.757	0.041	15.979	0.037	43.864	0.101	0.852	0.001	2.3385	0.0015	0.952	0.959
RRSW1	4	26.517	0.446	16.616	0.289	41.429	0.718	0.627	0.003	1.5624	0.0066	0.965	0.970
RRSW1	5	41.743	1.180	18.250	0.672	40.705	1.635	0.437	0.010	0.9752	0.0278	0.768	0.704
RRSW1	6	34.974	0.216	17.431	0.109	38.623	0.241	0.498	0.000	1.1043	0.0009	0.990	0.991
RRSW1	7	19.426	0.149	15.736	0.122	38.542	0.298	0.810	0.001	1.9840	0.0020	0.991	0.991
HLM2	1	37.797	0.186	17.765	0.089	59.734	0.298	0.470	0.000	1.5804	0.0011	0.986	0.991
HLM2	2	45.402	0.474	18.559	0.222	76.605	0.970	0.409	0.002	1.6873	0.0120	0.874	0.826
HLM2	3	1677.631	33.149	196.701	3.889	3090.085	61.100	0.117	0.000	1.8419	0.0011	0.999	1.000
HLM2	4	3995.921	116.892	449.895	13.166	8011.526	234.450	0.113	0.000	2.0049	0.0013	1.000	1.000
HLM2	5	536.743	16.885	71.414	2.287	856.483	26.966	0.133	0.001	1.5957	0.0019	0.982	0.999
HLM2	6	174.755	3.914	32.993	0.740	52.707	1.182	0.189	0.000	0.3016	0.0003	0.999	0.999
HLM2	7	27.430	0.113	16.624	0.070	41.234	0.175	0.606	0.001	1.5033	0.0013	0.981	0.981
TRMR2	1	18.894	0.106	16.128	0.092	38.175	0.217	0.854	0.001	2.0204	0.0015	0.987	0.991
TRMR2	2	18.372	0.015	16.070	0.017	36.969	0.040	0.875	0.000	2.0122	0.0011	0.846	0.873
TRMR2	3	136.272	0.251	34.957	0.069	318.879	0.639	0.257	0.000	2.3400	0.0015	0.950	0.946
TRMR2	4	763.992	7.754	136.613	1.405	2642.261	26.897	0.179	0.000	3.4585	0.0022	0.987	0.998
TRMR2	5	92.844	0.930	27.406	0.283	292.663	2.995	0.295	0.001	3.1522	0.0065	0.969	0.979
TRMR2	6	37.812	0.239	19.895	0.127	39.279	0.251	0.526	0.001	1.0388	0.0010	0.989	0.989
TRMR2	7	22.161	0.220	16.342	0.163	40.530	0.405	0.737	0.001	1.8289	0.0018	0.994	0.995
TRWC1	1	47.168	0.269	18.894	0.109	65.938	0.380	0.401	0.000	1.3979	0.0010	0.989	0.993
TRWC1	2	37.737	0.180	18.044	0.091	107.519	0.525	0.478	0.001	2.8492	0.0026	0.945	0.983
TRWC1	4	81.231	2.562	20.445	0.693	136.974	4.348	0.252	0.003	1.6862	0.0061	0.930	0.994
TRWC1	5	47.776	0.496	18.877	0.209	62.963	0.698	0.395	0.002	1.3179	0.0051	0.938	0.938
TRWC1	6	43.431	0.390	18.370	0.166	44.061	0.398	0.423	0.000	1.0145	0.0008	0.994	0.996
TRWC1	7	20.782	0.203	15.879	0.156	38.684	0.381	0.764	0.001	1.8614	0.0019	0.992	0.994

* $r_1 = {}^{206}Pb/{}^{204}Pb$ vs. $^{207}Pb/^{204}Pb$ error correction (Ludwig, 1990)

† $r_2 = {}^{206}Pb/{}^{204}Pb$ vs. $^{208}Pb/^{204}Pb$ error correction (Ludwig, 1990)

Errors are to 2 standard deviations absolute (Ludwig,1990)

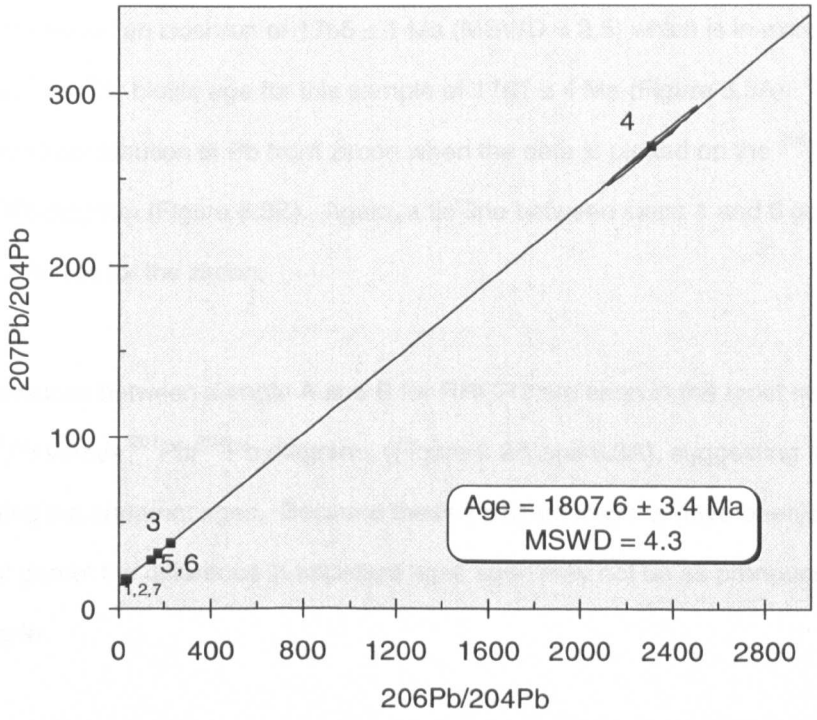

A) Uranogenic PbSL spectrum

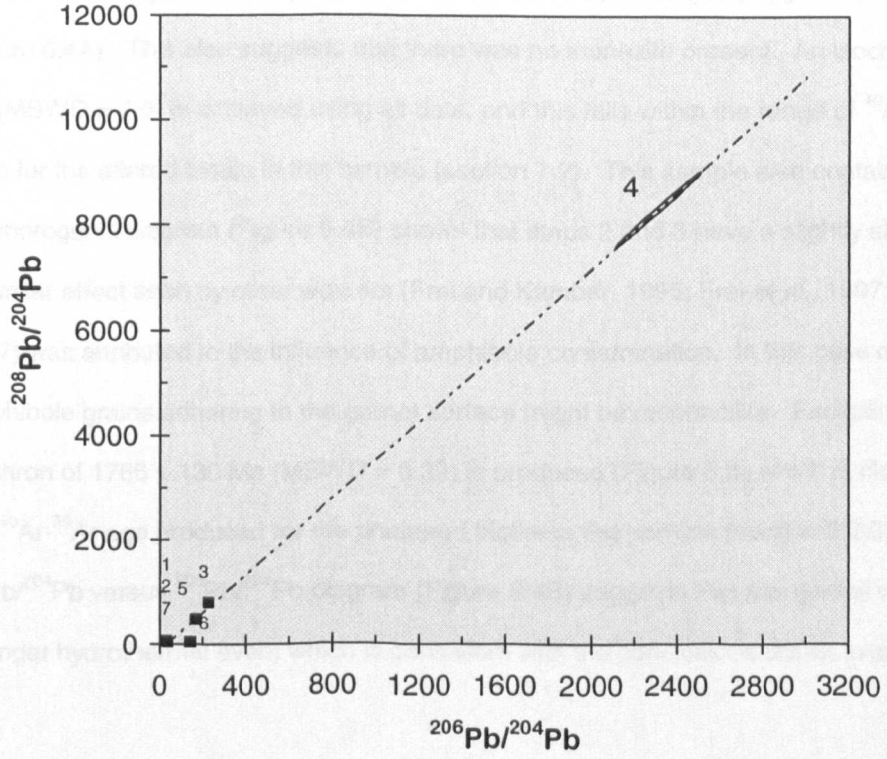

B) Thorogenic PbSL spectrum

Figure 6.2: PbSL spectra for RRCR2A

as a minor contribution of Pb from zircon. A tie-line between steps 1 and 6 gives a minimum bulk age for the zircon of 1768 ± 29 Ma.

Sample B defined an isochron of 1765 ± 1 Ma (MSWD = 2.5) which is in excellent agreement with the mean ^{40}Ar-^{39}Ar biotite age for this sample of 1761 ± 4 Ma (Figure 6.3A). This sample too shows a very small contribution of Pb from zircon when the data is plotted on the $^{206}Pb/^{204}Pb$ versus $^{208}Pb/^{204}Pb$ diagram (Figure 6.3B). Again, a tie-line between steps 1 and 6 gave a minimum bulk age of 1756 ± 64 Ma for the zircon.

The differences between sample A and B for RRCR2 are seen in the most radiogenic points on the $^{206}Pb/^{204}Pb$ versus $^{207}Pb/^{204}Pb$ diagrams (Figure 6.2A and 6.3A), suggesting that monazites are dominating the apparent ages. Because these samples may not have been pure separates of each phase of garnet the difference in apparent ages seen may not be as pronounced as if pure separates were made.

B) RRSW1

Sample RRSW1 produced a poor spread in $^{206}Pb/^{204}Pb$, leading to a high level of uncertainty in age (Figure 6.4A). This also suggests that there was no monazite present. An isochron of 1676 ± 270 Ma (MSWD = 7.6) is achieved using all data, and this falls within the range of ^{40}Ar-^{39}Ar apparent ages for the altered biotite in this sample (section 7.2). This sample also contained hornblende and the thorogenic diagram (Figure 6.4B) shows that steps 2 and 3 have a slightly elevated $^{208}Pb/^{206}Pb$. A similar effect seen by other workers (Frei and Kamber, 1995; Frei *et al.*, 1997; Schaller *et al.*, 1997) was attributed to the influence of amphibole contamination. In this case minute relic amphibole grains adhering to the garnet surface might be responsible. Excluding steps 2 and 3, an isochron of 1766 ± 130 Ma (MSWD = 0.39) is produced (Figure 6.5) which is close to the 1771 ± 32 Ma ^{40}Ar-^{39}Ar age produced for the unaltered biotite in this sample (section 5.2.3). The complex $^{206}Pb/^{204}Pb$ versus $^{208}Pb/^{204}Pb$ diagram (Figure 6.4B) suggests that this garnet was overprinted by a younger hydrothermal event which is consistent with the conclusions drawn in section 7.2.

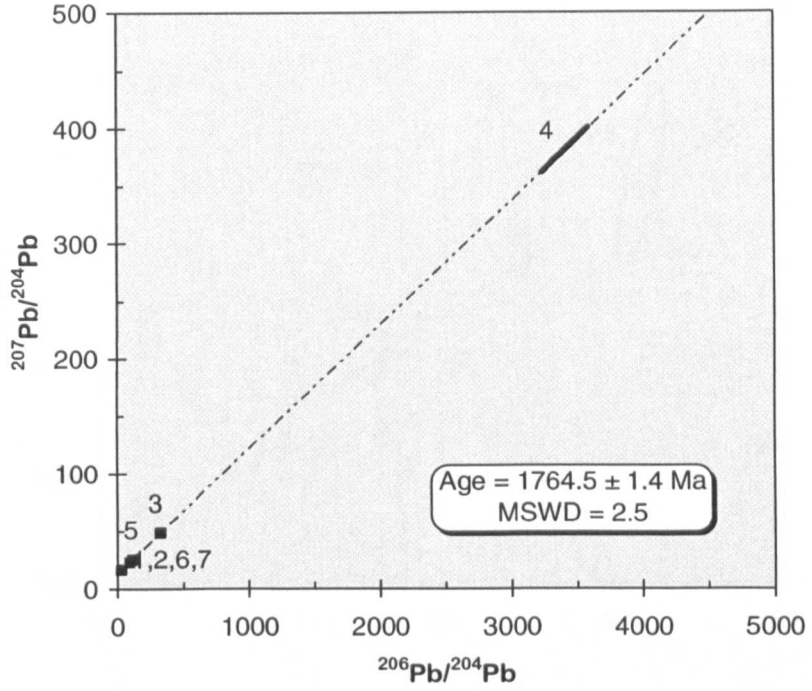

A) Uranogenic PbSL spectrum

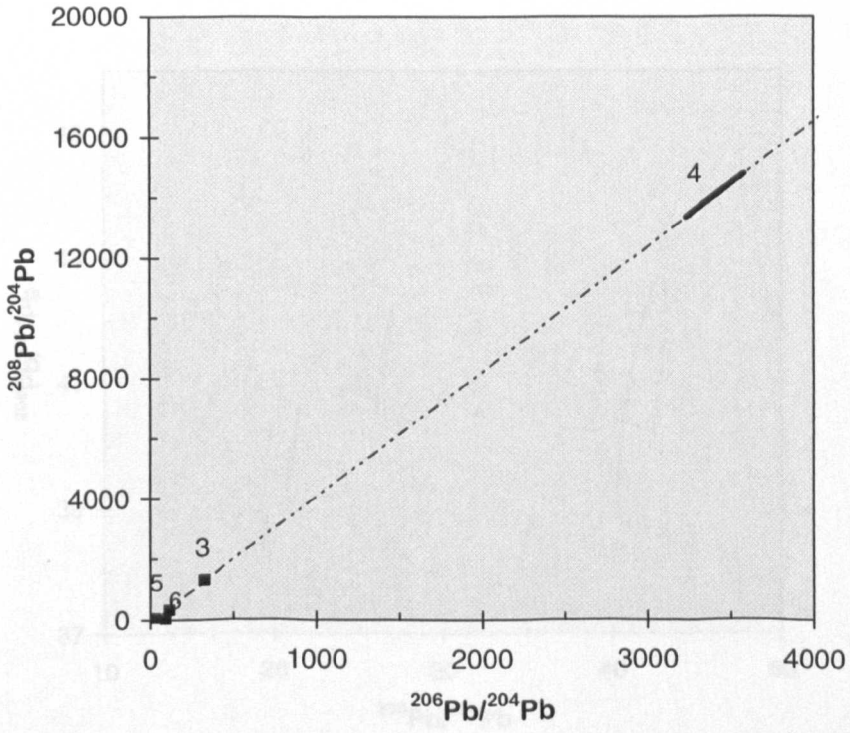

B) Thorogenic PbSL spectrum

Figure 6.3: PbSL spectra for RRCR2B

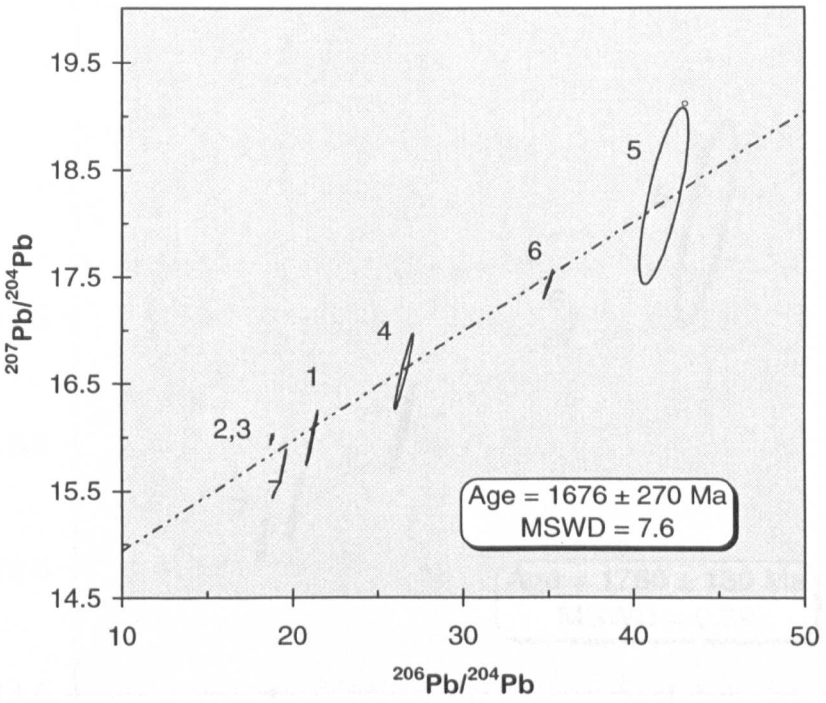

A) Uranogenic PbSL spectrum

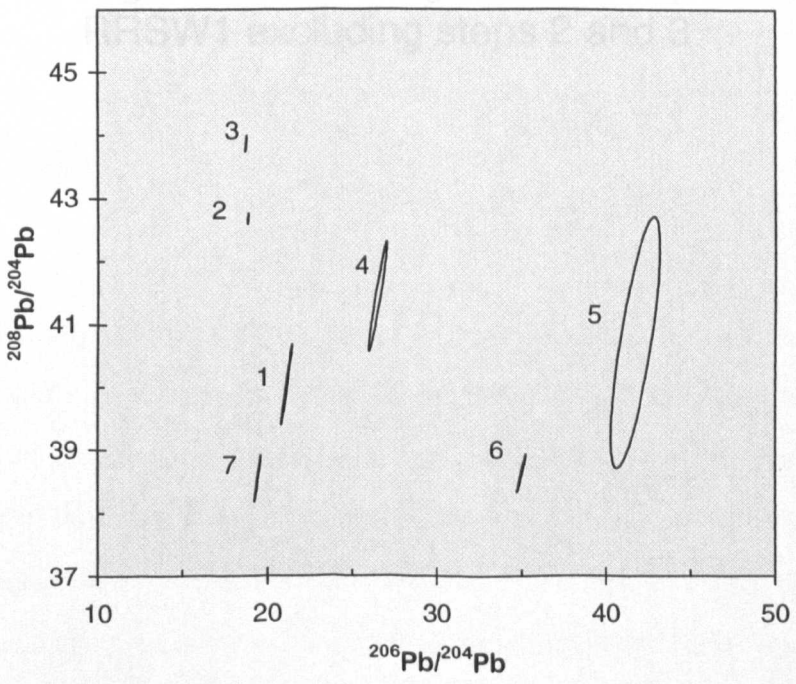

B) Thorogenic PbSL spectrum

Figure 6.4: PbSL spectra for RRSW1

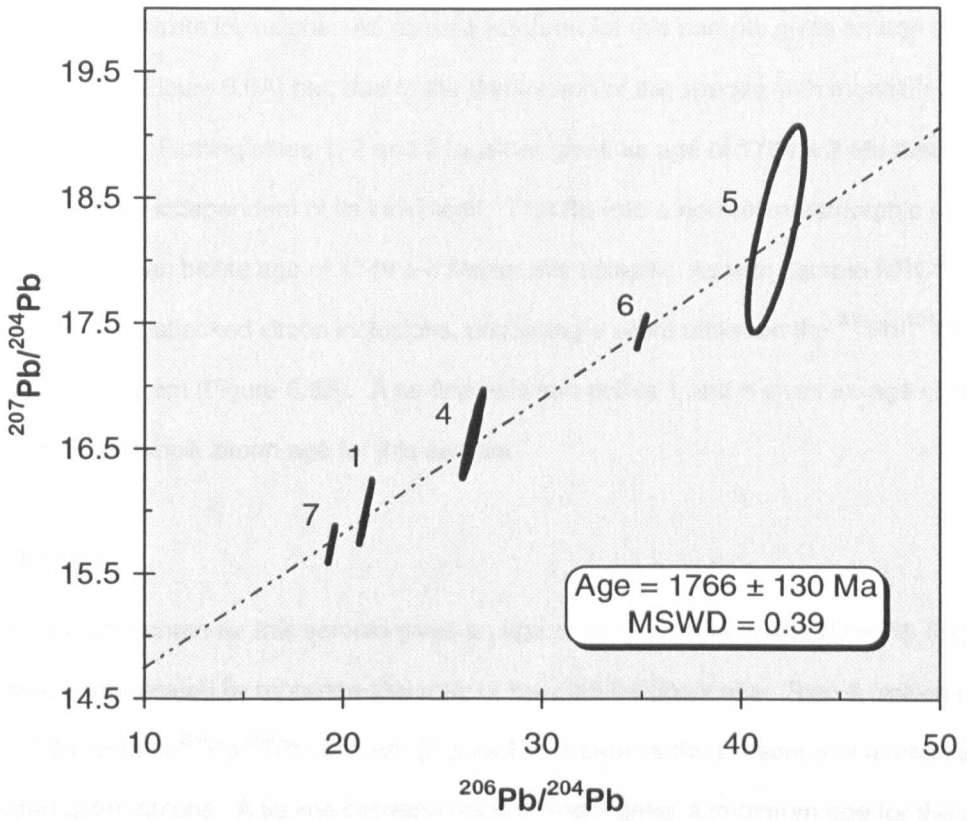

Figure 6.5: Uranogenic PbSL spectrum for RRSW1 excluding steps 2 and 3

C) HLM2

Leach step 4 for sample HLM2 was extremely radiogenic, producing a $^{206}Pb/^{204}Pb$ ratio of 3996 (Table 6.3). This gives as excellent spread in data with a good level of precision, and identifies the presence of monazite inclusions. An all data isochron for this sample gives an age of 1786 ± 4 Ma (MSWD = 2.2) (Figure 6.6A) but, due to the domination of the spectra with monazite, this represents a monazite age. Plotting steps 1, 2 and 3 together gives as age of 1784 ± 3 Ma that most likely dates the garnet independent of its inclusions. This fits into a normal metamorphic sequence with the ^{40}Ar-^{39}Ar mean biotite age of 1749 ± 6 Ma for this sample. As with sample RRCR2, the HF step 6 appears to have attacked zircon inclusions, producing a slight offset on the $^{206}Pb/^{204}Pb$ versus $^{208}Pb/^{204}Pb$ diagram (Figure 6.6B). A tie-line between points 1 and 6 gives an age of 1819 ± 37 Ma for the minimum bulk zircon age for this sample.

D) TRMR2

An all data errorchron for this sample gives an age of 2474 ± 19 Ma (MSWD = 79) (Figure 6.7A). This age is dominated by monazite that may or may not be cogenetic. Step 6 plotted on the $^{206}Pb/^{204}Pb$ versus $^{208}Pb/^{204}Pb$ diagram (Figure 6.7B) betrays the presence of a small amount of inherited older zircons. A tie line between steps 1 and 6 gives a minimum age for the zircons as 2819 ± 46 Ma (Figure 6.8). The $^{206}Pb/^{204}Pb$ versus $^{208}Pb/^{204}Pb$ diagram (Figure 6.7B) indicates that the less thorogenic steps appear to have been disturbed which explains why this sample does not produce an isochron. This is consistent with this sample being reset by the Tobacco Root Batholith (section 7.3)

E) TRWC1

This sample is very disturbed (Figure 6.9A and B) and it is difficult to deduce any age information from it. The all data errorchron of 1054 ± 900 Ma (MSWD = 25) produced is clearly meaningless (Figure 6.9A). Once again this rock is hornblendic and it is likely that it is the influence of contamination by minute relic amphibole grains adhering to the garnet surface that disturbed the PbSL dating of this sample. A tie-line between steps 1 and 2 yields and age of 1428 ± 250 Ma (1 σ) which may be dating the garnet independent of it inclusions. Within (very large) errors this

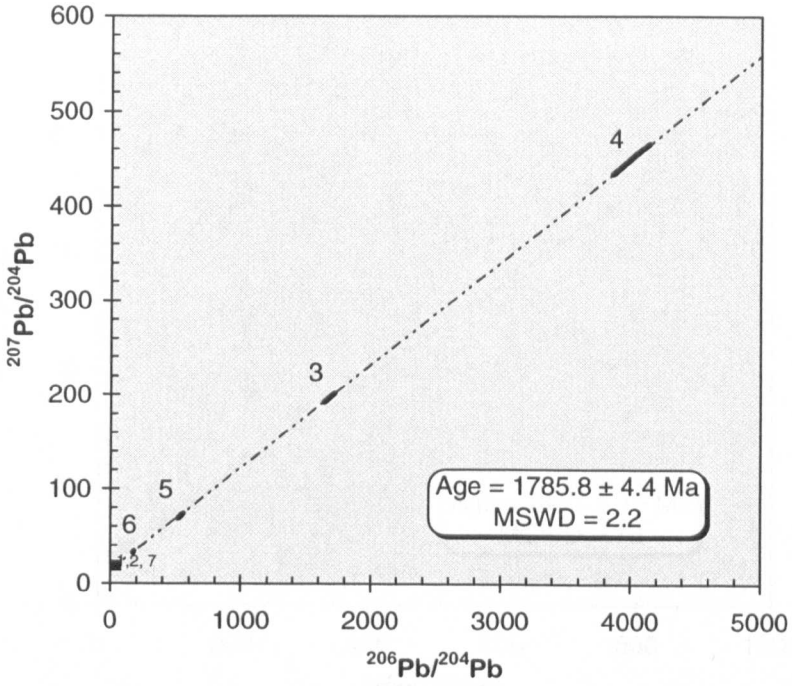

A) Uranogenic PbSL spectrum

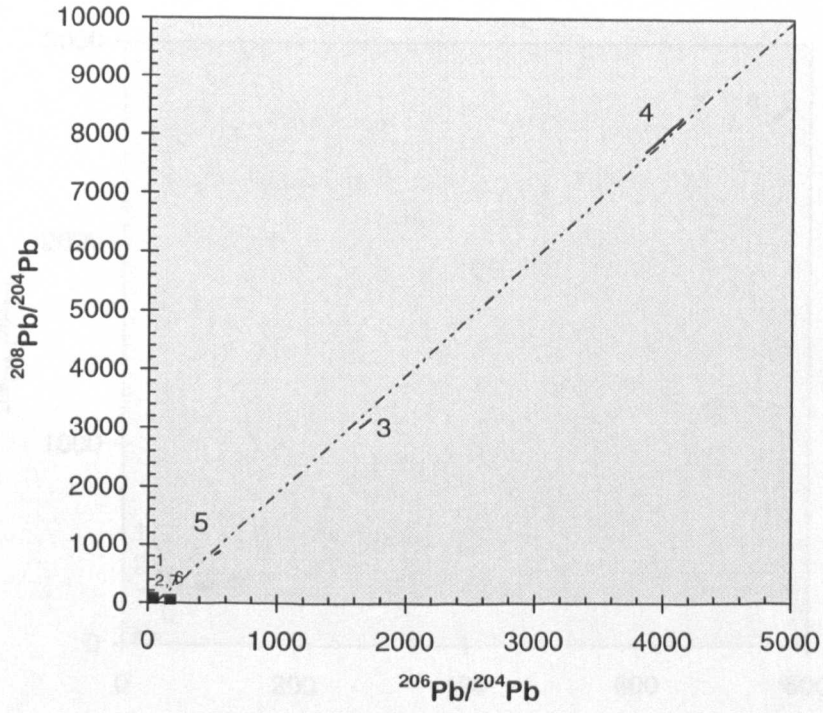

B) Thorogenic PbSL spectrum

Figure 6.6: PbSL spectra for HLM2

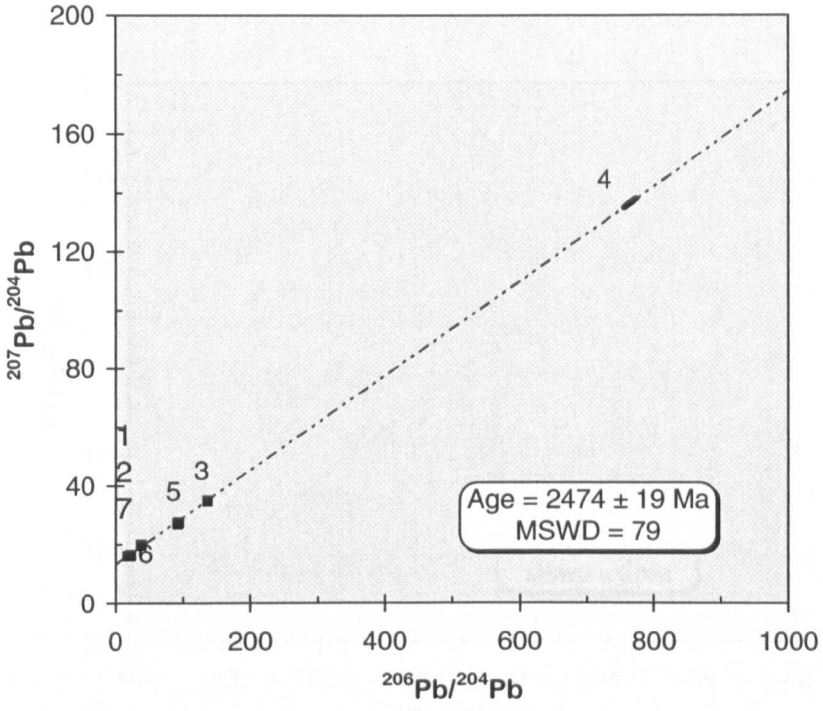

A) Uranogenic PbSL spectrum

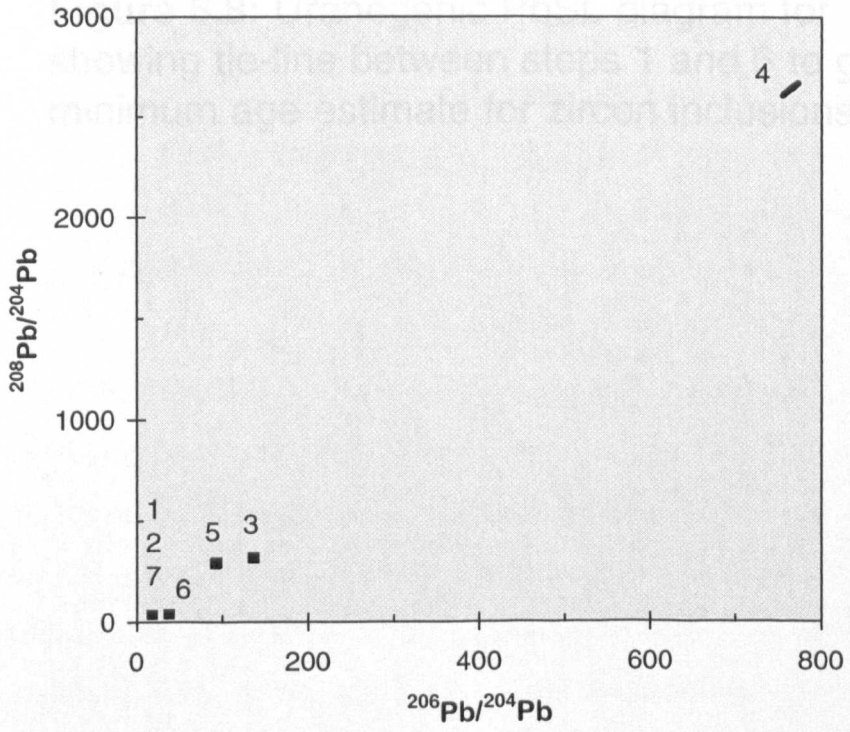

B) Thorogenic PbSL spectrum

Figure 6.7: PbSL spectra for TRMR2

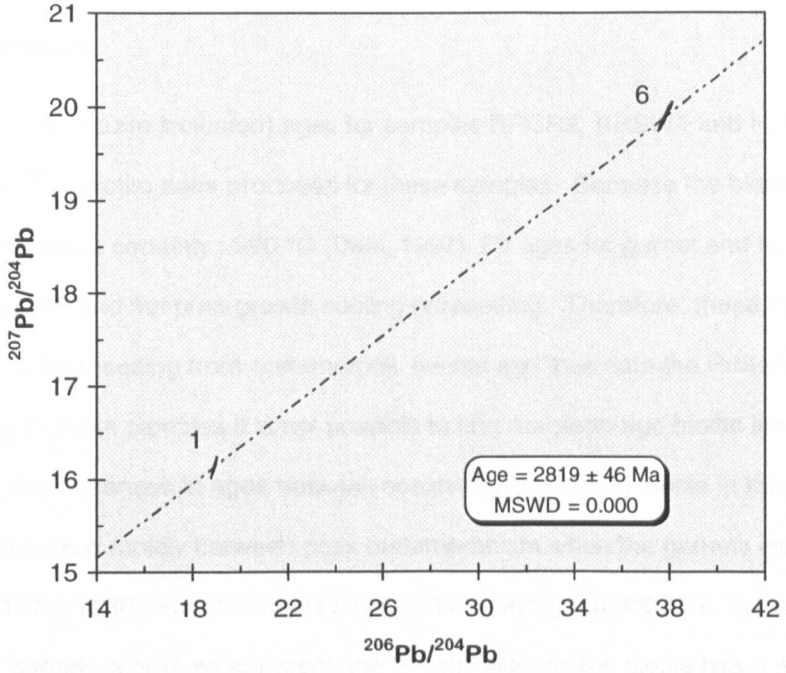

Figure 6.8: Uranogenic PbSL diagram for TRMR2 showing tie-line between steps 1 and 6 to give minimum age estimate for zircon inclusions

corresponds with the 1634 ± 34 and 1689 ± 10 Ma biotite and hornblende ^{40}Ar-^{39}Ar ages for this sample but clearly demonstrates that this sample is very disturbed. A tie-line between steps 6 and 7 suggests a minimum bulk zircon age of 1799 ± 130 Ma.

6.4.2.6. Discussion

The garnet (and monazite inclusion) ages for samples RRCR2, RRSW1 and HLM2 all correspond well to the ^{40}Ar-^{39}Ar biotite ages produced for these samples. Because the blocking temperature for Pb in garnet is almost certainly >900 °C (Dahl, 1997), Pb ages for garnet and its inclusions date crystal date growth and not post-growth cooling or resetting. Therefore, these ages cannot have been influenced by resetting from metamorphic events and thus date the Proterozoic metamorphic event. Clearly in these samples it is not possible to find Archæan age biotite inclusions. Furthermore, the closeness in ages between coexisting garnet and biotite in these rocks suggests that they were cooled rapidly between peak metamorphism when the garnets were formed (c.665 ± 50 °C; Dahl, 1979, 1980), and the biotite blocking temperature (c.300 °C). For sample RRCR2, for example, the garnet records an apparent age of 1808 Ma and the biotite has a mean age of 1761 Ma. These T-t data represent a cooling rate of 7.7 °C/m.y between 665 and 300 °C. From this a linear, time-integrated exhumation rate can be calculated, assuming a retrograde geotherm of between 20 to 25 °C/km. This implies very rapid exhumation of between 320 and 400 m/m.y. Similarly, sample HLM2 suggests a cooling rate of 10.4 °C/m.y. between these two temperatures, relating to an exhumation rate of between 416 and 520 m/m.y. These rapid exhumation rates are typical of rates in active orogens such as the Alps and Himalaya.

It is possible that the differences in the two apparent generations of garnet in sample RRCR2 is due to the monazite inclusions within them. In both these samples the $^{206}Pb/^{204}Pb$ versus $^{207}Pb/^{204}Pb$ spectra, and that of HLM2, are dominated by monazite inclusions and the integrity of the monazite inclusions could be the influential factor determining the apparent ages. RRCR2A garnet was well formed and had few fractures (Plate 6.1) and gave an age of 1808 ± 3 Ma, which is in good agreement with the 1822 ± 32 Ma PbSL age for garnet from sample RMC200 (Dahl *et al.*, 1998). In

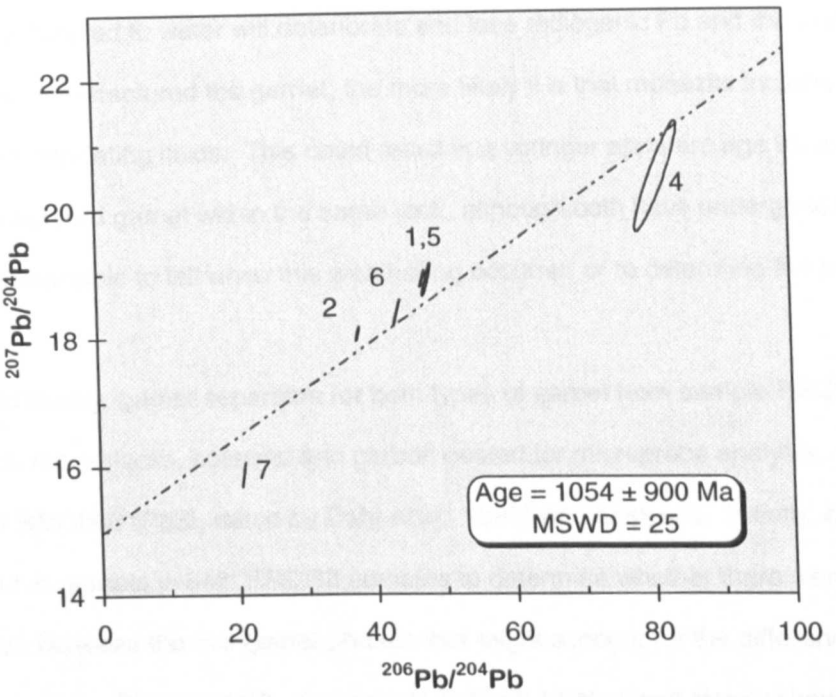

A) Uranogenic PbSL spectrum

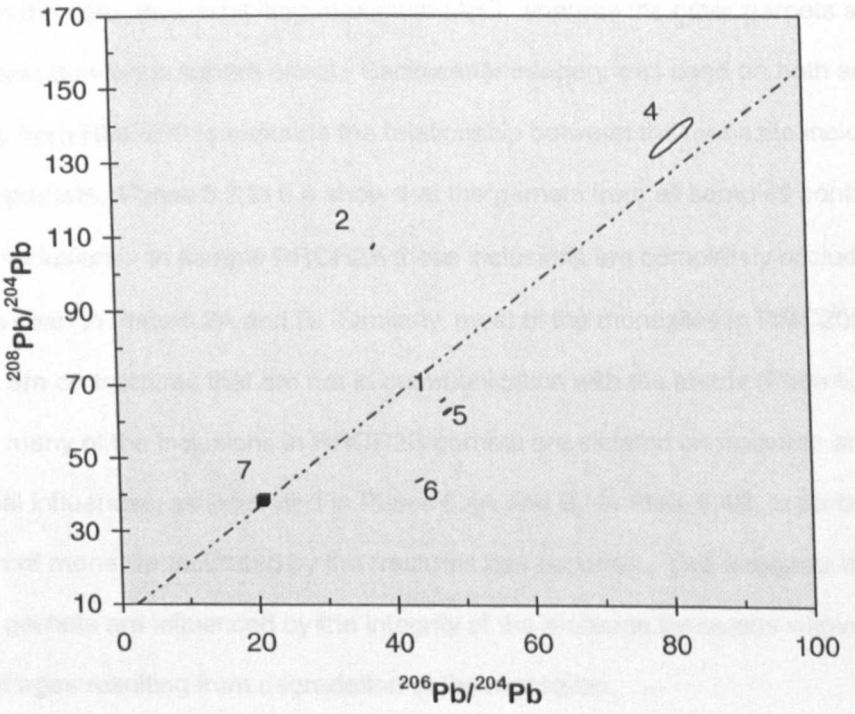

B) Thorogenic PbSL spectrum

Figure 6.9: PbSL spectra for TRWC1

contrast RRCR2B garnet was poorly formed and highly fractured (Plate 6.1) and gave an age of 1765 ± 1 Ma.

Monazites subjected to water will deteriorate and lose radiogenic Pb and thus appear younger. Clearly, the more fractured the garnet, the more likely it is that monazite inclusions will come into contact with circulating fluids. This could result in a younger apparent age for a fractured garnet than for a non-fractured garnet within the same rock, although both have undergone the same history. It would be impossible to tell when this weathering occurred or to determine the true age of the garnet.

To test this theory, garnet separates for both types of garnet from sample RRCR2 were picked, mounted in resin blocks, polished and carbon coated for microprobe analysis. In addition, the probe section of RMC200 (PbSL dated by Dahl *et al.*, 1998) was analysed. Initially, two traverses were carried out in garnets in both RRCR2 samples to determine whether there were any chemical differences between the two garnet phases that might account for the difference in apparent ages between the two. These results are given in Table 6.4 below and clearly show that the chemistry is similar. The apparently higher MnO concentration in RRCR2A1 is probably due to this garnet being cut through the core, thus exhibiting maximum MnO, whereas the other garnets show lower MnO concentration due to the sphere effect. Backscatter imagery was used on both sample RRCR2 and on garnets from RMC200 to examine the relationship between the monazite inclusions and fractures within the garnets. Plates 6.2 to 6.4 show that the garnets from all samples contain numerous tiny (<30 μm) inclusions. In sample RRCR2A these inclusions are completely occluded within the garnet, as can be seen in Plate 6.2A and B. Similarly, most of the monazites in RMC200 are occluded in the garnet or are on fractures that are not in communication with the matrix (Plate 6.3A and B). In contrast, many of the inclusions in RRCR2B garnets are situated on fractures and are therefore open to external influences, as illustrated in Plates 6.4A and B. In Plate 6.4B, in particular, it is clear that alteration of monazite facilitated by the fractures has occurred. This suggests that the apparent ages of these garnets are influenced by the integrity of the monazite inclusions within them, with younger apparent ages resulting from degradation of the monazites.

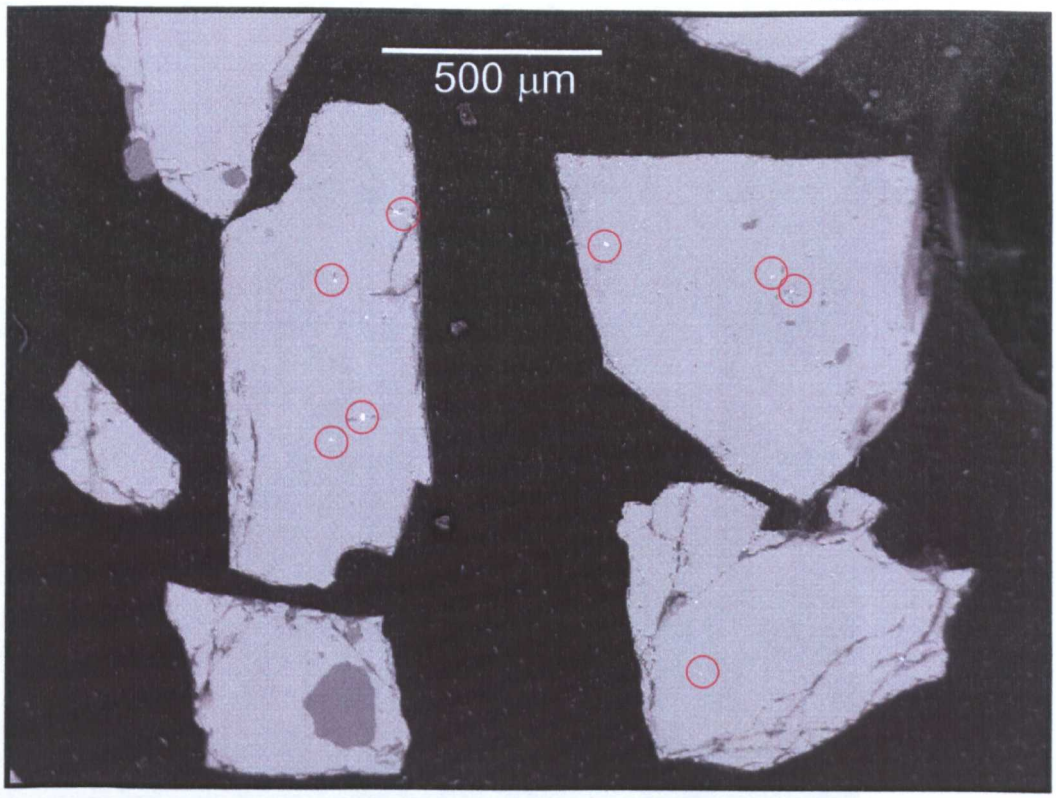

A) Backscattered image of garnet separates from RRCR2A showing tiny monazite inclusions circled in red

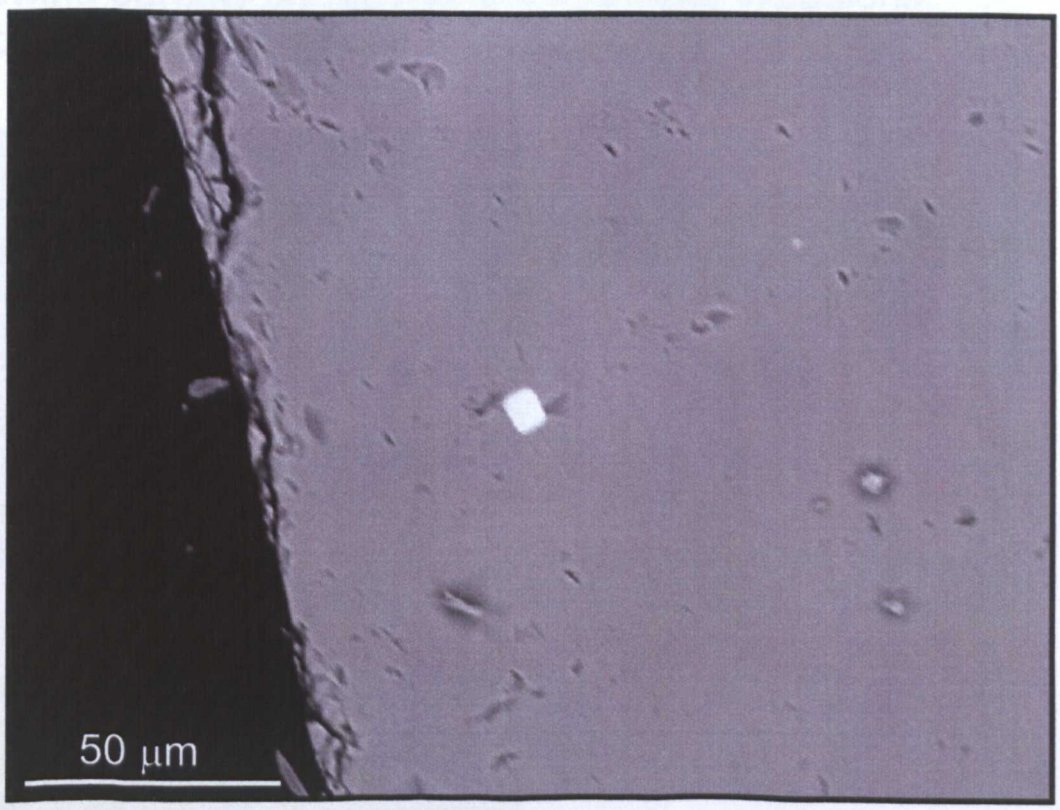

B) Backscattered imagine of a garnet separate from RRCR2A showing a tiny monazite inclusion completely enclosed in garnet

Plate 6.2: Backscattered images of RRCR2A garnet separates showing tiny monazite inclusions completely occluded in garnet

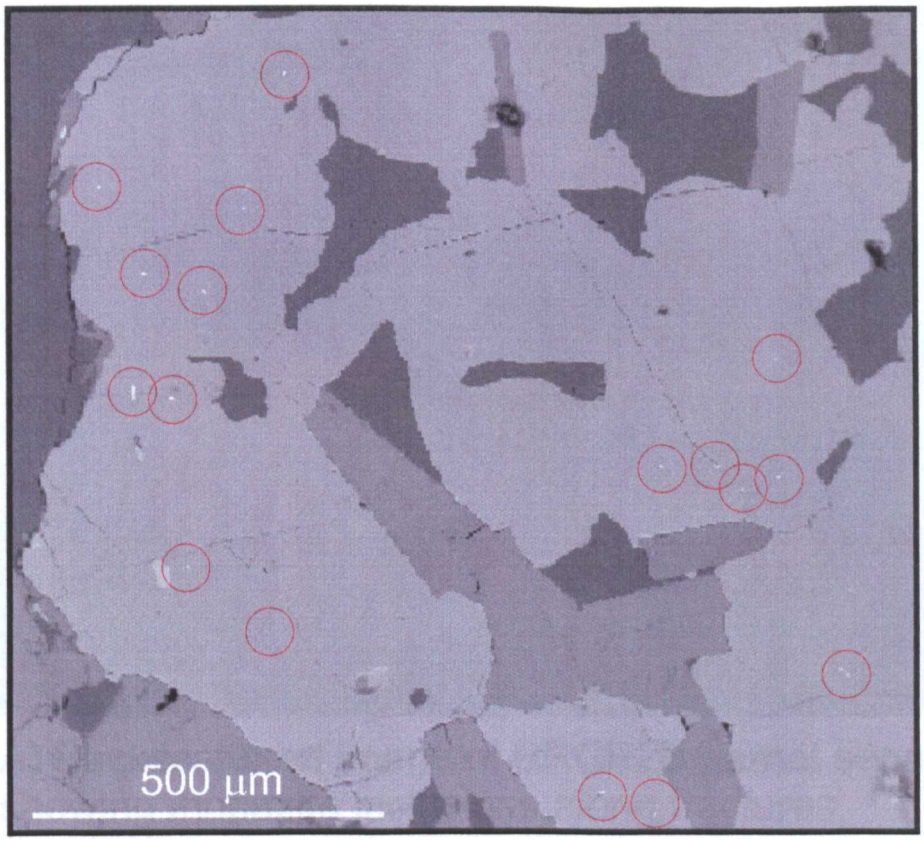

A) Backscattered image of RMC200 probe section showing garnets containing tiny monazite inclusions (monazite circled in red)

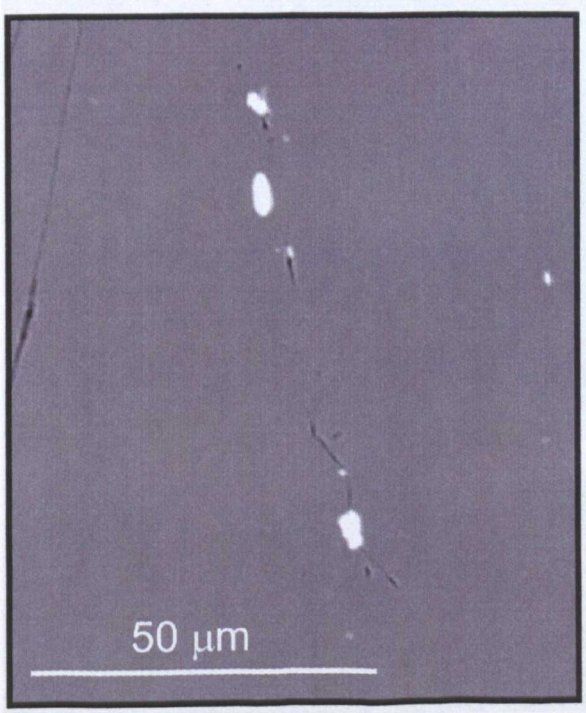

B) Backscattered image of RMC200 garnet showing monazite enclosed within the garnet

Plate 6.3: Backscattered images of RMC200 showing monazite inclusions within garnet

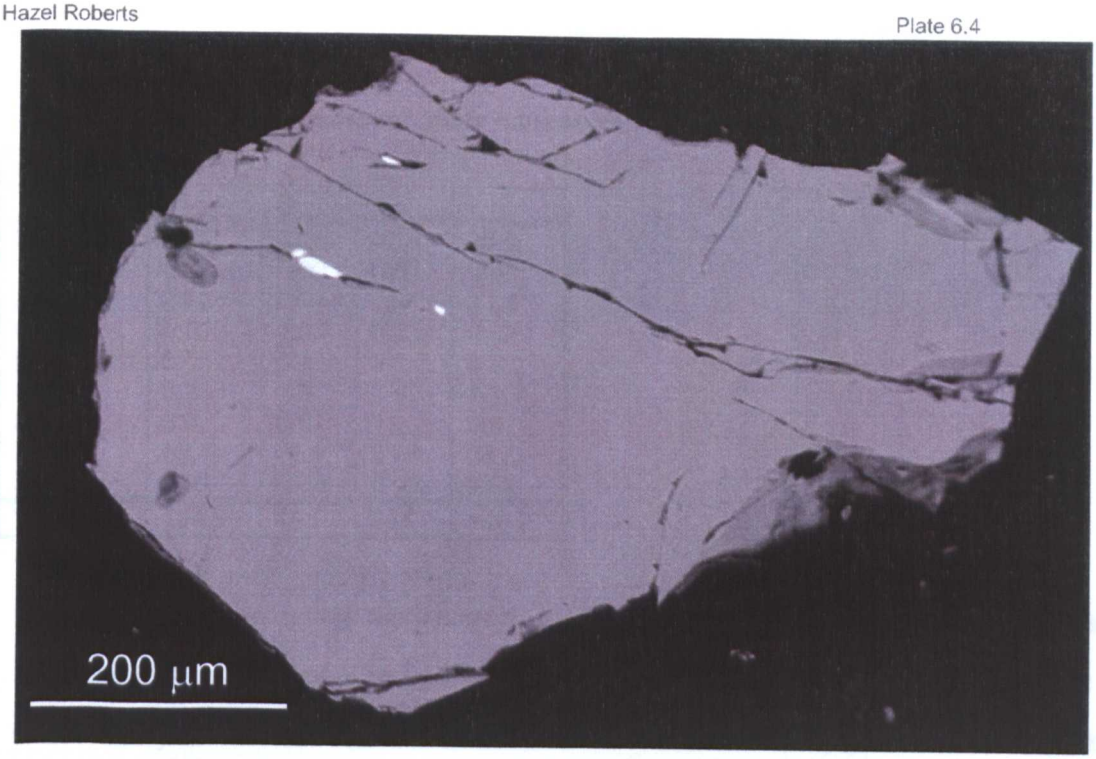

A) Backscattered image of RRCR2B garnet separate showing monazite inclusions along fractures

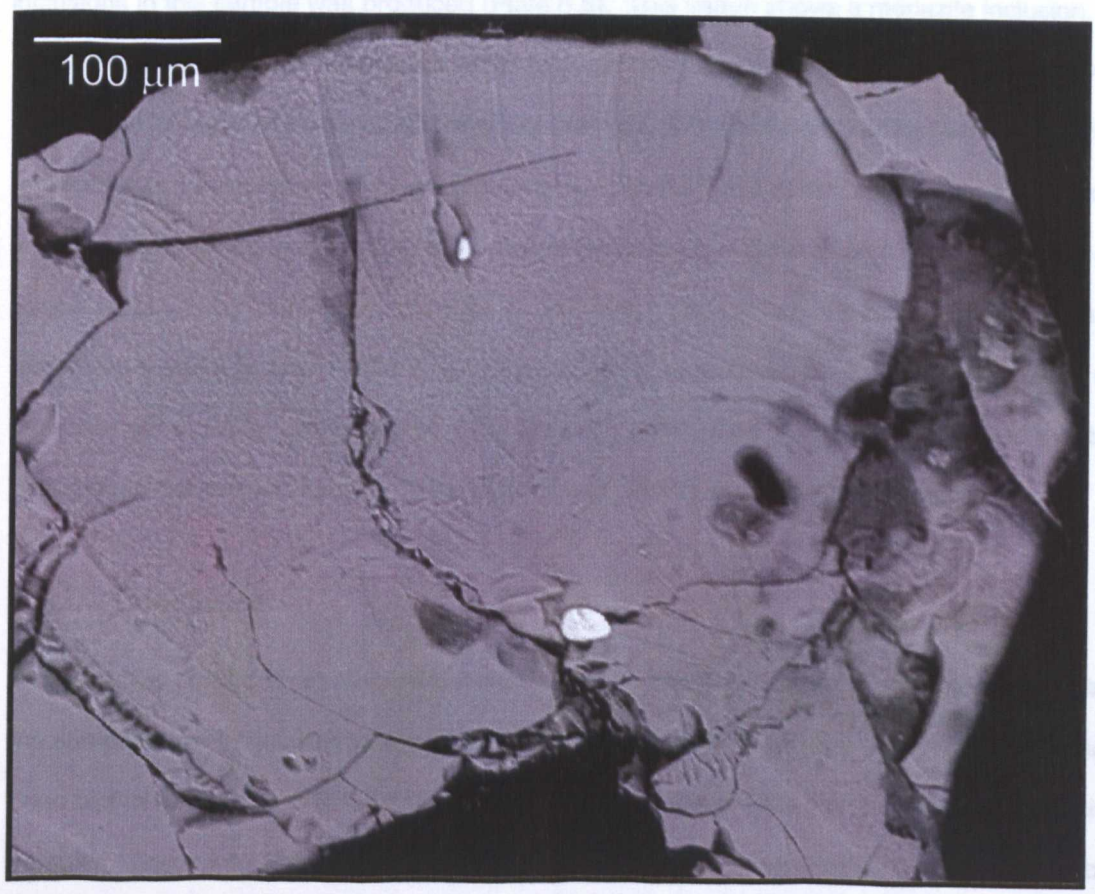

B) Backscattered image of RRCR2B garnet separate showing an apparently altered monazite inclusion on a fracture

Plate 6.4: Backscattered images of RRCR2B garnet separates showing monazite inclusions along fractures

Table 6.4. Mean weight percent oxide concentration for garnets from RRCR2A and B

Oxide %	RRCR2A		RRCR2B	
	1	2	1	2
SiO_2	36.9	37.5	37.4	36.5
TiO_2	0.01	0.02	0.01	0.01
Al_2O_3	21.3	21.4	21.6	21.4
Cr_2O_3	0.01	0.03	0.02	0.02
MgO	3.1	3.4	3.5	3.2
CaO	2.2	1.9	1.9	2.1
MnO	3.9	0.8	1.1	0.8
FeO	33.1	35.9	35.3	36.2
ZnO	0.01	0.02	0.02	0.02
TOTAL	**100.5**	**101**	**101**	**100.2**

Sample TRMR2 is somewhat more problematic. This is the only near-Archæan age achieved in this study and its validity needs to be questioned. Firstly, this age is dominated by monazite and influenced by zircon inclusions. The $^{206}Pb/^{204}Pb$ versus $^{208}Pb/^{204}Pb$ diagram from the PbSL dating of the garnets in this sample (Figure 6.7B) show that leach step 6 is off-set, demonstrating that the zircons are older. Using the electron microprobe, a backscattered image of one of the monazite inclusions in this sample was produced (Plate 6.5). This image shows a monazite inclusion, resting on the prismatic face, and clearly showing highly complex and irregular zonation. Chemical dating by electron microprobe of single monazite grains from this sample carried out by Dahl *et al.* (1999b) revealed 10-15 μm patches of an Archæan generation (~2770 Ma) enclosed within a large volume of younger Archæan material (~2590 Ma). These monazite generations are further overgrown and deeply embayed by Proterozoic monazite (~1780 Ma). Clearly then, the monazites in this sample are extremely complex and the PbSL date obtained for this sample will be a mixed age of these different monazite generations. Furthermore, if the monazite is inherited then the date obtained by PbSL dating does not date garnet growth but instead reflects the age of detrital inclusions.

6.4.2.7. Conclusion

By dating this small subset of garnets it has become clear that most (and possibly all) garnets within the samples are Proterozoic in age. This unfortunately means that they will not contain Archæan aged biotite inclusions. It is therefore difficult to assess the shielding properties of garnet using these samples. Some information can, however, be obtained from samples TRGC5 and TRMR2 by assessing the shielding properties of garnet in relation to resetting by the Cretaceous batholith.

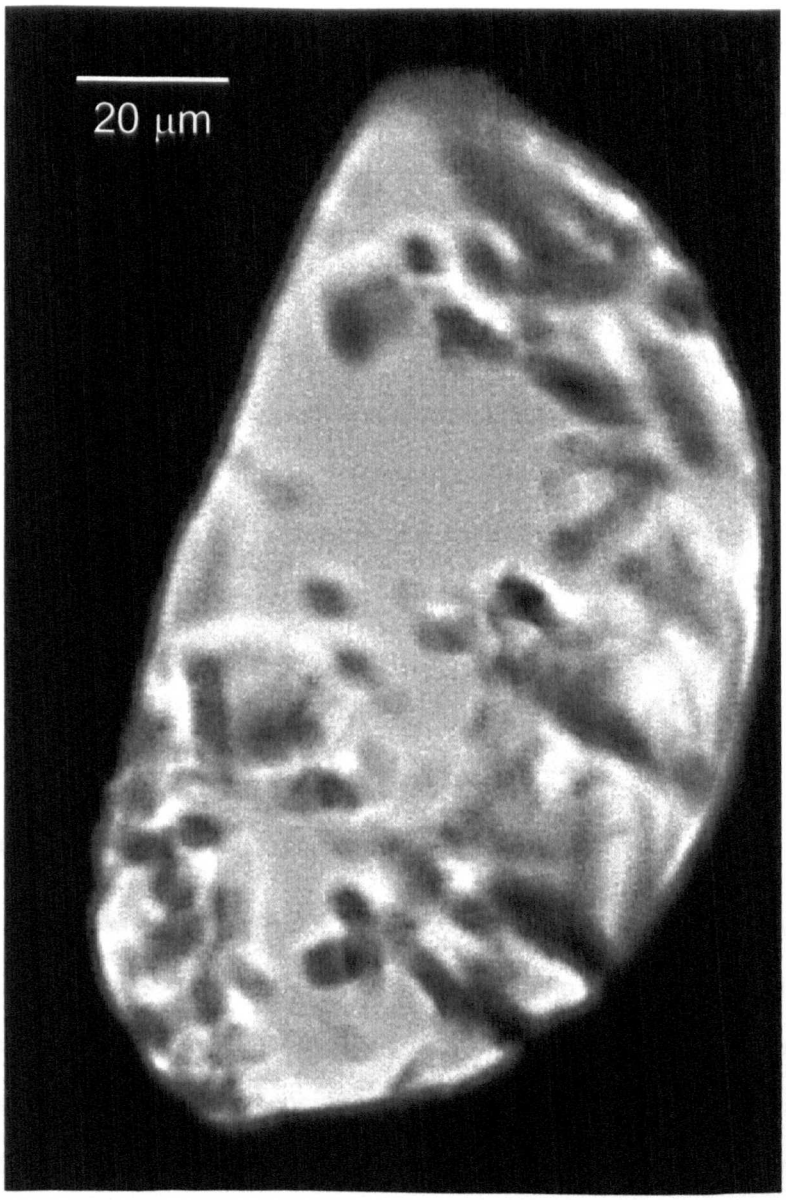

Plate 6.5: Backscattered image of monazite inclusion in garnet from TRMR2 showing complex overgrowths

Despite the claim by Frei and Kamber (1995), Frei *et al.* (1997), and Dahl and Frei (1998) that PbSL dating is able to date garnet independent of its inclusions, this has not been possible in this case. The PbSL dating was useful for discerning whether zircon inclusions were older than their garnet hosts, and for detecting contamination by amphibole. However, samples RRCR2 and RMC200 demonstrated that the integrity of the monazite inclusions was able to significantly alter the apparent age achieved for garnets. Furthermore, where $^{206}Pb/^{204}Pb$ versus $^{207}Pb/^{204}Pb$ spectra were dominated by monazite it was impossible to discern whether the age achieved dated the garnet or the monazite inclusions. This was particularly a problem for sample TRMR2 where an older age was obtained, clearly dominated by monazite, and it was not possible to demonstrate using textures whether the monazite was inherited or not.

6.5. Establishing the Blocking Temperature of Argon in Garnet

6.5.1. Introduction

In order to determine whether garnet, in theory, can shield biotite inclusions within them it is necessary to establish the blocking temperature of argon in garnet. To do this the diffusion rate of argon needs to be measured in garnet, at various temperatures and pressures, to determine the activation energy (E) and pre-exponential factor (D_0) for argon in garnet. Because of the large atomic radius of argon, argon diffusion in garnet is likely to be extremely slow and therefore difficult to measure over an experimental time scale. Preliminary experiments (Wartho pers. comm.) show that even long term experiments fail to measure argon diffusion. Helium, being smaller, diffuses faster than argon, so can be used as a proxy for argon in laboratory experimentation, setting at least a minimum rate of diffusion for argon.

The measurement of diffusion of large cations, such as Mg, in the past has been possible due to the high spatial resolution of apparatus such as the ion microprobe (0.3 μm; Chakraborty and Ganguly, 1992). He and Ar are measured using a laser and mass spectrometer which has a lower spatial resolution, therefore, diffusion paths have to be larger in order to be measured.

To date there have only been two studies to measure the diffusion of helium. The first was by Trull and Kurz (1993) who measured the diffusion of He contained within fluid inclusions in olivine and diopside; the second was by Dunai and Roselieb (1996) who measured He trapped within the crystal lattice of garnet. Because of the limited amount of previous work directly relevant to the present study, it has been necessary to investigate other work that has measured the diffusion coefficients of different cations within garnet (Appendix 6.3). It is the aim of the present study to add to the data set created by Dunai and Roselieb (1996) and to ultimately obtain a more reliable diffusion coefficient for He in garnet. This can then be used to set limits to diffusion of argon in garnet.

6.5.2. Other Investigations of Diffusion Coefficients

6.5.2.1. The Reason for Using High Temperature Experiments and the Associated Problems

A) Experimental Constraints

Elemental diffusion in garnet is very slow, therefore, relatively high temperature experiments are required in order to achieve measurable diffusion profiles within a realistic laboratory time-scale (less than 1 year) and within the spatial resolution of the apparatus used. However, experimental temperatures for experiments in garnet (750-1475 °C) are higher than those relevant to crustal metamorphism (300-700 °C) and extrapolation to lower temperatures is required. Numerous problems are associated with the high temperature experiments and the subsequent extrapolation of results, as indicated below.

B) The Stability of Garnet

A study by Boyd and England (1962) showed that pyrope breaks down to aluminous enstatite, sapphirine and sillimanite at temperatures down to 1100 °C at any pressure below 25 Kb. This suggests that any experiment carried out below 25 Kb would be measuring the diffusion coefficient in a mineral that is no longer pyrope. This is supported by work carried out by Schwandt *et al.* (1995) who found that examination using SEM and XRD after experimentation showed evidence of sample breakdown. Their pyrope garnets held at 1050 and 1100 °C became opaque and blackened. XRD

analysis revealed that surfaces of annealed garnet consisted of a combination of garnet, periclase, enstatite, augite, anorthite, hercynite and magnetite.

Almandine is also considered to be meta-stable at about 820 °C and 250 bars (Dunai and Roselieb, 1996) and breaks down as shown below:

Almandine ⇔ fayalite + cordierite + hercynite + fluid

Chakraborty and Rubie (1996) found that the workable range of conditions at which measurable diffusion profiles could be induced without decomposing the garnet was a narrow window between 750-900 °C and oxygen fugacity between 10^{-15} and 10^{-19} bars. However, their attempt to measure pure grossular garnet even within these constraints failed due to decomposition of the sample.

C) High Pressure Experimental Problems

In order to maintain the stability of garnet at the high temperatures necessary for diffusion to occur, high pressures are required. Elphick *et al.* (1985) attempted experiments on garnet-garnet couples at 35-40 Kb of pressure to overcome the problems of garnet breakdown. However, they found that at such high pressures it was very difficult to preserve the mechanical integrity of the garnet-garnet couple of cylindrical geometry over sufficiently large domains to ensure volume diffusion. Chakraborty and Rubie (1996) also found that at high pressures it is difficult to preserve the mechanical integrity of brittle single crystals of garnet during compression and decompression.

D) Extrapolation of Results

Many researchers have undertaken examination of cation diffusion in garnet in experiments above 1100 °C (Appendix 6.3). Diffusion data for temperatures typical of crustal metamorphic conditions (e.g. 700 °C) are then extrapolated. The diffusion coefficients calculated have a degree of uncertainty that is increased with the distance extrapolated away from the measured data.

This problem is further compounded by the possibility of a change in diffusion mechanism with temperature (Ayres and Vance, 1997). Schwandt *et al.* (1995) show that there may be significant

changes in the mechanisms and activation energies of diffusion at temperatures of 1100-1300 °C compared to 600-1000 °C. Volume diffusion of a cation through a mineral crystal structure is controlled by the occurrence, type and abundance of point defects (Schwandt *et al.*, 1995). It is believed that at high temperatures diffusion is dominated by thermally generated point defects and is therefore an intrinsic process. In contrast, at low temperatures the cation impurities influence the defect structure to a larger extent than does temperature and diffusion is an extrinsic process (Schwandt *et al.*, 1995; Ayres and Vance, 1997).

Chakraborty and Ganguly (1992) extrapolated their data (obtained from experiments at 1100-1200 °C; 14-35 Kb) to compare it to that of Cygan and Lasaga (1985) (750-900 °C; 2 Kb). They found the results were in good agreement, suggesting there was little change in the diffusion mechanism in garnet due to temperature variation. Ayres and Vance (1997) compared their data obtained at low temperatures (~ 700 °C) with the extrapolated results of Chakraborty and Ganguly (1992) and Elphick et al. (1985) (1300-1475; 35-40 Kb) and also found a good agreement. However, Ayres and Vance (1997) suggested that because of the large errors within the experimentation and the extrapolation, the possibility of a change in diffusion mechanism cannot be excluded. Elphick *et al.* (1985) extrapolated their findings and that of Freer (1979) to 5 Kb pressure. They found that their high temperature data yielded a much higher activation energy than that required by Freer's data in the temperature range 822 to 1000 °C. This supports the notion of a change in diffusion mechanism with temperature. However, a recent study by Chakraborty and Rubie (1996) compared new data with that of Chakraborty and Ganguly (1991), Cygan and Lasaga (1985), and Schwandt *et al.* (1995) and reported an excellent agreement between the low and high temperature data sets. This, they stated, proves that there is no change in activation energy between 1475 and 750 °C corresponding to any change of mechanism.

6.5.2.2. Experimental Techniques Used by Other Authors

The majority of diffusion experiments in garnet have used one of two experimental techniques. The first involves the sintering of two highly polished garnet slices of different composition at high temperature (usually 1000 °C). Resultant binary diffusion profiles are measured by an electron microprobe (e.g. Elphick *et al.*, 1985; Chakraborty and Ganguly, 1992). The second method requires

doping a highly polished garnet surface with a minor isotope of the cation being measured. Diffusion profiles are measured by depth profiling using an ion microprobe (e.g. Cygan and Lasaga, 1985; Schwandt *et al.*, 1995; Chakraborty and Rubie, 1996).

Ayres and Vance (1997) attempted to measure the diffusion of Mg in garnet at lower temperatures by calculating the diffusion data from naturally produced diffusion profiles in metamorphic garnet. This bypassed the problems associated with high temperature experiments but they experienced other problems, such as determining the thermal history of the sample and the initial distribution of the element concerned.

The measurement of helium differs from measuring cations such as Mg and Fe in that it requires a gas source mass spectrometer rather than a microprobe. Dunai and Roselieb (1996) dismissed the use of step-wise heating experiments for measuring helium diffusion in garnet because temperatures above 900 °C would have to be used in order to release accurately measurable fractions of He in a reasonable time. The instability of the almandine component in their samples during *in vacuo* heating experiments would make it impossible to prove the (meta)stability of samples throughout the experiments. Also rejected was the use of high-temperature release experiments (to allow the investigation of phase transition). These were found to be unsuitable for the highly variable natural He concentrations in sample material (see section 6.5.3).

A reverse conventional step-wise heating experiment was eventually chosen by Dunai and Roselieb (1996). This involved loading the garnet at high pressure with He and subsequently measuring the incorporated He. Although this also required loading the samples with temperatures exceeding the almandine stability field, the garnet could be studied for signs of instability after loading and prior to He analysis. The additional problem of iron loss in the Pt capsule causing a redox reaction was prevented by using a double capsule technique. This required a garnet crucible made from the same material as the sample (see Dunai and Roselieb, 1996 for more details).

6.5.2.3. Comparisons Between Studies

Volume diffusion obeys the Arrhenius relationship:

$D = D_0 e^{-(E/RT)}$ Equation [6.1]

where:

D_0 = diffusion coefficient

E = activation energy

R = the gas constant

T = Temperature

An Arrhenius plot presents the temperature dependence of the diffusion coefficient (D). Log values of D are plotted against the reciprocal of the anneal temperature. The slope of the resulting line is related to the activation energy and the intercept is log D_0.

Schwandt *et al.* (1995) indicated that comparison of data by normalisation to a common set of conditions could be misleading. In previous studies (e.g. Trull and Kurz, 1992; Schwandt *et al.*, 1995; Dunai and Roselieb, 1996) data were presented on an Arrhenius plot without correction for the different pressure and oxygen fugacity conditions. The effect of variable experimental factors upon diffusion coefficients is discussed below.

A) Composition

Elphick *et al.* (1985) found a strong link between the diffusion coefficients of Mg and Fe and composition in garnet. The amount of Fe^{2+} present was particularly influential on diffusion rates, with diffusion coefficients increasing with Fe^{2+}. Similar effects have been reported by Misener (1974), and Buening and Buseck (1973) (referenced in Elphick *et al.*, 1985) in olivine. This was due to the increased equilibrium concentration of cation vacancies and Fe^{3+} owing to the increase of Fe^{2+} at constant oxygen fugacity, and to the higher ionic porosity (Buening and Buseck, 1973; Morioka, 1980; Lasaga, 1981; referenced in Elphick *et al.*, 1985).

In contrast, a study by Chakraborty and Rubie (1996) reported that there was practically no compositional dependence of Mg tracer diffusivity in garnet for the range of compositions studied

($Alm_{73}Pyr_{21}$-$Alm_{38}Pyr_{50}$). This was consistent with the inference of Loomis *et al.* (1985) (referenced in Chakraborty and Rubie, 1996) from high pressure and temperature experiments. However, when Chakraborty and Rubie (1996) took a mean from the data set of the two compositions, a trend of weak increase of Mg tracer diffusivity with increasing Fe content of the garnet was found. They concluded that the weak compositional dependence of Mg tracer diffusivities found suggests that Mg tracer diffusion coefficients measured in various studies on garnet crystals of different composition should be directly comparable.

B) Oxygen Fugacity

Diffusion experiments use either constant oxygen fugacity throughout or a specific oxygen fugacity buffer. To compare results from the differing experiments Chakraborty and Rubie (1996) recommended normalisation to either a specific oxygen fugacity or to a particular buffer assemblage. The activation energies for experiments using a constant oxygen fugacity or an oxygen fugacity buffer are different, with temperature changes along an oxygen fugacity buffer being due to changes in oxygen fugacity and temperature. As a consequence, on the Arrhenius plot the diffusivity data show an exaggerated temperature dependence (steep slope) (Chakraborty and Rubie, 1996).

C) Site of Entrapment

Trull and Kurz (1992) found that in natural olivine He was contained almost exclusively in CO_2 rich fluid inclusions, whereas Dunai and Roselieb (1996) reported that the He was trapped within lattice defects in garnet. Dunai and Roselieb (1996) point out that the diffusion data on olivine and diopside from Trull and Kurz (1992) is complicated by the partitioning between fluid and crystalline phases. This means that the diffusion coefficients obtained by Trull and Kurz (1992), for example, may be several orders of magnitude too low. Therefore, the experimentally derived diffusion coefficients for He in olivine and diopside can only be considered as a minimum value (Dunai and Roselieb, 1996). Dunai and Roselieb (1996) indicate that their study of garnet shows that garnet is probably the most retentive silicate mineral for He known because the values they obtained are probably maximum values (see Figure 6.10).

D) Arrhenius Plot

The activation energies and diffusion coefficients from the majority of the work referenced above (and detailed in Appendix 6.3) have been plotted together on an Arrhenius plot without normalisation (Figure 6.10). Measured data are indicated by the solid line, with the dotted line representing extrapolated data between 300 and 1500 °C. Although there are difficulties associated with comparing data in this way, as indicated above, it is evident that the diffusivity data for helium in garnet define a significantly different slope from that for other cations in garnet. A steeper line is also seen for the helium experiments by Trull and Kurz (1992) although these are in diopside and olivine. This would suggest that either the data are incorrect or the diffusion rate of helium in garnet is controlled by a very different mechanism than other cations in garnet. This present study will attempt to show which of these is the case.

6.5.3. Helium Diffusion Experiment Using Zircon Inclusions in Garnet

6.5.3.1. Introduction

The halo surrounding a zircon will contain helium emitted as alpha particles by uranium and thorium fission. The helium can be released by ablating the zircon and halo using the UV laser microprobe and can be measured in a mass spectrometer. Using similar methods to those reported in Chapter 5 for argon diffusion in biotite, a profile of the size and shape of the halo can be constructed. If several zircons and halos in garnet were to be measured, a characteristic profile might be produced and the size and shape of any halo in garnet predicted. If a similar garnet containing zircons is then heated and the resultant profile from the zircon and halo is measured, comparison to the predicted

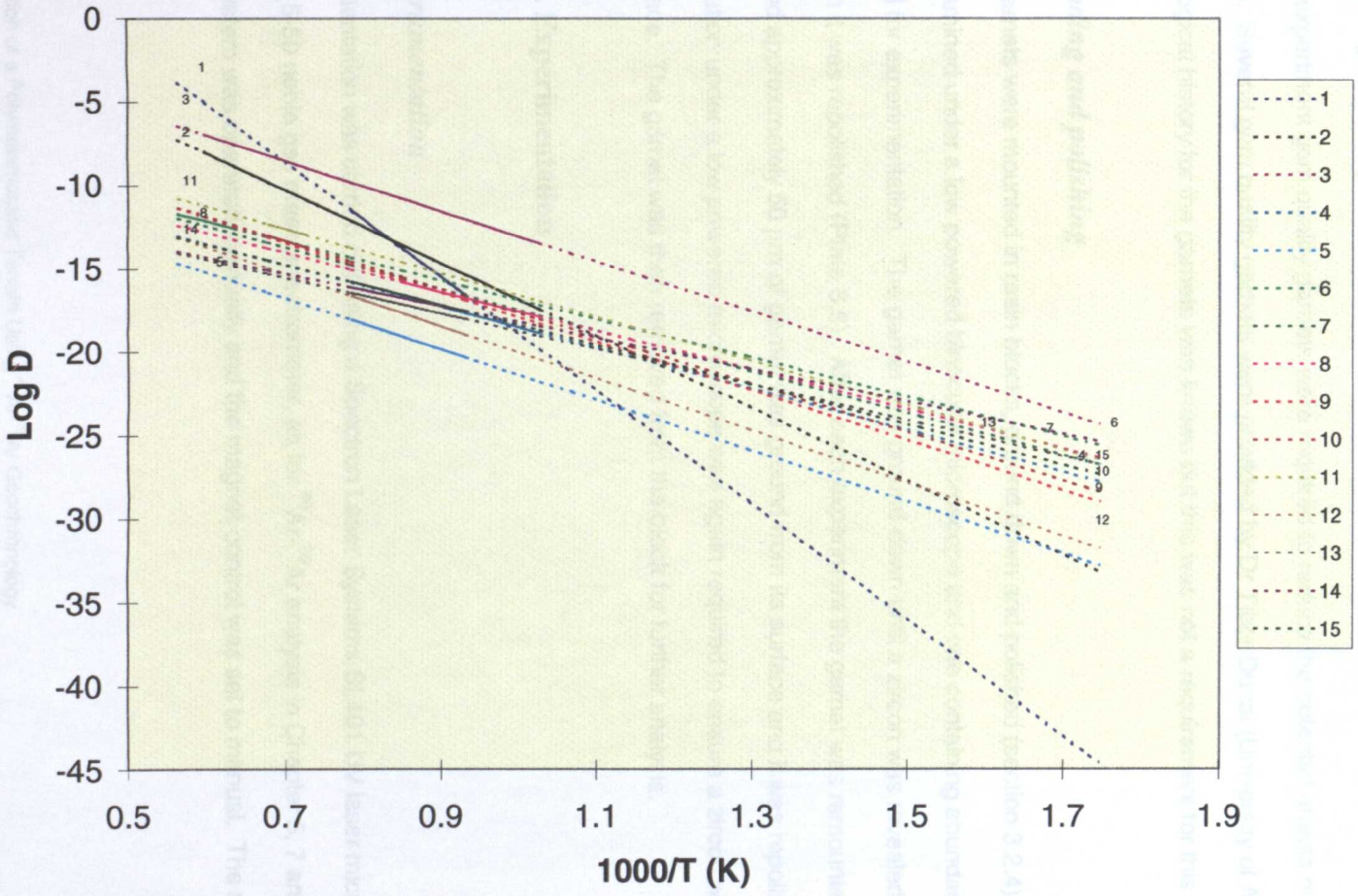

1. Dunai and Roselieb (1996) He in garnet
2. Trull and Kurz (1992) He in olivine
3. Trull and Kurz (1992) He in diopside
4. Cygan and Lasaga (1985) Mg in garnet
5. Schwandt *et al.* (1995) Mg in garnet
6. Elphick *et al.* (1985) Mg in Fe-garnet
7. Elphick *et al.* (1985) Mg in Mn-garnet
8. Chakraborty & Rubie (1996) Mg in gt
9. Chakraborty & Ganguly (1992) Mg in gt
10. Chakraborty & Ganguly (1992) Fe in gt
11. Chakraborty & Ganguly (1992) Mn in gt
12. Coghlan (1990) O_2 in garnet
13. Coghlan (1990) Sr in garnet
14. Coghlan (1990) Nd in garnet
15. Coghlan (1990) Er in garnet

For more details see Appendix 6.2

Figure 6.10: Arrhenius plot of previous diffusion experiments relevant to present study

profile before heating will determine the amount of diffusion due to heating. Because the helium associated with zircons is naturally contained within the mineral, no artificial method of forcing helium into the garnet at high temperature is necessary, thus reducing the possibility of introducing unrealistic behaviour of the helium and garnet, or of altering the composition of the garnet. This also overcomes the problems faced by Vance and Ayres (1997) of having to know the thermal history of the sample and the initial distribution of the helium.

6.5.3.2. Sample Preparation

A) Origin of the Sample

For this experiment gem quality garnets were required to reduce the potential affects of defects on diffusion. Several gem quality garnets were provided by Dr Tibor Dunai (University of Amsterdam). No geological history for the garnets was known but this was not a requirement for this experiment.

B) Grinding and polishing

Three garnets were mounted in resin blocks, ground down and polished (section 3.2.4). They were then examined under a low powered binocular microscope and one containing abundant zircons was selected for experimentation. The garnet was ground down until a zircon was revealed at the surface and then it was repolished (Plate 6.6). After each experiment the garnet was remounted in a resin block and approximately 50 μm of garnet was ground from its surface and it was repolished. Examination under a low powered microscope was again required to ensure a zircon was close to the surface. The garnet was then removed from the block for further analysis.

6.5.3.3. Experimentation

A) Instrumentation

Experimentation was carried out using a Spectron Laser Systems SL401 UV laser microprobe and a MAP 215-50 noble gas mass spectrometer, as for ^{40}Ar-^{39}Ar analysis in Chapter 5, 7 and 8. The valve system was operated manually and the magnet control was set to manual. The mass

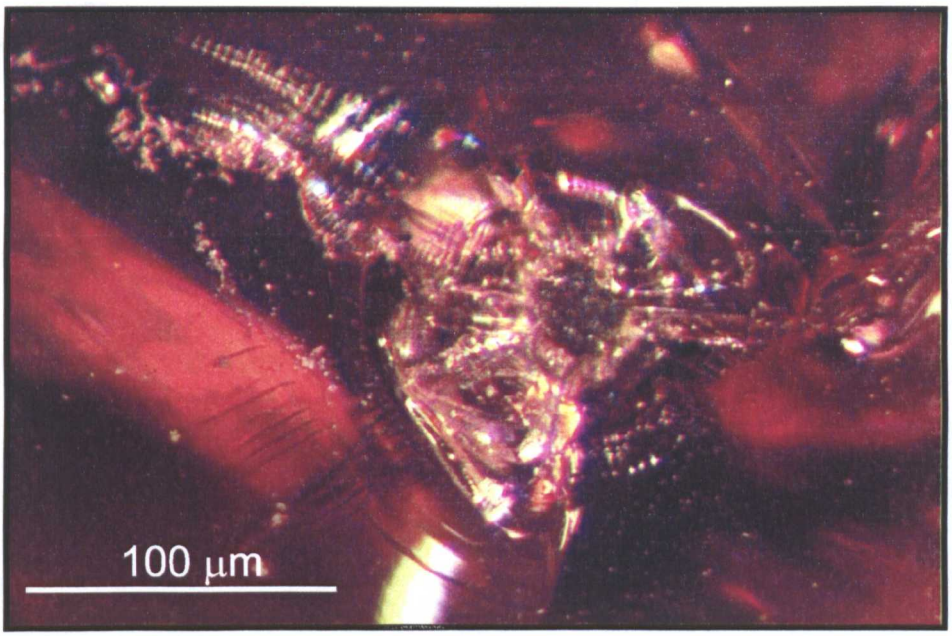

Plate 6.6: Zircon inclusion in gem-quality garnet surrounded by halo and fractures

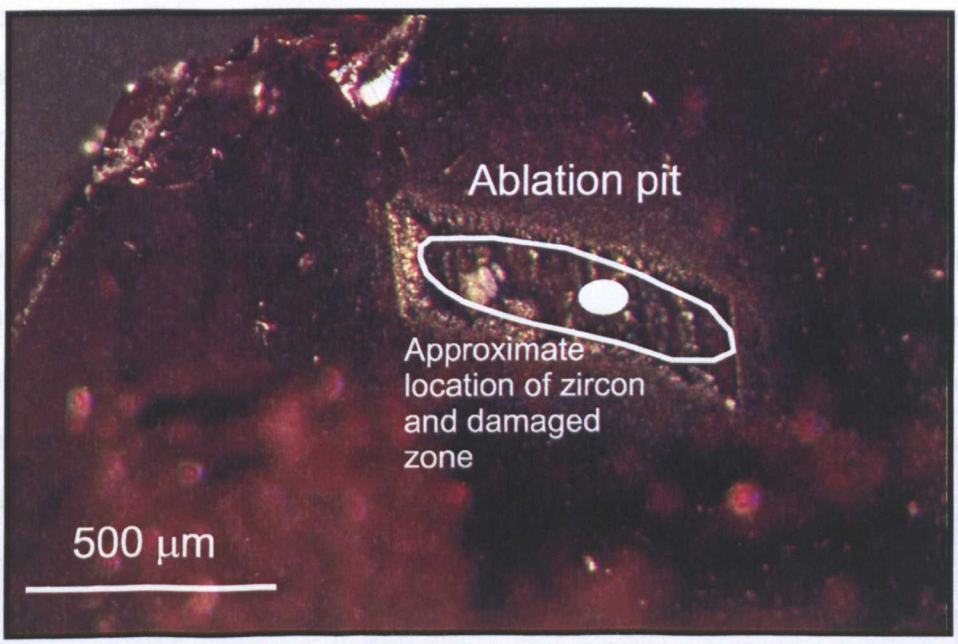

Plate 6.7: Ablation pit over zircon inclusion and halo in gem-quality garnet (Profile 3)

spectrometer magnet was adjusted to a Hall probe setting of 0.5226 volts for the ^{4}He peak calculated from the ^{40}Ar (1.65 volts) as follows:

$$\frac{M}{e} = \frac{H^2 r^2}{2V}$$ Equation [6.2]

(McDougall and Harrison, 1988; p.74)

$$\Rightarrow \quad \frac{M_1}{M_2} = \frac{H_1^{\,2}}{H_2^{\,2}}$$ Equation [6.3]

$$\Rightarrow \quad \frac{\sqrt{M_1}}{\sqrt{M_2}} = \frac{H_1}{H_2}$$ Equation [6.4]

where:

M = Mass of the ion
e = charge of the ion
H = magnetic field strength
r = radius of the flight tube
V = source voltage

To carry out a blank, the ion pump on the extraction line was closed for five minutes, then mass spectrometer ion pump was closed and the inlet valve opened to allow He into the mass spectrometer. This provided a measure of the amount of helium contained within the system. Five readings from the mass spectrometer were made and a mean taken. Blanks were taken after every 2 to 4 analyses.

For an analysis the extraction system was isolated from the pumps as in the blank, the sample was ablated using the UV laser and after five minutes the mass spectrometer ion pump was closed and the inlet valve was opened to allow the sample ^{4}He into the mass spectrometer. Once again five readings from the mass spectrometer were made and a mean taken. After each analysis the valves were returned to their start positions.

B) Determining the shape of helium concentration in zircon and halo prior to heating

The initial intention for this experiment was to drill progressively into the zircon from above using 50 µm square ablation pits repeated over the same area to construct a profile. However, it was difficult to judge how close the zircon was to the surface and numerous blank runs were performed without

hitting the zircon or He in the halo. It was found that completing a series of traverses across the zircon was more effective. Because the zircon and the halo are both roughly spherical this was effectively the same as approaching from above but it was easier to monitor.

Profile 1 was carried out on a zircon on the surface of the garnet. Each traverse was approximately 100 μm long and 10 μm wide. The profiling started outside the visible halo on one side of the zircon (Plate 6.6) and continued across the zircon (0 μm in Figure 6.11A) to the other side of the halo until a blank level was reached for several runs. The total area ablated was 100 μm by 160 μm.

Profile 2 was undertaken on a zircon close to but not at the surface. Once again the traverses started outside the damaged zone on one side of the zircon and continued across the zircon until outside the damaged zone on the other side of the zircon. Each traverse was about 125 μm long and 10 μm wide. 14 traverses were undertaken across the halo without releasing significant levels of helium. Another series of traverses directly over the first were then attempted.

For profile 3 the zircon was just below the surface. This zircon and halo had an elongate shape, being approximately 650 μm long and 200 μm wide. 65 traverses, approximately 10 μm wide and 200 μm long were carried out across the halo (Plate 6.7).

6.5.3.4. Results

The profiles produced are illustrated in Figure 6.11A-C and the data tabulated in Appendix 6.4.

A) Profile 1

As can be seen in Figure 6.11A that the maximum amount of helium released in Profile 1 was about 1940×10^{-9} cc/g, concentrated around the area of the zircon. Small 'blips' were also seen 20 to 30 μm away from the main signal on either side of the zircon but these were only slightly above blank levels.

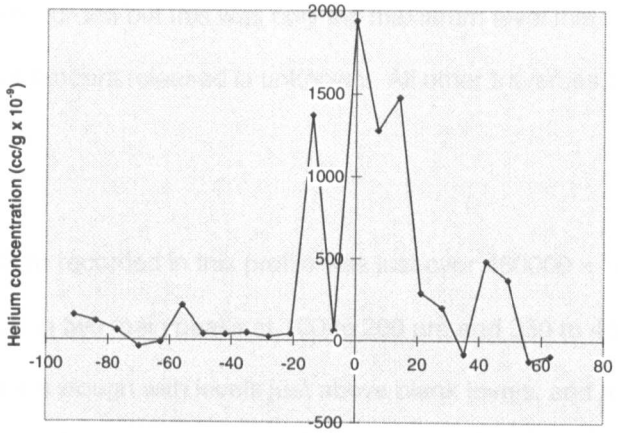

A) Profile 1

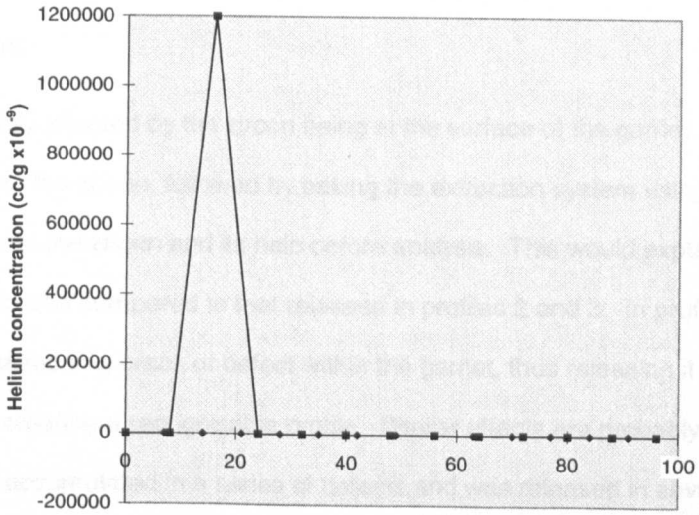

B) Profile 2

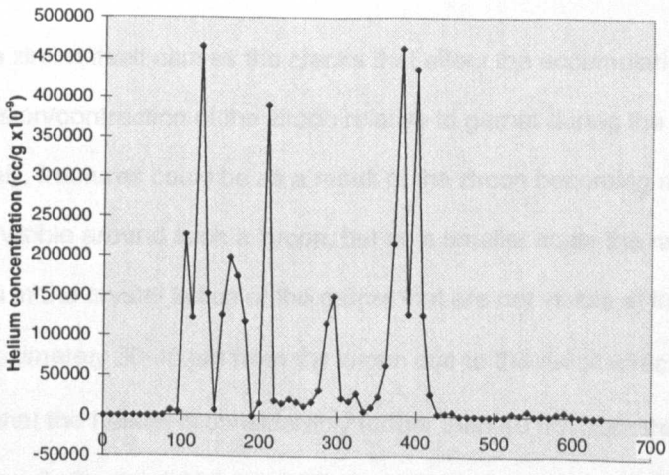

C) Profile 3

FIgure 6.11: Helium concentration profiles associated with zircon inclusions in garnet

B) Profile 2

In Profile 2 all the helium was released from the zircon in one analysis (Figure 6.11B). Over 1200000 $\times 10^{-9}$ cc/g of helium were recorded but this was only the maximum level that the mass spectrometer could record and the actual amount released is unknown. All other traverses yielded blank levels.

C) Profile 3

The maximum level of helium recorded in this profile was just over 460000 $\times 10^{-9}$ cc/g, as shown in Figure 6.11C) and occurred in two main peaks at 100 to 200 μm and 350 to 450 μm across the halo. Between the two peaks was a trough with levels just above blank levels, and a lesser peak at 300 μm. Blank levels were recorded on either edge of the halo.

6.5.3.5. Discussion

Profile 1 was probably affected by the zircon being at the surface of the garnet. It is possible that grinding off the top of the zircon, followed by baking the extraction system using a heat lamp, allowed helium to escape from the zircon and its halo before analysis. This would explain the relatively low levels of helium recorded compared to that released in profiles 2 and 3. In profile 2, it is likely that all the helium had collected in a crack or defect within the garnet, thus releasing it all as if bursting a balloon rather than creating a recognisable profile. Similar effects are probably evident in profile 3. It is likely that helium accumulated in a series of defects and was released in several bursts rather than as a smooth profile.

It is possible that the zircon itself causes the cracks that affect the accumulation of helium around it by differential expansion/contraction of the zircon relative to garnet during the geological history of the rock. Alternatively, fractures could be as a result of the zircon becoming metamict. Plate 6.6 shows the fractures visible around such a zircon, but on a smaller scale the radioactive decay could have caused defects in the crystal lattice of the garnet that are not visible at this magnification. Alpha particles travel approximately 30-40 μm from the zircon due to the recoil effect. These profiles, particularly 3, show that the helium is considerably further than 40 μm from the zircon, suggesting that it continues to travel after the initial recoil. Defects in the garnet structure would allow rapid diffusion away from the zircon and accumulation of helium within them.

It is clear that no "characteristic" profile has been found in zircon and there are no reproducible halos prior to heating that can be compared to zircons after heating. The three different profiles constructed show that it is not possible to predict the size and shape of the helium distribution around a zircon. This means that heating a sample and measuring the resultant profile would not be a useful exercise because it is not possible to relate it to the distribution before heating.

6.5.4. Helium Diffusion Experiment in Garnet Using Helium Doping

6.5.4.1. Introduction

This experimental technique was similar in some ways to that used by Dunai and Roselieb (1996) in that the garnets were doped with helium. However, Dunai and Roselieb (1996) measured bulk grains. In this experiment the UV laser microprobe was used to systematically depth profile single garnet grains to measure the concentration versus depth for helium.

In their experiment, Dunai and Roselieb (1996) used tumbled almandine-rich pyrope with a diameter of 5-10 mm from which spheres were manufactured by cutting the garnet into cubes and abrading them. Final diameter of the spheres ranged from 6 to 2280 μm. The smallest garnet spheres were loaded with helium for a sufficient length of time and at a sufficient temperature (based on the comparative ion-porosity between garnet and olivine) that the sphere became saturated with helium. Assuming that the smallest spheres had reached equilibrium, they measured the bulk gain of the larger spheres by heating to 1800 °C without prior baking in the extraction line. In this way, assuming the helium gain was a result of diffusion into the sphere, Dunai and Roselieb (1996) calculated diffusion coefficients for their experiments.

6.5.4.2. Sample Selection and Preparation

Again gem quality garnets were used for this experiment in order to reduce the effects of fractures and other defects. Three garnets of different compositions were analysed. These were: a colourless Fe-free pyrope and an Fe-bearing pyrope both from the Dora Maira Massif in the Italian Alps, supplied by Dr Richard Brooker (University of Bristol); and an almandine-rich pyrope with minor

grossular and spessartine components ($Pyr_{55}Alm_{40}Gro_4Sp_1$) from Orissa, India, supplied by Dr Tibor Dunai (University of Amsterdam). This garnet was from the same sample set used in the experiment conducted by Dunai and Roselieb (1996). All garnets were between 1 and 2 cm in diameter (Plates 6.8-6.10).

The garnets were mounted in resin blocks and polished. They were then removed from the blocks, cleaned in an ultrasonic bath in methanol, and mechanically broken into several pieces. Pieces from the same original garnet, each with a polished surface, were then used for the different experiments (Plates 6.8-6.10).

6.5.4.3. Helium Doping Conditions

A 2-3 mm sized garnet fragment of each garnet type was loaded into 2 separate 4 mm diameter platinum tubes, each garnet separated by gentle crimping of the tubing, and the ends of the capsule gently folded. The loaded samples were isothermally heated in internally heated gas bombs at the Experimental Petrology facility at the University of Edinburgh by Dr Steve Elphick. Two isothermal runs were undertaken, one at 1000 °C, pressurised at 250 bars He, with an Ni/NiO oxygen fugacity buffer of 10.18 log (fO_2), for a duration of 114 hours, and one at 892 °C, pressurised at 250 bars He, with an Ni/NiO oxygen fugacity buffer of 10.18 log (fO_2), for 49 days. The temperature and duration of these experiments was calculated to optimise diffusion profiles in the garnet based upon the helium diffusion data obtained by Dunai and Roselieb (1996) in order to allow sufficient diffusion into the garnet that it could be measured using 5-20 depth profile steps.

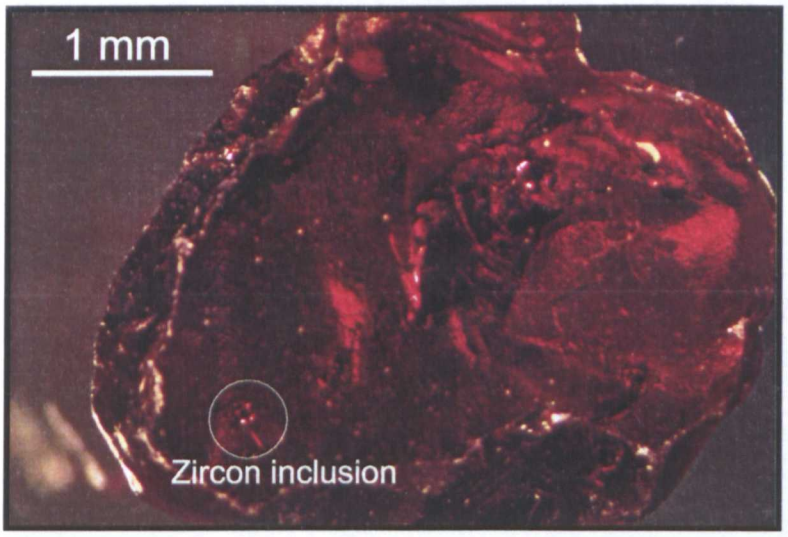

A) Not subjected to helium loading (can see through garnet to other side of the crystal)

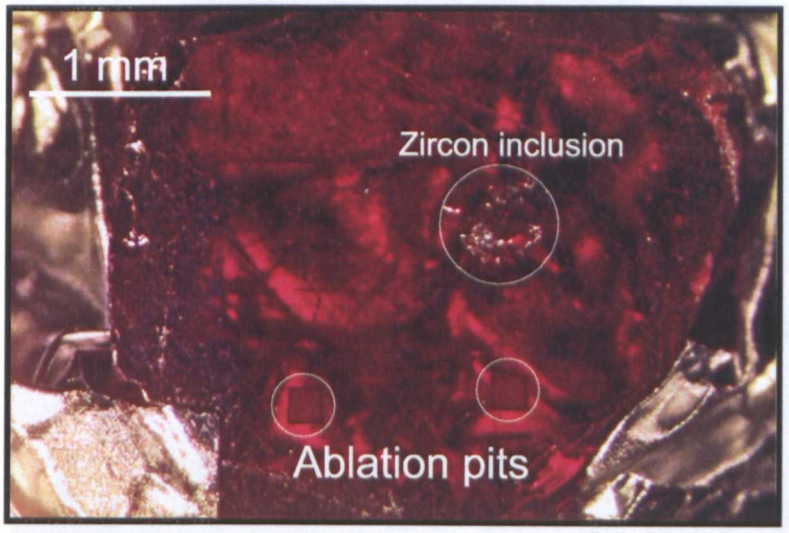

B) 900 °C - Garnet apparently unaffected (can see through garnet to aluminium foil beneath)

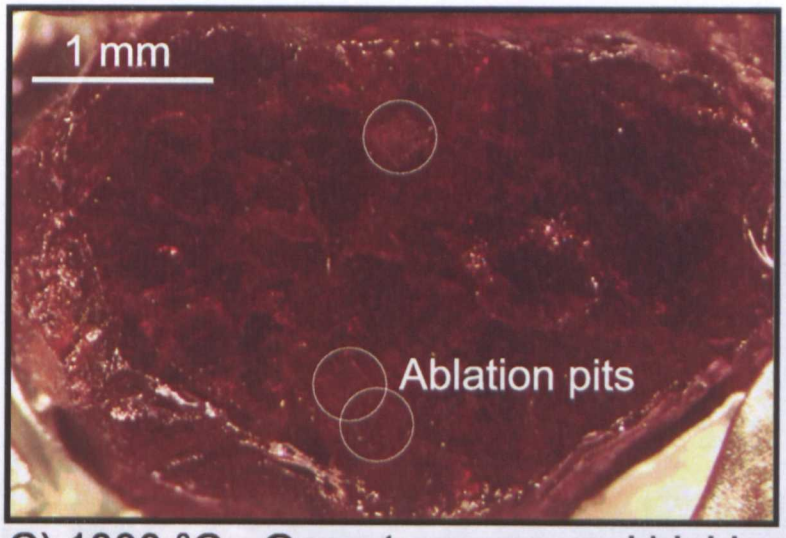

C) 1000 °C - Garnet opaque and highly fractured

Plate 6.8: Gem-quality almandine garnet fragments used in helium doping experiment

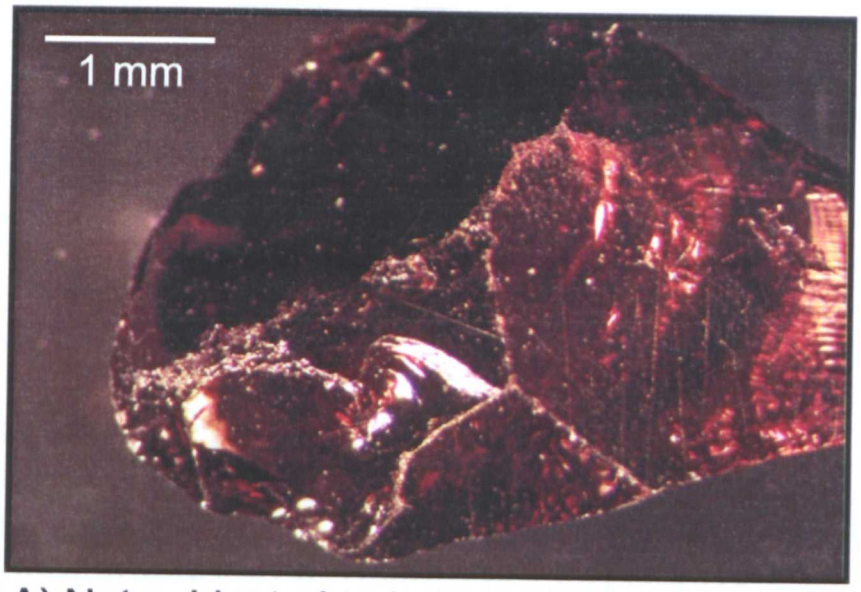

A) Not subjected to helium doping

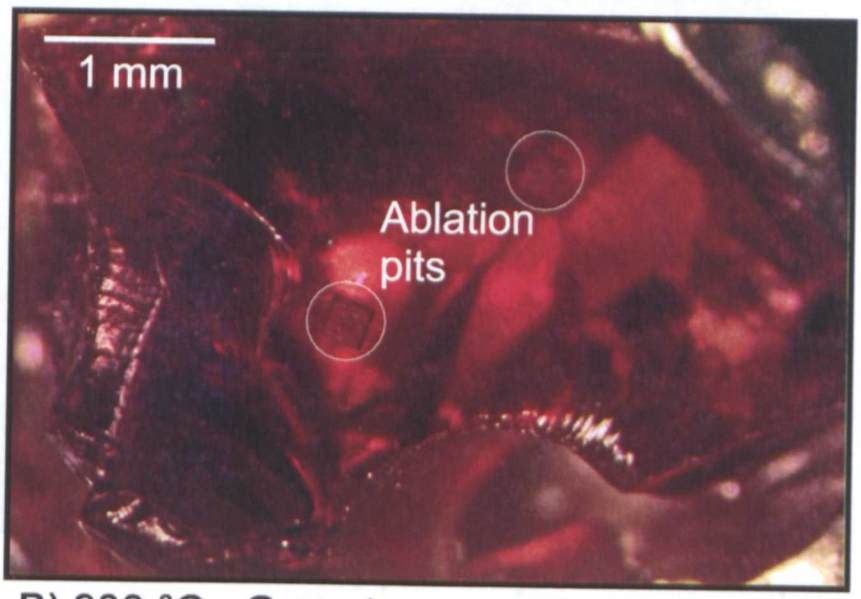

B) 900 °C - Garnet apparently unaffected

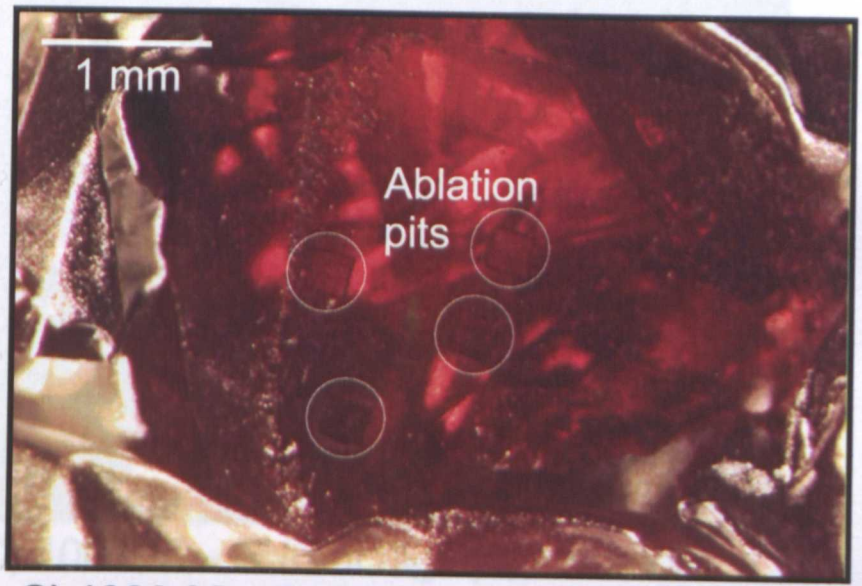

C) 1000 °C - Garnet apparently unaffected

Plate 6.9: Gem-quality Fe-rich pyrope garnet fragments used in helium doping experiment

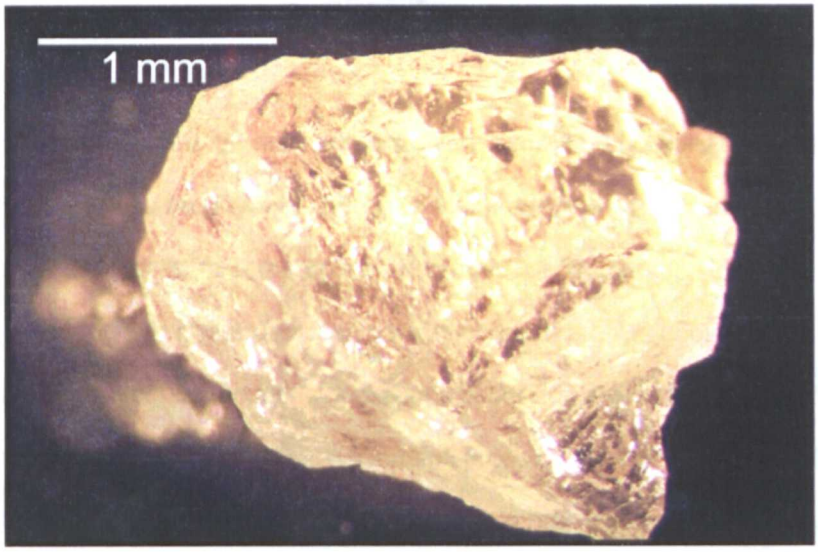

A) Not subjected to helium doping (can see through garnet to other side of crystal)

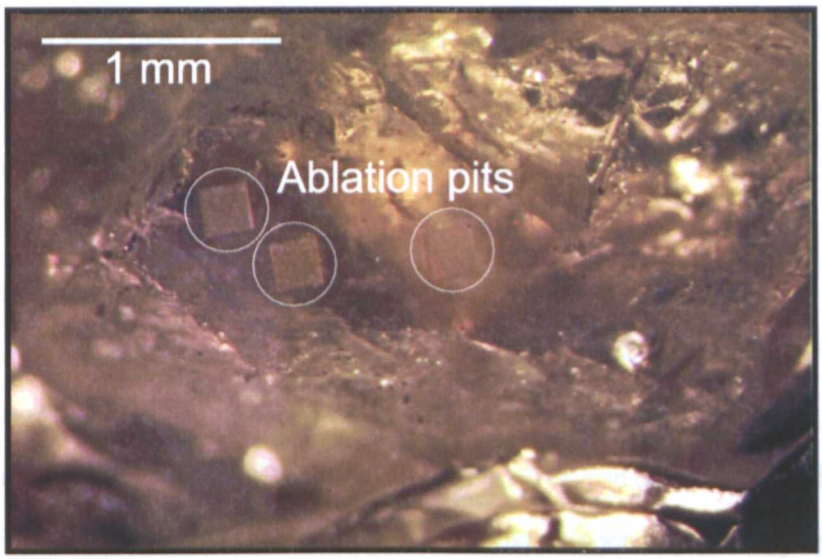

B) 900 °C - Garnet apparently unaffected (tiny dark inclusions visible)

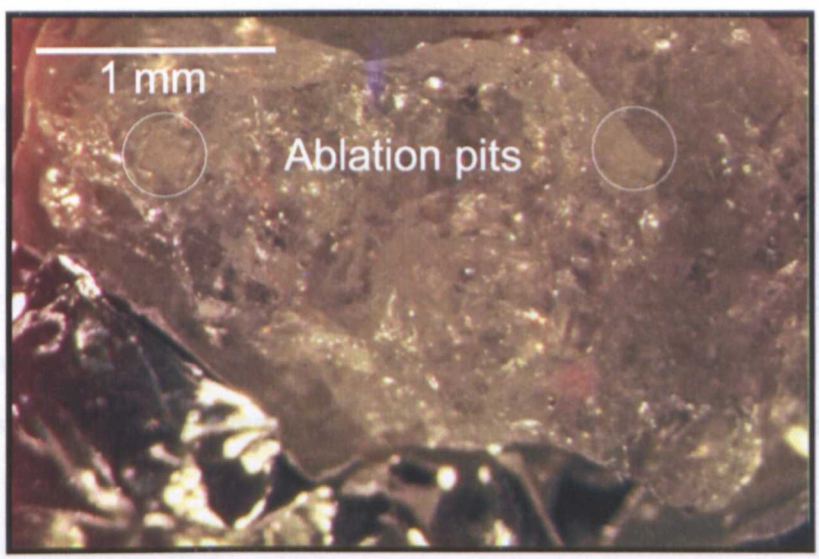

C) 1000 °C - Garnet highly fractured

Plate 6.10: Gem-quality Fe-free pyrope garnet fragments used in helium doping experiment

6.5.4.4. Analytical Technique

After the doping process, the garnet fragments were examined optically for signs of instability. Plate 6.8 shows that there was no physical change in the almandine garnet loaded at 892 °C but that the fragment loaded at 1000 °C became opaque and internally fractured. However, these fractures did not reach the surface and it was possible to conduct depth profiles above them. This plate also shows that this garnet contained zircon inclusions of varying sizes. Plate 6.9 shows that the Fe-rich pyrope did not change noticeably after the loading process in either experiment. Plate 6.10 shows that the Fe-free pyrope loaded at 1000 °C also became highly fractured. Indeed, the fracturing was so intense that it was not possible to find areas of unfractured garnet large enough to ablate a 200 μm square. An attempt to run 100 μm depth profiles in this sample failed to release enough gas so 200 μm squares were used despite the fracture problem. Also visible in Plate 6.10B are tiny (5-10 μm) brown inclusions. It is not known what these inclusion are but depth profiles were made avoiding them.

In order to ensure that the polished surface of the garnet was facing uppermost, the garnet fragments were mounted into pieces of aluminium foil before being placed into the laser port. Loading of the laser port was as for samples for ^{40}Ar-^{39}Ar dating, as described in section 3.3.5 and was baked out overnight at 120 °C using a heat lamp. This is in contrast to the procedure used by Dunai and Roselieb (1996) who stored samples in liquid nitrogen between doping and analysis and did not bake out. Again the mass spectrometer was adjusted as described in section 6.5.3.3, and the valves operated manually.

Depth profiles were measured by ablating 200 μm squares repeatedly over the same area of garnet. Each analysis consisted of 14 minutes of ablation time, followed by 2 minutes of getter time. Blanks were run for 16 minutes. A mean of ten readings from the mass spectrometer were taken for both blank and analytical runs. Because of variations of blank values throughout the day, the blanks were taken after every two sample runs and that blank reading used to correct the two sample values. Experiments were run until the measured helium in the sample fell to blank levels.

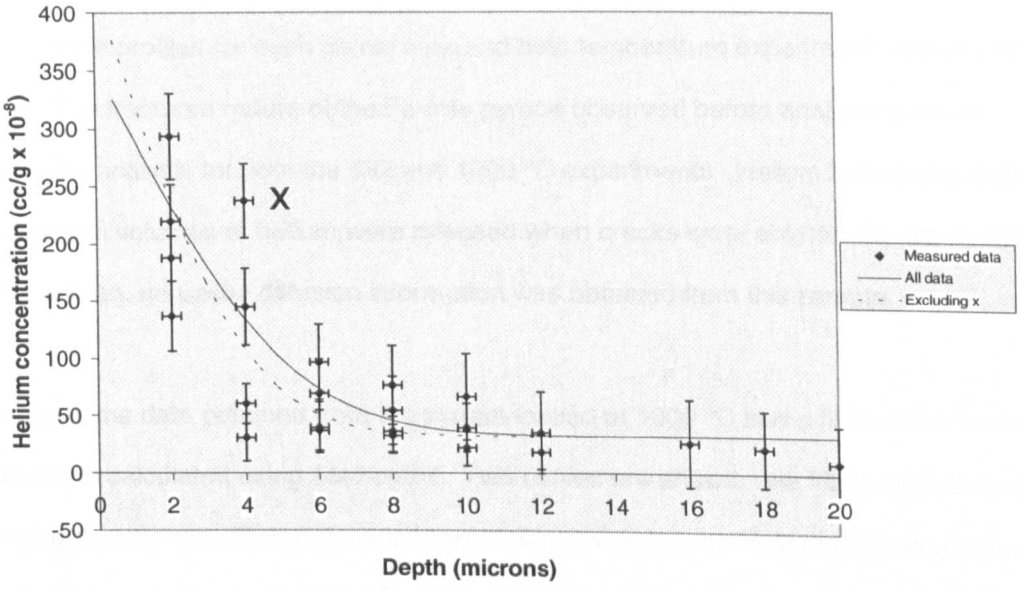

A) Pyrope held at 1000 °C

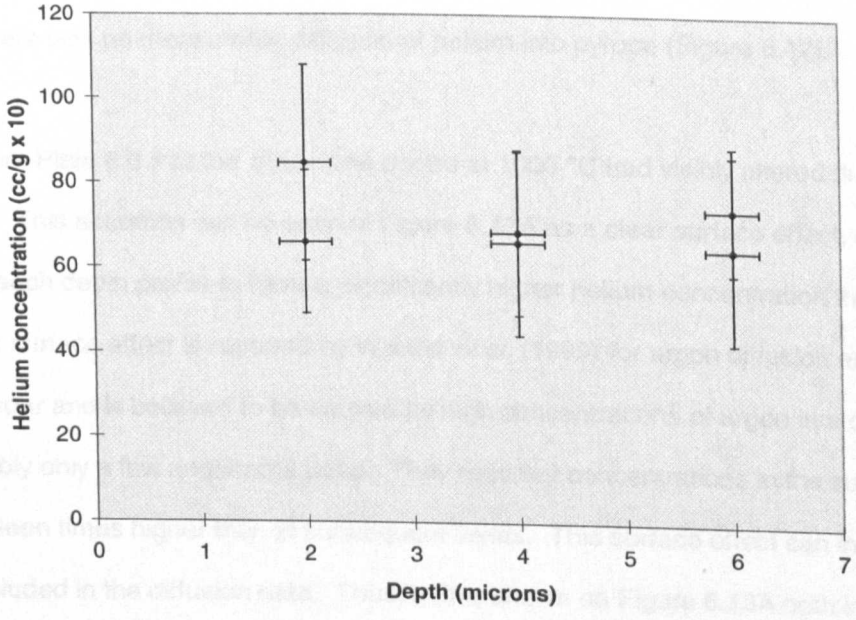

B) Pyrope held at 892 °C

Figure 6.12: Helium diffusion profiles for pyrope

Where possible, the depth profiling was conducted away from any visible fractures or inclusions (Plates 6.8-6.10).

6.5.4.5. Results

The data for the depth profiles for each garnet type and both temperature experiments are tabulated in Appendix 6.5. The fractured nature of the Fe-free pyrope observed before analyses proved problematical during analysis for both the 892 and 1000 °C experiments. Helium accumulated along the fractures and high volumes of helium were released when cracks were ablated, disturbing the profile. For this reason, no useful diffusion information was obtained from this sample.

Figure 6.12A shows the data obtained from the pyrope loaded at 1000 °C and a fit for diffusion into a semi-infinite medium calculated using *Mathcad 5*. Two curves are shown, one fitting all data and one fitted by removing data point x. This point appeared to lie outside the curve of the diffusion data and probably resulted from a surface contamination of helium associated with defects similar to that seen in argon diffusion experiments (Wartho *et al.*, 1999). The surface concentration (C_0) and diffusion coefficient (D) for these two curves are shown in Table 6.5 below.

At 892 °C there was no measurable diffusion of helium into pyrope (Figure 6.12B).

It is clear from Plate 6.8 that the almandine doped at 1000 °C had visibly altered during the experiment. This alteration can be seen in Figure 6.13A as a clear surface effect, causing the first analysis of each depth profile to have a significantly higher helium concentration than analyses at depth. This surface effect is reported by Wartho *et al.* (1999) for argon diffusion experiments in gem-quality feldspar and is believed to be caused by high concentrations of argon in a defect-rich surface layer probably only a few angstroms deep. They reported concentrations in the surface layer as much as fifteen times higher than in subsequent layers. This surface effect can introduce significant errors if included in the diffusion data. Thus, a fit is shown on Figure 6.13A both including and excluding the surface data. The diffusion coefficients based upon these data are included in Table 6.5.

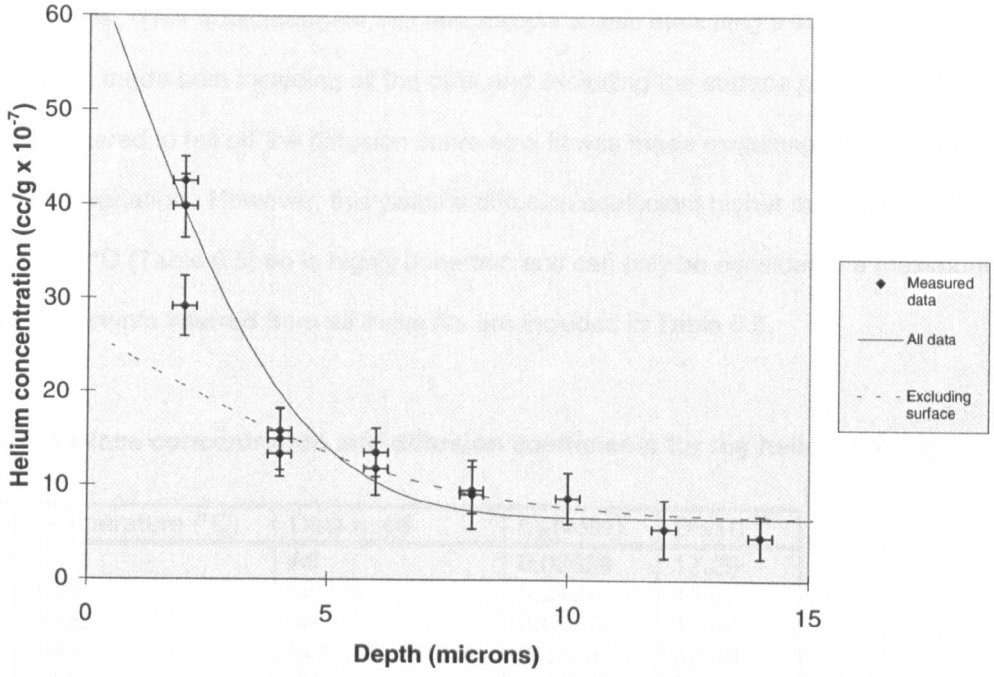

A) Almandine held at 1000 °C

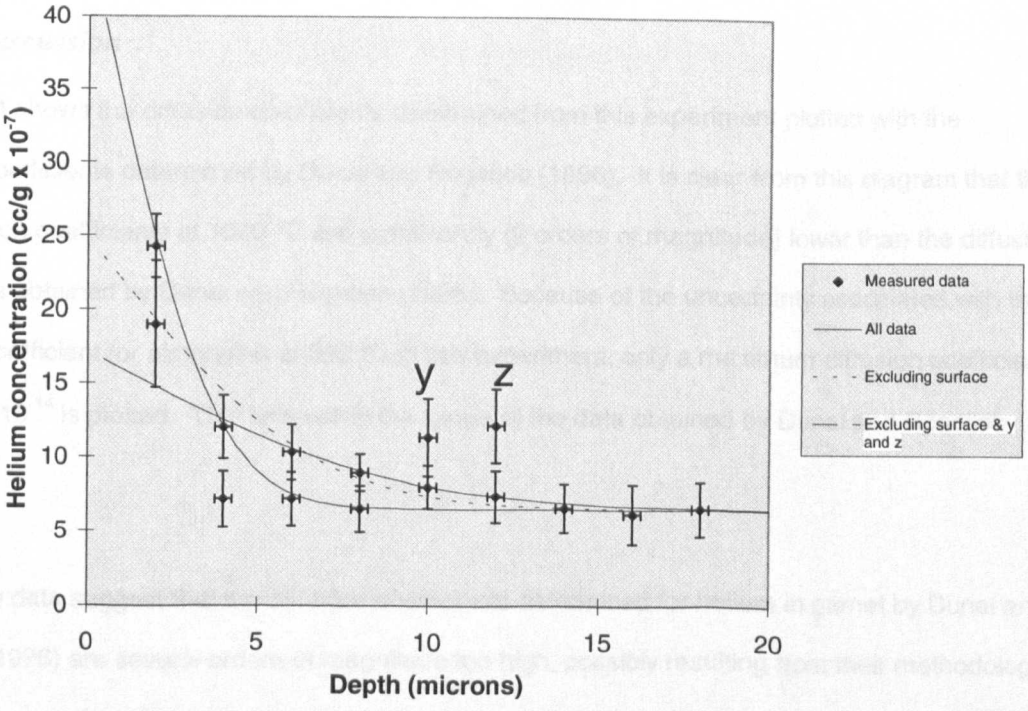

B) Almandine held at 892 °C

Figure 6.13: Helium diffusion profiles for almandine

No visible alteration of the almandine was detected in the 892 °C experiment (Plate 6.8). However, in Figure 6.13B the surface points again show an elevated concentration of helium in comparison to subsequent analyses. This would suggest that this sample is also exhibiting a surface effect. Therefore, fits were made both including all the data and excluding the surface points. In addition, points y and z appeared to fall off the diffusion curve so a fit was made excluding these points to check for possible variation. However, this yields a diffusion coefficient higher than obtained for almandine at 1000 °C (Table 6.5) so is highly uncertain and can only be considered a maximum. The diffusion coefficients inferred from all these fits are included in Table 6.5.

Table 6.5. The surface concentration and diffusion coefficients for the helium doping experiments

Garnet	Temperature (°C)	Data used	C_0 (volts)	D $\times 10^{-15}$
Pyrope	1000	All	0.03589	17.29
Pyrope	1000	Without x	0.04228	10.07
Almandine	1000	All	0.06475	11.68
Almandine	1000	Without surface	0.02259	32.49
Almandine	892	All	0.04085	8.037
Almandine	892	Without surface	0.02087	29.24
Almandine	892	Without surface or y and z	0.01243	54.44

6.5.4.6. Discussion

Figure 6.14 shows the diffusion coefficients determined from this experiment plotted with the diffusion coefficients determined by Dunai and Roselieb (1996). It is clear from this diagram that the new diffusion coefficients at 1000 °C are significantly (2 orders of magnitude) lower than the diffusion coefficients obtained by Dunai and Roselieb (1996). Because of the uncertainty associated with the diffusion coefficient for almandine at 892 °C in this experiment, only a maximum diffusion coefficient of 5.444×10^{-14} is plotted. This falls within the range of the data obtained by Dunai and Roselieb (1996).

These new data suggest that the diffusion coefficients determined for helium in garnet by Dunai and Roselieb (1996) are several orders of magnitude too high, possibly resulting from their methodology. Firstly, their samples were prepared by grinding fragments of garnet into spheres

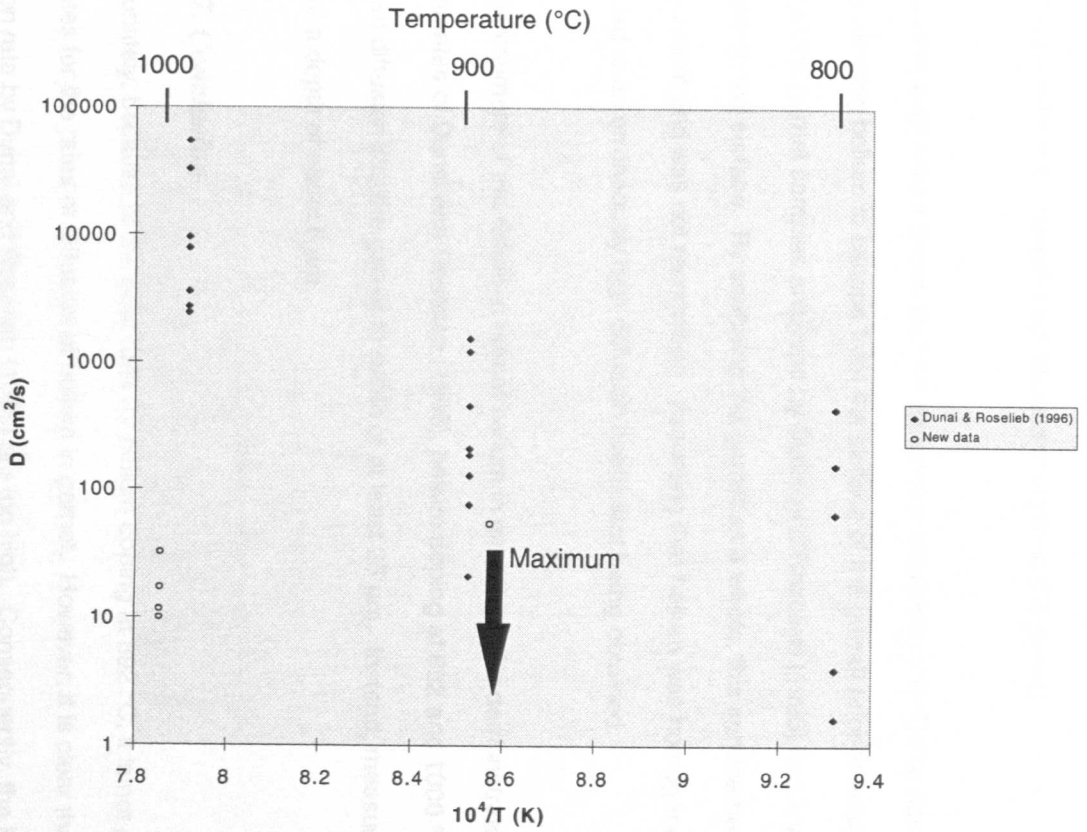

Figure 6.14: Arrhenius diagram for diffusion coefficients of helium in garnet showing data from Dunai and Roselieb (1996) and this study

and polishing them. This results in a large surface to volume ratio and a surface filled with defects caused by the polishing process. The micro-pitted surface allows helium to concentrate on the surface layer, leading to the surface effect described by Wartho *et al.* (1999). Furthermore, whereas samples in this research were left at room temperature for several weeks after doping, Dunai and Roselieb (1996) stored their samples in liquid nitrogen to prevent helium diffusion. This prevented helium concentrated on the surface from escaping. In addition, unlike this experiment, Dunai and Roselieb (1996) did not bake the samples prior to analysis which again prevented the release of helium from surface defects. Finally, their bulk extraction technique prevented any separation of surface helium from that which had diffused to depth in the garnet.

Because this experiment shows that the almandine provided by Dr Dunai has a slight surface effect, despite allowing helium to escape from the surface of the garnet prior to analysis, it seems highly likely that the garnet samples analysed by Dunai and Roselieb (1996) had a very large concentration of helium on the surface. By analysing the garnet as a whole, this surface helium was included in measurement and was not recognised. Assuming that helium was homogeneous throughout the garnet led to an erroneously high diffusion coefficient being obtained.

This overestimate of the diffusion rate of helium in garnet can be demonstrated by this study. Using the estimates of Dunai and Roselieb (1996), helium doping at 892 and 1000 °C should have resulted in helium diffusion into the garnet to depth of at least 25 μm. Instead, measurable helium was only found to a depth of about 6 μm.

6.5.4.7. Conclusion

Unfortunately, because of the poor data for helium doping at 892 °C, it is not possible to produce new estimates for the rates of diffusion of helium in garnet. However, it is clear that the estimates of the diffusion rate by Dunai and Roselieb (1996) are too high. Consequently, the blocking temperature of helium in garnet of between 590 and 630 °C determined by Dunai and Roselieb (1996) is also too low. Therefore, the blocking temperature for helium in garnet is higher than 630 °C. The implication this has for the blocking temperature for argon in garnet, given that argon atoms are larger and thus will diffuse even more slowly, is that the argon closure temperature will greatly exceed 630 °C. This implies that garnet should theoretically prevent biotite inclusions within it from being reset by

metamorphism at least up to the upper amphibolite/granulite facies boundary. Therefore, the c.1780 Ma amphibolite facies event recorded by the matrix mica did not reach sufficient temperatures to cause resetting of biotite inclusion ^{40}Ar-^{39}Ar ages.

6.6. Investigation of Fast Diffusion Paths in Garnet

The site of the argon within biotite inclusions becomes particularly significant when the effects of fast diffusion paths are considered. If a garnet containing biotite inclusions is heated beyond the blocking temperature of argon within biotite, then the argon within the inclusion will become mobile and migrate. It is possible that the argon will diffuse out of the biotite and into the grain boundary space between the inclusion and the garnet. It will then theoretically be prevented from moving any further by the dense garnet structure. However, any defects within the garnet structure will allow this accumulation of argon gas to escape into the grain boundary network.

Despite not yielding reproducible profiles, the zircon inclusion experiment has provided useful information with regard to the site of the gas within inclusions in garnet. The results of this experiment indicate that the majority of the helium in profile 1 was released before analysis, and the helium in profiles 2 and 3 was released from accumulations within defects. This suggests that the helium is contained within the grain boundary space and surrounding cracks and defects.

It may be possible to relate this to argon behaviour in a biotite inclusion in garnet. If argon is located in the grain boundary space or in defects in the garnet rather than in the biotite inclusion itself then this can have implications for the apparent ages obtained from inclusions. For example, a biotite inclusion exposed at the surface of a garnet before analysis may lose argon and thus record a younger age. Alternatively, if the gas has migrated into a defect that is punctured by the UV laser then an effect similar to excess argon would occur, producing an older apparent age. If an inclusion is ablated but the gas has escaped into a defect that is not ablated at the same time then a younger apparent age would be recorded.

However, this assumes that the behaviour of argon in biotite inclusions is the same as helium diffusion from zircons. Clearly, these situations have differences that might affect the location of the

gas and the way it diffuses. For example, the alpha particles from zircon are propelled into the surrounding garnet whereas argon diffuses. Furthermore, the alpha particles cause damage to the garnet that may facilitate different diffusion/accumulation effects than for argon escaping a biotite inclusion. However, at the very least these experiments highlight some of the potential problems that might occur when using the spot analysis method to release gas from an inclusion.

6.7. Overall Conclusions

PbSL dating of garnets demonstrated that the garnets measured in this set of experiments were formed during a Proterozoic metamorphic event in south-western Montana. Therefore, it will not be possible to obtain Archæan ages for inclusions in these garnets regardless of the shielding properties of garnet. This is supported by the Proterozoic ages obtained for biotite inclusions in garnet which are in excellent agreement with matrix biotite from the same samples. However, there is some indication that garnet has had some shielding effect on inclusions in samples TRMR2 and TRGC5 where matrix biotites were partially reset by the Cretaceous batholith but at least some of the inclusions appeared to retain Proterozoic ages consistent with those samples unaffected by the batholith.

The PbSL ages acquired for the garnets can be compared to the mean matrix biotite ages obtained for the same samples in order to give an estimate of the cooling rate of the rocks between metamorphic peak and biotite blocking temperature. Because of the influence of monazite inclusions in the PbSL ages and the possibility that the monazites along fractures have been degraded by circulating fluids, the best estimate will come from sample RRCR2A. In this sample the monazite inclusions were completely occluded in garnet and appeared unaffected by alteration. Estimates from this sample suggest a cooling rate of 7.7 °C/m.y. between 665 °C and approximately 300 °C. This is in contrast to the slow cooling rates of 1-3 °C/m.y. from approximately 350 °C implied by the slow cooling profiles in Chapter 5. It seems likely that from metamorphic peak the samples were exhumed rapidly, gradually slowing down to the cooling rate of 1-3 °C/m.y. seen in the closure profiles in biotite. The cooling history of these rocks cannot be further constrained using the current data. For this, intermediate ages and closure temperatures would be required. However, it is

evident that cooling was not extremely slow, and the process appears to resemble orogeny in modern settings such as the Alps or Himalaya.

Helium diffusion experiments on gem quality garnet suggests the blocking temperature of argon in garnet is in excess of 700 °C. This implies that biotite inclusions in garnet would be shielded from resetting by any event that did not reach this temperature. Clearly then, the theoretical shielding effects of garnet are valid. The lack of experimental support is obviously due to the garnet and biotite being contemporary. However, in samples where the matrix biotite is affected by resetting, the presence of apparently reset included biotite must be related to fast diffusion pathways within garnet.

Evidence from the diffusion of helium in garnet suggests that argon diffusing from a biotite inclusion in garnet would accumulate in the grain boundary space between the biotite and garnet and is therefore capable of rapid escape if defects communicate with this space or the polishing technique brings the inclusion to the surface. As natural garnet samples have numerous fractures, defects and possible subgrain networks, the chances of argon escaping from the garnet are great.

Inclusions will yield an age older than the main metamorphic event only if:

1) The garnet formed in an earlier event than that producing the matrix mica.

2) The resetting event did not exceed the blocking temperature of argon in garnet (i.e. >700 °C).

3) The inclusion is completely enclosed by fracture- and defect-free garnet.

4) The inclusion is still enclosed by garnet after sample preparation and polishing.

5) The ablation method removes the entire inclusions and the argon located in the grain boundary space.

The final conclusion would therefore be, garnet is capable of shielding biotite inclusions from resetting events but because of the precise set of circumstances required for this it is an unusual occurrence in nature.

Chapter 7 - Dating Younger Geological Events in South-western Montana

7.1. Introduction

One aim of this research was to date events within south-western Montana that are younger than the main metamorphic event. From Chapter 5 it is clear that the main metamorphic event measured by the ^{40}Ar-^{39}Ar dating technique is an amphibolite facies event that occurred between 1780 and 1740 Ma. It is also evident that some rocks have ages apparently younger than this because they have lost argon or undergone various degrees of resetting. These samples and the events influencing them are discussed in detail in this chapter.

7.2. Samples Affected by Alteration

7.2.1. Introduction

Secondary alteration of biotite to phases such as chlorite and clinozoisite is a common and widespread occurrence, which almost always correlates with ^{40}Ar-^{39}Ar age spectra that are seriously disturbed (Lo and Onstott, 1989). Because many rocks are geologically unique and/or representative of key localities, it is desirable to obtain meaningful biotite ages from all rocks regardless of condition and to identify apparent ages that are adversely influenced by alteration. However, producing geologically meaningful ages from highly altered biotite using incremental step-heating is virtually impossible, and even those biotites which appear pristine in thin section can yield unconvincing plateaux and unexpected apparent ages (e.g. Lo and Onstott, 1989; Onstott *et al.*, 1991; Ruffet *et al.*, 1991; Adams and Kelley, 1998). Indeed, it is likely that the vast majority of natural biotites are altered to some extent. Therefore, overcoming the effects of secondary alteration on biotite ages is a problem of universal importance in geochronology.

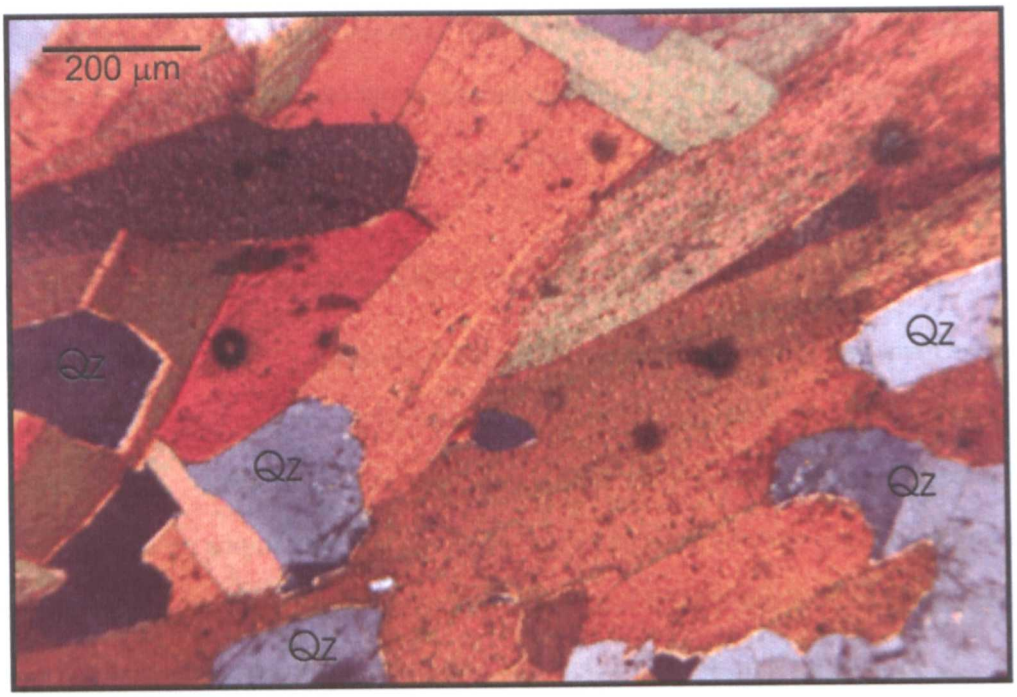

Plate 7.1: Photomicrograph of sample RRCR3 showing pristine biotite

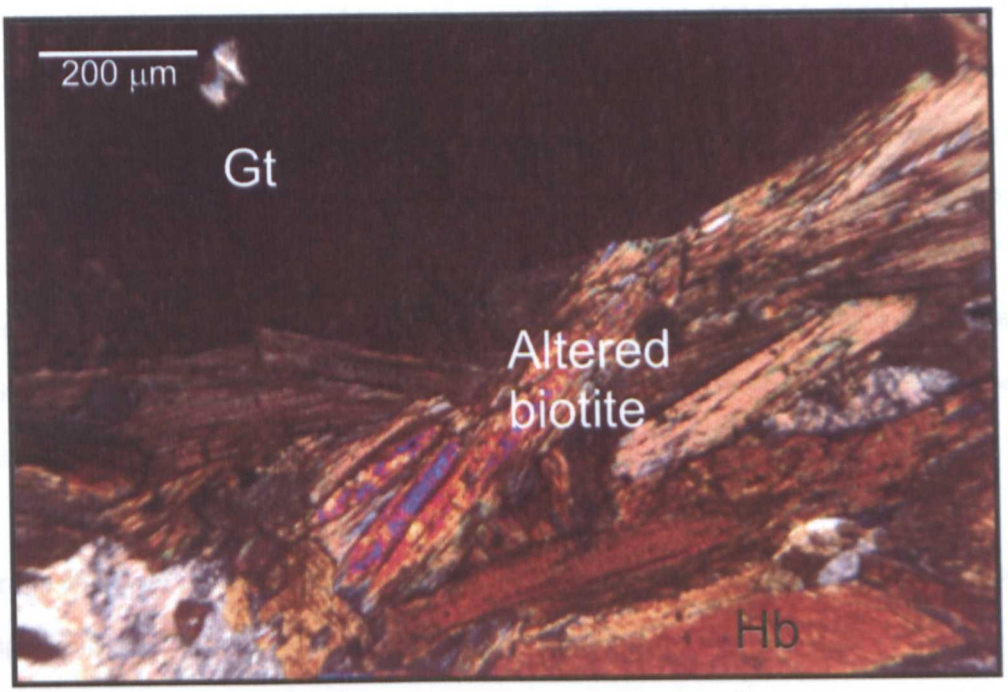

Plate 7.2: Photomicrograph of sample RRSW1 showing biotite altered along cleavage

This experiment is an investigation of the affects of alteration of biotite on ages produced using both the step-heating and UV laser microprobe ^{40}Ar-^{39}Ar age dating techniques. It is an attempt to obtain geologically meaningful ages from highly altered metamorphic rock, to recognise meaningless ages resulting from alteration, and to assign an age to the alteration event within south-western Montana.

7.2.2. Sample Selection and Experimental Methods

The biotite in sample RRCR3 appeared pristine in thin section (Plate 7.1) and when analysed using the UV laser microprobe it gave very consistent ages and a tightly constrained mean age of 1765 ± 6 Ma (section 5.2.3). Therefore, this sample was selected for this experiment as an example of an unaltered sample for comparison with those samples that were altered. During determination of mean matrix mica ages (section 5.2.) samples RRSW1, RRSW2 and RRCR5 were found to have a younger age population that might be caused by alteration of the biotite grains.

When the thin section for sample RRSW1 was examined, the majority of the biotite appeared highly altered to chlorite, clinozoisite and prehnite along the cleavage, and the feldspar had been heavily sericitized (section 4.2.1.2, Plate 7.2). Furthermore, chemical maps produced on the electron microprobe revealed a depletion of potassium and increase in calcium along the cleavages in relation to alteration, as shown in Plate 7.3A-F. In contrast, under the petrological microscope, biotite from sample RRSW2 appears almost pristine (Plate 7.4) and a good candidate for ^{40}Ar-^{39}Ar dating. At higher magnification, however, slight green and brown mottling of the grains was evident as patches less than 50 μm across. Sample RRCR5 was found to have pristine biotites when examined in thin section (see section 4.2.2.1 and Plate 4.3).

Average chemical composition of the biotite in these samples and the chlorite and clinozoisite in sample RRSW1 can be found in Tables 4.2 and 4.4.

For details of sample preparation procedure, irradiation, and analytical technique for these samples using the UV laser microprobe see sections 3.2, 3.4 and 5.2. In addition to standard UV laser microprobe analysis, detailed work on age variations occurring along the cleavage planes of biotite

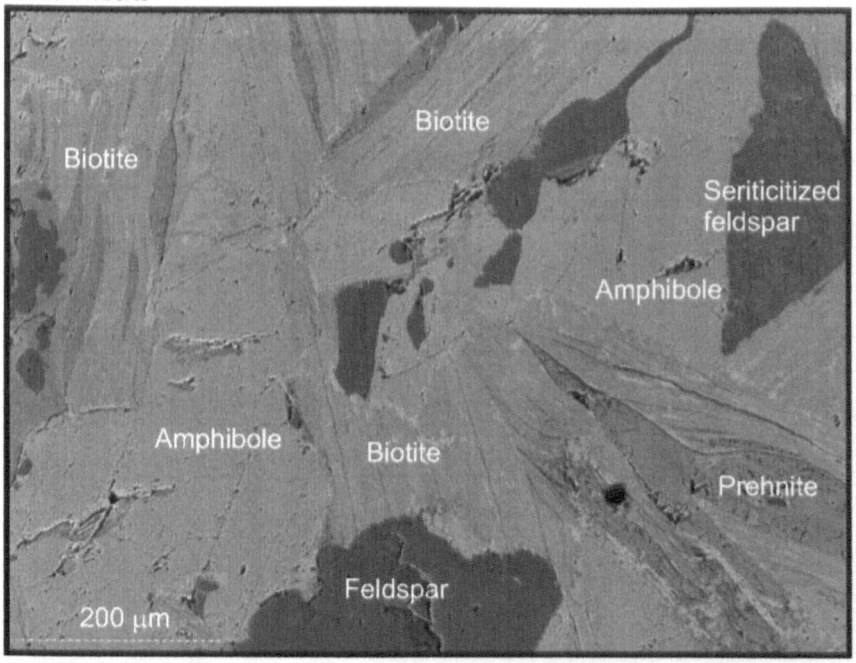

A) Backscatter image

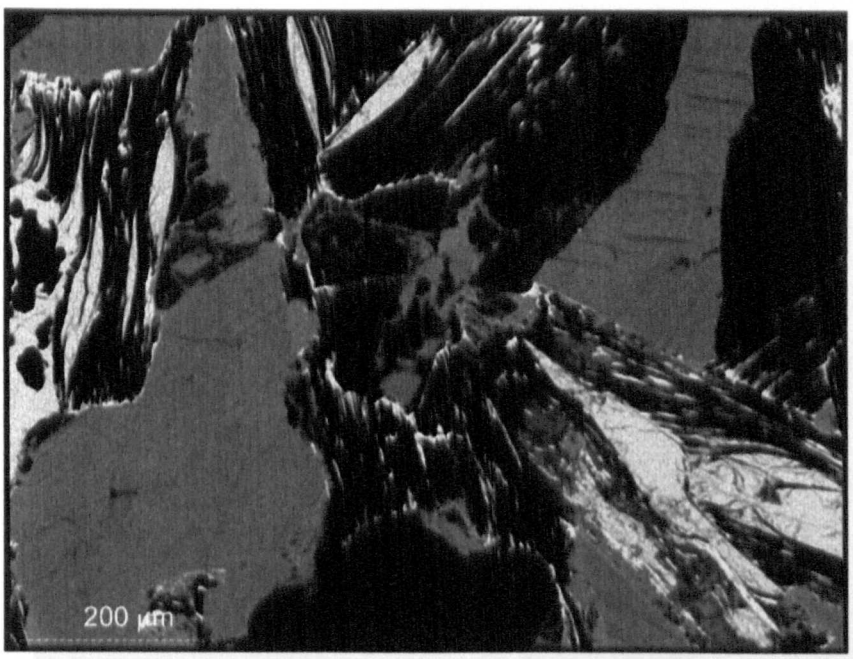

B) Calcium map

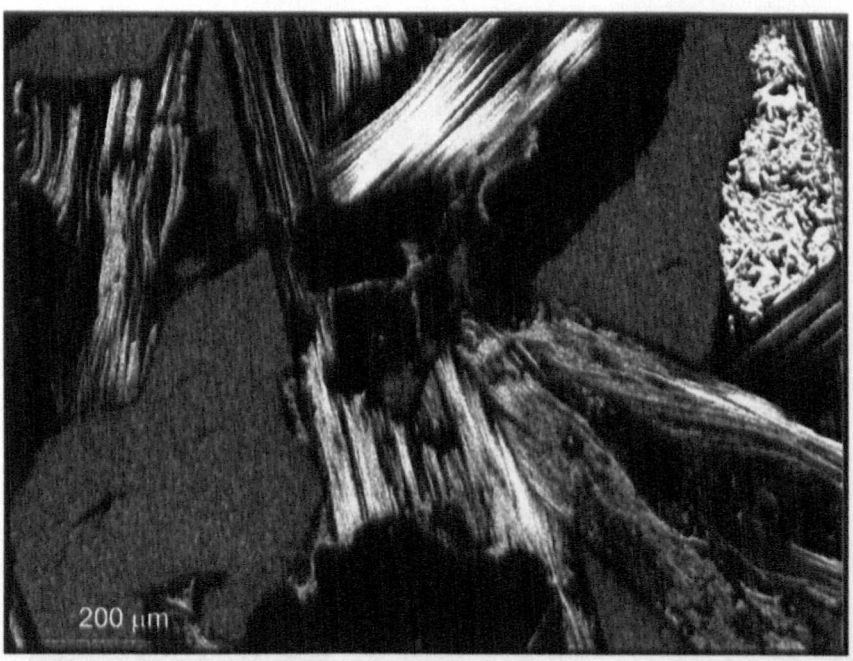

C) Potassium map

Plate 7.3: Electron microprobe chemical maps of RRSW1

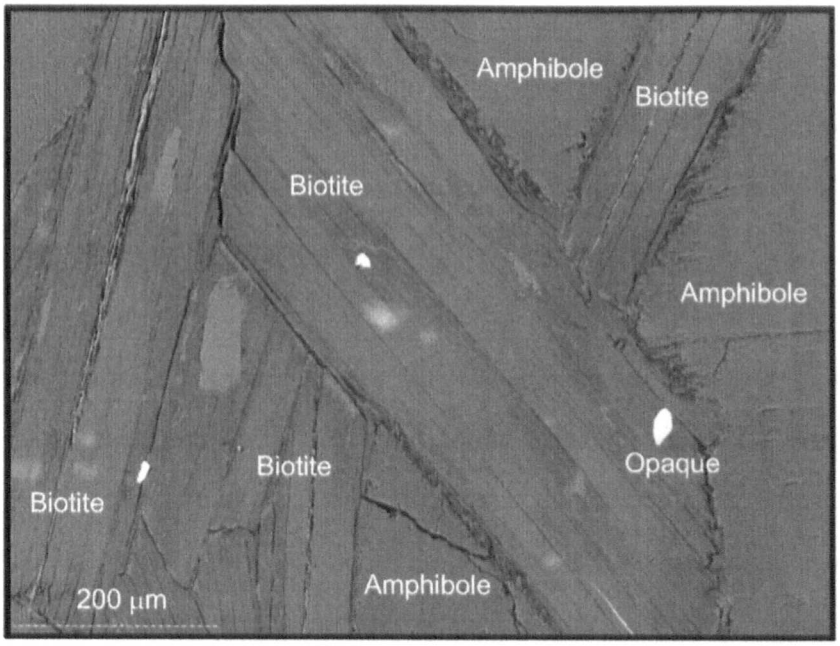

D) Backscatter image

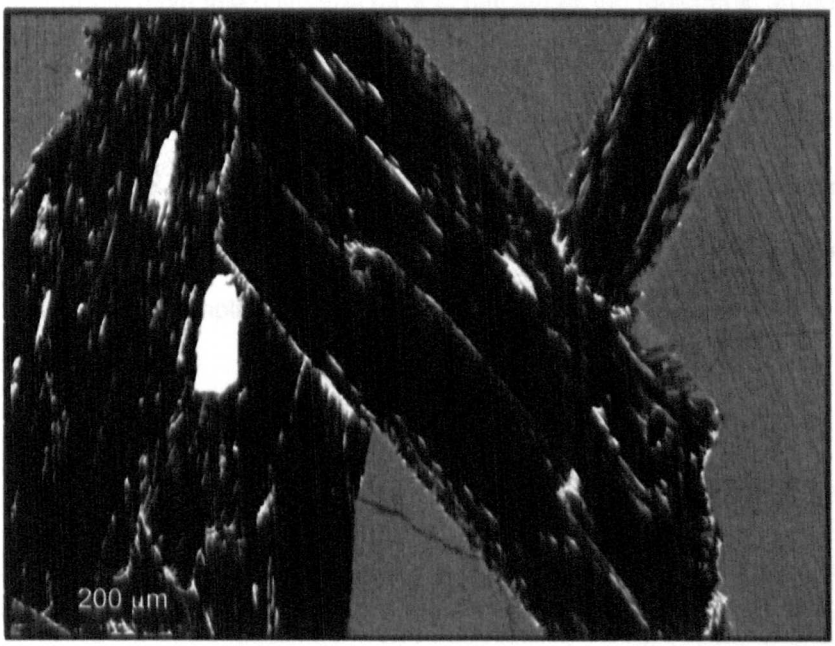

E) Calcium map

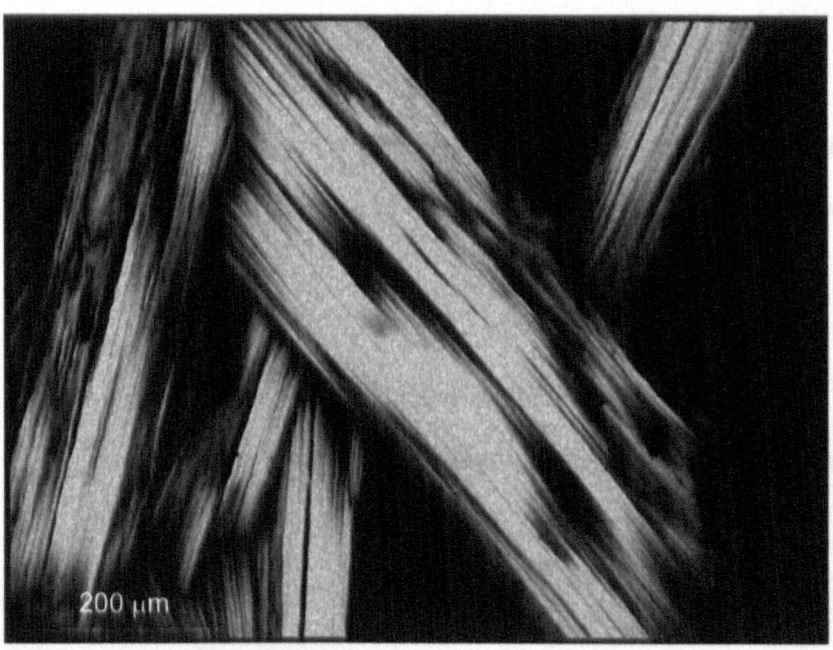

F) Potassium map

Plate 7.3 continued

separates from sample RRSW1 was carried out by depth profiling of biotite in basal section (3.4.1). Further to the UV laser microprobe analysis, samples RRCR3 and RRSW1 were step-heated using the IR system. UV laser microprobe analysis was undertaken first and fragments of the same grains were subsequently used for the step-heating experiments.

Due to the high concentration of argon accumulated within Precambrian biotite, only small fragments of the grains analysed by UV laser microprobe were used for the IR laser step-heating experiment. Step-heating began with a very gentle heating that caused little visible alteration to the grain. For sample RRCR3 the experiment was stopped when the fragment first began to bubble, and the data was processed at this point. This was a large fragment that contained a considerable volume of gas and would have taken several days to release all the radiogenic argon. However, as the data showed that a plateau had already been reached, the experiment was not continued beyond 14 steps. Since the biotite fragments from sample RRSW1 were smaller than RRCR3 and contained less gas, the experiment on sample RRSW1 was continued until the fragments melted into a spherical bead and little gas was released upon additional heating. Two fragments (1 and 2) were analysed for sample RRSW1. Fragments 1 and 2 underwent 13 and 19 incremental-heating steps respectively .

7.2.3. Results

A) IR Step-heating

Incremental-release step-heating of biotite in sample RRCR3 yielded a well-defined plateau corresponding to an age of 1776 ± 6 Ma (Figure 7.1A, Appendix 7.1). In fact, only 5 - 10% of the total gas within the fragment was released during the experiment, which represents only the very beginning of the total spectrum. Clearly there is little spectral disruption, as would be expected from a pristine grain.

In contrast, spectra for the two biotite fragments from sample RRSW1 both show argon loss at low temperature steps, indicating the release of argon from weakly bonded sites (Figure 7.1B and C).

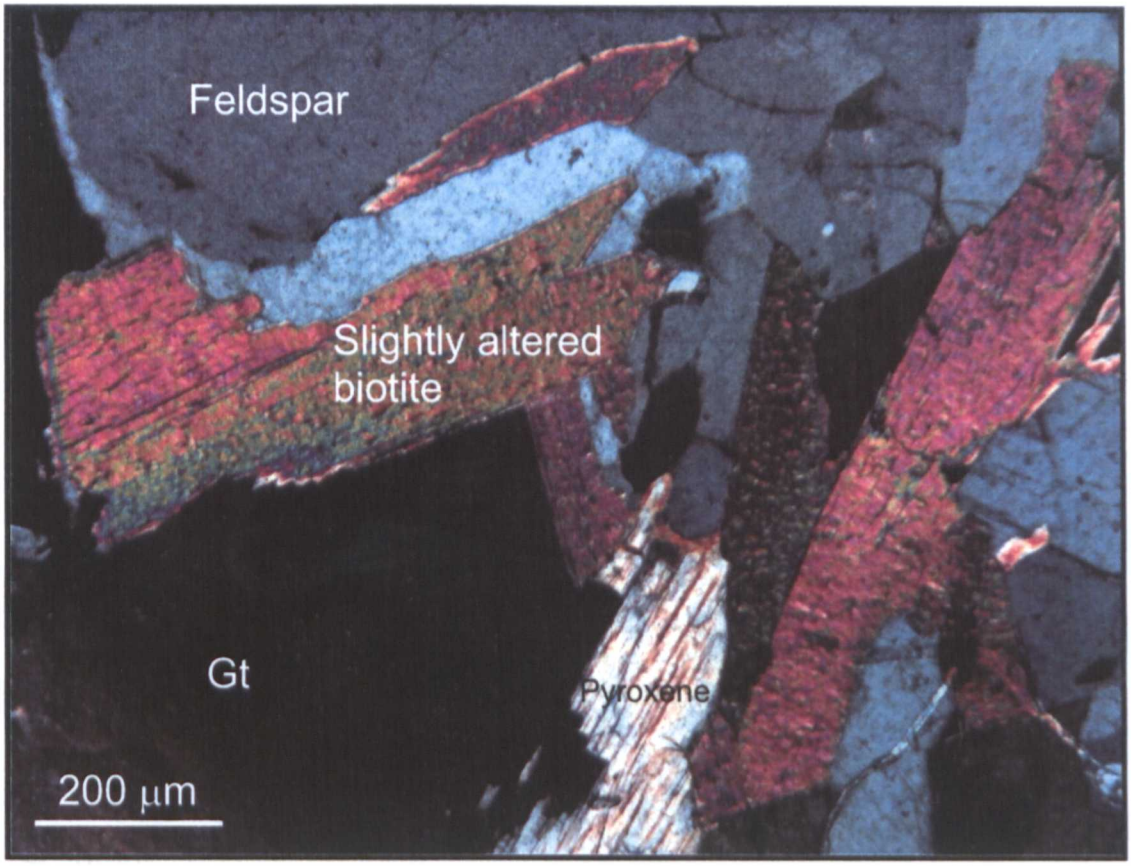

Plate 7.4: Photomicrograph of RRSW2 showing only slight alteration in the biotite

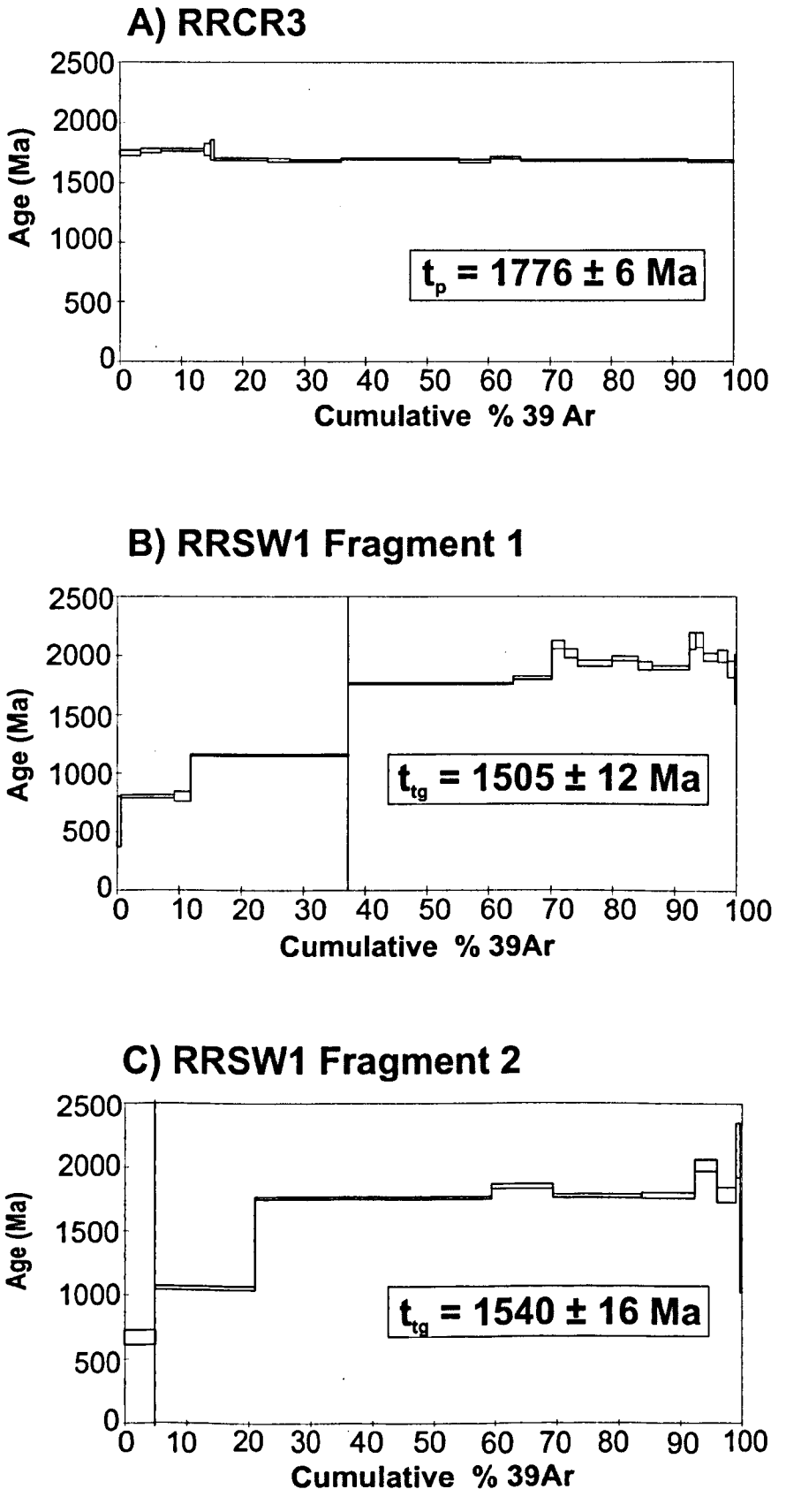

Figure 7.1: Step-heating spectra for RRCR3 and RRSW1 biotite

Both the profiles reach noisy plateaux between 2134 ± 428 and 1760 ± 20 Ma. Total gas ages for biotite fragments 1 and 2 of sample RRSW1 are 1505 ± 12 Ma and 1540 ± 16 Ma respectively.

B) UV microprobe analysis

The UV microprobe results are reported in 5.2.3 and Appendix 5.2. Here it is seen that RRCR3 gave a weighted mean of 1765 ± 6 Ma. A total of 14 analyses (8 from grain 1 alone) were carried out on biotite from sample RRSW1. Apparent ages from 50 μm squares and linear traverses for grain 1 ranged from 1697 ± 56 to 1565 ± 78 Ma (Plate 7.5). Another six ages were obtained from other grains in this sample and ranged from 1806 ± 72 to 1740 ± 96 Ma.

Two age-depth profiles were produced for sample RRSW1 grain 1 (Plate 7.5, Figure 7.2) to further investigate the cause of the anomalous ages. Because of the small amount of material ablated in each analysis, the errors associated with these dates produced were relatively high. However, both profiles reveal significant age variations with depth. Apparent ages of biotite layers range from 1730 ± 226 to 1511 ± 186 Ma (profile 1) and from 1741 ± 290 to 956 ± 230 Ma (profile 2) as indicated in Figure 7.2, Appendix 7.2.

In RRSW2 alteration of the biotite could be identified under high magnification as brown and green mottling of grains and attempts were made to analyse areas both affected and unaffected by this mottling. Apparently unaltered areas within single grains gave ages ranging from 1772 ± 52 to 1721 ± 92 Ma, consistent with the biotite age obtained in sample RRCR3. In contrast, visibly altered areas gave apparently lower ages ranging from 1690 ± 124 to 1359 ± 200 Ma, with the low levels of argon released leading to relatively large errors (see Appendix 5.2). Thus, within a single grain an apparent difference of ~360 m.y. was recorded from the altered to unaltered parts of the grain.

Sample RRCR5 also showed a population of younger ages. Whilst constructing closure profiles (section 5.4) two profiles showing apparent age variations at the edge were achieved. However, profile A had a weighted mean age of 1617 ± 16 Ma, whereas profile E had mean ages of 1720 ± 18 Ma (5.4.3.2). In order to verify that these ages were true and not an analytical artefact, two 100 μm

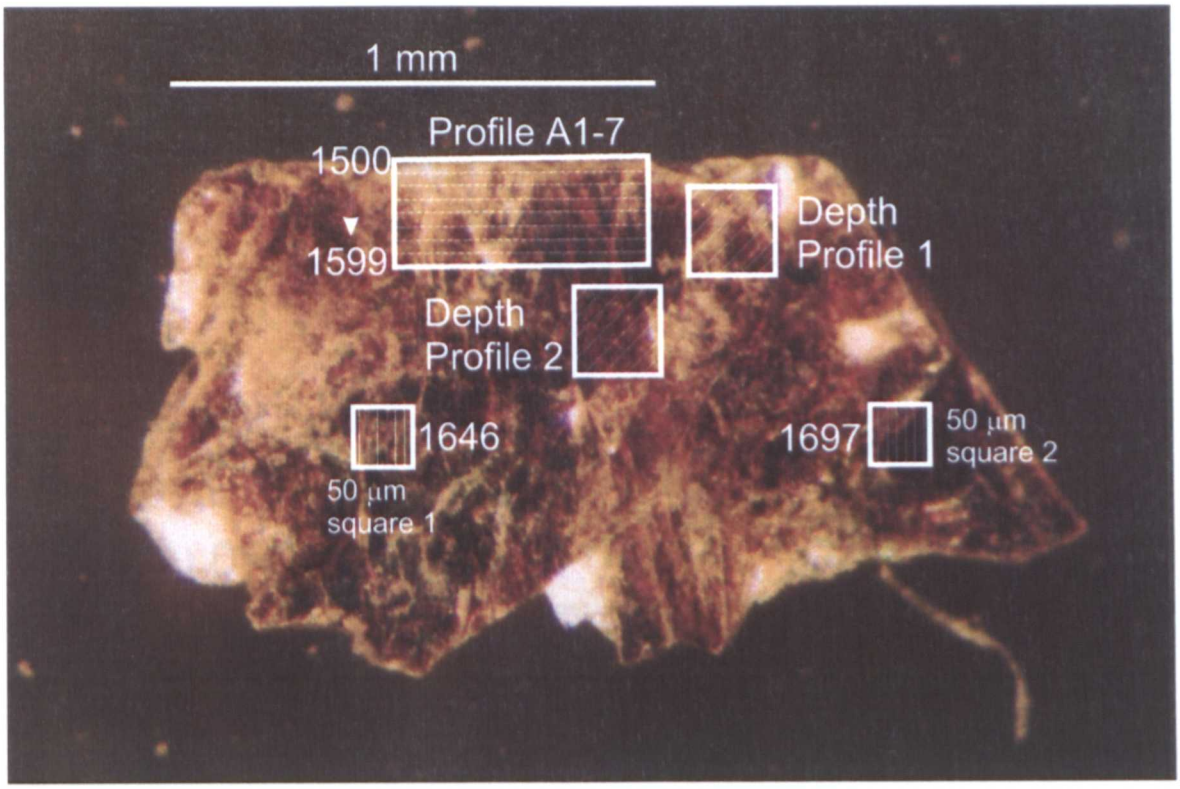

Plate 7.5: RRSW1 grain 1 showing position of ablation pits within grain and apparent ages in Ma

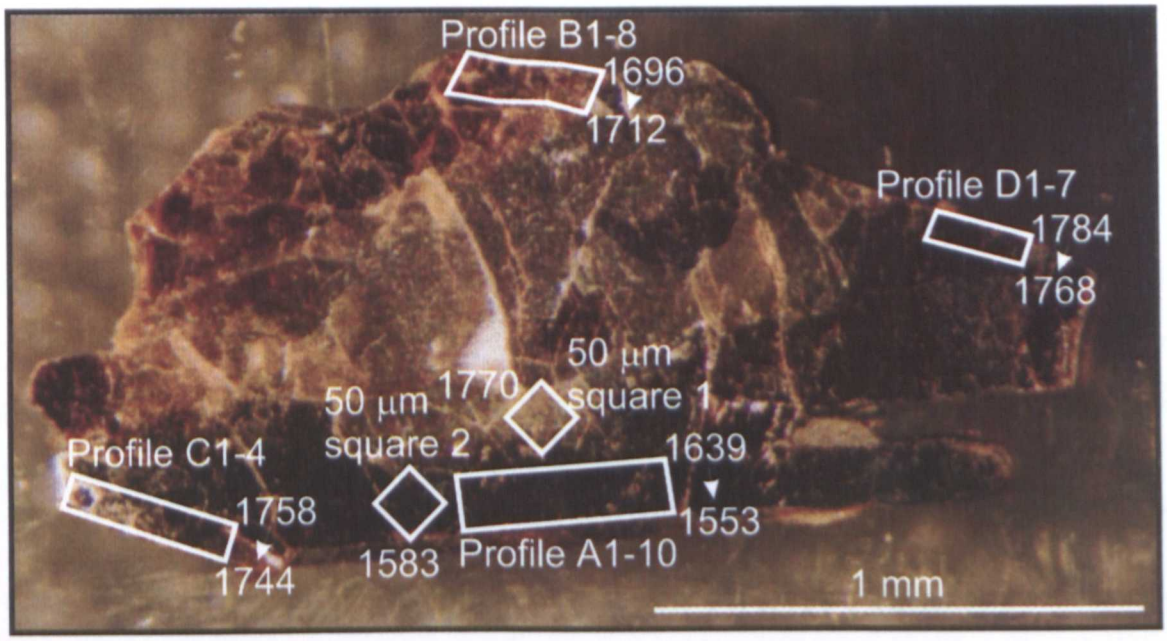

Plate 7.6: RRCR5 grain 1 showing position of ablation pits within grain and apparent ages in Ma

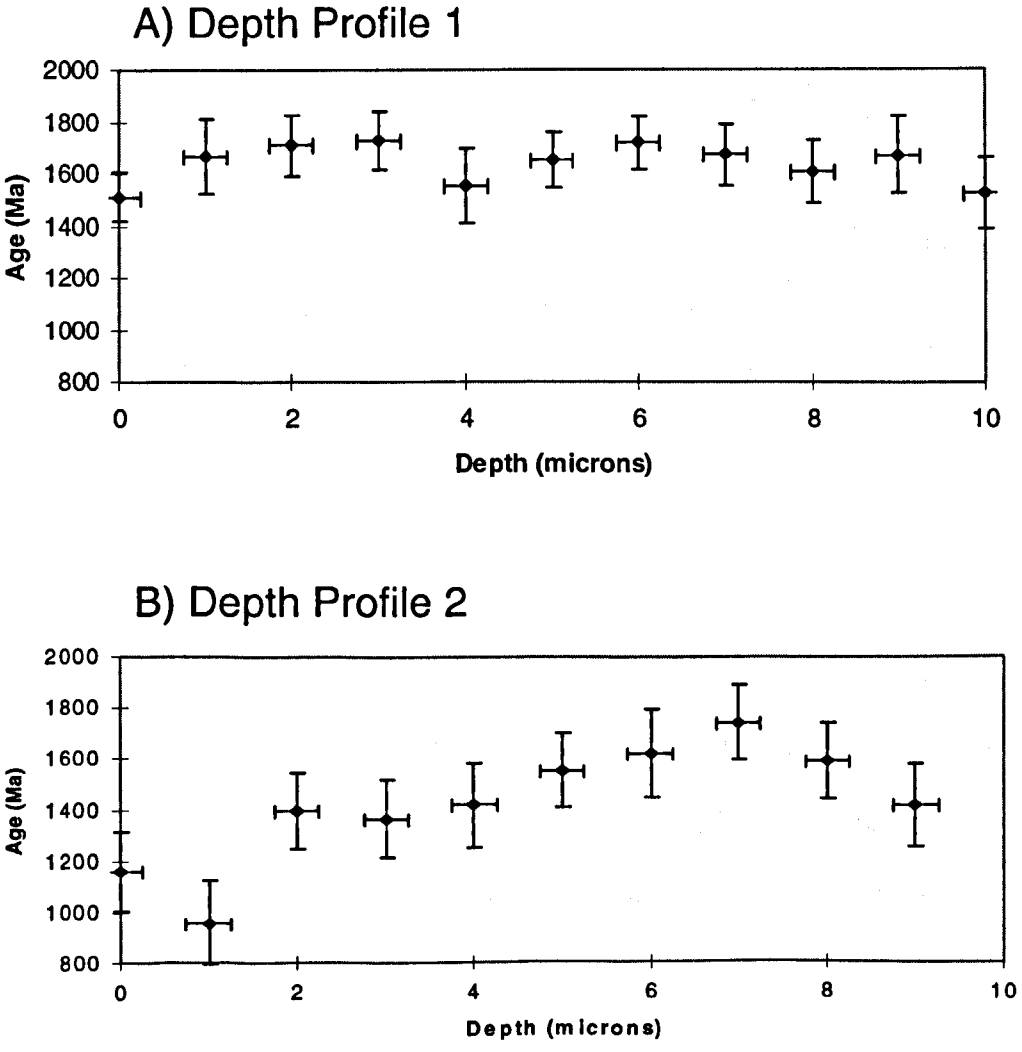

Figure 7.2: Depth profiles for RRSW1 biotite

squares were ablated in the same grain immediately adjacent to the profile A (Plate 7.6). One square gave an age of 1583 ± 39 Ma, comparable to those from the first profile, and one square gave an age of 1770 ± 38 Ma, comparable to profile E. Other profiles carried out along other edges of the same grain also gave apparent ages consistent with the apparent age of profile E (Plate 7.6, Appendix 5.2).

In order to investigate potential relationships among apparent age, biotite composition, and/or atmospheric content, the ratios of $^{38}Ar/^{39}Ar$, $^{37}Ar/^{39}Ar$ and $^{36}Ar/^{39}Ar$ were calculated for all the data from all samples and plotted against age (Appendix 5.2, 7.2). Figure 7.3A-F shows that in samples RRSW1 and RRSW2 there is a strong correlation between the $^{36}Ar/^{39}Ar$ ratio and the apparent age, with the younger ages corresponding to the higher $^{36}Ar/^{39}Ar$ ratios. However, in sample RRCR5 there is no correlation between age and $^{36}Ar/^{39}Ar$ ratios. The $^{36}Ar/^{39}Ar$ ratios for altered sample RRSW1 range from 0 to 0.072, whereas in unaltered sample RRCR3 the ratios only range from 0 to 0.023 (Appendix 5.2, 7.2); similarly, samples RRSW1 and RRCR3 exhibit maximum atmospheric argon of 25% and 5% respectively (Figure 7.3). These trends show that apparent age is inversely correlated with degree of alteration in the cleavage. The $^{37}Ar/^{39}Ar$ and $^{38}Ar/^{39}Ar$ ratios failed to exhibit similar correlations.

7.2.4. Discussion

7.2.4.1. Obtaining Meaningful Ages from Altered Samples

Sample RRCR3 biotite represents an ideal grain for ^{40}Ar-^{39}Ar dating, giving reproducible ages with a high level of confidence (Figure 7.1A, Appendix 7.1). In contrast, "ages" from sample RRSW1 biotite vary considerably with each analysis and technique. However, it is possible to extract reliable ages from such samples.

As shown in Figures 7.1B and 7.1C, sample RRSW1 biotite yields disturbed spectra when step-heated using the IR laser. Thus, in the absence of other data, all that normally could be inferred for this biotite is that its true age lies between the total gas age of ~1500 Ma and the near-plateau of

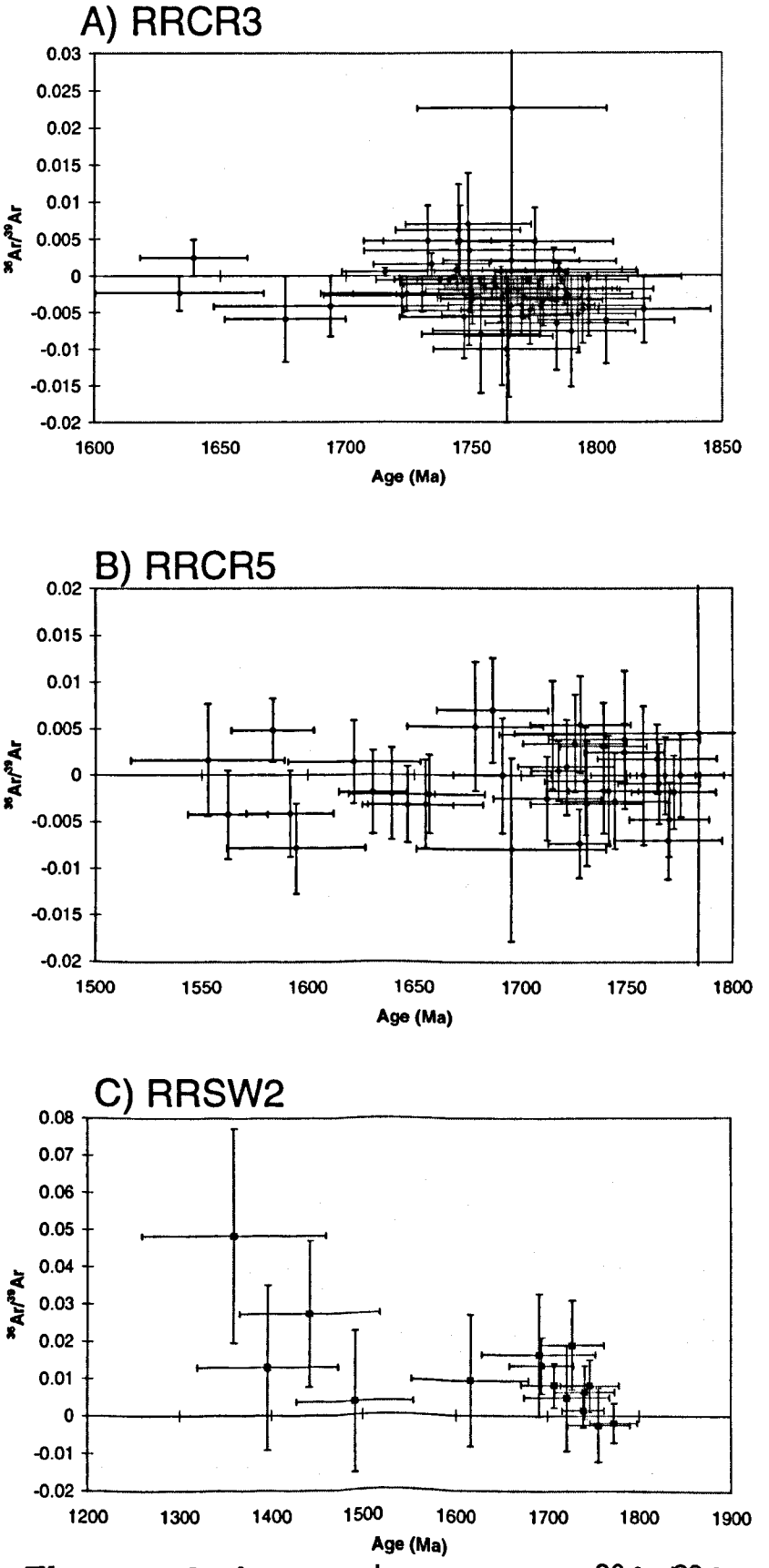

Figure 7.3: Apparent age versus $^{36}Ar/^{39}Ar$

D) RRSW1 spot dates

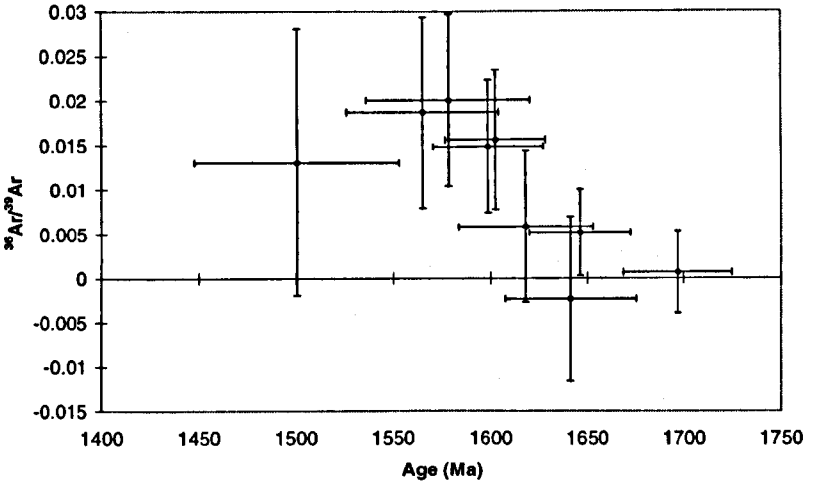

E) RRSW1 depth profile 1

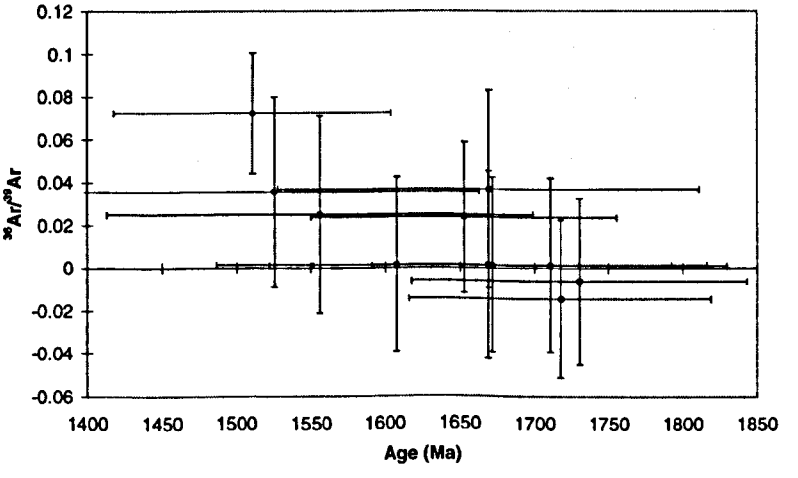

F) RRSW1 depth profile 2

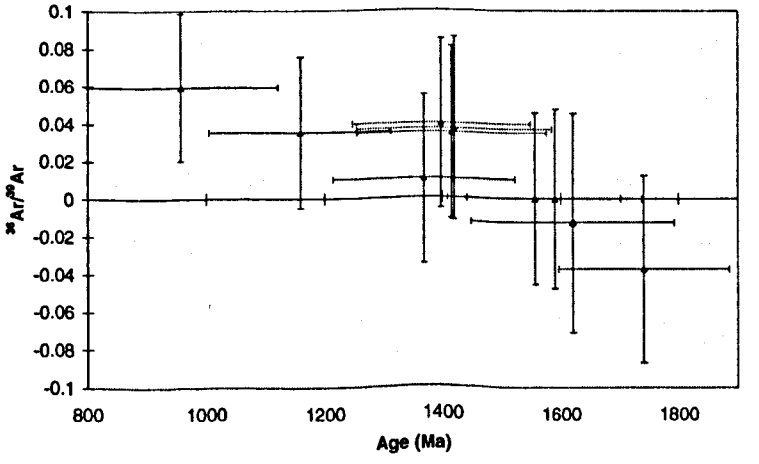

Figure 7.3 continued

1900 Ma. However, the UV microprobe data can further refine the age of this sample, as discussed below.

UV laser microprobe dating of sample RRCR3 biotite (Appendix 5.2) indicates that the age of unaltered rocks from the Ruby Range is 1765 ± 6 Ma. For sample RRSW1 biotite, the majority of the age variation was confined to grain 1; in contrast, the six ages from grains 2 to 4 define a mean age of 1770 ± 40 Ma, which represents excellent agreement with sample RRCR3. For a rock containing both altered and unaltered biotite, such concordance suggests that a meaningful age can be acquired by rigorous exclusion of altered grains.

7.2.4.2. Influence of ^{39}Ar Recoil

In sample RRSW1, alteration of biotite occurs principally along the cleavage planes as indicated microscopically and by electron microprobe chemical mapping (Plates 7.2 and 7.3). Isotopic depth profiling of the most altered grain (grain 1) seems to have discriminated between altered and less altered areas, with different layers showing variations of several hundred million years (Figure 7.2). Conceivably, the younger apparent ages revealed by the UV depth profiles might be caused by loss of ^{40}Ar, or gain in ^{39}Ar due to recoil that ultimately affects the $^{40}Ar/^{39}Ar$ ratio. Previous work has shown that ^{39}Ar is locally recoiled during neutron irradiation (Turner and Cadogan, 1974, Onstott *et al.*,1995, and Villa, 1997). When ^{39}Ar from the K-rich layer recoils into an adjacent K-poor layer, the ^{39}Ar abundance in the K-poor layer increases in relation to that of the ^{40}Ar. This results in a lower $^{40}Ar/^{39}Ar$ ratio, thereby giving an apparent age that is anomalously young. In theory, loss of potassium might cause age increases, but evidence from K-Ar studies shows that K loss is accompanied by greater loss of ^{40}Ar and thus results in younger apparent ages (Mitchell and Taka, 1984). Alteration tends to produce biotite interlayered with minerals such as clinozoisite or chlorite, thereby introducing a K-poor layer. Depth profiling through such a mineral would encounter K-rich biotite layers, K-poor alteration layers, or a combination of the two. Published data show that K-poor layers tend to produce lower ages in agreement with the bulk K-Ar data (Mitchell and Taka, 1984).

Given that previous step-heating studies have shown age variations assigned to recoil (Lo and Onstott, 1989; Ruffet *et al.*, 1991), it is possible that the UV laser age variations described in this

study are also caused by ^{39}Ar recoil. Recoil distance has been determined to be around ~0.1 μm (Villa, 1997 and references therein). The depth of each ablated volume analysed in the UV laser microprobe experiments in this study was calculated to be ~1 μm, based upon ^{39}Ar release (section 3.4.1). With these boundary conditions, a simple model can be erected to determine whether ^{39}Ar recoil could cause the age variations observed in the depth profiles (Figure 7.4).

Figure 7.4 shows two layers within a hypothetical altered biotite grain. Layer 1 is a 1 μm layer of unaltered biotite that is rich in potassium. Layer 2 is a 1 μm layer of altered biotite that is poor in potassium, containing half the concentration of K found in layer 1 (an estimate based upon experimental measurements). If two consecutive squares were drilled into this grain, their common point being the interface between altered and unaltered material, then the first square would measure the argon within layer 1 and the second would measure the argon in layer 2. During irradiation, ^{39}Ar from the K-rich layer 1 would recoil ~0.1 μm into layer 2 which effectively results in 10% of the K leaving layer 1 and entering layer 2. Because layer 2 only contains half the K content of layer 1, the net result in a 20% enrichment in K in layer 2. The $^{40}Ar/^{39}Ar$ ratio measured for altered biotite layers in sample RRSW1 ranged from 85.0 (1359 Ma) to 109.6 (1616 Ma); see Appendix 5.2. If maximum recoil had occurred then these measurements were enriched in ^{39}Ar by 20% and had correspondingly lowered $^{40}Ar/^{39}Ar$ ratios by 20%. In other words, the recoil-removed $^{40}Ar/^{39}Ar$ ratios should have been 102 and 131.5, respectively, indicating older actual ages of 1539 and 1819 Ma. Likewise, the mean 126.5 ratio recorded for the K-rich layer is 10% too high if recoil occurred and should have been 113.9, indicating an original age of 1651 Ma.

Clearly the age variations observed in this study fall within the bounds of ^{39}Ar recoil effects, but the model calculation above represents an extreme case of maximum recoil, which would only be recorded when the analyses were made on the exact boundary between the K-rich and K-poor layers. Moreover, had such an effect been important, the higher K-layers would not have yielded ages reproducibly close to ages from the unaltered sample RRCR3. An analysis that straddled this

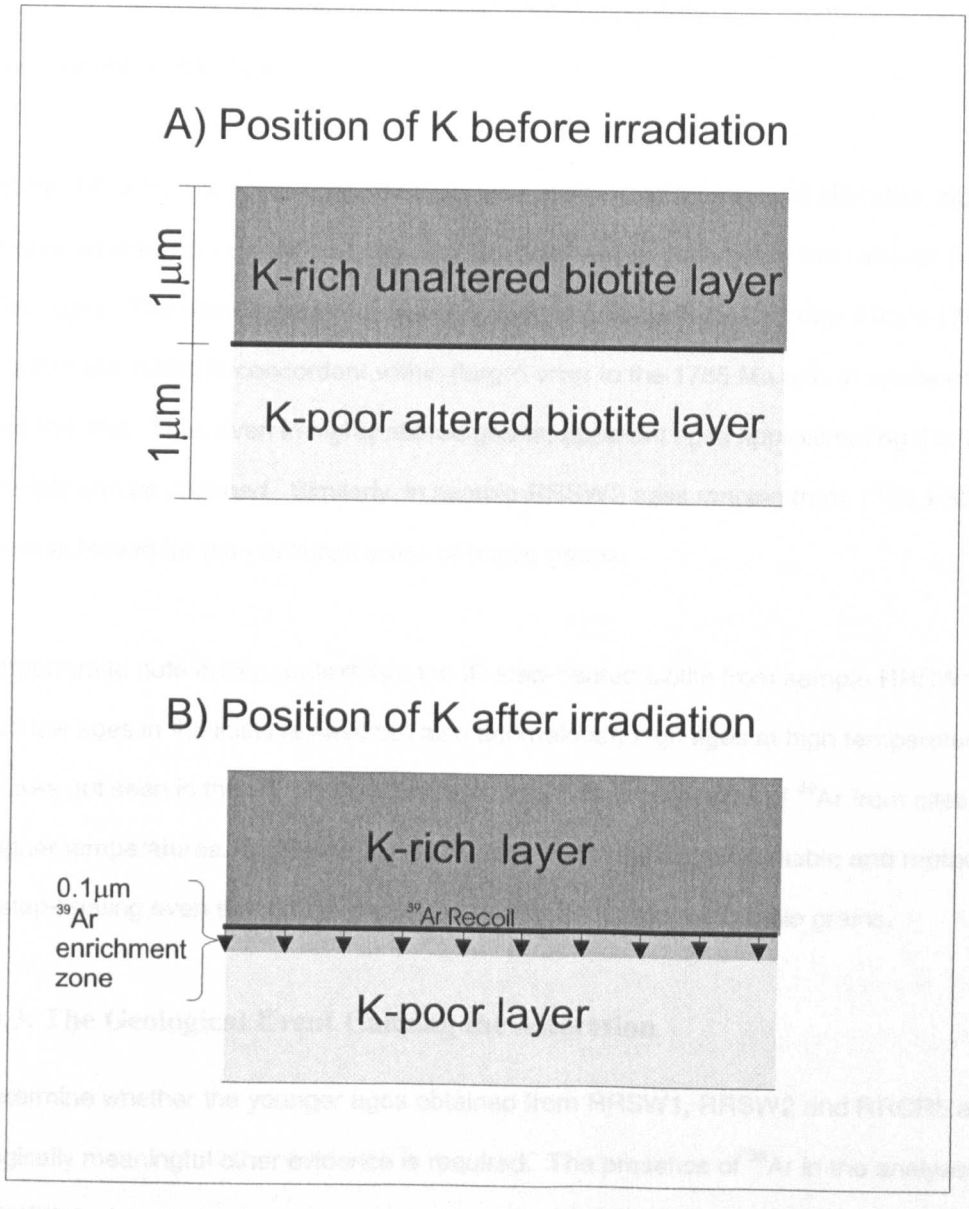

Figure 7.4: A cartoon to illustrate the possible movement of ^{39}Ar by recoil during irradiation in an altered biotite

boundary would measure both the K-rich layer from which the ^{39}Ar was recoiled and the K-poor layer into which it recoiled. The net result would be a cancellation of the two recoil related effects. Furthermore, the model calculation does not account for recoil of ^{39}Ar from the K-poor layer into the K-rich layer. Therefore, although recoil may be contributing to the age variations seen it is unlikely to be an important consideration.

It is inferred that the youngest apparent ages were dominated by zones of alteration along the cleavages, whereas the oldest ages are locally preserved in unaltered or less altered biotite between the cleavages. The older ages in the depth profiles in sample RRSW1 ranged from 1741 ± 290 to 1711 ± 238 Ma, which is concordant within (large) error to the 1765 Ma age of unaltered biotite in sample RRCR3. Thus even in highly altered grains, apparent ages approximating the 'true' age of the sample can be obtained. Similarly, in sample RRSW2 ages ranging from 1772 ± 52 to 1721 ± 92 Ma were achieved for the unaltered areas of biotite grains.

It is important to note in this context that the IR step-heated biotite from sample RRSW1 not only yielded low ages in the initial release but also anomalously high ages at high temperature. This effect was not seen in the UV analysis and may truly result from recoil of ^{39}Ar from sites releasing at the higher temperatures. In this case the UV analysis revealed more reliable and reproducible ages than step-heating even though the step-heating was undertaken on single grains.

7.2.4.3. The Geological Event Causing the Alteration

To determine whether the younger ages obtained from RRSW1, RRSW2 and RRCR5 are geologically meaningful other evidence is required. The presence of ^{36}Ar in the analyses in RRSW1 and RRSW2 giving younger apparent ages suggests that they contain an atmospheric component of argon. If this is the case then it would most likely have been introduced during an alteration process by meteoric water. This premise is further supported by the amphibole in RRSW1 yielding younger apparent ages than coexisting biotite (section 5.3), suggesting that defects allowed water into the amphibole structure, encouraging secondary minerals and removing argon, and resulting in a younger apparent age. Furthermore, the presence of sericite, chlorite, clinozoisite and prehnite within RRSW1 is indicative of low grade metamorphism, metasomatism or hydrothermal alteration.

Although other literature on the south-western Montana area refers to an M3 greenschist metamorphic event (Mueller and Cordua, 1976; Vitaliano *et al.*, 1979) this is currently undated. It is possible that mild reheating in the presence of meteoric water is responsible for the alteration and young ages seen in RRSW1 and RRSW2. RRCR5 may also have undergone reheating but in the absence of fluids. This would account for the lack of mineral alteration and ^{36}Ar within the sample but still allow for the younger grain ages, especially those seen at the edge (section 5.4.3). Indeed, younger apparent ages seen at the edge of several grains in RRCR3 (section 5.4.3) may also be due to this reheating.

A difficulty with interpreting the younger ages is the spread of ages seen. Furthermore, the low levels of gas released from altered areas of biotite led to high errors being recorded. The younger ages in RRSW1 and RRSW2 ranged from 1690 to 956 Ma with errors as high as ± 340 Ma (2σ). It is possible that some analyses measured are a combination of unaltered and younger age material and that this spread is caused by mixing of two ages. However, if a geological event is responsible for these ages then it is probably younger than 1400 Ma.

Ages around 1400 Ma do appear in the literature for this region, related to the formation of the Belt basin to the west of south-western Montana (section 9.3.7). For example, Rb-Sr whole rock dating of dykes in the Tobacco Root Mountains by Wooden *et al.* (1978) gave an age of 1455 ± 125 Ma. These Proterozoic dykes signal a rifting event throughout western Montana related to the Belt basin formation. In east-central Idaho, approximately 100 km to the south-west of the Ruby Range, Doughty and Chamberlain (1996) produced U-Pb zircon dates of 1370 Ma from dolerite, diorite, and migmatites within a large magmatic complex that they believed dated the East Kootenay orogeny. The East Kootenay orogeny resulted in magmatism, basin rifting, and renewed subsidence and sedimentation towards the end of deposition in the Belt basin. In the Ruby Range itself ^{40}Ar-^{39}Ar dating by Kovaric *et al.* (1996) of sericite that grew during the formation of the talc deposit gave a good plateau age of 1360 Ma. These authors believed that the sericite age confirmed that the talc formed during the Proterozoic rifting that created the Belt basin. The coincidence of the 1370 Ma East Kootenay orogeny nearby, the 1360 Ma Ruby Range talc deposit and the new ages in this study would suggest that the influence of the Belt basin tectonics was felt to some extent within the Ruby Range.

In order for these rocks to have undergone hydrothermal alteration at approximately 1360 Ma they would need to be near the surface at this time and in the presence of meteoric water. Evidence from the LaHood Formation (see section 9.3.7.2) within the Belt basin sediments shows that metamorphic Precambrian rocks were eroding at that time, suggesting that they these rocks were close to the surface. Furthermore, the influx of the Belt "sea" between 1500 and 1360 Ma provides a large expanse of surface water close by. This evidence accommodates the possibility of low temperature hydrothermal alteration of these rocks within the age range recorded.

7.2.5. Conclusions

This experiment has highlighted some of the problems associated with dating altered biotite using ^{40}Ar-^{39}Ar dating techniques. If, for example, sample RRSW1 had only been analysed by step-heating the age could only have been poorly constrained between the total gas age of c.1500 Ma and the poor plateau age of c.1900 Ma. Step-heating of altered biotite grains frequently produces disturbed $^{40}Ar/^{39}Ar$ spectra that are difficult to interpret, which propagates as loss of analytical confidence in the inferred ages. The interaction of recoil phenomena and variable release from low- and high-K phases leads to both low ages and anomalously high ages.

Selective UV laser microprobe analysis of unaltered biotite grains within an altered sample, or of unaltered domains within altered biotite grains, can produce ages that are consistent with the apparent age obtained from samples unaffected by alteration. In the case of highly altered biotites, only minimum ages close to the 'true' age can be expected. Furthermore, the presence of alteration in biotite can be identified in many cases by a high $^{36}Ar/^{39}Ar$ ratio.

Sample RRSW2 demonstrates that even when thin section examination reveals only incipient alteration this can still have a significant effect on apparent ages, unless selective microanalysis is undertaken. UV laser microprobe analysis is eminently suited for this work. Moreover, the UV microprobe can yield good ages even for highly altered samples. This is possible because the areas extracted can be tightly controlled rather than released from a bulk sample and mixed with gas from altered areas.

Sample RRCR5 shows that not all anomalous ages can be identified by a higher $^{36}Ar/^{39}Ar$ ratio. However, here the anomalous ages were identified by repeated analyses within the same sample and same mineral grain, a technique not possible when undertaking bulk analysis.

By being able to separate dates obtained from altered and unaltered samples it is possible to not only produce ages close to the 'true' age of the sample, but to obtain a possible timing for the alteration event. As a result an age from altered grains has been obtained and a possible geological reason for the alteration identified.

7.3. Samples Affected by Resetting by Cretaceous Plutons

7.3.1. Introduction

Dominating the central Tobacco Root Mountains is the Tobacco Root Batholith, a silicic pluton with an exposed extent of several tens of square kilometres (Figure 2.4). In the adjacent Highland Mountains the Hell Canyon and Rader Creek Plutons are exposed (Figure 2.5). Some of the units of the Tobacco Root Batholith were dated as 74 to 71 Ma by K/Ar by Vitaliano *et al.* (1979), and the plutons in the Highland Mountains are believed to be concordant. Giletti (1966) reported that two samples from the Rochester mining district in the Highland Mountains, close to the plutons, had K/Ar ages reset to 176 and 75 Ma, a third sample from north of the Tobacco Root Mountains had a Rb-Sr age of less than 80 Ma, and two samples adjacent to the Tobacco Root Mountains had K/Ar ages of 75 and 52 Ma. These ages were believed to have been reset by the batholith but as other samples within the Tobacco Root Mountains and North Madison Range were not apparently reset, the influence of the intrusions was found to be intense but sharply limited in extent. Kovaric *et al.* (1996) reported that biotite samples dated from the Spuhler Peak Metamorphic Suite, that outcrops within 1 km of the Tobacco Root Batholith, were apparently reset by the batholith to 112 and 125 Ma. Kovaric *et al.* (1996) also used ^{40}Ar-^{39}Ar on sericite in the talc deposit in the Highland Mountains and yielded a disturbed total gas age of 122 Ma that was believed to have been reset by a nearby pluton. The aim of this research was to further investigate the extent of resetting of dates in the Precambrian rocks by these plutons.

7.3.2. Sample Selection

Some samples collected from the Tobacco Root Mountains and Highland Mountains during the field sampling trip in June 1997 were selected because of their close proximity to the exposed plutons. Figure 7.5 is an aeromagnetic map of the northern portion of the Tobacco Root Mountains and the south-east area of the Highland Mountains, modified from Johnson *et al.* (1965). This can be used to infer the underground extent of the batholith for the area covered. Unfortunately, the source map did not extend south of Twin Bridges so only some of the sample locations within the northern Tobacco Root Mountains and Highland Mountains are included. However, 16 of the rock samples collected in June 1997 from the Tobacco Root Mountains and Highland Mountains can be located on this map and their proximity to both the exposed and underground extent of the batholith inferred.

Of the 16 rock samples located on this map, 6 were selected for analysis, and a further 5 samples within the Tobacco Root Mountains but outside the map area were also selected. Both biotite and amphibole were analysed, with samples TRMR3, TRER2, and TRWC1 containing both. The UV laser microprobe was used for biotite analysis, and the IR system was used for amphibole analysis. Details of the analytical techniques used are given in Chapter 5 and Appendix 5.1.

7.3.3. Results

The weighted mean ages obtained for each sample are contained in Table 7.1 below, listed in order of horizontal distance from exposed pluton, and details of the analytical results are in Appendix 5.2 and 5.4. Figure 7.6 shows the ages relative to geographical location.

Figure 7.5

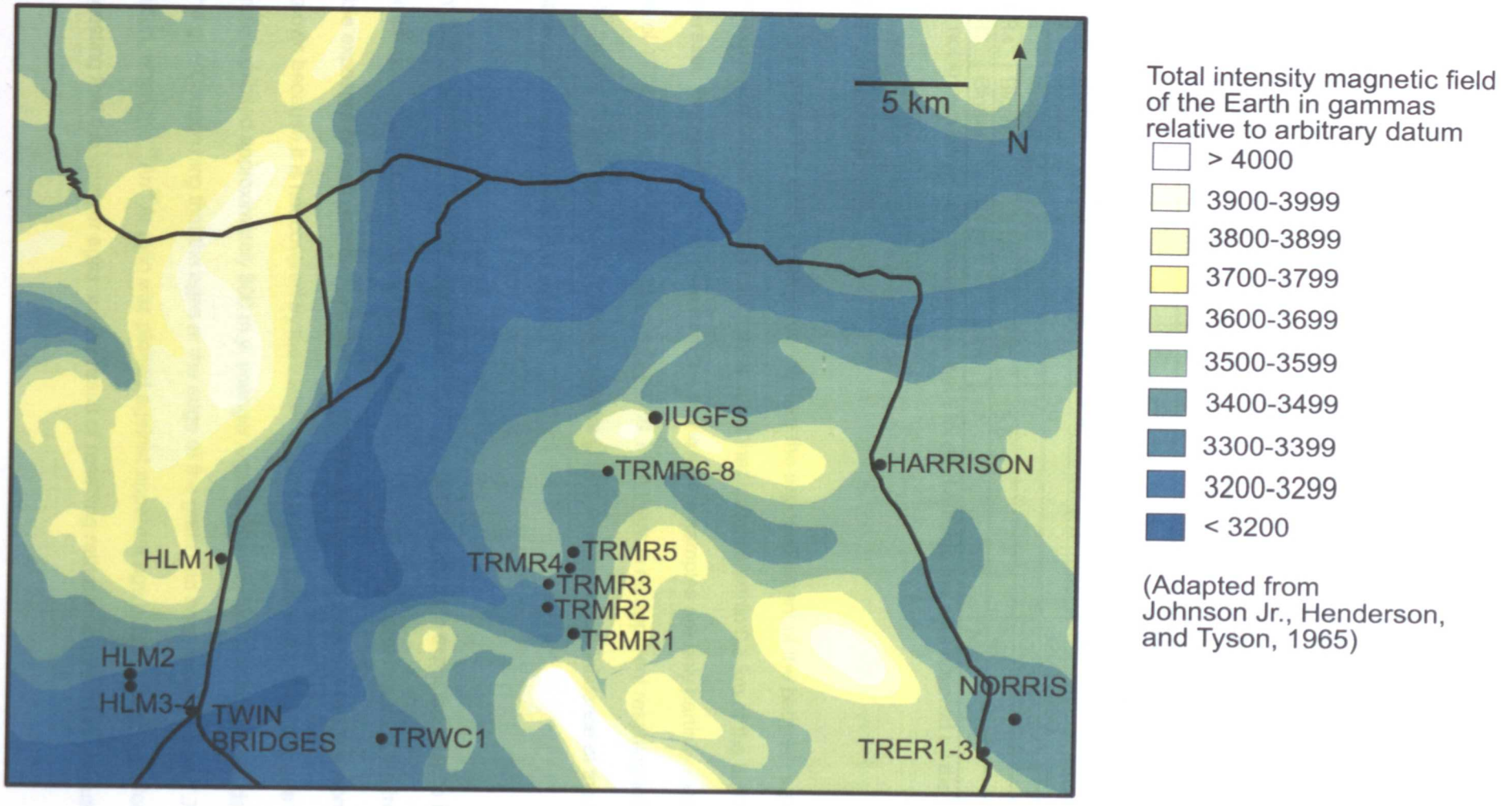

Figure 7.5: Aeromagnetic Map of the Northern Tobacco Root and Eastern Highland Mountains

Table 7.1. Summary of Mean Ages Achieved in Relation to Distance from an Exposed Pluton

Sample	Mineral	Mean Age (Ma)	± 2σ	Approx. distance from exposed pluton (km)	Magnetic field intensity at location
TRMR3	Amphibole	248	44	0.1	3500-3599
TRMR3	Biotite	80	36	0.1	3500-3599
TRER2	Amphibole	83	90	0.25	3500-3599
TRER2	Biotite	72	8	0.25	3500-3599
TRER1	Amphibole	1272	16	0.5	3500-3599
TRMR2	Biotite	1581	8	1	3300-3399
TRMC5	Amphibole	1803	34	3	NK
TRGC5	Biotite	1666	12	5.5	NK
TRWC1	Amphibole	1634	34	7.5	3300-3399
TRWC1	Biotite	1689	10	7.5	3300-3399
TRMC3	Biotite	1745	14	7.5	NK
HLM2	Biotite	1749	10	10	3200-3299
HLM4	Amphibole	XS		11	3200-3299
TRER4	Biotite	1723	20	15.5	NK
TRER7	Biotite	1711	16	17	NK

NK = not known because these samples were located outside the area covered by the aeromagnetic map.

7.3.4. Discussion

Figure 7.6 shows the approximate distance from the exposed extent of the batholith against the apparent age obtained. From this it can be seen that samples within 0.5 km of the batholith have been reset. Between 0.5 and 1 km from the batholith the samples are only partially reset, yielding ages of 1272 ± 16 and 1581 ± 8 Ma, and beyond 1 km there is no apparent resetting influence from the batholith. This supports the findings of Giletti (1966) who found the influence of the intrusions to be intense but sharply limited in extent.

Samples TRGC5 and TRWC1 also exhibit slightly younger ages than expected despite being several kilometres from the exposed extent of the batholith. TRGC5 was approximately 5 km from the visible exposure of the Tobacco Root Batholith but the unexposed extent of the intrusion here is unknown because it is not covered by the aeromagnetic map. Two matrix biotite grains from this sample exhibited approximately 300 m.y. younger ages at the margin than ages towards the centre of the grain, suggesting that the ages at the edge of the grain had been reset (Figure 7.7). In addition, when the $^{36}Ar/^{39}Ar$ ratio was plotted against apparent age no correlation was found, suggesting that the younger ages are the result of resetting rather than alteration. Inclusions of

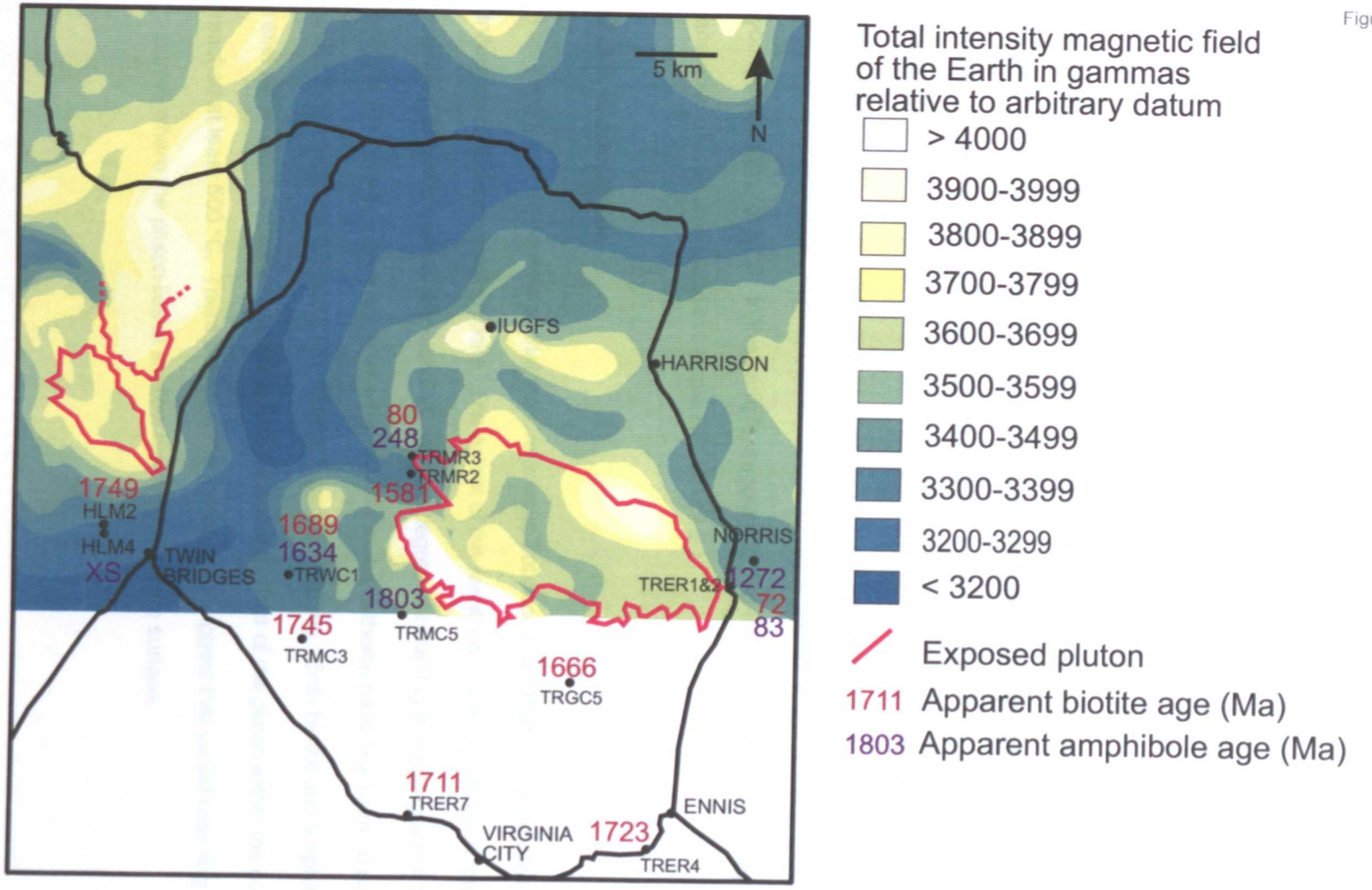

Figure 7.6: Apparent ages relative to geographical location and distance from plutons

biotite within garnet were also analysed in this sample (section 6.3.) and some inclusions had older apparent ages than matrix biotite, suggesting they had been shielded from resetting by the garnet. Collectively this information suggests that this sample has been reset and it is possible that the batholith underlies the country rock in this area, influencing the apparent age of the sample. Alternatively this sample may have been reset by a nearby pegmatite as suggested in section 7.4 below for sample RMC42, but no pegmatites were seen during the collection of this sample.

Sample TRWC1 yielded apparent ages of 1689 ± 10 Ma for biotite and 1634 ± 34 Ma for amphibole that might also be a consequence of partial resetting by unexposed batholith or pegmatites at this location. However, the relatively low magnetic intensity shown on the aeromagnetic map at this location suggests that the batholith is not present. When the $^{36}Ar/^{39}Ar$ ratio is plotted against age for the biotite in this sample there is a good correlation between the younger ages and higher $^{36}Ar/^{39}Ar$ ratio (Figure 7.8). This would suggest that the younger apparent ages for the biotite have been influenced by alteration. Further support comes from the apparent age of the amphibole which is younger than that of biotite in this sample, suggesting that the amphibole has lost argon due to alteration as was also found in sample RRSW1 (7.2.).

7.3.5. Conclusion

This experiment demonstrates that the Cretaceous Tobacco Root Batholith does have a resetting influence on the surrounding rocks. The extent of the resetting influence has been found to be restricted to within 1 km of the batholith, with the degree of resetting increasing within that 1 km towards the pluton. Those samples within 0.5 km of the batholith have been almost completely reset whilst those between 0.5 and 1 km show only partial resetting. Both biotite and amphibole have been reset within the 1 km zone suggesting that the heating effect of the pluton within the country rocks reached at least 500 °C. There is also some evidence to suggest that partial resetting has also occurred where the pluton lies at shallow depth beneath the surface.

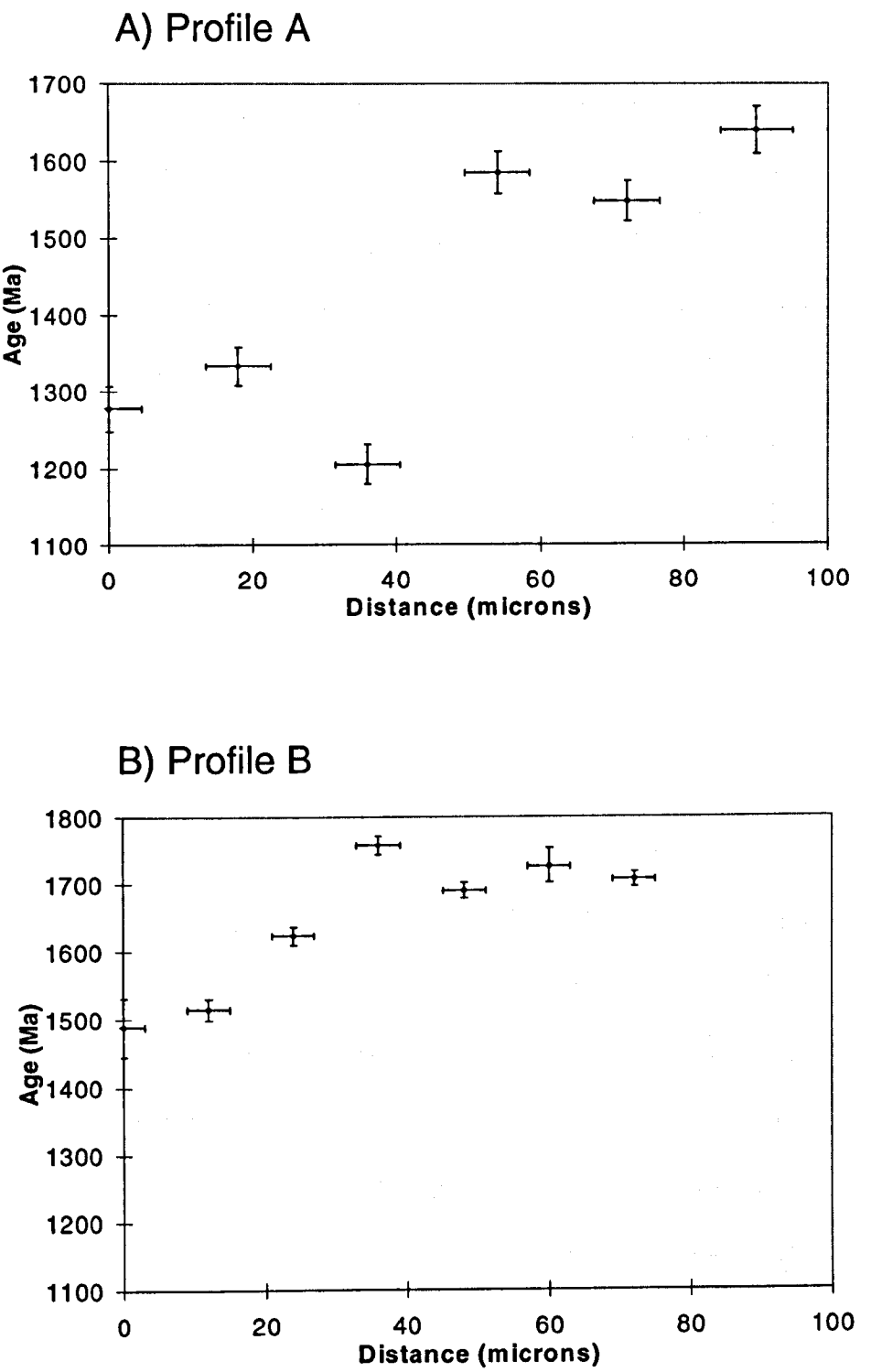

Figure 7.7: Closure profiles for TRGC5

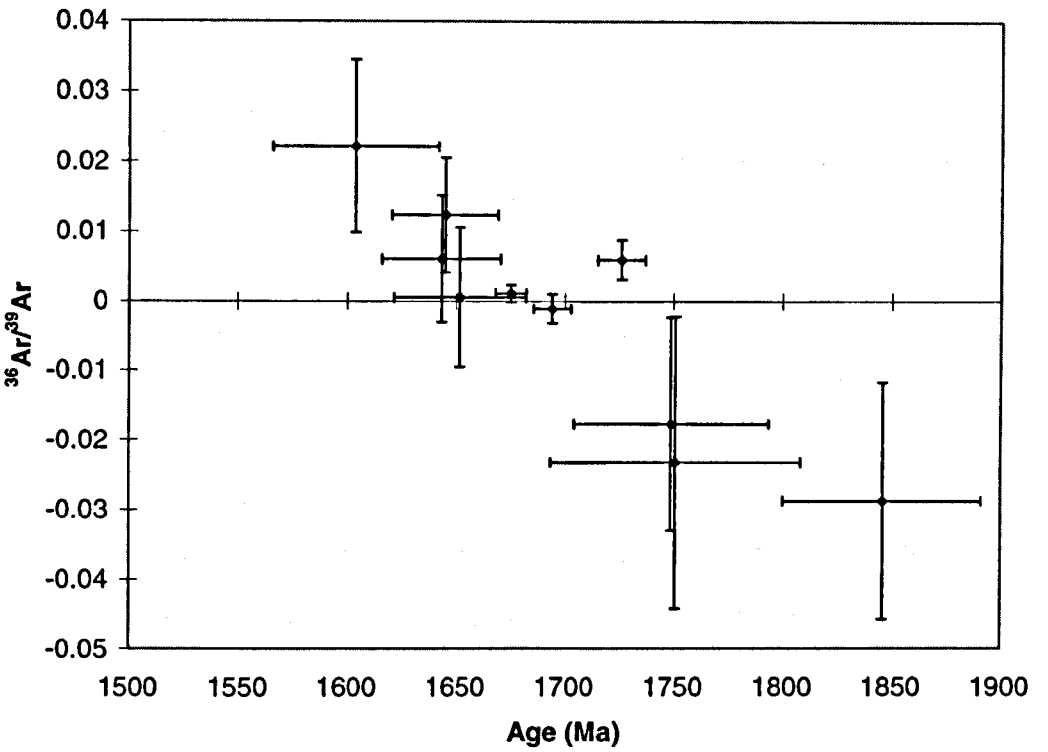

Figure 7.8: Apparent age versus $^{36}Ar/^{39}Ar$ for TRWC1

7.4. Samples Affected by Resetting by Pegmatites

Sample RMC42 was supplied by Dr Dahl as an example of a rock containing both muscovite and biotite. It was located approximately 125 m south of a small pod of tourmaline pegmatite (Dahl, pers. comm.). The pegmatite was mapped by James (1990) as a post-tectonic (undeformed, unmetamorphosed), medium-grained, schorl-rich pegmatite. Although there are no dates directly from this pegmatite body, Giletti (1966) dated muscovite in a similar, possibly related, pegmatite in the Tobacco Root Mountains and obtained a K-Ar muscovite age of 1643 Ma and Rb-Sr muscovite and feldspar ages of 1640 and 1672 Ma, respectively (corrected for decay constants after Steiger and Jäger, 1977).

For both biotite and muscovite in RMC42 four 50 μm square analyses and 1 profile were measured. For biotite the apparent ages ranged from 1668 to 1522 Ma, yielding a weighted mean of 1611 ± 8 (2σ). The apparent ages for muscovite ranged from 1716 to 1636 Ma and gave a weighted mean of 1671 ± 6 (2σ). Full analytical results can be found in Appendix 5.2.

The coincidence of the mean apparent mica ages for this rock and the possible age of the adjacent pegmatite strongly suggests that the mica in this sample has been reset by the same event that gave rise to the pegmatite intrusion.

7.5. Overall Conclusions

This chapter has dealt with the anomalously young ages that became evident when producing mean matrix mica and amphibole ages for south-western Montana. It is clear that because of the relatively low blocking temperature of the ^{40}Ar-^{39}Ar geochronological system it can be readily influenced by reheating events, and ages partially or totally reset. Using this aspect of the system it has been possible to date events that post-date the main metamorphic event affecting this region. Conversely, this feature of ^{40}Ar-^{39}Ar dating can also cause problems when attempting to date the main metamorphic event.

In this chapter three events that occurred after the 1780 to 1740 Ma amphibolite facies metamorphic event have been found to have resetting effects on the metamorphic rocks of this region. Firstly, the Belt basin rifting event between 1500 and 1360 Ma that occurred to the west and north of south-western Montana is manifested in south-western Montana as hydrothermal alteration of some samples within the Ruby Range. Secondly, the intrusion of Cretaceous plutons has been shown to have a resetting effect on the surrounding country rock up to 1 km away. Thirdly, resetting by an event that gave rise to localised pegmatite intrusion has also occurred within the Ruby Range. These represent three more events within the geological history of the metamorphic rocks of south-western Montana that have been dated using the ^{40}Ar-^{39}Ar geochronological technique.

Although valuable in terms of expanding the geological information that has been obtained for this area, these three resetting events demonstrate that the ^{40}Ar-^{39}Ar system can be reset at low temperatures, below the commonly accepted closure temperature (Dodson, 1973). Therefore, awareness of this is required when interpreting the meaning of any age obtained using this system. Alteration is widespread problem that has been shown to particularly disturb ages produced using the IR laser step-heating method. However, despite its common occurrence, alteration is less problematic when undertaking selective analysis using the UV laser microprobe. This research has demonstrated that ages influenced by alteration can often be identified by the occurrence of a higher $^{36}Ar/^{39}Ar$ ratio, and geologically meaningful ages obtained from even highly altered samples.

The resetting influences of plutons are less of a problem to general ^{40}Ar-^{39}Ar geochronology. The size of plutons means that they are usually well mapped and their locations well known. This research has shown that the extent of the resetting influence of even large epizonal plutons may be restricted to a narrow zone immediately around the pluton. Therefore, sampling rocks outside this zone will avoid resetting problems. Only when the pluton extends beneath the surface may it have a resetting influence on samples apparently beyond the limit of the exposed pluton. If geophysical data are available then this problem may also be overcome. The resetting influence of pegmatites may be more problematic because pegmatites can be numerous and small-scale in metamorphic regions, so their locations may be less well documented. However, again, their affects are localised.

Chapter 8 - ^{40}Ar-^{39}Ar Geochronology of the South Madison Range

8.1. The Context of the South Madison Range within South-western Montana

The Giletti Line represents the best-defined south-eastern boundary for the 1600 Ma metamorphic terrane determined by Giletti (1966) and divides south-western Montana into two geochronological regions. The boundary was found by Giletti to be in the Gravelly Range south-east of Virginia City and in the Gallatin River canyon south of Bozeman (Figure 8.1) but he stated that it was unlikely to be a straight line as drawn and further work was likely to redefine it. The north-west boundary of the terrane could not be defined because of the resetting effect of the Boulder Batholith and its apophyses.

In addition to the geochronological boundary within the south-western Montana portion of the Wyoming province, the region has been divided on a lithological basis into two separate Late Archæan subprovinces (Figure 8.1). The Wyoming Province as a whole was divided into the Wyoming greenstone terrane (WGT), the Beartooth-Big Horn magmatic terrane (BBMT), and the Montana metasedimentary terrane (MMT) (Mogk *et al.*, 1992, Mueller *et al.*, 1993 and references therein). The MMT comprises the Highland Mountains, Tobacco Root Mountains, Ruby Range, Greenhorn and Madison Ranges and is distinguished by metasupracrustal sequences within volumetrically dominant quartzofeldspathic gneisses. The BBMT is dominated by Late Archæan igneous and meta-igneous rocks, primarily of tonalite-trondhjemite-granodiorite composition and encompasses principally the Beartooth Mountains and the Bighorn Mountains (Mogk *et al.*, 1992 and references therein). The nature of the boundary between the BBMT and MMT has remained

Chapter 8 - ^{40}Ar-^{39}Ar Geochronology of the South Madison Range

8.1. The Context of the South Madison Range within South-western Montana

The Giletti Line represents the best-defined south-eastern boundary for the 1600 Ma metamorphic terrane determined by Giletti (1966) and divides south-western Montana into two geochronological regions. The boundary was found by Giletti to be in the Gravelly Range south-east of Virginia City and in the Gallatin River canyon south of Bozeman (Figure 8.1) but he stated that it was unlikely to be a straight line as drawn and further work was likely to redefine it. The north-west boundary of the terrane could not be defined because of the resetting effect of the Boulder Batholith and its apophyses.

In addition to the geochronological boundary within the south-western Montana portion of the Wyoming province, the region has been divided on a lithological basis into two separate Late Archæan subprovinces (Figure 8.1). The Wyoming Province as a whole was divided into the Wyoming greenstone terrane (WGT), the Beartooth-Big Horn magmatic terrane (BBMT), and the Montana metasedimentary terrane (MMT) (Mogk *et al.*, 1992, Mueller *et al.*, 1993 and references therein). The MMT comprises the Highland Mountains, Tobacco Root Mountains, Ruby Range, Greenhorn and Madison Ranges and is distinguished by metasupracrustal sequences within volumetrically dominant quartzofeldspathic gneisses. The BBMT is dominated by Late Archæan igneous and meta-igneous rocks, primarily of tonalite-trondhjemite-granodiorite composition and encompasses principally the Beartooth Mountains and the Bighorn Mountains (Mogk *et al.*, 1992 and references therein). The nature of the boundary between the BBMT and MMT has remained

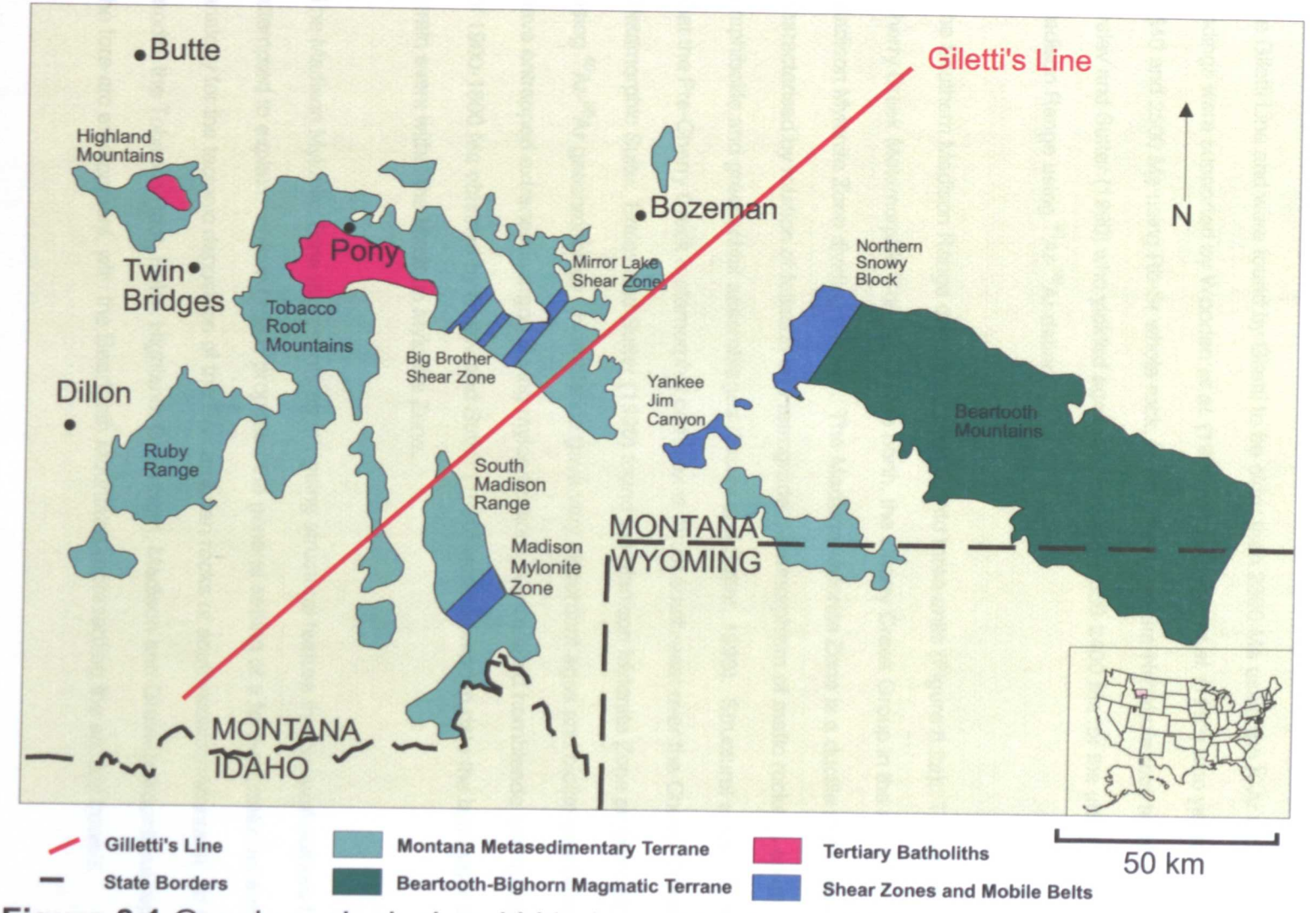

Figure 8.1 Geochronological and Lithological Divisions Within South-western Montana (modified from Mogk *et al.*, 1992)

speculative but it is constrained geographically to be between or within the South Madison Range and Beartooth Ranges (Mueller *et al.*, 1993).

The rocks investigated in this research thus far originated on the north-west of the Giletti Line, within the MMT (Figure 8.1). The rocks of the South Madison Range lie predominantly to the south-east of the Giletti Line and were found by Giletti to be older than 2300 Ma using the K-Ar technique. Those findings were supported by Wooden *et al.* (1988) and Mueller *et al.* (1993) who yielded ages between 3540 and 2500 Ma using Rb-Sr whole rock, U-Pb zircon and Sm-Nd whole rock techniques; and by Erslev and Sutter (1990) who yielded ages ranging from 2530-2400 Ma for the units in the South Madison Range using ^{40}Ar-^{39}Ar dating.

The Southern Madison Range can be subdivided into three units (Figure 8.2a). These are the Pre-Cherry Creek Metamorphic Complex in the north, the Cherry Creek Group in the south, and the Madison Mylonite Zone dividing the two. The Madison Mylonite Zone is a ductile shear zone characterised by rotation of foliation and retrograde metamorphism of mafic rocks to epidote-amphibolite and greenschist assemblages (Erslev and Sutter, 1990). Structural evidence suggests that the Pre-Cherry Creek metamorphic complex is thrust south-east over the Cherry Creek Metamorphic Suite. Erslev and Sutter (1990) found the Madison Mylonite Zone problematic to date using ^{40}Ar-^{39}Ar geochronology. Hornblende gave very discordant ages and biotite was believed to have entrapped extraneous argon during mylonitization. A combined hornblende and muscovite age of 1900-1800 Ma obtained by Erslev and Sutter (1990) was believed to date the last major ductile strain event within the Madison Mylonite Zone.

The Madison Mylonite Zone represents an intriguing structural feature that several authors have attempted to explain. Wilson (1981) proposed the general setting of a fore-arc basin as a modern analogy for the tectonic deposition of the Precambrian rocks of south-western Montana. In his model, the Tobacco Root, Ruby, Highland, Greenhorn, Madison and Gravelly Mountains represent the fore-arc environment, with the Beartooth Mountains representing the eroded bowels

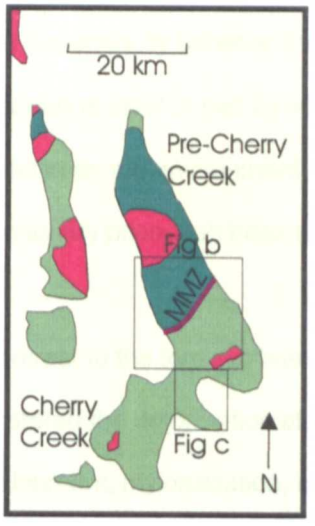

Supracrustal Rocks
Granitic Plutons
Qtz-Feldspar Gneiss

a) Basic Subdivisions of the South Madison Range

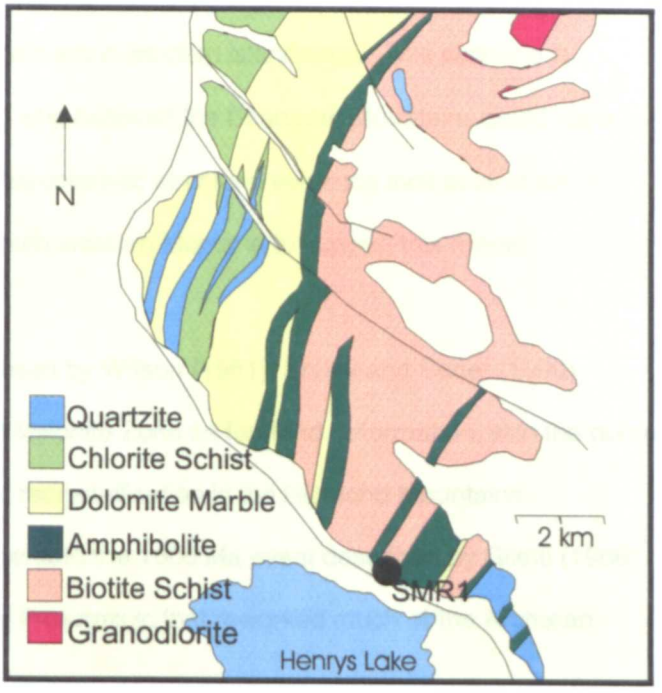

c) Geology of the Henrys Lake Area

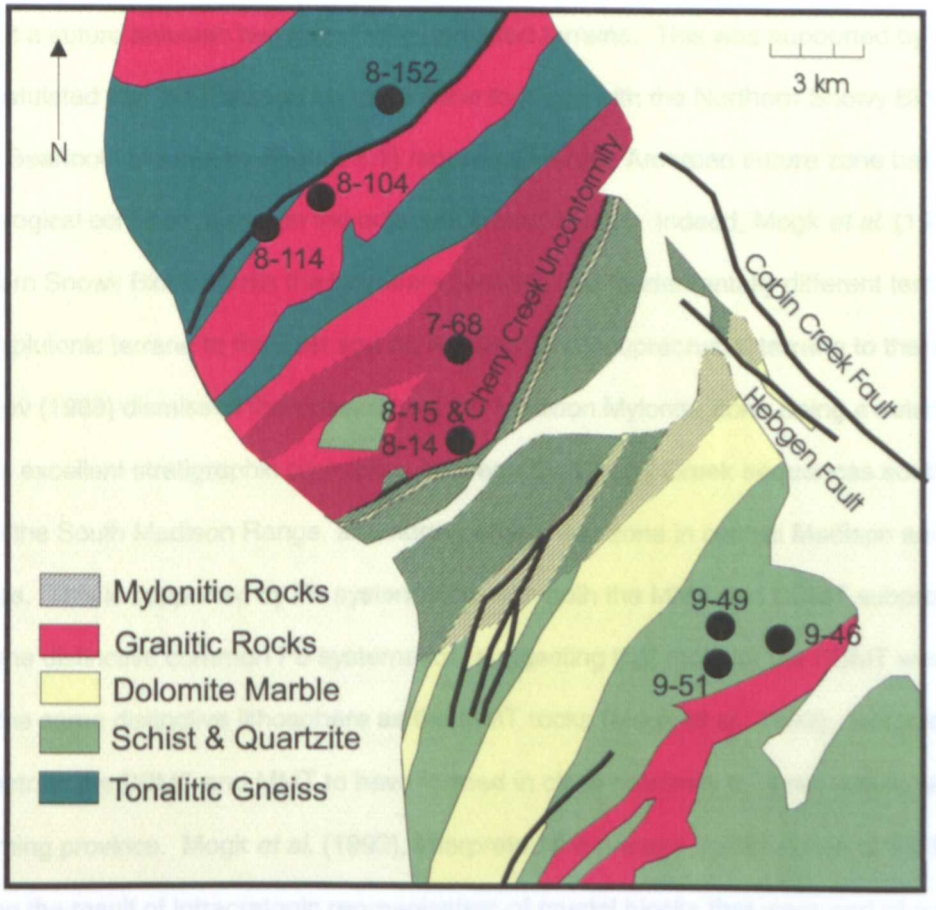

b) Geology of Central South Madison Range

Figure 8.2: Basic Geological Subdivisions of the South Madison Range with Sample Locations

of the main-arc. Wilson believed that the Madison Mylonite Zone could represent the faulted upper-slope discontinuity between the fore-arc and main-arc in modern island-arcs. This scenario is supported at least in part by Mogk *et al.* (1992) who believed the Beartooth Mountains could have formed in an arc environment. However, no characteristic structural evidence indicative of an accretionary prism has been reported within south-western Montana to support this model.

In contrast to the fore-arc basin scenario proposed by Wilson (1981), Erslev and Sutter (1990) interpreted the deformation along the Madison Mylonite Zone as foreland deformation, with the dome development, mylonitization, and metamorphic recrystallisation in the Highland Mountains representing hinterland deformation. In this scenario the 1600 Ma event described by Giletti (1966) was caused by major compression in the Early Proterozoic that reworked much of the Archæan basement.

Wilson (1981), pointed out that as the origin of the shear is unknown, the Madison Mylonite Zone could represent a suture between two genetically unrelated terrains. This was supported by Hoffman (1989) who postulated that the Madison Mylonite Zone together with the Northern Snowy Block in the north-western Beartooth Mountains (Figure 8.1) represents a Late Archæan suture zone based on purported lithological contrasts between the adjacent crustal blocks. Indeed, Mogk *et al.* (1988) state that the Northern Snowy Block marks the boundary between two fundamentally different terranes - a Late Archæan plutonic terrane to the east and an Archæan metasupracrustal terrane to the west. However, Erslev (1988) dismissed the possibility of the Madison Mylonite Zone being a suture because of the excellent stratigraphic correlation between the Cherry Creek sequences south of the shear zone, in the South Madison Range, and north of the shear zone in central Madison and Gravelly ranges. This is supported by Pb systematics, with both the MMT and BBMT subprovinces having the same distinctive common Pb systematics, suggesting that rocks of the BBMT were derived from the same distinctive lithosphere as the MMT rocks (Mogk *et al.*, 1992). Isotopic data, therefore, constrain the BBMT and MMT to have formed in close proximity to, if not within, what is now the Wyoming province. Mogk *et al.* (1992), interpreted the present configuration of the BBMT and MMT to be the result of intracratonic reorganisation of crustal blocks that were part of a more extensive Early to Middle Archæan craton, rather than accretion of exotic terranes.

Despite the somewhat contradictory models proposed for the tectonic history of this region, taken together, the Giletti Line, the MMT/BBMT subprovince division, and the Madison Mylonite Zone/Northern Snowy Block (Figure 8.1) form compelling evidence that there is at least one major discontinuity between the western and eastern halves of the south-western Montana region. The discontinuity appears to be located near or within the South Madison Range making it an important range for the investigation of this division.

Dating the South Madison Range provides important information towards understanding the history of south-western Montana. Firstly, rocks from south-east of the Giletti Line were unaffected by the Proterozoic metamorphic event that reset rocks in the north-west. Secondly, due to the different metamorphic conditions recorded in these rocks compared to the Ruby Range and Tobacco Root Mountains, muscovite mica is more abundant, and muscovite and biotite occur in the same rocks. This allows the further investigation of closure profiles within the two micas and direct comparison of the apparent age variations recorded in muscovite and biotite, and thus any variations in diffusion mechanisms between the two micas. Furthermore, the Madison Mylonite Zone apparently represents a ductile thrusting event within the geological history of this area that has so far failed to be satisfactorily dated. Understanding this zone and the nature of the discontinuity between western and eastern parts of this region allows a fuller picture of the history of south-western Montana to be built up.

8.2. Sample Selection and Irradiation

During the 1997 field work a muscovite-rich metapelite from the Cherry Creek unit (SMR1) was collected from the South Madison Range (Figure 8.2c). It was crushed and separated and 7 muscovite grains were selected for analysis. A further 9 samples were supplied by Dr Eric Erslev, Colorado University, USA (Figure 8.2b). These were supplied as thin-section off-cuts from which thick sections were prepared for analysis. Four of these samples (9-49, 8-152, 8-104, and 8-14a) had previously been analysed by Erslev and Sutter and the results published in the 1990 paper.

Sample SMR1 was irradiated in the McMaster 3 irradiation (Appendix 5.1) and the other 9 samples were irradiated in the McMaster 5 irradiation (Appendix 5.1).

8.3. Analytical Technique

For each sample five 50 μm squares were ablated in five mica separates using the UV laser microprobe to give general ages, then a series of traverses were made in order to construct closure profiles. Traverses ranged in length from approximately 100 μm to 170 μm, and there were 3 to 8 traverses in each profile. Where possible attempts were made to analyse both biotite and muscovite in each sample. However, in some samples only one mica species was present, whilst in others the second mica species was in limited abundance, making it impossible to attempt closure profiles. Occasionally, the grains of the second mica species were too small to allow 50 μm square analyses. In the mylonites the grain sizes were too fine to attempt profiles so additional 50 μm squares were ablated instead. Where possible the 50 μm squares in the mylonites were confined to single mineral grains but in very fine grained sample squares were across numerous grains of mica.

8.4. Mean Age

8.4.1. Results

A mean age for each sample was achieved by excluding the first two traverses in each profile and any other anomalous apparent ages in order to avoid any possible age variations caused by late stage cooling and defects. The weighted mean of each sample is shown in Table 8.1. and in Figure 8.3. Full analytical results are contained within Appendix 8.1.

Table 8.1. Mean ages for matrix mica (error to 2 σ)

Sample	Matrix Biotite				Matrix Muscovite				Fine Grained Composite*			
	No. of analyses	Age range (Ma)	Mean Age (Ma)	± 2σ	No. of analyses	Age range (Ma)	Mean Age (Ma)	± 2σ	No. of analyses	Age range (Ma)	Mean Age (Ma)	± 2σ
CHERRY CREEK												
SMR1					45	2581-1709	2448	8				
9-49	16	2460-2066	2368	6	8	2567-2452	2514	10				
9-51	14	2152-1959	2026	8	8	2516-1976	2396	14				
9-46	21	2200-1726	2053	6								
PRE-CHERRY CREEK												
8-152	17	2652-2377	2571	8								
8-114	16	2423-2198	2301	6								
8-104					27	2168-1576	1830	4				
MADISON MYLONITE ZONE												
7-68	6	2103-1953	2026	10	5	2207-1823	2076	12	5	1939-1852	1898	12
8-15a									8	1688-1624	1633	6
8-14a									10	1686-1605	1659	6

* The term 'fine grained composite' refers to a collection of very fine grained material that could not be analysed as individual grains.

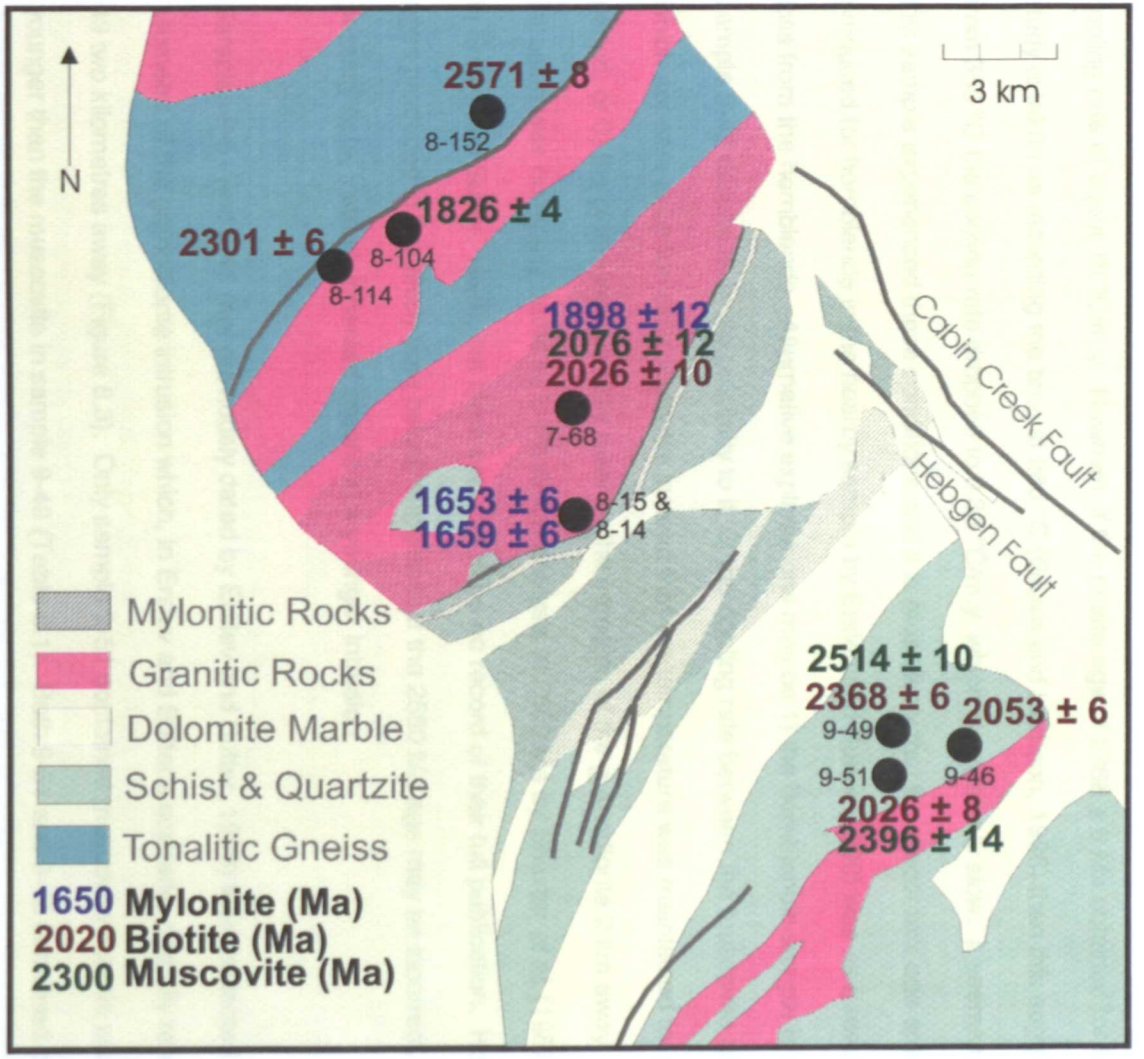

Figure 8.3: Central South Madison Range Showing Mean Age Obtained

8.4.2. Discussion

8.4.2.1. Cherry Creek

Sample 9-49 yielded a mean muscovite age of 2514 ± 10 Ma which is in excellent agreement with the 2520 Ma age obtained by Erslev and Sutter (1990) for this sample. Also dated by Erslev and Sutter was hornblende from a nearby rock that gave a discordant spectrum with an age plateau of 2530 Ma. They believed that the closeness of ages between the hornblende in this sample and muscovite in 9-49 was caused by rapid cooling after resetting by a granodiorite intrusion 2 km away (Figure 8.3). If the blocking temperature for hornblende is taken as 500 °C (Harrison, 1981), and the blocking temperature for muscovite is about 350 °C (Hames and Bowring, 1994), then this is a rapid cooling rate of about 15 °C/m.y. However, if the biotite age of 2368 ± 6 Ma obtained for 9-49 in the study is taken as recording the time at 280 °C (Grove and Harrison, 1996) then this suggests that from 350 °C the cooling rate dropped to 0.35 °C/m.y. which is extremely slow. It seems unlikely that this sample experienced these conditions and it is most likely that the discordant age spectrum produced for hornblende in the nearby sample by Erslev and Sutter (1990) was as a result of argon loss from the hornblende. Alternative explanations may be 1) the hornblendic sample is unrelated to sample 9-49 despite its close proximity to it; 2) the cooling rate between the muscovite and biotite, which appears to be too slow, indicates instead that the temperature was maintained for an extended period; or 3) the biotite was partially reset by the intrusion of the granodiorite 2 km away. This intrusion was nominally dated by U-Pb zircon analysis at 2580 Ma by Shuster *et al.* (1987, referenced in Erslev and Sutter, 1990), but there appears to be no record of their full publication. However, new ages produced in this study (see below) suggest that the 2580 Ma age may be incorrect, and may possibly date, instead, inherited zircons in a younger intrusion.

Samples 9-51 and 9-46 (not previously dated by Erslev and Sutter, 1990) were collected within a kilometre of the granodiorite intrusion which, in Erslev and Sutter's scenario, partially reset sample 9-49 two kilometres away (Figure 8.3). Only sample 9-51 contained muscovite but this was c.120 m.y. younger than the muscovite in sample 9-49 (Table 8.1). Both 9-51 and 9-46 contained biotite, yielding mean ages of 2026 ± 8 and 2053 ± 6 Ma, which are in excellent agreement with each other but over 300 m.y. younger than the biotite from 9-49. This suggests that the micas in both 9-51 and

9-46 have been at least partially reset. It is possible that overthrusting of the mylonites to the south-east was responsible for this partial resetting, but it seems more likely that the nearby granodiorite is responsible (see discussion of sample SMR1 below). If so, the intrusion cannot be older than c.2020 Ma and reached a temperature that was close to the blocking temperature of biotite, thus resetting the biotite ages but only partially resetting the muscovite. Its effects are lessened with distance from the intrusion, therefore, only partially resetting, or recrystallising, the biotite in 9-49 and having little or no effect on the muscovite in this sample. See also sections 8.4.2.2 and 8.5.2.3, below.

Sample SMR1 was taken more than 10 km to the south of samples 9-46, 9-49 and 9-51 (Figure 8.2c), i.e. far away from any potential influence from the granodiorite intrusion, but still within the range of influences from overthrusting in the mylonite zones. Because muscovite from this sample gave a mean age of 2448 ± 8 Ma, it is suggested that the c.2500 Ma age obtained for muscovite in sample 9-49 was unaffected by resetting. This scenario is possible if the intrusion was responsible for the resetting but unlikely if mylonites were the cause.

8.4.2.2. Pre-Cherry Creek

The three samples dated in this study from the Pre-Cherry Creek metamorphic complex also vary considerably in ages and may have been influenced by proximity to intrusions and mylonite zones. Hornblende from sample 8-152 was dated by Erslev and Sutter (1990) and gave an essentially concordant age spectrum with a plateau age of 2510 Ma. Biotite dated from the same rock (this study) gives a mean age of 2571 ± 8 Ma (Table 8.1) which is slightly older than the age of coexisting hornblende. It is possible that the biotite analysed contained a small amount of excess argon, although there is nothing in the analytical results to suggest this. As no analytical information is available from Erslev and Sutter (1990), it is difficult to critically evaluate validity of their hornblende age determine. Nominally, however, the closeness in the two ages would suggest rapid cooling.

Biotite dated in sample 8-114 gave a mean age of 2301 ± 6 Ma (Table 8.1). This age is in close agreement with the biotite age for sample 9-49 from the Cherry Creek Metamorphic Suite and may reflect partial resetting by the nearby granodiorite intrusion (Figure 8.3).

Erslev and Sutter (1990) obtained a discordant age spectrum for 8-104 muscovite and they interpreted the total gas age of 1960 Ma as having been affected by an Early Proterozoic retrograde event. New muscovite ages produced in this study gave a mean age of 1826 ± 4, with ages ranging from 2168 to 1576 Ma (Table 8.1). These results support the findings of Erslev and Sutter (1990) that this sample was disturbed. It is possible that this sample was affected by a nearby mylonite zone within the Pre-Cherry Creek Complex (Erslev pers. comm.) but, again, this sample is also close to a granodiorite intrusion that may be influencing the ages (Figure 8.3). Disturbed spectra and variable age profiles observed in several of the samples indicate a prolonged thermal history. Separating the localised effects of reheating during granite intrusion and high strain during mylonization related to overthrusting may prove very difficult.

8.4.2.3. The Madison Mylonite Zone

Erslev and Sutter (1990) found that minerals from the Madison Mylonite Zone gave very discordant age spectra, and that biotite total gas ages commonly exceeded co-existing hornblende ages. This they attributed to the entrapment of extraneous argon during mylonization which thus precluded geologically meaningful ages being obtained from biotite. Discordant hornblende spectra were interpreted as indicating a diffusive loss event (or partial recrystallisation) at approximately 1850 to 1800 Ma in hornblende that had originally cooled to closure temperature at about 2500 Ma. This interpretation was supported by the muscovite spectrum from sample 8-14b which gave a total gas age of 1800 Ma and was believed to be completely reset during shearing. The discordant spectrum produced by this sample was interpreted as indicating that the muscovite had re-equilibrated or crystallised at 1850 to 1900 Ma and later (1600 Ma or younger) experienced minor argon loss, possibly due to subsequent retrogression in the Madison Mylonite Zone. Therefore, according to Erslev and Sutter (1990), the timing of the last major ductile strain event in the Madison Mylonite Zone was constrained between 1900 and 1800 Ma and between the temperatures of 500 and 350 °C.

Three samples from the Madison Mylonite Zone were dated in this study, including sample 8-14a previously dated by Erslev and Sutter (1990). In sample 7-68 some larger grains were preserved that were large enough for 50 μm squares to be ablated in individual grains. Both biotite and

muscovite were analysed, yielding mean ages of 2026 ± 10 and 2076 ± 12 Ma, respectively, although all showed a significant age range down to the ages implied for hornblende recrystallisation by Erslev and Sutter (1990). In addition, 50 μm squares over collections of very fine grains (≤5 μm) of unidentified mica were ablated, giving a mean age of 1898 ± 12 Ma. This sample was located on the edge of the mylonite zone (Erslev pers. comm.) and the coarsest mica grains in this sample were clearly relatively unaffected by the mylonization. Therefore, it is possible that the 2026 Ma biotite age constrains the age of the rocks prior to the mylonization event. Indeed, the 1898 Ma age for the finer grained mica may simply reflect a lower closure temperature related to the smaller grain size. As this sample is located within rocks with an igneous precursor (Figure 8.3), it is possible that this 2026 age represents the original crystallisation date. This is supported by the closeness in ages between biotite in this sample and those from samples 9-51 (2026 Ma) and 9-46 (2053 Ma) from the Cherry Creek Metamorphic Suite, believed to have been reset by the granodiorite intrusion. The closeness in ages between the biotite and muscovite in this sample is also suggestive of a rapid igneous event. This further implies that the timing of the intrusion was c.2020 Ma.

Samples 8-15a and 8-14a were very fine grained and it was not possible to analyse individually recognisable mica grains. Instead, 50 μm squares were ablated over collections of fine grained (≤5 μm) mica. In 8-14a muscovite was the only mica present but in 8-15a both muscovite and biotite were present (although muscovite was in higher abundance) and analyses of multiple mineral grains probably contained both mica species in varying amounts. The 1659 ± 6 and 1653 ± 6 Ma mean ages for 8-14a and 8-15a respectively are in very good agreement with each other, indicating that any difference in the ages between muscovite and biotite was slight. This good agreement in ages between samples and the narrow age ranges (1688-1624 and 1686-1605 Ma) suggest that this is a true event and not a mixture of two or more ages. Therefore, it seems likely that this c.1655 Ma age is the timing of movement along the Madison Mylonite Zone.

The spectra produced for muscovite from the Madison Mylonite Zone by Erslev and Sutter (1990) was a typical staircase shape, commonly found when muscovite from mylonites are step-heated, and interpreted as representing protracted neocrystallisation and growth of white mica during low temperature ductile deformation (Kirschner *et al.* 1996). It is believed that the maximum and minimum ages within the spectra record the time span over which mica formed and grew. For the

muscovite step-heated by Erslev and Sutter (1990) this would suggest a neocrystallisation period between 1900 Ma and 1600 Ma. This time period encompasses the c.1655 Ma age of mylonization recorded in samples 8-14a and 8-15a, the 1826 ± 4 Ma age for sample 8-104 believed to be influenced by localised mylonization within the Pre-Cherry Creek unit, and the 1800 to 1900 Ma age obtained by Erslev and Sutter (1990). This, coupled with the intrusion of the granodiorite, implies a complex Proterozoic tectonic history for this region, involving igneous intrusions and repeated mylonitization.

8.4.3. Conclusions

The rocks of the South Madison Range do not reveal a simple picture but instead, reflect localised resetting influences of granodiorite and/or high strain. Those rocks that appear to be beyond the range of influential factors include SMR1 and 9-49 in the Cherry Creek Metamorphic Suite, and 8-152 in the Pre-Cherry Creek Metamorphic Complex. Muscovite from SMR1 and 9-49, and biotite from 8-152 have the respective ages of 2448 ± 8, 2514 ± 10 and 2571 ± 8 Ma, confirming the 2500 Ma cooling age from a peak metamorphism at 2750 Ma inferred by Erslev and Sutter (1990).

The reoccurrence of the c.2026 Ma age in two Cherry Creek biotites and a Madison Mylonite Zone biotite related to proximity to granodiorite intrusions may indicate that the U-Pb zircon age of 2580 Ma by Shuster *et al.* (1987) is not the magmatic crystallisation age. Given that this date is only referenced in an abstract it is difficult to critically evaluate its validity and ideally a fresh attempt to date the crystallisation of the granodiorite is required before dismissing it. It is likely, however, that at least some of the zircons dated were inherited, allowing the intrusion of the granodiorite to be much younger. A resetting event at approximately 2020 Ma that reheated rocks 1 km away to between around 300 °C and 350 °C would account for the biotite and muscovite ages in the three samples from the Cherry Creek Suite, and possibly for the ages obtained for 7-68 from the Madison Mylonite Zone.

The new ages obtained for samples 8-15a and 8-14a from the Madison Mylonite Zone suggest that there was movement along the mylonite zone at c.1650 Ma. This is younger than the 1800 to 1900 Ma age inferred by Erslev and Sutter (1990) but step-heating spectra from their paper showed that ages as young as 1600 Ma were recorded in muscovite from the mylonite zone. Therefore, it is

seems likely that the Madison Mylonite Zone was a complex zone of repeated movement active probably between 1800 and 1600 Ma.

No neat boundary was found within the South Madison Range between 1800-1600 Ma ages and ages greater than 2300 Ma that might represent the Giletti Line. Although the Madison Mylonite Zone recorded ages comparable to those found to the north-west in the Ruby Range and Tobacco Root Mountains, ages of 2301 ± 6 and 2571 ± 8 Ma were found in sample 8-152 and 8-114 between the Madison Mylonite Zone and the current position of the Giletti Line. However, it is possible that the geochronological boundary found by Giletti may in fact be a wide zone of complex age variations of which the Madison Mylonite Zone is a part.

8.5. Closure Profiles

8.5.1. Results

Data tables in Appendix 8.1 and figures in Appendix 8.2 contain details of the data and profiles produced.

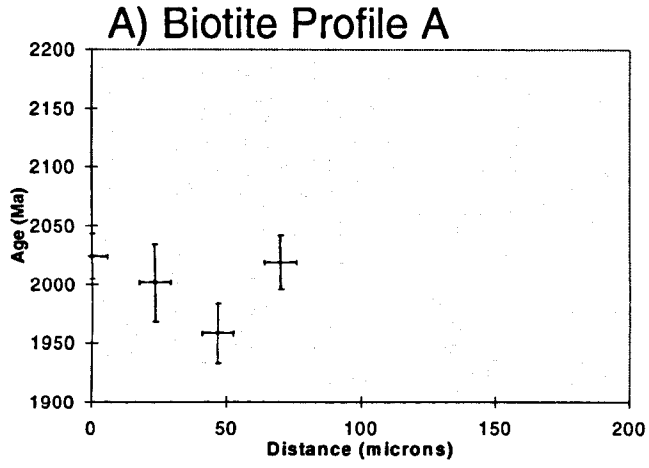

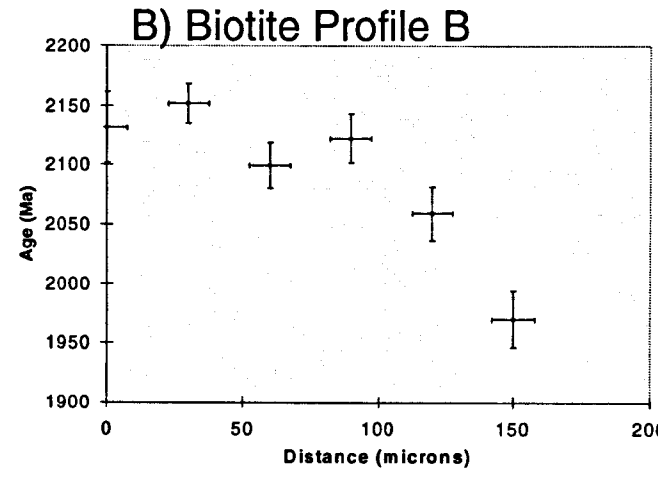

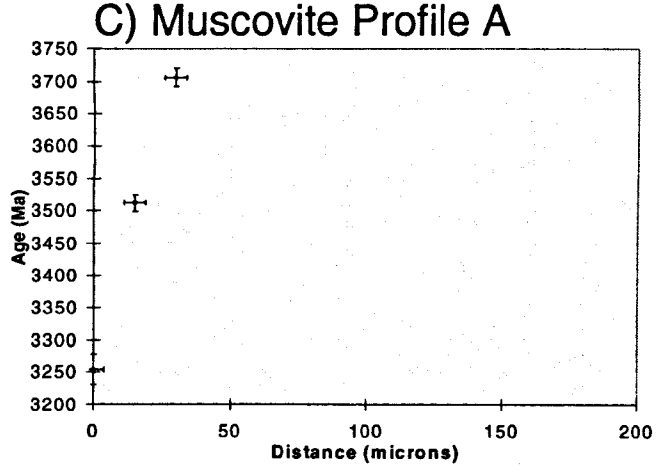

Figure 8.4: Profiles for 9-51 Biotite and Muscovite

Of the 24 age profiles produced for South Madison Range samples 13 showed younger ages at the edge of the grain with a systematic increase in ages with distance across the grain. 13 profiles were made in biotite, of which 7 showed systematic age variations, and 11 profiles were made in muscovite, of which 6 showed systematic age variations.

8.5.2. Discussion

8.5.2.1. Excess Argon

Only sample 9-51 shows any evidence of excess argon. Profile B in biotite (Figure 8.4B) exhibited a rapid decline in ages from the rim into the grain suggesting that the rim may have excess argon within it, whereas profile A (Figure 8.4A) showed only ages younger than those seen at the edge of profile B and no variation with distance from the margin. Further evidence of excess argon is seen in the muscovite in this sample where ages exceeded 3200 Ma (Figure 8.4C). All other ages achieved for the Cherry Creek unit, both from this study and previous work (Wooden *et al.*, 1988; Erslev and Sutter, 1990; and Mueller *et al.* 1993) yield ages younger than 2950 Ma, suggesting that the 3200+ Ma ages have no geological meaning.

8.5.2.2. Disturbed Profiles

As mentioned in section 8.4.2 above, biotite in sample 8-104 (Pre-Cherry Creek Metamorphic Complex) was found to be disturbed, probably by the presence of a nearby localised mylonite zone, leading to preservation of an 1830 ± 4 Ma mixed (mean) age. Indeed, it is possible that this sample is also part of the wider band of complex age variations that separate the two parts of south-western Montana. None of the 4 profiles produced for this sample gave systematic age profiles and no information can be gained from them. Sample 8-114 also failed to produce profiles with systematic age variations so no further information can be gained for this sample.

8.5.2.3. Interpretation of the Profiles Produced

Samples SMR1, 8-152 and muscovite from 9-49 appear to be the samples least affected by the influences of features that might have caused resetting to occur so are most likely to provide

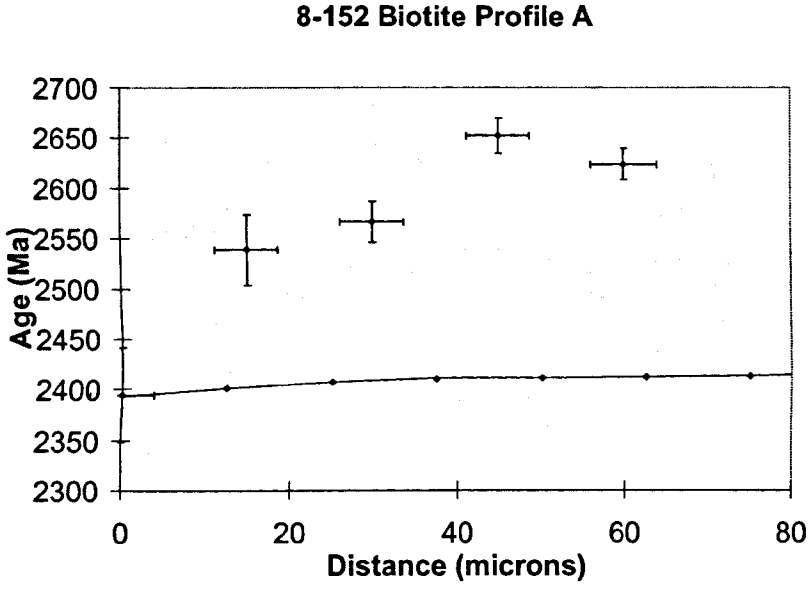

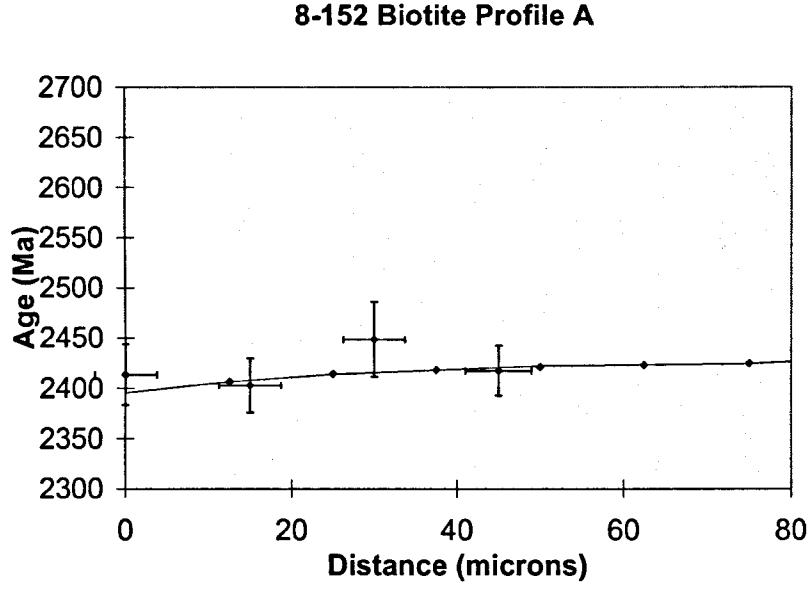

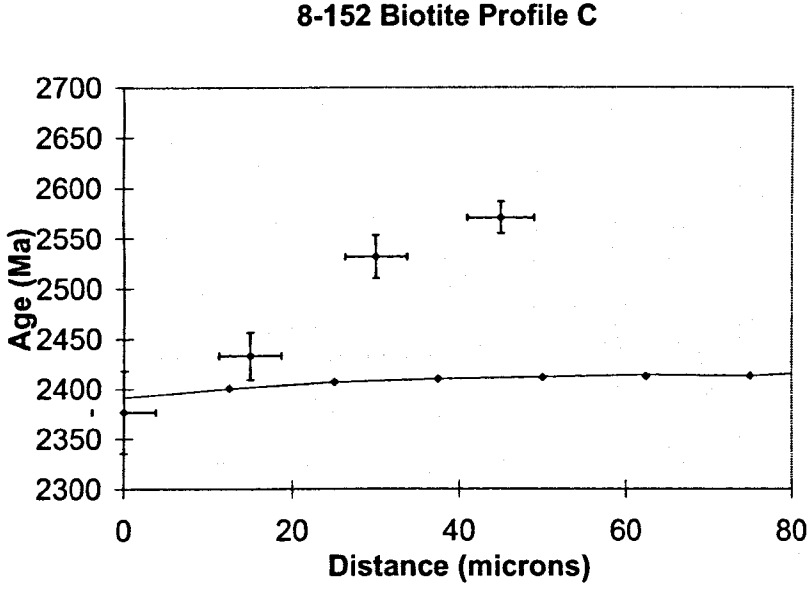

Figure 8.5: Profiles for 8-152 with theoretical 2.2 °C/m.y. linear cooling curve

information about the general cooling history of this area. Erslev and Sutter (1990) found that hornblende from the South Madison Range yielded an age of 2510 Ma and biotite an age of 2410 Ma. These were believed to be ages of cooling to closure temperatures of 500 and 280 °C respectively after a metamorphic maximum at approximately 2750 Ma. This is a drop of 220 °C in 100 m.y. between these two blocking temperatures, suggesting a mean cooling rate of 2.2 °C/m.y.

The program *DIFFARG* (Wheeler, 1996) was used to model a theoretical closure profile for a linear cooling history of 2.2 °C/m.y., in order to determine whether or not samples 8-152, SMR1 and 9-49 had actually undergone such a cooling history. A 250 μm grain size was used for simplicity, and the history was started at 400 °C for muscovite and 300 °C for biotite. It can be seen from Figures 8.5 that the biotite in sample 8-152 does not generally fit on the cooling curve, plotting above it instead, with only profile B and the edge points of profiles A and C reaching the values of the theoretical curve. This result suggests, as was proposed in section 8.4.2.2, that the biotite contains some excess argon. This suggestion is consistent with the biotite yielding a mean age older than the hornblende age obtained by Erslev and Sutter (1990).

The theoretical curve fits profiles A and D in sample SMR1 reasonably well, although the end point of profile D is too young (Figure 8.6). This suggests that for this sample the cooling rate is applicable. However, profiles C and E do not fit on the theoretical curve, indicating that these grains have been influenced by other factors. This might be related to the internal structures of the mineral grains or might reflect a more complex history for this sample, for example neocrystallisation related to the intrusion of granodiorite at c. 2020 Ma.

Figure 8.7 demonstrates that the theoretical linear cooling curve does not fit any of the profiles in sample 9-49. Here it can be seen that the although the points on the measured curves for the biotite reach the values for the theoretical curve towards the centre of the grain, considerably younger ages are recorded at the edge. These points cannot be modelled by simple linear cooling and imply that resetting has taken place.

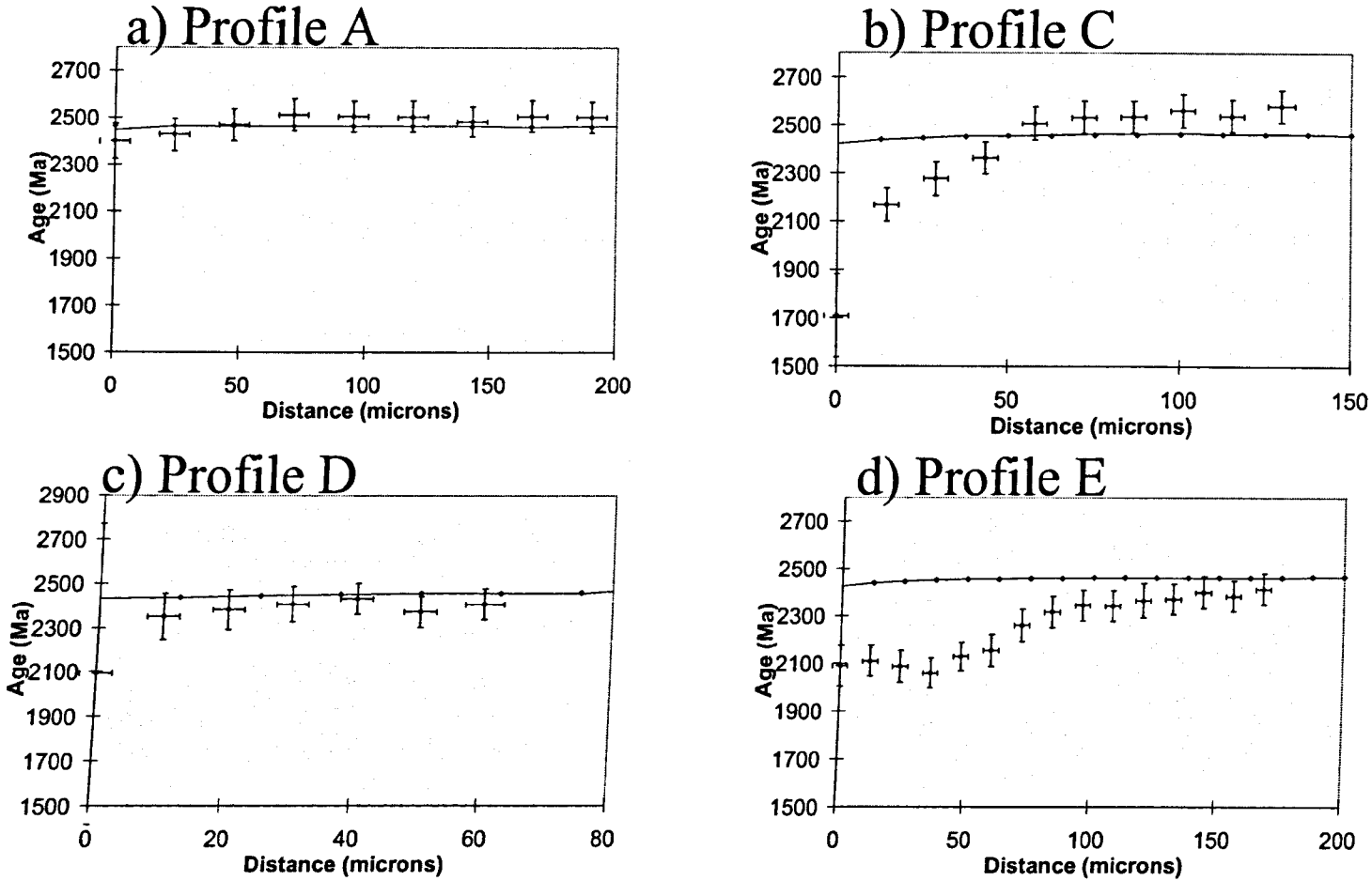

Figure 8.6: SMR1 profiles with theoretical 2.2 °C/m.y linear cooling curves

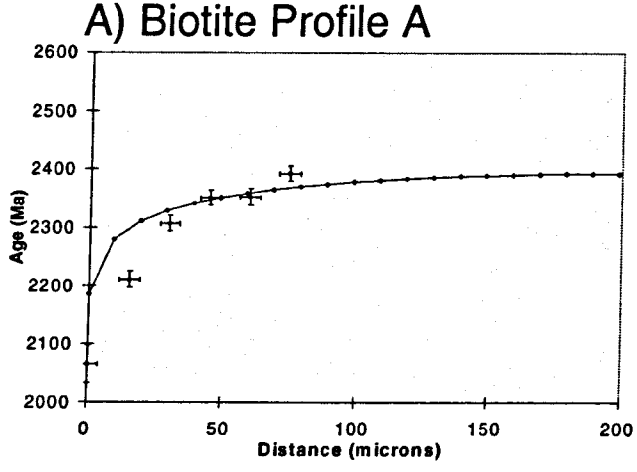

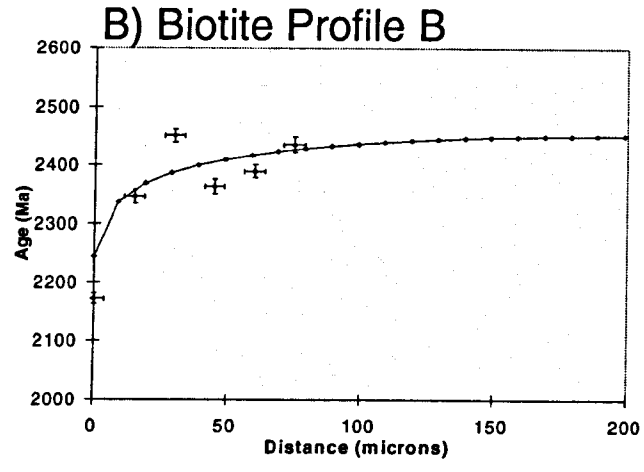

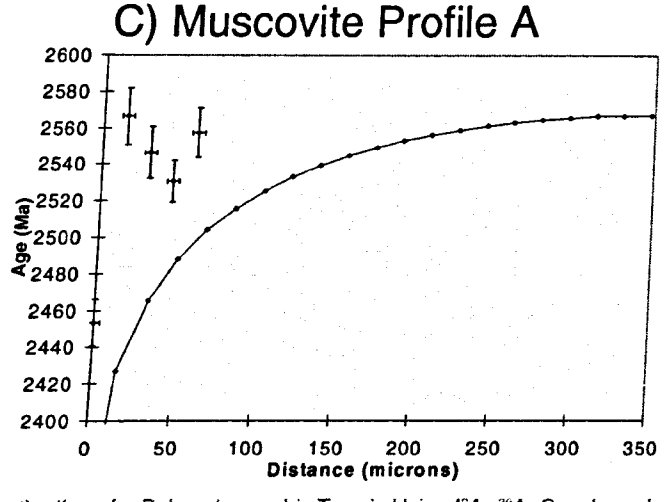

Figure 8.7: 9-49 Profiles with 2.2 °C/m.y Theoretical Closure Profile

The partial resetting scenario for samples 9-49 and 9.46 (section 8.4.2.1, above) was modelled using *DIFFARG* (Section 3.7.3). Initially models were attempted using a 2.2 °C/m.y. cooling rate from 350°C, through biotite blocking temperature, and down to 20°C. The intrusion was modelled at 2020 Ma, lasting for 10 m.y. followed by rapid cooling back to 20°C. This 2020 Ma age for the intrusion of the granodiorite was based on timing of intrusion inferred from mean ages from samples 9-51, 9-46 and 7-68 (8.4.2). The heating influence of the intrusion was adjusted until a fit was found with the measured curves produced for 9-49 and 9-46. As can be seen in Figure 8.8A an excellent fit is obtained for biotite in sample 9-49 when a temperature of 275°C for the heating influence of the intrusion is modelled. Unfortunately, a similar fit is not found when muscovite is modelled (Figure 8.8B). Higher temperature intrusion models were attempted for 9-46 as this is 1 km closer to the intrusion. Figure 8.9 demonstrates that although the intrusion model is a closer fit than simple linear cooling, the edge points of the measured profiles are still younger than can be obtained using this model since the model can only result in ages above 2020 Ma.

A second attempt was made to model the closure profiles, assuming an intrusion age of 1800 Ma. Again the heating influence of the intrusion was modelled at 275 °C for sample 9-49 but Figure 8.10 demonstrates that this is not as close a fit to the measured profile as an intrusion age at 2020 Ma. For sample 9-46 the heating influence of the intrusion was modelled at 300 and 325°C to account for the closer proximity to the intrusion of this sample and Figure 8.11 shows that these two temperatures give a reasonable fit to the measured profiles, therefore constraining the temperature of reheating at 1 km from the intrusion.

8.5.3. Conclusion

Again, as was found for the Ruby Range and Tobacco Root Mountains, not all profiles attempted gave the systematic age variations predicted. The possible reasons for this were discussed in section 5.4.3.3. and are not repeated here. However, the South Madison Range region appears to have undergone an extremely complex history that further influences the shape of the closure profiles. Although a linear cooling history appeared to fit two of the profiles, it is clear that closure

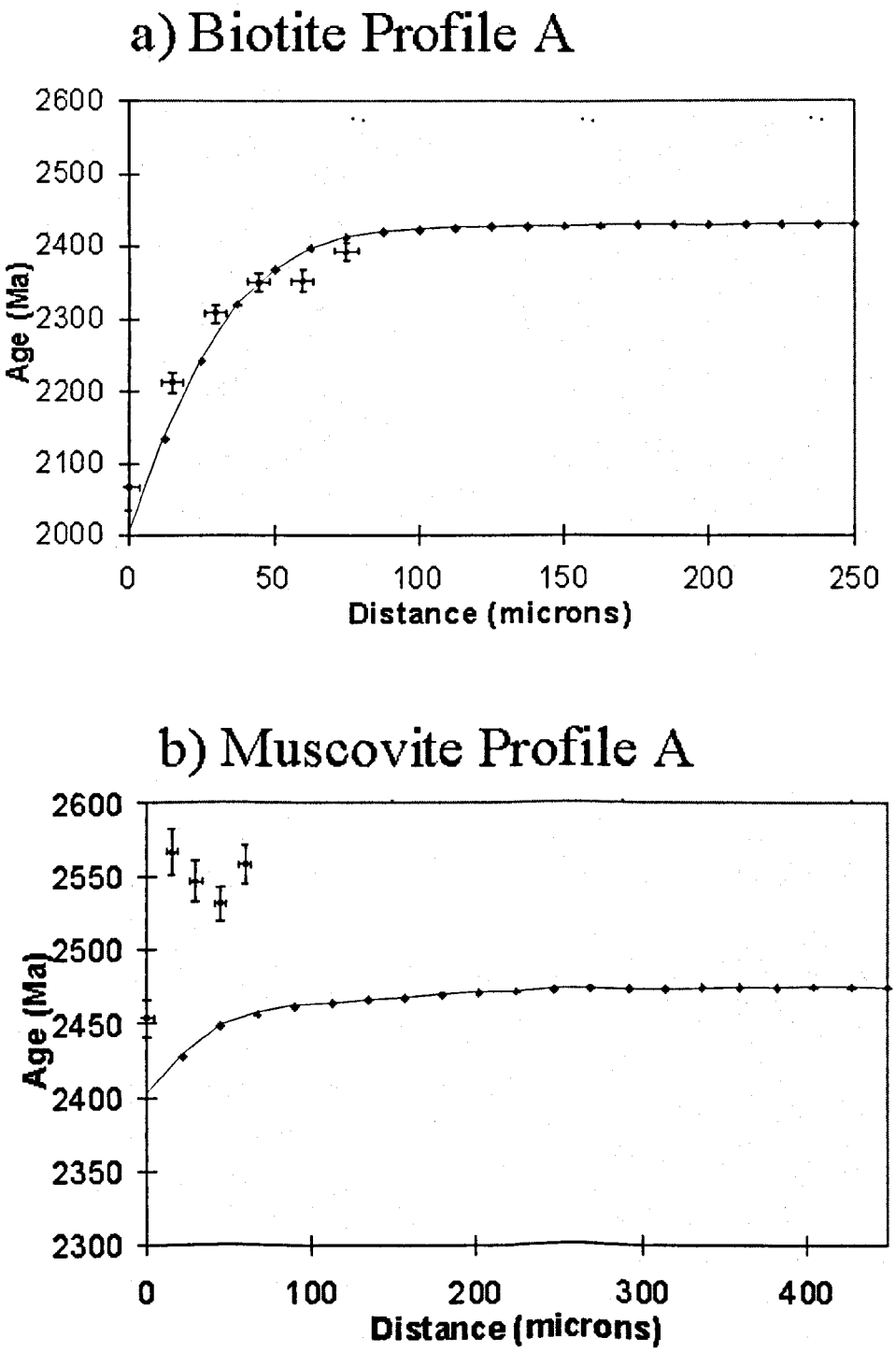

Figure 8.8: 9-49 biotite and muscovite profiles with intrusion model for 2020 Ma intrusion at 275 °C

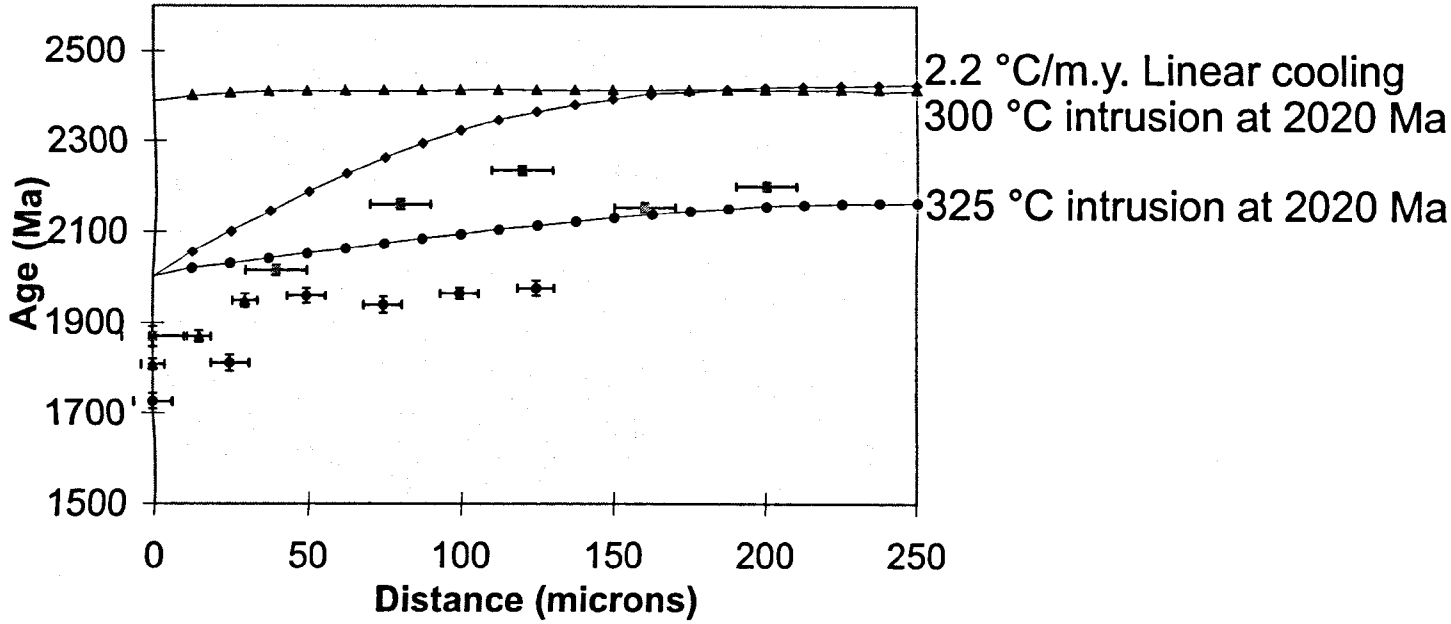

Figure 8.9: 9-46 Biotite profiles with 2.2 °C/m.y. closure profile, and 300 °C and 325 °C intrusion at 2020 Ma models

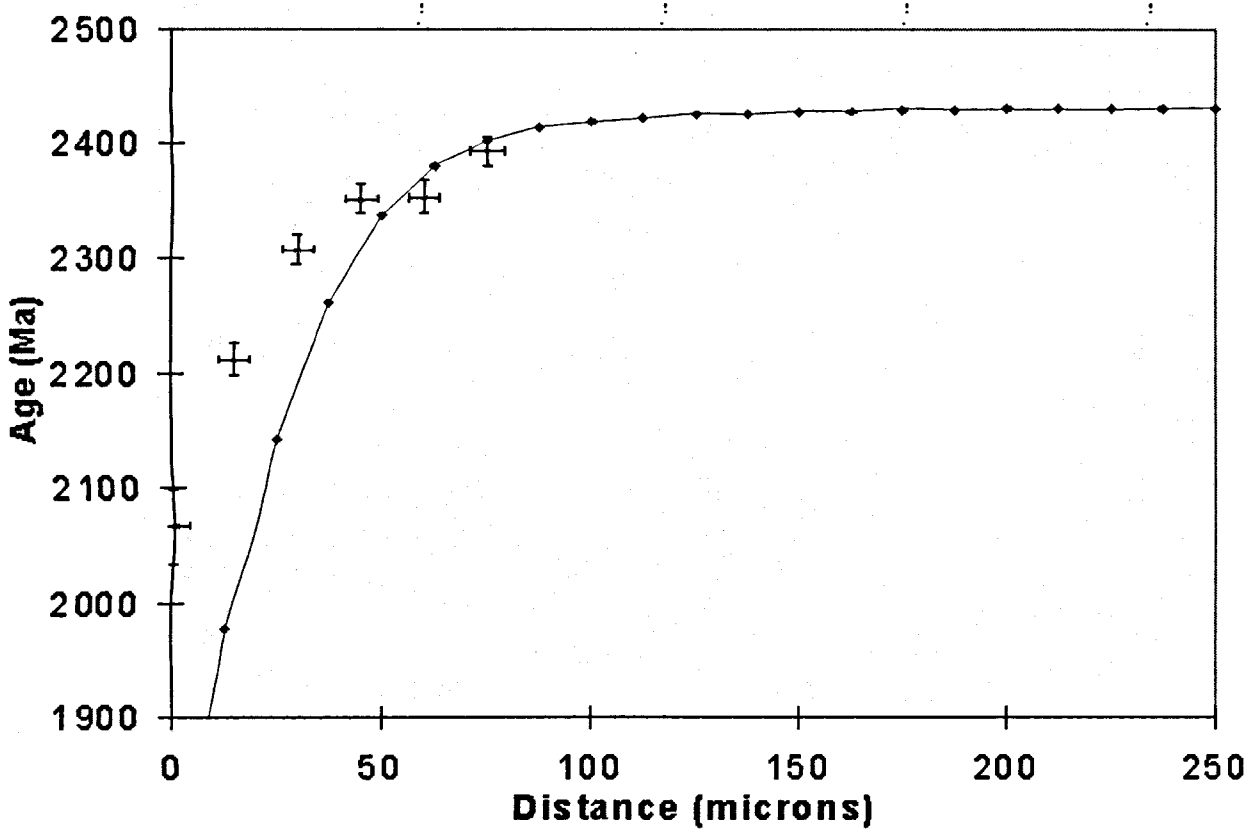

Figure 8.10: 9-49 biotite profile A with 275 °C intrusion at 1800 Ma

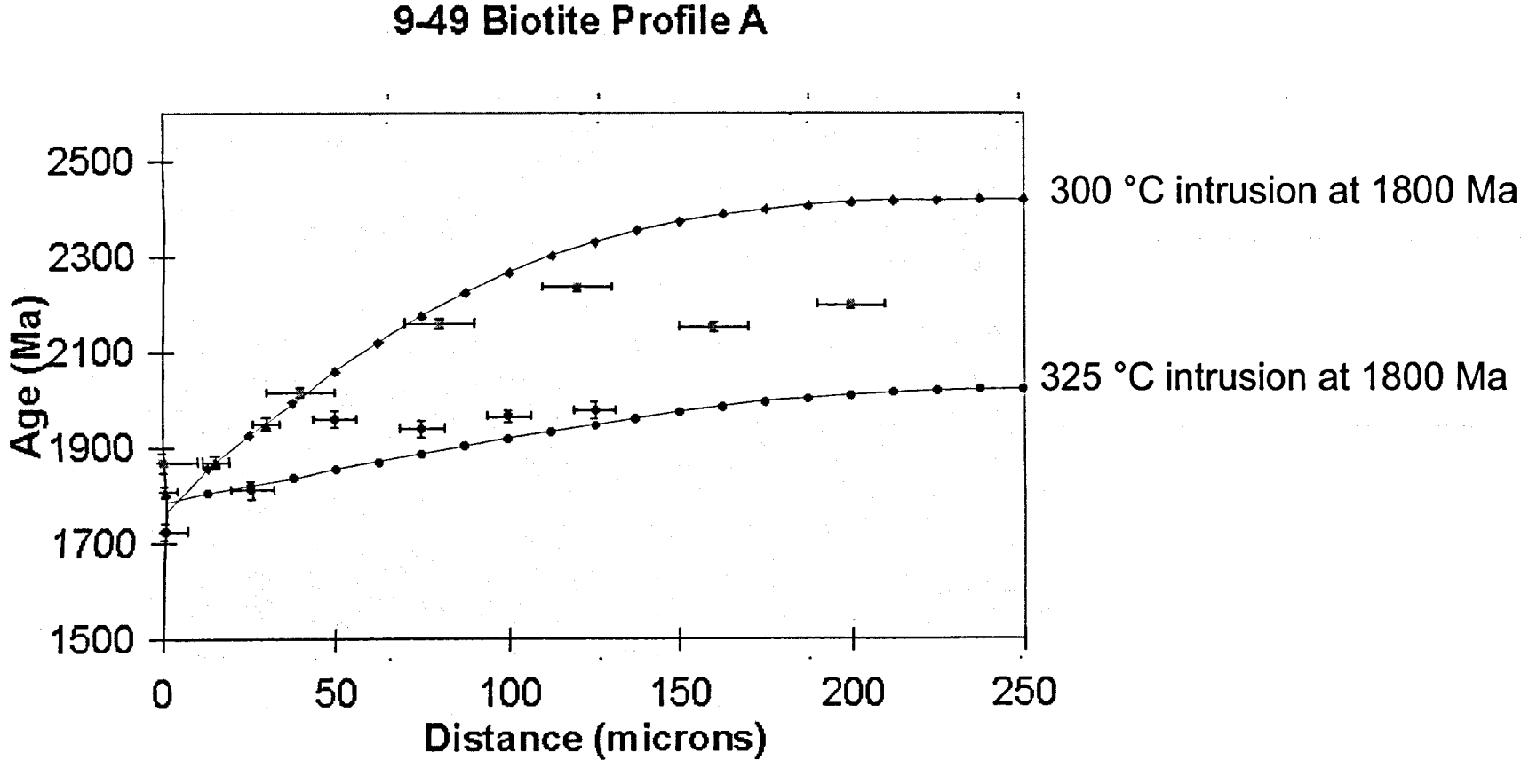

Figure 8.11: 9-46 Biotite profiles with 300 and 325 °C intrusion models at 1800 Ma

profiles generally record more information than just simple linear cooling. Unravelling this history can be difficult.

Using the experimentally obtained closure profiles it was possible to model the hypothesis of resetting caused by proximity to the intrusion as proposed in section 8.4. The modelling exercise demonstrated that simple scenarios cannot be successfully fitted to all the data obtained. However, modelling does help to eliminate some scenarios and can be used to provide some constraints for the geological history. In this instance, the models showed that simple linear cooling could not have produced the closure profiles measured, thereby supporting the notion that the rocks were reset. The models further suggest that that resetting event occurred between 1800 and 2000 Ma and heated the surrounding rocks to 275 °C up to 2 km away and to 300-325 °C 1 km from the intrusion. This further supports the earlier suggestion that the 2580 Ma U-Pb zircon age obtained for the intrusion by Shuster *et al.* (1987) dates inherited zircons rather than recrystallisation of the intrusion. Together with the data from the mean ages, particularly those from the Madison Mylonite Zone, a complex picture of the tectonic history begins to emerge for the South Madison Range, involving repeated mylonitization events and possibly several intrusion episodes, indicating a period of high tectonic activity here between 2000 and 1600 Ma.

8.5.4. Comparison Between Ruby Range and Tobacco Root Mountains Closure Profile Experiment to South Madison Range Closure Profile Experiment

8.5.4.1. Geological Histories

The region to the north-west of the Giletti line was extensively and thoroughly reset by Early Proterozoic tectonometamorphism, whilst the South Madison Range to the south-east has retained Archæan ages. Only those rocks reset by granodiorite intrusions or shearing in the South Madison Range record Early Proterozoic ages. However, it is possible that these ages can be related to ages and rock units found within the Ruby Range, Tobacco Root Mountains or Highland Mountains.

It is possible that the Quartzofeldspathic Gneiss and Granite Gneiss found within the Ruby Range and Tobacco Root Mountains could be related to the granodiorite intrusions within the South Madison Range. The origin of the Quartzofeldspathic Gneiss in both the Ruby Range and Tobacco Root Mountains has been disputed in the past by authors working in this region (Heinrich, 1960; Garihan and Okuma, 1974; Garihan, 1979a; 1979b; Vitaliano *et al.*, 1979; Karasevich *et al.* 1981; and James 1990) and it is unclear whether the units are predominantly sedimentary or igneous in origin. It is possible that these units include granite bodies that intruded at c.2020 Ma as part of a regional event that included the South Madison Range, Ruby Range and Tobacco Root Mountains. Whereas in the South Madison Range these ages were preserved, thorough reworking by the amphibolite facies event at c. 1780 to 1740 Ma within the Ruby Range and Tobacco Root Mountains would have reset the crystallisation date of these units as well as obscured their origins.

Another possible correlation could be between the timing of movement along the Madison Mylonite Zone and the ages of pegmatites with the Ruby Range and Tobacco Root Mountains. The c.1650 Ma age of rocks from the Madison Mylonite Zone dated in this study are in close agreement with 1611 Ma (biotite) and 1671 Ma (muscovite) mean apparent ages obtained for sample RMC42 from the Ruby Range believed to have been reset by an adjacent pegmatite (section 7.4). This age is supported by Giletti (1966), who dated muscovite in a pegmatite in the Tobacco Root Mountains and found K-Ar muscovite of 1643 Ma and Rb-Sr muscovite and feldspar ages of 1640 and 1672 Ma respectively. These ages are widely distributed over the region which would suggest a regional event that had a far reaching influence. In the Black Hills, Nabelek and Liu (1999) proposed shear heating to account for post-tectonic magmatism (including pegmatites) related to the Proterozoic Trans-Hudson orogeny. It is possible that a similar scenario can be applied in the south-western Montana portion of the Wyoming Province, linking the movement along the Madison Mylonite shear zone with the emplacement of pegmatites to the north-west of the Giletti Line.

8.5.4.2. Diffusion Mechanisms in Biotite and Muscovite

It is well known that biotite loses or gains Ar more readily than muscovite although the specific reasons for this have not been extensively investigated. Dahl (1996) suggested that one possible reason for this is that higher abundance of interlayer vacancies in biotite compared to muscovite means that fewer lattice distortions are needed for an Ar atom to diffuse out of the grains. For this

reason it is possible that muscovite would be more likely to preserve closure profiles than biotite. In this study, from both the Ruby Range and Tobacco Root Mountains region (Chapter 5) and the South Madison Range, a total of 51 profiles were made in biotite and 16 in muscovite. Of these only 18 profiles in biotite were successful whereas 9 of the profiles in muscovite showed the predicted shape of a cooling curve. Furthermore, in biotite grains that had the youngest ages at the edge, apparently random age variations were found away from the rim area, whereas in muscovite the almost constant ages from core to near rim predicted by the Dodson (1986) equation were found. This would indeed suggest that the diffusion mechanisms for argon in these two mica species are different.

The possibility that biotite consists of a number of subgrains bounded by fast diffusion paths is discussed in sections 5.4 and 5.5 and could account for the apparently random age variations seen throughout the grain. Similar variations are not as commonly observed in muscovite, suggesting that muscovite does not comprise a series of subgrains or that the subgrains are larger.

Evidence for alteration affecting the age of biotite is outlined in section 7.2 and is potentially another reason why biotite fails to produce closure profiles. Clauer (1981) found that although biotite in progressively more weathered samples lost more ^{40}Ar, the Ar balance in muscovite was maintained as long as no crystallographic changes occurred in the mineral structure. This means that biotite could have anomalously young ages even when only slightly weathered, whereas muscovite ages are maintained even during very intensive weathering. This was supported by Dahl (1996, and references therein) who reported that the relatively lower K - O bond strength inferred for biotite versus muscovite means that biotite is consistently more susceptible than muscovite to diagenetic alteration and K loss during weathering. Therefore, the susceptibility of biotite to alteration could significantly affect the apparent ages of a biotite grain and could cause apparently random age variations within a grain that distort and mask the profile produced by volume diffusion. Although it may be due to the geological difference between the South Madison Range and the Ruby Range/Tobacco Root Mountains rather than mineralogy, none of the muscovites studied showed any evidence of alteration, supporting the notion that muscovite is less prone to alteration than biotite.

One of the difficulties associated with interpreting closure profiles is discerning whether the profile is caused by slow cooling or reheating. One way to distinguish reheating from cooling profiles is by using the known geological history of the area. Hodges *et al.* (1994) interpreted their age variations as cooling because there was no evidence for a heat source close by. In the polymetamorphic rocks of the Wyoming Province, with its abundance of igneous intrusions, the possibility that the rocks have been reheated needs to be considered when attempting to fit a closure profile. As demonstrated with samples RRCR3 (from the Ruby Range) (section 5.4) and 9-46 (section 8.5), for example, reheating was indicated as an influential factor because the shape of the age profile was too steep to have been caused by simple linear cooling. In the case of sample 9-46 this was supported by the presence of a nearby granodiorite intrusion, and for RRCR3 the reheating could have been caused by the Belt basin rifting event to the west of the region.

8.5.4.3. Sample Format and Grain Size

Two other factors which may influence whether or not a closure profile is found are sample format (thick section or mineral separates) and grain size. Of the samples analysed from the South Madison Range, only SMR1 was analysed as separates and of the 5 profiles attempted 4 were successful. The other samples were analysed as thick sections, producing 19 profiles of which 9 were successful. When these results are combined with those from the Ruby Range and Tobacco Root Mountains it is found that 52% of the profiles that were from mineral separates were successful compared to 55% from thick sections. This reiterates the conclusion drawn in section 5.4.3.3 that loss of the true grain boundary during the crushing and separating processes is only a minor problem.

If volume diffusion was the only diffusion mechanism in operation then only rapid cooling would prevent a cooling profile from forming in micas. Clearly, then, multipath diffusion (as defined by Lee, 1995) (section 3.7.4) or the influence of subgrains must have an affect. Lee (1995) predicted that as the grain size increased, so would the abundance of multipaths and in larger grains multipath diffusion may override the controls of volume diffusion, resulting in cooling ages and closure temperatures that were dependent, instead, on effective diffusion dimension. Wright *et al.* (1991) measured the relationship between apparent ages and grain size and found that smaller grains yielded younger ages but that grains larger than about 225 μm yielded similar ages (section 3.7.4).

This, they believed, suggested that the effective diffusion dimension never exceeded 225 μm. If this were the case, then in mineral grains over about 225 μm closure profiles would be absent. In this research it was not possible to measure the radius of the basal section in grains that were analysed in non-basal section in thick sections. However, the visible part of the grains were measured and this gives an indication of the scale of the mica. Figure 8.12 shows the relationship between the dimensions of the mica and whether the profile had a systematic age variation from the grain edge. This shows that there is no apparent relationship between size of the grain and success of the profile. This suggests that multipaths that may disturb the distribution of argon within a grain are present in all grain sizes and that subgrains (in biotite at least) are smaller than the 225 μm size inferred by Wright *et al.* (1991).

8.6. Overall Conclusions

8.6.1. South Madison Range Geological History

It has become evident that the South Madison Range underwent a complex metamorphic history that is apparent both from mean age analysis and through the production of closure profiles. This history has been partially resolved by this study by determining a 2020 to 1800 Ma age range for the intrusion of granodiorites, and a new c.1650 Ma age for timing of movement along the Madison Mylonite Zone. Clearly then, the South Madison Range was very active between 2020 and 1650 Ma and it seem likely that only a fraction of the events occurring in this time frame can now be detected by geochronological techniques.

None of the ages found in the South Madison Range can be found within the rocks studied to the north-west of the Giletti Line and vice-versa. This would suggest that these two regions have

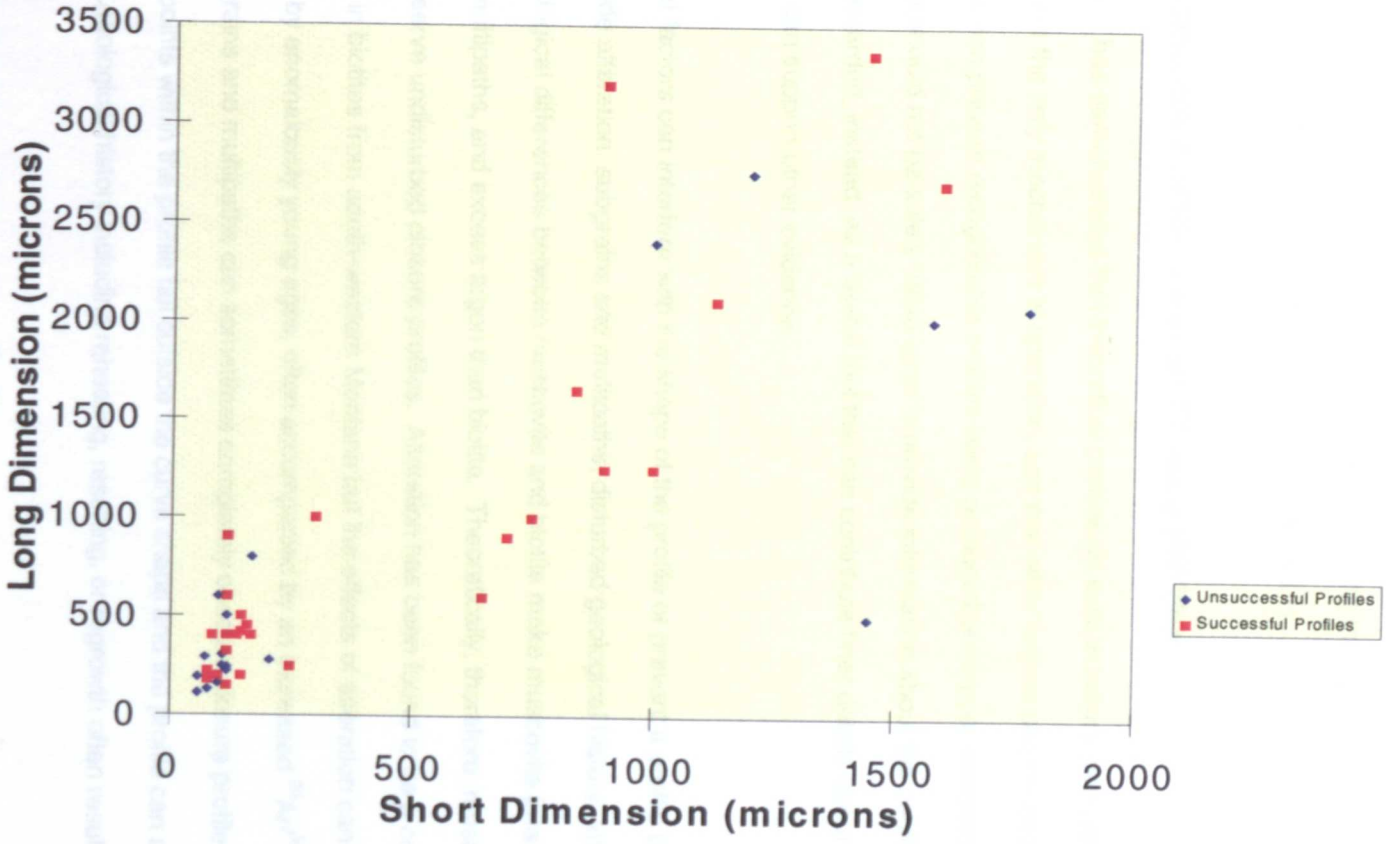

Figure 8.12: Relationship Between Mica Dimensions and Success of Profiles

undergone different geological histories. However, stratigraphic correlation by Erslev (1988) across these two regions, together with related Pb systematics reported by Mogk *et al.* (1992), suggests that the two regions are closely related. Therefore, it seems likely that the two areas were involved in intracratonic reorganisation rather than accretion of exotic terranes, as proposed by Mogk *et al.* (1992).

In this research no clear geochronological boundary that might mark the discontinuity between the two regions was found, so the specific boundary between the two geochronological regions is still unknown. However, it is proposed, instead, that the two geochronological regions are separated by a wide band of complex age variations rather than the single line defined by the Giletti Line, possibly related to the series of shear zones and mobile belts occurring through the centre of the south-western Montana portion of the Wyoming Province (Figure 8.1).

8.6.2. Assessment of the Value of Closure Profiles

This research has demonstrated that theoretical profiles do exist in natural samples, that volume diffusion is not the only mechanism in operation, and that other factors cause distortion of the profile shape. This can prevent recognisable profiles being produced or hamper interpretation. Because of this, profiles should not be solely relied upon to provide information about the cooling history but should be regarded, instead, as a useful tool that can contribute finer details about the geological history and can support other evidence.

A number of factors can interfere with the shape of the profile or prevent a profile being produced. These include alteration, subgrains and multipaths, disturbed geological history, and excess argon. The mineralogical differences between muscovite and biotite make muscovite less prone to alteration, multipaths, and excess argon than biotite. Theoretically, therefore, muscovite is more likely to preserve undisturbed closure profiles. Alteration has been found to be a common occurrence in biotites from south-western Montana but the effects of alteration can usually be recognised by anomalously young ages, often accompanied by an increased $^{36}Ar/^{39}Ar$ ratio (section 7.2.). Subgrains and multipaths can sometimes completely obscure closure profiles, but usually only one or two points within the profile fall outside the curve shape and the profile can still be interpreted. A disturbed geological history including reheating, resetting, or regrowth often results in a steeper

decline in ages at the edge of the profile than can be produced by simple linear cooling. If the cause of the reheating/resetting is known then this can be modelled using a piece-wise history in *DIFFARG*. The amount of excess argon varies in different areas but is fortunately only a minor problem within south-western Montana and has only occasionally influenced the shape of a profile or increased the ages within a profile. Other factors that could potentially prevent the detection of closure profiles are 1) the loss of true edges during sample preparation when analysing mineral separates, and 2) grain size - with larger grains having more multipaths than smaller. However, this research has found that these factors have only very minor effects.

Chapter 9 - Precambrian Tectonic Overview of South-western Montana

9.1. Proterozoic Tectonics of North America

Below is a summary of the Proterozoic tectonics pertinent to the south-western Montana study area. It is not an exhaustive history of Proterozoic accetionary or other collisonal events related to the formation of Laurentia but is designed to give a brief summary of some of the wider tectonics.

The Precambrian tectonics of the North American continent are concerned primarily with the formation of the Laurentian supercontinent, until the rifting events at the end of the Proterozoic that gave North America its approximate present day shape. In addition to North America, Laurentia included Greenland and north-west Scotland until their separation in the Late Cretaceous.

Laurentia was formed from the aggregation of seven former Archæan microcontinents, namely the Superior, Wyoming, Slave, Nain, Hearne, Rae and Burwell provinces (Figure 9.1). These provinces were welded together by Early Proterozoic collisional orogens, active between 2000 and 1750 Ma (Figure 9.1). These orogens were characterised by deformed passive margins, deformed foredeep sedimentary prisms, and foreland thrust-fold belts (Hoffman, 1989; and references therein).

Hoffman (1989) reported that the oldest igneous suites associated with formation of the supercontinent were intruded between 1850 and 1650 Ma in the interior of the Archæan protocraton while tectonic accretion was ongoing at its margins. Between 1500 and 1100 Ma, anorogenic gabbro-anorthosite-granite suites were intruded in the eastern part of the Archæan protocraton, and widespread syenogranite-rhyolite suites were emplaced in the southern and south-western parts of the Early Proterozoic accreted terranes. Finally, between 1300 and 1100 Ma scattered alkaline igneous complexes and extensive mafic dyke swarms penetrated the craton, the latter feeding

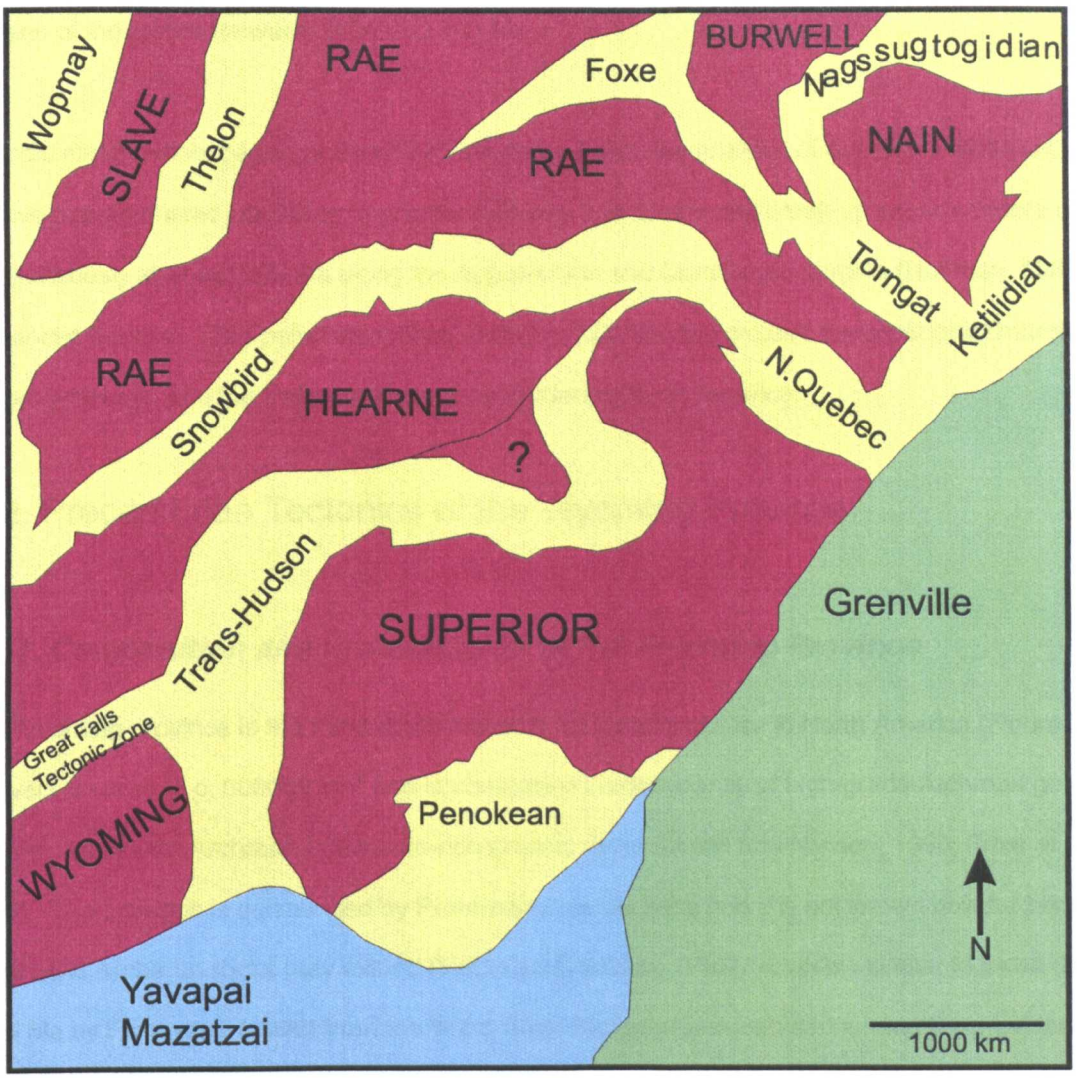

Figure 9.1: Orogenic age map of central Laurentia
(modified from Hoffman, 1989)

plateau lava fields. Deep localised sedimentary basins formed along the western and northern margins of the craton between 1600 and 800 Ma.

Episodic rifting events began at about 800 Ma and subsidence analysis of the early Palaeozoic passive margin prisms bordering Laurentia indicates that continental break-up occurred more or less simultaneously at about 600 Ma along the Appalachian and Cordilleran margins (Hoffman, 1989; and references therein). This polyphase rifting ended by 500 Ma and created the continental margins that would evolve into the Palaeozoic orogens bordering North America.

9.2. Precambrian Tectonics of the Wyoming Province

9.2.1. Composition and Cratonisation of the Wyoming Province

The Wyoming province is the most south-western Archæan province in North America (Figure 9.1). It covers an area of c. 500000 km^2 and is composed predominantly of high-grade Archæan gneiss and deformed Late Archæan potassium-rich granitic rocks (Dutch and Nielsen, 1990; Frost *et al.*, 1998). The province is surrounded by Proterozoic mobile belts and it is not known how far beneath these belts Archæan rocks may extend (Dutch and Nielsen, 1990). Granites similar to those dated at 2800 Ma by Frost *et al.* (1998) from the Wind River Range are widespread across the province. They are derived predominantly from pre-existing crust but have also involved the incorporation of substantial amounts of isotopically juvenile material either from depleted mantle or younger continental crust.

The chemical/isotopic signatures of the Wyoming and Superior provinces are very different (Dahl *et al.*, 1999a and references therein) indicating that these two provinces are discrete entities. The main distinction of the Wyoming Province from other Archæan provinces in North America is its lack of granite-greenstone associations. In addition, where other provinces, such as Superior and Slave, reflect the progressive assembly of arcs and small plates to form a craton, isotopic evidence suggests that the Wyoming province cratonised before 3000 Ma and was repeatedly reworked during an extensive later Archæan history (Frost *et al.*, 1998 and references therein). Evidence for this older crust is indirect, coming from detrital zircons. For example, Mueller *et al.* (1992) obtained 3960

Ma ages from zircons from quartzite in the Beartooth Plateau using U-Pb dating, and Aleinikoff *et al.* (1989) produced an age of c.3800 Ma from zircons from paragneiss-rich migmatites from the Wind River Range.

Prior to the formation of Laurentia (i.e. pre-1900 Ma) the movement and location of the Wyoming microcontinent is unknown. However, Dahl *et al.* (1999a) constrained the timing of the collision of Wyoming province with the Superior continent to be within the interval from ≤ ~1770 Ma to ~1715 Ma within the western Dakotas, whereas in south-western Montana the collision between the Wyoming and Hearne Provinces is believed to have begun at ~1820 Ma.

9.2.2. The Boundaries of the Wyoming Province

The most likely location of the boundaries of the Wyoming Province is discussed in detail by Dutch and Nielsen (1990), and a summary of their findings is below.

9.2.2.1. Southern Boundary

The southern boundary of the Wyoming Province is the best located and understood boundary around the province. It can be found within the Cheyenne Belt as a south-east dipping shear zone of ~1780-1740 Ma island-arc accretion (Chamberlain, 1998, as referenced in Dahl *et al.*, 1999a) (Figure 9.2). The shear zone is up to 7 km wide and separates two significantly different Proterozoic sequences. North of the shear zone is the Snowy Lake Supergroup believed to represent a transgressive continental margin sequence, progressing upwards from fluvial facies through deltaic to marine carbonate facies. Within this lithology are poorly dated widespread dykes and sills that appear to represent a rifting episode between 2200 Ma and 1900 Ma. The rocks to the south of the shear zone are dominated by bimodal calc-alkaline volcanic rocks and volcanogenic sediments of the Green Mountain Formation. These rocks are characterised by unusual mafic intrusives that may represent dismembered fragments of ophiolites. The common occurrence of syntectonic felsic intrusives (dated around 1780, 1700 and 1650 Ma) suggest that the

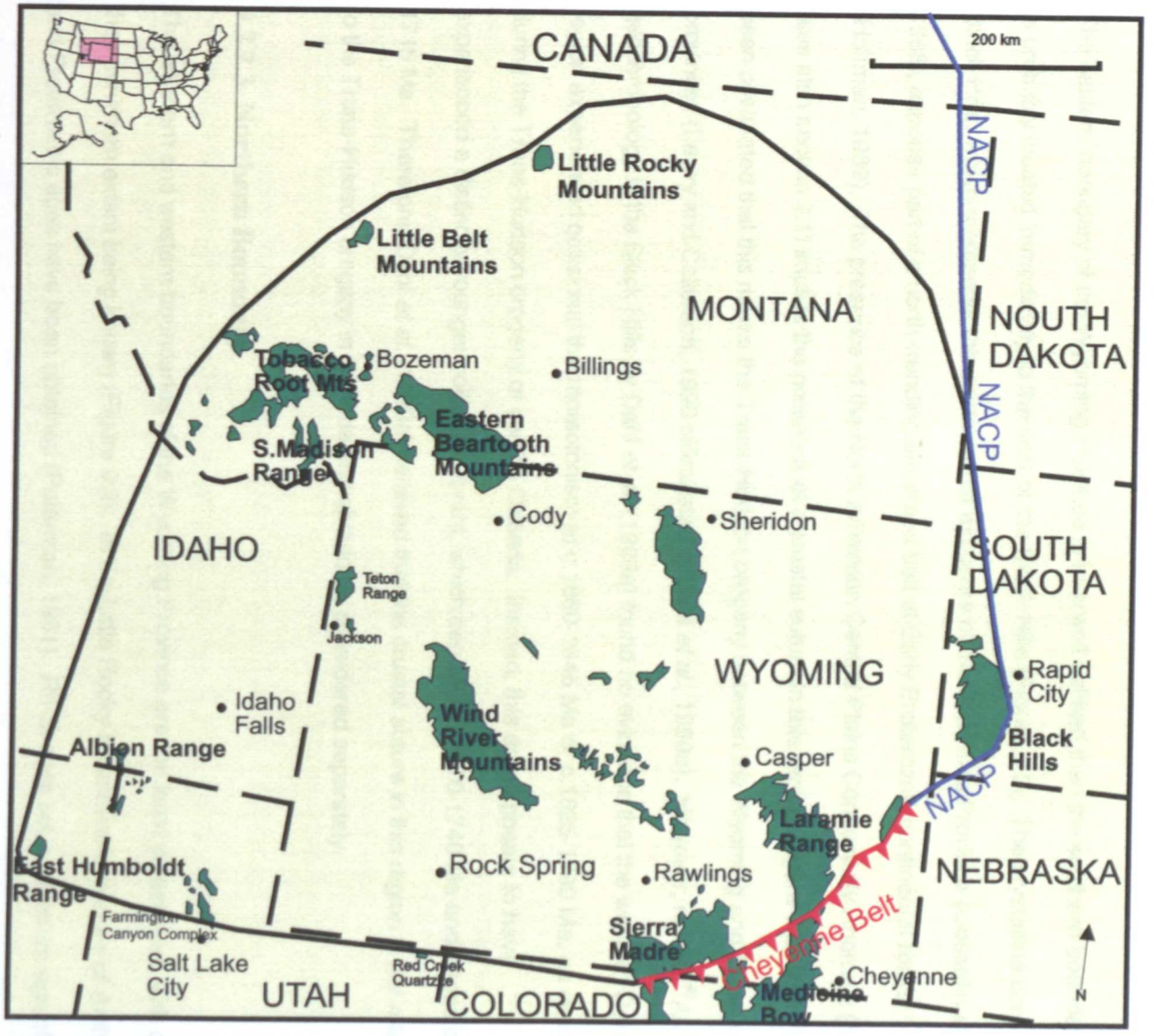

Figure 9.2: Map of the Wyoming Province showing the inferred boundaries (exposed boundary shown in red)
(modified from Dutch and Nielsen, 1990)

southern assemblage may have been a volcanic arc complex over a south-dipping subduction zone. Sm-Nd dating attempts failed to detect any Archæan basement south of the shear zone.

The southern boundary can be traced around to the Red Creek Quartzite located where Utah, Colorado and Wyoming meet (Figure 9.2). This unusual lithology was interpreted by Hansen (1965, referenced in Dutch and Nielsen, 1990) as having formed on a stable, slowly subsiding shelf, and schists within the unit have a Rb-Sr age of 2320 Ma. It is believed that the Red Creek Quartzite has a similar tectonic setting to the Cheyenne Belt, i.e. northward directed overthrusting probably due to collision of the Wyoming block with a south-dipping subduction zone.

9.2.2.2. Eastern Boundary

The eastern boundary of the Wyoming Province is less well defined than the southern boundary but is probably located immediately to the east of the Black Hills (Figure 9.2). The crystalline core of the Black Hills, which represents the easternmost exposure of the Wyoming Province (Gosselin *et al.*, 1988), exposes part of a north-trending deformed belt of Early Proterozoic continental rocks (Hoffman, 1989). The presence of the North American Central Plains Conductivity Anomaly (NACP) (see also section 2.1) implies the presence of a crustal suture in this region (Figure 9.2) and it has been postulated that this marks the Trans-Hudson orogeny between the Wyoming and Superior provinces (Lewry and Collerson, 1990 referenced in Dahl *et al.*, 1999a). However, recent ^{40}Ar-^{39}Ar geochronology in the Black Hills by Dahl *et al.* (1999a) found no evidence that the western Dakotas region experienced collisional thermotectonism at c.1860-1845 Ma or c.1825-1790 Ma, as occurred during the Trans-Hudson orogeny of central Canada. Instead, this area appears to have experienced a distinctly younger collisional event, which began at c.1770-1740 Ma and ended by 1715 Ma. Therefore, Dahl *et al.* (1999a) believed that the crustal suture in this region is not related to the Trans-Hudson orogeny in Canada and should be considered separately.

9.2.2.3. Northern Boundary

The northern and western boundaries of the Wyoming Province are the least understood, with only their minimum extent being known (Figure 9.2). In the Little Rocky Mountains a mixture of Archæan and Proterozoic ages have been obtained (Peterman, 1981). Rb-Sr data set a minimum age of 2550

Ma for the rocks in this area. Although this is not a precise isochron it is believed that these rocks are Archæan. K-Ar ages fall in the range of 1750 to 1700 Ma because of Proterozoic resetting. This implies that the Wyoming Province boundary is not far away. Indeed, reworked Archæan rocks from the Little Rocky Mountains along the north-east trending Great Falls tectonic zone (Figure 9.1) have yielded ~1750-1715 Ma mineral dates (K-Ar dating of hornblende and biotite; Peterman, 1981). This is considered as provisional evidence of an ~1800 Ma thermotectonic overprint. In the Little Belt Mountains, north-easterly structural trends, extensive cataclasis and mafic intrusives similar to those south of the Cheyenne Belt suggest that the north-western margin of the Wyoming Province is nearby.

9.2.2.4. Western Boundary

The exposures of south-western Montana play a key part in defining the north-western extent of the Wyoming Province but this area is discussed in more detail in section 9.3 below. The south-western limit of the Wyoming Province is defined by several exposures of Archæan and Proterozoic crystalline rock in Utah and Nevada. These include the Albion Range, the East Humboldt Range and the Farmington Canyon Complex (Figure 9.2). Phanerozoic thrusting has caused tectonic disruption to much of Utah and this hinders interpretation of the Proterozoic assemblages within Utah.

9.3. Precambrian Tectonics of South-western Montana

9.3.1. Introduction

Early radiometric dating in this region suggested an age gradation from Archæan in the Beartooth Mountains to Proterozoic in the Tobacco Root Mountains, Ruby Range and Highland Mountains (Giletti, 1966; Wooden *et al.*, 1978; DePaolo and Wasserburg, 1979; Vitaliano *et al.*, 1979; Wooden and Mueller, 1988; Wooden *et al.*, 1988; Erslev and Sutter, 1990; Mueller *et al.*, 1992; 1993; Brady *et al.*, 1994.). However, the 2760 ± 115 Ma Rb-Sr isochron age found by James and Hedge (1980) in the Tobacco Root Mountains and Ruby Range suggested that in this region Archæan crust had been reworked by an Early Proterozoic collisional event. Dahl *et al.* (1999a) have proposed that a collision causing orogenic heating and metamorphism occurred between the Wyoming and Hearne Provinces at ~1820 to 1800 Ma and that the Great Falls tectonic zone was the continental suture (Figure 9.1).

The present research was initiated on the basis that the 2760 Ma age of quartzofeldspathic gneisses obtained by James and Hedge (1980) dated M1 granulite facies metamorphism, and that the M2 amphibolite facies event occurred between 1800 and 1600 Ma (Giletti, 1966; Arth *et al.*, 1986; O'Neill *et al.*, 1988; Brady *et al.*, 1994; Harlan *et al.*; 1996; and Kovaric *et al.*, 1996). In this case, ^{40}Ar-^{39}Ar dating of matrix mica would confirm the 1800 to 1600 Ma age, PbSL dating of garnets might record the 2760 Ma age, and biotite inclusions in garnet might also reflect the earlier age. Clearly, the 1800 to 1600 Ma age has been confirmed by this study. Unfortunately, no evidence has been found in this research to confirm the existence of the Archæan age metamorphic event. A near-Archæan age for garnet from sample TRMR2 using PbSL dating is most likely dominated by detrital monazite.

In the light of these findings, the validity of the 2667 ± 66 Ma (Mueller and Cordua, 1976), and 2760 ± 115 Ma (James and Hedge, 1980) Rb-Sr whole rock ages is questionable. These ages were believed to date the timing of M1 metamorphism in this region and to show conclusively that the major stratigraphic sequences of the region are Archæan in age. The study by James and Hedge (1980) produced a whole rock isochron using quartzofeldspathic rocks collected from the Tobacco Root Mountains, North Madison Range, Ruby Range and Gallatin Range, and included the samples analysed by Mueller and Cordua (1976). They acknowledged that the lithological character of the Precambrian terrane differs between these mountain ranges, particularly in the amount and nature of material of recognisable sedimentary origin. However, they believed that the apparent general homogeneity in structure, degree of metamorphism, and presence of quartzofeldspathic gneiss across the area was sufficient to consider these mountain ranges as continuous. They also accepted that dating metasedimentary rocks, or sequences with an appreciable component of original sediments, presents problems. Those mentioned by James and Hedge (1980) were:

1) material derived from different geological terranes may be of different ages and may have different initial ratios of $^{87}Sr/^{86}Sr$;

2) sediments generally contain appreciable contents of water which, during metamorphism, is an effective medium of diffusion of elements, resulting in an open system.

Despite these obvious difficulties, probable differences in ultimate origin, and separation of around a hundred kilometres the samples were considered by James and Hedge (1980) to represent a single population. However, for these reasons, these age data cannot be considered sound and, because this age has not been substantiated by this or other regional geochronological studies, it should be discounted. There is, therefore, no evidence that these rocks were metamorphosed at c.2760 Ma or even that they were deposited in the Archæan.

9.3.2. Archæan and Proterozoic Relationships

Because of the lack of any credible evidence to suggest that the rocks of the Ruby Range, Tobacco Root Mountains, and Highland Mountains are Archæan in origin, the possible origins of this terrane and the implications for the Wyoming Province need to be re-evaluated.

Firstly, even though the Rb-Sr whole rock age obtained by James and Hedge (1980) is extremely questionable, it is still possible that the rocks of the Ruby Range, Tobacco Root Mountains, and Highland Mountains are thoroughly reworked Archæan basement. In this model, the most likely boundary for the Wyoming Province is the Great Falls tectonic zone, as proposed by Dahl *et al.*, (1999a). Thorough Proterozoic reworking during the 1820-1740 Ma orogeny completely reset all geochronological systematics, and/or minerals such as mica and garnet were crystallised during this high-grade metamorphic event.

However, the lack of Archæan rocks in the Ruby Range, Tobacco Root Mountains and Highland Mountains may be due to these rocks being Proterozoic in origin. Indeed, Dutch and Nielsen, (1990) considered the abundance of marble, quartzite and iron formation in the supracrustal rocks of south-western Montana to be more typical of Proterozoic than Archæan stratigraphy. It is most likely that the rocks of these mountain ranges are a Proterozoic sedimentary sequence deposited in a passive margin environment on Archæan basement. In this case, a possible source for the sediments could be the tonalite-trondhjemite-granodiorite rocks of the Beartooth Mountains. This would constrain the timing of deposition to between the c.2800 Ma age of the Beartooth Mountains (DePaolo and Wasserburg, 1979; Wooden and Mueller, 1988; Wooden *et al.*, 1988; Mueller *et al.*, 1992), and the 1820 Ma age of the oldest garnets in the Ruby Range (Dahl and Frei, 1998). If the Beartooth Mountains were the source of the sediments then, if the James and Hedge (1980) date means

anything at all, it might relate to the age of the source rocks, thus yielding an age comparable to the age of the Beartooth Mountains orogeny. Further, this would allow the rocks of the BBMT and MMT to have the same distinctive common Pb systematics as reported by Mogk *et al.* (1992), despite being of different ages.

From this Late Archæan/Proterozoic origin, two possible tectonic environments might lead to the geochronological situation now observed.

Firstly, during the collision between the Wyoming and Hearne Provinces along the Great Falls tectonic zone, the Proterozoic sediments and underlying basement were deformed together, resulting in an extremely complex boundary between rocks of Archæan and Proterozoic origin. For example, some (if not all) of the quartzofeldspathic gneiss in these mountain ranges may be reworked Archæan basement derived from tonalite-trondhjemite-granodiorite similar to that seen in the Beartooth Mountains. The obvious supracrustal rocks (i.e. quartzite, iron formation, marble etc.) would represent a Proterozoic cover sequence now tectonically intercalated with the reworked Archæan basement. Thus, any contact between quartzofeldspathic gneiss and supracrustal rocks might be an Archæan and Proterozoic boundary.

Alternatively, a thick sequence of Proterozoic supracrustals were metamorphosed and deformed in the Ruby Range, Tobacco Root Mountains and Highland Mountains during the collision of the Wyoming and Hearne Provinces. In this case, the quartzofeldspathic gneiss is part of the Proterozoic sequence, with the sediments sourced from the Beartooth Mountains and metamorphosed for the first time at c.1820 Ma. The boundary between the Archæan and the Proterozoic rocks would now occur somewhere around the Giletti Line. Although no contacts between the Archæan and Proterozoic rocks have been identified in this area, it is possible that the boundary is beneath the Phanerozoic rocks separating the Precambrian uplift blocks, or that the contact is exposed but not yet identified.

9.3.3. Archæan Metamorphism

By using ^{40}Ar-^{39}Ar dating a number of events within the complex geological history of this region have been dated and these events, and evidence supporting their ages, are considered here and in the following sections.

As discussed above, there is no reliable evidence to support an Archæan metamorphic event within the Ruby Range, Tobacco Root Mountains, and Highland Mountains. In contrast, apparent Archæan ages in the South Madison Range are readily detectable using several different techniques, including Rb-Sr, ^{40}Ar-^{39}Ar, Sm-Nd, U-Pb and Pb-Pb (Wooden *et al.*, 1988; Erslev and Sutter, 1990; Mueller *et al.*, 1993, Vargo, 1990; this study). Clearly, then, an Archæan event, of at least amphibolite grade, occurred in this part of south-western Montana. From the data presented in Chapter 8 it seems likely that cooling from this metamorphic peak was protracted and, as they passed through the blocking temperature of biotite, the rocks cooled at a rate of about 2 °C/m.y.

The existence of Archæan apparent ages in the South Madison Range confirms the validity of Giletti's (1966) geochronological division through south-western Montana separating Proterozoic apparent ages in the west and north from Archæan in the east and south. However, the reason for this division is still unknown and can only be speculative. It seems likely that the Giletti Line (1966) comprises a wide band of complex age variations, possibly related to the shear zones and mobile belts that run parallel to it (Figure 8.1).

9.3.4. Intrusion of Granodiorites

The younger apparent ages and shape of the closure profiles produced for mica in rocks within 1 to 2 km of granodiorite intrusions within the South Madison Range (Figure 8.3) suggested that these intrusions had a resetting influence on the surrounding rocks. From modelling the closure profiles it was inferred that the granodiorites were intruded at about 2020 Ma and had heated the country rock to 275 °C up to 2 km from the intrusion.

9.3.5. Movement Along the Madison Mylonite Zone

Erslev and Sutter (1990) suggested an age of between 1900 and 1800 Ma for mylonitized rocks from the Madison Mylonite Zone. New ages from the same area in this study suggest that the shear zone within the South Madison Range was active at c.1650 Ma. Together, Erslev and Sutter's (1990) age and this new age suggests that the Madison Mylonite Zone was active from c.1800 to at least c.1650 Ma.

9.3.6 Proterozoic Metamorphism

New data from this study (as outlined in Chapter 5) support the findings of previous authors that a metamorphic event took place in the Ruby Range, Tobacco Root Mountains and Highland Mountains between 1800 and 1600 Ma (Giletti, 1966; Brady *et al.*, 1991; Brady *et al.*, 1994; Kovaric *et al.*, 1996; and Harlan *et al.*, 1996). However, the new data suggest that the timing of this metamorphism can be constrained between 1820 Ma (PbSL garnet age) and 1740 Ma (^{40}Ar-^{39}Ar biotite age). This was clearly a widespread and penetrative thermotectonic event that thoroughly reworked supracrustal rocks in the Ruby Range, Tobacco Root Mountains and Highland Mountains. It is possible that metamorphism occurred due to the collision of the Wyoming Province with the Hearne Province along the Great Falls Tectonic Zone as proposed by Dahl *et al.* (1999a). Dutch and Nielsen (1990) reported that Proterozoic ages can be found in most exposures on the periphery of the Wyoming Province (section 9.3.2.2), and the Proterozoic ages found in south-western Montana may indicate that this region is close to the boundary.

Given the absence of Archæan ages it is perhaps necessary to reinterpret the timing of the metamorphic events discussed in section 2.7.4.2 to fit into the Proterozoic time-frame. Mueller and Cordua (1976) and Vitaliano et al. (1979) found textural and field relations suggesting that three metamorphic events had occurred within the Tobacco Root Mountains. Mueller and Cordua (1976) showed these to be an M1 granulite facies event, an M2 upper amphibolite facies event, and an M3 greenschist facies event. They inferred that their 2667 ± 66 Ma Rb-Sr whole rock age dated the M2 event, but that M1 and M2 were not greatly separated in time. In contrast, Vitaliano et al. (1979) believed Mueller and Cordua's (1976) age dated the timing of the granulite facies event and inferred the ~1600 Ma age produced by Giletti (1966) to be the timing of the amphibolite facies event.

However, Vitaliano *et al.* (1979) also pointed out that Immega and Klein (1976) believed that the granulite and amphibolite events could have been part of a single multiphase thermal event. With no sound evidence of an Archæan event, however, a reinterpretation might be that the granulite (M1) and amphibolite (M2) facies events were indeed closely related in time or part of a multiphase event. According to this scenario, the 1780 to 1740 Ma ^{40}Ar-^{39}Ar biotite ages date the M2 event, and the 1820-1808 Ma PbSL garnet ages may date the earlier M1 event. In this case, some biotite inclusions in M1 garnet might have been shielded from resetting by the M2 event whereas matrix micas were not shielded. However, given the closeness in time between the M1 and M2 events the mica age differences are indistinguishable from each other outside error.

9.3.7 Intrusion of Pegmatites

A pegmatite dated from the Tobacco Root Mountains by Giletti (1966), yielded a K-Ar muscovite age of 1643 Ma and Rb-Sr muscovite and feldspar ages of 1640 and 1672 Ma respectively (corrected for decay constants after Steiger and Jäger, 1977). The coincidence of the mean apparent mica ages of 1611 ± 8 (biotite) and 1671 ± 6 (muscovite) from sample RMC42 adjacent to a late, undeformed pegmatite (section 7.4) and the age of such pegmatites in this area strongly suggested that the mica in this sample had been reset by the same event that gave rise to the pegmatite intrusion. This age is also coincident with the later age of movement along the Madison Mylonite Zone and it is possible that localised tectonism occurring at this time reactivated the Madison Mylonite Zone and shear heating, similar to that proposed by Nabelek and Lui (1999) in the Black Hills, along the Madison Mylonite Zone could have given rise to late pegmatite intrusions in the Ruby Range and Tobacco Root Mountains.

9.3.8. The Formation of the Belt Basin and Associated Events

9.3.8.1. The Belt Basin

The Belt basin is a north-westerly trending elongate depositional trough, extending from British Columbia to Idaho and Montana (Figure 9.3). It is believed to have begun forming around 1500 Ma (Evans, 1986; and references therein). Continental crust underlying the Belt basin was cut by a network of nearly west-trending extensional faults (the Perry, Garnet and Jocko Lines, Figure 9.3),

separating the region into blocks. During regional extension central blocks subsided to form the Belt basin, and other blocks rose to form the bordering source areas that fed sediments to the basin (Figure 9.3) (Winston, 1986). Initial tectonic subsidence of the Belt basin was accompanied by the inundation of the Belt "sea" that extended to, and in some cases beyond, the bounding faults of the basin (Winston, 1986). The north-east/south-west extension that formed the Belt basin lead to dyke emplacement, granite plutonism and activation of north-west trending faults. Influx of sediments from all source areas started with inundation of the "sea" and continued until after 1370 Ma. The oldest sedimentary deposits are in the northern Belt basin and consist of deep water turbidites that are locally intruded by mafic sills (O'Neill *et al.*, 1986). The Crossport C sill has been dated at 1430 Ma by Zartman *et al.* (1982; referenced in O'Neill *et al.* 1986), and places a minimum age on the oldest sedimentary rocks in the basin.

9.3.8.2. The Perry Line and LaHood Formation

The Perry Line is the southernmost of the major faults and marks the southern edge of the Belt basin. It separates the uplifted Dillon block of crystalline basement from the downdropped Belt basin blocks (Figure 9.3) (Winston, 1986). The Perry Line became a very steep shoreline during Beltian times and as the uplifted crystalline rocks of the Dillon block eroded, boulders were carried northwards into the basin and deposited in subaqueous fans along the Perry Line as the LaHood conglomerate (Winston, 1986). The LaHood formation is a 3500 m wedge of arkosic conglomerate, arkose and interbedded arkose, argillite and limestone, occurring towards the base of the Belt sediments. It outcrops along the southern margin of the Belt basin and now extends from the Bridger Range north of Bozeman to the western Highland Mountains south of Butte (Figure 9.3).

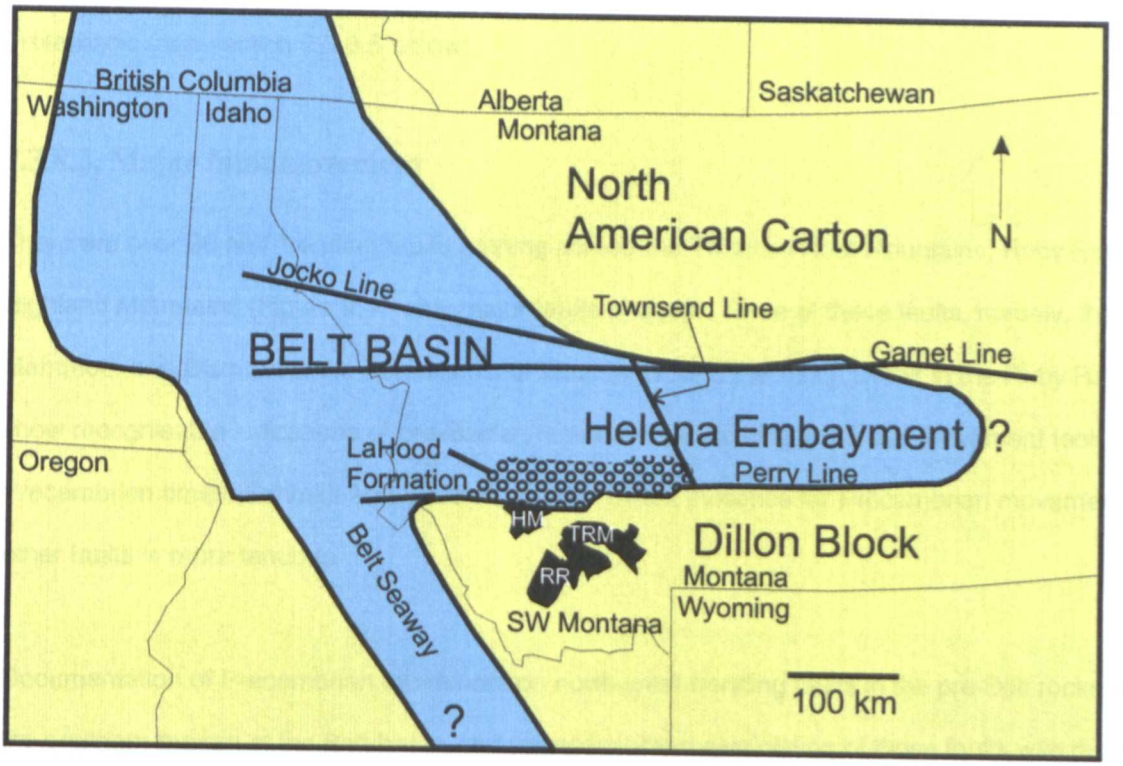

Figure 9.3: Generalised map of the extent of the Middle Proterozoic Belt basin in relation to the Precambrian uplift blocks (RR, TRM, HM) in south-western Montana
(modified from Winston,1986)

The LaHood formation provides evidence that the Dillon block was uplifted during the Late Proterozoic (see section 9.3.8.5 below).

9.3.8.3. Major fault movement

There are over 30 NW-trending faults running across the Tobacco Root Mountains, Ruby Range and Highland Mountains (Figure 9.4 - only major faults shown). Three of these faults, namely, the Mammoth and Bismark in the Tobacco Root Mountains, and the Hinch Creek in the Ruby Range, show recognisable indications of pre-Beltian movement, indicating that initial movement took place in Precambrian times (Schmidt and Garihan, 1986). Direct evidence for Precambrian movement on other faults is more tenuous.

Documentation of Precambrian movement on north-west trending faults in the pre-Belt rocks along the southern margin of the Belt basin, and the widespread association of those faults with mafic dykes of known or inferred Middle Proterozoic age (see below), establishes the north-west-trending fault set as an important tectonic element immediately south of the basin during its development. Schmidt and Garihan (1986) inferred that the fault movement was largely extensional and may have been related to the opening of the Belt basin itself. Wooden *et al.* (1978) suggested that the subsidence of the crust along the north-south Belt seaway (Figure 9.3) is indicated by the tensional opening of fractures subparallel to the sea in the Ruby Range. Furthermore, Wooden *et al.* (1978) inferred that the opening of fractures in the Tobacco Root Mountains was dominated by the subsidence of the Helena Embayment to the north (Figure 9.3). Belt age grabens in the Highland Mountains suggests that tectonism and sedimentation related to the formation of the Belt basin extended south of the present margin of the basin (O'Neill *et al.*, 1986, and references therein; Schmidt and Garihan, 1986).

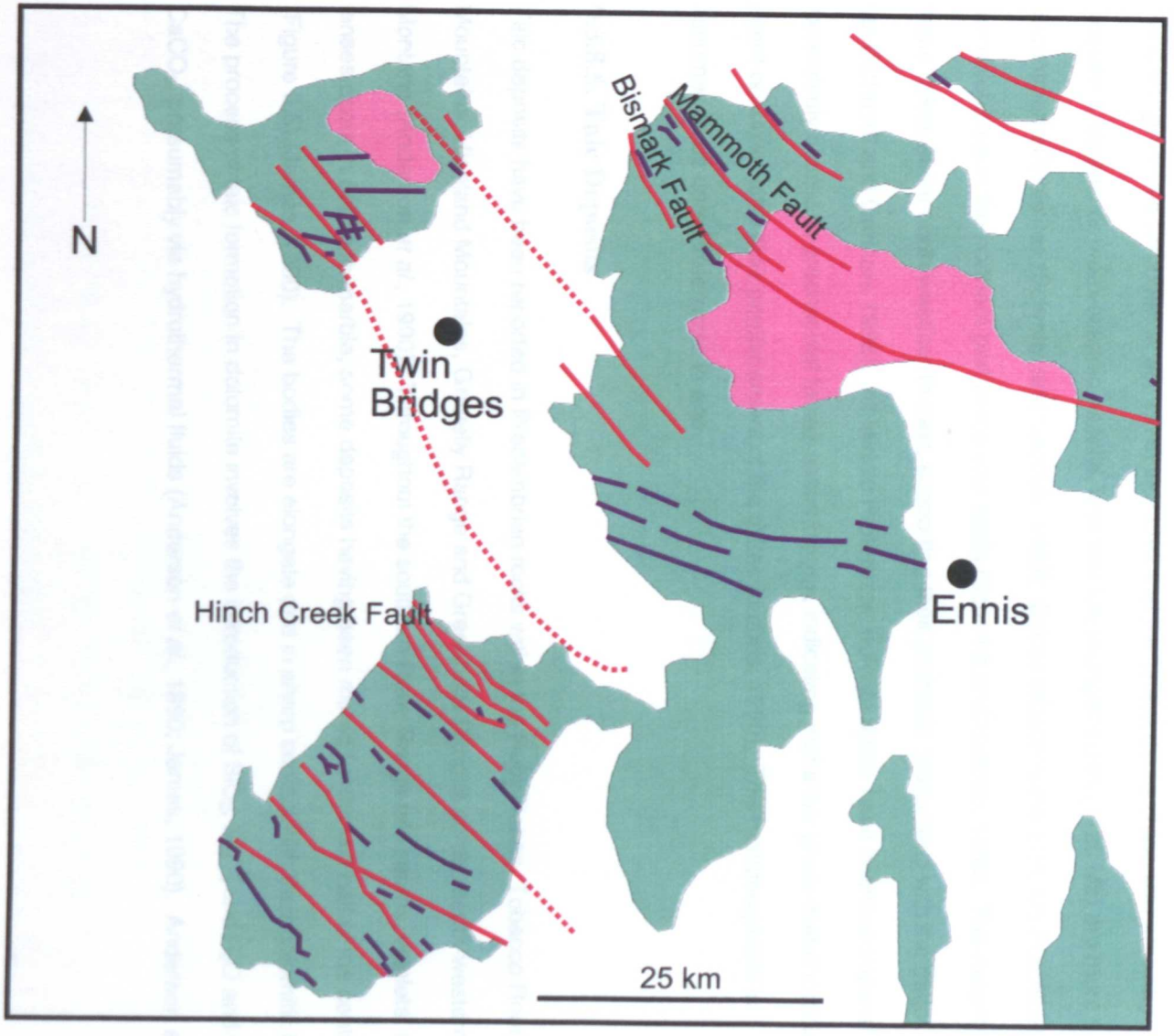

Tertiary basin sediments

Cretaceous plutons

Precambrian uplift blocks

Dykes

Faults

Figure 9.4: Location of major north-west trending faults and dykes in south-western Montana (modified from Schmidt and Garihan, 1986)

9.3.8.4. Intrusion of dykes

Two episodes of dyke emplacement at c.1455 ± 125 and 1120 ± 185 Ma (Rb-Sr whole rock dating) are recognised in the Tobacco Root Mountains and Ruby Range (Wooden *et al.*, 1978), and two sets of undated mafic dykes intrude the Precambrian rocks of the southern Highland Mountains (Figure 9.4) (O'Neill *et al.*, 1986). Most dykes with grain size and compositional characteristics similar to the dated dykes can either be shown to be Precambrian because they crosscut Archæan foliation and end at the Precambrian-Palaeozoic boundary, or are assumed to be late Precambrian because they have trends that parallel dykes of established late Precambrian age (Schmidt and Garihan, 1986). These episodes of dyke emplacement suggest at least one major episode of approximately north-east/south-west extension. The trace-element composition of the Tobacco Root Mountains and Ruby Range dykes (Wooden *et al.*, 1978) indicates that the oldest dykes (1455 Ma) probably represent oceanic or proto-oceanic basalts, whereas the younger dykes (1120 Ma) are more typical of continental tholeiites (Schmidt and Garihan, 1986). Dykes related to the 1100 Ma Purcell lavas are ubiquitous in the northern part of the Belt basin (Schmidt and Garihan, 1986). The majority of these dykes strike north-west/south-east, supporting their probable relationship with the major fault set (Schmidt and Garihan, 1986). All Middle Proterozoic dolerite dykes have been incompletely but extensively altered to greenschist facies assemblages, indicating that a low grade metamorphic event occurred after their emplacement of the dykes (James, 1990). This metamorphism is assumed to be Late Proterozoic in age.

9.3.8.5. Talc Deposits

Talc deposits have been reported in Precambrian rocks within the Ruby Range, Tobacco Root Mountains, Highland Mountains, Gravelly Range and Greenhorn Ranges across south-western Montana (Anderson *et al.*, 1990). Throughout the southern Ruby Range talc seams, veinlets, and lenses occur in dolomite marble, some deposits having been mined for the last half of the century (Figure 9.5) (James, 1990). The bodies are elongate and in sharp contact with their dolomitic host. The process of talc formation in dolomite involves the introduction of SiO_2, Mg^{+2}, and H_2O and loss of $CaCO_3$, presumably via hydrothermal fluids (Anderson *et al.*, 1990; James, 1990). Anderson *et*

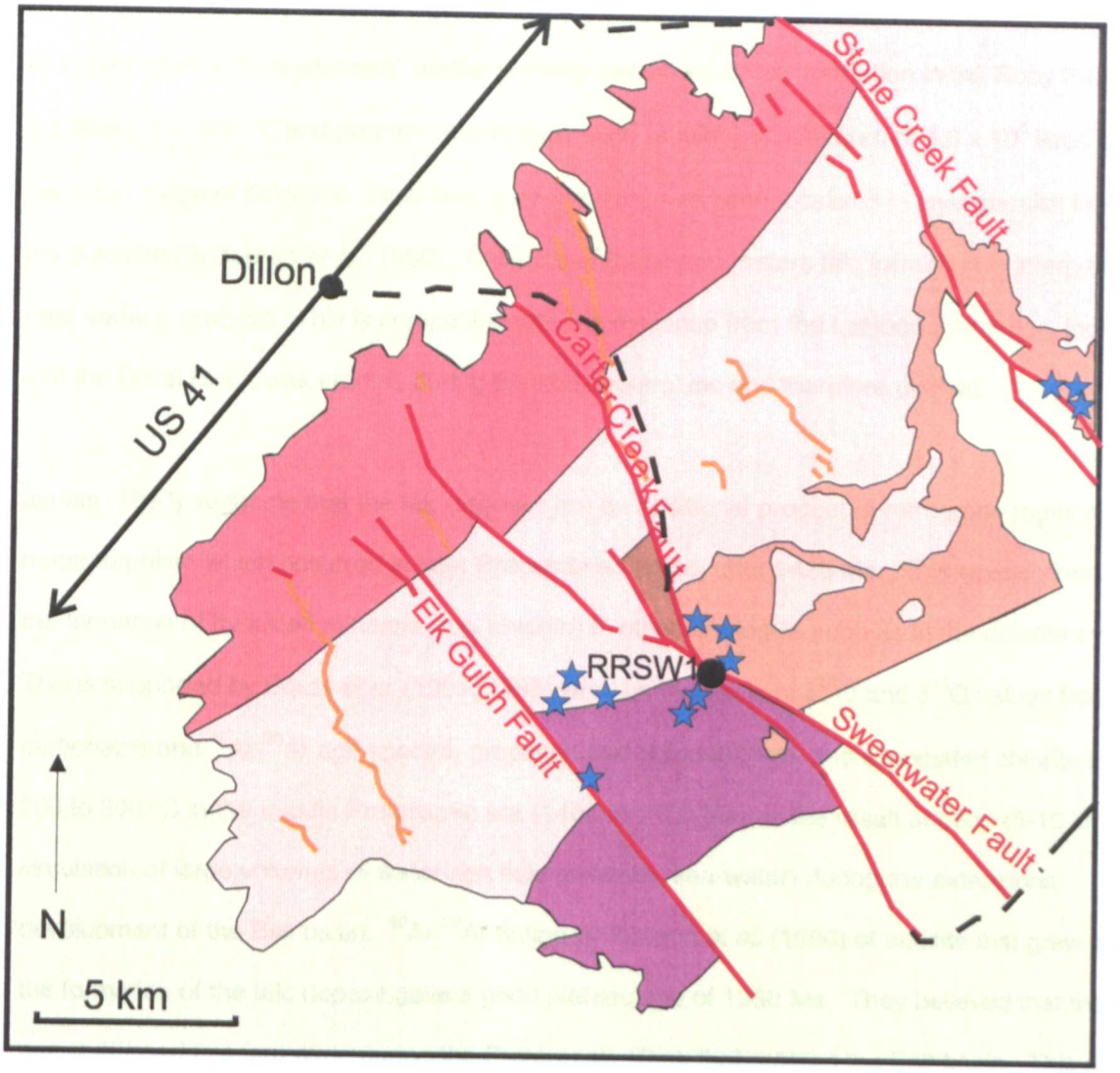

Figure 9.5: Location of sample RRSW1 and principal talc mines (blue stars) in southern Ruby Range (modified from James, 1990)

al. (1990) gave a "best estimate" for the physical conditions of talc formation in the Ruby Range as P < 2 kbars, T < 400 °C and probably much lower, and requiring a minimum of 4.8×10^5 litres of water per cubic metre of dolomite. Fluid flow is believed to have been localised in layer-parallel fractures in the dolomite (Anderson *et al.*, 1990). Because of these parameters talc formation is interpreted as a near-surface process. This is compatible with the evidence from the LaHood Formation, indicating that the Dillon Block was eroding during the Mid-Proterozoic and therefore uplifted.

James (1990) suggests that the talc deposits are an additional product of retrograde regional metamorphism which occurred in later Precambrian times, after 1425 Ma. This typically resulted in the formation of hydrated minerals (e.g. chlorite) in other lithologies such as in the dolerite dykes. This is supported by Brady *et al.* (1991; 1998) who, on the basis of $\delta^{18}O$ and $\delta^{13}O$ values from carbonates and ^{40}Ar-^{39}Ar age spectra, proposed that dolomite, talc, and associated chlorite formed at 200 to 300 °C in the middle Proterozoic era (1400 to 1100 Ma) as the result of deep (5-10 km) circulation of large volumes of water-rich fluid (probably sea-water) during the extensional development of the Belt basin. ^{40}Ar-^{39}Ar dating by Kovaric *et al.* (1996) of sericite that grew during the formation of the talc deposit gave a good plateau age of 1360 Ma. They believed that the sericite age confirmed talc formation during the Proterozoic rifting that created the Belt basin. This age is in good agreement with 1370 Ma U-Pb zircon dates on dolerite, diorite, and migmatites within a large magmatic complex at Salmon in east-central Idaho produced by Doughty and Chamberlain (1996). This they believed dated the East Kootenay orogeny, a tectonic event that resulted in magmatism, basin rifting, and renewed subsidence and sedimentation towards the end of deposition in the Belt basin.

Younger apparent ages found in samples RRSW1 and RRSW2 in this study can also be attributed to the affects of Belt basin tectonics within the Ruby Range. The presence of ^{36}Ar in these samples demonstrate that they have been affected by meteoric water. In addition, the presence of sericite, chlorite, clinozoisite and prehnite in sample RRSW1 is suggestive of low grade metamorphism, metasomatism or hydrothermal alteration. The presence of calcic minerals such as clinozoisite and prehnite in this sample (see particularly Plate 7.3B) suggests that this rock has experienced calcium metasomatism. This can be related to release of calcium into hydrothermal fluids during the conversion of dolomite to talc at this location (Figure 9.5).

9.3.9. Intrusion of Silicic Plutons

The Phanerozoic history of this region is not a principal concern of this research. However, during ^{40}Ar-^{39}Ar dating of rocks in close proximity to the Tobacco Root Batholith it became apparent that this major silicic Tertiary pluton had a resetting influence on the surrounding Precambrian gneisses. The youngest apparent age produced by resetting of biotite from samples within 0.25 km of the exposed extent of the pluton was 72 Ma, implying that the 74-71 Ma K-Ar age obtained by Vitaliano *et al.* (1979) correctly dated the emplacement of the pluton. The extent of complete or almost complete resetting of biotite is limited to within 0.25 km of the batholith and within this limit amphibole is not completely reset. Between 0.5 and 1 km only partial resetting occurs, and beyond that the samples are not reset. This indicates that the country rocks were heated to between 300 and 500 °C within 0.25 km of the pluton, but that beyond this distance the heating effect on the country rock quickly declined. This is consistent with the findings of Giletti (1966) who found the resetting influence of the batholith on the country rock to be intense but sharply limited in extent.

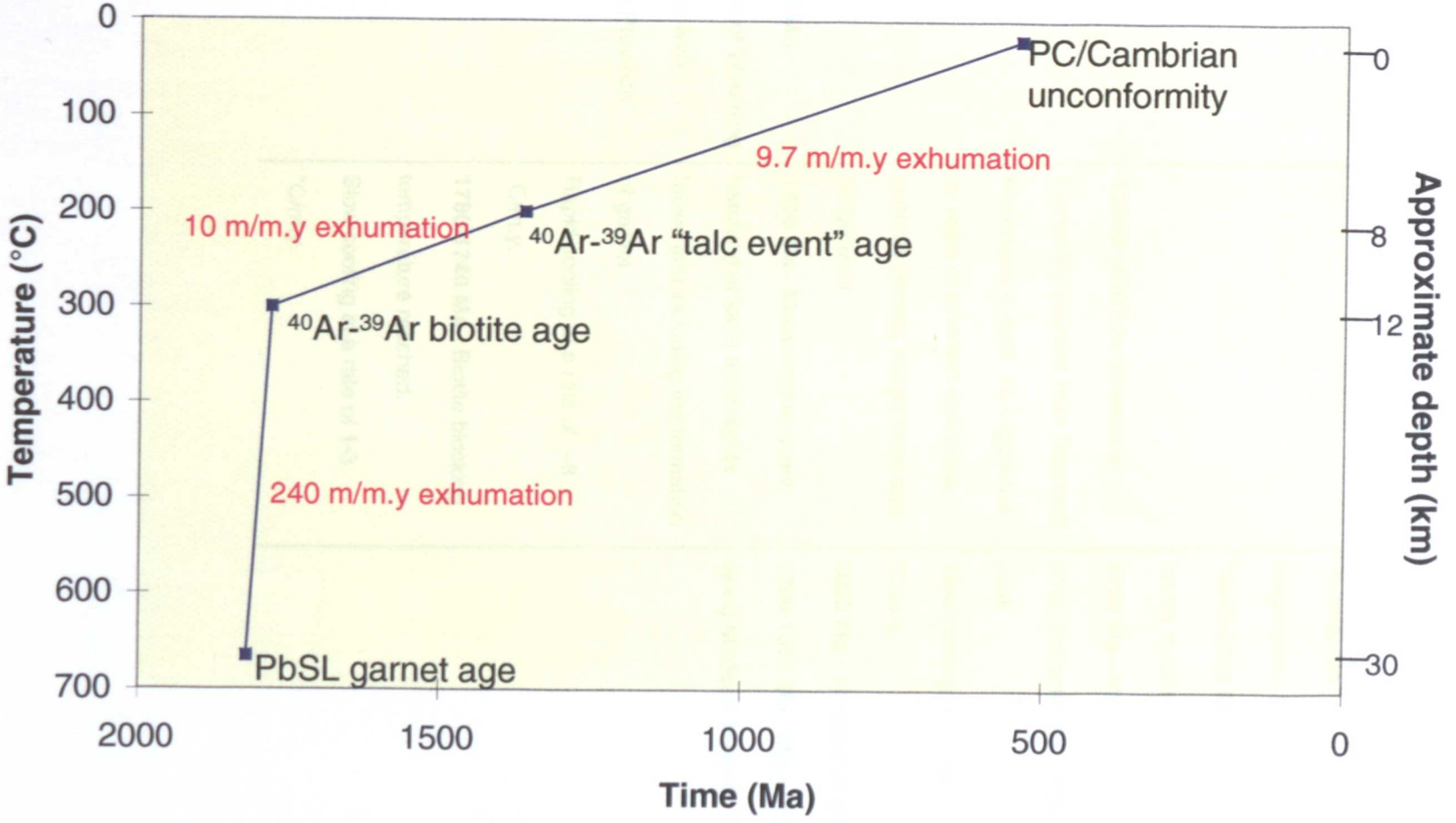

Figure 9.6: A possible T-t path for the rocks of the Ruby Range

9.3.10. Summary of the Precambrian Geological History of South-western Montana

See also Figure 9.6.

Outside south-western Montana	Ruby Range, Tobacco Root Mountains, Highland Mountains	South Madison Range
		[1]**c.3400 Ma** - Sedimentation, magmatism and orogenesis [2]**3250-3100 Ma** - M1 Granulite facies metamorphism **2750 Ma** - M2 - Upper amphibolite facies metamorphic peak Slow cooling at a rate of about 2 °C/m.y. **2020 Ma** - Intrusion of granitoids **1800-1650 Ma** - Movement along Madison Mylonite Zone
[3]**c.1820 Ma** - Collision of Wyoming Province with Hearne Province	**?2800-1820?** Sedimentation (?possibly sourced from Beartooth Mountains in east, as suggested by ages of inherited inclusions, such as zircon), magmatism and orogenesis **1820 Ma** - Metamorphic event reaching at least amphibolite facies and including the formation of garnet. Rapid cooling at a rate of ~8 °C/m.y. **1780-1740 Ma** - Biotite blocking temperature reached. Slow cooling at a rate of 1-3 °C/m.y.	

	1650 Ma - Intrusion of pegmatites
[4]**c.1500 Ma** - Formation of the Belt basin	[5]Dillon block uplifted and eroding to form the LaHood Conglomerate
	[6]**c.1450 Ma** - Formation of north-west trending faults and intrusion of dolerite dykes
[6]**c.1370 Ma** - East Kootenay orogeny	**c.1360 Ma** - Low grade metamorphism and metasomatism of the talc forming event
	[5]**c.1120 Ma** - intrusion of dolerite dykes

[1]Wooden *et al.* (1988)

[2]Erslev and Sutter (1990)

[3]Dahl *et al.* (1999a)

[4]Evans (1986)

[5]Wooden *et al.* (1978)

[6]Doughty and Chamberlain (1996)

All other events found or corroborated by this study

Chapter 10 - Conclusions

10.1. Conclusions

This research has clearly demonstrated that the laser-based ^{40}Ar-^{39}Ar geochronological technique is capable of providing more information from a polymetamorphic terrain than simply the timing of the last major event. Using this single geochronological technique and existing information on the geological history of south-western Montana, it has been possible to provide a comprehensive insight into the Precambrian tectonic history of this region and to fit it into the wider tectonic environments of the Wyoming Province, the Belt basin and Laurentia.

The apparent ages recorded by matrix mica from the Ruby Range, Tobacco Root Mountains, and Highland Mountains constrain the timing of the amphibolite facies metamorphic event between 1780 and 1740 Ma. It is not certain whether the mica was reset or created in this event but it is clear that this event thoroughly influenced the rocks across all three of these ranges. Therefore, these three mountain ranges were closely related at that time and the event was significant on a regional scale. Where recognisable closure profiles were produced, a cooling rate of 1 to 3 °C/m.y. can be inferred from metamorphic peak. This is consistent with a cooling rate of 1.2 °C/m.y. estimated from biotite and muscovite ages.

Attempts to date earlier events in this region were unsuccessful. However, evidence suggesting that there was an Archæan aged metamorphic event here is poor and it seems most likely that the main metamorphism in the area is Proterozoic. PbSL dating of garnet yielded ages between 1820 (Dahl *et al.*, 1998) and 1765 Ma (this study), proving that the garnet was formed during a Proterozoic event. Therefore, dating biotite inclusions in garnet failed to yield Archæan ages because there were no Archæan ages to detect rather than because garnet did not shield biotite inclusions.

If the garnet was formed in the same event as the matrix mica, the difference in apparent ages between garnet and biotite suggests a cooling rate of c.8 °C/m.y. between the blocking temperatures

of these two minerals. However, it is possible that the garnet was formed in an earlier metamorphic event than the mica. This would imply that the M1 event occurred around 1820 Ma and the M2 event occurred shortly before 1780 Ma, supporting the notion by Mueller and Cordua (1976) that the M1 and M2 events were closely related in time. If this is the case, then distinguishing biotite inclusions that had been shielded from those that had been reset would be extremely difficult. Having said that, it is clear from samples that were reset by Cretaceous events (c.74 Ma), that inclusions in garnet are shielded from resetting influences only in the rare absence of cracks and defects. It seems most likely that the high abundance of fractures, subgrain boundaries and defects in natural garnet will facilitate the rapid diffusion of argon into and out of garnet and will prevent any inclusions situated on them from being shielded.

Events occurring after the main 1780 Ma metamorphic event are more readily detectable because these mainly occurred below or close to the blocking temperature of argon in biotite and were not on a similar regional scale as the amphibolite facies event. The effects of a talc-forming metamorphic event are manifest in sample RRSW1 from the southern Ruby Range as highly altered biotite with chlorite, prehnite and clinozoisite interlayers. This event is believed to have only reached temperatures of 250 to 350 °C, and its influence was limited to only a few areas. The high spatial resolution of the UV laser ^{40}Ar-^{39}Ar technique proved to be valuable when dating samples affected by alteration. Whereas bulk sampling might have produced a meaningless mixed age of altered and unaltered biotite, the UV laser microprobe was able to date both altered and unaltered biotite from the same sample and consequently provided two apparent ages. Selective ^{40}Ar-^{39}Ar dating of sample RRSW1 was able to detect a 1771 Ma age, consistent with the timing of the main Proterozoic metamorphic event, and younger ages that could be related to the formation of the Belt basin to the north and west.

Heating of the country rocks by the Tobacco Root Batholith led to resetting of the country rock to apparent ages between 248 and 72 Ma for biotite and amphibole within 0.25 km of the batholith. This suggests heating that generated temperatures of up to about 500 °C in this zone. Between 0.5 km and 1 km only partial resetting of biotite and amphibole occurred in the country rock, and beyond 1 km there was no apparent resetting. This implies a limited and sharply bounded heating influence of the batholith on the surrounding country rocks.

The high spatial resolution of the UV laser microprobe has also allowed the investigation of apparent age variations within single mineral grains. This has provided valuable insights into the information recorded by single mineral grains and has allowed for more detailed interpretation of the geological history of the samples. Dodson's (1986) theoretical profiles of age variations across mineral grains related to the cooling rate of the rock have been shown to be valid, although often more complex than his models predicted. Natural samples are affected by defects, fractures, cleavages, and subgrains, etc. that disturb the volume diffusion process and influence the apparent ages of the profile. This can result in no recognisable profile being produced or can hamper interpretation of the profile. However, where profiles are recognisable it is possible to infer more about the geological history of the sample than can be gained from bulk samples. Indeed, it has proved possible to model more complex histories than the simple linear cooling modelled by Dodson's profiles, and consequently infer periods of reheating or resetting from the profiles. For example, it was possible to model periods of reheating by granodiorite intrusions for samples the Cherry Creek unit of the South Madison Range, and therefore infer a timing of emplacement for the intrusions. It has also been shown in this study that in rocks of Precambrian age it is possible to increase the spatial resolution of the technique further and to investigate the age variations within single mineral grains to a resolution of 15 μm. Further refinement of this technique might provide more insights to the mechanisms of diffusion of argon in mica.

10.2. Further Work

1) Repeat closure profile experiments in a region where there is a higher abundance of cogenetic biotite and muscovite to further investigate the different diffusion mechanisms between the two mica species.

2) Refine the high spatial resolution experiment technique to reduce blank levels (particularly on the ^{40}Ar and ^{36}Ar peaks) by adjusting the power of the laser beam, the length of analysis and degree of irradiation. This would allow more meaningful apparent ages to be produced for Precambrian aged samples that would allow a fuller investigation of the small-scale controls of argon diffusion in mica.

3) Repeat the experiments on inclusions in garnet in rocks where garnet is definitely formed in an older metamorphic event than the matrix mica in order to further evaluate the shielding effects of garnet on mica inclusions.

4) Assess the abundance and influence of fast diffusion paths in garnet on the shielding properties of garnet. In part this could be achieved by using the forescatter SEM technique, as reported by Prior *et al.* (1996), to examine garnet for subgrains.

5) Repeat the helium diffusion experiment, extending the doping periods in order to allow helium to diffuse further into garnet and to thus produce longer depth profiles. By doping at 3 or more temperatures more points can be plotted on the Arrehnius diagram from which a new diffusion coefficient and activation energy can be calculated for helium in garnet. This can then be related to the blocking temperature of argon in garnet.

6) Investigate further the influence of monazite and zircon inclusions in garnet on PbSL dating. A further examination of the effects of the integrity of monazite inclusions with respect to PbSL ages is required.

7) Evaluated further the data from PbSL dating and new chemical dating by electron microprobe of sample TRMR2 to fully understand the meaning of the Archæan and near-Archæan ages obtained.

8) Produce a new age determination of the granodiorites in South Madison Range to date the emplacement of the intrusion independent of inherited inclusions. This would assess the validity of the 2020 Ma intrusion models produced from ^{40}Ar-^{39}Ar closure profiles in adjacent country rock.

9) Undertake detailed structural mapping and geochronology on the Madison Mylonite Zone in order to further constrain the movement episodes.

10) Undertake detailed field mapping of the south-western Montana region to improve the understanding of the lithological, structural, chemical and geochronological difference between the MMT and BBMT. Particular attention should be paid to the Giletti Line and adjacent mobile belts in

order to further understand the nature of this division and its importance to the Wyoming Province boundary.

References

Adams, C.J. and Kelley, S. (1998); Provenance of Permian-Triassic and Ordovician metagraywacke terranes in New Zealand: evidence from $^{40}Ar/^{39}Ar$ dating of detrital micas; Geological Society of America Bulletin; 110; 422-432.

Aleinikoff, J.N., Williams, I.S., Compston, W., Stuckless, J.S. and Worl, R.G. (1989); Evidence for an early Archean component in the Middle to Late Archean gneisses of the Wind River Range, west-central Wyoming; conventional and ion microprobe U-Pb Data; Contributions to Mineralogy and Petrology; 101; 198-206.

Anderson, D.L., Mogk, D.W., and Childs, J.F. (1990); Petrogenesis and timing of talc formation in the Ruby Range, Southwestern Montana; Economic Geology; 85; 585-600.

Arnaud, N. and Kelley, S. (1997); Argon behaviour in gem-quality orthoclase from Madagascar; experiments and some consequences for $^{40}Ar/^{39}Ar$ geochronology; Geochimica et Cosmochimica Acta; 61; 3227-3255.

Arth, J.G., Zen, E.A., Sellars, G. and Hammarstrom, J. (1986); High initial Sr isotopic ratios and evidence from magma mixing in the Pioneer Batholith of southwest Montana; Journal of Geology; 94; 419-430.

Ayres, M.W., Vance, D. (1997); A comparative study of diffusion profiles in Himalayan and Dalradian garnets: constraints on diffusion data and the relative duration of the metamorphic events; Contributions to Mineralogy and Petrology; 128; 66-80.

Boyd, F.R., and England, J.L. (1962); Mantle minerals; effects of pressure on the melting of pyrope; Carnegie Institute of Washington Yearbook; 61; 109-112.

Brady, J.B., Cheney, J.T., Duvall, M.L., Green, C., Kaufman, L., Kogut, A.I., Larson, A.C. and Vasquez, A. (1991); Metasomatic talc deposits in southwestern Montana: geochemical evidence for deep circulation of water-rich fluids; Geological Society of America Abstracts with Programs; 23 (5); A-263.

Brady, J.B., Burger, H., Cheney, J.T., King, J.T, Tierney, K.A., Peck, W.H., Poulsen, C.J., Cady, P., Lowell, J., Sincock, M.J., Archuleta, L.L., Fisher, R. and Jacob, L. (1994); Geochemical and $^{40}Ar/^{39}Ar$ evidence for terrane assembly in the Archean of southwestern Montana; American Geological Society Abstracts with Programs; 26 (7); A-232-233.

Brady, J.B, Cheney, J.T, Larson Rhodes, A., Vasquez, A., Green, C., Duvall, M., Kogut, A., Kaufman, L., and Kovaric, D. (1998); Isotope geochemistry of Proterozoic talc occurrences in Archean marbles of the Ruby Mountains, southwest Montana, U.S.A; Geological Materials Research; 1; 1-41.

Burgess, R., Kelley, S.P., Parsons, I., Walker, F.D.L. and Worden, R.H. (1992); $^{40}Ar/^{39}Ar$ analysis of perthite microtextures and fluid inclusions in alkali feldspars from the Klokken syenite, south Greenland; Earth and Planetary Science Letters; 109; 147-167.

Chakraborty, S. and Ganguly, J. (1992); Cation diffusion in aluminosilicate garnets: experimental determination in spessartine-almandine diffusion couples, evaluation of effective binary diffusion coefficients, and applications; Contributions to Mineralogy and Petrology; 111; 74-86.

Chakraborty, S. and Ruble, D.C. (1996); Mg tracer diffusion in aluminosilicate garnets at 750-850 °C, 1 atm and 1300 °C, 8.5 GPa; Contributions to Mineralogy and Petrology; 122; 4; 406-414.

Clauer, N. (1981); Strontium and argon isotopes in naturally weathered biotites, muscovites and feldspars; Chemical Geology; 31; 325-334.

Coghlan, R.A.N. (1990); Studies in diffusional transport: grain boundary transport of oxygen in feldspars, diffusion of oxygen, strontium and the REEs in garnets and thermal histories of granitic intrusions in south-central Maine using oxygen isotopes; unpublished PhD thesis, Brown University, Providence, Rhode Island.

Condie, K.C. (1976); The Wyoming Archean Province in the western United States; *in* Windley, B.F.; The Early History of the Earth; Wiley and Sons; 499-510.

Cygan, R.T. and Lasaga, A.C. (1985); Self-diffusion of magnesium in garnet at 750 °C to 900 °C; Americal Journal of Science; 285; 328-350.

Dahl, P.S. (1979); Comparative geothermometry based on major-element and oxygen isotope distribution in Precambrian metamorphic rocks from southwestern Montana; American Mineralogist; 64; 1280-1293.

Dahl, P.S. (1980); The thermal-compositional dependence of Fe^{2+}-Mg distribution between coexisting garnet and pyroxene: applications to geothermometry; American Mineralogist; 65; 852-866.

Dahl, P.S. (1996); The crystal-chemical basis for Ar retention in micas: inferences from interlayer partitioning and implications for geochronology; Contributions to Mineralogy and Petrology; 123; 22-39.

Dahl, P.S. and Holm, D.K. (1996); Implications of hornblende and mica thermochronology on the 1800-1400 Ma tectonothermal evolution of the Black Hills, South Dakota; South Dakota School of Mines Bulletin; 19; 200-209.

Dahl, P.S. (1997); A crystal-chemical basis for Pb retention and fission-track annealing systematics in U-bearing minerals, with implications for geochronology; Earth and Planetary Science Letters; 150; 277-290.

Dahl, P.S., and Frei, R. (1998); Step-leach Pb-Pb dating of inclusion-bearing garnet and staurolite, with implications for Early Proterozoic tectonism in the Black Hills collisional orogen, South Dakota, United States; Geology; 26; 111-114.

Dahl, P.S., Frei, R. and Dorais, M.J. (1998); When did the Wyoming Province collide with Laurentia?: New clues from step-leach Pb-Pb dating of garnet independent of its inclusions; Geological Society of America Abstracts with Programs; 30 (7); A-109.

Dahl, P.S., Holm, D.K., Gardener, E.T., Hubacher, F.A. and Foland, K.A. (1999a); New constraints on the timing of Early Proterozoic tectonism in the Black Hills (South Dakota), with implications for docking of the Wyoming Province with Laurentia; Geological Society of America Bulletin; 111 (9); in press.

Dahl, P.S., Dorais, M.J., Roberts, H.J., Kelley, S.P, and Frei, R. (1999b); Electron microprobe geochronometry of age-zone monazite crystals in Archean metapelites from the Wyoming Province: the nature of Pb rejuvenation and implications for regional tectonism; Geological Society of America Abstracts with Programs; 31 (7); in press.

Dalrymple, G.B., and Lanphere, M.A. (1969); Potassium-Argon dating, principles, technique and applications to geochronology; W.H.Freeman.

Davidson, C.M. (1991); Tectonometamorphic evolution of the Maclaren glacier metamorphic Belt, South-central Alaska; PhD dissertation, Princeton University, Princeton, New Jersey.

DePaolo, D.J. and Wasserburg, G.J. (1979); Sm-Nd age of the Stillwater Complex and the mantle evolution curve for neodymium; Geochimica et Cosmochimica Acta; 43; 999-1008.

Desmarais, N.R. (1981); Metamorphosed Precambrian ultramafic rocks in the Ruby Range, Montana; Precambrian Research; 16; 67-101.

DeWolf, C.P., Belshaw, N. and O'Nions, R.K. (1993); A metamorphic history from micron scale $^{207}Pb/^{206}Pb$ chronometry of Archean monazite; Earth and Planetary Science Letters; 120; 207-220.

DeWolf, C.P., Zeissler, C.J., Halliday, A.N., Mezger, K and Essene, E.J. (1996); The role of inclusions in U-Pb and Sm-Nd garnet geochronology: stepwise dissolution experiments and trace-uranium mapping by fission track analysis: Geochimica et Cosmochimica Acta; 60; 121-134.

Dodson, M.H. (1973); Closure temperature in cooling geochronological and petrological systems; Contributions to Mineralogy and Petrology; 40, 259-274.

Dodson, M.H. (1986); Closure profiles in cooling systems; Material Science Forum; 7, 145-154.

Doughty, P.T. and Chamberlain, K.R. (1996); Salmon River Arch revisited: new evidence for 1370 Ma rifting near the end of deposition in the Middle Proterozoic Belt basin; Canadian Journal of Earth Science; 33; 1037-1052.

Dunal, T. and Roselieb, K. (1996); Sorption and diffusion of helium in garnet: implications for volatile tracing and dating; Earth and Planetary Science Letters; 139, 411-432.

Dutch, S.I. and Nielsen, P.A. (1990); The Archean Wyoming Province and its relations with adjacent Proterozoic provinces; Geological Association of Canada Special Paper 37; 287-300.

Elphick, S.C., Ganguly, J. and Loomis, T.P. (1985); Experimental determination of cation diffusivities in aluminosilicate garnets: I. experimental methods and interdiffusion data; Contributions to Mineralogy and Petrology; 90, 36-44.

Erslev, E.A. (1988); Field Guide to Pre-Beltian geology of the Southern Madison and Gravelly Ranges, southwest Montana; *in* Lewis, S.E. and Berg, R.B. (eds); Precambrian and Mesozoic Plate Margins; Montana Bureau of Mines and Geology Special Publication 96, 141-149.

Erslev, E.A. and Sutter, J.F. (1990); Evidence for Proterozoic mylonitization in the northwestern Wyoming Province; Geological Society American Bulletin; 102, 1681-1694.

Evans, K.V. (1986); Middle Proterozoic deformation and plutonism in Idaho, Montana and British Columbia; *in* Roberts, S.M. (ed); The Belt Supergroup: a guide to Proterozoic rocks of western Montana and adjacent area; Montana Bureau of Mines and Geology Special Publication 94; 237-243.

Faure, G. (1986); Principles of isotope geology; 2nd ed.; John Wiley and Sons, Inc.

Freer, R. (1979); An experimental measurement of cation diffusion in almandine garnet; Nature; 280; 220-222.

Frei, R. and Kamber, B.S. (1995); Single mineral Pb-Pb dating: Earth and Planetary Science Letters; 129; 261-268.

Frei, R., Villa, I.M., Nägler, Th. F., Kramers, J.D., Przybylowicz, W.J., Prozesky, V.M, Hojman, B.A. and Kamber, B.S. (1997); Single mineral dating by the Pb-Pb step-leaching methods: assessing the mechanisms; Geochimica et Cosmochimica Acta; 64; 393-414.

Frost, C.D., Frost, B.R., Chamberlain, K.R., and Hulsebosch, T.P. (1998); The Late Archean history of the Wyoming Province as recorded by granitic magmatism in the Wind River Range, Wyoming; Precambrian Research; 89; 145-173.

Gaber, L.J., Foland, K.A. and Corbato, C.E. (1988) On the significance of argon release from biotite and amphibole during $^{40}Ar/^{39}Ar$ vacuum heating; Geochimica et Cosmochimica Acta; 52, 2457-2465.

Garihan, J.M. and Okuma, A.F. (1974); Field evidence suggesting a non-igneous origin for the Dillion quartzo-feldspathic gneiss, Ruby Range, southwestern Montana; Geological Society of America Abstracts with Programs; 6; 510.

Garihan, J.M. (1979a); Geology and structure, central Ruby Range, Montana - Summary; Geological Society of America Bulletin, Part I; 90, 4, 323-326.

Garihan, J.M. (1979b); Geology and structure of the Central Ruby Range, Madison County, Montana; Geological Society of America Bulletin, Part II; 90, 695-788.

Giletti, B.J. (1966); Isotope ages from southwestern Montana; Journal of Geophysical Research; 71; 4029-4036.

Gosselin, D.C., Papike, J.J., Zartman, R.E, Peterman, Z.E., and Laul, J.C. (1988); Archean rocks of the Black Hills, South Dakota: Reworked basement from the southern extension of the Trans-Hudson Orogen; Geological Society of America; 100; 1244-1259.

Grove, M. and Harrison, T.M. (1996); $^{40}Ar^{*}$ diffusion in Fe-rich biotite; American Mineralogist; 81; 940-951.

Hames, W.E. and Andresen, A. (1996); Timing of Paleozoic orogeny and extension in the continental shelf of north-central Norway as indicated by laser $^{40}Ar/^{39}Ar$ muscovite dating; Geology; 24; 1005-1008.

Hames, W.E. and Bowring, S.A. (1994); An empirical evaluation of the argon diffusion geometry in muscovite; Earth and Planetary Science Letters; 124; 161-167.

Hames, W.E. and Hodges, K.V. (1993); Laser $^{40}Ar/^{39}Ar$ evaluation of slow cooling and episodic loss of ^{40}Ar from a sample of poly-metamorphic muscovite; Science; 261; 1721-1723.

Harlan, S.S., Geissman, J.W., Snee, L.W., and Reynolds, R.L. (1996); Late Cretaceous remagnetization of Proterozoic mafic dikes, southern Highland Mountains, southwestern Montana: a paleomagnetic and $^{40}Ar/^{39}Ar$ study; Geological Society of America Bulletin; 108; 653-668.

Harrison, T.M., (1981); Diffusion of ^{40}Ar in hornblende; Contributions to Mineralogy and Petrology; 78; 324-331.

Harrison, T.M., Duncan, I. and McDougall, I. (1985); Diffusion of ^{40}Ar in biotite: temperature, pressure and compositional effects; Geochimica et Cosmochimica Acta; 49; 2461-2468.

Harrison, T.M. and Fitz Gerald, J.D. (1986); Exsolution in hornblende and its consequences for $^{40}Ar/^{39}Ar$ age spectra and closure temperatures; Geochimica et Cosmochimica Acta; 50; 247-253.

Heinrich, E. W. (1960); Pre-Beltian geology of the Cherry Creek and Ruby Mountains areas, southwestern Montana: Part 2 - Geology of the Ruby Mountains; Montana Bureau of Mines and Geology Memoir 38; 15-40.

Hodges, K.V. and Bowring, S.A. (1995); $^{40}Ar/^{39}Ar$ thermochronology of isotopically zoned micas: insights from the southwestern USA Proterzoic orogen; Geochimica et Cosmochimica Acta; 59; 3205-3220.

Hodges, K.V., Hames, W.E. and Bowring, S.A. (1994); $^{40}Ar/^{39}Ar$ age gradients in micas from a high temperature-low-pressure metamorphic terrain: evidence for very slow cooling and implications for the interpretation of age spectra; Geology; 22, 55-58.

Hoffman, P.F. (1989); Precambrian geology and tectonic history of North America; *in* Bally, A.W., and Palmer, A.R. (eds); The geology of North America - an overview; Geological Society of America, Boulder, Colorado; 447-512.

Immega, I.P. and Klein, C. Jr. (1976); Mineralogy and petrology of some metamorphic Precambrian iron-formations in southwestern Montana; American Mineralogist; 61; 1117-1144.

James, H.L. and Hedge, C.E. (1980); Age of the basement rocks of southwestern Montana; Geological Society America Bulletin; 91; 11-15.

James, H.L. (1990); Precambrian geology and bedded iron deposits of the southwestern Ruby Range, Montana; U.S. Geological Survey Professional Paper1495; 1-39.

Johnson, Jr., R.W., Henderson, J.R., and Tyson, N.S. (1965); Aeromagnetic map of the Boulder Batholith area southwestern Montana; U.S. Geological Survey; Geophysical Investigations Map GP-538.

Karasevich, L.P., Garihan, J.M., Dahl, P.S. and Okuma, A.F. (1981); Summary of Precambrian metamorphic and structural history, Ruby Range, southwest Montana; Montana Geological Society Field Conference and Symposium Guidebook to Southwest Montana; 225-237.

Kelley, S.P., Parsons, I , Worden, R.H. and Walker, F.D.L. (1989); A laser $^{40}Ar/^{39}Ar$ study of preheat and alkali feldspars; Terra Abstracts; 1; 353.

Kelley, S.P. and Turner, G. (1991) Laser probe $^{40}Ar/^{39}Ar$ measurements of loss profiles within individual hornblende grains from the Giant Range granite, Northern Minnesota, USA; Earth and Planetary Science Letters; 107; 634-648.

Kelley, S.P. (1995); Ar-Ar dating by laser microprobe *in* Potts, P.J., Bowles, J.F.W., Reed, S.J.B. and Cave, M.R. (eds); Microprobe techniques in the Earth Sciences; Chapman and Hall; 328-358.

Kelley, S.P., Bartlett, J.M. and Harris, N.B.W. (1997); Pre-metamorphic Ar-Ar Ages from biotite inclusions in garnet; Geochimica et Cosmochimica Acta; 61; 3873-3878.

Kirschner, D.L., Cosca, M.A., Masson, H. and Hunziker, J.C. (1996); Staircase $^{40}Ar/^{39}Ar$ spectra of fine-grained white mica: timing and duration of deformation and empirical constraints on argon diffusion; Geology; 8; 747-750.

Kovaric, D.N., Brady, J.B., Cheney, J.T., Grove, M., Jacob, L.T. and King, J.T. (1996); $^{40}Ar/^{39}Ar$ evidence for reheating events affecting basement rocks in the Tobacco Root, Ruby and Highland Mountains, south-west Montana; Geological Society of America Abstracts with Programs; 28 (7); A-493.

Lee, J.K.W. (1993); The argon release mechanism of hornblende in vacuo; Chemical Geology (Isotope Geoscience); 106; 133-170.

Lee, J.K.W. (1995); Multipath diffusion in geochronology; Contributions of Mineralogy and Petrology; 120; 60-82.

Lo, C.H. and Onstott, T.C. (1989); ^{39}Ar recoil artifacts in chloritized biotite; Geochimica and Cosmochimica Acta; 53; 2697-2711.

Ludwig, K.R. (1990); ISOPLOT for MS-DOS - A plotting and regression program for radiogenic isotope data, for IBM-PC compatible computers, version 2.03; U.S. Geological Survey Open-File Report OF-88-0557.

Ludwig, K.R. (1998); Using *Isoplot/Ex version 1.00*: A geochronological toolkit for Microsoft Excel; Berkeley Geochronology Center Special Publication No.1.

McDougall, I. and Harrison, T.M. (1988); Geochronology and thermochronology by the $^{40}Ar/^{39}Ar$ method; Clarendon Press.

Miller, W.M., Fallick, A.E., Leake, B.E., Macintyre, R.M. and Jenkin, G.R.T. (1991); Fluid disturbed hornblende K-Ar ages from the Dalradian rocks of Connemara, Western Ireland; Journal of the Geological Society of London; 148; 985-992.

Mitchell, J.G. and Taka, A.S. (1984); Potassium and argon loss patterns in weathered micas: implications for detrital mineral studies, with particular reference to the Triassic palaeogeography of the British Isles; Sedimentary Geology; 39; 27-52.

Mogk, D.M. and Henry, D.J. (1988) Metamorphic petrology of the Nothern Archean Wyoming Province, southwestern Montana: evidence for Archean collisional tectonics *in* Ernst, W.G., (ed.); Metamorphism and Crustal Evolution of the Western United States (Rubey Volume VII); Prentice-Hall, Inc.; 362-382.

Mogk, D.W., Mueller, P.A., and Wooden, J.L. (1988); Archean tectonics of the North Snowy Block, Beartooth Mountains, Montana; Journal of Geology; 96; 125-141.

Mogk, D.W., Mueller, P.A., and Wooden, J.L. (1992); The nature of Archean terrane boundaries: an example from the northern Wyoming Province; Precambrian Research; 55, 155-168.

Mueller, P.A. and Cordua, W.S. (1976); Rb-Sr whole rock ages of gneiss from the Horse Creek Area, Tobacco Root Mountains, Montana; Isochron/West; 16; 33-36.

Mueller, P.A., Wooden, J.L. and Nutman, A.P. (1992); 3.96 Ga zircons from an Archean quartzite, Beartooth Mountains, Montana; Geology; 20; 327-330.

Mueller, P.A., Shuster, R.D., Wooden, J.L., Erslev, E.A. and Bowes, D.R. (1993); Age and composition of Archean crystalline rocks from the Southern Madison Range, Montana: implications for crustal evolution in the Wyoming craton; Geological Society of America Bulletin; 105; 437-446.

Nabelek, P.I. and Liu, M. (1999); Leuogranites in the Black Hills of South Dakota: the consquences of shear heating during continental collision; Geology; 27; 523-526.

O'Neill, J.M., Ferris, D.C., Schmidt, C.J. and Hanneman, D.L. (1986); Recurrent movement along northwest-trending faults at the southern margin of the Belt basin, Highland Mountains, southwestern Montana *in* Roberts, S.M. (ed); The Belt Supergroup: a guide to Proterozoic rocks of western Montana and adjacent area; Montana Bureau of Mines and Geology Special Publication 94; 209-215.

O'Neill, J.M., Duncan, M.S., and Zartman, R.E. (1988); An Early Proterozoic gneiss dome in the Highland Mountains, southwestern Montana; Montana Bureau of Mines and Geology Special Publication 96; 80-88.

Onstott, T.C. and Peacock, M.W. (1987); Argon rententivity of hornblendes: a field experiment in a slowly cooled metamorphic terrane; Geochimica et Cosmochimica Acta; 51; 2891-2903.

Onstott T.C., Phillips, D. and Pringle-Goodell, L. (1991); Laser microprobe measurement of chlorine and argon zonation in biotite; Chemical Geology; 90, 145-168.

Onstott, T.C., Miller, M.L., Ewing, R.C., Arnold, G.W. and Walsh, D.S. (1995); Recoil refinements; implications for the $^{40}Ar/^{39}Ar$ dating technique; Geochimica et Cosmochimica Acta; 59; 1821-1834.

Parsons, I, Rex, D.C., Guise, P and Halliday, A.N. (1988); Argon-loss by alkali feldspars; Geochimica et Cosmochimica Acta; 52; 1097-1112.

Peterman, Z.E. (1979); Geochronology and the Archean of the United States; Economic Geology; 74; 1544-1562.

Peterman, Z.E. (1981); Dating of Archean basement in northeastern Wyoming and southern Montana; Geological Society of America Bulletin; 92, 1, 139-146.

Pickles, C.S., Kelley, S.P., Reddy, S.M. amd Wheeler, J. (1997); Determination of high spatial resolution argon isotope variations in metamorphic biotites; Geochimica et Cosmochimica Acta; 61; 3809-3833.

Pouchou, J.L. and Pichoir, F. (1985); "PAP" procedure for improved quantitative analysis; Microbeam Analysis; 20; 104-105.

Prior, D.J., Trimby, P.W., Weber, U.D. and Dingley, D.J. (1996); Orientation contact imaging of microstructures in rocks using forescatter detectors in the scanning electron microscope; Mineralogical Magazine; 6; 859-869.

Reddy S.M., Kelley S.P. and Wheeler J. (1996); An $^{40}Ar/^{39}Ar$ laser probe study of micas from the Sesia Zone, Italian Alps: implications for metamorphic and deformation histories; Journal of Metamorphic Geology; 14, 493-508.

Rex, D.C., and Guise, P.G. (1995); Evaluation of argon standards with special emphasis on time scale measurements in Odin, G.S. (ed); Phanerozoic time scale; Bull. Liais. Inform. IUGS Subcom. Geochronol. 13, Offset Paris, 21-23.

Robbins, G.A. (1972); Radiogenic argon diffusion in muscovite under hydrothermal conditions; Unpublished M.S. Thesis, Brown University, Providence, Rhode Island.

Rosholt, J.N., Zartman, P.E. and Nkomo, I.T. (1973); Lead isotope systematics and uranium depletion in the Granite Mountains, Wyoming; Geological Society of America Bulletin; 84; 989-1002.

Ruffet, G., Féraud, G., and Amouric, M. (1991); Comparison of ^{40}Ar-^{39}Ar conventional and laser dating of biotites from the North Trégor Batholith; Geochimica et Cosmochimica Acta; 55; 1675-1688.

Schaller, M., Steiner, O., Studer, I., Frei, R. and Kramers, J.D. (1997); Pb stepwise leaching (PbSL) dating of garnet - addressing the inclusion problem; Schweizerische Mineralogische Petrographische Mitteilungen; 77; 113-121.

Schmidt, C.J. and Garihan, J.M. (1986); Middle Proterozoic and Laramide tectonic activity along the southern margin of the Belt basin; *in* Roberts, S.M. (ed); The Belt Supergroup: a guide to Proterozoic rocks of western Montana and adjacent area; Montana Bureau of Mines and Geology Special Publication 94; 217-235.

Schwandt, C.S., Cygan, R.T. and Westrich, H.R. (1995); Mg self-diffusion in pyrope garnet; American Mineralogist; 80; 483-490.

Steiger, R. and Jäger, E. (1977); Sub-commission on geochronology: convention on the use of decay constants in geo- and cosmochronology; Earth and Planetary Science Letters; 36; 359-362.

Stuckless, J.S, Hedge, C.E, Worl, R.G., Simmons, K.R. and **Nkomo, I.T.** (1985); Isotopic studies of the Late Archean plutonic rocks of the Wind River Range, Wyoming; Geological Society of America Bulletin, 96, 850-860.

Sumner, W. and Erslev, E.A. (1988); Late Archean thin-skinned thrusting of the Cherry Creek metamorphic suite in the Henry's Lake Mountains, southern Madison Range, Montana and Idaho; Montana Bureau of Mines and Geology Special Publication 96; 69-80.

Titterington, D.M., and Halliday, A.N. (1979); On the fitting or parallel isochrons and the methods of maximum likelihood; Chemical Geology; 46; 1-12.

Todt, W, Cliff, R.A., Hausen, A., and Hofmann, A.W. (1993); Re-calibration of NBS lead standards using a $^{202}Pb + ^{205}Pb$ double spike; Terra Abstracts 5; Supplement 1; 396.

Trull, T.W. and Kurtz, M.D. (1993); Experimental measurements of ^{3}He and ^{4}He mobility in olivine and clinopyroxene at magmatic temperatures; Geochimica et Cosmochimica Acta; 57; 1313-1324.

Turner, G. (1971); Argon 40-argon 39 dating: the optimization of irradiation parameters; Earth and Planetary Science Letters; 10; 227-234.

Turner, G. and Cadogan, P.H. (1974); Possible effects of ^{39}Ar recoil in ^{40}Ar-^{39}Ar dating; Proceedings of the Fifth Lunar Science Conference; 2; 1601-1615.

Vance, D. and O'Nions, R.K. (1992); Prograde and retrograde thermal histories from the central Swiss Alps; Earth and Planetary Science Letters; 114; 113-129.

Vance, D., Meier, M. and Oberli, F. (1998); The influences of high U-Th inclusions on the U-Th-Pb systematics of almandine-pyrope garnet: Results of a combined bulk dissolution, stepwise-leaching and SEM study; Geochimica et Cosmochimica Acta; 62; 3527-3540.

Vargo, A.G. (1990); Structure and petrography of the Pre-Beltian rocks of the north-central Gravelly Range, Montana; Unpublished M.S. Thesis, Colorado State University, Boulder, Colorado.

Villa, I. (1997); Direct determination of ^{39}Ar recoil distance; Geochimica et Cosmochimica Acta; 61; 689-691.

Vitaliano, C.J., Cordua, W.S., Burger, H.R., Hanley, T.B., Hess, D.F. and Root, F.K. (1979); Geology and structure of the southern part of the Tobacco Root Mountains, southwestern Montana: Map Summary; Geological Society of America Bulletin; 90; 712-715.

Wartho, J., Dodson, M.H., Rex, D.C. and Guise, P.G. (1991); Mechanisms of Ar release from Himalayan metamorphic hornblende; American Mineralogist; 76, 1446-1448.

Wartho, J. (1995); Apparent argon diffusive loss $^{40}Ar/^{39}Ar$ Age spectra in amphiboles; Earth and Planetary Science Letters; 134; 393-407.

Wartho, J., Kelley, S.P., Brooker, R.A., Carroll, M.R., Villa, I.M. and Lee, M.R. (1999); Direct measurement of Ar diffusion profiles in a gem-quality Madagascar K-feldspar using the ultra-violet laser ablation microprobe (UVLAMP); Earth and Planetary Science Letters; 170; 141-153.

Wheeler, J. (1996); DIFFARG: A program for simulating argon diffusion profiles in minerals; Computers and Geoscience; 22; 919-929.

Wilson, M.L. (1981); Origin of Archean lithologies in the southwestern Tobacco Root and nothern Ruby Ranges of southwestern Montana; Montana Geological Society Field Conference and Symposium Guidebook to Southwest Montana; 37-43.

Winston, D. (1986); Middle Proterozoic tectonics of the Belt basin, western Montana and northern Idaho; *in* Roberts, S.M. (ed); The Belt Supergroup: a guide to Proterozoic rocks of western Montana and adjacent area; Montana Bureau of Mines and Geology Special Publication 94; 245-257.

Wooden, J.L., Vitaliano, C.J., Koehler, S.W. and Ragland, P.C. (1978); The Late Precambrian mafic dikes in the Southern Tobacco Root Mountains, Montana - Geochemistry, Rb-Sr geochronology and relationship to Belt tectonics; Canadian Journal of Earth Sciences; 15; 467-479.

Wooden, J.L. and Mueller, P.A. (1988); Pb, Sr, and Nd isotopic composition of a suite of late Archean, igneous rocks, Eastern Beartooth Mountains: implications for crust-mantle evolution; Earth and Planetary Science Letters; 87; 59-72.

Wooden, J.L., Mueller, P.A. and Mogk, D.W. (1988); A review of the geochemistry and geochrononology of the Archean rocks of the northern part of the Wyoming Province *in* Ernst, W.G., (ed); Metamorphism and crustral evolution of the western United States; Prentice-Hall, Inc.; 384-410.

Wright, N., Layer, P.W., York, D. (1991); New insights into thermal history from single grain analysis of biotite; Earth and Planetary Science Letters; 104, 70-79.

York, D. (1969); Least-squares fitting of a stright line with correlated errors; Earth and Planetary Science Letters; 5; 320-324.

Appendix 2.1: Tables summarising previous geochronology within the Wyoming Province

1. General Geochronology of Black Hills

Author	Date	Site/lithology	Technique	Method	Sample	Age Ma	Event	Problem
Peterman, Z. E.	1979	Little Elk Granite	U-Pb	Concordia intercept	Zircon	2520		
			Rb-Sr	Isochron	Whole rock	1800	Metamorphism	
		Granite of Bear Mt.	Rb-Sr	Isochron	Whole rock	2450		
			Rb-Sr			2640 ± 160	Metamorphic & igneous event - Archæan	
			Rb-Sr		Plagioclase, biotite & whole rock	2160		Artefact of partial response of these systems to a younger event
			K-Ar		Biotite	2090		
					Hornblende	2420		
			^{87}Sr-^{86}Sr			2800		
			U-Pb & Th-Pb			2800		
			Rb-Sr		Plagioclase, microcline & whole rock	2130		
					Biotite	1610	Metamorphic & igneous event - Proterozoic	Possibly incorporation of ^{40}Ar into the biotite lattice during younger event
			K-Ar		Biotite	2480		
Holm, D.K., Dahl, P.S. and Lux, D.R.	1997	Metasedimentary rocks surrounding HPG and HPG	^{40}Ar-^{39}Ar	Step-heating	Biotite and muscovite	~1818 - ~1270	Metamorphic event	
Dahl *et al.*	1999 a		^{40}Ar-^{39}Ar	Step-heating	Amphiboles - hornblende-actinolitic	1883 -1715	Cooling age	Disturbed by transient Laramide reheating/ alteration.
						<1770, 1736, 1691	Syn-collisional regional metamorphism and deformation - post HPG intrusion.	
					Micas	1457 - 1221 cluster 1330 - 1400	Cooling ages	Laramide ^{40}Ar loss. Also Homestake Mine - indicate partial thermal resetting by nearby Early Tertiary dykes & sills.
						1650 - 1600	Initial cooling due to regional uplift	
						1500 - 1270	Middle Proterozoic cooling during slow uplift of S. Black Hills	

Appendix 2.1 continued

Author	Date	Site/lithology	Technique	Method	Sample	Age Ma	Event	Problem
Dahl, P.S. and Frei, R.	1998	Kyanite Zone metapelite	^{207}Pb-^{206}Pb	PbSL	Garnet	1762 ± 15	Maximum age for Wyoming-Superior	
					Staurolite	1759 ± 8	continental collision	
					Garnet-staurolite (combined)	1760 ± 7		
Dahl *et al.*	1999 a	Little Elk Granite and Homestake Mine	^{40}Ar-^{39}Ar	Total gas	Mica	1457-1221		
				Total gas	Hornblende	1959-1037		Highly discordant and XS argon in some

2. General Geochronology of Bighorn Mountains

Author	Date	Site/lithology	Technique	Method	Sample	Age Ma	Event
Peterman, Z. E.	1979	Granitic rocks - N. Terrane	U-Pb		Zircon & monazite	2850	
		Gneiss - S. Terrane	U-Pb Rb-Sr	Concordia intercept Isochron	Zircon Whole rock	3007, 2972, 2900, 2710	
		Granitic rocks - S. Terrane	Rb-Sr	Isochron	Whole rock	2800	
		N. plutonic terrane	K-Ar		Fresh biotite	2730	
		S. terrane	K-Ar		Fresh biotite	2510	
Peterman, Z. E.	1981		Rb-Sr			2780 ± 270	
Wooden, J.L., Mueller, P.A. and Mogk, D.W.	1988		K-Ar U-Pb Rb-Sr		Biotite Whole rock	2730 north 2510 south 2865 - 2840 north 2905 - 2890 south 2805 ± 60	
		Trondhjemitic tonalitic, and amphibolite samples	Rb-Sr U-Pb		Whole rock Zircon	3007 ± 68 2947 ± 100	E1 - older event
		Biotite tonalites, biotite granodiorites & biotite granites	Rb-Sr		Whole rock	2801 ± 62	E2 - Younger event

3. General Geochronology of the Wind River Range

Author	Date	Site/lithology	Technique	Model	Method	Age Ma	Event
Peterman, Z.	1979	Bears Ear Pluton	U-Pb	Concordia Intercept	Zircon	2570	
Aleinikoff *et al.*	1989	Bears Ears pluton	U-Pb Pb-Pb		Zircon Whole rock	2562 ± 75 2545 ± 30	Intrusion

Appendix 2.1 continued

Author	Date	Site/lithology	Technique	Model	Method	Age Ma	Event
Stuckless *et al.*	1985	Bears Ears Pluton (Granite)	Zircon fractions Rb-Sr, Th-Pb Pb-Pb			2575 ± 48 2511 ± 34 2572 ± 19	Intrusion and metasomatism
Aleinikoff *et al.*	1989	Bridger batholith	Rb-Sr U-Pb			2650 ± 150 2700	Intrusion during final stages of metamorphism
Rosholt, Zartman & Nkomo	1973	Granodiorite pluton - south	U-Pb Rb-Sr		Zircon Whole rock	2687 ± 15 2630 ± 20	
Aleinikoff *et al.*	1989	Granodioritic	Rb-Sr			2642 ± 13	Intrusion
Peterman, Z.	1979	Louis Lake batholith	U-Pb Rb-Sr	Isochron	Zircon Whole rock	2650 2570	
Stuckless *et al.*	1985	Louis Lake Batholith	Rb-Sr Th-Pb Pb-Pb			2631 ± 35 2620 ± 27 2629 ± 21	Intrusion
Aleinikoff *et al.*	1989	Louis Lake Batholith	Rb-Sr			2630 ± 20	
Aleinikoff *et al.*	1989	Metavolcanics (S. Part of range)	Rb-Sr			2800 ± 100	
Peterman, Z.	1979	Miners Delight Formation	Rb-Sr	Isochron	Whole rock	2790 ± 170	
Aleinikoff *et al.*	1989	Orthogneiss (N. Part of range)	Rb-Sr			3000 - 2800	

4. General Geochronology of Other Wyoming Mountain Ranges

Region	Author	Date	Site/lithology	Technique	Method	Sample	Age Ma	Event
Bow River Quartzite	Stevenson, Ross K, & Patchett, P. Jonathan	1990		Hf	T(CHUR)	Zircon	2610	
Granite Mountains,	Peterman, Z.	1979	Gneisses	Rb-Sr Pb-Pb	Isochron	Whole rock Single zircon	2860+ 3200	
			Granite Batholith	Rb-Sr U-Pb	Isochron Concordia Intercept	Whole rock Zircon	2550 2640, 2595	
	Rosholt, Zartman & Nkomo	1973	Biotite Granite	Rb-Sr Pb-Pb		Whole rock Whole rock	2610 ± 70 2820	
			Metamorphic rocks	Rb-Sr		Whole rock	2925 ± 80	
			Paragneisses	Pb-Pb		Whole rock	2950 ± 110	
Laramie Range	Peterman, Z.	1979	Granitic Gneiss	Rb-Sr	Isochron	Whole rock	2700	
			Laramie Batholith	Rb-Sr	Isochron	Whole rock	2510	
			Leucogranite	Rb-Sr	Isochron	Whole rock	2720	
			Migmatite	Rb-Sr	Isochron	Whole rock	2960	
Medicine Bow Mountains	Peterman, Z.	1979	Baggot Rock Granite	U-Pb Rb-Sr	Concordia Intercept Isochron	Zircon Whole rock	2365 2420	

Appendix 2.1 continued

Region	Author	Date	Site/lithology	Technique	Method	Sample	Age Ma	Event
	Stevenson, Ross K, & Patchett, P. Jonathan	1990		Hf	T(CHUR)	Zircon	3560 - 3040	
			Medicine Peak Quartzite	Hf	T(CHUR)	Magnetic fraction Non-magnetic fraction	2840 2750	
Owl Creek Mountains	Wooden, J.L., Mueller, P.A. and Mogk, D.W.	1988	Dacite	U-Pb Rb-Sr		Zircon	2906 ± 10 2755 ± 96	Igneous crystallisation. Metamorphism
	Peterman, Z.	1979	Greenstone sequence - gneiss	Rb-Sr	Isochron	Whole rock	2950	
Seminoe Mountains	Rosholt, Zartman & Nkomo	1973	Granite	Rb-Sr		Microcline & Whole rock	1700	
Sierra Madre	Peterman, Z.	1979	Baggot Rock Granite	Rb-Sr	Isochron	Whole rock	2510	
			Tonalitic to granodioritic gneiss	Pb-Pb Rb-Sr		Single zircon Model whole rock	2630 2800	
Teton Range	Peterman, Z.	1979	Mount Owen Quartz monzonite - unfoliated granite	Rb-Sr	Isochron	Whole rock	2440	
Teton Range	Peterman, Z.	1979	Webb Canyon Gneiss	Rb-Sr	Isochron	Whole rock	2815	

5. General Geochronology of the Beartooth Mountains

Region	Author	Date	Site/lithology	Technique	Method	Sample	Age Ma	Event	Problem
Central & Eastern Beartooth Mountains	Peterman, Z.	1979	Granite dykes	Rb-Sr	Isochron	Whole rock	2730, 2700, 2620		
			Metasedimentary rocks	U-Pb	Concordia intercept	Zircon	3100		
			Mouat Quartz Monzonite	U-Pb	Concordia intercept	Zircon	2710		
Eastern Beartooth Mountains	Wooden, J.L. & Mueller, P.A.	1988	Andesitic Amphibolites	U-Pb Pb			2789 ± 5 2790 ± 45		
			Long Lake Granite	U-Pb			2739 ± 25		
	Wooden, J.L., Mueller, P.A. and Mogk, D.W.	1988	Long Lake granite				2748 ± 25		60% discordant
	Wooden, J.L. & Mueller, P.A.	1988	Long Lake Granodiorite	U-Pb Pb			2783 ± 3 2775 ± 90		

Appendix 2.1 continued

Region	Author	Date	Site/lithology	Technique	Method	Sample	Age Ma	Event	Problem
			Andesitic Amphibolites, Long Lake granite, and Long Lake Granodiorite	Rb-Sr Sm-Nd Pb		Whole rock Whole rock & feldspar separates	2790 ± 35 2780 2775 ± 50		
	Wooden, J.L., Mueller, P.A. and Mogk, D.W.	1988	Andesitic Amphibolites, Long Lake granite, and Long Lake Granodiorite	Rb-Sr Pb-Pb Sm-Nd	 Chondritic Initial ε_{Nd}	Whole rock Whole rock & feldspar	2790 ± 45 2770 ± 60 3020 - 2880 2780		
			Granitic migmatite				3220		
			Granitic migmatite Quartzite	Rb-Sr Sm-Nd Pb U-Pb	 Chondritic 	 Zircon	3500 3500-3300 3300 3295		 Problematic
	Mueller, P.A., Wooden, J.L. & Nutman, A.P.	1992	Hellroaring and Quad Creek	Rb-Sr & Pb U-Pb and ^{207}Pb-^{206}Pb SHRIMP ^{207}Pb-^{206}Pb SHRIMP U-Pb		Whole rock Zircon Zircon	3300 3200 3960 - 2690 3400- 3200 (min)		
North Central Beartooth Mountains	Wooden, J.L., Mueller, P.A. and Mogk, D.W.	1988	Ms rock separated from BT Mts. by faults	Rb-Sr U-Pb		Granitoid rocks	2700 ± 100 2752 ± 14		
North Snowy Block	Wooden, J.L., Mueller,	1988	Pine Creek Heterogeneous Gneiss	Sm-Nd Rb-Sr	Chondritic	 Whole rock	3200 3400		
	P.A. and Mogk, D.W.		Mount Cowen Augen Gneiss	Rb-Sr		Whole rock	2740 ± 50		
			Trondhjemite-Amphibolite Complex	Rb-Sr Sm-Nd	 Chondritic	Whole rock	3400 3590 & 3260		
North-western Beartooth Mountains	Peterman, Z.	1979	Crevice Mt.	Rb-Sr	Isochron	Whole rock	2600		
			NW Beartooth	Pb-Pb		Single zircon	2990, 2600, 2580,		
			Portal Creek	Rb-Sr	Isochron	Whole rock	2750		

Appendix 2.1 continued

Region	Author	Date	Site/lithology	Technique	Method	Sample	Age Ma	Event	Problem
South-western Beartooth Mountains	Wooden, J.L., Mueller, P.A. and Mogk, D.W.	1988	2-Mica-granites Ms sequence Granitoids	Rb-Sr Rb-Sr & Sm-Nd Rb-Sr & U-Pb			2740 (min) 3100 - 2900 2780	2nd period of amphibolite facies metamorphism	Significant reheating in Proterozoic has complicated Rb-Sr systematics.
Stillwater Complex	DePaolo, D.J. & Wasserburg, G.J.	1979	Stillwater Complex Gabbro	Sm-Nd		Major elements & whole rock	2701 ± 8	Crystallisation	
	Peterman, Z.	1979	Hornfels -Stillwater Complex	Rb-Sr	Isochron	Whole rock	2700, 2660		
			Stillwater Complex	U-Pb Sm-Nd	Concordia intercept Isochron age	Zircon	2700 2710		
	Wooden, J.L., Mueller, P.A. and Mogk, D.W.	1988	Stillwater Complex	U-Pb		Zircon Chondritic (hornfel).	3090 - 3060 3130		

6. General Geochronology of the Madison and Gravelly Ranges

Region	Author	Date	Site/lithology	Technique	Method	Sample	Age Ma	Event	Problem
Northern Terrain	Wooden, J.L., Mueller, P.A. and Mogk, D.W.	1988	Tonalitic Gneiss Granitic Gneiss	Rb-Sr		Whole rock	3400 2700		Disturbed systematics
	Erslev, E.A. & Sutter, J.F.	1990	Pre-Cherry Creek	^{40}Ar-^{39}Ar		Hornblende Biotite	2510 2410	Cooling following metamorphic maximum at 2750	
	Mueller, Paul A. *et al.*	1993	Tonalitic & Trondhjemitic Gneiss	Rb-Sr Sm-Nd U-Pb	Chondritic Depleted mantle Initial ε_{Nd}	Whole rock Zircons	3300 3430 - 3260 3540 - 3380 3300 3140 - 3100	Emplacement	Sm-Nd ratios too limited to construct isochron Variable degrees of discordance & only moderately precise upper intercept ages

Appendix 2.1 continued

Region	Author	Date	Site/lithology	Technique	Method	Sample	Age Ma	Event	Problem
			Granitic Gneiss	Rb-Sr Sm-Nd U-Pb ^{207}Pb-^{206}Pb		Whole rock Whole rocks Zircons Hb bearing gneiss	2760 2760 2760 2690-2660	Crystallisation of original granitic magma. Crystallisation of protolith.	Shows disturbances
			Granodioritic Gneiss	Rb-Sr U-Pb		Whole rock Zircons	2600 2600		Slightly disturbed
Southern Terrain	Wooden, J.L., Mueller, P.A. and Mogk, D.W.	1988		Rb-Sr & U-Pb zircon			2500		
	Erslev, E.A. & Sutter, J.F.	1990	Cherry Creek	^{40}Ar-^{39}Ar		Hornblende Muscovite	2530 2520	Possible resetting by granodiorite intrusion.	
	Vargo, A.G.	1990	Biotite Schist	Sm-Nd	CHUR		2730	Possibly reset by granodiorite	
	Mueller, Paul A. *et al.*	1993	Cherry Creek Metamorphic Suite	^{207}Pb-^{206}Pb Sm-Nd Lu-Hf	 Chondritic Chondritic	Metavolcanic Zircons	2680 2950 2950	Crystallisation	
Madison Mylonite Zone	Erslev, E.A. & Sutter, J.F.	1990	Madison Mylonite Zone	^{40}Ar-^{39}Ar		Hornblende Biotite Muscovite/ Hornblende	1850 - 1800 1900 - 1800	Diffusive loss or partial resetting Last major ductile strain event in Madison Mylonite Zone	Very discordant ages Entrapment of extraneous argon during mylonization.
South Madison & North Gravelly Range	Vargo, A.G.	1990	Pelitic metasedimentary rocks	Sm-Nd	CHUR		3450 - 3230		
North-central Gravelly Range	Vargo, A.G.	1990	Goethite-calcite-chlorite schist	^{40}Ar-^{39}Ar	Plateau	Muscovite	1692		
			Muscovite quartzite	^{40}Ar-^{39}Ar	Plateau	Muscovite	1669		
			Actinolite-hornblende gneiss	^{40}Ar-^{39}Ar	Total gas	Hornblende-actinolite	2640		Excess argon - probably no geological significance
North Gravelly Range	Vargo, A.G.	1990	Biotite-muscovite schist	^{40}Ar-^{39}Ar	Plateau	Muscovite	1676		
			Muscovite-kyanite pegmatite	^{40}Ar-^{39}Ar	Plateau	Muscovite	1566		

Appendix 2.1 continued

7. General Geochronology of Montana

Region	Author	Date	Site/lithology	Technique	Method	Sample	Age Ma	Event	Problem
Little Belt Mountains & Little Rocky Mountains	Peterman, Z.	1979	Amphibolite and quartzofeldspathic gneiss	Rb-Sr U-Pb	Concordia intercept	Whole rock Zircon	2600 2590		
South-western Montana	Giletti, Bruno J.	1966	Central and Western Wyoming and Southern Montana	K-Ar and Rb-Sr			2600 ± 200	Regional metamorphism and/or igneous intrusion	
			South-western Montana	K-Ar and Rb-Sr			<1800; 1730 - 1410	Regional metamorphism	
Tobacco Root Mountains	Mueller and Cordua	1976	Quartzofeldspathic gneiss	Rb-Sr		Whole rock	2667 ± 66	Minimum timing of M_2 event	
	Peterman, Z.	1979	Tobacco Root	Rb-Sr	Isochron	Whole rock	2605		
	Brady *et al.*	1994	Indian Creek Metamorphic Suite metabasites & Sphuhler Peak Metamorphic Suite amphibolites	^{40}Ar-^{39}Ar			1800		
	Kovaric *et al.*	1996	Sphuhler Peak Metamorphic Suite amphibolites, Indian Creek Metamorphic Suite and dykes and sills	^{40}Ar-^{39}Ar laser single-crystal fusion and furnace step-heating	Plateau, isochron and integrated total gas	Hornblende	~1700		
			Sphuhler Peak Metamorphic Suite	^{40}Ar-^{39}Ar	Total gas	Biotite	125 and 112	Resetting by 75 Ma batholith	
Tobacco Root Mountains (Dykes)	Wooden *et al.*	1978	A - fine/ medium grained clean dolerite (Ruby Range)	Rb-Sr		Whole rock	1455 ± 125	Intrusion	
			B - fine grained to gabbroic or medium grained - weathered	Rb-Sr		Whole rock	1160 - 1130	Intrusion	
			C - fine/ medium grained	Rb-Sr		Whole rock	1130	Intrusion	
Tobacco Root Batholith	Vitaliano *et al.*	1979	Zoned composite pluton	K-Ar			74 - 71		(unpublished data)
Ruby Range	Peterman, Z.	1979	Ruby Range	Rb-Sr	Isochron	Whole rock	2750		
	Brady, John B *et al.*	1991	Ruby Range - metasomatic talc deposits	^{40}Ar-^{39}Ar	Plateau and total gas	Phlogopite, biotite and hornblende	~ 1700		Mica spectra were "disturbed"

Appendix 2.1 continued

Region	Author	Date	Site/lithology	Technique	Method	Sample	Age Ma	Event	Problem
	Kovaric *et al.*	1996	Basement	^{40}Ar-^{39}Ar		Hornblende & 2 phlogopites	1720		
			Marble adjacent to talc deposit	^{40}Ar-^{39}Ar		Phlogopite	1720		
			Metasomatic talc deposit	^{40}Ar-^{39}Ar	Plateau	Sericite	1360	Belt Basin resetting	
Ruby and Tobacco Root Ranges	James, H.L and Hedge, C.E.	1980	Ruby and Tobacco Root Ranges	Rb-Sr			2760 ± 115	Approximate time of metamorphism	Different rocks many have difference initial rations of ^{87}Sr-^{86}Sr. Sediment contain water - open system.
Highland Mountains	O'Neill *et al.*	1988	Leucocratic Gneiss and mylonite biotite gneiss	U-Pb	Zircon		~ 1800	Metamorphic growth	
	Harlan *et al.*	1996	Layered gneiss	^{40}Ar-^{39}Ar	Total gas	Hornblende Biotite	1839 1776		Discordant spectrum
			Metabasite sill	^{40}Ar-^{39}Ar		Hornblende			
	Kovaric *et al.*	1996	Chlorite deposit	^{40}Ar-^{39}Ar	Total gas	Sericite	122	Resetting by 75 Ma pluton	Disturbed
Pioneer Mountains	Arth *et al.*	1985	Microcline-plagioclase gneiss and interbanded amphibolite	Rb-Sr	Linear isochron	Whole rock	1640	Original magmatism or total re-equilibration during metamorphism	
			Leucocratic gneiss	U-Pb and ^{207}Pb-^{206}Pb		Zircon	~ 1800	Could indicate presence of inherited zircon	Discordant ages

Appendix 3.1: Formation of theoretical closure profiles using Dodson (1986) equation

"CALSHEET.XLS" is an Excel spreadsheet I set up in order to automatically produce slow cooling curves using the equation derived by Dodson (1986) for comparison to measured profiles. Below is the explanation of the workings of the spreadsheet and the source of the parameters used.

Column Heading	Explanation
1. Parameters	These are used in formulas to calculate other columns. **Core Age** = for an approximation usually took the highest age in measured profile **Cooling rate** = determined by user to fit known geological events or proposed model **Tc** = approximately 350 for muscovite (Hames and Bowring, 1994) and 280 for biotite (Grove and Harrison, 1996) but can be adjusted to suit grain size **Do** = either 0.03 for muscovite (Robbins, 1972) or 0.077 for biotite (Grove and Harrison, 1996) **e** = 2.718 **E** = either 52000 for muscovite (Robbins, 1972) or 47000 for biotite (Grove and Harrison, 1996) **R** = 1.987 **grain radius** = radius of the mica grain in basal section in microns Other parameters are used to calculate τ and are explained in 4.
2. x	This is the position with the grain where **x=0** relates to core and **x=0.995** relates to very near rim fro Dodson (1986)
3. Gx	Closure function directly related to **x**. From Dodson (1986) for cylinder

geometry appropriate for micas

4. **Temp C** Temperature in °C for the grain at location **x**. This is calculated using Dodson equation $E/RTc(x) = Ln(\tau Do/a^2)+Gx$.

This is rearranged in Excel to: $=(E/(R*(Ln((\tau*Do/a^2)+Gx)))-273$

E = either 52000 for muscovite or 47000 for biotite

R = 1.987

Do = either 0.03 for muscovite or 0.077 for biotite

$\mathbf{a^2}$ = the radius of the mica grain in basal section in microns - squared

Gx = fixed values from Dodson (1986)

-273 converts it from K to °C

τ = time taken for D to diminish by a factor of e^{-1} where $D = Do_e^{(-E/RT)}$

where **T** is the blocking temperature of the mica.

First calculate D. Then calculate **DI** which is D after a drop in e, therefore,

DI = D + 2.718

So $\tau = \mathbf{T-T_I}$ **where T** is the blocking temperature and **TI** is the temperature at Di which is:

TI = -E/(ln(Di/Do)*R)

This gives τ in Ma but it needs to be in seconds so it is multiplied by 60*60*24*365*1000000

5. **Core dis** For a specific grain of a known size, **x** position can be related to the distance from the core i.e. **x=0** = core and **x=0.995** = rim. The distance from the core is therefore **x** × **grain radius.**

6. Edge dis Because when measuring a grain the position of the core is unknown, the edge is usually taken as 0 distance. So to compare a theoretical profile to a measured profile it is necessary to turn the theoretical profile round. To do this for each **x** position subtract the core distance at that **x** position (i.e. previous column) away from core distance at **x=0.995**.

7. Age Ma To calculate the age at each **x** position first subtract the temperature at that **x** position away from the temperature at the **x=0** position. Then subtract this value from the age at the core.

Finally plot **Edge Distance** against **Age** for theoretical profile.

Appendix 3.1 continued - CALSHEET.XLS

Parameters			x	Gx	Temp C	Core dis	Edge dis	Age Ma
			0	1.60161	307.8507	0	248.75	2410
Core Age	2410		0.05	1.61553	307.6522	12.5	236.25	2409.802
Cooling rate	2.2		0.1	1.61712	307.6295	25	223.75	2409.779
Tc	280		0.15	1.63666	307.3511	37.5	211.25	2409.5
Do	0.07		0.2	1.6645	306.955	50	198.75	2409.104
e	2.718		0.25	1.70115	306.4343	62.5	186.25	2408.584
E	47000		0.3	1.74733	305.7796	75	173.75	2407.929
R	1.987		0.35	1.80398	304.9784	87.5	161.25	2407.128
grain radius	250		0.4	1.87237	304.0141	100	148.75	2406.163
a2	0.000625		0.45	1.95417	302.865	112.5	136.25	2405.014
			0.5	2.05161	301.5022	125	123.75	2403.652
T	553		0.55	2.16773	299.8865	137.5	111.25	2402.036
RT	1098.811		0.6	2.30671	297.9646	150	98.75	2400.114
E/RT	42.77351		0.65	2.47454	295.6608	162.5	86.25	2397.81
_E/RT	-42.7735		0.7	2.68013	292.864	175	73.75	2395.013
e(pow)_E/RT	2.66E-19		0.75	2.93748	289.4016	187.5	61.25	2391.551
Do(pow)_E/RT	1.87E-20		0.8	3.27039	284.9849	200	48.75	2387.134
Di	6.86E-21		0.85	3.72396	279.0779	212.5	36.25	2381.227
Di/Do	9.8E-20		0.9	4.40072	270.4931	225	23.75	2372.642
LnDi/Do	-43.769		0.95	5.63193	255.5409	237.5	11.25	2357.69
(LnDi/Do)R	-86.9689		0.995	10.05229	208.0285	248.75	0	2310.178
Ti	540.4228							
T-Ti	12.57718							
Ma taken	27.66979							
in seconds	8.73E+14							

Appendix 3.1 continued - CALSHEET.XLS (formulas)

	A	B	C	D	E	F	G	H	I
1	Parameters			x	Gx	Temp C	Core dis	Edge dis	Age Ma
2				0	1.60161	=($B$8/($B$9*(LN(($B$26*$B$6)/$B$11)+E2)))-273	=D2*$B$10	=$G$22-G2	=B3-(F2-F2)
3	Core Age	2410		0.05	1.61553	=($B$8/($B$9*(LN(($B$26*$B$6)/$B$11)+E3)))-273	=D3*$B$10	=$G$22-G3	=$B$3-($F$2-F3)
4	Cooling rate	2.2		0.1	1.61712	=($B$8/($B$9*(LN(($B$26*$B$6)/$B$11)+E4)))-273	=D4*$B$10	=$G$22-G4	=$B$3-($F$2-F4)
5	Tc	280		0.15	1.63666	=($B$8/($B$9*(LN(($B$26*$B$6)/$B$11)+E5)))-273	=D5*$B$10	=$G$22-G5	=$B$3-($F$2-F5)
6	Do	0.07		0.2	1.6645	=($B$8/($B$9*(LN(($B$26*$B$6)/$B$11)+E6)))-273	=D6*$B$10	=$G$22-G6	=$B$3-($F$2-F6)
7	e	2.718		0.25	1.70115	=($B$8/($B$9*(LN(($B$26*$B$6)/$B$11)+E7)))-273	=D7*$B$10	=$G$22-G7	=$B$3-($F$2-F7)
8	E	47000		0.3	1.74733	=($B$8/($B$9*(LN(($B$26*$B$6)/$B$11)+E8)))-273	=D8*$B$10	=$G$22-G8	=$B$3-($F$2-F8)
9	R	1.987		0.35	1.80398	=($B$8/($B$9*(LN(($B$26*$B$6)/$B$11)+E9)))-273	=D9*$B$10	=$G$22-G9	=$B$3-($F$2-F9)
10	grain radius	250		0.4	1.87237	=($B$8/($B$9*(LN(($B$26*$B$6)/$B$11)+E10)))-273	=D10*$B$10	=$G$22-G10	=$B$3-($F$2-F10)
11	a2	=(B10/10000)*(B10/10000)		0.45	1.95417	=($B$8/($B$9*(LN(($B$26*$B$6)/$B$11)+E11)))-273	=D11*$B$10	=$G$22-G11	=$B$3-($F$2-F11)
12				0.5	2.05161	=($B$8/($B$9*(LN(($B$26*$B$6)/$B$11)+E12)))-273	=D12*$B$10	=$G$22-G12	=$B$3-($F$2-F12)
13	T	=B5+273		0.55	2.16773	=($B$8/($B$9*(LN(($B$26*$B$6)/$B$11)+E13)))-273	=D13*$B$10	=$G$22-G13	=$B$3-($F$2-F13)
14	RT	=B9*$B$13		0.6	2.30671	=($B$8/($B$9*(LN(($B$26*$B$6)/$B$11)+E14)))-273	=D14*$B$10	=$G$22-G14	=$B$3-($F$2-F14)
15	E/RT	=B8/$B$14		0.65	2.47454	=($B$8/($B$9*(LN(($B$26*$B$6)/$B$11)+E15)))-273	=D15*$B$10	=$G$22-G15	=$B$3-($F$2-F15)
16	_E/RT	=-($B$15)		0.7	2.68013	=($B$8/($B$9*(LN(($B$26*$B$6)/$B$11)+E16)))-273	=D16*$B$10	=$G$22-G16	=$B$3-($F$2-F16)
17	e(pow)_E/RT	=POWER(B7,$B$16)		0.75	2.93748	=($B$8/($B$9*(LN(($B$26*$B$6)/$B$11)+E17)))-273	=D17*$B$10	=$G$22-G17	=$B$3-($F$2-F17)
18	Do(pow)_E/RT	=B6*$B$17		0.8	3.27039	=($B$8/($B$9*(LN(($B$26*$B$6)/$B$11)+E18)))-273	=D18*$B$10	=$G$22-G18	=$B$3-($F$2-F18)
19	Di	=$B$18/B7		0.85	3.72396	=($B$8/($B$9*(LN(($B$26*$B$6)/$B$11)+E19)))-273	=D19*$B$10	=$G$22-G19	=$B$3-($F$2-F19)
20	Di/Do	=$B$19/B6		0.9	4.40072	=($B$8/($B$9*(LN(($B$26*$B$6)/$B$11)+E20)))-273	=D20*$B$10	=$G$22-G20	=$B$3-($F$2-F20)
21	LnDi/Do	=LN($B$20)		0.95	5.63193	=($B$8/($B$9*(LN(($B$26*$B$6)/$B$11)+E21)))-273	=D21*$B$10	=$G$22-G21	=$B$3-($F$2-F21)
22	(LnDi/Do)R	=$B$21*B9		0.995	10.05229	=($B$8/($B$9*(LN(($B$26*$B$6)/$B$11)+E22)))-273	=D22*$B$10	=$G$22-G22	=$B$3-($F$2-F22)
23	Ti	=-(B8)/$B$22							
24	T-Ti	=B13-$B$23							
25	Ma taken	=B24*B4							
26	in seconds	=B25*60*60*24*365*1000000							

Appendix 3.2: Procedure for Electron Microprobe Analysis

The majority of the samples were prepared as polished thin sections of standard thickness (~30 μm). In addition, garnet separates from sample RRCR2 were mounted in resin blocks, the surface of which was highly polished. Both sample formats were carbon-coated to provide a conductive layer and to minimise charge build-up under the electron beam. Analyses were performed on a wavelength dispersive Cameca SX100 microprobe. Spectrometer angles, count times, crystal selection, specimen movement and on line PAP (Pouchou and Pichoir, 1985) corrections are all performed automatically. An accelerating potential of 20 kV and a beam current of 20 nA were used. The electron beam was defocused to about 10 μm to reduce the possibility of sample decomposition.

Primary standards used were feldspar (Si, K, Al), bustamite, (Mn, Ca), willemite (Zn), hæmatite (Fe), forsterite (Mg), rutile (Ti), jadeite (Na), synthetic potassium chlorite (Cl) and synthetic LiF (F). The calibration was checked against a secondary standard, KKA (a kærsutitic amphibole). If any element fell outside the expected range for KKA then a recalibration of that element was attempted on the primary standard until a satisfactory value was obtained. Reproducibility of KKA major element abundancies was generally better than 2 % (2σ).

Appendix 4.1: Electron microprobe analyses of garnet (oxide weight percent)

Sample	Analysis	SiO_2	TiO_2	Al_2O_3	MgO	CaO	MnO	FeO*	MgO/FeO	Total
70-30-2	Non-specific	37.17	0.06	22.91	6.76	1.14	0.55	28.79	0.23	97.37
70-30-2	Non-specific	37.88	0.00	21.58	6.79	1.35	0.71	32.40	0.21	100.70
70-30-2	Non-specific	37.77	0.00	21.57	6.41	1.86	0.76	32.35	0.20	100.70
70-30-2	Non-specific	37.50	0.01	21.55	6.07	1.36	0.80	33.08	0.18	100.37
70-30-2	Non-specific	37.98	0.00	21.59	7.26	1.43	0.71	31.79	0.23	100.76
70-30-2		**37.66**	**0.01**	**21.84**	**6.66**	**1.43**	**0.70**	**31.68**	**0.21**	**99.98**
RRSW1	Traverse A1	36.72	0.04	21.61	5.19	5.19	1.19	30.09	0.17	100.04
RRSW1	Traverse A2	36.84	0.05	21.39	5.03	5.27	1.28	30.20	0.17	100.07
RRSW1	Traverse A3	37.01	0.04	21.59	5.06	5.35	1.26	30.11	0.17	100.41
RRSW1	Traverse A4	37.68	0.05	21.72	4.97	5.25	1.30	30.36	0.16	101.32
RRSW1	Traverse A5	37.46	0.04	21.64	5.07	5.31	1.23	30.14	0.17	100.88
RRSW1	Traverse A7	37.31	0.00	21.51	3.98	5.09	1.80	30.98	0.13	100.67
RRSW1	Traverse B1	37.61	0.02	21.70	4.42	5.26	1.60	30.78	0.14	101.39
RRSW1	Traverse B2	38.17	0.07	21.98	5.20	5.44	1.19	30.21	0.17	102.24
RRSW1	Traverse B4	37.77	0.03	21.91	5.28	5.35	1.20	29.87	0.18	101.39
RRSW1	Traverse B5	37.78	0.06	21.81	5.20	5.45	1.19	30.17	0.17	101.66
RRSW1	Traverse B6	37.91	0.03	22.02	5.20	5.18	1.18	30.42	0.17	101.93
RRSW1	Traverse B8	37.51	0.04	21.74	4.30	5.21	1.65	30.89	0.14	101.34
RRSW1		**37.53**	**0.04**	**21.73**	**4.95**	**5.28**	**1.31**	**30.34**	**0.16**	**101.19**
RRCR2	Traverse A1	36.32	0.01	21.01	2.77	1.96	1.22	36.45	0.08	99.74
RRCR2	Traverse A2	36.63	0.00	21.51	3.45	2.07	0.96	35.87	0.10	100.47
RRCR2	Traverse A4	36.97	0.01	21.40	3.10	2.06	1.08	36.07	0.09	100.68
RRCR2	Traverse A5	36.91	0.00	21.27	3.26	1.91	1.02	36.52	0.09	100.89
RRCR2	Traverse A6	36.10	0.04	21.12	3.23	1.96	1.04	36.55	0.09	100.04
RRCR2	Traverse A7	36.64	0.01	21.25	3.12	2.18	1.04	36.40	0.09	100.63
RRCR2	Traverse A8	36.66	0.00	21.26	2.95	2.16	1.11	36.11	0.08	100.24
RRCR2		**36.64**	**0.01**	**21.27**	**3.16**	**2.05**	**1.05**	**36.24**	**0.09**	**100.42**
RRCR3	Traverse A1	36.26	0.01	21.02	2.83	1.30	0.81	38.23	0.07	100.46
RRCR3	Traverse A2	37.24	0.01	21.45	3.70	1.34	0.63	37.17	0.10	101.52
RRCR3	Traverse A4	37.51	0.00	21.55	3.75	1.30	0.64	37.20	0.10	101.95
RRCR3	Traverse A5	37.02	0.01	21.60	3.06	1.33	0.74	37.95	0.08	101.70
RRCR3	Traverse B1	36.36	0.01	21.27	3.76	1.36	0.63	37.09	0.10	100.47
RRCR3	Traverse B2	36.77	0.01	21.44	3.73	1.27	0.60	37.28	0.10	101.11
RRCR3	Traverse B3	36.60	0.00	21.30	3.67	1.27	0.62	37.32	0.10	100.78
RRCR3	Traverse B4	36.98	0.00	21.34	3.64	1.29	0.61	37.42	0.10	101.28
RRCR3	Traverse B5	36.54	0.01	21.45	3.64	1.23	0.63	37.51	0.10	101.01
RRCR3	Traverse B6	36.65	0.00	21.56	3.40	1.31	0.65	37.54	0.09	101.12
RRCR3	Traverse B7	36.47	0.00	21.21	3.40	1.23	0.69	37.50	0.09	100.49
RRCR3	Traverse C1	35.24	0.02	20.62	2.92	1.31	0.84	37.44	0.08	98.39
RRCR3	Traverse C2	36.66	0.02	21.42	3.45	1.26	0.66	37.59	0.09	101.06
RRCR3	Traverse C3	36.95	0.02	21.62	3.59	1.29	0.64	37.36	0.10	101.45
RRCR3	Traverse C4	35.75	0.01	20.86	3.52	1.29	0.62	36.14	0.10	98.21
RRCR3	Traverse C5	36.68	0.02	21.24	3.56	1.30	0.63	37.81	0.09	101.25
RRCR3	Traverse C6	35.61	0.00	20.74	3.43	1.26	0.68	37.49	0.09	99.20
RRCR3	Traverse C7	36.26	0.00	21.13	3.60	1.15	0.65	37.54	0.10	100.32
RRCR3	Traverse C8	36.63	0.00	21.56	3.59	1.37	0.65	37.20	0.10	101.01
RRCR3	Traverse C9	36.70	0.00	21.44	2.99	1.34	0.79	38.06	0.08	101.33
RRCR3		**36.54**	**0.01**	**21.28**	**3.50**	**1.29**	**0.66**	**37.40**	**0.09**	**100.68**
RRCR5	Traverse A1	36.37	0.01	21.19	3.18	1.10	0.96	37.75	0.08	100.55
RRCR5	Traverse A2	36.28	0.00	21.40	3.32	1.11	0.80	37.94	0.09	100.84
RRCR5	Traverse A3	36.66	0.00	21.34	3.54	1.06	0.74	37.77	0.09	101.11
RRCR5	Traverse A4	36.76	0.00	21.42	3.24	1.00	0.79	38.10	0.08	101.32
RRCR5	Traverse A5	36.57	0.01	21.39	3.28	1.08	0.79	38.16	0.09	101.29
RRCR5	Traverse A6	36.69	0.00	21.37	2.76	1.13	1.08	38.21	0.07	101.23
RRCR5	Traverse B1	37.34	0.00	21.49	2.73	1.11	1.10	38.10	0.07	101.85
RRCR5	Traverse B2	36.96	0.00	21.21	3.34	1.09	0.83	37.93	0.09	101.36
RRCR5	Traverse B3	37.18	0.00	21.09	3.41	1.07	0.76	37.63	0.09	101.13
RRCR5	Traverse B4	36.90	0.02	21.28	3.28	1.05	0.76	38.13	0.09	101.41
RRCR5	Traverse B5	36.61	0.00	21.04	3.25	1.07	0.87	38.01	0.09	100.85
RRCR5	Traverse C1	35.41	0.00	21.11	2.45	1.22	1.16	38.57	0.06	99.91
RRCR5	Traverse C2	36.87	0.02	21.31	3.10	1.14	0.91	37.98	0.08	101.32
RRCR5	Traverse C3	36.70	0.01	21.33	2.97	1.20	0.94	38.25	0.08	101.40
RRCR5	Traverse C4	36.40	0.01	21.12	2.66	1.06	1.07	38.63	0.07	100.95
RRCR5	Traverse C5	36.37	0.01	21.23	2.39	1.08	1.13	38.78	0.06	100.99
RRCR5	Traverse C6	36.08	0.01	21.20	2.96	1.09	1.00	38.10	0.08	100.43
RRCR5	Traverse C7	35.99	0.01	21.19	3.17	1.14	0.91	38.03	0.08	100.43
RRCR5	Traverse C8	36.19	0.04	21.23	2.55	1.19	1.12	38.31	0.07	100.63
RRCR5		**36.54**	**0.01**	**21.26**	**3.03**	**1.10**	**0.93**	**38.12**	**0.08**	**101.00**

Appendix 4.1 continued

Sample	Analysis	SiO_2	TiO_2	Al_2O_3	MgO	CaO	MnO	FeO*	MgO/FeO	Total
RMC200	Non specific	38.48	0.00	21.77	8.02	2.27	0.14	30.21	0.27	100.88
RMC200	Non specific	38.03	0.05	21.51	6.20	2.12	0.37	32.63	0.19	100.90
RMC200	Non specific	37.45	0.00	21.50	6.97	2.20	0.36	31.97	0.22	100.44
RMC200	Non specific	37.81	0.00	21.63	7.08	2.18	0.30	31.55	0.22	100.53
RMC200	Non specific	38.09	0.00	21.61	7.09	2.12	0.28	31.93	0.22	101.11
RMC200	Edge bounding sericite	37.87	0.06	21.13	5.59	2.14	0.48	33.15	0.17	100.41
RMC200	Edge bounding sericite	38.22	0.02	21.54	5.15	2.21	0.56	33.82	0.15	101.52
RMC200	Edge bounding sericite	37.87	0.10	21.38	5.69	2.18	0.48	33.01	0.17	100.71
RMC200	Edge bounding biotite	38.19	0.06	21.48	6.59	2.16	0.27	32.15	0.21	100.89
RMC200	Edge bounding biotite	38.39	0.00	21.50	6.91	2.53	0.27	31.31	0.22	100.92
RMC200	Edge bounding biotite	38.40	0.02	21.53	6.24	2.22	0.33	32.46	0.19	101.20
RMC200	Edge bounding chlorite	38.41	0.00	21.39	5.58	2.02	0.41	33.32	0.17	101.13
RMC200	Edge bounding chlorite	37.89	0.00	21.15	5.58	2.32	0.43	33.20	0.17	100.58
RMC200	Edge bounding chlorite	38.35	0.01	21.31	5.16	2.02	0.61	34.06	0.15	101.51
RMC200	Non-edge	38.51	0.00	21.67	7.81	2.25	0.10	30.32	0.26	100.66
RMC200	Non-edge	38.70	0.00	21.64	8.07	2.27	0.16	29.92	0.27	100.77
RMC200	Non-edge	38.76	0.07	21.72	7.92	2.54	0.17	30.10	0.26	101.28
RMC200	Non-edge	38.74	0.00	21.85	7.41	2.11	0.28	30.94	0.24	101.32
RMC200	Non-edge	38.76	0.00	21.55	7.51	2.09	0.13	30.71	0.24	100.76
RMC200	Non-edge	38.80	0.01	21.47	7.44	2.19	0.07	30.77	0.24	100.76
RMC200	Non-edge	38.58	0.03	21.59	7.49	2.21	0.14	30.86	0.24	100.89
RMC200	Traverse A1	37.91	0.03	21.63	7.75	1.60	0.29	31.21	0.25	100.43
RMC200	Traverse A2	37.61	0.00	21.56	7.52	1.76	0.30	31.80	0.24	100.55
RMC200	Traverse A3	37.68	0.00	21.62	6.33	2.00	0.44	32.83	0.19	100.90
RMC200	Traverse B1	37.85	0.00	21.31	5.66	1.98	0.48	33.59	0.17	100.89
RMC200	Traverse B2	38.12	0.08	21.56	6.66	2.01	0.38	32.33	0.21	101.14
RMC200	Traverse B3	38.24	0.01	21.70	6.86	2.04	0.37	32.05	0.21	101.27
RMC200	Traverse B4	38.26	0.03	21.64	6.59	2.04	0.37	32.31	0.20	101.22
RMC200	Traverse B5	37.97	0.00	21.57	5.24	1.92	0.62	34.06	0.15	101.38
RMC200		**38.21**	**0.02**	**21.53**	**6.69**	**2.13**	**0.33**	**32.02**	**0.21**	**100.93**
RRCR12	Traverse A1	37.75	0.00	21.61	4.49	5.17	0.84	31.60	0.14	101.45
RRCR12	Traverse A2	37.61	0.01	21.63	4.86	4.61	0.89	31.67	0.15	101.28
RRCR12	Traverse A3	37.63	0.02	21.43	4.06	4.75	1.20	32.24	0.13	101.32
RRCR12	Traverse A4	37.11	0.03	21.32	3.42	5.67	1.53	31.69	0.11	100.77
RRCR12	Traverse A5	37.18	0.03	21.52	3.36	6.08	1.69	31.21	0.11	101.05
RRCR12	Traverse A6	37.34	0.00	21.46	4.06	5.31	1.29	31.63	0.13	101.09
RRCR12	Traverse A7	37.18	0.03	21.52	4.23	5.22	1.07	31.49	0.13	100.76
RRCR12	Traverse A8	37.22	0.02	21.42	4.55	5.16	0.81	31.46	0.14	100.63
RRCR12	Traverse A9	37.51	0.03	21.73	4.62	5.20	0.79	30.92	0.15	100.80
RRCR12	Traverse B1	37.49	0.00	21.68	5.07	5.17	0.62	30.86	0.16	100.89
RRCR12	Traverse B3	37.25	0.00	21.75	4.63	4.12	0.76	31.98	0.14	100.51
RRCR12	Traverse B4	36.97	0.02	21.46	4.49	4.23	0.79	32.66	0.14	100.62
RRCR12	Traverse B6	37.13	0.03	21.44	4.56	5.00	0.68	31.42	0.15	100.27
RRCR12	Traverse B7	37.68	0.02	21.67	4.88	5.42	0.63	31.11	0.16	101.40
RRCR12	Traverse B8	37.24	0.04	21.72	5.04	5.32	0.61	30.84	0.16	100.81
RRCR12	Traverse B9	38.18	0.01	21.88	4.86	5.22	0.72	31.05	0.16	101.91
RRCR12		**37.40**	**0.02**	**21.58**	**4.45**	**5.10**	**0.93**	**31.49**	**0.14**	**100.97**
RM37	Traverse A1	37.09	0.09	20.86	2.83	1.22	0.62	38.32	0.07	101.04
RM37	Traverse A2	37.14	0.02	20.92	2.74	1.36	0.53	38.41	0.07	101.12
RM37	Traverse A3	37.07	0.04	20.87	2.52	1.41	0.72	38.24	0.07	100.87
RM37	Traverse A4	36.95	0.10	20.78	2.44	1.41	0.77	38.30	0.06	100.75
RM37	Traverse A5	36.94	0.00	20.91	2.06	1.50	0.80	38.65	0.05	100.85
RM37		**37.04**	**0.05**	**20.87**	**2.52**	**1.38**	**0.69**	**38.38**	**0.07**	**100.93**
RM39	Traverse A1	36.38	0.04	20.94	2.63	1.30	0.58	38.48	0.07	100.34
RM39	Traverse A2	37.04	0.03	20.96	3.33	1.32	0.48	37.78	0.09	100.94
RM39	Traverse A3	36.89	0.00	20.84	3.51	1.44	0.50	37.95	0.09	101.11
RM39	Traverse A4	37.27	0.13	20.71	3.49	1.41	0.45	37.68	0.09	101.14
RM39	Traverse A5	37.31	0.00	20.78	3.54	1.38	0.47	37.53	0.09	101.01
RM39	Traverse A6	37.02	0.00	20.67	3.39	1.37	0.47	37.72	0.09	100.64
RM39	Traverse A7	36.85	0.06	20.75	3.50	1.37	0.43	37.65	0.09	100.61
RM39	Traverse A8	37.26	0.03	20.98	3.51	1.41	0.46	37.87	0.09	101.52
RM39	Traverse A9	37.41	0.09	21.10	2.64	1.27	0.60	37.90	0.07	101.01
RM39	Traverse B1	37.10	0.12	21.00	3.07	1.31	0.49	38.02	0.08	101.12
RM39	Traverse B2	37.30	0.00	20.92	3.33	1.34	0.42	37.75	0.09	101.05
RM39	Traverse B3	37.03	0.00	20.93	3.42	1.42	0.45	37.63	0.09	100.87
RM39	Traverse B4	37.38	0.07	21.03	3.37	1.37	0.43	37.58	0.09	101.24
RM39	Traverse B5	37.13	0.01	20.86	3.35	1.23	0.39	37.53	0.09	100.49
RM39	Traverse B6	37.36	0.00	20.89	3.39	1.29	0.37	37.47	0.09	100.76
RM39	Traverse B7	37.28	0.10	20.73	3.50	1.34	0.51	37.53	0.09	100.98

Appendix 4.1 continued

Sample	Analysis	SiO_2	TiO_2	Al_2O_3	MgO	CaO	MnO	FeO*	MgO/FeO	Total
RM39	Traverse B8	37.24	0.07	20.89	3.40	1.34	0.46	37.78	0.09	101.18
RM39	Traverse B9	37.26	0.13	21.01	3.31	1.26	0.50	37.57	0.09	101.04
RM39	Traverse B10	37.25	0.05	21.02	2.51	1.19	0.58	38.50	0.07	101.11
RM39	Traverse B11	37.23	0.00	21.05	2.77	1.29	0.56	38.34	0.07	101.23
RM39	Traverse B12	37.19	0.07	20.79	2.80	1.25	0.54	38.47	0.07	101.12
RM39	Traverse B13	36.97	0.05	20.53	2.30	1.23	0.58	38.67	0.06	100.32
RM39	Traverse B14	36.81	0.03	20.67	2.18	1.35	0.61	38.66	0.06	100.30
RM39	Traverse C1	37.20	0.00	20.91	2.97	1.25	0.44	37.81	0.08	100.58
RM39	Traverse C2	37.34	0.02	20.75	3.27	1.31	0.50	37.76	0.09	100.96
RM39	Traverse C3	37.27	0.03	21.00	3.37	1.33	0.41	37.52	0.09	100.94
RM39	Traverse C4	37.30	0.07	20.99	3.37	1.34	0.45	37.55	0.09	101.07
RM39	Traverse C5	37.13	0.00	20.71	3.26	1.41	0.48	37.54	0.09	100.52
RM39	Traverse C6	37.44	0.00	20.55	3.43	1.35	0.47	37.60	0.09	100.83
RM39	Traverse C7	36.03	2.35	20.42	3.45	1.29	0.43	37.85	0.09	101.82
RM39	Traverse C8	37.39	0.23	20.88	3.40	1.32	0.47	37.60	0.09	101.29
RM39	Traverse C9	37.38	0.10	20.72	3.30	1.37	0.41	37.61	0.09	100.89
RM39	Traverse C10	37.42	0.07	20.86	3.08	1.27	0.50	37.91	0.08	101.10
RM39	Traverse C12	37.33	0.00	20.81	2.83	1.29	0.57	38.15	0.07	100.98
RM39	Traverse C13	37.23	0.00	21.05	2.77	1.29	0.56	38.34	0.07	101.23
RM39	Traverse C14	37.37	0.00	20.91	3.17	1.33	0.42	37.80	0.08	101.00
RM39	Traverse C15	37.35	0.00	20.74	2.73	1.40	0.55	38.45	0.07	101.22
RM39	Edge	37.31	0.00	20.92	2.62	1.31	0.49	38.61	0.07	101.25
RM39	Edge	36.74	0.01	20.77	2.37	1.27	0.53	38.50	0.06	100.19
RM39	Edge	36.83	0.01	20.94	2.68	1.32	0.59	38.49	0.07	100.85
RM39	Non-edge	37.30	0.00	20.77	3.32	1.35	0.50	37.88	0.09	101.11
RM39	Non-edge	37.40	0.02	20.96	3.13	1.36	0.36	37.87	0.08	101.10
RM39	Non-edge	37.29	0.12	20.98	3.10	1.42	0.52	38.17	0.08	101.61
RM39		**37.16**	**0.10**	**20.85**	**3.11**	**1.33**	**0.49**	**37.93**	**0.08**	**100.97**
RM40	Edge bounding biotite	36.94	0.06	20.94	3.24	1.23	3.78	34.17	0.09	100.35
RM40	Edge bounding biotite	36.66	0.01	21.04	3.40	1.18	3.34	34.65	0.10	100.27
RM40	Edge bounding biotite	37.30	0.00	21.21	3.58	1.39	2.94	34.76	0.10	101.18
RM40	Edge bounding biotite	36.80	0.06	20.97	3.81	1.22	2.90	34.70	0.11	100.45
RM40	Edge bounding feldspar	37.17	0.05	21.21	4.48	1.18	2.61	33.96	0.13	100.66
RM40	Edge bounding feldspar	37.10	0.11	21.00	4.40	1.32	3.03	33.61	0.13	100.56
RM40	Non-edge	37.62	0.00	21.05	5.09	1.80	1.59	33.89	0.15	101.02
RM40	Non-edge	37.50	0.14	21.33	5.28	1.67	1.13	33.98	0.16	101.04
RM40	Non-edge	36.92	0.01	20.97	4.66	1.37	2.56	33.81	0.14	100.30
RM40	Non-specific	37.33	0.00	20.92	3.12	1.30	3.84	34.14	0.09	100.65
RM40		**37.13**	**0.04**	**21.06**	**4.10**	**1.36**	**2.77**	**34.16**	**0.12**	**100.65**
RRSW2	Traverse A1	37.23	0.02	22.19	10.59	0.94	0.27	26.73	0.40	97.97
RRSW2	Traverse A2	38.43	0.00	22.63	10.81	1.03	0.28	27.64	0.39	100.82
RRSW2	Traverse A3	38.45	0.01	22.53	10.85	1.15	0.27	27.72	0.39	100.97
RRSW2	Traverse A4	38.66	0.02	22.56	10.87	1.00	0.27	27.80	0.39	101.18
RRSW2	Traverse A5	39.06	0.04	22.57	10.78	1.09	0.27	27.69	0.39	101.49
RRSW2	Traverse A6	38.97	0.02	22.51	10.86	1.12	0.29	27.67	0.39	101.44
RRSW2	Traverse A7	38.76	0.01	22.36	10.76	1.10	0.28	27.85	0.39	101.11
RRSW2	Traverse A8	38.93	0.00	22.54	10.82	1.10	0.26	27.91	0.39	101.58
RRSW2	Traverse A9	38.81	0.02	22.76	10.89	1.07	0.28	27.71	0.39	101.54
RRSW2	Traverse B1	38.77	0.00	22.60	10.74	1.01	0.27	27.99	0.38	101.38
RRSW2	Traverse B2	38.66	0.00	22.41	10.64	1.14	0.28	27.87	0.38	100.99
RRSW2	Traverse B3	38.54	0.01	22.46	10.60	1.19	0.29	27.79	0.38	100.87
RRSW2	Traverse B4	38.26	0.00	22.32	10.67	1.10	0.29	28.05	0.38	100.70
RRSW2	Traverse B5	38.58	0.00	22.42	10.69	1.14	0.29	28.21	0.38	101.34
RRSW2	Traverse B6	38.04	0.01	22.31	9.97	1.15	0.30	28.74	0.35	100.51
RRSW2		**38.54**	**0.01**	**22.48**	**10.70**	**1.09**	**0.28**	**27.82**	**0.38**	**100.93**
RRSW3	Traverse A1	35.72	0.01	21.04	2.86	2.16	2.40	35.60	0.08	99.78
RRSW3	Traverse A2	36.14	0.00	21.53	4.13	2.06	1.57	34.97	0.12	100.40
RRSW3	Traverse A3	36.29	0.00	21.31	4.24	2.00	1.54	34.77	0.12	100.16
RRSW3	Traverse A4	37.04	0.01	21.66	4.28	1.98	1.50	34.86	0.12	101.32
RRSW3	Traverse A5	36.93	0.01	21.50	4.18	1.96	1.58	35.04	0.12	101.19
RRSW3	Traverse A6	36.20	0.00	21.45	3.10	1.89	2.48	35.50	0.09	100.61
RRSW3	Traverse B1	35.47	0.05	20.83	2.32	1.90	3.11	35.82	0.06	99.49
RRSW3	Traverse B2	36.48	0.01	21.32	3.81	2.33	1.62	34.87	0.11	100.43
RRSW3	Traverse B3	36.64	0.01	21.49	3.97	2.38	1.59	34.87	0.11	100.95
RRSW3	Traverse B4	36.31	0.02	21.22	3.99	2.37	1.57	34.76	0.11	100.24
RRSW3	Traverse B5	36.49	0.04	21.39	4.06	2.33	1.59	34.66	0.12	100.56
RRSW3	Traverse B6	36.41	0.01	21.47	3.97	2.35	1.60	34.71	0.11	100.51
RRSW3	Traverse B7	36.25	0.00	21.35	3.28	1.93	2.19	35.57	0.09	100.57
RRSW3		**36.34**	**0.01**	**21.35**	**3.71**	**2.13**	**1.87**	**35.08**	**0.11**	**100.48**

Appendix 4.1 continued

Sample	Analysis	SiO_2	TiO_2	Al_2O_3	MgO	CaO	MnO	FeO*	MgO/FeO	Total
RRSW4	Traverse A1	38.61	0.01	22.25	10.56	3.16	0.50	24.71	0.43	99.80
RRSW4	Traverse A2	39.04	0.02	22.57	10.82	2.87	0.50	25.17	0.43	101.00
RRSW4	Traverse A3	38.83	0.03	22.63	10.83	2.84	0.50	25.11	0.43	100.78
RRSW4	Traverse A4	37.53	0.03	21.61	10.39	2.37	0.48	25.12	0.41	97.65
RRSW4	Traverse A5	38.54	0.02	22.50	10.72	2.80	0.51	25.40	0.42	100.55
RRSW4	Traverse A6	38.58	0.05	22.66	10.83	2.29	0.52	25.87	0.42	100.82
RRSW4	Traverse A7	38.85	0.03	22.43	10.74	2.61	0.51	25.63	0.42	100.81
RRSW4	Traverse A8	38.53	0.03	22.51	11.06	2.26	0.51	25.78	0.43	100.69
RRSW4	Traverse A9	39.45	0.00	22.94	11.30	2.36	0.49	25.63	0.44	102.17
RRSW4	Traverse A10	38.79	0.00	22.47	10.62	3.24	0.51	25.06	0.42	100.67
RRSW4	Traverse A11	39.02	0.02	22.51	10.78	3.50	0.50	24.73	0.44	101.08
RRSW4	Traverse A12	39.04	0.00	22.26	11.27	2.25	0.49	24.89	0.45	100.21
RRSW4	Traverse A13	39.33	0.01	22.71	11.36	2.21	0.48	25.47	0.45	101.59
RRSW4	Traverse B1	38.80	0.00	22.27	10.90	2.30	0.62	25.58	0.43	100.47
RRSW4	Traverse B2	38.62	0.02	22.61	10.89	2.50	0.62	25.48	0.43	100.74
RRSW4	Traverse B3	38.66	0.02	22.47	11.10	2.25	0.61	25.63	0.43	100.74
RRSW4	Traverse B4	38.21	0.02	22.39	10.62	3.11	0.59	25.31	0.42	100.27
RRSW4	Traverse B5	38.08	0.01	22.47	10.98	2.45	0.58	25.66	0.43	100.23
RRSW4	Traverse B6	38.15	0.01	22.28	11.02	2.29	0.58	25.54	0.43	99.87
RRSW4	Traverse B7	37.88	0.26	22.37	10.96	2.20	0.61	25.46	0.43	99.74
RRSW4	Traverse B8	37.72	0.00	22.28	10.84	2.56	0.58	25.06	0.43	99.05
RRSW4	Traverse B9	37.94	0.01	22.37	10.74	2.83	0.56	25.27	0.43	99.75
RRSW4	Traverse B10	39.89	0.04	23.39	11.04	3.28	0.59	25.16	0.44	103.40
RRSW4	Traverse B11	38.33	0.01	22.34	10.86	2.84	0.59	25.37	0.43	100.34
RRSW4	Traverse B12	38.61	0.01	22.67	11.02	2.65	0.57	25.23	0.44	100.77
RRSW4	Traverse B13	38.81	0.00	22.75	11.35	2.21	0.56	25.41	0.45	101.10
RRSW4	Traverse B14	38.37	0.03	22.55	11.18	2.36	0.55	25.31	0.44	100.36
RRSW4	Traverse B15	38.78	0.01	22.64	11.35	2.20	0.53	25.38	0.45	100.88
RRSW4	Traverse B16	38.30	0.01	22.26	9.85	1.87	0.67	27.85	0.35	100.82
RRSW4		**38.60**	**0.02**	**22.49**	**10.90**	**2.57**	**0.55**	**25.42**	**0.43**	**100.56**
TRBC2	Traverse A1	38.89	0.01	22.63	10.45	1.18	0.46	27.91	0.37	101.53
TRBC2	Traverse A2	39.28	0.01	22.62	10.44	1.22	0.49	28.16	0.37	102.22
TRBC2	Traverse A5	39.31	0.02	22.50	10.42	1.12	0.54	28.20	0.37	102.10
TRBC2	Traverse A8	38.26	0.01	22.28	10.20	1.17	0.53	28.04	0.36	100.49
TRBC2	Traverse A9	39.40	0.01	22.82	10.53	1.21	0.53	28.24	0.37	102.73
TRBC2	Traverse A10	38.78	0.00	22.55	10.29	1.20	0.50	27.95	0.37	101.27
TRBC2	Traverse A11	38.99	0.00	22.75	10.51	1.22	0.50	28.09	0.37	102.05
TRBC2	Traverse A12	39.78	0.00	23.17	10.52	1.25	0.50	27.97	0.38	103.19
TRBC2	Traverse A13	37.98	0.02	22.39	10.14	1.21	0.51	28.02	0.36	100.27
TRBC2	Traverse A14	39.03	0.01	22.75	10.37	1.20	0.51	28.15	0.37	102.02
TRBC2	Traverse A15	39.48	0.03	23.19	10.65	1.23	0.52	28.09	0.38	103.18
TRBC2	Traverse A16	40.12	0.00	23.28	10.59	1.23	0.51	27.83	0.38	103.55
TRBC2	Traverse A18	38.66	0.00	22.68	10.30	1.20	0.50	28.17	0.37	101.51
TRBC2	Traverse A21	38.45	0.01	22.49	10.33	1.12	0.53	28.27	0.37	101.19
TRBC2	Traverse A22	37.92	0.00	22.19	10.07	1.14	0.50	28.19	0.36	100.01
TRBC2	Traverse A23	38.41	0.01	22.73	10.28	1.17	0.49	28.22	0.36	101.29
TRBC2	Traverse A24	38.51	0.00	22.59	10.17	1.31	0.49	28.08	0.36	101.14
TRBC2	Traverse A25	38.40	0.01	22.45	10.08	1.43	0.51	27.98	0.36	100.86
TRBC2	Traverse A28	38.74	0.01	22.75	10.47	1.15	0.49	28.07	0.37	101.68
TRBC2	Traverse A29	37.69	0.01	22.60	10.79	1.14	0.44	26.96	0.40	99.62
TRBC2	Traverse A30	39.01	0.01	22.80	10.29	1.44	0.51	27.92	0.37	101.98
TRBC2	Traverse B1	38.84	0.01	22.35	10.01	1.69	0.46	27.87	0.36	101.23
TRBC2	Traverse B2	38.78	0.00	22.44	10.32	1.19	0.47	28.07	0.37	101.27
TRBC2	Traverse B3	38.53	0.00	22.48	10.24	1.31	0.48	28.02	0.37	101.05
TRBC2	Traverse B4	38.41	0.01	22.36	10.23	1.45	0.49	27.78	0.37	100.73
TRBC2	Traverse B5	38.86	0.02	22.65	10.22	1.47	0.47	27.95	0.37	101.64
TRBC2	Traverse B6	40.04	0.03	23.62	10.71	1.54	0.46	27.80	0.39	104.20
TRBC2	Traverse B7	38.77	0.01	22.44	10.08	1.55	0.49	27.84	0.36	101.18
TRBC2	Traverse B8	38.88	0.02	22.47	10.20	1.59	0.48	27.84	0.37	101.47
TRBC2	Traverse B9	38.56	0.00	22.39	10.07	1.62	0.49	27.83	0.36	100.96
TRBC2	Traverse B10	38.49	0.00	22.26	9.99	1.55	0.50	27.72	0.36	100.51
TRBC2	Traverse B11	37.39	0.01	21.85	9.89	1.60	0.47	27.77	0.36	98.98
TRBC2	Traverse B12	37.98	0.00	22.35	9.97	1.54	0.48	27.90	0.36	100.23
TRBC2	Traverse B14	39.52	0.00	23.01	10.67	1.32	0.46	27.22	0.39	102.20
TRBC2	Traverse B15	38.66	0.00	22.58	10.27	1.32	0.48	27.69	0.37	100.99
TRBC2	Traverse B16	38.10	0.00	22.35	10.12	1.24	0.44	28.05	0.36	100.30
TRBC2	Traverse B17	38.49	0.00	22.48	10.35	1.29	0.48	27.96	0.37	101.06
TRBC2	Traverse B18	38.67	0.00	22.50	10.13	1.46	0.48	27.82	0.36	101.06
TRBC2	Traverse B19	37.88	0.01	21.91	9.80	1.51	0.48	28.09	0.35	99.67
TRBC2	Traverse B20	38.46	0.02	22.34	9.35	1.84	0.51	28.50	0.33	101.01

Appendix 4.1 continued

Sample	Analysis	SiO_2	TiO_2	Al_2O_3	MgO	CaO	MnO	FeO*	MgO/FeO	Total
TRBC2	Traverse C1	38.58	0.01	22.50	9.88	1.45	0.50	28.26	0.35	101.18
TRBC2	Traverse C2	38.53	0.00	22.46	9.99	1.13	0.50	28.45	0.35	101.06
TRBC2	Traverse C4	38.79	0.00	22.46	9.94	1.32	0.50	28.40	0.35	101.41
TRBC2	Traverse C5	38.19	0.01	21.97	9.70	1.39	0.49	28.51	0.34	100.25
TRBC2	Traverse C6	38.58	0.02	22.33	9.74	1.51	0.49	28.22	0.35	100.90
TRBC2	Traverse C7	38.70	0.02	22.34	9.83	1.58	0.51	28.19	0.35	101.17
TRBC2	Traverse C8	38.56	0.01	22.54	9.80	1.71	0.51	28.14	0.35	101.28
TRBC2	Traverse C9	38.16	0.00	22.11	9.40	1.74	0.53	28.37	0.33	100.31
TRBC2	Traverse C11	38.99	0.00	22.56	9.68	1.75	0.52	28.33	0.34	101.83
TRBC2	Traverse C12	39.22	0.00	22.94	9.79	1.77	0.53	28.35	0.35	102.59
TRBC2	Traverse C13	38.49	0.01	22.34	9.58	1.84	0.54	28.36	0.34	101.16
TRBC2	Traverse C14	37.29	0.01	21.45	9.15	1.87	0.55	28.20	0.32	98.52
TRBC2	Traverse C15	38.48	0.00	22.32	9.55	1.91	0.52	28.17	0.34	100.94
TRBC2	Traverse C16	38.78	0.01	22.52	9.79	1.79	0.51	28.22	0.35	101.60
TRBC2	Traverse C18	37.54	0.01	21.49	9.10	1.84	0.50	28.04	0.32	98.51
TRBC2	Traverse C19	39.34	0.02	22.94	9.92	1.82	0.51	28.28	0.35	102.83
TRBC2	Traverse C20	39.04	0.01	22.64	9.84	1.79	0.52	28.43	0.35	102.27
TRBC2	Traverse C21	40.36	0.02	23.24	10.08	1.77	0.48	28.05	0.36	104.01
TRBC2	Traverse C22	38.60	0.01	22.35	9.70	1.74	0.53	28.13	0.34	101.06
TRBC2	Traverse C23	38.62	0.01	22.17	9.60	1.73	0.51	28.16	0.34	100.78
TRBC2	Traverse C24	39.23	0.00	22.77	9.76	1.62	0.50	28.38	0.34	102.25
TRBC2	Traverse C25	39.07	0.01	22.62	9.94	1.55	0.52	28.20	0.35	101.89
TRBC2	Traverse C26	39.13	0.00	22.64	10.04	1.39	0.51	28.33	0.35	102.03
TRBC2	Traverse C27	38.62	0.02	22.32	9.99	1.23	0.49	28.40	0.35	101.06
TRBC2	Traverse C28	37.55	0.00	21.64	9.67	1.18	0.48	28.26	0.34	98.78
TRBC2	Traverse C29	40.32	0.00	23.45	10.39	1.46	0.48	28.39	0.37	104.50
TRBC2	Traverse C30	39.12	0.00	22.60	9.95	1.50	0.52	28.10	0.35	101.79
TRBC2		**38.72**	**0.01**	**22.52**	**10.06**	**1.45**	**0.50**	**28.08**	**0.36**	**101.34**
TRER7	Traverse A1	36.83	0.00	21.55	4.95	1.37	2.11	33.62	0.15	100.42
TRER7	Traverse A2	37.18	0.01	21.85	6.36	1.56	1.75	31.89	0.20	100.59
TRER7	Traverse A3	37.43	0.01	21.91	6.85	1.56	1.66	31.45	0.22	100.87
TRER7	Traverse A4	37.82	0.01	22.23	7.05	1.54	1.66	31.22	0.23	101.52
TRER7	Traverse A5	37.61	0.00	21.97	6.93	1.50	1.61	31.18	0.22	100.80
TRER7	Traverse A6	37.48	0.01	21.93	7.04	1.56	1.62	31.10	0.23	100.75
TRER7	Traverse A7	37.58	0.00	21.90	6.96	1.52	1.66	31.37	0.22	100.98
TRER7	Traverse A8	37.72	0.00	21.97	6.78	1.39	1.65	31.46	0.22	100.97
TRER7	Traverse A9	37.52	0.01	21.94	6.19	1.51	1.87	32.06	0.19	101.10
TRER7	Traverse A10	37.72	0.03	21.82	4.70	1.50	2.32	33.94	0.14	102.03
TRER7	Traverse B1	36.50	0.00	21.40	5.16	1.44	2.15	33.13	0.16	99.79
TRER7	Traverse B2	37.49	0.00	22.36	6.66	1.44	1.74	31.67	0.21	101.37
TRER7	Traverse B3	36.66	0.00	21.62	6.68	1.56	1.63	31.31	0.21	99.46
TRER7	Traverse B4	36.95	0.00	21.83	6.89	1.48	1.63	30.70	0.22	99.46
TRER7	Traverse B5	38.73	0.01	22.22	7.36	1.48	1.57	30.53	0.24	101.90
TRER7	Traverse B6	37.15	0.03	21.94	6.37	1.50	1.77	31.91	0.20	100.66
TRER7	Traverse C1	36.56	0.01	21.61	5.64	1.71	2.02	32.21	0.18	99.75
TRER7	Traverse C2	36.51	0.01	21.86	6.71	1.76	1.77	31.28	0.21	99.89
TRER7	Traverse C3	36.60	0.01	21.44	6.16	1.46	1.90	32.09	0.19	99.66
TRER7		**37.26**	**0.01**	**21.86**	**6.39**	**1.52**	**1.79**	**31.80**	**0.20**	**100.63**
TRMR2	Traverse A1	35.58	0.01	21.22	7.06	0.90	0.64	31.81	0.22	97.21
TRMR2	Traverse A2	35.82	0.01	21.31	7.55	1.36	0.54	31.46	0.24	98.06
TRMR2	Traverse A3	35.63	0.00	21.45	7.68	1.40	0.52	31.04	0.25	97.72
TRMR2	Traverse A4	35.62	0.00	21.45	7.81	1.40	0.52	31.13	0.25	97.93
TRMR2	Traverse A5	36.11	0.00	21.56	8.01	1.24	0.53	30.98	0.26	98.44
TRMR2	Traverse A6	35.95	0.00	21.62	8.00	1.05	0.52	30.91	0.26	98.05
TRMR2	Traverse A7	35.97	0.00	21.63	8.25	0.95	0.52	31.07	0.27	98.39
TRMR2	Traverse A8	36.07	0.01	21.64	8.20	0.95	0.50	31.16	0.26	98.54
TRMR2	Traverse A9	36.12	0.00	21.67	8.17	0.99	0.52	31.11	0.26	98.57
TRMR2	Traverse A10	36.21	0.02	21.69	8.24	1.00	0.53	31.06	0.27	98.76
TRMR2	Traverse A11	36.21	0.00	21.68	8.21	1.02	0.55	30.96	0.27	98.63
TRMR2	Traverse A12	36.41	0.00	21.84	8.17	1.05	0.51	31.12	0.26	99.10
TRMR2	Traverse A13	36.70	0.00	21.75	8.14	0.99	0.52	31.16	0.26	99.26
TRMR2	Traverse A14	36.26	0.00	21.72	8.11	0.96	0.52	31.20	0.26	98.78
TRMR2	Traverse A15	36.73	0.00	21.82	8.18	1.04	0.54	31.26	0.26	99.56
TRMR2	Traverse A16	36.54	0.00	21.73	7.92	1.15	0.53	31.14	0.25	99.01
TRMR2	Traverse A17	36.51	0.02	21.86	7.80	1.37	0.50	31.12	0.25	99.18
TRMR2	Traverse A18	36.61	0.02	21.85	7.63	1.52	0.56	31.23	0.24	99.42
TRMR2	Traverse A19	36.89	0.00	21.76	7.50	1.27	0.55	31.70	0.24	99.68
TRMR2	Traverse A20	36.59	0.00	21.62	6.89	1.16	0.60	32.95	0.21	99.82
TRMR2	Traverse B1	35.60	0.01	21.19	6.54	1.24	0.48	33.02	0.20	98.09
TRMR2	Traverse B2	35.95	0.01	21.58	7.89	1.39	0.45	31.09	0.25	98.35

Appendix 4.1 continued

Sample	Analysis	SiO_2	TiO_2	Al_2O_3	MgO	CaO	MnO	FeO*	MgO/FeO	Total
TRMR2	Traverse B3	36.18	0.01	21.65	8.31	1.18	0.46	30.71	0.27	98.51
TRMR2	Traverse B4	36.28	0.02	21.76	8.58	1.06	0.44	30.69	0.28	98.82
TRMR2	Traverse B5	36.00	0.01	21.58	8.71	1.03	0.45	30.40	0.29	98.20
TRMR2	Traverse B6	36.15	0.00	21.60	8.69	1.06	0.42	30.14	0.29	98.07
TRMR2	Traverse B7	36.45	0.00	21.70	8.64	1.07	0.42	30.42	0.28	98.70
TRMR2	Traverse B8	36.17	0.02	21.58	8.77	1.10	0.42	30.40	0.29	98.47
TRMR2	Traverse B9	36.46	0.00	21.69	8.79	1.08	0.43	30.24	0.29	98.69
TRMR2	Traverse B10	36.26	0.00	21.79	8.78	1.07	0.41	30.20	0.29	98.52
TRMR2	Traverse B11	36.38	0.00	21.66	8.71	1.07	0.44	30.15	0.29	98.42
TRMR2	Traverse B12	36.22	0.01	21.65	8.79	1.13	0.42	30.21	0.29	98.43
TRMR2	Traverse B13	36.38	0.01	21.69	8.85	1.12	0.40	30.15	0.29	98.60
TRMR2	Traverse B14	42.87	0.01	25.49	10.80	0.97	0.41	29.52	0.37	110.09
TRMR2	Traverse B15	36.39	0.00	21.75	8.87	1.11	0.42	30.03	0.30	98.57
TRMR2	Traverse B16	36.62	0.00	21.60	8.90	1.06	0.42	30.05	0.30	98.67
TRMR2	Traverse B17	36.38	0.00	21.76	8.80	1.12	0.42	29.91	0.29	98.40
TRMR2	Traverse B18	36.39	0.01	21.81	8.88	1.08	0.42	30.14	0.29	98.73
TRMR2	Traverse B19	36.49	0.00	21.76	8.91	1.13	0.41	29.91	0.30	98.62
TRMR2	Traverse B20	36.49	0.00	21.71	8.96	1.11	0.44	30.04	0.30	98.76
TRMR2	Traverse B21	36.21	0.01	21.83	8.95	1.12	0.43	30.07	0.30	98.63
TRMR2	Traverse B22	36.41	0.02	21.81	8.81	1.06	0.41	29.93	0.29	98.46
TRMR2	Traverse B23	36.30	0.00	21.82	8.87	1.05	0.42	30.05	0.30	98.50
TRMR2	Traverse B24	36.43	0.00	21.62	8.93	1.04	0.41	29.94	0.30	98.39
TRMR2	Traverse B25	36.50	0.00	21.67	8.91	0.98	0.41	30.06	0.30	98.54
TRMR2	Traverse B26	36.68	0.00	21.75	8.86	0.99	0.43	30.18	0.29	98.91
TRMR2	Traverse B27	36.91	0.01	21.69	9.00	1.00	0.43	30.22	0.30	99.27
TRMR2	Traverse B28	36.87	0.00	21.95	9.01	1.10	0.45	30.08	0.30	99.48
TRMR2	Traverse B29	37.00	0.00	21.77	8.74	1.34	0.43	29.99	0.29	99.30
TRMR2	Traverse B30	36.44	0.02	21.63	8.61	1.38	0.44	29.62	0.29	98.15
TRMR2		**36.45**	**0.01**	**21.75**	**8.41**	**1.12**	**0.47**	**30.66**	**0.27**	**98.87**
TRER6B	Traverse A1	36.54	0.08	20.71	3.23	5.97	1.47	31.88	0.10	99.88
TRER6B	Traverse A2	37.06	0.04	21.18	3.80	6.14	1.33	30.78	0.12	100.34
TRER6B	Traverse A3	37.09	0.05	20.79	3.71	6.19	1.33	31.16	0.12	100.31
TRER6B	Traverse A4	36.61	0.04	20.98	3.84	6.20	1.26	30.86	0.12	99.79
TRER6B	Traverse A5	36.67	0.08	21.07	3.85	6.33	1.30	30.76	0.13	100.05
TRER6B	Traverse A6	36.82	0.02	21.35	3.39	5.75	1.38	31.66	0.11	100.38
TRER6B	Traverse B1	36.39	0.12	20.96	3.16	6.92	1.15	31.29	0.10	99.99
TRER6B	Traverse B2	37.58	0.07	21.46	3.26	10.33	0.65	27.40	0.12	100.74
TRER6B	Traverse B3	37.79	0.04	21.37	3.30	9.97	0.68	27.96	0.12	101.11
TRER6B	Traverse B4	37.45	0.05	21.47	3.19	10.11	0.65	28.10	0.11	101.02
TRER6B	Traverse B5	37.58	0.05	21.67	3.03	7.65	1.12	30.67	0.10	101.78
TRER6B	Traverse C1	37.59	0.03	21.43	3.25	7.82	1.22	30.14	0.11	101.48
TRER6B	Traverse C2	37.34	0.03	21.64	3.81	8.58	1.03	28.42	0.13	100.86
TRER6B	Traverse C3	37.40	0.06	21.56	3.80	8.50	1.01	28.65	0.13	100.97
TRER6B	Traverse C4	37.26	0.05	21.43	3.69	9.01	1.02	28.38	0.13	100.85
TRER6B	Traverse C5	37.01	0.04	21.25	3.32	6.42	1.24	31.45	0.11	100.73
TRER6B	Traverse D1	37.06	0.04	21.18	3.80	6.14	1.33	30.78	0.12	100.34
TRER6B	Traverse D2	37.09	0.05	20.79	3.71	6.19	1.33	31.16	0.12	100.31
TRER6B	Traverse D3	36.61	0.04	20.98	3.84	6.20	1.26	30.86	0.12	99.79
TRER6B	Traverse D4	36.67	0.08	21.07	3.85	6.33	1.30	30.76	0.13	100.05
TRER6B	Traverse E2	37.58	0.07	21.46	3.26	10.33	0.65	27.40	0.12	100.74
TRER6B	Traverse E3	37.79	0.04	21.37	3.30	9.97	0.68	27.96	0.12	101.11
TRER6B	Traverse E4	37.45	0.05	21.47	3.19	10.11	0.65	28.10	0.11	101.02
TRER6B	Traverse F2	37.34	0.03	21.64	3.81	8.58	1.03	28.42	0.13	100.86
TRER6B	Traverse F3	37.40	0.06	21.56	3.80	8.50	1.01	28.65	0.13	100.97
TRER6B	Traverse F4	37.26	0.05	21.43	3.69	9.01	1.02	28.38	0.13	100.85
TRER6B		**37.17**	**0.05**	**21.28**	**3.53**	**7.82**	**1.08**	**29.69**	**0.12**	**100.63**
HLM2	Traverse A1	36.12	0.00	21.01	2.47	2.09	3.04	35.30	0.07	100.03
HLM2	Traverse A2	35.85	0.01	21.29	3.32	2.30	2.14	34.61	0.10	99.53
HLM2	Traverse A3	36.16	0.01	21.23	3.41	2.28	1.94	34.82	0.10	99.83
HLM2	Traverse A4	36.93	0.02	20.40	3.18	2.23	2.12	34.17	0.09	99.04
HLM2	Traverse A5	36.57	0.00	21.36	3.14	1.55	2.63	35.23	0.09	100.47
HLM2	Traverse B1	36.56	0.00	21.28	3.95	1.64	1.96	35.06	0.11	100.45
HLM2	Traverse B2	36.45	0.01	21.48	3.99	2.18	1.60	34.69	0.12	100.41
HLM2	Traverse B3	36.18	0.00	21.45	4.01	2.14	1.51	34.64	0.12	99.95
HLM2	Traverse B4	36.60	0.00	21.39	4.15	2.13	1.50	34.45	0.12	100.22
HLM2	Traverse B5	36.65	0.00	21.55	4.14	2.04	1.51	34.77	0.12	100.66
HLM2	Traverse B6	36.32	0.02	21.28	4.04	2.06	1.57	34.96	0.12	100.25
HLM2	Traverse B7	36.38	0.02	21.16	3.63	2.03	1.66	35.42	0.10	100.29
HLM2	Traverse B8	36.74	0.01	21.44	3.91	2.02	1.73	34.84	0.11	100.69
HLM2	Traverse B9	36.87	0.00	21.52	3.57	2.12	2.02	35.16	0.10	101.26

Appendix 4.1 continued

Sample	Analysis	SiO_2	TiO_2	Al_2O_3	MgO	CaO	MnO	FeO*	MgO/FeO	Total
HLM2	Traverse B10	36.51	0.02	21.46	2.54	1.41	3.05	36.16	0.07	101.15
HLM2	Traverse C1	36.76	0.00	21.47	3.34	1.51	2.49	35.24	0.09	100.81
HLM2	Traverse C2	36.63	0.00	21.41	3.47	2.12	2.29	34.86	0.10	100.78
HLM2	Traverse C3	36.55	0.01	21.48	3.49	2.35	2.17	34.68	0.10	100.73
HLM2	Traverse C4	36.71	0.02	21.51	3.60	2.28	2.03	34.97	0.10	101.13
HLM2	Traverse C5	36.89	0.01	21.57	3.56	2.33	1.98	34.81	0.10	101.13
HLM2	Traverse C6	36.90	0.01	21.64	3.56	2.37	2.01	34.84	0.10	101.34
HLM2	Traverse C7	36.97	0.00	21.59	3.45	2.35	2.10	34.95	0.10	101.41
HLM2	Traverse C8	37.05	0.00	21.57	3.35	2.28	2.25	34.98	0.10	101.48
HLM2	Traverse C9	36.95	0.00	21.55	3.02	2.36	2.69	34.98	0.09	101.55
HLM2	Traverse C10	37.02	0.01	21.57	2.39	1.86	3.44	35.41	0.07	101.70
HLM2		**36.61**	**0.01**	**21.39**	**3.47**	**2.08**	**2.14**	**34.96**	**0.10**	**100.65**

*Total iron reported as FeO

Appendix 4.2: Electron microprobe analyses of biotite (oxide weight percent)

Sample	Analysis	SiO_2	TiO_2	Al_2O_3	MgO	CaO	MnO	FeO*	Na_2O	K_2O	MgO/FeO	Total
70-30-2	Matrix	34.70	4.71	17.30	10.70	0.11	0.00	16.55	0.09	9.25	0.65	93.55
70-30-2	Matrix	35.29	4.09	17.47	11.45	0.05	0.00	16.64	0.12	9.16	0.69	94.27
70-30-2	Matrix	35.59	3.78	18.00	10.79	0.02	0.00	16.25	0.11	9.19	0.66	93.74
70-30-2	Matrix	35.83	4.16	17.52	11.31	0.00	0.00	16.60	0.19	9.48	0.68	95.09
70-30-2	**Matrix**	**35.36**	**4.18**	**17.57**	**11.06**	**0.05**	**0.00**	**16.51**	**0.13**	**9.27**	**0.67**	**94.16**
RM42	Matrix	31.44	8.09	17.66	9.04	0.08	0.10	19.41	0.06	6.50	0.47	92.37
RM42	Matrix	34.88	4.40	17.94	8.94	0.00	0.00	18.84	0.10	9.38	0.47	94.49
RM42	Matrix	34.94	5.06	17.82	8.48	0.00	0.03	18.93	0.05	9.62	0.45	94.92
RM42	Matrix	33.17	6.94	18.41	9.04	0.02	0.08	19.22	0.04	6.40	0.47	93.44
RM42	**Matrix**	**34.87**	**1.01**	**19.63**	**10.34**	**0.04**	**0.08**	**19.17**	**0.21**	**9.51**	**0.54**	**94.86**
RRSW1	Inclusion in garnet	34.85	3.57	15.09	12.67	0.08	0.07	19.38	0.27	6.55	0.65	92.53
RRSW1	Inclusion in garnet	35.39	4.62	15.09	11.91	0.03	0.02	18.00	0.30	8.12	0.66	93.48
RRSW1	Inclusion in garnet	35.23	3.89	14.93	11.89	0.06	0.02	19.27	0.24	7.52	0.62	93.05
RRSW1	Inclusion in garnet	31.51	4.85	14.60	11.05	2.81	0.08	23.34	0.02	1.49	0.47	89.76
RRSW1	Inclusion in garnet	35.34	4.59	15.01	10.89	0.00	0.08	19.51	0.26	8.32	0.56	93.99
RRSW1	Inclusion in garnet	35.58	5.00	14.76	11.61	0.28	0.02	17.27	0.32	8.37	0.67	93.21
RRSW1	**Inclusion in garnet**	**34.65**	**4.42**	**14.91**	**11.67**	**0.54**	**0.05**	**19.46**	**0.24**	**6.73**	**0.61**	**92.67**
RRSW1	Matrix	32.06	1.74	17.17	11.67	0.97	0.14	24.18	0.04	1.08	0.48	89.06
RRSW1	Matrix	33.90	3.08	15.16	11.22	0.10	0.09	22.94	0.11	5.61	0.49	92.21
RRSW1	Matrix	35.44	4.94	14.75	10.34	0.00	0.06	20.22	0.16	9.05	0.51	94.97
RRSW1	Matrix	35.18	4.46	14.71	10.46	0.02	0.06	20.53	0.19	8.71	0.51	94.32
RRSW1	Matrix	32.12	2.82	13.48	10.99	0.08	0.05	20.73	0.14	5.93	0.53	86.33
RRSW1	Matrix	31.11	1.93	14.84	12.93	0.12	0.11	25.15	0.06	2.75	0.51	88.98
RRSW1	Matrix	34.49	5.14	14.09	10.49	1.43	0.06	20.67	0.12	6.48	0.51	92.97
RRSW1	Matrix	33.39	1.12	14.02	12.94	1.23	0.11	24.91	0.04	1.60	0.52	89.36
RRSW1	Matrix	32.26	3.03	15.01	12.40	0.29	0.10	24.24	0.06	4.41	0.51	91.79
RRSW1	**Matrix**	**33.33**	**3.14**	**14.80**	**11.49**	**0.47**	**0.09**	**22.62**	**0.10**	**5.07**	**0.51**	**91.11**
RRCR2	Inclusion in garnet	33.82	2.12	18.44	7.30	0.07	0.06	22.70	0.19	8.71	0.32	93.41
RRCR2	Matrix	33.35	3.44	17.77	7.02	0.01	0.05	22.63	0.16	9.37	0.31	93.78
RRCR2	Matrix	33.73	3.49	18.17	7.04	0.01	0.04	22.74	0.13	9.55	0.31	94.90
RRCR2	Matrix	33.44	3.47	18.02	7.02	0.00	0.04	22.36	0.18	9.60	0.31	94.13
RRCR2	Matrix	33.16	3.39	18.11	6.99	0.03	0.07	22.48	0.17	9.14	0.31	93.54
RRCR2	Matrix	33.52	3.13	18.19	7.33	0.01	0.04	22.23	0.18	9.50	0.33	94.12
RRCR2	Matrix	33.88	3.11	18.27	7.27	0.00	0.05	22.24	0.17	9.43	0.33	94.42
RRCR2	Matrix	33.63	3.33	17.86	7.17	0.00	0.05	22.47	0.16	9.56	0.32	94.24
RRCR2	Matrix	33.64	3.29	18.07	7.37	0.01	0.04	22.59	0.20	9.48	0.33	94.67
RRCR2	Matrix	33.75	3.21	18.25	7.26	0.03	0.05	21.97	0.20	9.19	0.33	93.90
RRCR2	Matrix	35.26	2.73	19.55	6.47	0.08	0.04	19.41	0.16	8.22	0.33	91.92
RRCR2	Matrix	33.56	3.19	18.20	7.48	0.11	0.06	22.06	0.18	9.06	0.34	93.89

Appendix 4.2 continued

Sample	Analysis	SiO_2	TiO_2	Al_2O_3	MgO	CaO	MnO	FeO*	Na_2O	K_2O	MgO/FeO	Total
RRCR2	Matrix	32.93	3.34	17.71	6.90	0.05	0.06	22.64	0.12	8.96	0.30	92.69
RRCR2	**Matrix**	**33.65**	**3.26**	**18.18**	**7.11**	**0.03**	**0.05**	**22.15**	**0.17**	**9.25**	**0.32**	**93.85**
RRCR2	Rimming garnet	33.24	2.05	18.78	7.19	0.00	0.05	22.90	0.17	9.45	0.31	93.83
RRCR2	Rimming garnet	33.25	2.44	18.64	7.10	0.00	0.04	22.76	0.19	9.30	0.31	93.72
RRCR2	Rimming garnet	33.65	1.89	19.51	7.39	0.05	0.05	22.12	0.21	8.71	0.33	93.59
RRCR2	Rimming garnet	33.49	2.44	19.10	7.01	0.01	0.06	21.64	0.21	9.33	0.32	93.28
RRCR2	Rimming garnet	34.86	3.76	19.67	6.60	0.07	0.04	20.72	0.22	8.02	0.32	93.95
RRCR2	**Rimming garnet**	**33.70**	**2.51**	**19.14**	**7.06**	**0.03**	**0.05**	**22.03**	**0.20**	**8.96**	**0.32**	**93.67**
RRCR3	Inclusion in garnet	35.07	4.19	18.33	9.04	0.00	0.01	19.30	0.22	9.46	0.47	95.61
RRCR3	Inclusion in garnet	35.09	4.37	18.59	8.96	0.00	0.00	19.27	0.19	9.31	0.47	95.79
RRCR3	Inclusion in garnet	35.79	3.78	18.95	9.95	0.01	0.01	17.73	0.19	9.70	0.56	96.10
RRCR3	Inclusion in garnet	35.13	4.04	18.33	9.85	0.02	0.01	18.04	0.27	9.14	0.55	94.81
RRCR3	Inclusion in garnet	35.07	3.66	18.73	9.27	0.01	0.00	18.86	0.30	9.18	0.49	95.06
RRCR3	Inclusion in garnet	35.12	3.70	18.75	9.28	0.01	0.01	18.92	0.28	9.37	0.49	95.44
RRCR3	Inclusion in garnet	34.86	4.37	18.32	9.16	0.01	0.00	18.98	0.33	9.16	0.48	95.19
RRCR3	Inclusion in garnet	35.27	4.20	18.88	9.19	0.03	0.01	18.98	0.32	9.11	0.48	95.99
RRCR3	Inclusion in garnet	34.52	3.70	18.68	9.09	0.02	0.01	19.46	0.47	8.91	0.47	94.85
RRCR3	Inclusion in garnet	34.57	3.66	18.29	9.04	0.00	0.00	19.82	0.36	9.16	0.46	94.90
RRCR3	Inclusion in garnet	34.63	3.86	18.24	9.22	0.01	0.02	19.30	0.36	9.00	0.48	94.63
RRCR3	**Inclusion in garnet**	**35.01**	**3.96**	**18.55**	**9.28**	**0.01**	**0.01**	**18.97**	**0.30**	**9.23**	**0.49**	**95.31**
RRCR3	Matrix	34.37	3.72	18.45	7.27	0.00	0.01	22.31	0.20	9.32	0.33	95.65
RRCR3	Matrix	33.68	3.62	18.60	7.22	0.00	0.03	22.36	0.23	9.30	0.32	95.03
RRCR3	Matrix	33.89	3.55	18.45	7.31	0.02	0.03	22.06	0.18	9.19	0.33	94.66
RRCR3	Matrix	34.13	3.67	18.40	7.31	0.00	0.03	21.81	0.26	9.16	0.34	94.78
RRCR3	Matrix	33.86	3.67	18.17	7.20	0.05	0.01	22.14	0.28	8.67	0.33	94.05
RRCR3	Matrix	33.80	3.59	18.31	7.22	0.01	0.03	22.16	0.21	9.29	0.33	94.62
RRCR3	Matrix	33.83	3.65	18.60	7.36	0.00	0.02	21.94	0.23	9.34	0.34	94.95
RRCR3	Matrix	33.97	3.67	18.53	7.20	0.01	0.02	21.64	0.23	9.14	0.33	94.40
RRCR3	Matrix	34.29	3.72	18.78	7.39	0.02	0.01	21.88	0.29	9.24	0.34	95.62
RRCR3	Matrix	32.98	3.70	17.95	7.10	0.01	0.03	22.08	0.24	9.26	0.32	93.35
RRCR3	Matrix	33.62	3.74	18.32	7.29	0.01	0.02	21.95	0.28	9.24	0.33	94.47
RRCR3	Matrix	33.99	3.58	18.58	7.19	0.01	0.02	21.27	0.24	9.10	0.34	93.97
RRCR3	Matrix	34.23	3.91	18.37	7.47	0.00	0.01	22.02	0.18	9.40	0.34	95.60
RRCR3	Matrix	33.82	3.89	18.06	7.04	0.05	0.02	22.21	0.33	9.14	0.32	94.55
RRCR3	Matrix	33.78	3.62	18.33	7.35	0.05	0.02	21.94	0.27	9.32	0.33	94.67
RRCR3	**Matrix**	**33.88**	**3.69**	**18.39**	**7.26**	**0.02**	**0.02**	**21.98**	**0.24**	**9.21**	**0.33**	**94.69**
RRCR3	Rimming garnet	35.09	3.61	19.07	7.52	0.00	0.02	21.67	0.26	9.27	0.35	96.50
RRCR3	Rimming garnet	34.64	3.45	18.60	7.54	0.01	0.03	22.32	0.28	9.05	0.34	95.92
RRCR3	Rimming garnet	34.90	3.56	19.15	7.33	0.01	0.03	21.62	0.28	9.20	0.34	96.07
RRCR3	Rimming garnet	34.60	3.83	18.29	7.33	0.01	0.00	21.95	0.30	9.14	0.33	95.45

Appendix 4.2 continued

Sample	Analysis	SiO_2	TiO_2	Al_2O_3	MgO	CaO	MnO	FeO*	Na_2O	K_2O	MgO/FeO	Total
RRCR3	Rimming garnet	34.47	3.48	18.54	7.36	0.02	0.03	22.13	0.24	9.22	0.33	95.48
RRCR3	Rimming garnet	34.02	3.58	18.42	7.30	0.01	0.02	21.60	0.30	9.22	0.34	94.47
RRCR3	Rimming garnet	34.76	3.40	18.71	7.50	0.01	0.02	21.77	0.26	9.01	0.34	95.41
RRCR3	Rimming garnet	34.40	3.50	18.65	7.38	0.01	0.02	22.00	0.21	9.26	0.34	95.43
RRCR3	Rimming garnet	34.29	3.63	18.85	7.32	0.01	0.02	21.74	0.24	9.37	0.34	95.46
RRCR3	**Rimming garnet**	**34.57**	**3.56**	**18.70**	**7.40**	**0.01**	**0.02**	**21.87**	**0.26**	**9.19**	**0.34**	**95.58**
RRCR5	Inclusion in garnet	33.43	3.06	18.64	6.98	0.03	0.01	22.06	0.24	8.84	0.32	93.29
RRCR5	Inclusion in garnet	33.40	3.12	19.05	7.25	0.00	0.02	22.04	0.21	8.96	0.33	94.06
RRCR5	Inclusion in garnet	33.73	3.24	18.85	7.86	0.00	0.01	21.60	0.10	9.29	0.36	94.68
RRCR5	Inclusion in garnet	33.43	3.29	18.81	7.14	0.02	0.02	21.38	0.31	8.89	0.33	93.31
RRCR5	Inclusion in garnet	33.68	3.34	19.05	7.18	0.01	0.00	21.46	0.28	9.15	0.33	94.15
RRCR5	Inclusion in garnet	34.16	3.28	19.17	7.13	0.01	0.01	21.84	0.26	9.28	0.33	95.12
RRCR5	Inclusion in garnet	32.24	3.21	18.29	7.15	0.09	0.02	21.16	0.33	8.76	0.34	91.25
RRCR5	Inclusion in garnet	33.98	3.24	19.18	7.10	0.00	0.04	21.95	0.29	9.26	0.32	95.02
RRCR5	Inclusion in garnet	34.29	3.85	18.87	7.90	0.02	0.02	20.46	0.27	8.94	0.39	94.63
RRCR5	Inclusion in garnet	34.14	3.85	18.82	7.96	0.05	0.02	20.01	0.28	8.96	0.40	94.08
RRCR5	Inclusion in garnet	34.23	3.71	18.97	7.59	0.00	0.03	21.10	0.30	9.14	0.36	95.05
RRCR5	Inclusion in garnet	35.20	3.34	19.65	8.51	0.00	0.00	19.67	0.26	9.46	0.43	96.09
RRCR5	Inclusion in garnet	35.13	3.22	19.57	8.55	0.01	0.02	19.20	0.35	9.26	0.44	95.30
RRCR5	Inclusion in garnet	35.66	3.42	19.73	8.82	0.00	0.01	19.24	0.30	9.35	0.46	96.55
RRCR5	Inclusion in garnet	35.37	4.00	19.45	8.48	0.04	0.02	19.14	0.36	9.17	0.44	96.01
RRCR5	Inclusion in garnet	35.29	3.31	19.48	8.64	0.00	0.02	19.41	0.25	9.38	0.44	95.78
RRCR5	Inclusion in garnet	35.77	3.25	20.01	9.16	0.00	0.02	18.81	0.29	9.41	0.49	96.72
RRCR5	Inclusion in garnet	34.38	3.25	19.18	8.74	0.02	0.02	19.16	0.38	9.24	0.46	94.37
RRCR5	Inclusion in garnet	35.51	3.32	19.72	8.88	0.02	0.01	19.14	0.27	9.34	0.46	96.20
RRCR5	Inclusion in garnet	34.90	2.54	19.55	9.14	0.04	0.02	19.11	0.29	9.20	0.48	94.77
RRCR5	Inclusion in garnet	35.38	3.28	19.46	8.42	0.00	0.01	19.51	0.25	9.23	0.43	95.54
RRCR5	**Inclusion in garnet**	**34.44**	**3.34**	**19.21**	**8.03**	**0.02**	**0.02**	**20.35**	**0.28**	**9.17**	**0.40**	**94.86**
RRCR5	Matrix	34.41	3.28	19.09	7.19	0.02	0.03	22.29	0.23	9.29	0.32	95.82
RRCR5	Matrix	34.71	3.38	18.94	7.07	0.01	0.02	21.88	0.25	9.39	0.32	95.66
RRCR5	Matrix	33.83	3.34	18.84	7.00	0.00	0.02	22.52	0.20	9.33	0.31	95.06
RRCR5	Matrix	34.14	3.56	19.26	6.79	0.00	0.03	21.77	0.21	9.44	0.31	95.18
RRCR5	Matrix	33.93	3.50	18.88	6.83	0.00	0.03	22.06	0.24	9.34	0.31	94.80
RRCR5	Matrix	33.93	3.50	18.76	6.92	0.00	0.04	22.23	0.23	9.33	0.31	94.93
RRCR5	Matrix	33.47	3.61	18.59	6.79	0.00	0.03	22.14	0.21	9.38	0.31	94.21
RRCR5	Matrix	32.81	3.49	17.98	6.73	0.00	0.03	21.16	0.17	9.02	0.32	91.38
RRCR5	Matrix	33.71	3.57	18.54	6.85	0.01	0.03	22.21	0.11	9.16	0.31	94.19
RRCR5	Matrix	33.70	3.58	18.91	6.94	0.00	0.04	21.83	0.16	9.53	0.32	94.70
RRCR5	Matrix	34.34	3.59	18.96	6.97	0.01	0.03	21.57	0.25	9.35	0.32	95.04
RRCR5	Matrix	33.53	3.55	18.77	6.80	0.00	0.02	21.62	0.21	9.41	0.31	93.92
RRCR5	Matrix	33.56	3.64	18.59	6.77	0.01	0.03	21.93	0.20	9.33	0.31	94.06
RRCR5	Matrix	34.03	3.59	18.72	6.88	0.00	0.05	22.10	0.19	9.39	0.31	94.95
RRCR5	Matrix	33.75	3.61	18.44	7.05	0.00	0.02	22.34	0.19	9.39	0.32	94.79

Appendix 4.2 continued

Sample	Analysis	SiO_2	TiO_2	Al_2O_3	MgO	CaO	MnO	FeO*	Na_2O	K_2O	MgO/FeO	Total
RRCR5	**Matrix**	**33.86**	**3.52**	**18.75**	**6.91**	**0.00**	**0.03**	**21.98**	**0.20**	**9.34**	**0.31**	**94.58**
RRCR5	Rimming garnet	33.86	3.26	18.85	6.93	0.04	0.04	22.07	0.30	8.95	0.31	94.30
RRCR5	Rimming garnet	33.61	3.13	19.28	7.07	0.01	0.04	21.98	0.27	9.24	0.32	94.62
RRCR5	Rimming garnet	33.66	3.29	19.18	6.99	0.00	0.03	21.90	0.28	9.21	0.32	94.55
RRCR5	Rimming garnet	33.64	3.07	18.83	6.93	0.01	0.02	22.22	0.32	9.11	0.31	94.15
RRCR5	Rimming garnet	33.86	3.07	18.86	6.99	0.02	0.02	21.53	0.32	8.82	0.32	93.48
RRCR5	Rimming garnet	34.38	3.23	19.29	7.14	0.01	0.03	22.10	0.27	9.11	0.32	95.56
RRCR5	Rimming garnet	34.80	3.45	19.22	7.08	0.00	0.03	22.06	0.25	9.30	0.32	96.19
RRCR5	Rimming garnet	35.26	2.18	20.65	8.08	0.01	0.02	20.20	0.26	9.47	0.40	96.15
RRCR5	Rimming garnet	34.63	3.05	19.29	7.24	0.00	0.04	22.08	0.21	9.51	0.33	96.05
RRCR5	Rimming garnet	34.55	3.23	19.21	7.22	0.03	0.02	22.00	0.23	9.19	0.33	95.67
RRCR5	Rimming garnet	34.40	3.18	18.99	7.16	0.01	0.03	21.36	0.27	9.36	0.34	94.74
RRCR5	Rimming garnet	34.75	3.22	19.26	7.21	0.01	0.03	21.80	0.25	9.20	0.33	95.73
RRCR5	Rimming garnet	33.80	3.20	19.01	7.14	0.05	0.02	21.86	0.25	9.10	0.33	94.44
RRCR5	Rimming garnet	34.94	3.35	19.11	7.20	0.00	0.01	21.85	0.29	9.27	0.33	96.03
RRCR5	Rimming garnet	34.98	3.09	19.73	7.55	0.00	0.01	21.49	0.20	9.53	0.35	96.60
RRCR5	Rimming garnet	34.98	3.11	19.52	7.36	0.06	0.03	21.70	0.28	9.13	0.34	96.17
RRCR5	**Rimming garnet**	**34.38**	**3.13**	**19.27**	**7.20**	**0.02**	**0.03**	**21.76**	**0.27**	**9.22**	**0.33**	**95.28**
RMC200	Inclusion in garnet	37.60	2.23	18.09	15.89	0.08	0.00	12.08	0.53	8.69	1.32	95.19
RMC200	Inclusion in garnet	36.55	2.81	17.75	13.91	0.00	0.02	15.09	0.46	8.47	0.92	95.14
RMC200	Inclusion in garnet	35.41	2.39	17.38	14.03	0.08	0.02	15.25	0.43	8.05	0.92	93.12
RMC200	Traverse in biotite inclusion A1	37.76	2.44	18.21	15.52	0.00	0.02	13.07	0.57	8.68	1.19	96.38
RMC200	Traverse in biotite inclusion A2	37.54	2.37	18.18	15.26	0.01	0.05	13.12	0.51	8.72	1.16	95.90
RMC200	Traverse in biotite inclusion A3	37.39	2.65	18.01	15.08	0.01	0.00	13.25	0.48	8.80	1.14	95.66
RMC200	Traverse in biotite inclusion A4	37.17	2.59	17.92	14.89	0.00	0.04	13.34	0.47	8.86	1.12	95.62
RMC200	Traverse in biotite inclusion A5	37.13	2.60	17.93	14.72	0.06	0.03	13.29	0.52	8.86	1.11	95.21
RMC200	Traverse in biotite inclusion A6	37.25	2.58	17.87	14.83	0.02	0.00	13.40	0.49	8.82	1.11	95.26
RMC200	Traverse in biotite inclusion A7	36.86	2.49	17.77	14.73	0.06	0.00	13.26	0.52	8.77	1.11	94.75
RMC200	**Inclusion in garnet**	**35.14**	**1.04**	**19.66**	**10.88**	**0.03**	**0.06**	**18.26**	**0.21**	**9.45**	**0.61**	**94.78**
RMC200	Matrix	36.31	2.19	17.61	13.47	0.00	0.03	17.19	0.35	7.96	0.78	95.12
RMC200	Matrix	37.06	2.16	17.70	13.70	0.06	0.00	15.70	0.45	8.72	0.87	95.55
RMC200	Matrix	36.93	2.60	17.66	13.28	0.03	0.04	16.32	0.38	8.53	0.81	95.77
RMC200	Matrix	36.91	2.32	17.54	13.44	0.05	0.01	15.72	0.44	8.39	0.85	94.82
RMC200	Matrix	37.20	2.18	17.78	13.73	0.01	0.00	15.68	0.36	8.72	0.88	95.65
RMC200	Matrix	36.92	2.74	17.59	13.54	0.00	0.06	15.58	0.39	8.86	0.87	96.02
RMC200	Matrix	37.01	3.10	17.33	13.51	0.00	0.00	15.62	0.55	8.76	0.87	95.88
RMC200	Matrix	37.13	2.86	17.47	13.44	0.00	0.08	16.02	0.46	8.90	0.84	96.36
RMC200	Matrix	35.24	2.99	16.89	13.38	0.00	0.03	15.38	0.49	8.42	0.87	93.12
RMC200	Matrix	36.89	3.06	17.26	13.75	0.00	0.00	15.61	0.38	8.82	0.88	95.84
RMC200	Traverse in matrix biotite A1	34.82	2.63	17.39	14.43	0.00	0.08	16.99	0.14	6.58	0.85	93.09

Appendix 4.2 continued

Sample	Analysis	SiO_2	TiO_2	Al_2O_3	MgO	CaO	MnO	FeO*	Na_2O	K_2O	MgO/FeO	Total
RMC200	Traverse in matrix biotite A2	36.71	2.84	17.30	13.45	0.08	0.00	15.97	0.42	8.78	0.84	95.64
RMC200	Traverse in matrix biotite A3	36.86	2.85	17.33	13.44	0.02	0.03	15.72	0.44	8.82	0.85	95.83
RMC200	Traverse in matrix biotite A4	36.82	2.84	17.37	13.48	0.04	0.00	15.63	0.33	8.81	0.86	95.30
RMC200	Traverse in matrix biotite A5	37.02	2.84	17.37	13.45	0.01	0.02	15.68	0.49	8.98	0.86	95.86
RMC200	Traverse in matrix biotite A6	36.75	2.94	17.46	13.56	0.00	0.03	15.75	0.37	8.96	0.86	95.82
RMC200	Traverse in matrix biotite A7	36.94	2.93	17.39	13.61	0.00	0.03	15.80	0.48	8.49	0.86	95.66
RMC200	Traverse in matrix biotite A8	36.86	2.73	17.49	13.68	0.00	0.03	15.83	0.40	8.84	0.86	95.85
RMC200	Traverse in matrix biotite A9	37.00	2.84	17.59	13.75	0.00	0.01	15.25	0.49	8.51	0.90	95.78
RMC200	Traverse in matrix biotite A10	36.35	2.71	17.42	13.68	0.00	0.00	15.88	0.52	8.51	0.86	95.08
RMC200	Traverse in matrix biotite B1	36.35	2.73	16.94	13.32	0.00	0.04	15.32	0.45	8.54	0.87	93.78
RMC200	Traverse in matrix biotite B2	37.15	2.81	17.11	13.56	0.00	0.04	15.59	0.42	8.72	0.87	95.72
RMC200	Traverse in matrix biotite B3	36.93	2.90	17.26	13.44	0.03	0.00	15.65	0.41	8.72	0.86	95.44
RMC200	Traverse in matrix biotite B4	36.98	2.83	17.28	13.49	0.10	0.02	15.57	0.30	8.64	0.87	95.21
RMC200	Traverse in matrix biotite B5	36.76	2.91	17.20	13.56	0.06	0.00	15.67	0.34	8.77	0.87	95.37
RMC200	**Matrix**	**35.20**	**1.11**	**19.62**	**10.73**	**0.02**	**0.06**	**18.43**	**0.19**	**9.42**	**0.59**	**94.83**
RMC200	Rimming garnet	35.18	0.59	18.53	13.99	0.22	0.00	15.61	0.29	7.08	0.90	91.50
RMC200	Rimming garnet	35.90	2.02	17.26	13.54	0.16	0.02	16.36	0.16	7.57	0.83	92.99
RMC200	Rimming garnet	38.38	2.73	20.84	10.91	0.03	0.00	13.93	0.11	6.97	0.78	93.89
RMC200	Rimming garnet	37.03	2.62	17.24	13.89	0.00	0.02	15.30	0.51	8.72	0.91	95.33
RMC200	Rimming garnet	37.68	2.73	17.45	13.62	0.00	0.05	15.15	0.53	8.79	0.90	96.16
RMC200	Traverse in biotite rimming garnet A1	37.02	2.54	17.74	14.15	0.05	0.00	14.59	0.41	8.39	0.97	95.00
RMC200	Traverse in biotite rimming garnet A2	36.60	2.83	17.58	13.87	0.02	0.05	15.06	0.41	8.53	0.92	94.95
RMC200	Traverse in biotite rimming garnet A3	36.19	2.86	17.76	13.15	0.05	0.05	15.42	0.17	7.88	0.85	93.86
RMC200	Traverse in biotite rimming garnet A4	37.26	3.11	17.51	13.51	0.01	0.00	15.67	0.47	8.76	0.86	96.58
RMC200	**Rimming garnet**	**36.62**	**2.63**	**17.60**	**13.38**	**0.03**	**0.02**	**15.75**	**0.38**	**8.47**	**0.85**	**94.98**
RM37	Deformed biotite	39.02	2.45	26.62	3.80	0.08	0.04	13.02	0.25	7.18	0.29	92.47
RM37	Deformed biotite	39.09	2.46	27.54	3.95	0.05	0.03	13.81	0.11	5.67	0.29	92.71
RM37	Deformed biotite	37.96	2.57	26.29	4.22	0.09	0.04	14.39	0.08	5.68	0.29	91.31
RM37	**Deformed biotite**	**38.69**	**2.49**	**26.82**	**3.99**	**0.07**	**0.04**	**13.74**	**0.15**	**6.18**	**0.29**	**92.16**
RM37	Inclusion in garnet	35.10	3.64	19.70	8.59	0.00	0.00	19.52	0.29	9.44	0.44	96.77
RM37	Matrix	34.97	3.77	19.66	6.22	0.10	0.00	20.42	0.19	8.20	0.30	93.77
RM37	Matrix	34.19	3.90	18.91	6.74	0.00	0.03	22.29	0.09	9.54	0.30	96.15
RM37	Matrix	31.77	2.66	19.62	6.68	0.04	0.11	26.03	0.11	6.39	0.26	93.57
RM37	Matrix	34.97	2.86	19.40	7.10	0.00	0.02	22.40	0.19	9.36	0.32	96.30
RM37	Matrix	35.03	4.05	18.96	6.58	0.00	0.05	22.02	0.13	9.13	0.30	95.94
RM37	Matrix	34.27	3.52	18.48	7.13	0.18	0.02	22.10	0.17	8.50	0.32	94.63
RM37	Matrix	36.15	3.56	21.35	5.64	0.00	0.00	19.49	0.18	8.22	0.29	94.60
RM37	**Matrix**	**34.55**	**3.49**	**19.51**	**6.83**	**0.04**	**0.03**	**21.78**	**0.17**	**8.60**	**0.32**	**95.22**
RM37	Rimming garnet	35.14	2.88	20.23	6.72	0.03	0.07	21.69	0.18	9.20	0.31	96.15
RM37	Rimming garnet	35.06	2.73	19.89	7.57	0.00	0.03	21.87	0.26	9.67	0.35	97.08
RM37	Rimming garnet	34.58	2.97	19.30	7.53	0.18	0.06	21.98	0.25	8.34	0.34	95.46
RM37	Rimming garnet	34.91	2.71	19.86	7.32	0.05	0.00	21.94	0.20	9.50	0.33	96.56

Appendix 4.2 continued

Sample	Analysis	SiO_2	TiO_2	Al_2O_3	MgO	CaO	MnO	FeO*	Na_2O	K_2O	MgO/FeO	Total
RM37	Rimming garnet	34.73	2.54	19.78	7.63	0.01	0.00	21.39	0.25	9.49	0.36	95.88
RM37	**Rimming garnet**	**34.88**	**2.77**	**19.81**	**7.35**	**0.05**	**0.03**	**21.77**	**0.23**	**9.24**	**0.34**	**96.23**
RM39	Inclusion in garnet	30.55	2.12	18.57	7.93	0.07	0.07	27.73	0.18	4.55	0.29	91.83
RM39	Inclusion in garnet	35.35	3.60	19.04	8.09	0.05	0.03	21.11	0.25	9.28	0.38	96.80
RM39	Inclusion in garnet	35.10	3.21	19.17	8.75	0.00	0.02	19.81	0.19	9.39	0.44	95.82
RM39	Inclusion in garnet	34.77	2.70	18.70	9.31	0.13	0.03	20.88	0.36	8.21	0.45	95.22
RM39	Inclusion in garnet	32.01	4.25	18.50	7.59	0.09	0.03	23.59	0.14	7.43	0.32	94.00
RM39	Traverse in biotite inclusion A1	34.92	3.62	19.01	7.83	0.00	0.01	21.63	0.08	9.27	0.36	96.37
RM39	Traverse in biotite inclusion A2	35.14	4.16	18.91	7.61	0.01	0.00	21.39	0.17	9.58	0.36	97.14
RM39	Traverse in biotite inclusion A3	35.34	3.95	18.91	7.88	0.02	0.00	20.96	0.12	9.59	0.38	96.94
RM39	Traverse in biotite inclusion A4	35.22	4.00	18.90	7.79	0.06	0.00	21.06	0.15	9.58	0.37	96.75
RM39	Traverse in biotite inclusion A5	35.37	3.97	18.78	7.82	0.04	0.01	20.89	0.19	9.58	0.37	96.82
RM39	Traverse in biotite inclusion A6	35.36	3.86	18.88	7.91	0.02	0.02	20.93	0.18	9.54	0.38	96.70
RM39	Traverse in biotite inclusion A7	35.19	3.79	18.90	8.05	0.02	0.00	20.79	0.07	9.68	0.39	96.49
RM39	Traverse in biotite inclusion A8	35.30	3.77	18.91	8.07	0.00	0.01	20.72	0.00	9.55	0.39	96.33
RM39	Traverse in biotite inclusion A9	35.17	3.41	19.24	8.36	0.00	0.00	20.46	0.23	9.35	0.41	96.21
RM39	Traverse in biotite inclusion A10	35.10	3.20	19.13	8.58	0.00	0.00	20.17	0.12	9.55	0.43	95.85
RM39	Traverse in biotite inclusion B1	34.98	2.97	17.89	9.14	0.01	0.01	21.12	0.37	8.88	0.43	95.36
RM39	Traverse in biotite inclusion B2	35.00	3.08	18.13	9.30	0.02	0.03	20.93	0.26	9.02	0.44	95.79
RM39	Traverse in biotite inclusion B3	34.70	2.95	17.76	8.83	0.11	0.04	20.88	0.23	8.33	0.42	94.04
RM39	Traverse in biotite inclusion B4	34.52	2.81	18.04	8.30	0.00	0.00	22.02	0.16	9.02	0.38	95.09
RM39	Traverse in biotite inclusion B4	35.38	3.37	19.42	8.37	0.01	0.08	20.61	0.26	9.30	0.41	96.79
RM39	Traverse in biotite inclusion B5	35.60	3.27	19.38	8.48	0.02	0.10	20.10	0.22	9.68	0.42	96.85
RM39	Traverse in biotite inclusion B6	35.38	3.43	19.32	8.45	0.04	0.00	19.98	0.21	9.58	0.42	96.53
RM39	Traverse in biotite inclusion B7	35.37	3.24	19.47	8.53	0.00	0.05	20.05	0.05	9.57	0.43	96.33
RM39	Traverse in biotite inclusion B8	35.67	3.25	19.45	8.57	0.04	0.02	20.00	0.18	9.54	0.43	96.72
RM39	Traverse in biotite inclusion B9	35.52	3.22	19.42	8.41	0.00	0.06	20.11	0.23	9.65	0.42	96.62
RM39	Traverse in biotite inclusion C1	35.23	3.79	19.03	7.63	0.00	0.00	20.97	0.24	9.40	0.36	96.29
RM39	Traverse in biotite inclusion C2	34.91	3.59	18.72	7.47	0.00	0.00	21.13	0.11	9.32	0.35	95.26
RM39	Traverse in biotite inclusion C3	35.33	3.57	19.08	7.58	0.03	0.03	21.35	0.18	9.38	0.36	96.67
RM39	Traverse in biotite inclusion C4	34.56	3.24	18.79	7.73	0.05	0.00	21.24	0.25	9.36	0.36	95.22
RM39	**Inclusion in garnet**	**35.12**	**3.08**	**20.65**	**6.80**	**0.06**	**0.03**	**20.61**	**0.19**	**8.18**	**0.33**	**94.86**
RM39	Matrix	34.69	3.74	18.88	7.07	0.00	0.00	22.09	0.23	9.51	0.32	96.20
RM39	Matrix	34.93	3.78	18.96	7.15	0.03	0.05	22.25	0.03	9.43	0.32	96.60
RM39	Matrix	34.90	3.27	18.79	7.14	0.02	0.05	21.85	0.25	9.51	0.33	95.78
RM39	Matrix	34.24	3.66	18.84	7.17	0.03	0.00	21.82	0.12	9.46	0.33	95.34
RM39	Matrix	34.36	3.73	18.72	7.06	0.02	0.00	22.42	0.07	9.15	0.32	95.68
RM39	Matrix	34.92	4.21	18.62	7.19	0.00	0.01	22.15	0.05	9.55	0.32	96.87
RM39	Matrix	34.93	3.98	18.66	7.09	0.04	0.00	22.17	0.19	9.53	0.32	96.58
RM39	Matrix	34.75	3.92	19.08	7.10	0.02	0.01	22.22	0.17	9.43	0.32	96.69

Appendix 4.2 continued

Sample	Analysis	SiO_2	TiO_2	Al_2O_3	MgO	CaO	MnO	FeO*	Na_2O	K_2O	MgO/FeO	Total
RM39	Traverse in matrix biotite A1	34.36	3.95	18.35	6.86	0.04	0.00	22.72	0.25	9.31	0.30	96.02
RM39	Traverse in matrix biotite A2	34.77	4.07	18.29	6.89	0.04	0.00	22.84	0.05	9.50	0.30	96.64
RM39	Traverse in matrix biotite A3	34.85	4.08	18.42	7.00	0.01	0.00	22.64	0.12	9.50	0.31	96.62
RM39	Traverse in matrix biotite A4	34.82	3.91	18.43	6.89	0.00	0.00	22.33	0.12	9.50	0.31	95.98
RM39	Traverse in matrix biotite A5	34.84	3.97	18.60	7.05	0.03	0.00	22.47	0.14	9.58	0.31	96.66
RM39	Traverse in matrix biotite A6	34.80	3.99	18.55	6.92	0.00	0.01	22.47	0.01	9.47	0.31	96.61
RM39	Traverse in matrix biotite A7	34.86	3.94	18.60	7.12	0.00	0.03	22.49	0.10	9.51	0.32	96.65
RM39	Traverse in matrix biotite A8	34.65	3.96	18.74	7.07	0.03	0.00	22.40	0.05	9.40	0.32	96.67
RM39	Traverse in matrix biotite A9	34.62	3.62	18.72	7.19	0.00	0.00	22.25	0.13	9.47	0.32	95.99
RM39	Traverse in matrix biotite B1	35.08	3.71	18.87	6.57	0.04	0.03	22.08	0.21	9.34	0.30	95.93
RM39	Traverse in matrix biotite B2	34.89	3.73	18.94	6.84	0.00	0.01	22.21	0.15	9.39	0.31	96.15
RM39	Traverse in matrix biotite B3	34.70	3.73	18.84	7.06	0.00	0.04	21.99	0.09	9.45	0.32	95.91
RM39	Traverse in matrix biotite B4	34.42	3.90	19.18	6.89	0.05	0.01	21.43	0.17	9.59	0.32	95.64
RM39	Traverse in matrix biotite B5	34.25	4.18	19.06	6.35	0.01	0.00	21.42	0.12	9.58	0.30	95.09
RM39	**Matrix**	**34.89**	**3.40**	**19.09**	**7.80**	**0.03**	**0.02**	**21.35**	**0.18**	**9.13**	**0.37**	**95.97**
RM39	Rimming garnet	34.61	3.70	18.88	7.22	0.04	0.06	21.82	0.23	9.60	0.33	96.14
RM39	Rimming garnet	34.25	3.67	19.01	7.04	0.00	0.07	22.09	0.27	9.45	0.32	95.85
RM39	Rimming garnet	34.92	3.34	19.17	7.31	0.03	0.00	21.62	0.19	9.42	0.34	95.99
RM39	Rimming garnet	35.31	3.23	19.25	8.16	0.05	0.01	20.33	0.19	9.24	0.40	95.90
RM39	Rimming garnet	33.76	2.79	19.17	7.35	0.00	0.02	22.00	0.25	9.14	0.33	94.48
RM39	Rimming garnet	34.51	3.87	18.86	7.12	0.00	0.05	21.80	0.13	9.50	0.33	95.94
RM39	Rimming garnet	34.59	3.79	18.97	6.98	0.00	0.00	21.94	0.24	9.37	0.32	96.23
RM39	Rimming garnet	34.15	2.94	19.70	7.28	0.06	0.02	22.71	0.19	8.52	0.32	95.96
RM39	**Rimming garnet**	**34.51**	**3.42**	**19.13**	**7.31**	**0.02**	**0.03**	**21.79**	**0.21**	**9.28**	**0.34**	**95.81**
RM40	Inclusion in garnet	35.89	0.32	20.31	13.63	0.00	0.07	14.58	0.19	9.28	0.93	94.45
RM40	Inclusion in garnet	35.72	0.81	20.07	12.41	0.03	0.00	15.94	0.24	9.33	0.78	94.71
RM40	Inclusion in garnet	35.63	2.25	18.96	12.28	0.00	0.06	16.00	0.24	9.42	0.77	94.95
RM40	Inclusion in garnet	35.49	0.81	19.98	11.66	0.03	0.01	16.79	0.29	9.41	0.69	94.46
RM40	Inclusion in garnet	35.06	0.91	19.52	10.24	0.00	0.03	18.80	0.09	9.48	0.54	94.28
RM40	**Inclusion in garnet**	**35.56**	**1.02**	**19.77**	**12.04**	**0.01**	**0.03**	**16.42**	**0.21**	**9.38**	**0.74**	**94.57**
RM40	Matrix	35.37	1.08	19.83	10.23	0.00	0.12	19.45	0.10	9.50	0.53	95.68
RM40	Matrix	35.29	1.11	19.47	9.98	0.04	0.00	19.29	0.19	9.20	0.52	94.56
RM40	Matrix	34.69	1.37	19.30	10.37	0.00	0.08	18.91	0.22	9.54	0.55	94.62
RM40	**Matrix**	**35.41**	**1.07**	**19.69**	**11.42**	**0.01**	**0.05**	**17.35**	**0.20**	**9.39**	**0.67**	**94.70**
RM40	Rimming garnet	34.87	1.01	19.63	10.34	0.04	0.08	19.17	0.21	9.51	0.54	94.86
RRSW2	Inclusion in garnet	38.32	2.67	17.93	18.08	0.02	0.00	8.25	0.92	7.68	2.19	93.86
RRSW2	Inclusion in garnet	37.00	2.44	17.63	17.72	0.11	0.00	7.75	1.14	7.73	2.29	91.52
RRSW2	**Inclusion in garnet**	**37.66**	**2.55**	**17.78**	**17.90**	**0.06**	**0.00**	**8.00**	**1.03**	**7.70**	**2.24**	**92.69**
RRSW2	Matrix	37.76	2.36	17.86	16.89	0.00	0.00	10.21	0.70	7.94	1.65	93.72
RRSW2	Matrix	37.06	2.69	17.60	16.04	0.01	0.00	11.26	0.76	7.82	1.42	93.23
RRSW2	Matrix	37.32	3.19	17.48	15.49	0.02	0.00	11.80	0.56	7.93	1.31	93.78
RRSW2	Matrix	36.82	3.37	16.69	15.44	0.03	0.00	12.23	0.62	7.69	1.26	92.88

Appendix 4.2 continued

Sample	Analysis	SiO_2	TiO_2	Al_2O_3	MgO	CaO	MnO	FeO*	Na_2O	K_2O	MgO/FeO	Total
RRSW2	Matrix	37.64	3.46	17.19	15.60	0.02	0.00	12.23	0.58	8.16	1.28	94.88
RRSW2	Matrix	37.46	3.30	16.93	15.49	0.00	0.00	11.85	0.63	8.20	1.31	93.85
RRSW2	Matrix	36.71	3.35	16.75	15.25	0.00	0.00	12.08	0.64	7.96	1.26	92.73
RRSW2	Matrix	37.48	3.47	16.94	15.28	0.00	0.00	12.43	0.64	7.93	1.23	94.18
RRSW2	Matrix	37.80	3.56	16.85	15.19	0.03	0.01	12.41	0.63	8.14	1.22	94.62
RRSW2	Matrix	37.94	2.81	17.24	15.51	0.02	0.01	12.47	0.49	8.02	1.24	94.51
RRSW2	Matrix	38.07	3.69	17.01	15.75	0.00	0.00	11.70	0.63	8.07	1.35	94.93
RRSW2	Matrix	37.52	3.03	17.17	16.00	0.18	0.00	11.22	0.54	7.19	1.43	92.86
RRSW2	Matrix	38.00	1.89	17.84	16.68	0.24	0.00	11.27	0.52	6.83	1.48	93.27
RRSW2	**Matrix**	**37.51**	**3.09**	**17.20**	**15.74**	**0.04**	**0.00**	**11.78**	**0.61**	**7.84**	**1.34**	**93.80**
RRSW2	Rimming garnet	38.50	2.91	17.81	17.34	0.01	0.01	9.62	0.86	7.63	1.80	94.69
RRSW2	Rimming garnet	38.42	2.05	18.31	17.38	0.05	0.01	9.91	0.68	7.81	1.75	94.63
RRSW2	Rimming garnet	39.16	3.11	17.93	16.56	0.00	0.00	11.98	0.78	7.96	1.38	97.48
RRSW2	Rimming garnet	37.06	2.10	17.94	16.91	0.01	0.01	9.73	0.73	7.49	1.74	91.96
RRSW2	Rimming garnet	37.92	1.87	17.63	17.68	0.14	0.01	10.59	0.71	6.86	1.67	93.40
RRSW2	Rimming garnet	37.59	2.20	17.98	17.06	0.02	0.01	10.21	0.70	7.52	1.67	93.29
RRSW2	Rimming garnet	38.12	1.72	18.17	17.67	0.02	0.00	9.87	0.49	8.24	1.79	94.30
RRSW2	Rimming garnet	38.66	2.14	18.41	18.07	0.02	0.00	8.52	0.91	7.62	2.12	94.35
RRSW2	Rimming garnet	38.21	2.55	18.01	16.81	0.02	0.01	11.08	0.57	7.98	1.52	95.23
RRSW2	Rimming garnet	36.79	2.22	17.62	16.05	0.02	0.01	11.51	0.39	8.66	1.39	93.26
RRSW2	Rimming garnet	35.95	2.24	18.39	16.87	0.03	0.01	12.36	0.44	6.72	1.36	93.02
RRSW2	Rimming garnet	37.24	3.03	16.73	15.37	0.08	0.01	12.06	0.52	7.33	1.27	92.37
RRSW2	Rimming garnet	38.21	2.68	18.11	16.45	0.02	0.00	11.42	0.69	7.93	1.44	95.49
RRSW2	**Rimming garnet**	**37.83**	**2.37**	**17.93**	**16.94**	**0.03**	**0.01**	**10.68**	**0.65**	**7.67**	**1.61**	**94.11**
RRSW3	Inclusion in garnet	36.26	3.67	18.96	11.79	0.00	0.04	15.14	0.25	9.40	0.78	95.52
RRSW3	Inclusion in garnet	35.53	2.51	18.77	11.55	0.02	0.02	16.75	0.42	8.98	0.69	94.55
RRSW3	Inclusion in garnet	34.40	3.72	17.92	7.64	0.00	0.08	21.93	0.12	9.53	0.35	95.35
RRSW3	Inclusion in garnet	34.50	5.33	16.85	10.90	0.01	0.01	16.18	0.61	8.73	0.67	93.12
RRSW3	Inclusion in garnet	34.48	5.23	17.80	9.20	0.01	0.03	18.45	0.31	9.13	0.50	94.62
RRSW3	Inclusion in garnet	35.99	1.97	19.93	10.49	0.05	0.04	15.66	0.14	9.18	0.67	93.46
RRSW3	Inclusion in garnet	35.52	3.63	18.87	10.88	0.04	0.05	15.67	0.26	9.29	0.69	94.21
RRSW3	Inclusion in garnet	33.17	2.23	17.82	8.24	0.11	0.06	21.84	0.40	8.41	0.38	92.28
RRSW3	Inclusion in garnet	34.60	1.51	18.52	8.78	0.05	0.08	21.78	0.35	8.71	0.40	94.39
RRSW3	Inclusion in garnet	35.60	2.46	19.63	11.05	0.01	0.02	15.54	0.20	9.62	0.71	94.12
RRSW3	Inclusion in garnet	34.73	4.77	17.65	9.16	0.02	0.04	19.11	0.33	9.14	0.48	94.95
RRSW3	**Inclusion in garnet**	**34.98**	**3.37**	**18.43**	**9.97**	**0.03**	**0.04**	**18.01**	**0.31**	**9.10**	**0.57**	**94.23**
RRSW3	Matrix	33.97	4.47	17.19	7.39	0.00	0.08	21.91	0.12	9.41	0.34	94.54
RRSW3	Matrix	33.61	4.66	17.10	6.72	0.03	0.09	21.52	0.13	8.97	0.31	92.82
RRSW3	Matrix	33.95	3.78	17.32	7.55	0.00	0.06	22.14	0.13	9.29	0.34	94.21
RRSW3	Matrix	34.45	4.04	17.52	7.50	0.01	0.08	22.79	0.15	9.43	0.33	95.97

Appendix 4.2 continued

Sample	Analysis	SiO_2	TiO_2	Al_2O_3	MgO	CaO	MnO	FeO*	Na_2O	K_2O	MgO/FeO	Total
RRSW3	Matrix	34.52	3.89	17.57	7.73	0.01	0.07	22.00	0.16	9.39	0.35	95.34
RRSW3	Matrix	33.99	3.69	17.24	7.66	0.01	0.08	22.41	0.18	9.19	0.34	94.44
RRSW3	Matrix	33.95	4.20	17.33	7.44	0.00	0.06	22.08	0.17	9.30	0.34	94.53
RRSW3	Matrix	34.49	3.04	18.05	8.09	0.00	0.08	21.72	0.13	9.34	0.37	94.94
RRSW3	Matrix	33.94	3.80	17.60	7.54	0.01	0.06	21.90	0.14	9.40	0.34	94.38
RRSW3	Matrix	33.92	3.88	17.69	7.56	0.02	0.07	21.75	0.13	9.31	0.35	94.33
RRSW3	Matrix	33.40	4.34	16.85	7.38	0.05	0.09	22.41	0.13	9.04	0.33	93.70
RRSW3	Matrix	33.97	4.71	17.10	7.23	0.00	0.09	22.60	0.10	9.50	0.32	95.30
RRSW3	Matrix	33.74	4.26	17.12	7.39	0.00	0.07	22.46	0.10	9.51	0.33	94.64
RRSW3	Matrix	33.58	4.61	17.08	7.28	0.00	0.07	22.30	0.09	9.42	0.33	94.43
RRSW3	Matrix	33.68	4.65	16.76	7.20	0.00	0.08	22.01	0.09	9.25	0.33	93.72
RRSW3	**Matrix**	**33.94**	**4.13**	**17.30**	**7.44**	**0.01**	**0.07**	**22.13**	**0.13**	**9.32**	**0.34**	**94.48**
RRSW3	Rimming garnet	34.20	4.25	17.34	7.41	0.02	0.07	21.90	0.19	9.31	0.34	94.69
RRSW3	Rimming garnet	35.05	3.24	18.41	8.36	0.01	0.06	21.69	0.17	8.84	0.39	95.82
RRSW3	Rimming garnet	35.52	3.15	18.62	8.16	0.01	0.09	21.48	0.14	9.29	0.38	96.47
RRSW3	Rimming garnet	34.47	3.25	17.98	7.75	0.02	0.08	22.28	0.22	9.24	0.35	95.29
RRSW3	Rimming garnet	34.52	3.16	17.27	7.51	0.07	0.06	20.74	0.19	8.54	0.36	92.04
RRSW3	Rimming garnet	35.14	3.71	17.52	7.63	0.07	0.08	21.90	0.17	9.07	0.35	95.30
RRSW3	Rimming garnet	34.37	4.15	17.91	7.56	0.01	0.07	21.88	0.17	9.42	0.35	95.56
RRSW3	Rimming garnet	34.63	3.93	18.00	7.64	0.01	0.07	21.65	0.15	9.37	0.35	95.45
RRSW3	Rimming garnet	34.58	3.58	17.91	7.86	0.01	0.06	21.87	0.13	9.38	0.36	95.38
RRSW3	Rimming garnet	34.37	3.34	17.94	8.01	0.01	0.06	21.79	0.19	9.35	0.37	95.05
RRSW3	Rimming garnet	33.68	3.31	17.32	7.50	0.00	0.07	21.14	0.14	9.09	0.35	92.26
RRSW3	Rimming garnet	34.01	3.90	17.61	7.63	0.00	0.07	21.99	0.13	9.30	0.35	94.64
RRSW3	Rimming garnet	33.91	3.47	17.48	7.90	0.00	0.07	21.67	0.16	9.15	0.36	93.80
RRSW3	Rimming garnet	32.82	4.06	16.90	6.56	0.10	0.08	22.31	0.20	8.85	0.29	91.87
RRSW3	Rimming garnet	33.43	3.99	17.64	7.30	0.02	0.08	21.67	0.17	9.35	0.34	93.65
RRSW3	**Rimming garnet**	**34.31**	**3.63**	**17.72**	**7.65**	**0.02**	**0.07**	**21.73**	**0.17**	**9.17**	**0.35**	**94.48**
RRSW4	*Inclusion in garnet*	39.42	1.50	17.40	19.03	0.09	0.01	8.52	0.58	8.01	2.23	94.56
RRSW4	**Inclusion in garnet**	**34.56**	**3.55**	**17.61**	**8.52**	**0.03**	**0.07**	**20.68**	**0.20**	**9.12**	**0.50**	**94.33**
RRSW4	Matrix	39.42	2.69	18.60	14.90	0.04	0.02	11.14	0.49	7.37	1.34	94.68
RRSW4	Matrix	37.84	3.21	16.72	15.53	0.00	0.02	12.19	0.54	8.35	1.27	94.40
RRSW4	Matrix	38.16	2.14	16.87	16.50	0.02	0.01	11.84	0.51	8.20	1.39	94.25
RRSW4	Matrix	38.37	1.69	17.07	16.86	0.24	0.01	11.36	0.54	7.58	1.48	93.72
RRSW4	Matrix	37.16	2.21	16.69	16.12	0.10	0.02	11.40	0.52	7.71	1.41	91.92
RRSW4	Matrix	38.27	2.10	16.85	16.79	0.03	0.02	11.65	0.45	8.00	1.44	94.16
RRSW4	Matrix	38.06	2.55	16.71	16.46	0.06	0.03	11.27	0.53	8.03	1.46	93.67
RRSW4	Matrix	37.84	2.38	16.80	16.53	0.00	0.00	11.23	0.54	8.34	1.47	93.65
RRSW4	Matrix	38.13	2.41	16.82	16.49	0.01	0.01	11.40	0.55	8.34	1.45	94.16
RRSW4	Matrix	38.25	1.94	17.04	16.70	0.06	0.02	11.37	0.51	8.13	1.47	94.01
RRSW4	Matrix	38.23	1.95	16.97	16.62	0.09	0.01	11.64	0.48	8.04	1.43	94.01
RRSW4	Matrix	38.26	2.28	17.10	16.61	0.03	0.01	11.88	0.47	7.81	1.40	94.43
RRSW4	Matrix	37.91	2.24	16.85	16.27	0.13	0.01	11.90	0.40	7.90	1.37	93.62

Appendix 4.2 continued

Sample	Analysis	SiO_2	TiO_2	Al_2O_3	MgO	CaO	MnO	FeO*	Na_2O	K_2O	MgO/FeO	Total
RRSW4	Matrix	37.69	2.40	16.66	16.17	0.08	0.02	11.66	0.46	7.97	1.39	93.10
RRSW4	Matrix	37.47	2.27	17.25	16.79	0.00	0.02	12.22	0.44	7.70	1.37	94.16
RRSW4	**Matrix**	**38.07**	**2.30**	**17.00**	**16.35**	**0.06**	**0.01**	**11.61**	**0.49**	**7.96**	**1.41**	**93.86**
RRSW4	Rimming garnet	38.52	1.95	16.94	16.92	0.07	0.00	11.25	0.51	7.94	1.50	94.08
RRSW4	Rimming garnet	38.43	1.34	16.55	17.35	0.04	0.02	12.12	0.42	7.31	1.43	93.58
RRSW4	Rimming garnet	37.86	1.38	17.41	17.26	0.06	0.02	11.21	0.49	7.30	1.54	92.99
RRSW4	Rimming garnet	37.74	2.61	16.98	16.93	0.01	0.01	10.85	0.55	8.05	1.56	93.73
RRSW4	Rimming garnet	36.23	1.27	17.39	17.82	0.23	0.01	11.87	0.32	5.24	1.50	90.37
RRSW4	Rimming garnet	38.26	1.60	16.93	17.15	0.20	0.00	11.07	0.42	7.22	1.55	92.85
RRSW4	Rimming garnet	38.77	1.38	17.22	17.75	0.06	0.03	11.20	0.54	7.83	1.58	94.79
RRSW4	Rimming garnet	38.92	1.81	17.06	16.86	0.15	0.02	11.58	0.55	7.59	1.46	94.54
RRSW4	Rimming garnet	39.21	1.81	17.01	17.25	0.19	0.02	11.22	0.56	7.75	1.54	95.01
RRSW4	Rimming garnet	38.51	1.98	17.27	17.17	0.08	0.02	10.77	0.54	8.10	1.60	94.44
RRSW4	Rimming garnet	38.59	1.31	17.24	17.66	0.16	0.02	11.44	0.49	7.15	1.54	94.05
RRSW4	Rimming garnet	38.63	1.35	17.32	17.39	0.09	0.02	11.38	0.56	7.69	1.53	94.43
RRSW4	Rimming garnet	37.92	1.56	16.96	16.99	0.28	0.02	11.32	0.48	7.13	1.50	92.65
RRSW4	Rimming garnet	37.16	1.56	16.96	17.25	0.24	0.01	10.97	0.44	6.84	1.57	91.42
RRSW4	Rimming garnet	38.33	0.37	17.29	18.42	0.45	0.01	10.01	0.49	6.08	1.84	91.45
RRSW4	**Rimming garnet**	**38.20**	**1.55**	**17.10**	**17.34**	**0.15**	**0.02**	**11.22**	**0.49**	**7.28**	**1.55**	**93.36**
TRBC2	Matrix	36.73	4.77	16.68	14.55	0.04	0.01	11.73	0.27	9.03	1.24	93.82
TRBC2	Matrix	36.50	5.42	16.49	14.41	0.00	0.02	12.22	0.29	9.23	1.18	94.58
TRBC2	Matrix	36.29	4.38	16.72	14.32	0.02	0.02	12.66	0.29	9.10	1.13	93.80
TRBC2	Matrix	35.43	5.78	15.55	13.12	0.02	0.01	13.21	0.21	9.34	0.99	92.66
TRBC2	Matrix	35.64	5.39	16.20	13.53	0.04	0.01	13.00	0.26	9.23	1.04	93.29
TRBC2	Matrix	38.89	4.31	18.64	11.26	0.12	0.02	10.79	0.21	9.09	1.04	93.31
TRBC2	Matrix	35.01	3.46	17.82	14.13	0.18	0.08	14.18	0.22	5.84	1.00	90.91
TRBC2	Matrix	35.82	4.28	16.41	14.21	0.08	0.02	12.97	0.21	8.30	1.10	92.30
TRBC2	Matrix	34.29	3.50	17.04	15.17	0.11	0.05	14.09	0.18	6.42	1.08	90.85
TRBC2	Matrix	36.04	4.10	17.21	14.49	0.03	0.03	12.51	0.27	8.01	1.16	92.68
TRBC2	Matrix	29.58	8.85	16.05	11.26	9.44	0.12	13.39	0.02	0.46	0.84	89.16
TRBC2	Matrix	34.68	6.71	16.89	12.30	0.15	0.04	12.49	0.18	6.54	0.98	89.96
TRBC2	Matrix	36.04	4.51	16.76	14.44	0.01	0.01	12.15	0.26	9.28	1.19	93.45
TRBC2	Matrix	35.27	4.93	16.23	13.58	0.04	0.00	12.72	0.26	9.14	1.07	92.18
TRBC2	**Matrix**	**35.44**	**5.03**	**16.76**	**13.63**	**0.73**	**0.03**	**12.72**	**0.22**	**7.79**	**1.07**	**92.35**
TRBC2	Rimming garnet	36.04	4.42	16.56	14.04	0.03	0.02	13.04	0.26	8.98	1.08	93.39
TRBC2	Rimming garnet	36.12	4.24	15.83	15.48	0.11	0.01	11.38	0.28	8.81	1.36	92.26
TRBC2	Rimming garnet	36.24	3.85	16.85	14.01	0.04	0.04	13.97	0.33	8.97	1.00	94.29
TRBC2	Rimming garnet	36.41	4.34	16.23	15.62	0.02	0.01	11.86	0.28	9.17	1.32	93.93
TRBC2	Rimming garnet	35.75	3.97	16.38	14.68	0.06	0.02	12.07	0.21	9.04	1.22	92.17
TRBC2	Rimming garnet	36.97	4.07	16.81	15.54	0.11	0.02	11.56	0.25	8.72	1.34	94.05
TRBC2	Rimming garnet	36.14	4.24	16.11	14.93	0.09	0.02	12.39	0.31	8.79	1.20	93.01
TRBC2	Rimming garnet	35.62	3.53	16.62	14.78	0.05	0.05	14.25	0.22	8.05	1.04	93.15
TRBC2	Rimming garnet	35.89	4.22	15.78	14.10	0.06	0.05	13.99	0.20	8.81	1.01	93.08

Appendix 4.2 continued

Sample	Analysis	SiO_2	TiO_2	Al_2O_3	MgO	CaO	MnO	FeO*	Na_2O	K_2O	MgO/FeO	Total
TRBC2	Rimming garnet	36.40	3.99	16.58	14.45	0.01	0.03	13.38	0.24	9.25	1.08	94.32
TRBC2	Rimming garnet	36.83	4.32	16.54	15.57	0.02	0.03	11.87	0.26	9.14	1.31	94.58
TRBC2	Rimming garnet	37.00	3.44	17.23	15.11	0.04	0.01	11.09	0.25	9.11	1.36	93.27
TRBC2	Rimming garnet	35.19	3.86	16.28	15.20	0.02	0.04	13.21	0.17	8.10	1.15	92.06
TRBC2	**Rimming garnet**	**36.20**	**4.04**	**16.44**	**14.88**	**0.05**	**0.03**	**12.62**	**0.25**	**8.84**	**1.19**	**93.35**
TRER7	Matrix	34.88	3.36	17.76	11.44	0.02	0.04	15.48	0.25	9.14	0.74	92.35
TRER7	Matrix	35.57	3.11	18.35	12.02	0.01	0.04	15.70	0.22	9.37	0.77	94.39
TRER7	Matrix	34.90	4.01	17.47	11.42	0.00	0.05	16.54	0.21	9.33	0.69	93.92
TRER7	Matrix	35.41	3.92	17.61	11.56	0.00	0.05	16.50	0.22	9.44	0.70	94.72
TRER7	Matrix	35.29	3.97	17.55	11.39	0.00	0.04	16.23	0.25	9.40	0.70	94.12
TRER7	Matrix	35.38	3.66	17.81	11.59	0.00	0.04	16.21	0.21	9.49	0.72	94.39
TRER7	Matrix	34.73	3.49	17.50	11.63	0.02	0.03	15.81	0.23	9.32	0.74	92.76
TRER7	Matrix	35.77	3.14	18.23	11.75	0.00	0.03	16.05	0.22	9.41	0.73	94.59
TRER7	Matrix	35.38	4.22	17.72	11.44	0.00	0.04	16.39	0.20	9.47	0.70	94.85
TRER7	Matrix	35.48	4.04	17.46	11.43	0.00	0.05	16.42	0.20	9.43	0.70	94.50
TRER7	Matrix	34.73	4.05	17.51	11.40	0.00	0.05	16.18	0.20	9.43	0.70	93.54
TRER7	Matrix	34.93	3.62	17.34	11.80	0.00	0.03	16.13	0.18	9.28	0.73	93.33
TRER7	Matrix	34.83	3.69	17.39	11.84	0.00	0.01	15.71	0.22	9.39	0.75	93.08
TRER7	Matrix	35.15	3.00	17.98	11.93	0.01	0.04	15.79	0.20	9.35	0.76	93.44
TRER7	Matrix	35.61	3.23	18.13	11.97	0.00	0.04	15.75	0.22	9.51	0.76	94.44
TRER7	**Matrix**	**35.20**	**3.63**	**17.72**	**11.64**	**0.00**	**0.04**	**16.06**	**0.21**	**9.38**	**0.73**	**93.90**
TRER7	Rimming garnet	35.90	3.51	17.84	12.46	0.01	0.03	15.37	0.25	9.34	0.81	94.70
TRER7	Rimming garnet	35.53	3.24	17.99	12.49	0.00	0.03	15.60	0.23	9.42	0.80	94.53
TRER7	Rimming garnet	35.15	2.76	17.79	12.97	0.00	0.03	14.77	0.21	9.38	0.88	93.06
TRER7	Rimming garnet	35.74	3.56	17.92	12.56	0.00	0.04	15.13	0.25	9.36	0.83	94.55
TRER7	Rimming garnet	34.96	2.82	17.60	12.34	0.01	0.04	15.59	0.23	9.18	0.79	92.77
TRER7	Rimming garnet	35.64	3.49	18.10	12.49	0.01	0.03	15.36	0.23	9.27	0.81	94.61
TRER7	Rimming garnet	34.33	3.32	17.26	11.44	0.28	0.04	18.16	0.26	8.82	0.63	93.91
TRER7	Rimming garnet	35.17	3.28	17.31	11.67	0.06	0.03	17.24	0.23	9.10	0.68	94.09
TRER7	Rimming garnet	35.58	3.27	17.81	12.20	0.00	0.03	15.93	0.21	9.40	0.77	94.44
TRER7	Rimming garnet	35.41	3.60	18.15	11.55	0.04	0.03	15.65	0.18	9.51	0.74	94.11
TRER7	Rimming garnet	36.53	2.20	18.58	14.61	0.00	0.03	12.89	0.22	9.33	1.13	94.39
TRER7	Rimming garnet	35.31	3.38	17.91	11.80	0.01	0.03	16.14	0.19	9.45	0.73	94.21
TRER7	Rimming garnet	35.48	2.69	18.23	12.33	0.01	0.03	15.89	0.23	9.28	0.78	94.15
TRER7	Rimming garnet	34.47	2.96	17.69	12.03	0.02	0.02	15.93	0.24	9.04	0.76	92.40
TRER7	Rimming garnet	35.73	3.37	17.99	11.82	0.00	0.03	16.00	0.21	9.42	0.74	94.57
TRER7	**Rimming garnet**	**35.40**	**3.16**	**17.88**	**12.32**	**0.03**	**0.03**	**15.71**	**0.22**	**9.29**	**0.79**	**94.03**
TRMR2	Inclusion in garnet	36.47	1.84	18.70	16.37	0.00	0.00	10.10	0.21	9.55	1.62	93.39
TRMR2	Inclusion in garnet	36.53	3.12	18.36	15.36	0.00	0.00	9.98	0.18	9.57	1.54	93.26

Appendix 4.2 continued

Sample	Analysis	SiO_2	TiO_2	Al_2O_3	MgO	CaO	MnO	FeO*	Na_2O	K_2O	MgO/FeO	Total
TRMR2	Inclusion in garnet	35.59	2.00	18.57	14.25	0.02	0.03	13.11	0.11	9.43	1.09	93.16
TRMR2	Inclusion in garnet	38.56	1.48	20.86	12.91	0.21	0.11	14.52	0.10	7.43	0.89	96.18
TRMR2	Inclusion in garnet	35.69	3.05	18.16	14.34	0.00	0.01	11.55	0.08	9.56	1.24	92.49
TRMR2	**Inclusion in garnet**	**36.57**	**2.30**	**18.93**	**14.64**	**0.05**	**0.03**	**11.85**	**0.14**	**9.11**	**1.28**	**93.70**
TRMR2	Matrix	34.37	2.29	18.31	13.54	0.06	0.02	13.89	0.06	8.64	0.98	91.17
TRMR2	Matrix	35.77	2.53	18.25	13.45	0.01	0.01	13.46	0.10	9.65	1.00	93.24
TRMR2	Matrix	35.04	2.38	18.44	13.47	0.00	0.00	12.97	0.13	9.24	1.04	91.68
TRMR2	Matrix	35.27	2.79	18.44	13.74	0.01	0.01	13.78	0.10	9.35	1.00	93.53
TRMR2	Matrix	34.85	2.55	17.93	13.40	0.00	0.01	13.35	0.12	9.58	1.00	91.81
TRMR2	**Matrix**	**35.06**	**2.51**	**18.27**	**13.52**	**0.02**	**0.01**	**13.49**	**0.10**	**9.29**	**1.00**	**92.29**
TRER6B	Inclusion in garnet	33.35	5.18	14.65	9.41	0.59	0.09	23.80	0.09	6.84	93.99	0.04
TRER6B	Matrix	26.27	0.30	18.07	11.32	0.06	0.27	31.52	0.02	0.45	88.28	0.03
TRER6B	Matrix	29.03	8.78	12.16	9.16	6.06	0.09	22.49	0.03	2.22	90.01	0.04
TRER6B	Matrix	29.70	5.83	13.64	10.03	3.32	0.10	24.52	0.03	3.04	90.21	0.04
TRER6B	Matrix	34.44	5.46	14.23	9.05	0.25	0.05	22.06	0.06	8.95	94.53	0.05
TRER6B	Matrix	30.88	6.88	12.96	9.34	3.47	0.08	22.65	0.08	4.59	90.92	0.04
TRER6B	Matrix	29.95	2.17	16.58	10.99	0.07	0.14	26.62	0.04	3.82	90.38	0.04
TRER6B	Matrix	32.03	4.53	12.82	9.56	1.89	0.08	22.56	0.09	5.82	89.37	0.04
TRER6B	Matrix	28.00	5.89	14.12	11.50	4.52	0.09	24.64	0.01	0.43	89.19	0.04
TRER6B	Matrix	27.68	0.74	16.17	13.89	0.57	0.11	28.08	0.02	0.11	87.38	0.04
TRER6B	**Matrix**	**29.78**	**4.51**	**14.53**	**10.54**	**2.25**	**0.11**	**25.02**	**0.04**	**3.27**	**90.03**	**0.04**
HLM2	Matrix	33.91	2.82	19.01	8.21	0.00	0.07	19.98	0.18	9.66	0.41	93.83
HLM2	Matrix	34.29	2.68	18.45	8.54	0.00	0.10	20.91	0.12	9.52	0.41	94.61
HLM2	Matrix	34.01	2.99	18.90	8.33	0.00	0.07	20.07	0.24	9.57	0.42	94.18
HLM2	Matrix	34.36	2.96	19.11	8.41	0.04	0.07	20.19	0.20	9.52	0.42	94.86
HLM2	Matrix	34.24	2.89	18.95	8.24	0.01	0.08	20.35	0.15	9.70	0.40	94.61
HLM2	Matrix	34.40	2.85	19.09	8.11	0.01	0.08	20.24	0.19	9.57	0.40	94.53
HLM2	Matrix	34.66	3.01	19.29	8.15	0.00	0.09	20.23	0.16	9.73	0.40	95.33
HLM2	Matrix	34.32	3.03	19.08	8.11	0.01	0.07	20.32	0.19	9.61	0.40	94.74
HLM2	Matrix	33.61	3.03	18.31	8.32	0.01	0.08	20.13	0.15	9.61	0.41	93.26
HLM2	Matrix	34.36	2.87	18.86	8.51	0.01	0.07	20.71	0.12	9.55	0.41	95.05
HLM2	Matrix	33.82	2.89	18.44	8.20	0.01	0.06	20.74	0.15	9.52	0.40	93.81
HLM2	Matrix	35.25	2.57	20.21	7.72	0.07	0.07	18.94	0.15	8.99	0.41	93.96
HLM2	Matrix	33.74	2.86	18.82	8.06	0.00	0.08	20.25	0.14	9.70	0.40	93.64
HLM2	Matrix	34.01	2.66	18.77	8.42	0.01	0.06	20.26	0.22	9.58	0.42	94.00
HLM2	**Matrix**	**34.21**	**2.86**	**18.95**	**8.24**	**0.01**	**0.07**	**20.24**	**0.17**	**9.56**	**0.41**	**94.32**
HLM2	Rimming garnet	34.13	2.48	19.07	8.34	0.02	0.09	20.14	0.17	9.57	0.41	93.99
HLM2	Rimming garnet	34.07	2.43	19.50	8.43	0.02	0.04	19.48	0.17	9.76	0.43	93.89

Appendix 4.2 continued

Sample	Analysis	SiO_2	TiO_2	Al_2O_3	MgO	CaO	MnO	FeO*	Na_2O	K_2O	MgO/FeO	Total
HLM2	Rimming garnet	34.09	2.12	19.80	8.79	0.00	0.05	19.05	0.21	9.68	0.46	93.79
HLM2	Rimming garnet	34.58	2.02	19.82	8.64	0.01	0.05	19.80	0.17	9.55	0.44	94.64
HLM2	Rimming garnet	34.00	2.48	19.43	8.42	0.02	0.04	19.58	0.20	9.69	0.43	93.86
HLM2	Rimming garnet	33.17	2.65	18.67	8.25	0.00	0.07	21.03	0.09	9.38	0.39	93.31
HLM2	Rimming garnet	34.56	2.15	19.52	9.56	0.03	0.05	18.48	0.12	9.65	0.52	94.12
HLM2	Rimming garnet	34.41	2.52	19.51	8.55	0.01	0.05	20.05	0.13	9.66	0.43	94.89
HLM2	Rimming garnet	34.36	2.42	19.30	8.37	0.01	0.05	19.86	0.15	9.77	0.42	94.30
HLM2	Rimming garnet	34.46	2.69	19.17	8.21	0.01	0.05	19.87	0.10	9.55	0.41	94.10
HLM2	Rimming garnet	34.07	2.49	19.04	8.55	0.03	0.07	20.74	0.17	9.61	0.41	94.75
HLM2	Rimming garnet	34.66	2.41	19.19	8.37	0.02	0.07	20.34	0.16	9.59	0.41	94.81
HLM2	Rimming garnet	33.93	2.30	18.87	8.25	0.02	0.05	20.26	0.08	9.74	0.41	93.51
HLM2	Rimming garnet	33.70	2.30	19.13	8.42	0.00	0.05	19.86	0.12	9.74	0.42	93.31
HLM2	Rimming garnet	34.78	2.73	19.68	8.64	0.03	0.05	19.67	0.15	9.70	0.44	95.44
HLM2	**Rimming garnet**	**34.20**	**2.41**	**19.31**	**8.52**	**0.01**	**0.05**	**19.88**	**0.15**	**9.64**	**0.43**	**94.18**

*Total iron reported as FeO

Appendix 4.3: Electron microprobe analyses of amphibole (oxide weight percent)

Sample	Analysis	SiO_2	TiO_2	Al_2O_3	MgO	CaO	MnO	FeO*	Na_2O	K_2O	Total
RRSW1	Matrix	43.68	1.52	10.76	10.27	10.62	0.18	17.88	1.32	0.53	96.75
RRSW1	Matrix	43.65	1.46	10.80	10.25	10.39	0.18	17.98	1.37	0.52	96.61
RRSW1	Matrix	44.22	1.30	10.66	10.50	11.16	0.17	17.31	1.29	0.51	97.12
RRSW1	Matrix	42.60	1.50	10.82	10.07	10.65	0.18	17.37	1.38	0.50	95.11
RRSW1	Matrix	43.60	1.46	10.77	10.14	10.67	0.18	18.06	1.36	0.50	96.73
RRSW1	Matrix	42.84	1.44	11.20	9.77	10.84	0.17	17.94	1.42	0.54	96.16
RRSW1	Matrix	43.36	1.40	10.48	9.96	10.99	0.19	17.96	1.24	0.51	96.10
RRSW1	Matrix	43.81	1.34	10.40	13.32	10.37	0.19	18.29	1.24	0.52	96.47
RRSW1	Matrix	43.91	1.44	10.99	10.06	10.82	0.20	18.08	1.33	0.52	97.36
RRSW1	Matrix	44.69	1.32	10.37	10.31	9.40	0.22	19.86	1.23	0.53	97.92
RRSW1	Matrix	44.05	1.43	10.67	10.33	10.66	0.18	18.02	1.26	0.52	97.13
RRSW1	Matrix	44.45	1.44	10.53	10.47	10.96	0.16	17.42	1.24	0.50	97.17
RRSW1	Matrix	44.87	1.39	10.01	10.65	10.55	0.19	17.95	1.24	0.47	97.31
RRSW1	Matrix	43.68	1.40	10.93	10.38	10.66	0.18	17.89	1.42	0.53	97.07
RRSW1	Matrix	44.60	1.26	10.14	10.60	11.02	0.16	17.54	1.18	0.44	96.94
RRSW1	Matrix	43.94	1.40	11.06	10.30	10.89	0.17	17.50	1.36	0.52	97.12
RRSW1	**Matrix**	**43.87**	**1.41**	**10.66**	**10.46**	**10.67**	**0.18**	**17.94**	**1.31**	**0.51**	**96.82**
RRSW1	Rimming garnet	43.80	1.30	10.62	9.81	10.26	0.22	19.24	1.29	0.48	97.00
RRSW1	Rimming garnet	44.65	1.44	11.12	9.63	11.19	0.16	18.26	1.30	0.49	98.23
RRSW1	Rimming garnet	44.30	1.13	11.27	10.66	11.06	0.14	16.86	1.30	0.51	97.22
RRSW1	Rimming garnet	45.92	1.00	10.11	11.29	9.73	0.13	18.11	1.10	0.42	97.81
RRSW1	Rimming garnet	45.25	1.31	10.14	10.61	10.13	0.14	18.45	1.16	0.41	97.59
RRSW1	**Rimming garnet**	**44.78**	**1.24**	**10.65**	**10.40**	**10.47**	**0.16**	**18.18**	**1.23**	**0.46**	**97.57**
RRCR12	Inclusion in garnet	42.62	1.02	13.61	10.26	11.07	0.09	16.23	1.59	0.39	96.88
RRCR12	Inclusion in garnet	42.64	0.96	13.69	10.21	11.11	0.09	15.96	1.73	0.40	96.79
RRCR12	Inclusion in garnet	42.54	0.87	14.43	10.11	10.97	0.08	16.08	1.66	0.37	97.10
RRCR12	Inclusion in garnet	43.49	1.01	13.73	10.51	10.93	0.08	15.85	1.63	0.38	97.60
RRCR12	Inclusion in garnet	43.21	0.74	14.02	10.56	10.94	0.07	15.97	1.66	0.36	97.52
RRCR12	Inclusion in garnet	43.47	1.10	13.65	10.48	11.04	0.07	16.06	1.64	0.35	97.85
RRCR12	Inclusion in garnet	43.44	1.13	13.55	10.61	10.94	0.06	15.77	1.65	0.39	97.55
RRCR12	Inclusion in garnet	42.40	1.05	14.40	10.08	10.99	0.07	16.33	1.80	0.45	97.58
RRCR12	Inclusion in garnet	42.42	1.02	14.09	10.30	10.99	0.08	15.68	1.71	0.41	96.70
RRCR12	Inclusion in garnet	42.88	0.62	14.79	10.01	9.32	0.25	18.41	1.71	0.25	98.22
RRCR12	**Inclusion in garnet**	**42.91**	**0.95**	**14.00**	**10.31**	**10.83**	**0.09**	**16.23**	**1.68**	**0.37**	**97.38**
RRCR12	Matrix	42.86	1.01	13.59	10.04	11.01	0.08	16.31	1.66	0.41	96.97
RRCR12	Matrix	42.27	1.07	13.96	9.76	10.90	0.08	16.66	1.76	0.47	96.93
RRCR12	Matrix	42.05	1.11	13.35	9.86	10.91	0.08	16.17	1.69	0.46	95.69
RRCR12	Matrix	41.07	1.03	13.20	9.48	10.85	0.08	16.43	1.64	0.41	94.20
RRCR12	Matrix	41.77	1.08	13.64	9.70	10.88	0.08	16.72	1.76	0.46	96.09
RRCR12	Matrix	43.01	0.92	13.69	9.84	10.85	0.08	16.54	1.61	0.38	96.92
RRCR12	Matrix	42.65	0.88	13.79	9.86	10.92	0.09	16.77	1.69	0.39	97.02
RRCR12	Matrix	45.14	0.95	13.48	10.35	10.90	0.11	16.95	1.60	0.44	99.93
RRCR12	Matrix	43.15	1.10	13.59	9.94	10.89	0.11	16.89	1.65	0.42	97.73
RRCR12	Matrix	42.76	1.04	13.41	9.88	10.97	0.10	16.94	1.62	0.40	97.11
RRCR12	Matrix	42.58	0.95	13.26	9.69	10.90	0.10	16.57	1.58	0.37	96.01
RRCR12	Matrix	42.31	1.07	13.38	9.60	11.09	0.10	16.68	1.61	0.44	96.28
RRCR12	Matrix	41.71	1.12	13.49	9.54	11.01	0.09	16.68	1.65	0.44	95.73
RRCR12	Matrix	46.90	0.81	13.99	11.05	10.88	0.09	16.63	1.64	0.35	102.34
RRCR12	**Matrix**	**42.87**	**1.01**	**13.56**	**9.90**	**10.93**	**0.09**	**16.64**	**1.65**	**0.42**	**97.07**
RRCR12	Rimming garnet	42.75	0.93	13.65	9.95	10.99	0.08	16.52	1.65	0.38	96.90
RRCR12	Rimming garnet	42.56	0.74	15.25	9.82	10.95	0.08	16.68	1.81	0.37	98.25
RRCR12	Rimming garnet	42.01	0.88	13.78	9.88	10.64	0.08	16.75	1.53	0.40	95.95
RRCR12	Rimming garnet	42.75	1.07	13.46	10.21	11.02	0.07	16.38	1.63	0.38	96.96
RRCR12	Rimming garnet	44.22	1.11	13.73	10.56	10.71	0.09	16.64	1.75	0.40	99.21
RRCR12	Rimming garnet	42.12	1.08	13.78	10.07	11.08	0.08	16.09	1.71	0.41	96.40
RRCR12	Rimming garnet	41.29	0.96	14.09	9.51	11.13	0.08	16.50	1.74	0.42	95.72
RRCR12	Rimming garnet	42.96	0.87	14.87	10.03	10.80	0.09	16.22	1.87	0.42	98.13
RRCR12	Rimming garnet	42.65	1.19	13.79	10.28	10.78	0.08	16.07	1.67	0.41	96.90
RRCR12	Rimming garnet	42.41	1.04	13.68	9.83	10.90	0.09	16.42	1.68	0.40	96.45
RRCR12	**Rimming garnet**	**42.57**	**0.98**	**14.01**	**10.01**	**10.90**	**0.08**	**16.43**	**1.70**	**0.40**	**97.09**
TRER6B	Inclusion in garnet	41.81	2.38	12.31	8.39	11.44	0.06	19.32	1.48	1.76	98.95
TRER6B	Inclusion in garnet	42.07	2.35	12.29	8.25	11.63	0.05	18.83	1.43	1.62	98.53
TRER6B	Inclusion in garnet	42.29	2.00	11.70	8.97	10.86	0.13	18.88	1.75	0.93	97.51
TRER6B	Inclusion in garnet	42.68	1.81	11.30	9.23	10.71	0.11	18.96	1.68	0.92	97.39
TRER6B	Inclusion in garnet	43.19	1.89	10.90	9.79	10.45	0.12	18.89	1.61	0.84	97.67
TRER6B	Inclusion in garnet	43.37	1.77	11.30	9.41	11.23	0.12	18.09	1.69	0.83	97.82
TRER6B	Inclusion in garnet	42.94	1.80	11.37	9.48	11.15	0.11	17.95	1.73	0.87	97.39
TRER6B	Inclusion in garnet	42.00	2.35	11.97	9.42	11.32	0.10	17.58	1.79	1.24	97.78
TRER6B	Inclusion in garnet	42.43	2.13	11.76	9.51	11.22	0.08	17.65	1.67	1.29	97.73
TRER6B	Inclusion in garnet	44.72	1.39	10.65	10.12	10.70	0.11	18.43	1.47	0.72	98.31

Appendix 4.3 continued

Sample	Analysis	SiO_2	TiO_2	Al_2O_3	MgO	CaO	MnO	FeO*	Na_2O	K_2O	Total
TRER6B	Inclusion in garnet	43.56	1.63	11.13	9.85	10.86	0.10	17.89	1.58	0.79	97.39
TRER6B	Inclusion in garnet	43.10	1.88	11.32	10.08	10.79	0.11	17.86	1.65	0.88	97.67
TRER6B	Inclusion in garnet	43.96	1.78	11.21	10.09	11.16	0.08	17.60	1.60	0.84	98.31
TRER6B	Inclusion in garnet	43.24	1.75	11.40	9.96	11.22	0.10	17.26	1.70	0.84	97.46
TRER6B	Inclusion in garnet	43.90	1.79	10.93	10.25	10.58	0.10	17.68	1.57	0.81	97.59
TRER6B	Inclusion in garnet	42.28	2.18	11.87	9.92	11.18	0.09	16.88	1.74	1.03	97.16
TRER6B	Inclusion in garnet	43.05	1.79	11.28	10.15	10.97	0.10	17.22	1.69	0.83	97.09
TRER6B	Inclusion in garnet	42.91	2.11	11.53	9.91	11.27	0.08	16.79	1.55	1.10	97.24
TRER6B	Inclusion in garnet	42.67	1.98	11.35	10.16	11.18	0.08	16.73	1.68	1.00	96.83
TRER6B	Inclusion in garnet	42.85	2.24	11.71	10.01	11.36	0.07	16.43	1.62	1.16	97.44
TRER6B	Inclusion in garnet	43.17	1.80	11.10	10.41	10.91	0.10	17.02	1.63	0.85	96.98
TRER6B	Inclusion in garnet	43.62	2.26	11.37	10.20	11.22	0.09	16.61	1.66	1.14	98.18
TRER6B	Inclusion in garnet	43.13	2.32	11.40	10.11	11.34	0.09	16.46	1.62	1.11	97.57
TRER6B	Inclusion in garnet	43.05	2.10	11.27	10.16	11.37	0.07	16.14	1.62	1.11	96.89
TRER6B	Inclusion in garnet	43.62	1.77	11.01	10.41	11.28	0.08	16.37	1.59	0.91	97.03
TRER6B	**Inclusion in garnet**	**43.02**	**1.97**	**11.42**	**9.77**	**11.10**	**0.09**	**17.58**	**1.63**	**1.02**	**97.59**
TRER6B	Matrix	41.26	2.28	11.10	8.70	10.61	0.16	19.70	1.70	0.95	96.45
TRER6B	Matrix	41.56	2.18	10.87	8.68	11.09	0.16	18.86	1.73	0.86	95.99
TRER6B	Matrix	41.65	2.18	11.11	8.90	10.93	0.15	19.15	1.69	0.89	96.64
TRER6B	Matrix	41.29	2.07	10.56	9.02	10.78	0.16	18.81	1.73	0.84	95.27
TRER6B	Matrix	40.92	2.26	11.33	8.78	10.86	0.16	19.36	1.69	1.04	96.40
TRER6B	Matrix	40.69	2.20	11.21	8.61	11.20	0.15	18.84	1.76	0.90	95.55
TRER6B	Matrix	40.30	2.27	11.14	8.49	10.70	0.16	19.06	1.76	0.93	94.82
TRER6B	Matrix	41.02	2.20	11.26	8.63	11.04	0.15	19.02	1.67	0.89	95.88
TRER6B	Matrix	41.25	2.06	10.47	8.48	11.23	0.13	19.39	1.62	0.85	95.48
TRER6B	Matrix	41.19	1.94	11.54	8.18	11.22	0.12	19.28	1.74	1.00	96.21
TRER6B	Matrix	41.86	1.95	11.14	8.53	11.14	0.12	19.66	1.64	0.87	96.91
TRER6B	**Matrix**	**41.18**	**2.14**	**11.07**	**8.64**	**10.98**	**0.15**	**19.19**	**1.70**	**0.91**	**95.96**
TRER6B	Rimming garnet	41.81	2.30	11.57	8.79	10.75	0.13	19.71	1.72	0.97	97.76
TRER6B	Rimming garnet	42.23	1.94	11.04	9.18	10.73	0.10	19.14	1.69	0.89	96.94
TRER6B	Rimming garnet	41.73	1.90	11.27	8.85	11.06	0.14	19.05	1.71	0.87	96.57
TRER6B	Rimming garnet	41.32	1.90	10.66	9.02	10.77	0.12	18.93	1.60	0.85	95.16
TRER6B	Rimming garnet	41.62	2.00	11.03	9.06	11.19	0.11	18.66	1.71	0.86	96.25
TRER6B	Rimming garnet	43.20	1.74	10.65	9.77	10.99	0.11	18.63	1.52	0.83	97.44
TRER6B	Rimming garnet	42.45	1.93	10.98	9.33	11.12	0.11	18.67	1.70	0.85	97.13
TRER6B	Rimming garnet	43.18	1.83	10.70	9.64	11.26	0.11	18.35	1.61	0.76	97.42
TRER6B	Rimming garnet	43.38	1.74	10.11	9.96	10.82	0.10	18.51	1.33	0.71	96.65
TRER6B	**Rimming garnet**	**42.44**	**2.02**	**11.29**	**9.42**	**11.04**	**0.11**	**18.10**	**1.66**	**0.96**	**97.05**

*Total iron reported as FeO

Appendix 4.4: Electron microprobe analyses of miscellaneous minerals (oxide weight percent)

Sample	Analysis	SiO_2	TiO_2	Al_2O_3	MgO	CaO	MnO	FeO*	Na_2O	K_2O	Total
70-30-2	Cordierite	49.03	0.02	33.02	9.73	0.00	0.01	6.23	0.10	0.03	98.16
70-30-2	Cordierite	48.91	0.00	32.64	9.64	0.02	0.00	6.09	0.12	0.02	97.44
70-30-2	Cordierite	49.20	0.00	33.03	9.82	0.02	0.08	6.20	0.14	0.01	98.51
70-30-2	**Cordierite**	**49.05**	**0.01**	**32.90**	**9.73**	**0.01**	**0.03**	**6.17**	**0.12**	**0.02**	**98.04**
70-30-2	Feldspar	60.06	0.00	23.93	0.00	0.71	0.00	4.34	0.27	0.69	91.92
70-30-2	Feldspar	57.94	0.00	24.75	0.00	0.28	0.00	3.42	0.39	3.81	92.81
70-30-2	Feldspar	57.74	0.00	26.14	0.00	8.03	0.00	0.01	6.75	0.16	98.84
70-30-2	Feldspar	57.76	0.00	25.82	0.00	7.96	0.00	0.04	6.85	0.11	98.55
70-30-2	Feldspar	58.07	0.00	26.16	0.00	8.11	0.00	0.07	6.85	0.12	99.37
70-30-2	Feldspar	57.23	0.00	26.68	0.00	8.91	0.00	0.17	6.18	0.00	99.18
70-30-2	Feldspar	58.37	0.00	26.00	0.00	8.12	0.00	0.00	6.80	0.11	99.44
70-30-2	**Feldspar**	**58.17**	**0.00**	**25.64**	**0.00**	**6.02**	**0.00**	**1.15**	**4.87**	**0.71**	**97.16**
70-30-2	Sillimanite	36.70	0.05	61.52	0.00	0.00	0.01	0.42	0.00	0.00	98.70
70-30-2	Sillimanite	36.52	0.00	61.40	0.00	0.03	0.02	0.35	0.08	0.00	98.41
70-30-2	Sillimanite	36.65	0.00	61.34	0.00	0.04	0.04	0.43	0.01	0.00	98.51
70-30-2	Sillimanite	36.64	0.05	61.73	0.02	0.00	0.05	0.35	0.00	0.00	98.83
70-30-2	Sillimanite	36.68	0.03	61.59	0.03	0.04	0.00	0.33	0.00	0.00	98.70
70-30-2	Sillimanite	36.73	0.07	61.39	0.03	0.00	0.00	0.25	0.00	0.00	98.46
70-30-2	Sillimanite	36.82	0.07	61.58	0.00	0.00	0.04	0.30	0.01	0.03	98.84
70-30-2	Sillimanite	36.61	0.00	61.40	0.01	0.00	0.02	0.78	0.00	0.00	98.82
70-30-2	**Sillimanite**	**36.67**	**0.03**	**61.49**	**0.01**	**0.01**	**0.02**	**0.40**	**0.01**	**0.00**	**98.66**
RM42	Feldspar	59.53	0.00	24.42	0.00	6.66	0.00	0.01	7.57	0.38	98.57
RM42	Feldspar	58.95	0.00	25.21	0.00	7.33	0.00	0.02	7.10	0.34	98.95
RM42	Feldspar	58.92	0.00	25.23	0.00	7.18	0.00	0.00	7.21	0.37	98.90
RM42	Feldspar	59.41	0.00	25.00	0.00	7.13	0.00	0.07	7.30	0.29	99.19
RM42	**Feldspar**	**59.20**	**0.00**	**24.96**	**0.00**	**7.07**	**0.00**	**0.03**	**7.30**	**0.34**	**98.91**
RRSW1	Chlorite	27.08	0.22	18.90	14.10	0.13	0.20	26.48	0.01	0.29	87.41
RRSW1	Chlorite	27.98	0.65	18.33	13.46	0.12	0.22	27.48	0.02	0.63	88.88
RRSW1	Chlorite	28.86	1.58	16.62	12.39	0.10	0.15	27.47	0.02	1.45	88.64
RRSW1	Chlorite	26.47	0.15	18.91	13.65	0.08	0.20	27.75	0.01	0.09	87.29
RRSW1	Chlorite	28.78	0.68	17.93	13.57	0.01	0.17	26.23	0.04	0.75	88.28
RRSW1	Chlorite	28.19	0.12	17.42	14.47	0.21	0.19	26.97	0.01	0.13	87.69
RRSW1	Chlorite	26.55	0.00	18.93	12.12	0.08	0.27	29.93	0.00	0.07	87.94
RRSW1	Chlorite	30.18	0.82	15.06	13.85	0.10	0.10	26.89	0.02	1.31	88.32
RRSW1	Chlorite	28.79	1.65	16.81	14.11	1.18	0.18	26.07	0.00	0.45	89.23
RRSW1	Chlorite	28.63	1.06	16.52	14.68	0.68	0.18	26.24	0.01	0.26	88.25
RRSW1	Chlorite	28.76	0.18	17.31	15.01	0.11	0.18	26.98	0.02	0.16	88.70
RRSW1	**Chlorite**	**28.21**	**0.65**	**17.52**	**13.76**	**0.25**	**0.19**	**27.14**	**0.01**	**0.51**	**88.24**
RRSW1	Prehnite	42.10	0.07	21.68	0.00	27.10	0.01	2.57	0.04	0.00	93.56
RRSW1	Prehnite	42.73	0.02	23.97	0.00	27.44	0.00	0.37	0.01	0.01	94.54
RRSW1	Prehnite	43.32	0.00	23.32	0.00	25.87	0.00	0.22	0.54	0.01	93.29
RRSW1	Prehnite	42.12	0.01	22.70	0.00	27.33	0.00	1.74	0.10	0.00	93.91
RRSW1	Prehnite	42.65	0.18	23.70	0.02	27.49	0.01	0.51	0.00	0.01	94.56
RRSW1	Prehnite	42.79	0.04	23.77	0.01	27.27	0.00	0.65	0.02	0.01	94.54
RRSW1	Prehnite	42.52	0.24	23.17	0.00	27.34	0.00	1.44	0.00	0.00	94.72
RRSW1	Prehnite	41.88	0.15	21.72	0.00	27.10	0.01	2.94	0.00	0.01	93.80
RRSW1	Prehnite	42.55	0.02	21.77	0.00	26.76	0.00	2.62	0.08	0.01	93.81
RRSW1	Prehnite	42.71	0.02	23.14	0.10	27.14	0.00	1.74	0.01	0.01	94.99
RRSW1	Prehnite	42.77	0.04	24.12	0.06	27.29	0.01	0.50	0.02	0.00	94.79
RRSW1	**Prehnite**	**42.56**	**0.07**	**23.01**	**0.02**	**27.10**	**0.00**	**1.39**	**0.07**	**0.01**	**94.23**
RMC200	Chlorite	26.25	0.11	22.99	19.33	0.00	0.08	19.73	0.00	0.04	88.53
RMC200	Chlorite	28.09	0.07	21.04	16.19	0.10	0.06	23.60	0.04	0.32	89.51
RMC200	Chlorite	26.40	0.08	23.13	19.32	0.00	0.01	19.52	0.00	0.02	88.47
RMC200	Chlorite	26.42	0.06	22.46	19.13	0.00	0.06	19.51	0.06	0.02	87.72
RMC200	Chlorite	26.95	0.00	22.94	18.99	0.01	0.03	19.98	0.00	0.05	88.94
RMC200	Chlorite	25.97	0.03	22.65	18.67	0.01	0.03	19.40	0.07	0.00	86.82
RMC200	Chlorite	26.28	0.01	22.41	18.56	0.00	0.00	19.55	0.05	0.08	86.94
RMC200	Chlorite	26.14	0.07	22.37	18.77	0.00	0.02	19.81	0.00	0.00	87.18
RMC200	**Chlorite**	**26.56**	**0.05**	**22.50**	**18.62**	**0.01**	**0.04**	**20.14**	**0.03**	**0.07**	**88.01**
RMC200	Feldspar	56.10	0.00	27.42	0.00	9.36	0.00	0.03	5.82	0.31	99.03
RMC200	Sericite	45.35	0.14	27.65	6.21	0.40	0.07	6.39	0.12	6.97	93.30
RMC200	Sericite	46.66	0.07	28.29	5.85	0.38	0.02	5.39	0.10	6.81	93.56
RMC200	Sericite	44.83	0.01	29.21	4.52	0.08	0.00	5.10	0.16	9.00	92.91
RMC200	Sericite	46.04	0.01	30.09	4.51	0.14	0.00	4.53	0.14	8.87	94.32
RMC200	Sericite	46.39	0.06	30.08	4.26	0.09	0.00	4.59	0.18	9.06	94.70
RMC200	Sericite	48.63	0.00	29.25	4.29	0.37	0.04	3.77	0.14	7.77	94.26
RMC200	Sericite	49.44	0.08	29.93	2.81	0.27	0.03	2.66	0.10	9.37	94.69
RMC200	**Sericite**	**47.93**	**0.05**	**28.99**	**4.06**	**1.39**	**0.02**	**4.06**	**0.84**	**7.27**	**94.60**

Appendix 4.4 continued

Sample	Analysis	SiO_2	TiO_2	Al_2O_3	MgO	CaO	MnO	FeO*	Na_2O	K_2O	Total
RM37	Sillimanite	47.83	0.00	37.30	0.17	0.22	0.00	0.27	0.14	0.85	86.79
RM37	Sillimanite	46.83	0.03	36.94	0.29	0.30	0.00	0.47	0.07	0.44	85.36
RM37	**Sillimanite**	**47.33**	**0.02**	**37.12**	**0.23**	**0.26**	**0.00**	**0.37**	**0.11**	**0.65**	**86.08**
RM39	Feldspar	61.29	0.00	24.08	0.00	5.75	0.00	0.02	8.07	0.23	99.44
RM39	Feldspar	61.32	0.00	24.11	0.00	5.80	0.00	0.02	8.09	0.18	99.51
RM39	Feldspar	61.40	0.00	24.10	0.00	5.55	0.00	0.00	8.16	0.26	99.47
RM39	Feldspar	61.40	0.00	24.15	0.00	5.89	0.00	0.07	8.15	0.20	99.87
RM39	Feldspar	61.34	0.00	23.86	0.00	5.70	0.00	0.14	8.33	0.17	99.54
RM39	Feldspar	61.84	0.00	23.81	0.00	5.30	0.00	0.00	8.33	0.28	99.56
RM39	**Feldspar**	**61.43**	**0.00**	**24.02**	**0.00**	**5.66**	**0.00**	**0.04**	**8.19**	**0.22**	**99.56**
RRSW2	Rutile	0.10	99.87	0.02	0.00	0.00	0.00	0.23	0.00	0.00	100.22
RRSW2	Rutile	0.09	99.70	0.03	0.00	0.00	0.02	0.36	0.01	0.01	100.22
RRSW2	Rutile	0.07	98.56	0.02	0.00	0.00	0.00	0.08	0.00	0.00	98.72
RRSW2	Rutile	0.09	99.53	0.08	0.00	0.00	0.01	0.35	0.02	0.00	100.08
RRSW2	Rutile	0.09	99.24	0.02	0.00	0.00	0.00	0.18	0.06	0.00	99.59
RRSW2	**Rutile**	**0.09**	**99.38**	**0.03**	**0.00**	**0.00**	**0.01**	**0.24**	**0.02**	**0.00**	**99.76**
RRSW2	Pyroxene	46.55	0.57	13.29	17.42	0.23	0.08	18.24	1.30	0.00	97.68
RRSW2	Pyroxene	45.62	0.57	13.25	17.22	0.22	0.08	18.37	1.36	0.00	96.67
RRSW2	Pyroxene	46.09	0.51	12.23	17.23	0.19	0.06	18.56	1.17	0.01	96.04
RRSW2	Pyroxene	46.83	0.58	12.12	17.46	0.23	0.08	18.72	1.23	0.00	97.24
RRSW2	Pyroxene	47.49	0.57	11.92	17.68	0.18	0.08	18.73	1.14	0.00	97.79
RRSW2	**Pyroxene**	**46.52**	**0.56**	**12.56**	**17.40**	**0.21**	**0.07**	**18.52**	**1.24**	**0.00**	**97.08**
TRER7	Epidote	57.94	0.01	23.55	0.00	6.26	0.01	0.05	8.08	0.08	95.96
TRER7	Epidote	58.68	0.01	24.05	0.00	6.40	0.00	0.05	8.39	0.08	97.66
TRER7	Epidote	58.92	0.01	24.07	0.00	6.48	0.00	0.03	8.27	0.08	97.87
TRER7	Epidote	59.86	0.01	24.24	0.00	6.07	0.00	0.08	8.53	0.07	98.85
TRER7	Epidote	58.98	0.00	23.86	0.00	6.37	0.00	0.09	8.40	0.06	97.75
TRER7	Epidote	58.43	0.00	24.08	0.00	6.45	0.00	0.03	8.27	0.09	97.35
TRER7	Epidote	58.78	0.00	23.76	0.00	6.25	0.00	0.09	8.40	0.05	97.33
TRER7	Epidote	58.72	0.00	23.82	0.00	6.20	0.00	0.07	8.51	0.07	97.38
TRER7	Epidote	59.82	0.00	24.12	0.00	6.38	0.00	0.03	8.43	0.10	98.88
TRER7	Epidote	59.22	0.00	24.00	0.00	6.19	0.01	0.07	8.56	0.06	98.10
TRER7	**Epidote**	**58.93**	**0.01**	**23.96**	**0.00**	**6.30**	**0.00**	**0.06**	**8.38**	**0.07**	**97.71**

*Total iron reported as FeO

Appendix 5.1: Irradiation details and analytical technique used for each sample

Irradiation ID	End Date of Irradiation	Irradi-ation Duration (hours)	Sample	Sample Format	Analytical Technique	J-Value †	Error ($\times 10^{-5}$)	Relevant Thesis Section
*BR2 Mol	25/4/97	198	70-30-2	Thick section	Squres and inclusions	0.0846	423	5.2, 6.3
			RM37	Thick section	Squares, inclusions and profiles	0.0846	423	5.2, 6.3
			RM39	Thick section	Squares and inclusions	0.0846	423	5.2, 6.3
			RM40	Thick section	Squares, inclusions and profiles	0.0846	423	5.2, 6.3
			RM42	Thick section	Sqares and inclusion	0.0846	423	5.2, 6.3
			RMC200	Thick section	Squares	0.0846	423	5.2
McMaster 1	12/12/97	28	RRCR2	Biotite Separates	Squares and profiles	0.013151	6.58	5.2
			RRCR3	Biotite Separates	Squares, profiles and step heating	0.013187	6.59	5.2
			RRCR5	Biotite Separates	Squares and profiles	0.013200	6.60	5.2
			RRSW1	Biotite Separates	Squares and profiles	0.013175	6.59	5.2
			RRSW2	Biotite Separates	Squares and profiles	0.013224	6.61	5.2
			RRSW3	Biotite Separates	Squares and profiles	0.013163	6.58	5.2
			RRSW4	Biotite Separates	Squares and profiles	0.013212	6.61	5.2
			RRSW1	Amphibole Separates	Total fusion and step heating	0.013236	6.62	5.3
McMaster 2	3/4/98	50	RRCR3	Garnet Separates	Inclusion ablations	0.01099	54.95	6.3
			RRSW2	Garnet Separates	Inclusion ablations	0.01099	54.95	6.3
McMaster 3	3/4/98	25	HLM2	Garnet Separates	Inclusion ablations	0.01047	52.35	6.3
			TRER7	Garnet Separates	Inclusion ablations	0.01047	52.35	6.3
			TRBC2	Garnet Separates	Inclusion ablations	0.01047	52.35	6.3
			SMR1	Muscovite Separates	Squares and profiles	0.01047	52.35	8.2
McMaster 4	9/7/98	50	70-30-2	Thick Section	Squares and inclusions	0.01185	59.25	5.2
			RMC200	Thick Section	Squares and inclusions	0.01185	59.25	5.2
			RM37	Thick Section	Squares and inclusions	0.01185	59.25	5.2
			RM39	Thick Section	Squares and inclusions	0.01185	59.25	5.2
			RM40	Thick Section	Squares and inclusions	0.01185	59.25	5.2
			HLM2	Thick Section	Squares	0.01185	59.25	5.2
			TRER4	Thick Section	Squares and profiles	0.01185	59.25	5.2
			TRER7	Thick Section	Squares and profiles	0.01185	59.25	5.2
			TRGC5	Thick Section	Squares and profiles	0.01185	59.25	5.2
			TRMC3	Thick Section	Squares and profiles	0.01185	59.25	5.2
			TRMR2	Thick Section	Squares and profiles	0.01185	59.25	5.2
McMaster 5	3/11/98	15	HLM4	Amphibole Separate	Total fusion	0.012065	60.35	5.3
			RRCR11	Amphibole Separate	Total fusion	0.012065	60.35	5.3
			RRCR12	Amphibole Separate	Total fusion	0.012065	60.35	5.3
			RRCR4	Amphibole Separate	Total fusion	0.012065	60.35	5.3
			TRER1	Amphibole Separate	Total fusion	0.012065	60.35	5.3
			TRER2	Amphibole Separate	Total fusion	0.012065	60.35	5.3
			TRER2	Biotite Separate	Squares	0.012065	60.35	5.3
			TRMC5	Amphibole Separate	Total fusion	0.012065	60.35	5.3
			TRMR2	Thick Section	Squares	0.012065	60.35	5.3, 6.3
			TRMR3	Amphibole Separate	Total fusion	0.012065	60.35	5.3
			TRMR3	Biotite Separate	Total fusion	0.012065	60.35	5.3

Appendix 5.1 continued

Irradiation ID	End Date of Irradiation	Irradi-ation Duration (hours)	Sample	Sample Format	Analytical Technique	J-Value	Error ($\times 10^{-5}$)	Relevant Thesis Section
			TRWC1	Amphibole Separate	Total fusion	0.012065	60.35	5.3
			TRWC1	Biotite Separate	Squares	0.012065	60.35	5.3
			RMC42	Thick section	Squares and profiles	0.012065	60.35	5.2
			9-49	Thick section	Squares and profiles	0.012065	60.35	8.2
			9-51	Thick section	Squares and profiles	0.012065	60.35	8.2
			9-46	Thick section	Squares and profiles	0.012065	60.35	8.2
			7-68	Thick section	Squares and profiles	0.012065	60.35	8.2
			8-15a	Thick section	Squares and profiles	0.012065	60.35	8.2
			8-14a	Thick section	Squares and profiles	0.012065	60.35	8.2
			8-152	Thick section	Squares and profiles	0.012065	60.35	8.2
			8-104	Thick section	Squares and profiles	0.012065	60.35	8.2
			8-114	Thick section	Squares and profiles	0.012065	60.35	8.2
McMaster 6	21/11/98	200	TRMR2	Thick Section	High resolution	0.04693	230.00	5.5

Correction factors for the BR2 reactor at Mol, Belguim are as follows:

Ca correction: $^{39}Ar/^{37}Ar$ = 0.000242
$^{36}Ar/^{37}Ar$ = 0.000727
K correction: $^{40}Ar/^{39}Ar$ = 0.000923

Correction factors for the McMaster University reactor are as follows:

Ca correction: $^{39}Ar/^{37}Ar$ = 0.000651
$^{36}Ar/^{37}Ar$ = 0.000254
K correction: $^{40}Ar/^{39}Ar$ = 0.0156

* Note: when the standards from the BR2, Mol irradiation were analysed they gave widely differing ages. This was probably because the irradiation package was packed by someone else and the standards were placed in a different part of the irradiation can from the samples. For this reason, parts of the same thick sections as contained within the BR2 irradiation, along with new standards, were later irradiated at the McMaster reactor, and the ages cross-calculated. This changed the J-value of the BR2 to that shown in the table above. The absolute ages of the samples in the BR2 irradiation should be viewed as compromised, with external errors of 2 to 3 %. However, this does not affect the internal age variations or comparisons between samples.

†Note: variations in flux were found to be insignificant in most irradiations so a mean J-value was used for all samples within that irradiation

Appendix 5.2: Data tables for matrix mica ^{40}Ar-^{39}Ar analyses from Ruby Range, Tobacco Root Mountains and Highland Mountains

Sample	Run	$^{40}Ar/^{39}Ar$	$^{38}Ar/^{39}Ar$	$^{37}Ar/^{39}Ar$	$^{36}Ar/^{39}Ar$	% Atmospheric	^{39}Ar (cc) $\times10^{-13}$	$^{40}Ar^*/^{39}Ar$	Age (Ma)	± 1 σ	Excluded from mean	Profile Diagram
70-30-2	50 µm square	133.79	0.01	0.00	0.002	0.35	970.78	133.31	1710	10		
70-30-2	50 µm square	135.29	0.01	0.01	0.004	0.94	1201.65	134.02	1716	9		
70-30-2	50 µm square	135.43	0.01	0.01	0.001	0.32	1064.59	135.00	1724	8		
70-30-2	50 µm square	137.69	0.01	0.01	0.002	0.38	1139.43	137.17	1741	7		
70-30-2	50 µm square	141.02	0.02	0.00	0.012	2.49	586.34	137.51	1744	11		
70-30-2	50 µm square	139.25	0.01	0.01	0.003	0.73	1491.80	138.23	1750	7		
70-30-2	50 µm square	139.67	0.01	0.01	0.002	0.35	936.76	139.18	1758	8		
70-30-2	50 µm square	140.84	0.01	0.01	0.004	0.89	902.74	139.60	1761	8		
70-30-2	50 µm square	142.67	0.01	0.00	0.005	1.12	1041.26	141.08	1773	8		
70-30-2	50 µm square	224.36	0.02	0.02	0.007	0.86	305.90	222.41	2329	14	*	
RM37	50 µm square	19.75	0.01	0.00	0.001	0.95	5947.12	19.56	1762	17		
RM37	50 µm square	19.84	0.01	0.00	0.000	0.48	2103.77	19.74	1772	24		
RM37	50 µm square	19.84	0.01	0.00	0.002	3.12	4129.30	19.22	1742	15		
RM37	50 µm square	19.85	0.01	0.00	0.001	1.47	7987.24	19.56	1762	10		
RM37	50 µm square	19.87	0.01	0.00	0.000	-0.72	3515.70	20.01	1787	16		
RM37	50 µm square	19.89	0.01	0.00	0.002	2.39	4889.98	19.42	1753	14		
RM37	50 µm square	98.62	0.03	0.37	0.074	-0.90	150.61	99.50	1405	33		
RM37	50 µm square	113.98	0.02	0.39	0.073	3.53	198.24	109.96	1505	24		
RM37	50 µm square	115.92	0.02	0.41	0.080	3.26	175.89	112.14	1525	27		
RM37	50 µm square	120.16	0.02	0.15	0.031	0.28	392.17	119.83	1594	16		
RM37	50 µm square	125.20	0.02	0.08	0.016	0.49	872.85	124.59	1636	8		
RM37	50 µm square	136.63	0.02	0.09	0.021	1.32	811.61	134.83	1722	8		
RM37	50 µm square	136.68	0.02	0.07	0.019	1.37	994.84	134.81	1722	8		
RM37	50 µm square	137.89	0.01	0.06	0.012	0.41	1170.78	137.32	1743	7		
RM37	50 µm square	138.41	0.01	0.11	0.019	-0.98	487.92	139.77	1762	11		
RM37	50 µm square	138.91	0.01	0.07	0.010	0.15	1254.38	138.69	1754	7		
RM37	50 µm square	140.10	0.02	0.07	0.013	0.00	874.31	140.10	1765	8		
RM37	50 µm square	141.92	0.01	0.06	0.012	-0.22	870.42	142.23	1782	8		
RM37	ProfileA1	19.86	0.01	0.00	0.001	1.83	2326.28	19.50	1758	38		5.7.1
RM37	ProfileA2	19.87	0.01	0.00	0.000	-0.23	1824.00	19.91	1782	46		5.7.1
RM37	ProfileA3	20.13	0.01	0.01	0.003	4.93	2062.09	19.13	1737	47		5.7.1
RM37	ProfileA4	19.78	0.01	0.00	0.001	2.12	2021.08	19.36	1750	44		5.7.1
RM37	ProfileA5	20.05	0.01	0.00	-0.001	-0.78	2236.26	20.21	1798	39		5.7.1

Appendix 5.2 continued

Sample	Run	$^{40}Ar/^{39}Ar$	$^{38}Ar/^{39}Ar$	$^{37}Ar/^{39}Ar$	$^{36}Ar/^{39}Ar$	% Atmos-pheric	^{39}Ar (cc) $\times10^{-13}$	$^{40}Ar^*/^{39}Ar$	Age (Ma)	± 1 σ	Excluded from mean	Profile Diagram
RM39	50 µm square	7.72	0.02	0.04	0.001	4.86	1108.81	7.34	871	90	*	
RM39	50 µm square	13.02	0.02	0.09	0.005	12.33	1418.27	11.42	1219	53	*	
RM39	50 µm square	16.06	0.02	0.04	0.010	18.82	577.24	13.04	1341	122	*	
RM39	50 µm square	18.42	0.01	0.01	0.001	1.72	2990.07	18.10	1675	21		
RM39	50 µm square	22.45	0.02	0.07	-0.009	-11.80	94.14	25.09	2055	431	*	
RM39	50 µm square	43.69	-0.08	-0.45	0.045	30.17	14.77	30.51	557	607	*	
RM39	50 µm square	138.79	0.01	-0.02	-0.004	-0.78	678.20	139.87	1763	9		
RM39	50 µm square	138.94	0.01	-0.01	-0.001	-0.29	851.22	139.34	1759	8		
RM39	50 µm square	141.55	0.01	-0.02	0.001	0.15	926.56	141.34	1775	8		
RM39	50 µm square	142.66	0.01	0.00	0.003	0.66	1203.59	141.72	1778	7		
RM39	50 µm square	143.25	0.01	-0.03	0.002	0.43	744.30	142.63	1785	9		
RM39	50 µm square	143.97	0.01	-0.01	0.001	0.21	654.38	143.67	1794	10		
RM39	50 µm square	144.15	0.01	-0.01	-0.002	-0.44	742.35	144.79	1802	9		
RM39	50 µm square	145.36	0.01	0.01	0.000	-0.07	731.17	145.46	1808	8		
RM39	50 µm square	145.89	0.01	-0.01	-0.001	-0.14	966.41	146.10	1813	8		
RM40	50 µm square	25.11	0.01	0.01	0.015	17.09	4629.48	20.82	1832	26		
RM40	50 µm square	127.49	0.02	0.12	0.011	2.65	294.24	124.12	1632	19		
RM40	50 µm square	129.78	0.01	0.00	0.005	1.22	710.27	128.19	1667	9		
RM40	50 µm square	143.87	0.01	0.01	0.004	0.90	1080.14	142.58	1785	7		
RM40	50 µm square	145.73	0.01	0.01	0.006	1.25	691.32	143.91	1795	9		
RM40	50 µm square	145.88	0.02	0.00	0.008	1.65	687.43	143.47	1792	10		
RM40	50 µm square	147.32	0.02	0.01	0.005	0.91	744.30	145.98	1812	10		
RM40	50 µm square	147.79	0.02	0.01	0.005	1.02	749.64	146.29	1814	10		
RM40	50 µm square	148.52	0.01	0.01	0.003	0.58	1146.24	147.66	1825	8		
RM40	50 µm square	149.15	0.01	0.00	0.003	0.59	970.78	148.26	1830	8		
RM40	ProfileA1	18.93	0.01	0.01	0.001	2.16	1220.56	18.52	1701	29	*	5.7.2
RM40	ProfileA2	20.05	0.01	0.01	0.002	3.38	1915.90	19.37	1750	19		5.7.2
RM40	ProfileA3	19.84	0.01	0.01	0.002	3.51	2817.88	19.15	1738	17		5.7.2
RM40	ProfileA4	19.69	0.01	0.02	0.003	3.78	3168.51	18.94	1726	15		5.7.2
RM40	ProfileA5	19.80	0.01	0.02	0.002	2.90	3420.51	19.23	1742	15		5.7.2
RM40	ProfileA6	20.27	0.01	0.02	0.003	5.08	3452.57	19.24	1743	14		5.7.2
RM40	ProfileB1	24.34	0.02	0.00	0.011	12.86	3577.63	21.21	1854	20		5.7.2

Appendix 5.2 continued

Sample	Run	$^{40}Ar/^{39}Ar$	$^{38}Ar/^{39}Ar$	$^{37}Ar/^{39}Ar$	$^{36}Ar/^{39}Ar$	% Atmospheric	^{39}Ar (cc) $\times 10^{-13}$	$^{40}Ar^*/^{39}Ar$	Age (Ma)	± 1 σ	Excluded from mean	Profile Diagram
RM40	ProfileB2	22.71	0.01	0.00	0.008	10.09	3840.98	20.42	1810	19		5.7.2
RM40	ProfileB3	23.93	0.01	0.00	0.009	11.50	4746.90	21.18	1852	15		5.7.2
RM40	ProfileC1	123.29	0.02	0.02	-0.002	-0.43	383.18	123.82	1629	15	*	5.7.2
RM40	ProfileC2	134.87	0.01	0.02	0.004	0.90	1035.42	133.65	1713	8	*	5.7.2
RM40	ProfileC3	139.40	0.01	0.00	0.003	0.72	1120.97	138.39	1751	7		5.7.2
RM40	ProfileC4	145.10	0.01	0.00	0.004	0.92	1148.18	143.77	1794	8		5.7.2
RM40	ProfileC5	133.19	0.01	0.01	0.007	1.60	1024.25	131.05	1691	8		5.7.2
RM40	ProfileC6	138.14	0.01	0.01	0.006	1.33	1115.62	136.30	1734	8		5.7.2
RM40	ProfileD1	20.57	0.01	0.03	0.000	0.44	2571.30	20.48	1814	14		
RM40	ProfileE1	145.55	0.01	0.02	0.010	2.00	752.07	142.64	1785	9		
RM42	50 µm square	18.97	0.01	0.00	0.001	0.94	3179.42	18.79	1717	20		
RM42	50 µm square	19.04	0.01	0.01	0.000	0.32	4926.46	18.98	1728	16		
RM42	50 µm square	19.12	0.01	0.05	-0.024	-37.63	180.16	26.32	2113	217	*	
RM42	50 µm square	19.14	0.01	0.00	0.001	1.67	4261.20	18.82	1719	16		
RM42	50 µm square	19.39	0.01	0.00	0.000	0.49	5957.11	19.30	1746	10		
RM42	50 µm square	20.08	0.01	0.04	-0.004	-5.46	333.56	21.18	1852	161		
RM42	50 µm square	20.38	0.02	0.04	0.004	6.27	338.36	19.10	1735	154		
RM42	50 µm square	21.67	0.01	0.23	-0.007	-9.48	178.03	23.72	1986	234	*	
RM42	50 µm square	22.64	0.01	0.10	0.015	19.43	128.50	18.24	1684	415	*	
RM42	50 µm square	23.80	0.00	0.15	0.013	16.45	110.39	19.89	1780	505	*	
RMC200	*50 µm square*	17.32	0.01	0.01	-0.006	-10.46	1725.20	19.13	1737	79		
RMC200	50 µm square	19.24	0.01	0.00	-0.002	-2.99	2197.11	19.81	1776	59		
RMC200	50 µm square	19.41	0.01	0.00	-0.003	-4.85	2329.21	20.35	1806	54		
RMC200	50 µm square	19.59	0.01	0.00	-0.002	-3.64	2701.52	20.30	1804	48		
RMC200	50 µm square	19.60	0.01	0.00	-0.003	-5.19	2681.81	20.62	1821	49		
RMC200	50 µm square	20.14	0.01	0.00	0.001	1.76	1690.58	19.79	1774	76		
RMC200	50 µm square	130.57	0.01	-0.01	-0.001	-0.24	842.28	130.89	1690	8		
RMC200	50 µm square	134.05	0.02	0.01	0.009	1.94	716.89	131.45	1694	7		
RMC200	50 µm square	134.95	0.01	0.00	0.004	0.78	630.37	133.90	1715	6		
RMC200	50 µm square	137.27	0.01	0.00	0.001	0.15	633.29	137.06	1741	7		
RMC200	50 µm square	139.74	0.01	0.00	0.003	0.57	669.74	138.94	1756	7		
RMC200	50 µm square	140.20	0.02	0.00	0.002	0.41	915.19	139.62	1761	8		

Appendix 5.2 continued

Sample	Run	$^{40}Ar/^{39}Ar$	$^{38}Ar/^{39}Ar$	$^{37}Ar/^{39}Ar$	$^{36}Ar/^{39}Ar$	% Atmospheric	^{39}Ar (cc) $\times10^{-13}$	$^{40}Ar^*/^{39}Ar$	Age (Ma)	± 1 σ	Excluded from mean	Profile Diagram
RMC200	50 µm square	140.35	0.01	0.00	0.001	0.13	724.66	140.17	1766	6		
RMC200	50 µm square	140.36	0.01	0.00	0.000	0.00	777.15	140.36	1767	7		
RMC200	50 µm square	140.43	0.01	0.00	0.006	1.22	699.88	138.72	1754	6		
RMC200	50 µm square	141.05	0.01	-0.01	0.001	0.14	657.59	140.85	1771	7		
RMC42B	50 µm square	112.03	0.02	0.01	0.006	1.48	641.51	110.37	1527	9		
RMC42B	50 µm square	116.26	0.01	0.00	0.005	1.27	632.27	114.79	1568	10		
RMC42B	50 µm square	121.66	0.01	0.00	0.005	1.10	696.92	120.32	1618	9		
RMC42B	50 µm square	126.41	0.01	0.01	0.001	0.27	772.74	126.06	1668	9		
RMC42B	ProfileA1	115.43	0.00	0.03	0.000	0.00	98.62	115.43	1574	48		5.7.3
RMC42B	ProfileA2	119.81	0.01	0.00	-0.003	-0.81	275.05	120.77	1622	18		5.7.3
RMC42B	ProfileA3	119.82	0.01	-0.01	0.004	0.99	448.56	118.63	1603	13		5.7.3
RMC42B	ProfileA4	124.37	0.01	0.00	0.002	0.51	624.98	123.73	1648	10		5.7.3
RMC42B	ProfileA5	123.27	0.01	-0.01	0.002	0.45	723.65	122.71	1639	9		5.7.3
RMC42B	ProfileB1	101.65	0.08	0.14	-0.028	-8.05	32.52	109.83	1522	145		
RMC42M	50 µm square	124.48	0.01	0.00	0.002	0.45	705.18	123.91	1649	10		
RMC42M	50 µm square	128.75	0.01	0.00	0.000	0.00	533.13	128.75	1691	11		
RMC42M	50 µm square	130.21	0.02	0.00	0.001	0.14	710.52	130.02	1702	10		
RMC42M	50 µm square	130.84	0.01	-0.01	-0.003	-0.66	464.60	131.70	1716	11		
RMC42M	ProfileA1	124.69	0.02	0.00	0.005	1.29	413.56	123.08	1642	12		5.7.3
RMC42M	ProfileA2	126.01	0.01	0.00	0.002	0.50	633.73	125.38	1662	9		5.7.3
RMC42M	ProfileA3	130.19	0.01	0.00	0.002	0.41	748.43	129.66	1699	9		5.7.3
RMC42M	ProfileA4	125.01	0.01	0.01	0.004	0.84	763.99	123.97	1650	8		5.7.3
RMC42M	ProfileA5	123.66	0.01	0.01	0.003	0.75	719.27	122.73	1639	9		5.7.3
RRCR2	ProfileA1	123.62	0.01	-0.01	-0.001	-0.21	755.19	123.88	1744	19		5.7.4
RRCR2	ProfileA2	124.23	0.01	-0.02	-0.003	-0.78	753.25	125.20	1756	23		5.7.4
RRCR2	ProfileA3	127.92	0.01	-0.01	0.000	0.08	662.36	127.82	1779	21		5.7.4
RRCR2	ProfileA4	126.69	0.01	0.00	-0.002	-0.53	691.03	127.37	1775	20		5.7.4
RRCR2	ProfileA5	123.63	0.02	0.01	0.006	1.35	595.28	121.95	1726	37		5.7.4
RRCR2	ProfileA6	127.35	0.01	0.01	0.011	2.57	669.16	124.08	1746	26		5.7.4
RRCR2	ProfileA7	128.25	0.01	0.01	0.015	3.48	520.92	123.79	1743	31		5.7.4
RRCR2	ProfileA8	127.83	0.02	0.07	0.032	7.30	362.95	118.49	1695	41		5.7.4
RRCR2	ProfileA9	128.07	0.01	0.04	0.000	0.08	655.53	127.97	1781	22		5.7.4

Appendix 5.2 continued

Sample	Run	$^{40}Ar/^{39}Ar$	$^{38}Ar/^{39}Ar$	$^{37}Ar/^{39}Ar$	$^{36}Ar/^{39}Ar$	% Atmos-pheric	^{39}Ar (cc) $\times10^{-13}$	$^{40}Ar^*/^{39}Ar$	Age (Ma)	± 1 σ	Excluded from mean	Profile Diagram
RRCR2	ProfileA10	128.33	0.01	0.02	0.004	1.03	651.17	127.00	1772	25		5.7.4
RRCR2	ProfileB1	124.89	0.01	0.05	0.000	0.09	572.42	124.78	1752	24		5.7.4
RRCR2	ProfileB2	126.32	0.01	0.02	0.001	0.18	865.02	126.09	1764	18		5.7.4
RRCR2	ProfileB3	125.61	0.01	-0.01	-0.002	-0.49	750.33	126.23	1765	24		5.7.4
RRCR2	ProfileB4	126.59	0.01	0.00	-0.004	-0.86	798.44	127.67	1778	17		5.7.4
RRCR2	ProfileB5	124.00	0.02	0.00	-0.002	-0.44	848.99	124.55	1750	17		5.7.4
RRCR2	ProfileC1	124.76	0.01	-0.02	-0.007	-1.68	602.10	126.86	1771	26		5.7.4
RRCR2	ProfileC2	127.73	0.01	-0.03	-0.007	-1.55	501.98	129.71	1796	23		5.7.4
RRCR2	ProfileC3	128.75	0.01	-0.01	-0.006	-1.48	523.84	130.65	1804	24		5.7.4
RRCR2	ProfileC4	126.28	0.01	0.02	0.000	-0.10	555.42	126.40	1767	23		5.7.4
RRCR2	ProfileC5	122.87	0.01	0.01	-0.004	-0.91	533.56	123.99	1745	30		5.7.4
RRCR2	ProfileC6	126.06	0.01	-0.02	-0.006	-1.33	514.61	127.74	1778	29		5.7.4
RRCR2	ProfileC7	128.62	0.01	0.00	-0.004	-0.93	498.57	129.82	1797	30		5.7.4
RRCR2	ProfileC8	124.97	0.01	0.01	-0.004	-0.96	498.56	126.17	1765	27		5.7.4
RRCR2	ProfileC9	125.32	0.01	-0.04	-0.011	-2.67	497.12	128.66	1787	26		5.7.4
RRCR2	ProfileC10	127.92	0.01	0.04	-0.003	-0.67	541.32	128.78	1788	25		5.7.4
RRCR2	ProfileC11	130.89	0.02	0.02	-0.005	-1.04	540.36	132.24	1818	20		5.7.4
RRCR2	ProfileD1	119.88	0.01	-0.02	-0.001	-0.21	784.84	120.14	1710	21		5.7.4
RRCR2	ProfileD2	124.26	0.01	-0.02	-0.001	-0.33	814.49	124.67	1751	20		5.7.4
RRCR2	ProfileD3	123.45	0.01	-0.01	-0.001	-0.19	868.92	123.68	1742	18		5.7.4
RRCR2	ProfileD4	125.03	0.01	-0.01	-0.002	-0.45	822.26	125.60	1759	18		5.7.4
RRCR2	ProfileD5	123.80	0.01	-0.02	-0.004	-1.06	858.72	125.12	1755	17		5.7.4
RRCR2	ProfileD6	125.79	0.01	-0.02	0.000	0.06	857.75	125.71	1760	20		5.7.4
RRCR2	ProfileD7	127.68	0.01	-0.01	-0.003	-0.77	746.93	128.66	1787	22		5.7.4
RRCR2	ProfileD8	122.76	0.01	0.03	-0.002	-0.44	865.99	123.30	1739	15		5.7.4
RRCR2	ProfileD9	121.99	0.01	0.00	0.001	0.29	927.24	121.63	1724	16		5.7.4
RRCR3	ProfileA1	111.04	0.01	0.00	-0.002	-0.626	267.65	111.73	1634	33	*	5.7.5
RRCR3	ProfileA2	120.66	0.01	-0.01	-0.002	-0.593	260.36	121.37	1724	34	*	5.7.5
RRCR3	ProfileA3	122.81	0.02	-0.01	-0.010	-2.408	242.87	125.76	1764	29		5.7.5
RRCR3	ProfileA4	122.66	0.01	-0.01	-0.001	-0.134	324.52	122.82	1737	26		5.7.5
RRCR3	ProfileA5	126.52	0.01	-0.01	-0.001	-0.131	322.09	126.68	1772	24		5.7.5
RRCR3	ProfileA6	128.63	0.01	-0.01	-0.002	-0.431	335.70	129.19	1794	28		5.7.5

Appendix 5.2 continued

Sample	Run	$^{40}Ar/^{39}Ar$	$^{38}Ar/^{39}Ar$	$^{37}Ar/^{39}Ar$	$^{36}Ar/^{39}Ar$	% Atmos-pheric	^{39}Ar (cc) $\times10^{-13}$	$^{40}Ar^*/^{39}Ar$	Age (Ma)	± 1 σ	Excluded from mean	Profile Diagram
RRCR3	ProfileA7	126.42	0.01	-0.02	-0.008	-1.771	320.63	128.66	1790	26		5.7.5
RRCR3	ProfileA8	126.12	0.01	0.00	0.007	1.627	362.92	124.07	1749	25		5.7.5
RRCR3	ProfileA9	128.47	0.02	-0.01	-0.006	-1.385	328.89	130.25	1804	27		5.7.5
RRCR3	ProfileA10	126.60	0.01	-0.01	-0.002	-0.428	343.47	127.14	1776	26		5.7.5
RRCR3	ProfileA11	125.42	0.01	-0.02	-0.005	-1.103	326.95	126.80	1773	27		5.7.5
RRCR3	ProfileA12	125.68	0.01	0.00	-0.002	-0.459	322.57	126.25	1768	31		5.7.5
RRCR3	ProfileA13	128.06	0.01	0.00	-0.001	-0.124	335.70	128.22	1786	27		5.7.5
RRCR3	ProfileA14	126.41	0.01	0.00	-0.003	-0.802	314.80	127.42	1779	23		5.7.5
RRCR3	ProfileA15	128.37	0.01	-0.02	0.001	0.179	347.36	128.14	1785	31		5.7.5
RRCR3	ProfileA16	124.58	0.01	0.00	-0.003	-0.743	344.93	125.51	1762	25		5.7.5
RRCR3	ProfileA17	123.74	0.01	-0.01	0.001	0.178	361.46	123.51	1744	28		5.7.5
RRCR3	ProfileA18	128.53	0.01	-0.01	-0.003	-0.735	337.64	129.47	1797	25		5.7.5
RRCR3	ProfileA19	128.34	0.01	-0.02	0.001	0.190	327.92	128.09	1785	25		5.7.5
RRCR3	ProfileA20	127.83	0.01	-0.01	-0.005	-1.066	331.81	129.20	1794	24		5.7.5
RRCR3	ProfileA21	127.49	0.01	-0.02	-0.002	-0.422	346.39	128.02	1784	22		5.7.5
RRCR3	ProfileA22	122.22	0.01	0.00	-0.006	-1.359	352.22	123.88	1747	26		5.7.5
RRCR3	ProfileA23	126.07	0.01	-0.01	-0.004	-0.970	369.72	127.29	1778	23		5.7.5
RRCR3	ProfileA24	125.64	0.01	-0.01	-0.003	-0.696	364.86	126.51	1771	23		5.7.5
RRCR3	ProfileA25	126.10	0.01	-0.01	-0.006	-1.511	307.02	128.00	1784	28		5.7.5
RRCR3	ProfileA26	125.45	0.01	-0.01	0.006	1.455	335.21	123.63	1745	25		5.7.5
RRCR3	ProfileA27	127.82	0.01	-0.01	-0.002	-0.435	334.73	128.38	1787	22		5.7.5
RRCR3	ProfileA28	122.26	0.01	0.00	-0.008	-1.936	359.51	124.62	1754	24		5.7.5
RRCR3	ProfileA29	123.09	0.01	0.00	0.000	-0.119	364.37	123.24	1741	22		5.7.5
RRCR3	ProfileA30	127.27	0.01	0.00	-0.002	-0.411	355.62	127.79	1782	26		5.7.5
RRCR3	ProfileA31	128.45	0.01	0.00	0.002	0.437	378.95	127.88	1783	25		5.7.5
RRCR3	ProfileA32	124.83	0.01	-0.01	-0.002	-0.385	387.22	125.31	1760	21		5.7.5
RRCR3	ProfileA33	127.43	0.01	-0.01	-0.005	-1.218	377.01	128.98	1793	23		5.7.5
RRCR3	ProfileA34	124.44	0.01	-0.01	0.000	-0.110	390.13	124.58	1753	25		5.7.5
RRCR3	ProfileA35	123.70	0.01	-0.01	0.000	-0.111	386.73	123.84	1747	27		5.7.5
RRCR3	ProfileA36	128.24	0.01	-0.01	-0.004	-0.955	369.23	129.47	1797	22		5.7.5
RRCR3	ProfileA37	122.71	0.01	-0.01	-0.005	-1.140	418.32	124.11	1749	26		5.7.5
RRCR3	ProfileB1	113.04	0.02	0.00	0.002	0.642	513.05	112.31	1639	21	*	5.7.5

Appendix 5.2 continued

Sample	Run	$^{40}Ar/^{39}Ar$	$^{38}Ar/^{39}Ar$	$^{37}Ar/^{39}Ar$	$^{36}Ar/^{39}Ar$	% Atmos-pheric	^{39}Ar (cc) $\times10^{-13}$	$^{40}Ar^*/^{39}Ar$	Age (Ma)	± 1 σ	Excluded from mean	Profile Diagram
RRCR3	ProfileB2	123.26	0.02	-0.01	-0.001	-0.251	516.45	123.56	1744	23	*	5.7.5
RRCR3	ProfileB3	123.59	0.01	0.00	-0.002	-0.440	537.84	124.13	1749	18		5.7.5
RRCR3	ProfileB4	124.89	0.01	0.00	-0.001	-0.230	555.82	125.17	1759	18		5.7.5
RRCR3	ProfileB5	130.63	0.01	-0.01	-0.005	-1.041	508.67	131.99	1819	27		5.7.5
RRCR3	ProfileB6	124.77	0.01	0.00	-0.004	-0.965	574.29	125.97	1766	16		5.7.5
RRCR3	ProfileC1	116.86	0.01	-0.03	-0.004	-1.052	237.96	118.09	1694	47	*	5.7.5
RRCR3	ProfileC2	125.14	0.01	-0.01	0.003	0.815	234.75	124.12	1749	42	*	5.7.5
RRCR3	ProfileC3	132.71	0.01	0.00	0.023	5.050	313.49	126.01	1766	38		5.7.5
RRCR3	ProfileD1	114.42	0.01	0.00	-0.006	-1.517	551.64	116.15	1676	24	*	5.7.5
RRCR3	ProfileD2	122.91	0.01	0.01	0.002	0.372	522.96	122.46	1734	23	*	5.7.5
RRCR3	ProfileD3	120.57	0.01	0.01	0.001	0.133	661.48	120.41	1715	17		5.7.5
RRCR3	ProfileD4	123.28	0.02	0.00	-0.003	-0.785	714.46	124.25	1750	13		5.7.5
RRCR3	ProfileD5	129.39	0.01	-0.01	0.000	-0.032	644.96	129.44	1797	37		5.7.5
RRCR3	ProfileD6	123.35	0.01	0.00	0.000	-0.033	655.16	123.39	1743	21		5.7.5
RRCR3	ProfileD7	126.59	0.01	-0.01	0.002	0.476	618.22	125.99	1766	27		5.7.5
RRCR3	ProfileE1	124.41	0.01	-0.01	-0.001	-0.285	268.08	124.77	1755	32	*	5.7.5
RRCR3	ProfileE2	120.37	0.01	0.00	-0.003	-0.670	282.66	121.18	1722	31	*	5.7.5
RRCR3	ProfileE3	123.34	0.01	0.00	-0.007	-1.792	283.63	125.55	1762	28		5.7.5
RRCR3	ProfileE4	123.67	0.01	0.00	0.005	1.133	311.82	122.27	1732	25		5.7.5
RRCR3	ProfileE5	124.19	0.01	-0.01	-0.005	-1.292	307.93	125.80	1764	26		5.7.5
RRCR3	ProfileE6	128.57	0.01	0.00	0.000	0.096	308.42	128.45	1788	28		5.7.5
RRCR3	ProfileE7	127.74	0.01	0.00	-0.003	-0.597	298.70	128.51	1788	26		5.7.5
RRCR3	ProfileE8	125.10	0.01	0.00	0.005	1.120	311.82	123.70	1745	31		5.7.5
RRCR3	ProfileE9	125.25	0.01	0.01	-0.004	-0.951	303.07	126.44	1770	29		5.7.5
RRCR3	ProfileE10	123.50	0.01	0.01	-0.003	-0.603	305.99	124.24	1750	30		5.7.5
RRCR3	ProfileE11	121.32	0.01	-0.01	-0.002	-0.599	313.76	122.04	1730	28		5.7.5
RRCR3	ProfileE12	123.89	0.01	0.00	-0.001	-0.248	309.39	124.19	1750	27		5.7.5
RRCR3	ProfileF1	128.39	0.01	0.00	0.005	1.059	567.00	127.03	1775	32		
RRCR3	ProfileF2	125.03	0.01	0.00	-0.002	-0.569	598.10	125.74	1764	17		
RRCR3	ProfileG1	123.42	0.01	-0.01	-0.008	-1.979	500.90	125.86	1765	18		
RRCR3	ProfileH1	125.70	0.01	0.00	0.001	0.145	582.26	125.52	1762	26	*	
RRCR5	50 µm square	107.89	0.01	0.00	0.005	1.33	510.25	106.46	1583	19	*	

Appendix 5.2 continued

Sample	Run	$^{40}Ar/^{39}Ar$	$^{38}Ar/^{39}Ar$	$^{37}Ar/^{39}Ar$	$^{36}Ar/^{39}Ar$	% Atmos-pheric	^{39}Ar (cc) $\times10^{-13}$	$^{40}Ar^*/^{39}Ar$	Age (Ma)	± 1 σ	Excluded from mean	Profile Diagram
RRCR5	50 µm square	124.91	0.02	-0.01	-0.005	-1.11	525.31	126.31	1770	19		
RRCR5	ProfileA1	103.88	0.01	0.01	0.002	0.47	366.54	103.40	1553	36	*	5.7.6
RRCR5	ProfileA2	107.35	0.01	0.00	-0.008	-2.16	382.58	107.58	1594	33	*	5.7.6
RRCR5	ProfileA3	103.09	0.01	0.00	-0.004	-1.21	391.33	104.34	1562	19	*	5.7.6
RRCR5	ProfileA4	106.06	0.02	0.00	-0.004	-1.15	400.57	107.28	1591	21	*	5.7.6
RRCR5	ProfileA5	110.79	0.01	-0.01	0.001	0.38	416.60	110.36	1622	31	*	5.7.6
RRCR5	ProfileA6	110.75	0.01	-0.01	-0.002	-0.48	414.17	111.28	1631	16	*	5.7.6
RRCR5	ProfileA7	112.94	0.01	-0.01	-0.003	-0.81	386.96	113.85	1655	27	*	5.7.6
RRCR5	ProfileA8	112.05	0.01	0.00	-0.003	-0.84	378.69	112.98	1647	21	*	5.7.6
RRCR5	ProfileA9	113.43	0.01	0.00	-0.002	-0.53	368.97	114.03	1657	26	*	5.7.6
RRCR5	ProfileA10	111.60	0.01	-0.01	-0.002	-0.53	373.35	112.19	1639	20	*	5.7.6
RRCR5	ProfileB1	115.80	0.01	0.01	-0.008	-2.02	141.84	118.14	1696	45	*	5.7.6
RRCR5	ProfileB2	121.11	0.01	0.00	-0.003	-0.73	374.64	121.99	1731	27	*	5.7.6
RRCR5	ProfileB3	124.18	0.01	-0.01	-0.007	-1.67	417.90	126.25	1769	25		5.7.6
RRCR5	ProfileB4	124.70	0.01	-0.01	0.003	0.59	448.52	123.96	1749	19		5.7.6
RRCR5	ProfileB5	120.69	0.01	-0.01	0.001	0.13	438.80	120.54	1718	13		5.7.6
RRCR5	ProfileB6	126.21	0.01	-0.01	0.002	0.42	373.19	125.68	1764	28		5.7.6
RRCR5	ProfileB7	119.44	0.01	0.00	-0.007	-1.80	463.10	121.60	1727	15		5.7.6
RRCR5	ProfileB8	119.24	0.01	0.01	-0.002	-0.60	462.13	119.95	1712	25		5.7.6
RRCR5	ProfileC1	124.95	0.02	-0.02	0.000	0.00	302.23	124.95	1758	25	*	5.7.6
RRCR5	ProfileC2	123.78	0.01	-0.01	0.003	0.75	431.02	122.86	1739	21	*	5.7.6
RRCR5	ProfileC3	121.22	0.01	0.01	0.001	0.22	499.07	120.95	1721	23		5.7.6
RRCR5	ProfileC4	122.65	0.01	0.01	-0.003	-0.66	495.18	123.46	1744	25		5.7.6
RRCR5	ProfileD1	129.22	0.00	-0.02	0.005	1.04	99.07	127.88	1784	87	*	5.7.6
RRCR5	ProfileD2	117.68	0.01	0.01	0.000	0.00	412.55	117.68	1691	23	*	5.7.6
RRCR5	ProfileD3	126.02	0.01	0.00	-0.002	-0.41	513.16	126.54	1772	20		5.7.6
RRCR5	ProfileD4	126.90	0.01	0.00	0.000	0.00	509.76	126.90	1775	21		5.7.6
RRCR5	ProfileD5	122.39	0.01	0.00	-0.002	-0.39	556.90	122.86	1739	16		5.7.6
RRCR5	ProfileD6	125.53	0.01	-0.01	-0.001	-0.20	522.88	125.78	1765	19		5.7.6
RRCR5	ProfileD7	126.09	0.01	0.00	0.000	0.00	544.27	126.09	1768	17		5.7.6
RRCR5	ProfileE1	117.88	0.01	0.00	0.005	1.32	377.35	116.33	1679	32	*	5.7.6
RRCR5	ProfileE2	125.11	0.02	0.00	0.004	0.91	396.31	123.97	1749	36	*	5.7.6

Appendix 5.2 continued

Sample	Run	$^{40}Ar/^{39}Ar$	$^{38}Ar/^{39}Ar$	$^{37}Ar/^{39}Ar$	$^{36}Ar/^{39}Ar$	% Atmos-pheric	^{39}Ar (cc) $\times10^{-13}$	$^{40}Ar^*/^{39}Ar$	Age (Ma)	± 1 σ	Excluded from mean	Profile Diagram
RRCR5	ProfileE3	119.27	0.01	0.00	0.007	1.74	410.89	117.20	1687	26		5.7.6
RRCR5	ProfileE4	121.54	0.01	0.00	0.004	1.07	450.25	120.24	1715	25		5.7.6
RRCR5	ProfileE5	122.41	0.01	0.01	0.003	0.83	443.45	121.39	1725	25		5.7.6
RRCR5	ProfileE6	122.63	0.01	0.01	-0.002	-0.39	442.48	123.11	1741	29		5.7.6
RRCR5	ProfileE7	123.28	0.02	0.01	0.005	1.31	443.94	121.66	1728	24		5.7.6
RRCR5	ProfileE8	121.76	0.01	0.01	-0.001	-0.15	449.28	121.94	1731	19		5.7.6
RRSW1	50 µm square	114.66	0.02	0.01	0.005	1.33	494.69	113.14	1646	26	*	
RRSW1	50 µm square	118.71	0.01	0.00	0.001	0.17	450.95	118.52	1697	28	*	
RRSW1	50 µm square	130.10	0.02	0.01	0.023	5.32	322.82	123.18	1740	48		
RRSW1	50 µm square	125.49	0.02	0.00	0.004	0.98	409.82	124.26	1749	39		
RRSW1	50 µm square	123.37	0.01	0.01	-0.006	-1.38	406.90	125.07	1757	38		
RRSW1	50 µm square	126.83	0.01	0.00	-0.003	-0.60	386.00	127.59	1779	40		
RRSW1	50 µm square	126.78	0.01	0.01	-0.006	-1.30	500.22	128.43	1787	40		
RRSW1	50 µm square	130.29	0.01	-0.01	-0.001	-0.28	430.72	130.66	1806	39		
RRSW1	ProfileA1	102.32	0.02	0.01	0.013	3.77	160.79	98.46	1500	53	*	5.7.7
RRSW1	ProfileA2	112.08	0.02	0.03	0.020	5.29	216.69	106.15	1578	42	*	5.7.7
RRSW1	ProfileA3	110.33	0.01	0.02	0.019	5.00	257.03	104.81	1565	39	*	5.7.7
RRSW1	ProfileA4	111.94	0.01	0.01	-0.002	-0.61	259.94	112.62	1641	34	*	5.7.7
RRSW1	ProfileA5	111.93	0.00	0.02	0.006	1.54	282.79	110.21	1618	35	*	5.7.7
RRSW1	ProfileA6	113.21	0.01	0.00	0.016	4.07	307.57	108.60	1602	26	*	5.7.7
RRSW1	ProfileA7	112.61	0.02	-0.01	0.015	3.90	323.13	108.22	1599	29	*	5.7.7
RRSW2	50 µm square	99.24	0.03	-0.03	0.048	14.391	88.46	84.96	1359	100	*	
RRSW2	50 µm square	115.11	0.03	0.53	0.033	8.489	6.80	105.34	1574	794	*	
RRSW2	50 µm square	121.58	0.01	0.00	0.013	3.242	286.75	117.63	1693	35		
RRSW2	50 µm square	123.03	0.01	0.00	0.001	0.346	468.04	122.60	1739	23		
RRSW2	50 µm square	125.73	0.01	-0.01	-0.002	-0.462	343.62	126.31	1772	26		
RRSW2	ProfileA1	122.03	0.01	0.01	0.005	1.143	214.46	120.63	1721	46		5.7.8
RRSW2	ProfileA2	122.14	0.02	0.01	0.016	3.920	201.34	117.35	1690	62	*	5.7.8
RRSW2	ProfileA3	112.32	0.01	0.00	0.009	2.457	156.62	109.56	1616	63	*	5.7.8
RRSW2	ProfileA4	100.56	0.02	0.02	0.027	8.008	152.73	92.51	1442	77	*	5.7.8
RRSW2	ProfileA5	98.21	0.02	0.02	0.004	1.064	159.05	97.17	1491	64	*	5.7.8
RRSW2	ProfileA6	92.09	0.02	-0.01	0.013	4.109	149.33	88.31	1396	77	*	5.7.8
RRSW2	ProfileB1	126.83	0.02	0.01	0.019	4.396	178.86	121.26	1726	35		5.7.8

Appendix 5.2 continued

Sample	Run	$^{40}Ar/^{39}Ar$	$^{38}Ar/^{39}Ar$	$^{37}Ar/^{39}Ar$	$^{36}Ar/^{39}Ar$	% Atmos-pheric	^{39}Ar (cc) $\times10^{-13}$	$^{40}Ar^*/^{39}Ar$	Age (Ma)	± 1 σ	Excluded from mean	Profile Diagram
RRSW2	ProfileB2	123.69	0.01	-0.01	-0.003	-0.620	260.02	124.46	1755	34		5.7.8
RRSW2	ProfileB3	124.62	0.01	0.00	0.006	1.475	253.22	122.78	1740	33		5.7.8
RRSW2	ProfileB4	125.74	0.01	0.00	0.008	1.844	258.08	123.42	1746	32		5.7.8
RRSW2	ProfileB5	121.55	0.02	0.01	0.008	1.963	250.79	119.17	1707	36		5.7.8
RRSW3	ProfileA1	125.80	0.01	-0.01	-0.004	-0.96	238.13	127.01	1773	36		5.7.9
RRSW3	ProfileA2	126.76	0.01	0.00	-0.004	-0.89	371.78	127.90	1781	26		5.7.9
RRSW3	ProfileA3	126.37	0.01	-0.01	0.002	0.47	411.83	125.78	1762	22		5.7.9
RRSW3	ProfileA4	129.15	0.02	0.00	-0.004	-0.94	456.38	130.36	1803	27		5.7.9
RRSW3	ProfileA5	125.53	0.01	0.00	0.004	0.86	471.68	124.45	1750	19		5.7.9
RRSW3	ProfileA6	128.23	0.01	0.00	-0.002	-0.46	493.73	128.81	1789	24		5.7.9
RRSW3	ProfileB1	120.85	0.02	-0.01	-0.009	-2.19	209.33	123.49	1741	40		5.7.9
RRSW3	ProfileB2	123.47	0.02	0.00	-0.005	-1.12	208.43	124.85	1754	57		5.7.9
RRSW3	ProfileB3	126.14	0.01	0.02	-0.013	-2.97	218.78	129.89	1798	51		5.7.9
RRSW3	ProfileB4	128.51	0.01	0.00	-0.002	-0.50	243.08	129.15	1792	40		5.7.9
RRSW3	ProfileB5	124.94	0.02	-0.02	0.004	0.83	235.43	123.91	1745	37		5.7.9
RRSW3	ProfileB6	124.62	0.02	0.00	-0.005	-1.26	268.73	126.19	1766	34		5.7.9
RRSW3	ProfileC1	130.33	0.01	0.02	0.008	1.86	543.38	127.91	1781	32		5.7.9
RRSW3	ProfileC2	130.18	0.01	0.03	0.003	0.75	527.82	129.20	1792	25		5.7.9
RRSW3	ProfileC3	128.14	0.01	0.02	0.005	1.11	550.67	126.72	1770	27		5.7.9
RRSW3	ProfileC4	130.17	0.02	0.03	0.011	2.53	439.37	126.87	1772	34		5.7.9
RRSW3	ProfileC5	124.78	0.01	0.01	0.001	0.17	558.93	124.57	1751	29		5.7.9
RRSW3	ProfileD1	118.69	0.02	0.00	0.014	3.54	249.33	114.48	1658	48		5.7.9
RRSW3	ProfileD2	125.53	0.01	0.00	0.003	0.63	315.43	124.73	1753	41		5.7.9
RRSW3	ProfileD3	126.37	0.01	-0.03	0.008	1.89	271.69	123.98	1746	52		5.7.9
RRSW3	ProfileD4	124.90	0.01	-0.01	0.006	1.33	311.54	123.24	1739	41		5.7.9
RRSW3	ProfileD5	125.80	0.01	-0.01	-0.006	-1.37	394.65	127.52	1778	33		5.7.9
RRSW3	ProfileD6	132.29	0.01	0.01	0.013	2.86	347.51	128.50	1786	37		5.7.9
RRSW3	ProfileD7	128.50	0.01	0.00	0.002	0.56	351.88	127.79	1780	36		5.7.9
RRSW3	ProfileD8	133.17	0.01	0.00	-0.008	-1.75	348.48	135.51	1847	35		5.7.9
RRSW3	ProfileD9	130.53	0.01	-0.02	-0.003	-0.63	343.62	131.35	1811	38		5.7.9
RRSW3	ProfileE1	126.29	0.01	-0.04	-0.009	-2.05	364.52	128.88	1790	33		
RRSW3	ProfileF1	120.47	0.00	-0.12	-0.029	-7.02	111.79	128.92	1790	97		

Appendix 5.2 continued

Sample	Run	$^{40}Ar/^{39}Ar$	$^{38}Ar/^{39}Ar$	$^{37}Ar/^{39}Ar$	$^{36}Ar/^{39}Ar$	% Atmos-pheric	^{39}Ar (cc) $\times10^{-13}$	$^{40}Ar^*/^{39}Ar$	Age (Ma)	± 1 σ	Excluded from mean	Profile Diagram
RRSW3	ProfileF2	130.72	0.01	-0.09	-0.019	-4.25	170.11	136.28	1854	65		
RRSW3	ProfileG1	123.94	0.01	-0.05	-0.014	-3.28	298.42	128.00	1782	44		
RRSW4	ProfileA1	126.32	0.00	-0.02	0.001	0.16	334.95	126.13	1769	36		5.7.10
RRSW4	ProfileA2	126.96	0.01	0.00	0.002	0.41	385.01	126.45	1772	18		5.7.10
RRSW4	ProfileA3	127.36	0.01	0.00	-0.008	-1.77	384.04	129.61	1800	27		5.7.10
RRSW4	ProfileA4	120.77	0.01	-0.01	0.006	1.39	435.07	119.08	1705	25		5.7.10
RRSW4	ProfileA5	127.09	0.01	-0.02	0.005	1.15	410.29	125.63	1765	30		5.7.10
RRSW4	ProfileB1	130.38	-0.03	-0.03	-0.022	-4.99	51.11	136.89	1863	116	*	5.7.10
RRSW4	ProfileB2	119.29	0.02	-0.02	0.012	3.06	163.87	115.64	1673	42		5.7.10
RRSW4	ProfileB3	120.59	0.01	0.01	-0.001	-0.26	215.39	120.90	1722	32		5.7.10
RRSW4	ProfileB4	121.08	0.01	0.00	0.015	3.61	258.65	116.71	1683	28		5.7.10
RRSW4	ProfileB5	121.22	0.01	0.00	-0.004	-0.97	283.43	122.39	1736	26		5.7.10
TRER4	50 µm square	135.52	0.01	0.01	0.011	2.46	370.07	132.18	1700	15		
TRER4	50 µm square	135.93	0.01	0.01	0.001	0.30	418.68	135.52	1728	14		
TRER4	50 µm square	137.98	0.02	0.00	0.004	0.80	394.37	136.87	1739	15		
TRER4	50 µm square	138.90	0.02	0.02	0.000	0.07	372.50	138.80	1755	14		
TRER4	ProfileA1	127.31	0.03	0.08	0.024	5.64	97.90	120.13	1597	53	*	5.7.11
TRER4	ProfileA2	135.28	0.02	0.05	0.021	4.68	174.21	128.96	1673	29		5.7.11
TRER4	ProfileA3	137.51	0.01	0.01	0.003	0.62	199.48	136.65	1737	26		5.7.11
TRER4	ProfileA4	138.50	0.01	0.02	0.013	2.84	246.14	134.57	1720	21		5.7.11
TRER4	ProfileB1	153.54	0.03	0.10	0.019	3.66	54.16	147.93	1827	85	*	5.7.11
TRER4	ProfileB2	133.34	0.01	0.03	-0.005	-1.14	149.42	134.86	1723	33		5.7.11
TRER4	ProfileB3	141.41	0.01	0.06	0.008	1.58	195.10	139.17	1758	26		5.7.11
TRER4	ProfileB4	135.25	0.02	0.01	0.007	1.50	215.03	133.22	1709	24		5.7.11
TRER7	50 µm square	130.83	0.01	0.01	0.004	0.86	576.81	129.71	1680	10		
TRER7	50 µm square	133.49	0.01	0.02	-0.002	-0.34	620.07	133.95	1715	9		
TRER7	ProfileA1	127.96	0.01	0.00	-0.009	-2.03	263.33	130.55	1687	18	*	5.7.12
TRER7	ProfileA2	137.66	0.01	0.03	-0.007	-1.45	341.58	139.66	1762	13		5.7.12
TRER7	ProfileA3	136.61	0.00	0.00	-0.001	-0.28	398.93	136.98	1740	12		5.7.12
TRER7	ProfileA4	136.20	0.01	-0.04	-0.006	-1.25	323.60	137.90	1747	15		5.7.12
TRER7	ProfileB1	194.68	0.00	-0.86	0.461	69.93	6.71	58.54	951	940	*	5.7.12

Appendix 5.2 continued

Sample	Run	$^{40}Ar/^{39}Ar$	$^{38}Ar/^{39}Ar$	$^{37}Ar/^{39}Ar$	$^{36}Ar/^{39}Ar$	% Atmos-pheric	^{39}Ar (cc) $\times10^{-13}$	$^{40}Ar^*/^{39}Ar$	Age (Ma)	± 1 σ	Excluded from mean	Profile Diagram
TRER7	ProfileB2	136.62	-0.05	-0.09	0.021	4.59	18.37	130.35	1685	226	*	5.7.12
TRER7	ProfileB3	131.33	0.01	0.04	-0.028	-6.36	113.63	139.68	1762	37		5.7.12
TRER7	ProfileB4	137.72	0.02	0.00	-0.004	-0.75	145.22	138.76	1754	29		5.7.12
TRER7	ProfileC1	126.06	0.03	-0.04	-0.009	-2.22	148.63	128.86	1672	32		5.7.12
TRER7	ProfileC2	131.62	0.01	0.00	-0.005	-1.06	298.81	133.01	1707	16		5.7.12
TRER7	ProfileC3	127.76	0.01	-0.03	-0.007	-1.62	328.94	129.84	1681	16		5.7.12
TRER7	ProfileD1	136.54	0.01	0.00	0.001	0.24	355.19	136.22	1734	15		5.7.12
TRER7	ProfileD2	129.62	0.01	0.02	0.012	2.67	302.21	126.16	1649	18		5.7.12
TRER7	ProfileD3	129.95	0.02	0.02	0.004	0.95	309.50	128.72	1671	18		5.7.12
TRER7	ProfileD4	127.03	0.01	0.00	-0.015	-3.54	299.29	131.54	1695	18		5.7.12
TRER7	ProfileE1	151.96	0.00	0.02	0.003	0.51	149.11	151.19	1852	29		
TRER7	ProfileE2	131.52	0.01	0.01	0.005	1.15	338.66	130.01	1682	15	*	
TRGC5	50 µm square	116.89	0.01	0.00	-0.004	-0.95	264.45	118.00	1578	15		
TRGC5	50 µm square	129.99	0.01	0.00	-0.005	-1.13	289.72	131.46	1694	17		
TRGC5	50 µm square	134.28	0.01	-0.01	0.000	-0.05	434.56	134.34	1718	12		
TRGC5	50 µm square	136.93	0.00	-0.03	0.007	1.44	187.66	134.96	1723	21		
TRGC5	50 µm square	139.27	0.01	0.02	0.003	0.62	432.61	138.41	1751	10		
TRGC5	ProfileA1	83.10	0.02	-0.01	-0.013	-4.56	147.80	86.89	1277	30	*	5.7.13
TRGC5	ProfileA2	88.75	0.01	0.00	-0.012	-3.96	159.47	92.26	1333	25	*	5.7.13
TRGC5	ProfileA3	79.40	0.02	0.03	-0.003	-0.98	206.61	80.18	1205	26	*	5.7.13
TRGC5	ProfileA4	113.17	0.00	-0.02	-0.019	-5.00	145.86	118.83	1586	27		5.7.13
TRGC5	ProfileA5	113.70	0.01	0.01	-0.003	-0.83	171.13	114.64	1548	26		5.7.13
TRGC5	ProfileA6	124.83	0.03	-0.01	-0.001	-0.19	119.13	125.06	1640	30		5.7.13
TRGC5	ProfileB1	103.52	0.02	0.08	-0.016	-4.53	90.94	108.22	1489	44	*	5.7.13
TRGC5	ProfileB2	112.36	0.01	0.03	0.004	1.16	283.40	111.05	1515	16	*	5.7.13
TRGC5	ProfileB3	121.41	0.02	0.02	-0.006	-1.45	392.27	123.17	1624	13		5.7.13
TRGC5	ProfileB4	138.26	0.01	0.02	-0.003	-0.65	326.17	139.16	1758	13		5.7.13
TRGC5	ProfileB5	133.69	0.01	0.02	0.009	2.02	383.53	130.99	1690	11		5.7.13
TRGC5	ProfileB6	134.23	0.02	0.02	-0.004	-0.84	259.59	135.36	1727	26		5.7.13
TRGC5	ProfileB7	135.16	0.02	0.02	0.008	1.68	398.59	132.89	1706	11	-	5.7.13
TRGC5	ProfileC1	173.32	0.05	-0.02	-0.001	-0.18	88.51	173.64	2016	34	*	
TRGC5	ProfileC2	122.73	0.05	-0.04	-0.002	-0.54	42.34	123.39	1626	83	*	
TRGC5	ProfileC3	11.55	-0.09	1.60	0.030	77.60	11.72	2.59	54	712	*	

Appendix 5.2 continued

Sample	Run	$^{40}Ar/^{39}Ar$	$^{38}Ar/^{39}Ar$	$^{37}Ar/^{39}Ar$	$^{36}Ar/^{39}Ar$	% Atmos-pheric	^{39}Ar (cc) $\times 10^{-13}$	$^{40}Ar^*/^{39}Ar$	Age (Ma)	± 1 σ	Excluded from mean	Profile Diagram
TRMC3	50 µm square	138.51	0.01	0.07	0.011	2.27	539.10	135.37	1727	14		
TRMC3	ProfileA1	120.00	0.01	0.06	0.004	1.08	384.55	118.70	1584	19	*	5.7.14
TRMC3	ProfileA2	142.96	0.02	0.07	0.006	1.27	347.12	141.15	1774	20		5.7.14
TRMC3	ProfileA3	142.16	0.01	0.07	0.010	1.99	410.79	139.33	1759	17		5.7.14
TRMC3	ProfileA4	147.83	0.00	0.08	0.005	1.02	330.60	146.33	1814	22		5.7.14
TRMC3	ProfileA5	137.90	0.01	0.13	0.001	0.20	361.22	137.63	1745	20		5.7.14
TRMC3	ProfileA6	148.52	0.01	0.07	0.008	1.62	372.88	146.12	1813	18		5.7.14
TRMC3	ProfileA7	134.81	0.01	0.11	-0.004	-0.97	331.57	136.12	1733	21		5.7.14
TRMC3	ProfileB1	190.90	0.03	0.32	-0.006	-0.96	91.48	192.74	2145	61	*	5.7.14
TRMC3	ProfileB2	141.17	0.01	0.13	-0.008	-1.64	245.06	143.49	1792	27		5.7.14
TRMC3	ProfileB3	131.79	0.00	0.07	-0.003	-0.72	176.53	132.74	1705	38		5.7.14
TRMC3	ProfileB4	122.39	0.01	0.08	0.012	2.91	251.86	118.83	1586	29		5.7.14
TRMC3	ProfileB5	131.55	0.01	0.09	-0.006	-1.30	253.81	133.26	1709	26		5.7.14
TRMC3	ProfileB6	126.88	0.01	0.06	0.003	0.59	310.19	126.14	1649	22		5.7.14
TRMC3	ProfileB7	135.19	0.01	0.05	0.006	1.28	362.68	133.46	1711	20		5.7.14
TRMC3	ProfileB8	136.61	0.01	0.04	-0.005	-1.03	402.05	138.02	1748	17		5.7.14
TRMC3	ProfileB9	140.91	0.01	0.05	-0.007	-1.56	317.96	143.11	1789	21		5.7.14
TRMC3	ProfileB10	133.72	0.02	0.10	-0.001	-0.12	215.41	133.89	1714	31		5.7.14
TRMC3	ProfileB11	204.60	0.02	0.16	-0.020	-2.82	98.28	210.37	2256	49	*	5.7.14
TRMC3	ProfileC1	135.19	0.01	0.11	0.008	1.84	253.32	132.71	1705	29		
TRMC3	ProfileD1	144.08	0.02	0.02	0.007	1.42	567.78	142.04	1781	14		
TRMC3	ProfileD2	146.14	0.01	0.03	0.006	1.15	689.77	144.45	1800	11		
TRMC3	ProfileD3	443.99	0.03	0.38	0.014	0.91	123.07	439.96	3296	25	*	
TRMC3	ProfileE1	157.39	-0.01	0.22	-0.027	-5.06	104.60	165.35	1957	55	*	
TRMC3	ProfileF1	135.71	0.01	0.05	0.003	0.73	499.74	134.71	1721	15		
TRMC3	ProfileF2	138.85	0.01	0.02	0.004	0.85	643.11	137.67	1745	12		
TRMC3	ProfileG1	137.39	0.02	0.21	-0.001	-0.20	126.95	137.67	1745	53	*	
TRMC3	ProfileG2	139.29	0.01	0.12	0.000	-0.10	261.10	139.43	1760	26		
TRMR2	50 µm square	106.13	0.01	0.04	0.003	0.91	511.32	105.17	1460	13		
TRMR2	50 µm square	108.45	0.02	0.00	0.004	1.11	850.08	107.25	1480	10		
TRMR2	50 µm square	108.54	0.01	0.07	0.001	0.16	536.11	108.36	1490	13		
TRMR2	50 µm square	109.53	0.01	0.04	0.003	0.76	913.75	108.69	1493	10		

Appendix 5.2 continued

Sample	Run	$^{40}Ar/^{39}Ar$	$^{38}Ar/^{39}Ar$	$^{37}Ar/^{39}Ar$	$^{36}Ar/^{39}Ar$	% Atmos-pheric	^{39}Ar (cc) $\times10^{-13}$	$^{40}Ar^*/^{39}Ar$	Age (Ma)	± 1 σ	Excluded from mean	Profile Diagram
TRMR2	50 µm square	111.10	0.01	0.01	0.005	1.46	799.05	109.49	1501	10		
TRMR2	50 µm square	113.90	0.01	0.01	0.003	0.72	761.14	113.08	1534	9		
TRMR2	50 µm square	114.07	0.01	0.00	0.002	0.44	990.54	113.57	1538	8		
TRMR2	50 µm square	119.32	0.01	0.00	0.002	0.47	891.39	118.77	1585	9		
TRMR2	50 µm square	119.83	0.01	0.03	-0.001	-0.21	688.72	120.08	1597	11		
TRMR2	50 µm square	128.07	0.01	0.00	0.002	0.44	1124.20	127.51	1661	9		
TRMR2	50 µm square	127.99	0.01	0.03	0.000	0.08	937.56	127.89	1664	9		
TRMR2	50 µm square	129.18	0.01	0.01	-0.003	-0.57	766.97	129.93	1681	11		
TRMR2	50 µm square	133.14	0.01	0.00	0.000	-0.03	852.51	133.18	1709	9		
TRMR2	50 µm square	136.27	0.01	-0.01	0.002	0.44	599.77	135.67	1729	14		
TRMR2	ProfileA1	114.27	0.01	0.07	0.007	1.90	473.89	112.10	1525	14		5.7.15
TRMR2	ProfileA2	132.52	0.01	0.06	0.001	0.29	590.05	132.13	1700	11		5.7.15
TRMR2	ProfileA3	126.15	0.01	0.08	0.001	0.15	515.69	125.97	1648	12		5.7.15
TRMR2	ProfileA4	130.52	0.01	0.09	0.003	0.79	480.21	129.49	1678	13		5.7.15
TRMR2	ProfileA5	125.91	0.01	0.07	0.004	0.91	664.42	124.77	1637	10		5.7.15
TRMR2	ProfileA6	119.46	0.01	0.03	0.002	0.48	868.55	118.89	1586	9		5.7.15
TRMR2	ProfileA7	124.39	0.01	0.03	0.002	0.51	777.17	123.76	1629	9		5.7.15
TRMR2	ProfileA8	117.59	0.02	0.06	0.001	0.14	566.24	117.42	1573	12		5.7.15
TRMR2	ProfileB1	94.65	0.01	0.04	0.001	0.43	237.69	94.25	1353	28		5.7.15
TRMR2	ProfileB2	78.34	0.01	0.05	-0.004	-1.65	338.29	79.63	1199	21		5.7.15
TRMR2	ProfileB3	84.60	0.01	0.04	0.001	0.34	329.06	84.31	1250	21		5.7.15
TRMR2	ProfileB4	83.81	0.01	-0.01	0.003	1.15	376.69	82.85	1234	19		5.7.15
TRMR2	ProfileB5	58.12	0.01	0.05	0.002	1.18	139.99	57.43	937	56		5.7.15
TRMR2	ProfileB6	54.47	0.02	0.09	0.022	11.79	97.71	48.05	813	88		5.7.15
HLM2	50 µm square	79.87	0.01	0.03	-0.005	-1.71	270.50	81.24	1217	24	*	
HLM2	50 µm square	123.01	0.01	0.02	0.001	0.18	1986.17	122.79	1620	7		
HLM2	50 µm square	128.99	0.01	0.01	0.002	0.47	1358.71	128.38	1668	7		
HLM2	50 µm square	130.70	0.01	0.02	0.004	0.84	874.63	129.61	1679	9		
HLM2	50 µm square	142.40	0.01	0.00	0.002	0.47	1224.57	141.72	1778	7		
HLM2	50 µm square	143.58	0.01	0.00	0.000	0.08	1496.26	143.48	1792	8		
HLM2	50 µm square	143.80	0.01	0.01	0.001	0.23	1311.08	143.48	1792	8		
HLM2	50 µm square	146.25	0.01	0.01	0.007	1.33	1790.30	144.30	1799	8		

Appendix 5.2 continued

Sample	Run	$^{40}Ar/^{39}Ar$	$^{38}Ar/^{39}Ar$	$^{37}Ar/^{39}Ar$	$^{36}Ar/^{39}Ar$	% Atmos-pheric	^{39}Ar (cc) $\times 10^{-13}$	$^{40}Ar^{*}/^{39}Ar$	Age (Ma)	± 1 σ	Excluded from mean	Profile Diagram
HLM2	50 µm square	146.25	0.01	0.00	0.002	0.32	1200.75	145.78	1810	8		
HLM2	50 µm square	151.94	0.01	0.00	0.002	0.42	1078.27	151.29	1853	8		

Appendix 5.3: Data tables for quartz and garnet ^{40}Ar-^{39}Ar analyses from Ruby Range, Tobacco Root Mountains and Highland Mountains to monitor excess argon

Sample	Mineral	$^{39}Ar \times 10^{-7}$	$^{40}Ar^{*} \times 10^{-4}$	$^{40}Ar/^{39}Ar$	$^{38}Ar/^{39}Ar$	$^{37}Ar/^{39}Ar$	$^{36}Ar/^{39}Ar$	%Atmos-pheric	^{39}Ar (cc) $\times 10^{-15}$	$^{40}Ar^{*}/^{39}Ar$	Age (Ma)	± 1 σ	Excess
70-30-2	Quartz	42.43	66.82	630.95	-0.05	3.40	0.064	3.02	1720.18	611.90	3807	108	
70-30-2	Quartz	3822.63	2339.08	1574.88	-9.04	-25.32	-3.619	-67.91	19.09	2644.40	6271	5346	
RM37	Quartz	96.00	-7.14	-80.59	-0.57	-10.46	1.471	-539.19	91.80	-515.13		2614	
RM37	Quartz	204.01	-105.09	-74.42	-0.12	-20.08	-2.083	827.19	43.20	541.17	3614	3885	
RM39	Quartz	-173.58	299.35	-8499.01	3.42	26.30	2.037	-7.08	-78.11	-9100.93		1272	
RM39	Quartz	-173.58	1475.26	-1724.56	0.39	22.75	3.189	-54.65	-78.11	-2666.95		1391	
RM39	Quartz	42.43	172.96	4076.29	-11.53	-97.91	-13.046	-94.58	19.09	7931.51	8215	5113	
RM40	Quartz	798.47	130.13	-13197.87	1.03	-35.28	-3.758	8.41	-29.51	-12087.39		3351	
RM40	Quartz	-173.58	408.59	-6822.28	1.74	-3.48	-0.520	2.25	-126.71	-6668.61		792	
RM40	Quartz	-65.57	792.63	-3113.88	1.60	-2.68	-2.572	24.41	-78.11	-2353.89		1423	
RM40	Quartz	150.44	1465.75	217.17	-0.08	0.97	0.183	24.95	359.31	162.98	1940	1173	Excess
RM40	Quartz	-281.59	1877.79	945.88	-0.26	6.97	2.501	78.14	116.30	206.76	2234	3019	Excess
RM40	Quartz	258.44	53.44	10423.80	0.25	1.05	2.303	6.53	67.70	9743.31	8583	1441	
TRER4	Garnet	46.29	-28.75	199.65	2.60	51.17	2.78	411.12	20.83	-621.14	-3005	10101	
TRER4	Quartz	1126.34	147.25	46.27	1.46	0.05	-0.46	-295.68	69.43	183.06	2081	5696	
TRER4	Quartz	46.29	52.48	107.29	-0.02	0.87	0.05	14.07	2013.53	92.19	1332	297	
TRER4	Quartz	154.29	7.14	130.73	0.11	2.92	-0.15	-34.40	506.85	175.71	2031	802	
TRER4	Quartz	4474.52	412.51	3031.65	-1.27	8.70	-1.11	-10.83	69.43	3359.96	6692	1034	
TRER4	Quartz	154.29	467.76	3869.81	-6.50	-33.11	9.26	70.70	20.83	1133.84	4816	5100	
TRER7	Quartz	-237.61	22.22	-1218.38	0.44	-7.11	-5.836	141.54	-106.93	506.11	3510	1940	
TRER7	Quartz	-237.61	-120.26	-1100.54	0.00	-97.28	-13.271	356.33	-9.72	2821.02	6385	14612	
TRER7	Quartz	-21.60	-60.94	-93.53	-3.55	-0.20	0.898	-283.67	-106.93	-358.83		3520	
TRER7	Quartz	-345.62	-237.35	-71.35	-0.61	-4.00	-2.565	1062.57	-155.53	686.75	3991	1108	
TRGC5	Quartz	3251.54	244.33	-14074.84	1.43	1.45	2.287	-4.80	-43.49	-14750.78		2720	
TRGC5	Quartz	2819.51	103.00	36.53	0.06	2.21	-0.043	-34.73	1268.78	49.22	829	430	
TRGC5	Quartz	-96.64	1360.15	75.14	0.05	1.19	-0.037	-14.64	1463.19	86.14	1269	279	
TRMC3	Quartz	11147.32	7390.31	-772.69	0.69	-4.42	-1.42	54.15	-86.97	-354.25		6217	
TRMC3	Quartz	9095.21	1435.04	157.78	0.04	1.31	-0.01	-2.60	4092.84	161.88	1932	141	
TRMC3	Quartz	22.74	3069.18	295.34	0.03	1.53	-0.01	-1.36	4190.05	299.35	2732	91	Excess
TRMC3	Quartz	9311.22	2749.96	599.51	-0.05	1.21	-0.02	-1.06	4724.68	605.88	3792	57	Excess

Appendix 5.3 continued

Sample	Mineral	$^{39}Ar \times 10^{-7}$	$^{40}Ar^* \times 10^{-4}$	$^{40}Ar/^{39}Ar$	$^{38}Ar/^{39}Ar$	$^{37}Ar/^{39}Ar$	$^{36}Ar/^{39}Ar$	%Atmos -pheric	^{39}Ar (cc) $\times 10^{-15}$	$^{40}Ar^*/^{39}Ar$	Age (Ma)	± 1 σ	Excess
TRMC3	Quartz	-193.27	68.47	662.97	0.00	0.91	0.00	-0.11	5016.29	663.67	3937	61	
TRMC3	Quartz	10499.28	6294.41	135937.43	-10.48	1.43	3.24	0.70	10.23	134979.84	13311	11384	Excess
TRMR2	Garnet	11668.93	327.29	10.19	0.09	1.43	0.10	288.033	779.58	-19.15	-464	2176	
TRMR2	Garnet	1732.41	-33.18	42.53	0.01	0.31	0.05	34.056	5251.02	28.05	518	187	
TRMR2	Garnet	4.32	14.21	3290.34	62.42	788.04	-6.48	-58.206	1.94	5205.51	7466	46978	
TRMR2	Quartz	39426.37	3491.02	70.32	-0.01	0.73	0.00	-0.495	10694.50	70.67	1098	69	
TRMR2	Quartz	1408.39	10.09	93.58	0.02	0.21	0.02	5.382	17741.87	88.55	1294	39	
TRMR2	Quartz	112.33	574.67	97.66	-0.01	1.45	-0.03	-8.441	6903.50	105.91	1467	87	
TRMR2	Quartz	15341.12	1498.25	106.20	0.19	-0.79	0.34	93.252	633.78	7.17	147	1951	
TRMR2	Quartz	23765.56	1671.23	197.13	-1.17	-4.59	-0.58	-87.086	99.15	368.79	3032	2626	
TRMR2	Quartz	5404.60	3079.67	569.82	-0.05	3.59	-0.02	-1.228	2432.07	576.82	3714	82	
TRMR2	Quartz	220.33	43.43	5116.09	-1.35	-6.25	-1.14	-6.582	50.55	5452.82	7548	1806	Excess
HLM2	Quartz	-48.00	9.97	-207.76	3.41	22.10	9.953	-1415.66	-21.60	-3148.93		6782	
HLM2	Quartz	600.03	-20.72	25.66	0.25	-1.43	0.204	234.58	270.01	-34.53	-949	7642	
HLM2	Quartz	60.00	-6.11	1485.01	6.05	18.25	5.370	106.86	27.00	-101.86		225739	

Appendix 5.4: Data tables for amphibole total fusion ^{40}Ar-^{39}Ar analyses from Ruby Range, Tobacco Root Mountains and Highland Mountains

Sample	Run	$^{40}Ar/^{39}Ar$	$^{38}Ar/^{39}Ar$	$^{37}Ar/^{39}Ar$	$^{36}Ar/^{39}Ar$	% Atmos-pheric	^{39}Ar (cc) $\times10^{-12}$	$^{40}Ar^*/^{39}Ar$	Age (Ma)	± 1 σ	Excluded from mean
RRCR4	Amphibole	115.47	0.01	5.76	0.000	0.10	121.93	115.36	1572	50	
RRCR4	Amphibole	126.62	0.01	7.69	0.008	1.87	85.65	124.25	1651	68	
RRCR4	Amphibole	121.42	0.02	6.28	0.000	0.00	96.75	121.42	1626	61	
RRCR4	Amphibole	95.12	0.02	5.35	0.000	0.12	102.05	95.00	1377	66	
RRCR4	Amphibole	129.45	0.01	8.02	0.039	8.82	22.11	118.03	1596	270	
RRCR11	Amphibole	127.15	-0.02	9.16	0.003	0.80	31.75	126.13	1667	181	
RRCR11	Amphibole	84.64	0.01	3.84	0.001	0.31	118.66	84.38	1266	61	
RRCR11	Amphibole	125.24	0.00	6.24	0.023	5.49	30.75	118.36	1599	194	
RRCR11	Amphibole	126.40	0.01	7.00	0.001	0.23	126.54	126.11	1667	46	
RRCR11	Amphibole	124.20	0.02	6.69	0.008	1.82	101.12	121.94	1631	58	
RRCR12	Amphibole	126.35	0.02	13.89	0.015	3.55	84.13	121.86	1630	70	
RRCR12	Amphibole	124.60	0.02	13.80	0.002	0.55	130.32	123.92	1648	45	
RRCR12	Amphibole	95.27	0.02	10.47	0.002	0.50	205.07	94.80	1375	33	
RRCR12	Amphibole	125.35	0.02	14.95	0.003	0.64	123.18	124.55	1654	49	
RRCR12	Amphibole	126.80	0.02	13.02	0.002	0.48	165.78	126.19	1668	35	
RRSW1	Amphibole	123.91	0.02	9.31	0.019	559.64	213.70	118.31	1700	7	
RRSW1	Amphibole	121.28	0.02	10.42	0.001	17.80	182.33	121.10	1726	7	
RRSW1	Amphibole	121.19	0.01	9.82	-0.001	-20.48	353.74	121.40	1729	7	
RRSW1	Amphibole	119.21	0.01	9.96	0.006	165.51	216.75	117.56	1693	7	
RRSW1	Amphibole	121.92	0.02	9.21	0.007	195.07	312.94	119.97	1715	6	
RRSW1	Amphibole	129.89	0.02	9.49	0.021	635.24	201.71	123.53	1748	11	
RRSW1	Amphibole	119.04	0.02	9.10	0.006	165.74	307.74	117.38	1691	6	
RRSW1	Amphibole	138.01	0.05	8.62	0.088	2611.26	198.36	111.89	1639	7	
RRSW1	Amphibole	128.23	0.02	9.81	0.020	597.36	309.49	122.26	1736	6	
RRSW1	Amphibole	124.54	0.02	10.52	0.008	241.44	241.42	122.13	1735	11	
TRER1	Amphibole	84.45	0.01	3.29	0.000	0.00	178.77	84.45	1266	41	
TRER1	Amphibole	74.35	0.02	2.92	0.001	0.44	599.54	74.02	1150	13	
TRER1	Amphibole	80.67	0.02	3.13	0.001	0.39	217.07	80.35	1222	34	
TRER1	Amphibole	66.88	0.01	3.00	0.003	1.26	397.09	66.04	1056	21	*

Appendix 5.4 continued

Sample	Run	$^{40}Ar/^{39}Ar$	$^{38}Ar/^{39}Ar$	$^{37}Ar/^{39}Ar$	$^{36}Ar/^{39}Ar$	% Atmos-pheric	39Ar (cc) $\times10^{-12}$	$^{40}Ar^{*}/^{39}Ar$	Age (Ma)	± 1 σ	Excluded from mean
TRER1	Amphibole	103.35	0.01	2.86	0.001	0.34	579.34	103.00	1456	12	
TRER2	Amphibole	6.43	0.03	14.22	0.003	11.68	116.75	5.68	119	116	
TRER2	Amphibole	5.47	0.03	6.86	0.000	0.00	94.63	5.47	115	143	
TRER2	Amphibole	4.33	0.03	3.99	0.003	17.12	255.46	3.59	76	54	
TRER2	Amphibole	3.79	0.03	6.55	0.009	67.78	82.53	1.22	26	173	
TRER2	Amphibole	14.62	0.79	119.74	0.000	0.00	5.12	14.62	293	2402	
TRER2	100 µm biotite	5.62	0.01	0.01	0.007	34.36	125.14	3.69	81	8	
TRER2	100 µm biotite	5.79	0.01	0.01	0.011	54.39	119.08	2.64	59	9	
TRER2	100 µm biotite	5.15	0.01	0.00	0.006	36.09	130.03	3.29	73	8	
TRER2	100 µm biotite	4.94	0.01	0.00	0.004	23.71	127.05	3.77	83	8	
TRER2	100 µm biotite	33.21	0.04	0.03	0.103	91.65	50.32	2.77	62	72	
TRER2	50 µm biotite	86.50	0.08	-0.01	0.280	95.76	16.24	3.66	81	64	
TRER2	50 µm biotite	14.30	0.02	0.01	0.041	84.11	23.42	2.27	51	45	
TRER2	50 µm biotite	24.53	0.03	-0.03	0.075	90.82	37.13	2.25	50	28	
TRER2	50 µm biotite	11.01	0.02	0.02	0.026	69.09	40.53	3.40	75	26	
TRER2	50 µm biotite	6.40	0.02	-0.02	0.011	52.34	36.47	3.05	67	29	
TRER2	50 µm biotite	9.62	0.03	0.04	0.016	49.17	11.77	4.89	107	87	
TRER2	50 µm biotite	6.61	0.00	0.00	0.018	80.12	15.54	1.31	29	66	
TRER2	50 µm biotite	7.87	0.01	0.01	0.019	70.22	60.57	2.34	52	17	
TRER2	50 µm biotite	7.70	0.02	-0.01	0.021	79.46	35.17	1.58	35	30	
TRER2	50 µm biotite	3.55	0.01	-0.01	-0.001	-4.61	65.98	3.72	82	16	
TRER2	50 µm biotite	3.72	0.02	0.00	0.002	18.85	60.43	3.02	67	17	
TRER2	50 µm biotite	3.98	0.01	0.00	0.003	22.88	61.23	3.07	68	17	
TRMC5	Amphibole	137.83	0.03	12.59	0.001	0.31	264.63	137.40	1762	21	
TRMC5	Amphibole	168.06	0.04	12.62	0.000	0.00	100.61	168.06	1997	48	
TRMC5	Amphibole	157.31	0.03	12.75	0.002	0.32	98.71	156.82	1914	51	
TRMC5	Amphibole	245.00	0.04	12.48	0.005	0.62	126.85	243.47	2471	30	
TRMC5	Amphibole	135.64	0.03	12.04	0.004	0.93	134.31	134.37	1737	42	
TRMR3	Amphibole	9.85	0.02	1.65	0.001	1.51	495.77	9.70	199	26	
TRMR3	Amphibole	18.23	0.02	4.34	0.001	2.19	201.36	17.83	351	59	

Appendix 5.4 continued

Sample	Run	$^{40}Ar/^{39}Ar$	$^{38}Ar/^{39}Ar$	$^{37}Ar/^{39}Ar$	$^{36}Ar/^{39}Ar$	% Atmos-pheric	39Ar (cc) $\times10^{-12}$	$^{40}Ar^*/^{39}Ar$	Age (Ma)	± 1 σ	Excluded from mean
TRMR3	Amphibole	25.39	0.02	4.95	0.000	0.00	136.08	25.39	482	81	
TRMR3	Amphibole	14.64	0.02	3.54	0.002	3.85	176.29	14.08	283	70	
TRMR3	50 µm biotite	61.25	0.05	0.02	0.195	94.08	58.66	3.63	80	18	
TRWC1	Amphibole	130.46	0.03	14.31	0.008	1.81	69.61	128.11	1684	82	
TRWC1	Amphibole	130.80	0.02	13.07	0.008	1.81	79.16	128.43	1687	72	
TRWC1	Amphibole	125.28	0.01	14.05	0.015	3.44	41.31	120.97	1622	143	
TRWC1	Amphibole	127.35	0.02	4.92	0.017	3.84	331.09	122.46	1635	18	
TRWC1	Amphibole	126.22	0.03	13.09	0.046	10.74	96.02	112.66	1547	64	
TRWC1	50 µm biotite	124.26	0.01	-0.03	-0.023	-5.52	7.39	131.13	1751	57	
TRWC1	50 µm biotite	120.69	0.02	-0.03	0.006	1.48	16.29	118.90	1643	27	
TRWC1	50 µm biotite	125.68	-0.01	0.05	-0.018	-4.15	9.72	130.90	1749	45	
TRWC1	50 µm biotite	122.78	0.01	0.00	0.001	0.27	129.10	122.46	1675	7	
TRWC1	50 µm biotite	124.27	0.01	-0.01	-0.001	-0.26	73.77	124.60	1694	9	
TRWC1	50 µm biotite	121.15	0.01	0.00	0.022	5.41	12.56	114.60	1604	38	
TRWC1	50 µm biotite	129.99	0.02	-0.02	0.006	1.34	54.70	128.24	1726	11	
TRWC1	50 µm biotite	119.99	0.02	0.07	0.001	0.13	15.50	119.83	1652	30	
TRWC1	50 µm biotite	122.73	0.01	0.05	0.012	2.97	18.90	119.08	1645	24	
TRWC1	50 µm biotite	134.05	0.01	-0.04	-0.029	-6.33	9.11	142.53	1846	45	
HLM4	Amphibole	221.88	0.02	6.54	0.003	0.33	141.72	221.14	2343	29	
HLM4	Amphibole	616.11	0.03	5.06	0.004	0.20	33.18	614.89	3842	53	
HLM4	Amphibole	201.30	0.02	4.67	0.005	0.76	63.45	199.77	2212	67	
HLM4	Amphibole	142.03	0.02	5.95	0.003	0.61	248.12	141.17	1793	22	
HLM4	Amphibole	133.28	0.02	6.03	0.000	0.00	98.85	133.28	1728	56	

Appendix 5.5: Data table for amphibole step-heating ^{40}Ar-^{39}Ar analyses for RRSW1

Sample	Step	$^{40}Ar/^{39}Ar$	$^{38}Ar/^{39}Ar$	$^{37}Ar/^{39}Ar$	$^{36}Ar/^{39}Ar$	% 39Ar	$^{40}Ar^{*}/^{39}Ar$	Age (Ma)	± 1 σ
RRSW1	1	96.66	0.01	7.77	0.007	0.69	94.54	1464	47
RRSW1	2	134.63	0.02	8.40	0.056	2.89	118.09	1698	16
RRSW1	3	125.91	0.02	8.75	0.012	6.49	122.31	1737	11
RRSW1	4	127.05	0.02	10.12	0.005	9.23	125.65	1767	13
RRSW1	5	126.81	0.02	9.75	0.007	12.50	124.86	1760	13
RRSW1	6	117.07	0.02	9.98	0.008	15.09	114.69	1666	14
RRSW1	7	-105.07	0.95	63.63	-0.662	15.09	90.65	1422	10037
RRSW1	8	100.98	0.01	0.18	0.190	15.26	44.95	842	239
RRSW1	9	58.84	0.06	1.69	0.089	16.36	32.46	645	39
RRSW1	10	97.01	0.04	4.46	0.042	18.65	84.50	1354	17
RRSW1	11	94.57	0.02	3.57	0.027	19.41	86.62	1378	46
RRSW1	12	93.27	0.03	2.28	0.012	21.04	89.61	1411	22
RRSW1	13	107.74	0.04	5.59	0.021	22.70	101.39	1535	20
RRSW1	14	72.38	0.04	3.54	0.055	22.85	56.16	1003	247
RRSW1	15	117.49	0.02	8.57	0.004	29.49	116.35	1682	9
RRSW1	16	119.21	0.03	8.61	0.006	31.37	117.54	1693	20
RRSW1	17	98.71	0.01	6.83	0.007	32.42	96.53	1485	32
RRSW1	18	103.33	0.00	6.60	-0.015	33.49	107.89	1600	31
RRSW1	19	99.51	-0.01	6.51	0.003	33.95	98.63	1507	71
RRSW1	20	105.54	0.00	7.11	0.005	34.41	104.03	1562	70
RRSW1	21	105.49	0.02	6.42	-0.003	35.14	106.40	1586	43
RRSW1	22	118.23	0.01	6.45	-0.009	36.29	120.89	1724	28
RRSW1	23	125.37	0.00	7.18	-0.007	37.13	127.40	1783	37
RRSW1	24	120.84	0.01	8.44	0.002	39.53	120.30	1719	15
RRSW1	25	114.61	0.01	8.96	0.028	40.20	106.43	1586	49
RRSW1	26	110.48	0.04	7.73	0.029	40.71	101.96	1541	62
RRSW1	27	115.21	0.01	7.85	0.000	41.58	115.08	1670	37
RRSW1	28	76.16	0.07	7.54	-0.033	41.69	85.89	1370	325
RRSW1	29	52.03	0.02	8.44	0.003	71.58	51.29	935	5
RRSW1	30	118.26	-0.01	5.35	-0.003	72.18	119.18	1708	52
RRSW1	31	111.41	0.02	8.32	0.004	75.74	110.36	1625	11
RRSW1	32	121.34	0.02	8.91	0.005	80.89	120.00	1716	9
RRSW1	33	115.94	0.02	7.27	0.003	82.07	115.16	1671	27
RRSW1	34	115.29	0.01	7.41	-0.003	83.27	116.10	1679	27
RRSW1	35	122.54	0.02	8.80	0.002	93.91	121.91	1733	8
RRSW1	36	113.11	0.01	8.12	0.000	95.03	113.16	1651	29
RRSW1	37	121.48	0.02	9.32	0.002	97.10	120.98	1725	18
RRSW1	38	115.39	0.02	9.10	-0.001	97.95	115.71	1676	37
RRSW1	39	97.59	0.02	8.57	0.005	98.58	96.24	1482	53
RRSW1	40	144.16	-0.01	5.38	-0.134	98.76	183.75	2225	168
RRSW1	41	118.90	-0.04	7.88	-0.063	99.22	137.58	1871	67
RRSW1	42	110.03	0.02	9.45	0.003	100.00	109.14	1613	44

Appendix 5.6: Data tables for high resolution ^{40}Ar-^{39}Ar analyses on TRMR2 biotite

Sample	Run	$^{40}Ar/^{39}Ar$	$^{38}Ar/^{39}Ar$	$^{37}Ar/^{39}Ar$	$^{36}Ar/^{39}Ar$	% Atmos-pheric	^{39}Ar (cc) $\times 10^{-13}$	$^{40}Ar^{*}/^{39}Ar$	Age (Ma)	± 1 σ
TRMR2	ExperimentA1	30.75	0.00	-0.01	0.014	13.02	163.11	26.74	1467	141
TRMR2	ExperimentA2	29.36	0.03	0.04	-0.006	-5.56	251.68	31.00	1620	93
TRMR2	ExperimentA3	26.57	0.01	-0.03	0.003	3.88	246.09	25.54	1421	96
TRMR2	ExperimentA4	30.16	0.02	0.04	0.016	15.79	192.95	25.40	1416	124
TRMR2	ExperimentA5	29.20	0.02	0.00	-0.005	-5.45	258.21	30.79	1613	83
TRMR2	ExperimentA6	29.83	0.02	0.01	-0.003	-3.20	151.92	30.78	1613	169
TRMR2	ExperimentA7	27.02	0.01	0.00	0.014	15.25	158.45	22.90	1317	175
TRMR2	ExperimentA8	26.10	0.01	0.05	-0.012	-14.04	257.28	29.76	1577	91
TRMR2	ExperimentA9	28.60	0.02	0.05	0.018	18.25	226.98	23.38	1336	112
TRMR2	ExperimentA10	29.11	0.01	0.04	-0.007	-7.54	187.35	31.31	1631	123
TRMR2	ExperimentA11	26.77	0.01	0.06	0.012	13.23	146.80	23.23	1330	173
TRMR2	ExperimentA12	27.14	0.01	0.05	-0.009	-9.50	159.38	29.72	1575	140
TRMR2	ExperimentA13	26.52	0.03	0.00	-0.028	-31.43	129.08	34.85	1748	158
TRMR2	ExperimentA14	27.85	0.02	0.07	0.019	20.00	164.98	22.28	1291	168
TRMR2	ExperimentA15	25.95	0.02	0.01	0.001	1.56	627.87	25.55	1422	46
TRMR2	ExperimentA16	27.32	0.01	0.07	0.002	2.40	184.56	26.67	1464	128
TRMR2	ExperimentA17	26.41	0.01	0.01	-0.002	-2.69	764.92	27.12	1481	31
TRMR2	ExperimentA18	24.71	0.00	0.00	0.000	-0.14	362.16	24.74	1390	68
TRMR2	ExperimentA19	26.62	0.03	0.03	-0.019	-21.27	143.07	32.28	1664	151
TRMR2	ExperimentA20	26.99	0.03	0.07	0.008	8.97	159.85	24.57	1384	151
TRMR2	ExperimentB1	46.61	-0.01	-0.12	0.036	22.81	41.23	35.98	1784	504
TRMR2	ExperimentB2	31.58	0.00	0.01	-0.002	-1.70	174.08	32.11	1658	136
TRMR2	ExperimentB3	34.83	0.02	0.01	0.014	11.77	269.18	30.73	1611	85
TRMR2	ExperimentB4	31.66	0.01	-0.06	0.004	3.59	151.71	30.52	1604	152
TRMR2	ExperimentB5	36.99	0.00	0.01	0.027	21.83	103.69	28.91	1547	229
TRMR2	ExperimentB6	33.85	0.00	-0.03	0.011	9.20	98.10	30.73	1611	229
TRMR2	ExperimentB7	35.40	-0.01	-0.03	0.013	10.44	118.61	31.71	1644	190
TRMR2	ExperimentB8	28.51	0.02	-0.13	-0.013	-13.27	59.88	32.30	1664	371
TRMR2	ExperimentB9	24.52	0.09	0.07	0.004	4.34	37.03	23.45	1339	718
TRMR2	ExperimentB10	28.07	-0.06	-0.08	-0.015	-16.09	20.72	32.59	1674	1067

Appendix 5.6 continued

Sample	Run	$^{40}Ar/^{39}Ar$	$^{38}Ar/^{39}Ar$	$^{37}Ar/^{39}Ar$	$^{36}Ar/^{39}Ar$	% Atmos-pheric	^{39}Ar (cc) $\times 10^{-13}$	$^{40}Ar^{*}/^{39}Ar$	Age (Ma)	± 1 σ
TRMR2	ExperimentB11	36.65	-0.16	-0.22	-0.294	-237.07	7.20	123.52	3458	1150
TRMR2	ExperimentB12	34.18	-0.06	0.20	-0.091	-78.90	3.47	61.14	2441	4169
TRMR2	ExperimentB13	30.67	-0.03	-0.01	0.016	15.37	36.57	25.96	1437	675
TRMR2	ExperimentB14	23.66	-0.03	-0.28	0.052	64.39	37.50	8.42	601	1046
TRMR2	ExperimentB15	22.19	0.00	0.01	0.008	10.65	72.93	19.83	1187	397
TRMR2	ExperimentB16	30.58	0.03	-0.01	-0.012	-11.31	142.39	34.03	1722	151
TRMR2	ExperimentB17	30.50	0.01	-0.03	0.001	0.80	161.96	30.26	1595	140
TRMR2	ExperimentB18	32.70	0.01	-0.01	-0.007	-6.16	112.55	34.71	1744	186
TRMR2	ExperimentB19	29.36	0.03	-0.01	0.016	15.66	95.30	24.76	1391	266
TRMR2	ExperimentB20	35.87	0.00	0.03	0.001	0.92	119.54	35.54	1770	173
TRMR2	ExperimentB21	33.19	0.01	0.00	0.017	14.93	168.96	28.24	1522	142
TRMR2	ExperimentB22	33.07	0.01	-0.06	0.024	21.51	99.03	25.95	1437	255
TRMR2	ExperimentB23	31.82	0.02	-0.09	0.025	23.46	94.37	24.35	1375	277
TRMR2	ExperimentB24	32.20	0.00	-0.03	0.001	1.00	122.34	31.88	1650	183
TRMR2	ExperimentB25	30.71	0.01	-0.05	0.020	19.34	140.99	24.77	1391	183
TRMR2	ExperimentB26	36.21	0.01	0.04	0.006	4.76	99.96	34.49	1737	214
TRMR2	ExperimentB27	34.00	0.00	-0.23	-0.040	-34.78	52.88	45.83	2071	336
TRMR2	ExperimentB28	19.58	-0.21	-0.72	0.362	546.93	5.33	-87.51		3308
TRMR2	ExperimentB29	26.78	-0.14	-0.40	0.163	179.88	11.86	-21.39		1206313
TRMR2	ExperimentB30	28.95	-0.01	0.08	0.098	100.11	15.12	-0.03	-3	3700
TRMR2	ExperimentB31	30.42	0.09	0.07	-0.076	-74.21	27.71	52.99	2253	579
TRMR2	ExperimentB32	38.14	0.03	0.00	0.050	38.78	56.61	23.35	1335	462
TRMR2	ExperimentB33	44.18	0.02	0.10	0.046	30.67	42.16	30.63	1607	545
TRMR2	ExperimentB34	32.90	0.04	-0.01	0.035	31.36	68.27	22.58	1304	398
TRMR2	ExperimentB35	28.36	0.02	-0.03	0.008	8.03	75.72	26.08	1442	325
TRMR2	ExperimentB36	33.10	0.05	-0.41	-0.032	-28.54	23.98	42.55	1980	762
TRMR2	ExperimentB37	28.20	0.02	0.09	0.007	7.52	81.32	26.08	1442	310
TRMR2	ExperimentB38	30.77	0.01	0.04	0.014	13.90	133.53	26.49	1458	187
TRMR2	ExperimentB39	29.14	0.01	0.01	0.009	9.45	159.17	26.38	1453	158
TRMR2	ExperimentB40	35.21	0.02	-0.03	-0.008	-6.96	92.51	37.66	1836	219

Appendix 5.6 continued

Sample	Run	$^{40}Ar/^{39}Ar$	$^{38}Ar/^{39}Ar$	$^{37}Ar/^{39}Ar$	$^{36}Ar/^{39}Ar$	% Atmos-pheric	^{39}Ar (cc) $\times10^{-13}$	$^{40}Ar^*/^{39}Ar$	Age (Ma)	± 1 σ
TRMR2	ExperimentB41	27.26	0.01	0.06	0.031	33.41	150.31	18.15	1112	201
TRMR2	ExperimentB42	30.25	0.01	-0.01	0.016	15.44	150.78	25.58	1423	169
TRMR2	ExperimentB43	31.39	0.02	-0.03	0.014	13.47	166.63	27.16	1483	145
TRMR2	ExperimentB44	28.54	0.00	-0.05	0.024	24.92	99.03	21.43	1256	276
TRMR2	ExperimentB45	47.14	0.00	-0.09	0.055	34.42	76.19	30.91	1617	299
TRMR2	ExperimentB46	30.32	-0.01	-0.20	-0.007	-7.01	44.03	32.44	1669	504
TRMR2	ExperimentB47	37.68	0.04	-0.07	0.011	8.50	53.82	34.48	1736	398
TRMR2	ExperimentB48	26.30	0.03	0.01	0.018	20.78	128.87	20.84	1230	219

Appendix 5.7: Closure Profiles for the Ruby Range and Tobacco Root Mountains

Appendix 5.7.1: Closure Profiles for RM37

RM37 Profile A

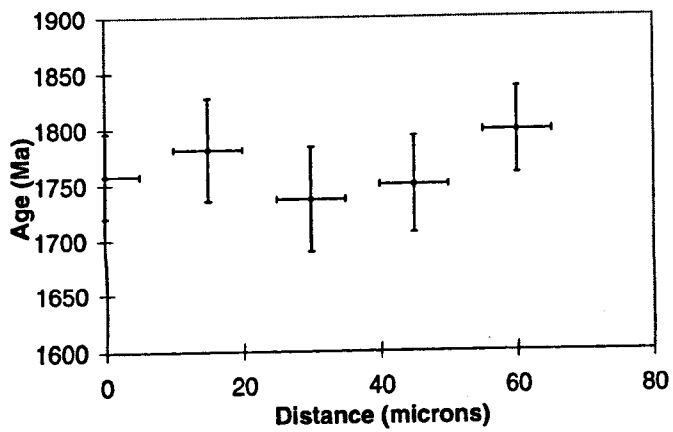

RM40 Profile B

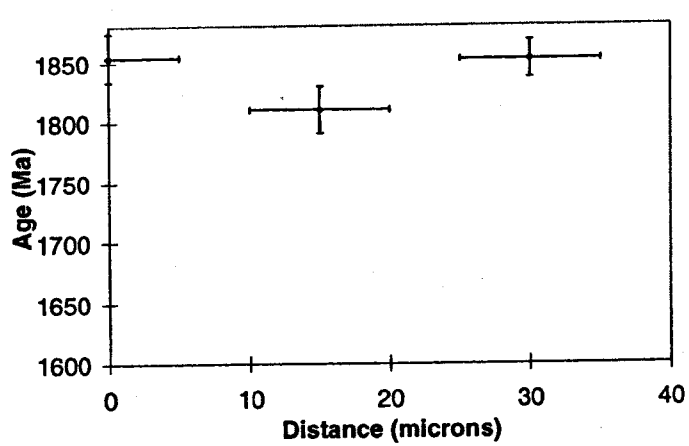

Appendix 5.7.2: Closure Profiles for RM40

RM40 Profile A

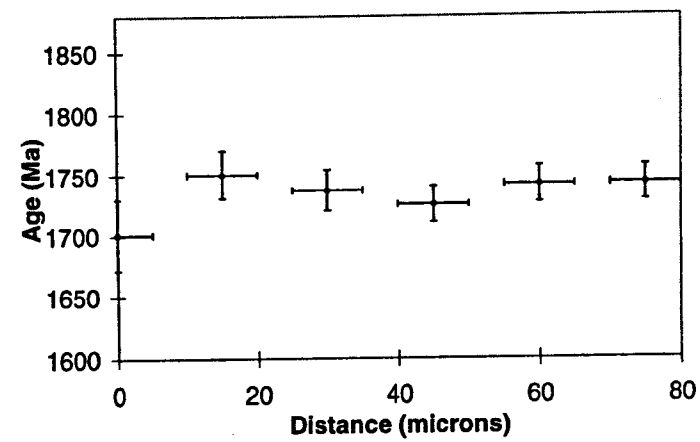

RM40 Profile C

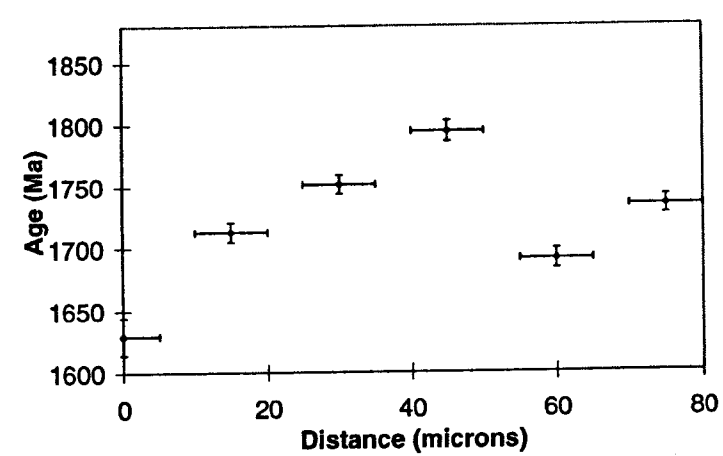

Appendix 5.7.3: Closure profiles for RMC42

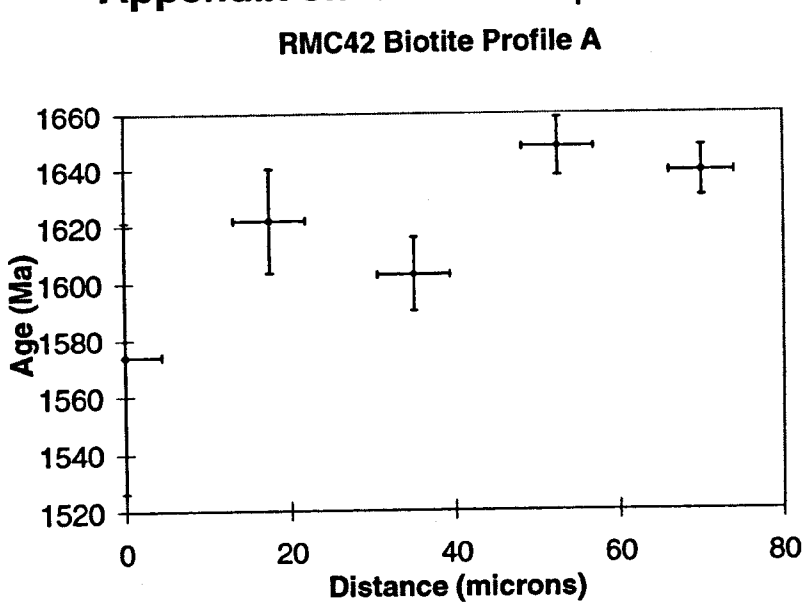

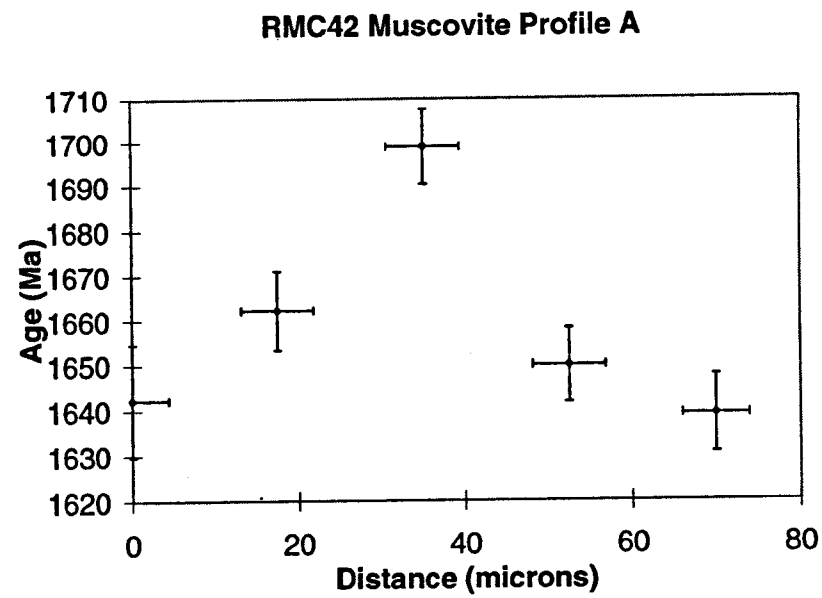

Appendix 5.7.4: Closure profiles for RRCR2

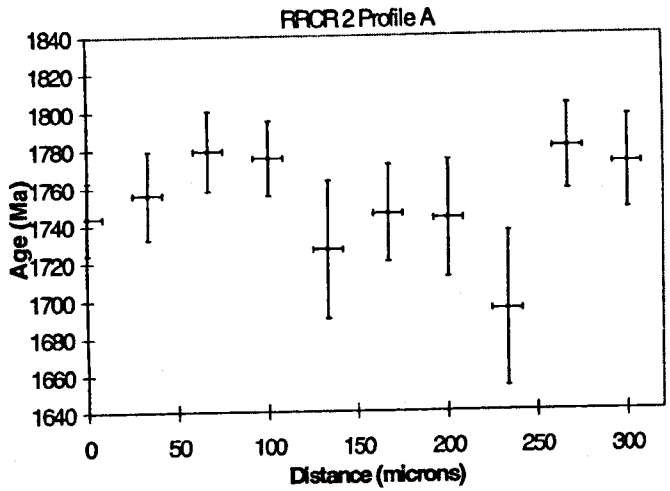

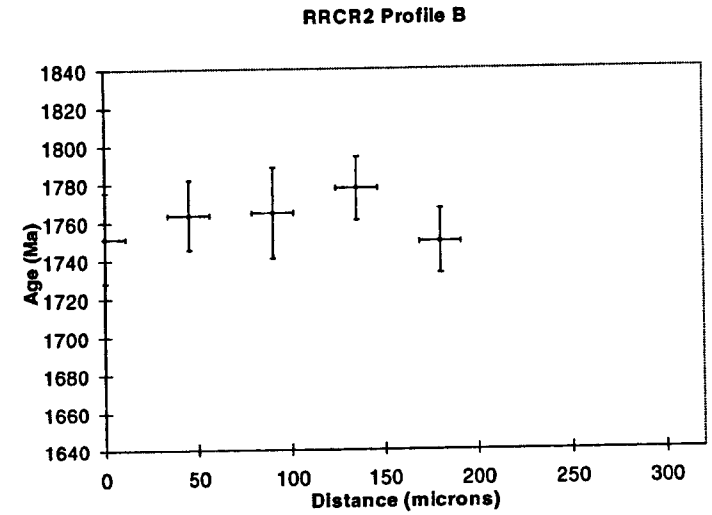

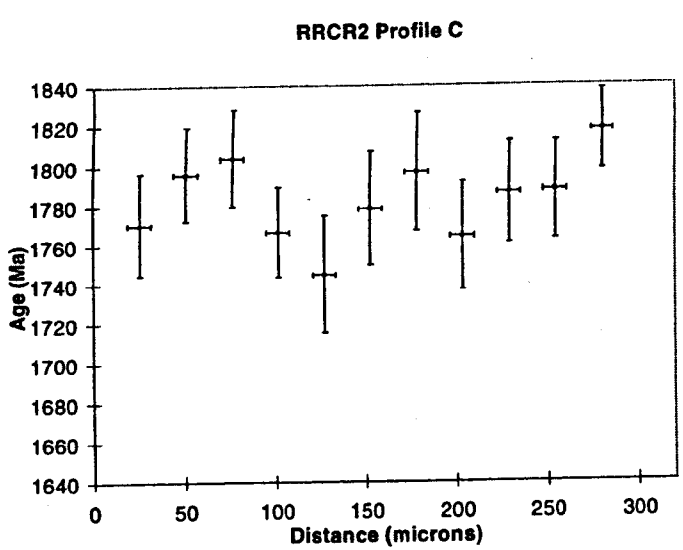

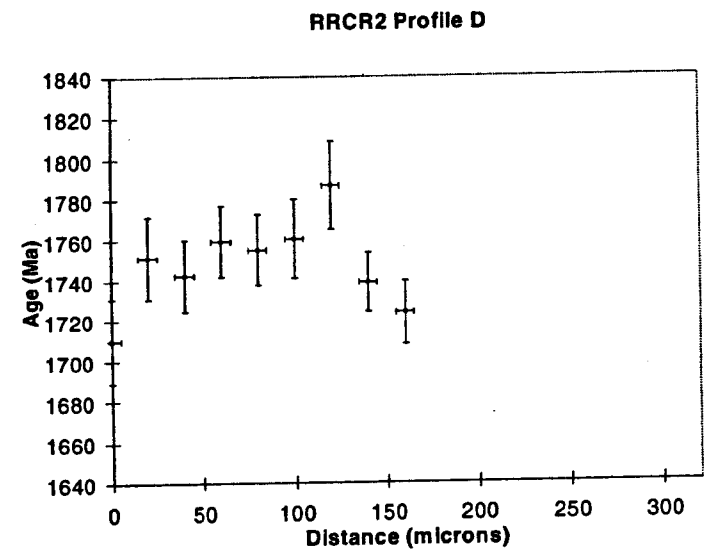

Appendix 5.7.5: Closure profiles for RRCR3

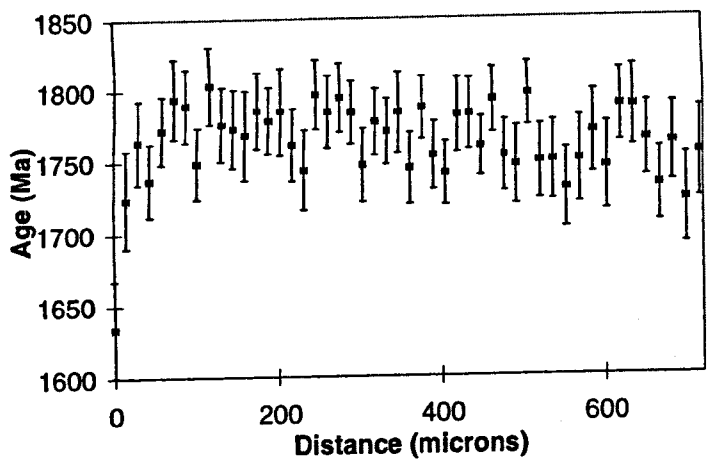

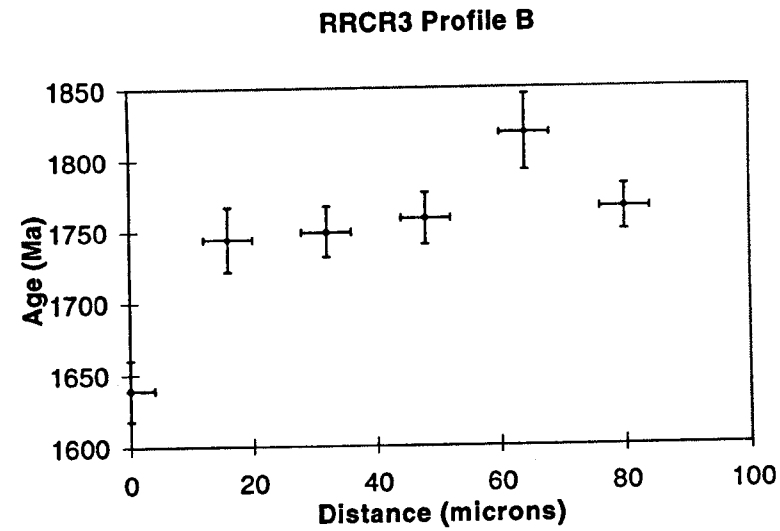

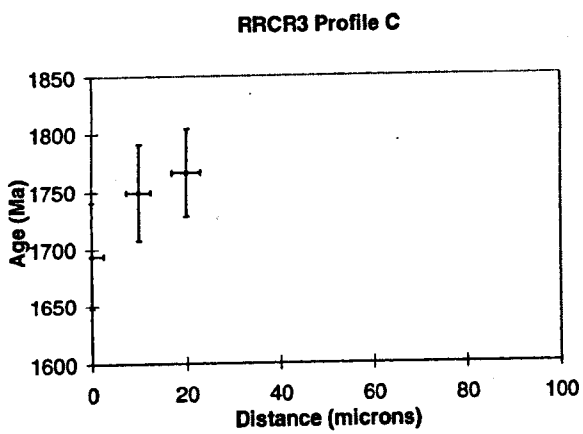

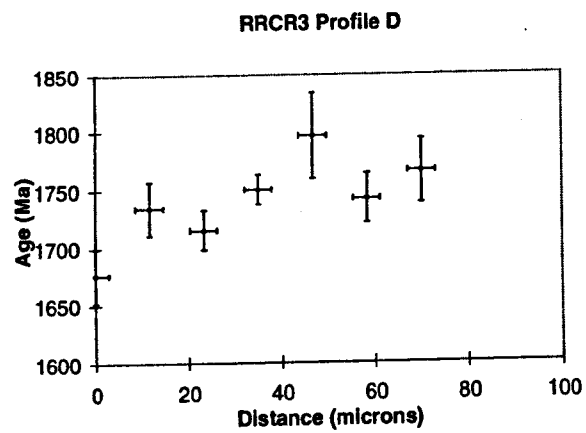

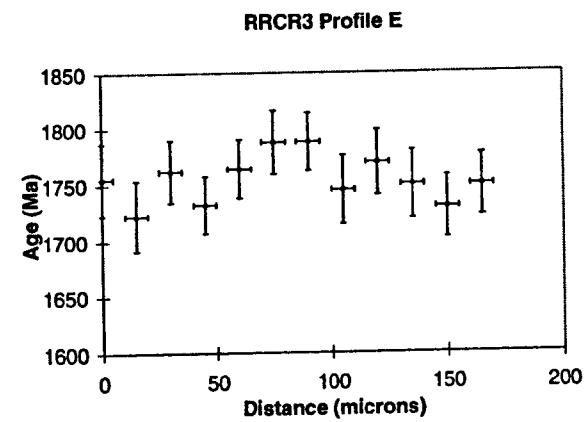

Appendix 5.7.6: Closure Profiles for RRCR5

RRCR5 Profile A

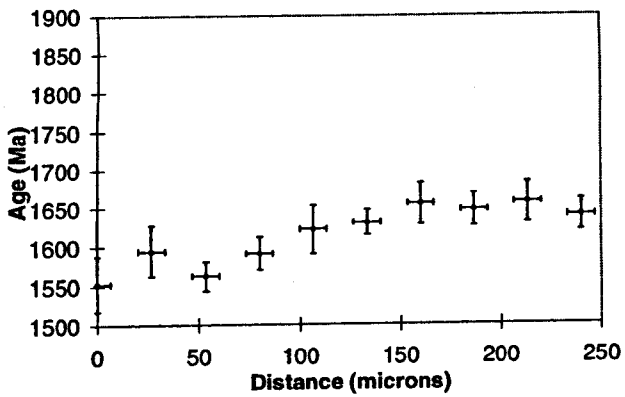

RRCR5 Profile B

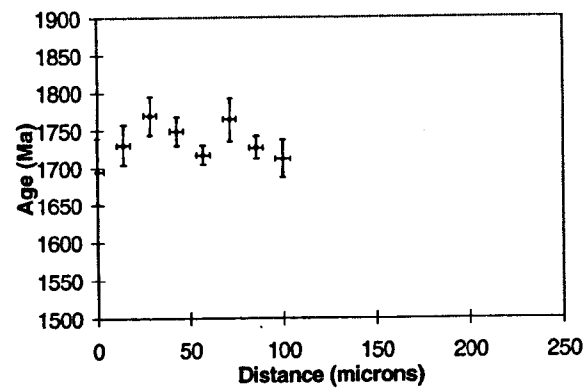

RRCR5 Profile C

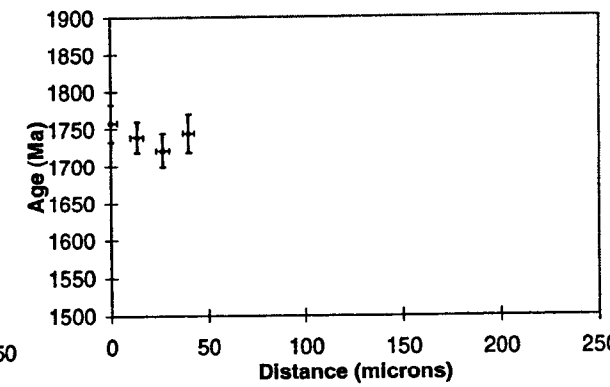

RRCR5 Profile D

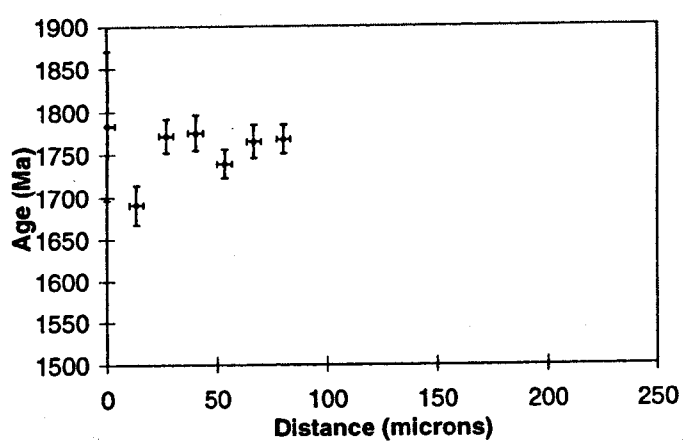

RRCR5 Profile E

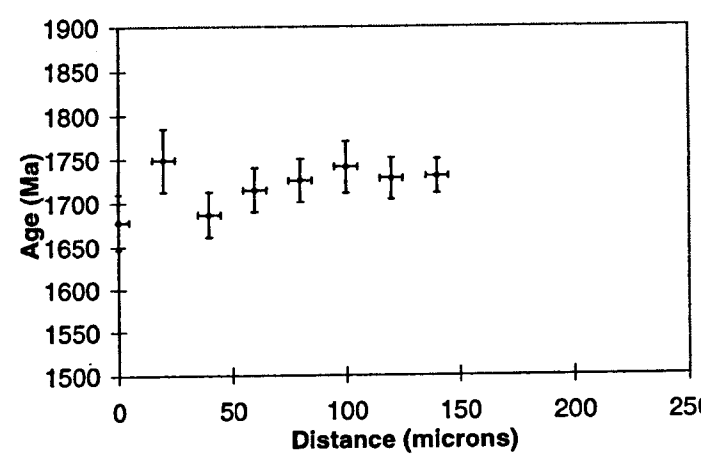

Appendix 5.7.7: Closure profiles for RRSW1

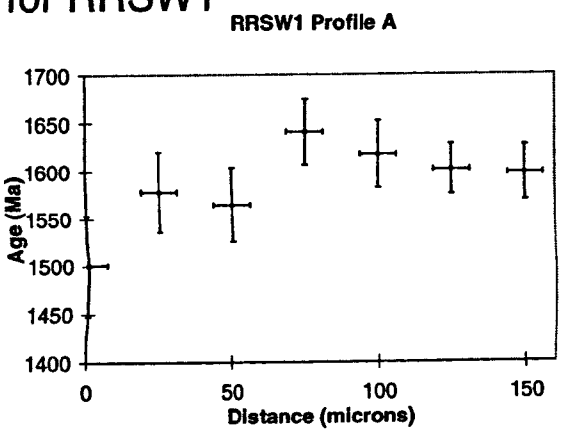

Appendix 5.7.8: Closure Profiles for RRSW2

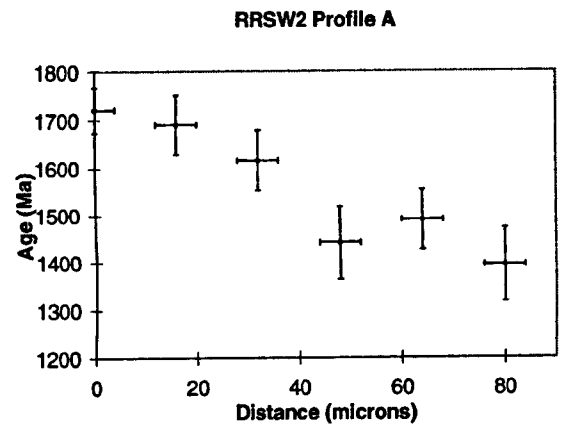

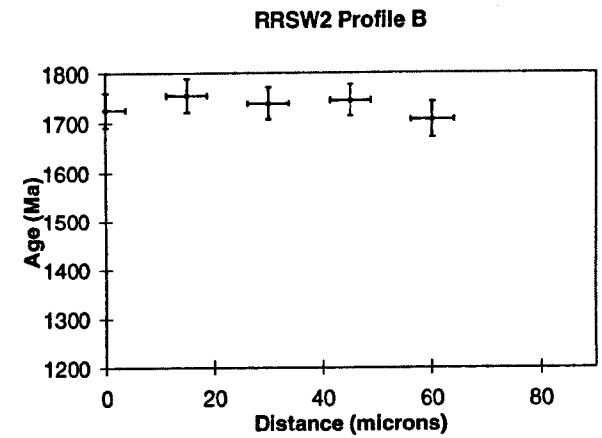

Appendix 5.7.10: Closure profiles for RRSW4

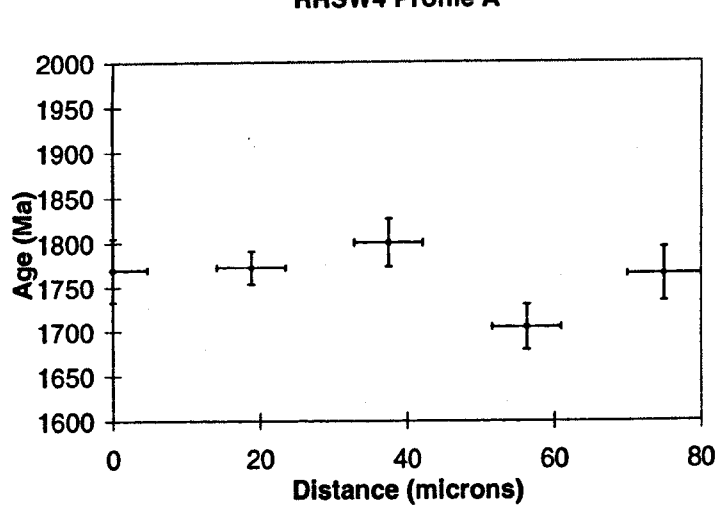

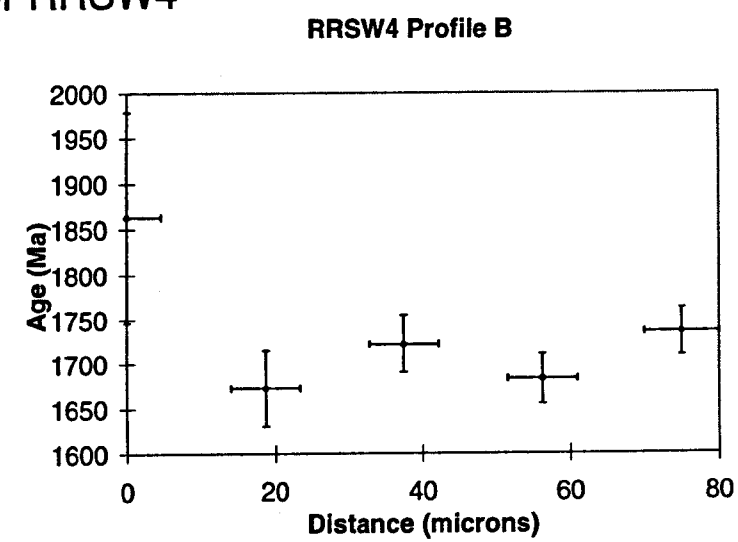

Appendix 5.7.9: Closure Profiles for RRSW3

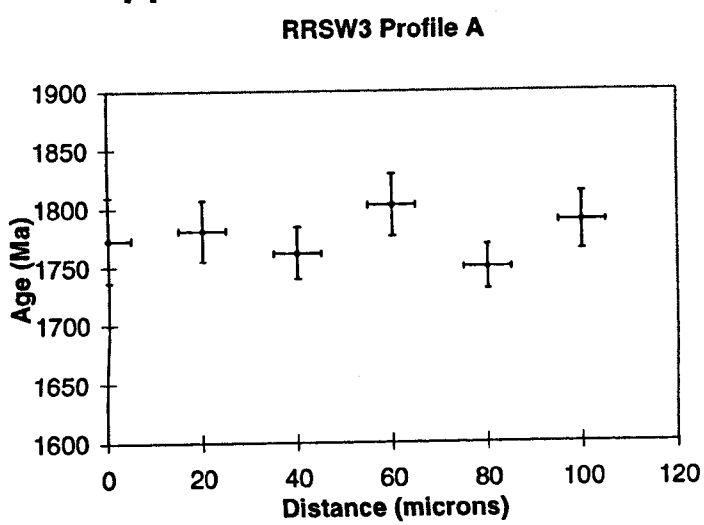

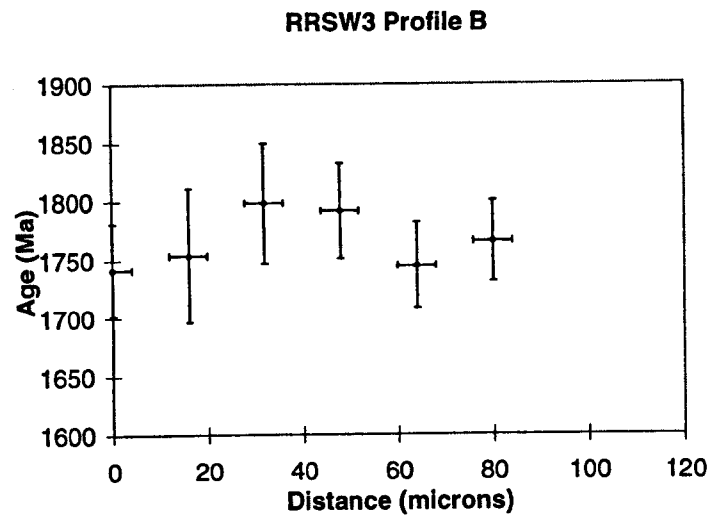

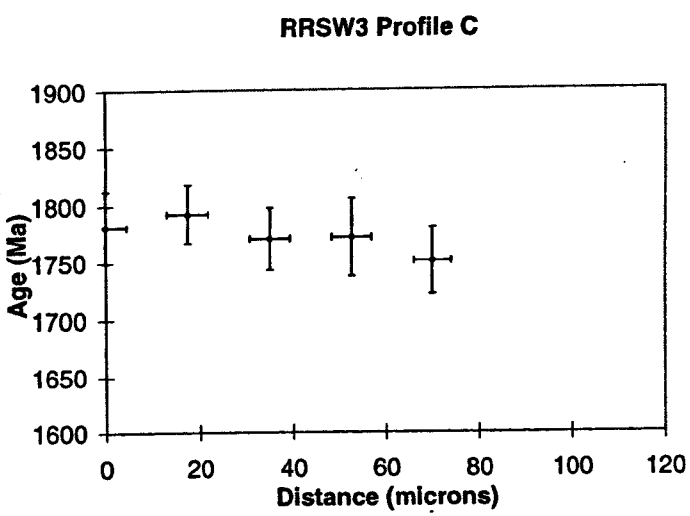

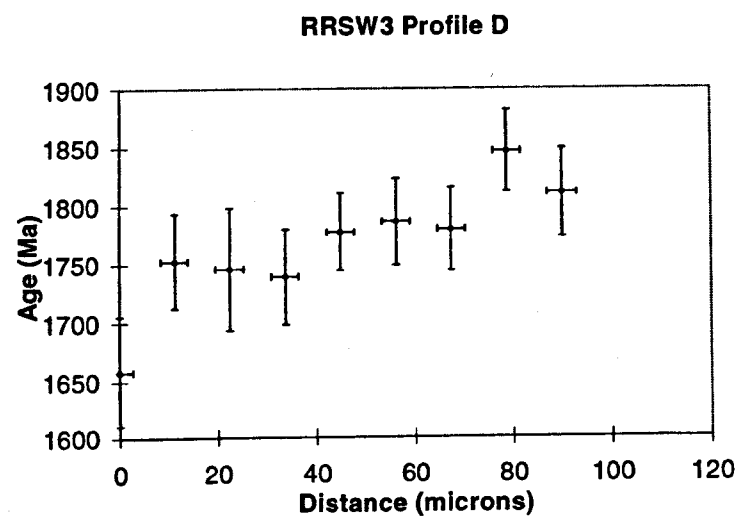

Appendix 5.7.11: Closure Profiles for TRER4

TRER4 Profile A

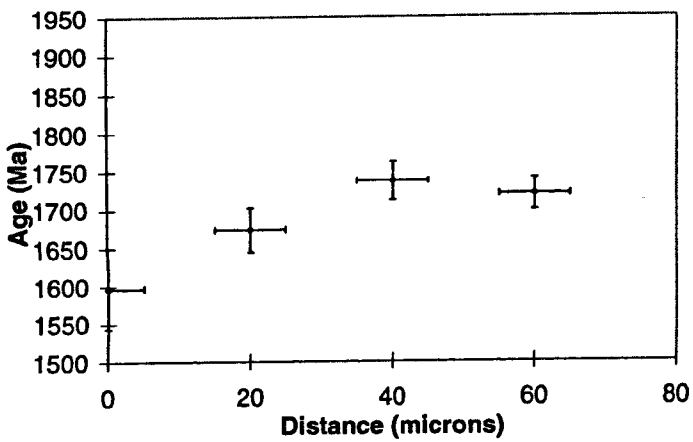

TRER4 Profile B

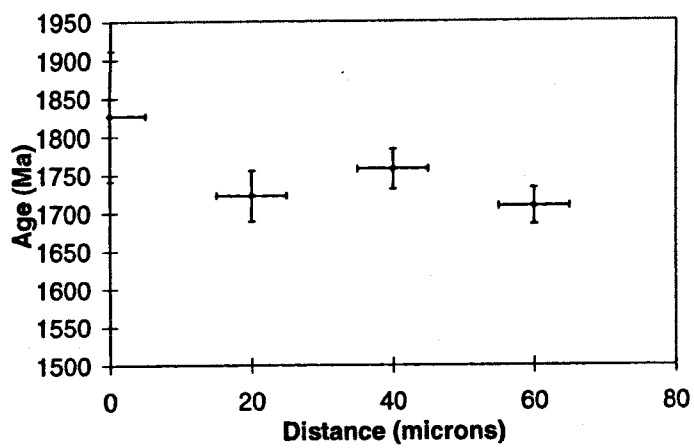

Appendix 5.7.13: Closure Profiles for TRGC5

TRGC5 Profile A

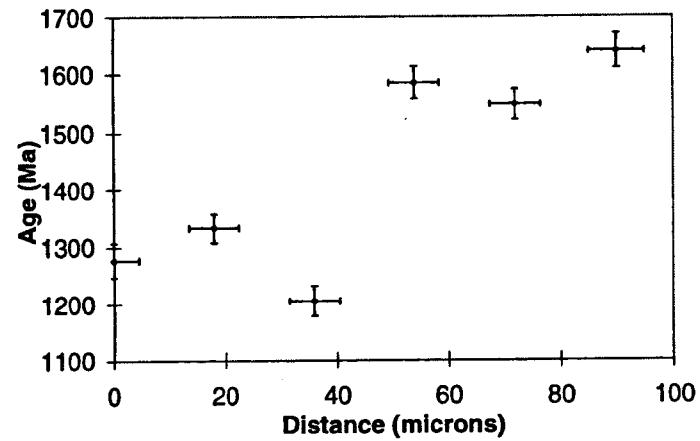

TRGC5 Profile B

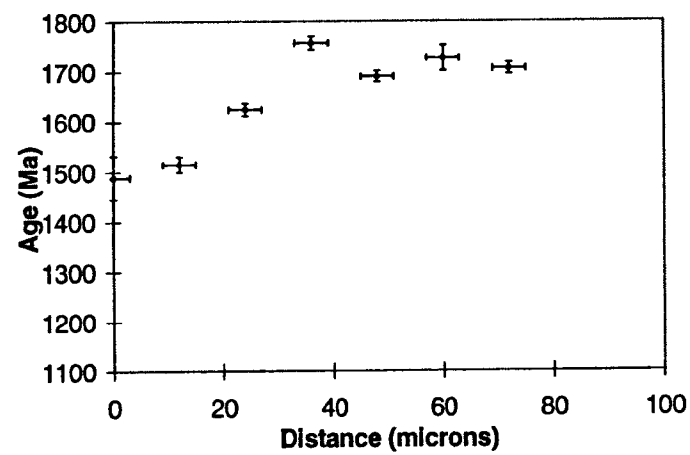

Appendix 5.7.12: Closure Profiles for TRER7

TRER7 Profile A

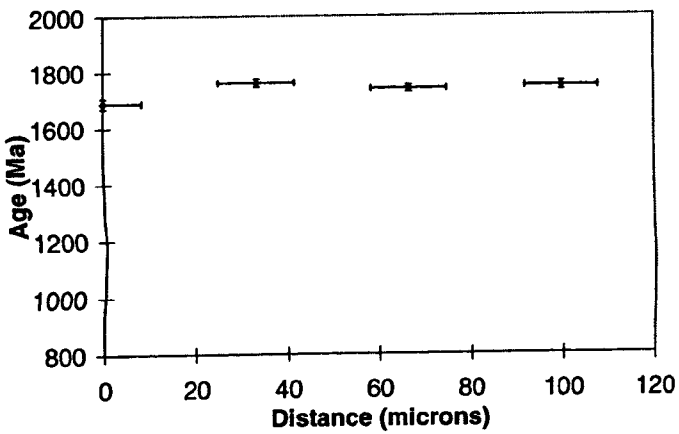

TRER7 Profile B

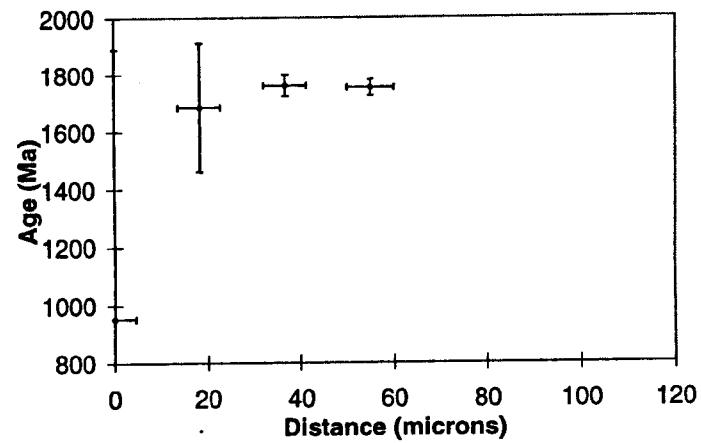

TRER7 Profile C

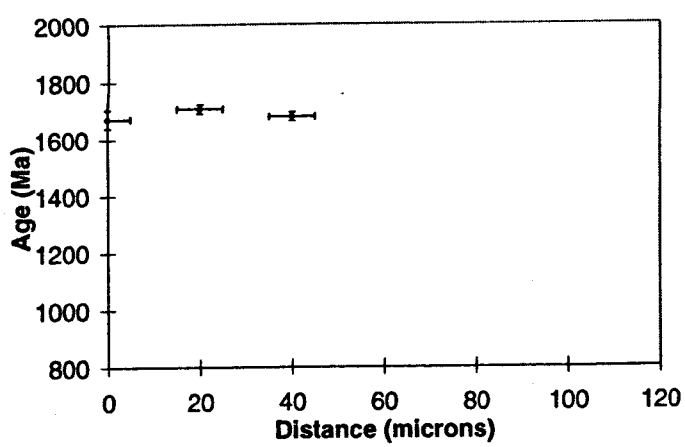

TRER7 Profile D

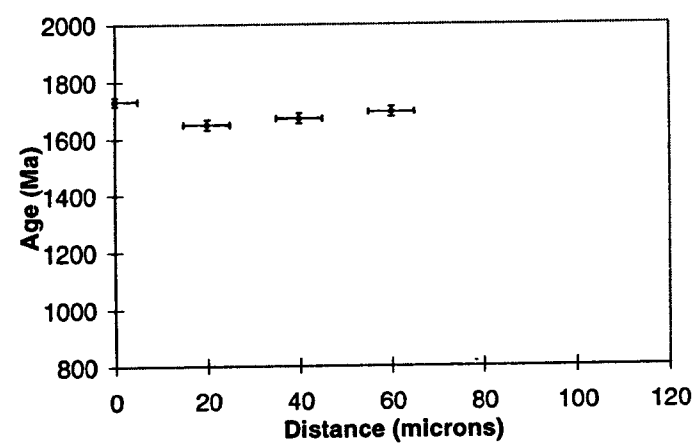

Appendix 5.7.14: Closure Profiles for TRMC3

TRMC3 Profile A

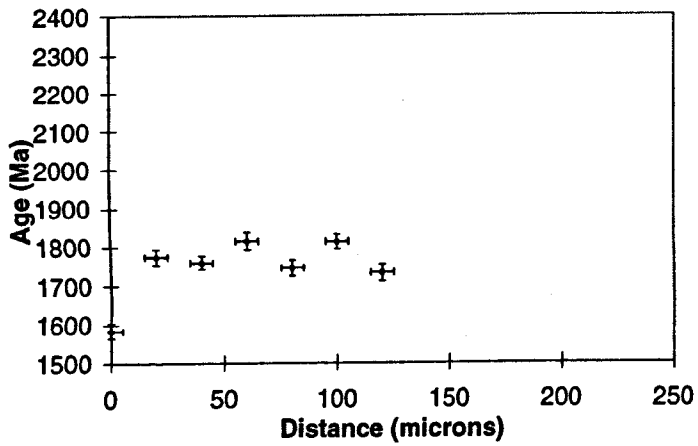

TRMC3 Profile B

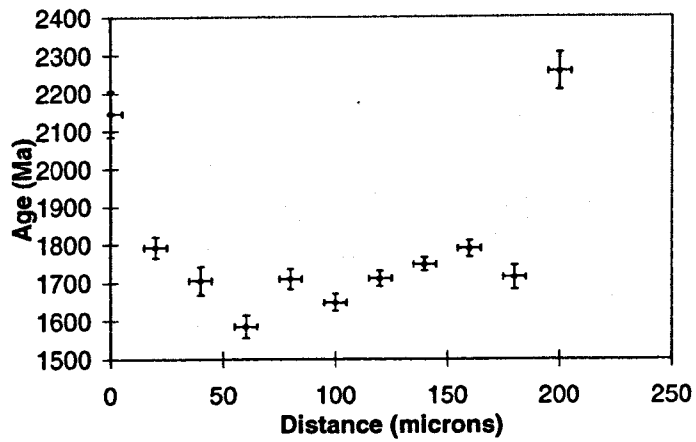

Appendix 5.7.15: Closure Profiles for TRMR2

TRMR2 Profile A

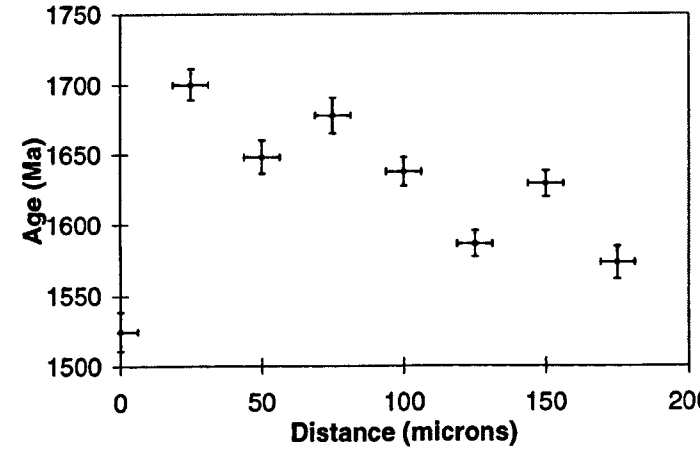

TRMR2 Profile B

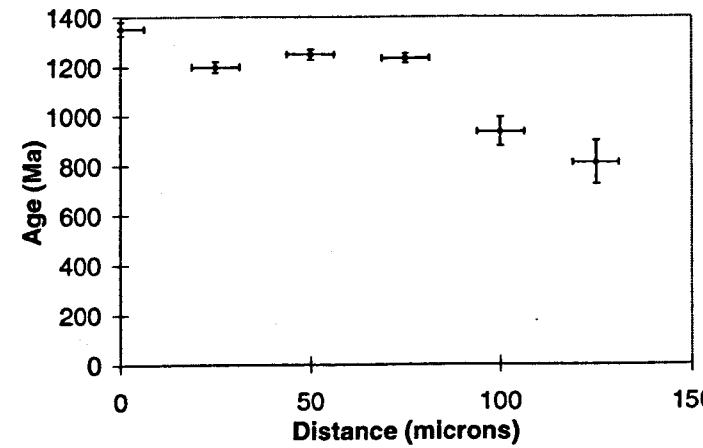

Appendix 6.1: Data tables for biotite inclusions in garnet ^{40}Ar-^{39}Ar analyses from Ruby Range and Tobacco Root Mountains

Sample	$^{40}Ar/^{39}Ar$	$^{38}Ar/^{39}Ar$	$^{37}Ar/^{39}Ar$	$^{36}Ar/^{39}Ar$	% Atmospheric	$^{39}Ar \times 10^{-12}$	$^{40}Ar^*/^{39}Ar$	Age (Ma)	± 1 σ
RM37	19.79	0.01	0.00	0.000	-0.63	3739.46	19.91	1782	15
RM37	19.43	0.01	0.00	0.002	2.61	1181.97	18.92	1724	47
RM37	19.39	0.01	0.02	0.004	6.77	1367.39	18.08	1674	33
RM37	19.98	0.01	0.04	0.002	3.53	659.72	19.28	1745	73
RM37	18.90	0.01	0.03	0.001	1.54	630.00	18.61	1706	142
RM37	17.59	0.01	0.01	0.000	0.62	2910.35	17.48	1638	33
RM37	18.61	0.01	0.04	0.003	5.29	1401.30	17.63	1647	66
RM37	17.22	0.01	0.01	0.001	1.18	1439.81	17.01	1609	42
RM39	22.45	0.02	0.07	-0.009	-11.80	94.14	25.09	2055	431
RM40	25.22	0.02	0.30	0.021	24.65	136.36	19.00	1729	625
RM40	20.38	0.01	0.02	0.002	3.28	2658.84	19.71	1770	32
RM40	20.21	0.01	0.02	0.002	2.75	2245.58	19.65	1767	42
RRCR3	142.52	0.05	0.18	0.083	17.26	46.57	117.91	1500	149
RRCR3	150.63	0.01	0.03	0.005	0.93	344.99	149.24	1752	25
RRCR3	153.45	0.02	0.00	0.003	0.53	425.19	152.63	1778	24
RRCR3	151.38	0.01	0.01	0.005	1.02	570.02	149.84	1757	15
RRCR3	150.76	0.01	0.01	0.009	1.85	698.82	147.98	1743	17
RRCR3	154.16	0.01	0.02	0.011	2.20	611.82	150.77	1764	17
RRCR3	159.24	0.01	0.01	0.013	2.44	602.10	155.35	1798	18
RRCR3	149.80	0.01	0.01	0.009	1.78	926.76	147.13	1737	14
RRCR3	149.80	0.01	0.04	0.011	2.20	508.30	146.50	1732	26
RRCR3	151.56	0.00	0.11	0.037	7.15	68.93	140.72	1687	113
RRCR3	158.92	0.02	0.02	0.002	0.29	466.01	158.46	1820	33
RRCR3	153.58	0.02	0.02	0.006	1.23	325.07	151.69	1771	22
RRCR3	153.43	0.01	0.03	-0.001	-0.20	161.76	153.75	1786	50
RRCR3	153.11	0.04	0.12	-0.024	-4.59	26.16	160.14	1833	223
RRCR3	157.44	0.02	0.39	0.058	10.87	28.10	140.32	1684	222
RRCR3	144.02	0.00	0.01	0.010	1.96	29.08	141.20	1691	262
RRCR3	149.86	0.01	0.00	0.000	-0.06	577.31	149.95	1758	16
RRCR3	153.10	0.01	0.00	-0.002	-0.46	447.54	153.81	1786	17
RRCR3	151.72	0.01	0.00	0.008	1.56	259.94	149.36	1753	45
RRCR3	153.51	0.02	0.01	0.004	0.84	582.17	152.22	1775	19
RRCR3	154.28	0.01	0.04	0.004	0.75	415.95	153.13	1781	21
RRCR3	146.78	0.01	0.02	0.005	1.08	472.82	145.20	1722	25
RRCR3	157.62	0.01	0.00	0.003	0.60	653.62	156.68	1808	25
RRCR3	156.11	0.01	-0.03	-0.003	-0.61	332.36	157.06	1810	23
RRSW2	146.93	0.01	0.00	0.005	1.08	554.96	145.34	1723	13
RRSW2	144.02	0.01	-0.01	0.001	0.20	731.87	143.72	1711	20
RRSW2	144.49	0.01	0.05	0.004	0.72	207.45	143.46	1709	40
TRER4	140.49	0.01	0.01	0.011	2.25	264.12	137.32	1743	23
TRER4	119.27	0.01	0.07	-0.014	-3.44	152.82	123.37	1625	33
TRER4	136.06	0.01	0.06	-0.001	-0.27	262.66	136.42	1735	20
TRGC5	121.67	0.01	0.02	-0.005	-1.20	201.75	123.12	1623	18
TRGC5	110.16	0.01	0.08	-0.001	-0.17	152.18	110.34	1509	25
TRGC5	142.01	0.02	0.00	0.006	1.25	358.74	140.24	1766	12
TRGC5	101.89	0.01	0.02	0.011	3.13	241.61	98.71	1397	20
TRGC5	136.87	0.02	0.02	-0.002	-0.35	331.52	137.36	1743	12
TRGC5	139.30	0.01	0.00	0.003	0.71	375.75	138.31	1751	11
TRMR2	145.75	0.01	0.00	0.00	-0.178	1171.83	146.00	1812	7
TRMR2	160.92	0.02	0.07	0.02	2.943	216.79	156.18	1890	24
TRMR2	127.55	0.01	0.03	0.00	0.180	417.03	127.32	1659	18
TRMR2	140.79	0.03	-0.01	0.00	-0.067	354.19	140.89	1771	14
TRMR2	138.19	0.01	0.02	0.00	-0.950	227.82	139.51	1760	18
TRMR2	83.77	0.04	0.19	0.144	50.78	24.38	41.23	750	284
TRMR2	116.16	0.01	0.01	0.002	0.46	697.04	115.63	1613	9
TRMR2	108.40	0.01	0.01	0.004	1.04	563.72	107.26	1534	10
TRMR2	125.98	0.01	0.02	0.015	3.42	240.68	121.67	1668	19
TRMR2	120.24	0.01	0.01	-0.020	-4.80	142.78	126.02	1707	30
TRMR2	131.22	0.03	0.00	-0.003	-0.73	307.34	132.18	1760	16
TRMR2	118.21	0.02	0.01	0.006	1.43	220.63	116.53	1621	21
TRMR2	106.26	0.01	0.08	0.002	0.62	161.90	105.60	1518	30
TRMR2	85.20	0.05	0.80	-0.004	-1.23	25.31	86.25	1320	203
TRMR2	98.19	0.01	0.02	0.003	0.85	445.79	97.35	1436	13
TRMR2	95.61	0.02	0.01	0.007	2.08	455.58	93.63	1398	13

Appendix 6.1 continued

Sample	$^{40}Ar/^{39}Ar$	$^{38}Ar/^{39}Ar$	$^{37}Ar/^{39}Ar$	$^{36}Ar/^{39}Ar$	% Atmospheric	$^{39}Ar \times 10^{-12}$	$^{40}Ar^*/^{39}Ar$	Age (Ma)	± 1 σ
TRMR2	123.10	0.01	0.02	-0.004	-1.01	449.98	124.34	1692	11
TRMR2	108.74	0.01	0.04	0.004	1.01	217.84	107.64	1538	23
TRMR2	137.28	0.01	0.01	0.003	0.58	961.82	136.48	1796	8
TRMR2	125.33	0.02	0.07	0.013	3.14	278.88	121.40	1666	18
TRMR2	90.54	0.01	0.03	-0.028	-9.05	174.46	98.73	1450	32
TRMR2	93.65	0.01	0.03	0.003	1.08	428.51	92.64	1388	15
TRMR2	73.34	0.00	0.04	-0.004	-1.54	324.56	74.47	1187	20
TRMR2	112.53	0.02	0.01	-0.001	-0.29	307.78	112.85	1587	19
TRMR2	125.11	0.01	0.05	-0.001	-0.30	268.62	125.48	1702	20

Appendix 6.2: Pb-Pb step-leaching procedure

1) Add appropriate acid to garnet grains and leave on hotplate for set duration.

2) Pipette off leachate into a clean beaker.

3) Rinse garnets with MQ H_2O twice, adding water to leachate in clean beaker.

4) Place next acid on garnets and put back on hotplate.

5) Leave leachate on hotplate with lid off until it has evaporated to dryness.

6) Pass through 0.5 ml glass columns and 200 µl Teflon columns as described in 6.1.1. below.

7) Load on filaments as outlined in 6.1.2. below.

8) Repeat for each acid leach step.

6.2.1. PbSL Column Recipe

6.2.1.1. 0.5 ml glass columns

1) Add 1 ml 1.5N HBr:2N HCl = 12:1 mix to evaporated leachate.

2) Place in an ultrasonic bath for 5 minutes.

3) Fill each column stem with AG 1x8 100-200 mesh resin.

4) Fill ½ a reservoir of each column with MQ H_2O and allow to drain through.

5) Fill ¾ a reservoir of each column with QD 6N HCl and allow to drain through.

6) Fill ½ a reservoir of each column with MQ H_2O and allow to drain through.

7) Fill ¼ a reservoir of each column with 1.5N HBr:2N HCl = 12:1 mix and allow to drain through.

8) Pipette all of sample/acid mix into column (leaving behind any undissolved residue) and allow to drain through. Wash beakers out with MQ H_2O.

9) Completely fill reservoir with 1N HBr and allow to drain through.

10) Completely fill reservoir with 2N HCl and allow to drain through.

11) Remove waste beakers from below column and replace with sample beakers.

12) Fill 1½ reservoirs with 6N HCl to collect Pb.

13) Place on hotplate lid off until it has evaporated to dryness.

6.2.1.2. 200 µl Teflon Columns

1) Add 1 ml 1.5N HBr:2N HCl = 12:1 mix to evaporated column Pb elute.

2) Place in an ultrasonic bath for 5 minutes.

3) Fill each column stem with AG 1x8 100-200 mesh resin.

4) Fill ½ a reservoir of each column with MQ H_2O and allow to drain through.

5) Fill ¾ a reservoir of each column with QD 7N HCl and allow to drain through.

6) Fill ½ a reservoir of each column with MQ H_2O and allow to drain through.

7) Fill ¼ a reservoir of each column with 1.5N HBr:2N HCl = 12:1 mix and allow to drain through.

8) Pipette all of sample/acid mix into column (including any undissolved residue) and allow to drain through. Wash beakers out with MQ H_2O.

9) Completely fill reservoir with 1N HBr and allow to drain through.

10) Completely fill reservoir with 2N HCl and allow to drain through.

11) Remove waste beakers from below column and replace with sample beakers.

12) Fill 1½ reservoirs with 7N HCl to collect Pb.

13) Place on hotplate lid off until it has evaporated to dryness.

6.2.2. Filament Loading

1) Use Re filament ribbon in centre filament holders.

2) Add 1.8 µl of silica gel onto centre of filament.

3) Pipette up 1.8 µl of phosphoric acid and drag over bottom of sample beaker to take up Pb.

4) Heat up filament and reduce silica gel.

5) Load Pb onto filament and heat up filament until phosphoric acid begins to smoke.

6.2.3. Regression Models

6.2.3.1. Model 1

Two-dimensional (X-Y) data are initially regressed using the algorithm of York (1969), with errors propagated using the algorithm of Titterington and Halliday (1979). This model assumes that the only cause for scatter from a straight line are the assigned errors. The points are weighted proportional to the inverse square of these errors (taking into account the error correlations).

This assumption is tested by the Probability of Fit value calculated by *Isoplot*. If this value is more than 15% then the Model 1 assumption is considered justified and the regression is complete. If this probably is less than 15% then another model may be more appropriate.

6.2.3.2. Model 2

A Model 2 fit assigns equal weights and zero error-correlations to each point. This avoids weights the points according to analytical errors when another cause of scatter is clearly involved. If little or nothing is known about the dominant cause of the scatter of the points this model should be used.

Appendix 6.3: Details of elemental diffusion experiments relevant to this study

Author	Publish Date	Mineral	Element	Pressure (bars)	Temperature °C	Time (hours)	Meter	Ea (KJ/mole)	LogDo (cm^2/sec)
Freer	1979	Almandine-rich (couple)	Mn (10 wt%) (15 wt%)	1	900-1000	300-501		-94 ± 16 -72 ± 25	-9.0 -9.7
Cygan and Lasaga	1985	Pyrope ($Py_{74}Alm_{15}Gr_{10}Uv_1$)	Mg	2000	750-900			239 ± 16	-6
Elphick et al.	1985	Sp-alm couple (Fe) (Mg)	Mg Fe	35000-40000	1300-1475	25-122	Ion Microprobe	225 ± 21 240 ± 35	-5.1 -4.9
Coghlan	1990	Garnet Garnet Spessartine Spessartine	O_2 Sr Nd Er	1000	800-1000		Ion Microprobe	302 ± 46 206 ± 17 185 ± 29 231 ± 38	-4.2 -5 -8.5 -6.3
Trull and Kurz	1992	Olivine Clinopyroxene	He He		960-1260 and 750-1400		Mass Spec	420 ± 20 290 ± 40	0.7 0.3
Chakraborty and Ganguly	1992	Alm-Sp couple	Fe Mg Mn	14000-35000	1100-1200	147-212	Ion Microprobe	276 ± 37 286 ± 38 254 ± 37	-3.2 -3 -3.3
Schwandt et al.	1995	Garnet ($Py_{66}Alm_{18}Gro_{14}Sp_2$)	Mg		800-1000		Ion microprobe	294 ± 51	-6
Dunai & Roselieb	1996	Garnet ($Py_{55}Alm_{40}Gro_4Sp_1$)	He	<250	800-990	18 - 500	Mass Spec	660 ($\pm^{190}_{120}$)	15.6
Chakraborty and Rubie	1996	Pyrope ($Alm_{38}Pyr_{50}Gr_{10}Sp_2$) Almandine ($Alm_{73}Pyr_{21}Gr_5Sp_1$)	Mg	80000	750-850			226 ± 21	-5.7

Appendix 6.4: Data tables for helium concentrations associated with zircon inclusions in garnet

6.4.1. Profile 1

Run	Distance	cc/g x 10^{-9}
Profile 1A	-91	151.404
Profile 1B	-84	113.96
Profile 1C	-77	60.236
Profile 1D	-70	-37.444
Profile 1E	-63	-9.768
Profile 1F	-56	213.268
Profile 1G	-49	37.444
Profile 1H	-42	36.63
Profile 1I	-35	45.584
Profile 1J	-28	22.792
Profile 1K	-21	42.328
Profile 1L	-14	1370.776
Profile 1M	-7	60.236
Profile 1N	0	1939.762
Profile 1O	7	1277.98
Profile 1P	14	1477.41
Profile 1Q	21	291.412
Profile 1R	28	200.244
Profile 1S	35	-82.214
Profile 1T	42	485.144
Profile 1U	49	369.556
Profile 1V	56	-124.542
Profile 1W	63	-95.238

6.4.2. Profile 2

Run	Distance	cc/g x 10^{-9}
Profile 2 Layer 1A	0	578.4284
Profile 2 Layer 1B	7	227.92
Profile 2 Layer 1C	14	239.316
Profile 2 Layer 1D	21	304.9244
Profile 2 Layer 1E	28	-103.785
Profile 2 Layer 1F	35	126.0072
Profile 2 Layer 1G	42	124.8676
Profile 2 Layer 1H	49	162.4744
Profile 2 Layer 1I	56	121.7744
Profile 2 Layer 1J	63	238.9904
Profile 2 Layer 1K	70	188.3596
Profile 2 Layer 1L	77	69.8412
Profile 2 Layer 1M	84	Lost analysis
Profile 2 Layer 1N	91	184.1268
Profile 2 Layer 2A	0	100.936
Profile 2 Layer 2B	8	11.396
Profile 2 Layer 2C	16	>1200000
Profile 2 Layer 2D	24	-39.886
Profile 2 Layer 2E	32	15.466
Profile 2 Layer 2F	40	-46.398
Profile 2 Layer 2G	48	32.56
Profile 2 Layer 2H	56	49.654
Profile 2 Layer 2I	64	-67.562
Profile 2 Layer 2J	72	956.45
Profile 2 Layer 2K	80	131.5424
Profile 2 Layer 2L	88	76.516
Profile 2 Layer 2M	96	113.96

6.4.3. Profile 3

Run	Distance	cc/g x 10^{-9}
Profile 3A	0	184.6152
Profile 3B	9.5	261.6196
Profile 3C	19	211.3144
Profile 3D	28.5	263.0848
Profile 3E	38	297.2728
Profile 3F	47.5	193.8948
Profile 3G	57	200.0812
Profile 3H	66.5	299.8776
Profile 3I	76	829.3032
Profile 3J	85.5	6995.679
Profile 3K	95	5281.232
Profile 3L	104.5	226746.2
Profile 3M	114	122034.9
Profile 3N	123.5	463752.1
Profile 3O	133	152915.4
Profile 3P	142.5	7538.291
Profile 3Q	152	125821
Profile 3R	161.5	198641.4
Profile 3S	171	175222.6
Profile 3T	180.5	118177.5
Profile 3U	190	Lost analysis
Profile 3V	199.5	15889.44
Profile 3W	209	390166.6
Profile 3X	218.5	19420.57
Profile 3Y	228	15590.05
Profile 3Z	237.5	21270.15
Profile 3AB	247	17522.49
Profile 3AC	256.5	12239.63
Profile 3AD	266	17709.71
Profile 3AE	275.5	32231.47
Profile 3AF	285	115595.5
Profile 3AG	294.5	150027.7
Profile 3AH	304	22983.94
Profile 3AI	313.5	18835.8
Profile 3AJ	323	28286.5
Profile 3AK	332.5	6157.259
Profile 3AL	342	11289.04
Profile 3AM	351.5	24511.66
Profile 3AN	361	63274.82
Profile 3AO	370.5	215979.6
Profile 3AP	380	461547.1
Profile 3AQ	389.5	126830.3
Profile 3AR	399	435179.2
Profile 3AS	408.5	126136
Profile 3AT	418	27525.41
Profile 3AU	427.5	2390.067
Profile 3AV	437	3795.194
Profile 3AW	446.5	5156.364
Profile 3AX	456	561.1716
Profile 3AY	465.5	634.92
Profile 3AZ	475	940.3328
Profile 3BA	484.5	-9.1168
Profile 3BB	494	-61.864
Profile 3BC	503.5	17.7452
Profile 3BD	513	174.3588
Profile 3BE	522.5	4538.213
Profile 3BF	532	2401.3
Profile 3BG	541.5	6954.979
Profile 3BH	551	759.462
Profile 3BI	560.5	2071.63
Profile 3BJ	570	269.434
Profile 3BK	579.5	3446.802
Profile 3BL	589	5692.465
Profile 3BM	598.5	1787.218
Profile 3BN	608	461.8636
Profile 3BO	617.5	-11.2332
Profile 3BP	627	43.142
Profile 3BQ	636.5	53.5612

Appendix 6.5: Helium diffusion data for pyrope and almandine doped at 1000 and 892 °C

Pyrope 1000 °C			
Run	Depth (μm)	^{4}He cc/g $\times10^{-8}$	±
Profile A1	2	219.6009	31.9324
Profile A2	4	237.7531	31.9324
Profile A3	6	69.41792	30.17332
Profile A4	8	54.28566	29.73597
Profile A5	10	39.71506	21.003
Profile B1	2	293.4063	37.15111
Profile B2	4	145.2095	33.61683
Profile B3	6	96.88228	32.66249
Profile B4	8	76.67066	34.43053
Profile B5	10	66.65846	37.75809
Profile B6	12	35.66948	35.46858
Profile B8	16	26.65036	37.74309
Profile B9	18	22.07568	32.79408
Profile B10	20	9.9308	32.20221
Profile C1	2	137.273	30.51044
Profile C2	4	31.14364	20.48809
Profile C3	6	37.06956	17.63659
Profile C4	8	36.54046	18.332
Profile D1	2	187.7165	19.82033
Profile D2	4	60.6023	17.47347
Profile D3	6	39.66622	22.07684
Profile D4	8	33.06468	15.80778
Profile D5	10	21.9373	15.44488
Profile D6	12	18.52664	14.71777
Pyrope 892 °C			
Run	Depth (μm)	^{4}He cc/g $\times10^{-8}$	±
Profile A1	2	66.08052	16.86573
Profile A2	4	65.9747	21.77611
Profile A3	6	64.70486	22.09217
Profile B1	2	84.76996	23.16371
Profile B2	4	68.47368	19.55181
Profile B3	6	74.09028	15.05179

Almandine 1000 °C			
Run	Depth (μm)	^{4}He cc/g $\times10^{-7}$	±
Profile A1	2	29.169	3.212099
Profile A2	4	13.34676	2.421184
Profile B1	2	39.83028	3.399946
Profile B2	4	14.95368	3.313533
Profile B3	6	11.8272	2.828295
Profile B4	8	9.09636	3.670606
Profile B5	10	8.70576	2.70926
Profile B6	12	5.4558	3.093724
Profile B7	14	4.62504	2.271303
Profile C1	2	42.55608	2.517023
Profile C2	4	15.78696	2.376737
Profile C3	6	13.52652	2.596046
Profile C4	8	9.55836	2.516419
Almandine 892 °C			
Run	Depth (μm)	^{4}He cc/g $\times10^{-7}$	±
Profile A1	2	24.30116	2.151706
Profile A2	4	7.189248	1.898179
Profile A3	6	7.189248	1.816956
Profile A4	8	6.531536	1.58539
Profile A5	10	11.40821	2.641345
Profile A6	12	12.19576	2.490419
Profile B1	2	19.01992	4.288988
Profile B2	4	12.06999	2.163765
Profile B3	6	10.37524	1.876865
Profile B4	8	8.98249	1.24231
Profile B5	10	8.021156	1.460729
Profile B6	12	7.390306	1.761956
Profile B7	14	6.603982	1.675012
Profile B8	16	6.21896	2.030333
Profile B9	18	6.5527	1.864324

Appendix 7.1: Data tables for biotite step-heating ^{40}Ar-^{39}Ar analyses for RRCR3 and RRSW1

Sample	Step	$^{40}Ar/^{39}Ar$	$^{38}Ar/^{39}Ar$	$^{37}Ar/^{39}Ar$	$^{36}Ar/^{39}Ar$	% ^{39}Ar	$^{40}Ar^*/^{39}Ar$	Age (Ma)	± 1σ
RRCR3	1	127.87	0.02	0.00	0.013	3.57	124.02	1748	22
	2	126.04	0.01	-0.03	0.000	7.10	126.12	1767	16
	3	127.30	0.01	-0.01	0.001	14.73	126.98	1775	11
	4	127.70	0.00	-0.02	0.001	15.79	127.45	1779	50
	5	131.42	0.03	-0.14	0.016	16.43	126.79	1773	82
	6	129.82	0.01	0.01	0.008	24.98	127.58	1780	12
	7	127.81	0.02	0.00	0.004	28.58	126.68	1772	16
	8	128.07	0.01	0.01	0.008	36.73	125.86	1765	9
	9	129.02	0.01	0.00	0.002	55.74	128.44	1788	7
	10	126.69	0.01	0.01	0.002	60.81	126.00	1766	12
	11	131.06	0.02	0.01	0.005	65.66	129.67	1798	13
	12	127.39	0.01	0.00	0.001	80.03	127.03	1775	7
	13	127.08	0.02	0.00	0.001	92.59	126.89	1774	7
	14	126.35	0.01	0.00	0.002	100.00	125.66	1763	9
RRSW1	1	13.09	0.47	0.50	-0.677	-0.12	213.13	2412	1255
Fragment 1	2	68.16	0.04	0.02	0.116	4.94	34.02	668	56
	3	20.00	0.31	-3.95	-1.946	4.89	595.11	3932	3061
	4	-52.98	-0.17	-4.24	0.556	4.85	-217.30		8453
	5	70.08	0.02	0.00	0.032	21.05	60.53	1058	14
	6	132.88	0.02	0.00	0.025	59.39	125.43	1760	10
	7	139.57	0.02	0.02	0.015	69.27	135.05	1844	19
	8	130.50	0.02	0.00	0.013	83.70	126.79	1772	14
	9	129.77	0.01	0.03	0.008	92.21	127.32	1777	22
	10	162.39	-0.02	-0.01	0.022	95.93	155.99	2015	45
	11	142.85	0.05	0.10	0.050	98.92	127.95	1782	58
	12	175.82	-0.01	-0.12	0.014	99.66	171.80	2134	214
	13	116.85	0.17	1.21	0.449	100.00	-15.87	-423	1443
RRSW1	1	123.05	0.05	-0.10	0.318	0.57	29.17	587	216
Fragment 2	2	61.10	0.03	0.00	0.063	9.19	42.50	802	13
	3	56.64	0.02	0.02	0.048	11.85	42.48	802	42
	4	74.33	0.02	0.00	0.021	37.24	68.24	1157	6
	5	120.16	0.41	3.03	1.037	37.28	-186.36		4566
	6	129.14	0.02	0.00	0.010	63.85	126.09	1766	7
	7	135.26	0.02	0.01	0.013	70.06	131.52	1814	14
	8	165.90	0.01	0.01	-0.002	72.16	166.53	2095	37
	9	154.51	0.00	-0.01	-0.007	74.27	156.50	2019	38
	10	143.67	0.01	0.00	-0.007	79.79	145.74	1933	25
	11	153.65	0.03	-0.02	0.009	84.05	150.91	1975	19
	12	144.19	0.01	0.05	0.002	86.30	143.49	1915	35
	13	140.25	0.01	0.02	-0.004	92.33	141.43	1898	16
	14	165.26	-0.01	0.06	-0.019	93.35	170.79	2127	72
	15	169.73	0.01	0.01	-0.008	94.56	172.01	2135	61
	16	154.32	0.02	0.03	0.006	96.92	152.44	1987	33
	17	147.18	-0.01	0.01	-0.022	98.46	153.67	1997	50
	18	145.18	0.03	0.04	0.017	99.63	140.13	1887	68
	19	126.77	0.15	-0.05	-0.012	100.00	130.35	1803	210

Appendix 7.2: Data table for depth profile ^{40}Ar-^{39}Ar analyses on sample RRSW1

Sample	Profile	Depth (μm)	$^{40}Ar/^{39}Ar$	$^{38}Ar/^{39}Ar$	$^{37}Ar/^{39}Ar$	$^{36}Ar/^{39}Ar$	% Atmos-pheric	^{39}Ar (cc) $\times10^{-12}$	$^{40}Ar^*/^{39}Ar$	Age (Ma)	± 1σ
RRSW1	1	0	120.88	0.01	0.03	0.072	18	7.56	99.47	1511	93
		1	126.49	-0.01	0.06	0.037	9	5.08	115.58	1669	141
		2	120.38	0.00	0.07	0.001	0	5.76	119.99	1711	119
		3	120.32	0.01	-0.02	-0.006	-2	6.05	122.15	1730	113
		4	111.28	-0.01	0.03	0.025	7	5.71	103.91	1556	143
		5	120.83	0.02	0.00	0.024	6	6.00	113.82	1653	103
		6	116.52	0.01	0.01	-0.014	-4	5.76	120.76	1718	102
		7	116.25	0.01	0.00	0.001	0	5.18	115.82	1672	120
		8	109.60	0.02	-0.03	0.001	0	5.18	109.17	1608	122
		9	115.98	0.00	-0.04	0.002	0	4.84	115.52	1669	147
		10	111.39	0.00	-0.06	0.036	9	5.27	100.88	1525	137
RRSW1	2	0	78.82	0.04	0.10	0.035	13	5.09	68.38	1159	154
		1	70.58	0.03	0.17	0.059	25	4.55	53.06	956	165
		2	100.50	0.02	0.02	0.040	12	4.55	88.81	1398	149
		3	89.05	0.01	0.03	0.010	3	4.55	86.13	1368	154
		4	101.71	0.03	-0.04	0.037	11	3.65	90.79	1419	165
		5	103.83	0.04	-0.03	0.000	0	3.52	103.83	1555	147
		6	106.65	0.02	-0.08	-0.013	-4	3.52	110.43	1620	173
		7	112.26	0.02	0.05	-0.037	-10	3.61	123.32	1741	145
		8	107.30	0.00	-0.06	0.000	0	3.74	107.30	1590	149
		9	100.68	0.04	-0.05	0.035	10	3.88	90.39	1415	159

Appendix 8.1: Data tables for matrix mica ^{40}Ar-^{39}Ar analyses from the South Madison Range

Sample	Run	$^{40}Ar/^{39}Ar$	$^{38}Ar/^{39}Ar$	$^{37}Ar/^{39}Ar$	$^{36}Ar/^{39}Ar$	%Atmos-pheric	$^{39}Ar \times 10^{-13}$	$^{40}Ar^*/^{39}Ar$	Age (Ma)	± 1 σ	Excluded from mean	Profile Diagram
SMR1	Muscovite Profile A1	267.78	0.01	0.03	0.006	0.72	21.0	265.86	2401	75		8.2.1
SMR1	Muscovite Profile A2	272.69	0.02	0.01	0.004	0.46	42.4	271.42	2428	69		8.2.1
SMR1	Muscovite Profile A3	281.94	0.01	0.02	0.005	0.57	58.6	280.35	2472	67		8.2.1
SMR1	Muscovite Profile A4	290.81	0.01	0.03	0.007	0.67	68.5	288.86	2512	67		8.2.1
SMR1	Muscovite Profile A5	288.15	0.01	0.00	0.002	0.18	76.2	287.61	2506	66		8.2.1
SMR1	Muscovite Profile A6	288.47	0.01	0.01	0.004	0.46	80.9	287.15	2504	67		8.2.1
SMR1	Muscovite Profile A7	284.96	0.01	0.02	0.007	0.72	78.4	282.91	2484	66		8.2.1
SMR1	Muscovite Profile A8	288.83	0.01	0.02	0.004	0.39	82.5	287.70	2506	68		8.2.1
SMR1	Muscovite Profile A9	287.73	0.02	0.00	0.003	0.28	82.1	286.91	2503	66		8.2.1
SMR1	Muscovite Profile B1	273.41	0.02	0.09	0.058	6.28	7.0	256.24	2352	100		8.2.1
SMR1	Muscovite Profile B2	274.91	0.02	0.05	0.009	0.94	15.6	272.32	2433	72		8.2.1
SMR1	Muscovite Profile B3	262.66	0.01	0.02	0.001	0.13	40.6	262.32	2383	71		8.2.1
SMR1	Muscovite Profile C1	179.53	0.06	0.02	0.097	16.00	4.2	150.80	1709	173		8.2.1
SMR1	Muscovite Profile C2	228.15	0.02	0.04	0.020	2.56	20.6	222.31	2169	69		8.2.1
SMR1	Muscovite Profile C3	250.31	0.02	0.04	0.028	3.26	29.4	242.14	2278	71		8.2.1
SMR1	Muscovite Profile C4	261.60	0.02	0.01	0.011	1.23	45.8	258.39	2363	67		8.2.1
SMR1	Muscovite Profile C5	288.84	0.01	0.01	0.004	0.39	60.2	287.73	2507	69		8.2.1
SMR1	Muscovite Profile C6	294.96	0.01	0.01	0.006	0.61	67.1	293.17	2532	67		8.2.1
SMR1	Muscovite Profile C7	295.20	0.01	0.01	0.006	0.56	73.1	293.56	2534	67		8.2.1
SMR1	Muscovite Profile C8	300.81	0.01	0.01	0.005	0.51	70.0	299.28	2560	69		8.2.1
SMR1	Muscovite Profile C9	294.63	0.02	0.01	0.000	0.00	47.6	294.62	2539	67		8.2.1
SMR1	Muscovite Profile C10	304.77	0.01	-0.01	0.003	0.31	71.5	303.84	2581	68		8.2.1
SMR1	Muscovite Profile D1	270.45	-0.04	-0.12	0.207	22.60	0.9	209.33	2094	678		8.2.1
SMR1	Muscovite Profile D2	252.21	0.01	-0.02	-0.013	-1.58	6.6	256.18	2352	104		8.2.1
SMR1	Muscovite Profile D3	268.99	0.02	0.05	0.023	2.52	9.9	262.20	2382	91		8.2.1
SMR1	Muscovite Profile D4	269.56	0.02	0.03	0.008	0.88	22.7	267.20	2407	80		8.2.1
SMR1	Muscovite Profile D5	273.93	0.02	0.01	0.006	0.61	24.1	272.25	2432	69		8.2.1
SMR1	Muscovite Profile D6	260.57	0.01	0.00	0.002	0.18	29.1	260.09	2372	69		8.2.1
SMR1	Muscovite Profile D7	267.42	0.01	0.01	0.001	0.13	39.6	267.07	2407	69		8.2.1
SMR1	Muscovite Profile E1	202.12	0.01	0.04	-0.023	-3.31	9.9	208.80	2091	86		8.2.1
SMR1	Muscovite Profile E2	212.70	0.02	0.02	0.002	0.24	26.9	212.19	2111	66		8.2.1
SMR1	Muscovite Profile E3	204.59	0.01	0.03	-0.013	-1.81	28.6	208.29	2088	68		8.2.1
SMR1	Muscovite Profile E4	202.61	0.01	0.00	-0.003	-0.40	48.3	203.43	2058	63		8.2.1
SMR1	Muscovite Profile E5	216.95	0.01	0.01	0.005	0.72	59.6	215.38	2129	62		8.2.1
SMR1	Muscovite Profile E6	220.27	0.01	-0.01	0.002	0.22	55.8	219.78	2155	67		8.2.1
SMR1	Muscovite Profile E7	237.37	0.01	-0.03	-0.006	-0.71	46.8	239.06	2262	67		8.2.1
SMR1	Muscovite Profile E8	248.49	0.01	-0.02	-0.003	-0.35	44.8	249.37	2316	66		8.2.1
SMR1	Muscovite Profile E9	251.60	0.01	-0.03	-0.012	-1.39	41.6	255.10	2346	65		8.2.1
SMR1	Muscovite Profile E10	253.51	0.01	-0.01	-0.003	-0.31	50.3	254.29	2342	65		8.2.1
SMR1	Muscovite Profile E11	257.66	0.01	-0.01	-0.004	-0.51	49.8	258.99	2366	72		8.2.1
SMR1	Muscovite Profile E12	259.89	0.01	-0.02	0.000	0.00	51.0	259.88	2371	65		8.2.1
SMR1	Muscovite Profile E13	263.27	0.01	-0.04	-0.008	-0.94	48.2	265.74	2400	66		8.2.1
SMR1	Muscovite Profile E14	259.06	0.01	-0.04	-0.012	-1.34	45.8	262.53	2384	66		8.2.1

Appendix 8.1 continued

Sample	Run	$^{40}Ar/^{39}Ar$	$^{38}Ar/^{39}Ar$	$^{37}Ar/^{39}Ar$	$^{36}Ar/^{39}Ar$	%Atmos -pheric	$^{39}Ar \times 10^{-13}$	$^{40}Ar^*/^{39}Ar$	Age (Ma)	± 1 σ	Excluded from mean	Profile Diagram
SMR1	Muscovite Profile E15	266.77	0.01	-0.05	-0.006	-0.63	47.0	268.46	2414	67		8.2.1
SMR1	Muscovite Profile F1	274.15	0.01	0.01	0.006	0.63	62.1	272.42	2433	68		
9-49	Biotite 50 µm square	242.81	0.01	0.01	0.005	0.65	76.0	241.24	2460	9		
9-49	Biotite 50 µm square	229.58	0.01	0.00	0.006	0.83	83.4	227.67	2383	9		
9-49	Biotite 50 µm square	215.16	0.02	0.01	0.003	0.47	65.6	214.15	2303	12		
9-49	Biotite 50 µm square	200.38	0.02	0.01	0.003	0.49	81.1	199.39	2211	10		
9-49	Biotite 50 µm square	178.92	0.00	0.00	0.004	0.73	20.3	177.61	2066	32		
9-49	Biotite 50 µm square	200.12	0.02	0.01	0.002	0.31	42.9	199.50	2212	14		
9-49	Biotite Profile A3	215.00	0.01	0.00	0.000	0.00	44.9	215.00	2308	13		8.2.2
9-49	Biotite Profile A4	222.38	0.01	0.01	0.000	0.00	44.5	222.38	2352	13		8.2.2
9-49	Biotite Profile A5	221.69	0.01	0.00	-0.003	-0.39	46.2	222.55	2353	14		8.2.2
9-49	Biotite Profile A6	229.89	0.01	0.01	0.002	0.25	46.8	229.32	2393	13		8.2.2
9-49	Biotite Profile B1	194.13	0.01	0.01	0.002	0.34	80.6	193.47	2173	9		8.2.2
9-49	Biotite Profile B2	223.50	0.00	0.01	0.006	0.85	62.8	221.59	2347	11		8.2.2
9-49	Biotite Profile B3	239.77	0.01	0.01	0.001	0.10	54.4	239.53	2451	11		8.2.2
9-49	Biotite Profile B4	225.56	0.01	0.01	0.003	0.45	65.0	224.53	2365	13		8.2.2
9-49	Biotite Profile B5	227.54	0.01	0.02	-0.005	-0.59	59.1	228.89	2390	11		8.2.2
9-49	Biotite Profile B6	237.33	0.01	0.01	0.002	0.20	55.9	236.85	2436	13		8.2.2
9-49	Muscovite 50 µm square	250.17	0.02	0.00	0.009	1.02	41.5	247.61	2495	14		
9-49	Muscovite 50 µm square	242.33	0.01	0.01	0.008	1.03	69.2	239.83	2452	10		
9-49	Muscovite 50 µm square	251.49	0.00	0.00	0.006	0.73	50.6	249.65	2506	12		
9-49	Muscovite Profile A1	240.34	0.01	-0.01	0.001	0.13	43.9	240.04	2454	13		8.2.2
9-49	Muscovite Profile A2	259.60	0.01	0.01	-0.004	-0.51	40.3	260.92	2567	15		8.2.2
9-49	Muscovite Profile A3	257.52	0.01	0.01	0.001	0.15	34.0	257.13	2547	14		8.2.2
9-49	Muscovite Profile A4	254.98	0.01	0.02	0.003	0.32	48.6	254.16	2531	12		8.2.2
9-49	Muscovite Profile A5	259.75	0.02	0.02	0.002	0.22	45.9	259.17	2557	13		8.2.2
9-51	Biotite 50 µm square	166.06	0.01	0.01	0.000	-0.07	70.7	166.18	1985	10		
9-51	Biotite 50 µm square	169.81	0.01	0.01	0.000	-0.06	77.3	169.91	2012	9		
9-51	Biotite 50 µm square	168.83	0.01	0.01	0.000	0.04	72.1	168.76	2004	10		
9-51	Biotite Profile A1	169.89	0.03	0.00	-0.006	-1.05	27.1	171.67	2024	19		8.2.3
9-51	Biotite Profile A2	164.75	0.01	0.04	-0.013	-2.28	16.3	168.51	2002	33		8.2.3
9-51	Biotite Profile A3	159.66	0.01	0.01	-0.010	-1.81	21.2	162.55	1959	26		8.2.3
9-51	Biotite Profile A4	169.15	0.00	0.00	-0.006	-1.06	26.7	170.95	2019	23		8.2.3
9-51	Biotite Profile B1	189.23	0.00	0.01	0.007	1.04	16.1	187.26	2132	30		8.2.3
9-51	Biotite Profile B2	189.21	0.01	0.04	-0.004	-0.59	31.2	190.32	2152	17		8.2.3
9-51	Biotite Profile B3	183.07	0.01	0.03	0.002	0.30	33.8	182.53	2100	19		8.2.3
9-51	Biotite Profile B4	186.62	0.02	-0.01	0.002	0.39	25.1	185.89	2122	21		8.2.3
9-51	Biotite Profile B5	173.98	0.01	-0.02	-0.009	-1.54	22.9	176.66	2059	23		8.2.3
9-51	Biotite Profile B6	163.28	0.01	0.03	-0.003	-0.58	22.7	164.22	1971	24		8.2.3
9-51	Muscovite 50 µm square	237.43	0.02	0.02	0.000	0.03	75.7	237.37	2439	9		
9-51	Muscovite 50 µm square	189.68	0.02	0.09	-0.021	-3.22	12.2	195.80	2188	38		
9-51	Muscovite 50 µm square	163.95	0.02	0.03	-0.003	-0.58	22.4	164.90	1976	25		

Appendix 8.1 continued

Sample	Run	$^{40}Ar/^{39}Ar$	$^{38}Ar/^{39}Ar$	$^{37}Ar/^{39}Ar$	$^{36}Ar/^{39}Ar$	%Atmos -pheric	$^{39}Ar \times 10^{-13}$	$^{40}Ar^*/^{39}Ar$	Age (Ma)	± 1 σ	Excluded from mean	Profile Diagram
9-51	Muscovite 50 µm square	175.48	0.01	0.00	-0.004	-0.71	17.2	176.73	2060	30		
9-51	Muscovite 50 µm square	252.84	0.01	0.01	0.005	0.57	40.7	251.41	2516	13		
9-51	Muscovite Profile A1	416.38	0.01	0.15	-0.014	-1.00	11.5	420.55	3255	24	*	8.2.3
9-51	Muscovite Profile A2	496.65	0.02	0.05	-0.004	-0.25	28.4	497.87	3512	13	*	8.2.3
9-51	Muscovite Profile A3	560.11	0.00	0.08	-0.012	-0.64	20.9	563.69	3706	14	*	8.2.3
9-46	Biotite 50 µm square	176.37	0.01	-0.02	0.003	0.44	60.2	171.27	2022	12		
9-46	Biotite 50 µm square	160.49	0.02	-0.03	0.001	0.10	45.4	156.45	1913	11		
9-46	Biotite 50 µm square	198.69	0.01	-0.01	0.004	0.65	46.4	192.49	2166	10		
9-46	Biotite 50 µm square	167.03	0.02	0.00	0.011	1.91	52.2	159.56	1936	10		
9-46	Biotite 50 µm square	185.91	0.01	0.01	0.006	0.92	58.9	179.59	2080	10		
9-46	Biotite 50 µm square	162.52	0.02	0.00	0.007	1.23	89.7	156.43	1913	8		
9-46	Biotite Profile A1	148.48	0.02	0.00	0.006	1.23	47.5	142.92	1808	12	*	8.2.4
9-46	Biotite Profile A2	156.53	0.02	0.03	0.006	1.19	39.4	150.74	1870	12	*	8.2.4
9-46	Biotite Profile A3	171.83	0.02	-0.01	0.020	3.43	30.5	161.32	1949	15		8.2.4
9-46	Biotite Profile B1	159.66	0.00	0.01	0.016	2.95	21.3	150.73	1869	22	*	8.2.4
9-46	Biotite Profile B2	177.23	0.01	0.00	0.008	1.26	44.7	170.53	2016	11	*	8.2.4
9-46	Biotite Profile B3	198.09	0.01	0.01	0.005	0.78	55.9	191.64	2161	11		8.2.4
9-46	Biotite Profile B4	208.99	0.01	0.00	0.002	0.31	51.3	203.24	2235	10		8.2.4
9-46	Biotite Profile B5	197.06	0.01	0.00	0.005	0.80	55.3	190.61	2154	10		8.2.4
9-46	Biotite Profile B6	202.99	0.02	0.00	0.001	0.18	55.8	197.70	2200	10		8.2.4
9-46	Biotite Profile C1	134.83	0.01	0.04	-0.004	-0.88	27.5	132.87	1726	17	*	8.2.4
9-46	Biotite Profile C2	145.58	0.01	0.04	-0.004	-0.82	27.5	143.35	1812	18	*	8.2.4
9-46	Biotite Profile C3	166.04	0.01	0.03	-0.002	-0.40	29.5	162.75	1960	17		8.2.4
9-46	Biotite Profile C4	163.71	0.00	-0.01	-0.001	-0.13	28.4	160.00	1940	18		8.2.4
9-46	Biotite Profile C5	171.55	0.01	0.01	0.013	2.16	34.2	163.42	1965	13		8.2.4
9-46	Biotite Profile C6	170.89	0.01	0.03	0.006	0.96	36.8	165.00	1976	17		8.2.4
8-152	Biotite 50 µm square	262.31	0.01	0.00	0.006	0.67	84.2	260.54	2565	13		
8-152	Biotite 50 µm square	267.71	0.01	0.00	0.009	1.04	67.8	264.93	2587	11		
8-152	Biotite 50 µm square	260.63	0.01	0.01	0.009	0.99	52.3	258.04	2551	16		
8-152	Biotite 50 µm square	269.08	0.02	-0.02	0.001	0.11	51.4	268.78	2607	13		
8-152	Biotite 50 µm square	256.07	0.01	0.00	0.002	0.24	67.5	255.44	2538	11		
8-152	Biotite Profile A1	229.88	0.01	0.04	0.001	0.10	10.8	229.66	2395	46	*	8.2.5
8-152	Biotite Profile A2	259.78	0.01	0.11	0.014	1.59	13.5	255.66	2539	35	*	8.2.5
8-152	Biotite Profile A3	262.69	0.01	0.02	0.006	0.67	23.9	260.92	2567	20		8.2.5
8-152	Biotite Profile A4	277.69	0.02	0.04	0.000	0.03	29.4	277.61	2652	17		8.2.5
8-152	Biotite Profile A5	273.22	0.01	0.04	0.004	0.43	36.4	272.05	2624	15		8.2.5
8-152	Biotite Profile B1	241.08	0.01	0.00	0.027	3.36	16.7	232.98	2414	30	*	8.2.5
8-152	Biotite Profile B2	238.74	0.02	0.01	0.026	3.20	19.5	231.10	2403	27	*	8.2.5
8-152	Biotite Profile B3	241.88	0.01	0.01	0.009	1.13	15.5	239.15	2449	37		8.2.5
8-152	Biotite Profile B4	236.02	0.01	0.02	0.008	1.00	23.6	233.66	2418	25		8.2.5
8-152	Biotite Profile C1	244.95	0.03	-0.02	0.062	7.48	12.5	226.62	2377	41	*	8.2.5
8-152	Biotite Profile C2	240.10	0.01	0.07	0.013	1.55	25.7	236.37	2433	24	*	8.2.5

Appendix 8.1 continued

Sample	Run	$^{40}Ar/^{39}Ar$	$^{38}Ar/^{39}Ar$	$^{37}Ar/^{39}Ar$	$^{36}Ar/^{39}Ar$	%Atmos -pheric	$^{39}Ar \times 10^{-13}$	$^{40}Ar^*/^{39}Ar$	Age (Ma)	± 1 σ	Excluded from mean	Profile Diagram
8-152	Biotite Profile C3	258.53	0.00	-0.01	0.014	1.60	23.0	254.39	2532	22		8.2.5
8-152	Biotite Profile C4	264.01	0.01	0.03	0.008	0.86	36.4	261.75	2571	15		8.2.5
8-114	Biotite 50 µm square	213.88	0.02	0.00	0.004	0.62	53	212.56	2293	9		
8-114	Biotite 50 µm square	229.85	0.02	0.00	0.030	3.88	59	220.94	2344	9		
8-114	Biotite 50 µm square	222.50	0.01	0.00	0.008	1.01	61	220.25	2339	9		
8-114	Biotite 50 µm square	213.28	0.01	0.00	0.001	0.14	56	212.97	2296	9		
8-114	Biotite 50 µm square	215.19	0.01	0.00	0.000	-0.06	77	215.31	2310	9		
8-114	Biotite Profile A1	213.48	0.01	-0.02	0.004	0.60	24	212.20	2291	15		8.2.6
8-114	Biotite Profile A2	221.76	0.02	0.03	0.022	2.98	19	215.16	2309	18		8.2.6
8-114	Biotite Profile A3	203.58	0.00	-0.02	0.021	3.01	22	197.45	2198	16		8.2.6
8-114	Biotite Profile B1	221.63	0.04	0.03	0.024	3.24	21	214.44	2305	17		8.2.6
8-114	Biotite Profile B2	213.75	0.01	0.01	0.022	3.01	27	207.31	2261	14		8.2.6
8-114	Biotite Profile B3	236.77	0.01	0.02	0.007	0.92	26	234.59	2423	14		8.2.6
8-114	Biotite Profile B4	218.23	0.01	0.00	0.017	2.25	39	213.32	2298	12		8.2.6
8-114	Biotite Profile C1	214.37	0.01	0.00	-0.008	-1.14	20	216.81	2319	18		8.2.6
8-114	Biotite Profile C2	214.37	0.01	-0.01	0.008	1.05	31	212.11	2290	15		8.2.6
8-114	Biotite Profile C3	210.65	0.02	-0.01	0.019	2.67	29	205.02	2246	13		8.2.6
8-114	Biotite Profile C4	205.10	0.01	-0.02	0.001	0.20	43	204.70	2244	10		8.2.6
8-104	Muscovite 50 µm square	130.23	0.01	0.02	-0.001	-0.34	50	130.67	1707	12		
8-104	Muscovite 50 µm square	137.74	0.01	0.01	-0.002	-0.41	62	138.31	1771	8		
8-104	Muscovite 50 µm square	194.01	0.01	0.02	0.004	0.66	66	192.74	2168	10		
8-104	Muscovite 50 µm square	130.40	0.01	0.01	-0.002	-0.41	66	130.93	1710	8		
8-104	Muscovite Profile A1	116.13	0.01	0.01	0.002	0.45	34	115.61	1576	14	*	8.2.7
8-104	Muscovite Profile A2	129.18	0.01	0.04	0.006	1.41	39	127.36	1679	14	*	8.2.7
8-104	Muscovite Profile A3	121.15	0.02	0.02	-0.004	-0.87	46	122.19	1634	12		8.2.7
8-104	Muscovite Profile A4	122.84	0.01	0.02	-0.003	-0.79	50	123.82	1649	11		8.2.7
8-104	Muscovite Profile A5	129.38	0.01	0.01	0.002	0.50	48	128.74	1691	9		8.2.7
8-104	Muscovite Profile A6	130.49	0.01	0.02	-0.003	-0.60	45	131.27	1713	10		8.2.7
8-104	Muscovite Profile A7	130.04	0.02	0.02	-0.002	-0.34	49	130.49	1706	11		8.2.7
8-104	Muscovite Profile A8	130.38	0.01	0.01	0.002	0.51	47	129.71	1699	10		8.2.7
8-104	Muscovite Profile B1	124.70	0.01	0.02	-0.007	-1.59	31	126.69	1674	14	*	8.2.7
8-104	Muscovite Profile B2	133.56	0.01	-0.01	0.003	0.62	37	132.73	1725	11	*	8.2.7
8-104	Muscovite Profile B3	125.95	0.01	0.00	0.004	0.86	41	124.88	1658	11		8.2.7
8-104	Muscovite Profile B4	133.37	0.01	0.01	-0.004	-0.97	48	134.66	1741	9		8.2.7
8-104	Muscovite Profile B5	127.88	0.01	0.00	0.007	1.66	52	125.75	1665	10		8.2.7
8-104	Muscovite Profile C1	155.52	0.02	0.01	0.000	0.09	32	155.38	1905	14	*	8.2.7
8-104	Muscovite Profile C2	143.86	0.02	0.03	0.000	0.07	44	143.76	1815	10	*	8.2.7
8-104	Muscovite Profile C3	140.50	0.01	0.00	0.001	0.26	48	140.13	1786	9		8.2.7
8-104	Muscovite Profile D1	137.38	0.01	0.00	0.003	0.60	53	136.55	1757	9	*	8.2.7
8-104	Muscovite Profile D2	161.65	0.01	0.01	0.001	0.17	63	161.37	1950	9	*	8.2.7
8-104	Muscovite Profile D3	168.37	0.01	0.01	0.002	0.28	65	167.89	1997	8		8.2.7
8-104	Muscovite Profile D4	163.71	0.01	0.02	0.001	0.26	73	163.28	1964	8		8.2.7

Appendix 8.1 continued

Sample	Run	$^{40}Ar/^{39}Ar$	$^{38}Ar/^{39}Ar$	$^{37}Ar/^{39}Ar$	$^{36}Ar/^{39}Ar$	%Atmos -pheric	$^{39}Ar \times 10^{-13}$	$^{40}Ar^*/^{39}Ar$	Age (Ma)	± 1 σ	Excluded from mean	Profile Diagram
8-104	Muscovite Profile D5	168.77	0.01	0.00	0.000	0.04	68	168.70	2003	9		8.2.7
8-104	Muscovite Profile D6	161.29	0.02	0.01	0.001	0.18	61	160.99	1947	9		8.2.7
8-104	Muscovite Profile E1	176.47	0.01	0.02	-0.009	-1.53	23	179.18	2077	16	*	
8-104	Muscovite Profile F1	141.84	0.02	0.02	-0.003	-0.72	35	142.87	1808	12	*	
8-104	Muscovite Profile F2	148.24	0.02	-0.01	-0.004	-0.73	45	149.33	1859	9	*	
8-104	Muscovite Profile F3	163.22	0.01	0.01	-0.005	-0.94	49	164.75	1975	9		
8-104	Muscovite Profile F4	161.65	0.02	0.01	-0.005	-0.88	53	163.07	1962	9		
7-68	Biotite 50 µm square	171.96	0.02	0.01	0.006	0.96	70	170.30	2015	12		
7-68	Biotite 50 µm square	182.80	0.01	0.02	-0.001	-0.10	76	182.99	2103	10		
7-68	Biotite 50 µm square	172.92	0.01	0.00	0.002	0.42	70	172.20	2028	11		
7-68	Biotite 50 µm square	164.14	0.01	0.01	0.008	1.42	55	161.80	1953	14		
7-68	Biotite 50 µm square	165.47	0.01	0.01	0.003	0.50	77	164.65	1974	12		
7-68	Muscovite 50 µm square	166.89	0.01	0.01	-0.001	-0.18	49	167.18	1992	13		
7-68	Muscovite 50 µm square	143.95	0.03	0.00	-0.003	-0.61	17	144.82	1823	35		
7-68	Muscovite 50 µm square	199.32	0.01	0.02	0.002	0.28	68	198.76	2207	10		
7-68	Muscovite 50 µm square	125.90	0.04	0.09	0.047	11.15	7	111.86	1541	89		
7-68	Muscovite 50 µm square	173.42	0.01	0.01	0.001	0.20	72	173.08	2034	10		
7-68	Composite 50 µm square	159.55	0.01	0.05	0.003	0.47	15	158.80	1931	38		
7-68	Composite 50 µm square	149.20	0.03	0.01	0.002	0.49	16	148.47	1852	36		
7-68	Composite 50 µm square	152.81	0.02	-0.01	0.004	0.74	22	151.69	1877	26		
7-68	Composite 50 µm square	151.14	0.01	0.01	0.004	0.72	22	150.05	1864	26		
7-68	Composite 50 µm square	163.69	0.02	0.01	0.013	2.35	30	159.85	1939	21		
8-15A	Composite 50 µm square	125.47	0.01	-0.01	0.001	0.29	65	125.10	1660	7		
8-15A	Composite 50 µm square	122.31	0.01	-0.01	0.002	0.58	52	121.60	1629	10		
8-15A	Composite 50 µm square	121.78	0.01	0.00	0.003	0.62	67	121.03	1624	10		
8-15A	Composite 50 µm square	124.13	0.00	0.00	-0.003	-0.69	34	124.99	1659	11		
8-15A	Composite 50 µm square	126.63	0.01	-0.01	0.005	1.25	74	125.04	1659	8		
8-15A	Composite 50 µm square	123.35	0.00	0.00	0.002	0.43	71	122.82	1640	8		
8-15A	Composite 50 µm square	112.23	0.01	0.00	0.005	1.43	65	110.63	1586	14	*	
8-15A	Composite 50 µm square	128.64	0.01	0.00	0.001	0.16	51	128.43	1688	8		
8-14A	Composite 50 µm square	129.67	0.02	0.01	0.006	1.40	75	127.85	1683	10		
8-14A	Composite 50 µm square	123.32	0.01	0.00	0.007	1.75	82	121.16	1625	10		
8-14A	Composite 50 µm square	124.17	0.01	0.01	0.005	1.28	86	122.59	1638	8		
8-14A	Composite 50 µm square	118.35	0.01	0.00	-0.002	-0.44	70	118.88	1605	12		
8-14A	Composite 50 µm square	126.99	0.01	0.01	0.003	0.74	74	126.05	1668	9		
8-14A	Composite 50 µm square	146.89	0.07	0.11	0.068	13.64	3	126.85	1675	157		
8-14A	Composite 50 µm square	128.67	0.01	0.00	0.002	0.44	75	128.10	1686	9		
8-14A	Composite 50 µm square	128.45	0.01	-0.01	0.001	0.31	74	128.05	1685	9		
8-14A	Composite 50 µm square	126.12	0.01	0.00	0.002	0.37	64	125.66	1665	13		
8-14A	Composite 50 µm square	125.98	0.01	0.00	0.002	0.42	82	125.46	1663	9		

Appendix 8.2: Closure Profiles for the South Madison Range

Appendix 8.2.1: Closure Profiles for SMR1

SMR1 Profile A

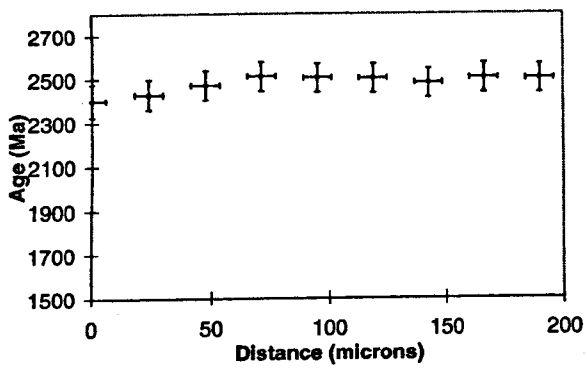

SMR1 Profile B

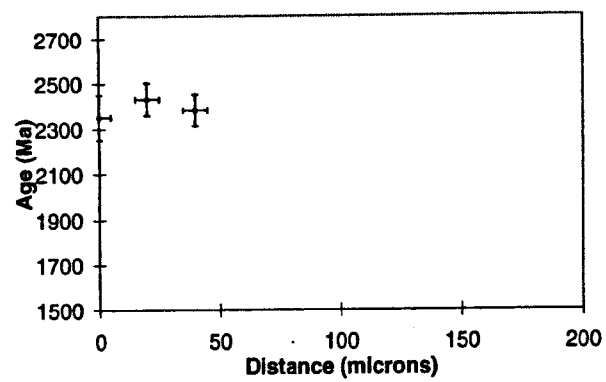

SMR1 Profile C

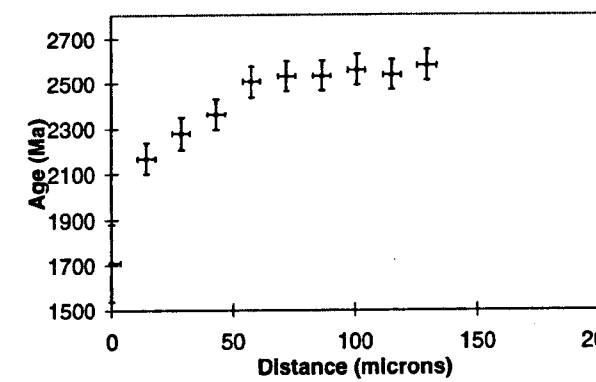

SMR1 Profile D

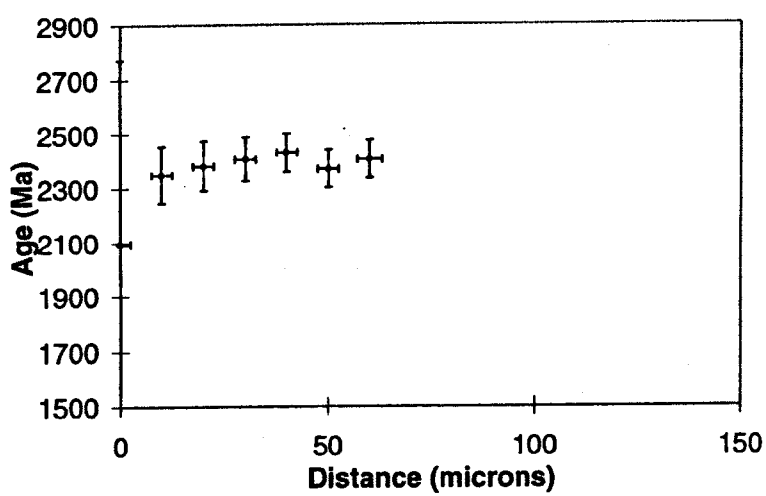

SMR1 Profile E

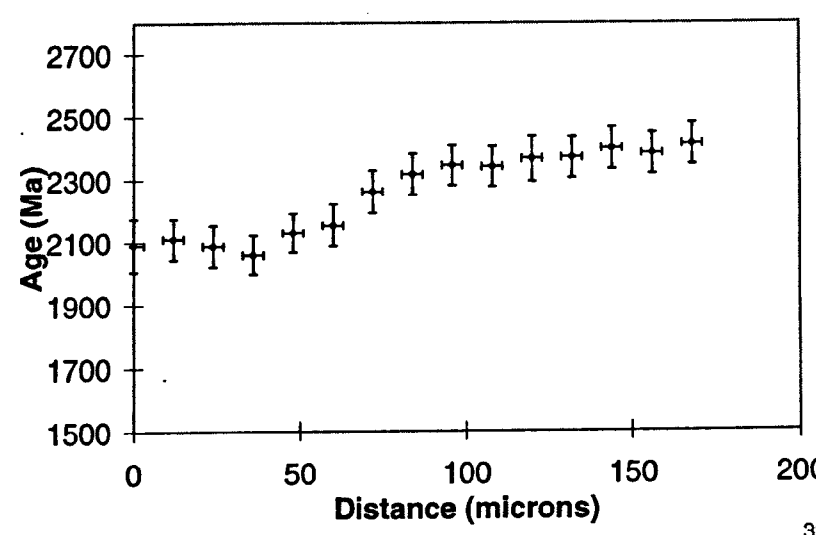

Appendix 8.2.2: Closure Profiles for 9-49

9-49 Biotite Profile A

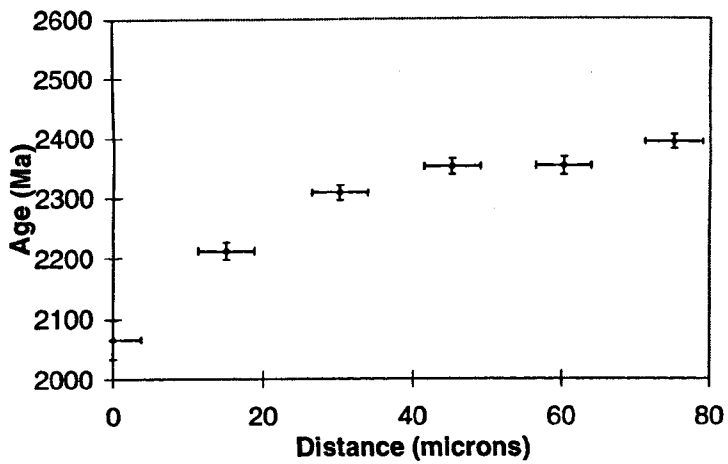

9-49 Biotite Profile B

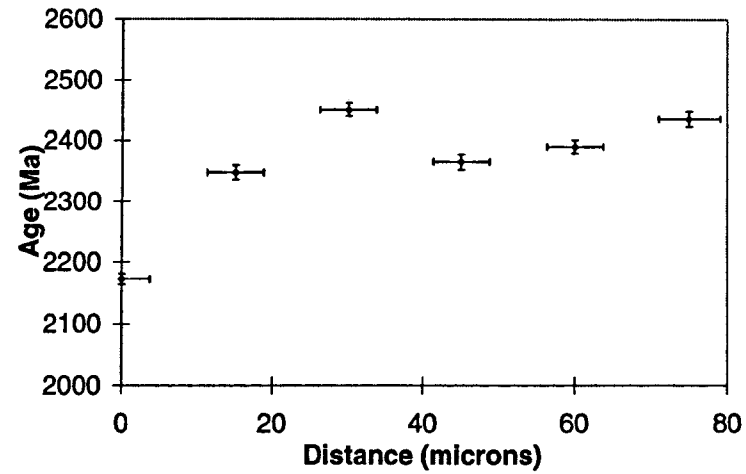

9-49 Muscovite Profile A

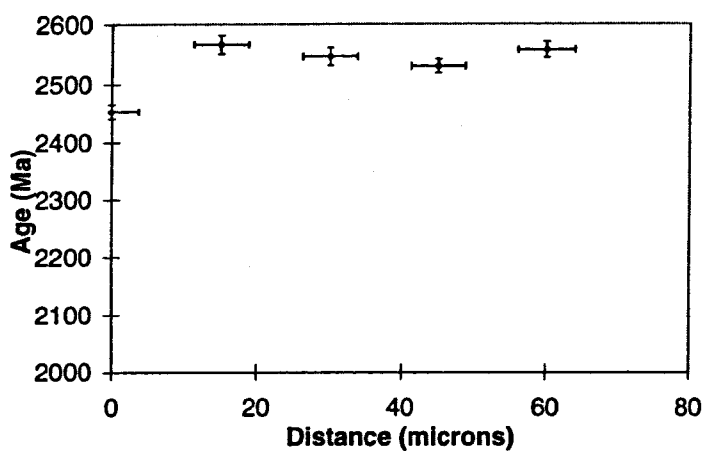

Appendix 8.2.3: Closure Profiles for 9-51

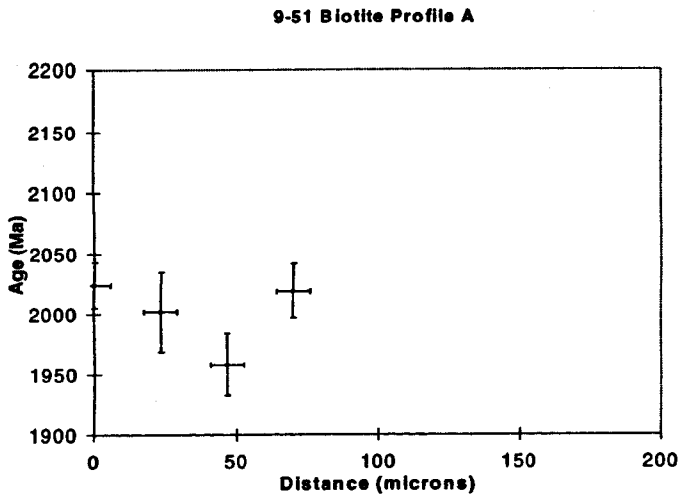

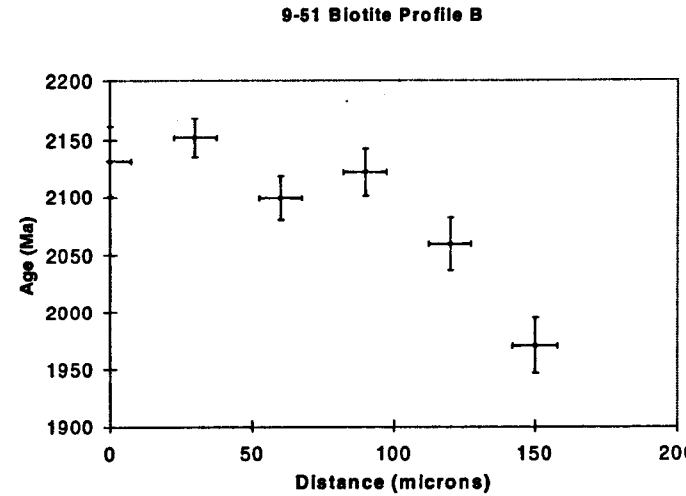

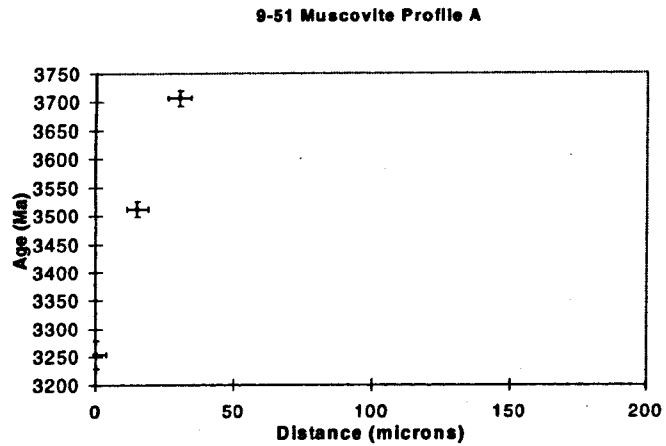

Appendix 8.2.4: Closure Profiles for 9-46

9-46 Biotite Profile A

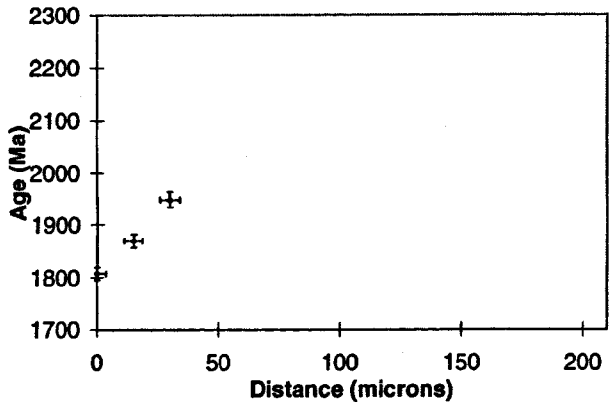

9-46 Biotite Profile B

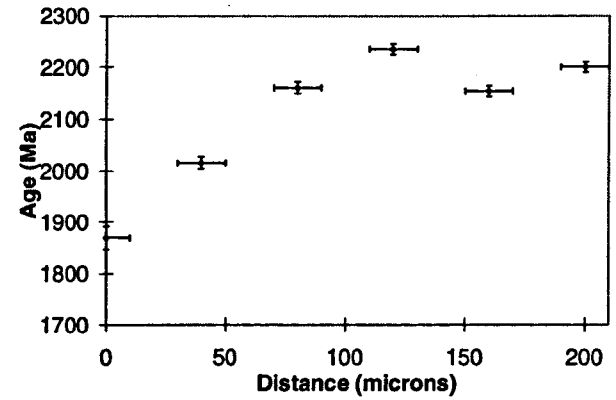

9-46 Biotite Profile C

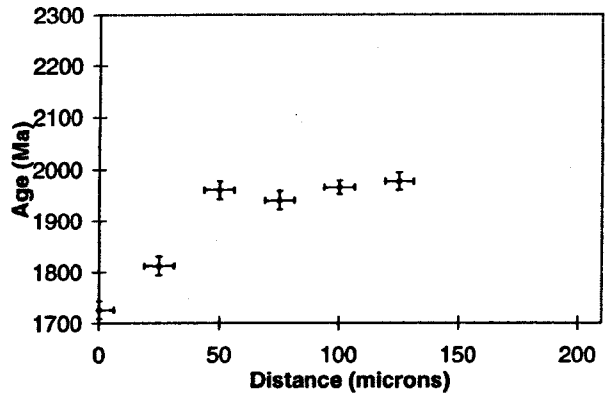

Appendix 8.2.5: Closure Profiles for 8-152

8-152 Biotite Profile A

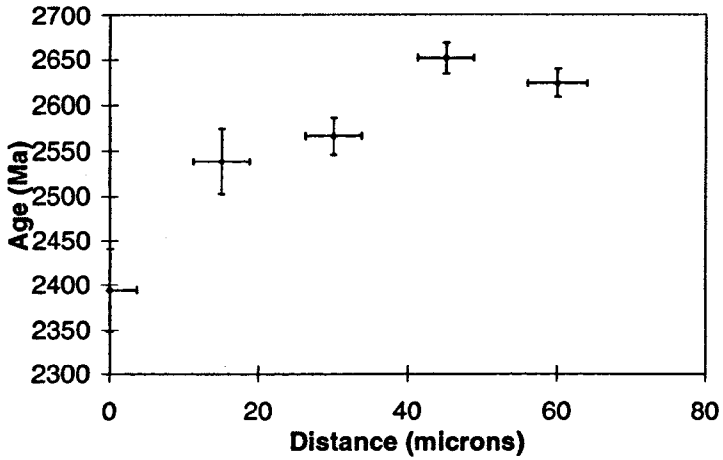

8-152 Biotite Profile A

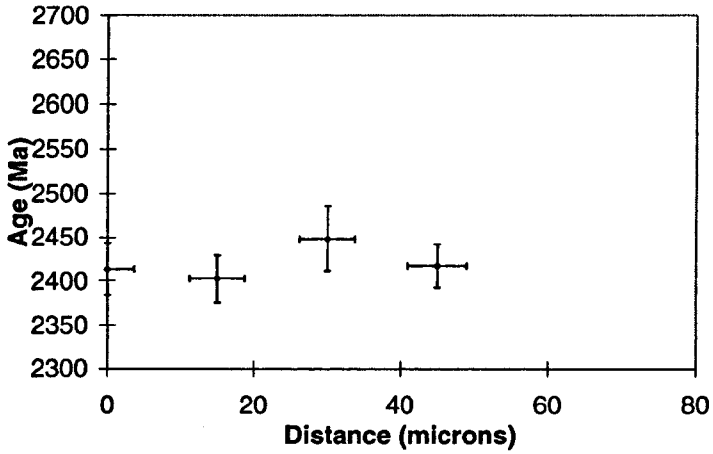

8-152 Biotite Profile C

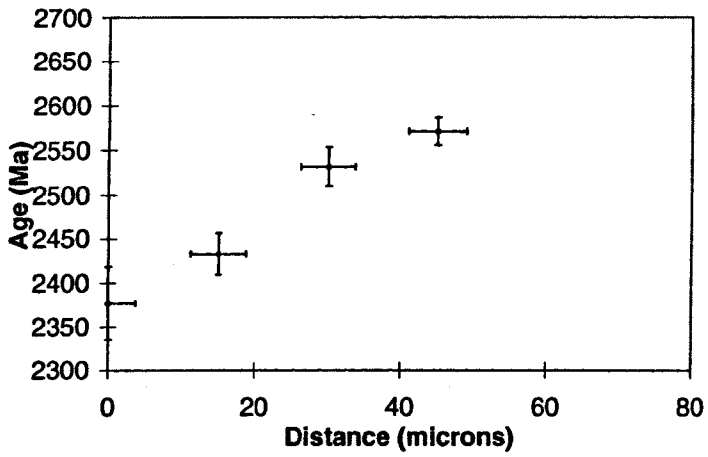

Appendix 8.2.6: Closure Profiles for 8-114

8-114 Biotite Profile A

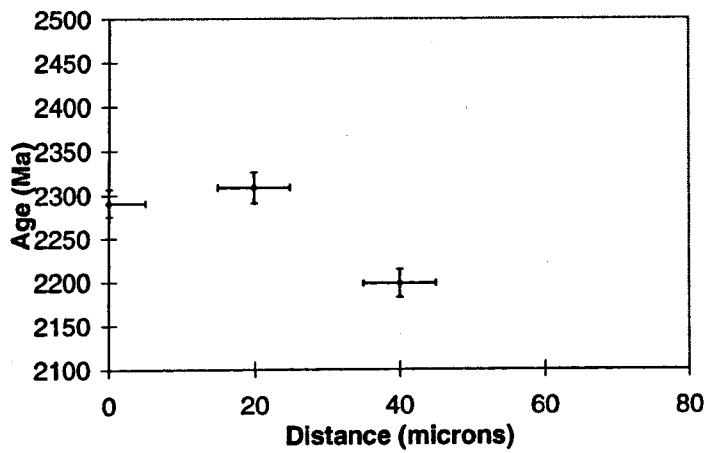

8-114 Biotite Profile B

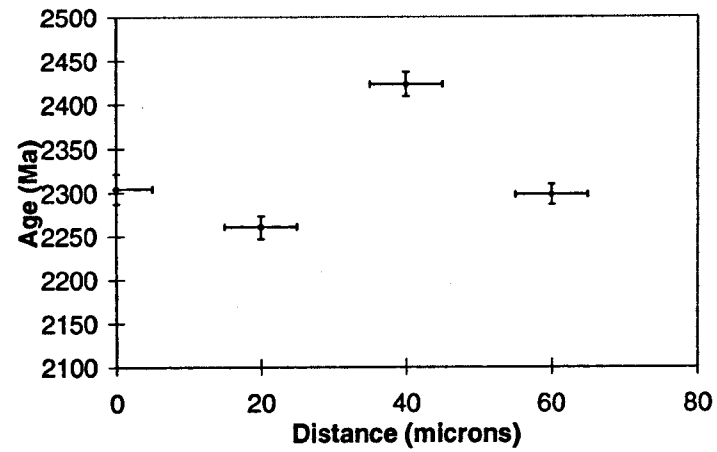

8-114 Biotite Profile C

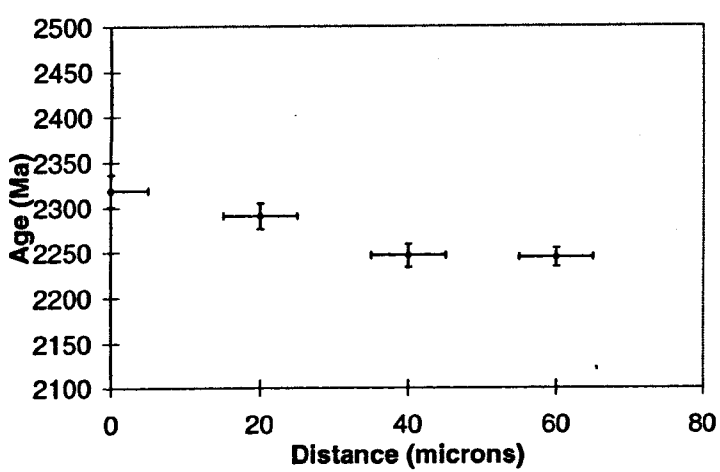

Appendix 8.2.7: Closure Profiles for 8-104

8-104 Muscovite Profile A

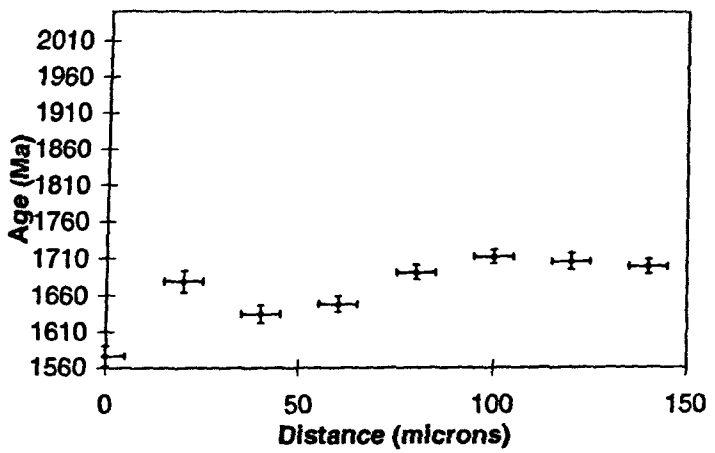

8-104 Muscovite Profile B

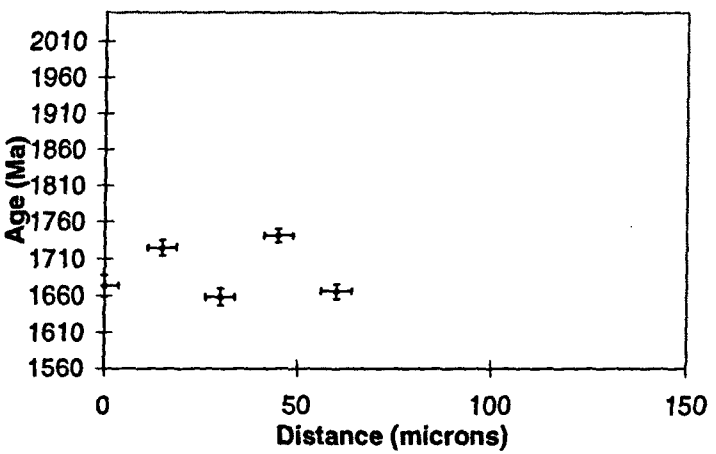

8-104 Muscovite Profile C

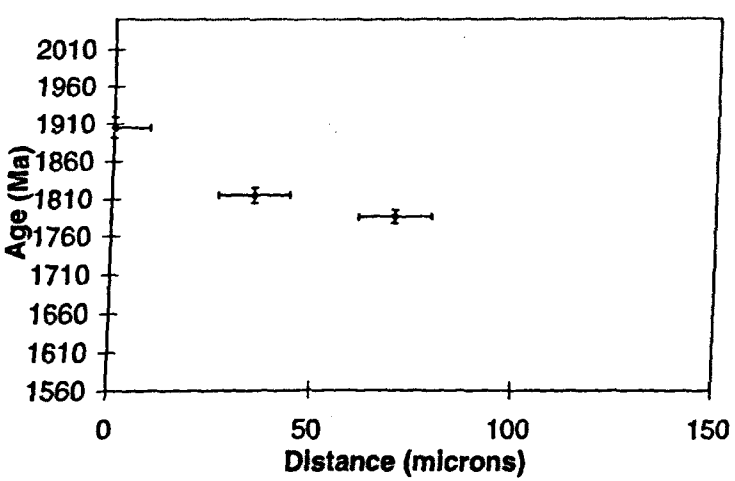

8-104 Muscovite Profile D